CRANFIELD UNIVERSITY

S M J HANSON

POWDER CO-INJECTION MOULDING

SCHOOL OF INDUSTRIAL AND MANUFACTURING SCIENCE

PhD THESIS

CRANFIELD UNIVERSITY

SCHOOL 0F INDUSTRIAL AND MANUFACTURING SCIENCE

PhD THESIS

ACADEMIC YEAR 1999-2000

S M J HANSON

Powder co-injection moulding

Supervisors: Prof D J Stephenson and Dr J R Alcock

September 2000

This thesis is submitted in partial fulfilment of the requirements
for the degree of Doctor of Philosophy

Abstract

A novel powder processing technique has been developed by combining conventional powder injection moulding with polymer co-injection moulding, to permit the in-situ surface engineering of metal or ceramic components as an integral step within the processing cycle.

The new technique has been used to produce surface engineered iron based components with either corrosion resistant or wear resistant surfaces, and to produce alumina based components with toughened surfaces.

The most critical factor for the feasibility of surface engineered components is that the sintering profiles of the skin and core materials must be well matched or differential shrinkage or delamination will result.

A particular requirement of surface engineering is the ability to control the surface engineered skin profile. Polymer injection moulding modelling software was applied to predict the surface engineered skin profiles of the surface engineered metal/ceramic components.

Successful skin profile prediction is dependent on the characterisation of the feedstock materials being injection moulded. Several feedstocks have been characterised for their material properties and first pass models developed to predict the feedstock material properties as a function of their individual material properties and mass or volume ratios.

It has been demonstrated that the design of the feedstock composition and injection moulding process conditions can be optimised by the use of computer-based injection moulding modelling software to achieve the desired surface engineered skin profile.

A methodology has been developed that outlines all the stages necessary for successful powder co-injection moulding.

Appendices

List of figures

Abbreviations

PIM	Powder injection moulding
MIM	Metal injection moulding
CIM	Ceramic injection moulding
PCM	Powder co-injection moulding
MCM	Metal co-injection moulding
CCM	Ceramic co-injection moulding
SHC	Specific heat capacity
PVT	Pressure - volume - temperature
LMWPP	Low molecular weight polypropylene

1. Introduction

As we enter a new century, more and more technological challenges face the materials scientist. The demands placed on metallic and ceramic materials are continually increasing, leading to increasing problems in the processing of metals and ceramics. The importance of net-shaped production techniques has increased[1]. Die pressing, injection moulding, tape casting, slip casting are all examples of well established net shape processing routes for the production of precision components to near net shape profiles. A common theme in all of these manufacturing processes is the use of metal or ceramic powders with diameters in the order of microns.

Low cost intricate parts are routinely formed by polymer injection moulding. Advances in materials processing have enabled the materials processor to produce components of increasing geometrical complexity with higher production yields, reductions in wastage, scrap materials, machining time and labour. This has led to reductions in the cost of materials and labour hours.

1.1 The origins of injection moulding

The very earliest work on injection moulding can be traced to the Hyatt brothers[2] who took out a patent in 1872, and subsequently used the injection moulding technique on pyroxiline. The first recorded injection moulding of ceramic materials dates back to 1937[3]. More recently, co-injection moulding was developed by Oxley and Sandiford[4] at ICI as an extension to injection moulding.

1.2 The origins of powder injection moulding

From 1977 onwards[5], the injection moulding technique has been applied to the manufacture of ceramic or metal parts by using a highly laden powder filled polymer instead of a pure polymer, which was made possible by improved injection moulding machine control systems. Powder injection moulding has been used successfully to produce the following components:

1. Bone staplers, computer disk drive parts[6]
2. Watch cases[7]
3. Orthodontic braces[8]
4. Percussive mining tips[9]
5. Jet engine actuator arms[10]
6. Turbine blades[11]
7. Radial rotors, turbocharger rotors, engine parts, airfoils[12]
8. Surgical tweezers, gas manifolds, gun and missile parts, fuel nozzles, drill bits[13]

Thus, powder injection moulding (PIM) was born and encompasses metal injection moulding (MIM) and ceramic injection moulding (CIM).

The further development of PIM was driven by the projected reductions that would arise in post-production machining operations and savings in material costs[9]. PIM has become a mature technique for the fabrication of small and difficult to machine parts with complex shapes. In recent years PIM[13] has been taken up in the medical devices, automotive, marine and aerospace industries, and the PIM[14] industry has forecast an average growth rate of between 20% to 40% over the next few years. Powder injection moulding permits the production of cost effective parts with complex geometries. PIM is most cost effective for high production quantities of intricately shaped metal or ceramic parts, illustrated by figure 1.1, showing alternative competing technologies. Figure 1.2 identifies the optimal application of PIM.

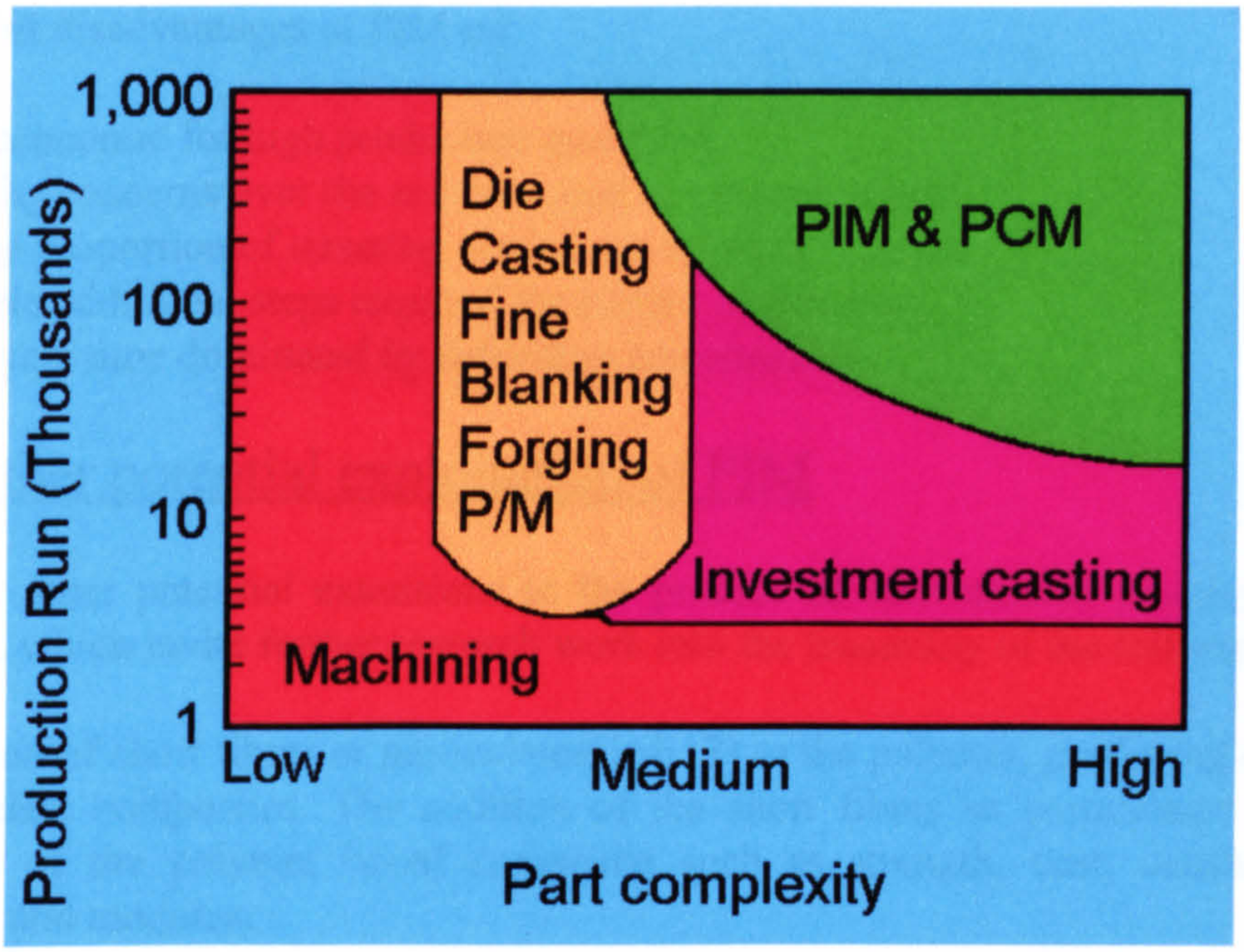

Figure 1.1 Competing metal component manufacturing technologies.[15]

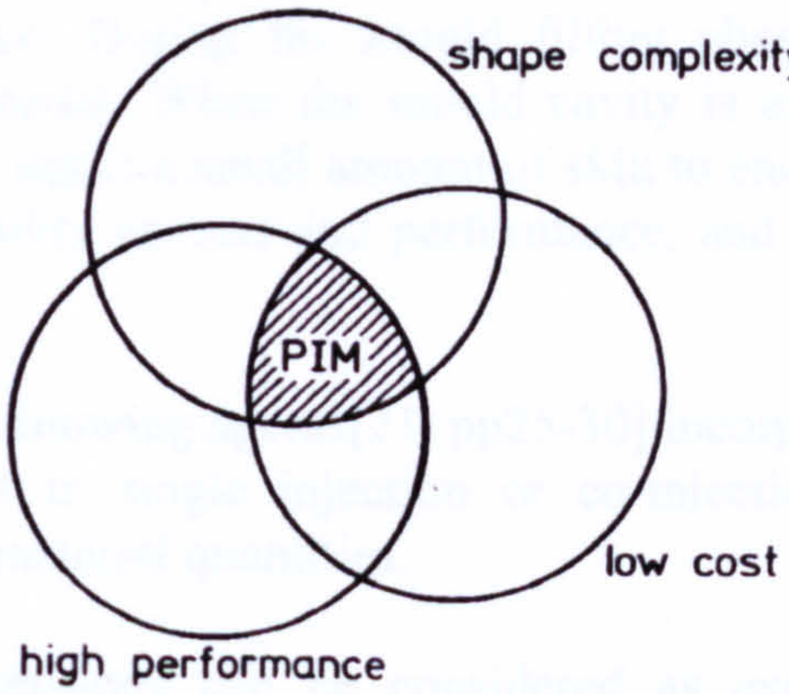

Figure 1.2 Venn diagram identifying the optimal application of PIM[5, pp7]

As can be seen, PIM is an attractive technology for high complexity and high production quantities. The advantages offered by conventional injection moulding are:

(a) High production rates
(b) Recycling of waste material
(c) Near net shape processing
(d) Economic manufacturing route
(e) High level of shape complexity achievable
(f) Minimal machining required
(g) Minimal labour required

The current disadvantages of PIM are:

(a) Only economic for high production quantities
(b) Toxicity concerns over the solvents used in binder removal
(c) A large proportion of sintering carried out in batch furnaces
(d) Possible additional steps required for surface engineering
(e) PIM cycle time dominated by debinding and sintering

1.3 Further potential exploitation of PIM

There are other potential extensions to the process of conventional powder injection moulding, which invite further research work into the feasibility of the following:

(a) Addition of short fibres or particulates[16][17] to the polymer, producing short fibre or particulate composites. The addition of the short fibres or particulates alters the properties of the polymer based composite such as strength, cost, density, impact resistance and modulus.

(b) Co-injection moulding[18][19][20], which is the sequential injection moulding of two different polymers. The sequential injection moulding process starts with the injection of skin material. During the mould filling phase, a changeover valve is switched to the core material. When the mould cavity is almost full, the changeover valve is switched back to inject a small amount of skin to encapsulate the core material. This offers greater flexibility on cost and performance, and enables recycling of scrap material for the core.

(c) Physical and chemical blowing agents[21, pp25-30] incorporated within the injection moulding process, either in single injection or co-injection moulding. This offers reductions in weight and material quantities.

The above potential extensions can be considered as examples of in-situ surface engineering, thus removing the need for extra steps necessary for surface engineering of components.

At Cranfield, powder co-injection moulding (PCM)[14][22] has been developed. PCM can be considered essentially the same process as PIM, but with the ability to carry out

in-situ surface engineering. The development of PCM provides an incentive for further commercial exploitation of powder processing, leading to cost and time savings.

1.4 Surface engineered profile prediction

In any surface engineering process, the surface engineered thickness and the skin thickness distribution around a PIM component are of particular importance. Hence there is a requirement to be able to predict and control the surface coating profile. There is considerable potential for further development of PIM for the mass production of intricately shaped components

It is only in recent years[23][24] that computers and commercial software have been employed routinely in the manufacturing industry to model the injection moulding cycle of polymers. This permits the optimisation of desired materials performance and predicts phenomena such as warpage or shrinkage in the mouldings ejected from the moulding machine. This extends the scope of analysis beyond that which is readily obtainable through normal experimental methods. The mould cavity geometry and process conditions can be optimised, avoiding the trial and error approach methods previously used.

2 Project objectives

The main objectives of the present work fall into two categories:

2.1 Powder co-injection moulding

To demonstrate the feasibility of PCM by developing three model PCM systems using well-matched skin and core feedstocks, avoiding delamination and differential densification. The model PCM systems should have one of the following desirable properties each.

(a) Corrosion resistance. This will be achieved using a stainless steel skin and an iron core.
(b) Wear resistance. This will be achieved by using an iron-alumina cermet skin and an iron core.
(c) Improved toughness. This will be achieved using a zirconia and alumina ceramic composite skin and an alumina core.

2.2 Computer modelling

(a) To demonstrate that computer modelling software can be used as a tool to predict the skin profile for polymer co-injection moulding.

(b) To investigate the effect of material properties and processing parameters on the polymer skin profile such as rheology, thermal properties and mould filling time.

(c) To determine the PCM feedstock material properties such as rheology, thermal properties and specific volume.

(d) To develop methods for predicting the feedstock material properties as a function of their individual material properties and volume or mass ratios.

(e) To demonstrate that any models that are used to model polymer material properties can also be used to model feedstock material properties.

(f) To run C-Mold modelling software using the material properties data of the PCM feedstocks and run skin profile predictions for the three model PCM systems. The predicted skin profiles can then be compared with the actual skin profiles achieved.

(g) To demonstrate the application of co-injection moulding modelling software to PCM.

(h) To investigate the effects of various material properties of the PCM feedstocks on the skin profile. This will provide important data for the feedstock design process.

3. Literature survey: Powder co-injection moulding

As stated previously, PCM allows the in-situ engineering of the skin and core to permit the properties of the skin and/or core to be modified. PCM is the combination of PIM and co-injection moulding, with the optional addition of particulates for the skin and/or core materials. This permits the achievement of optimal combinations of cost and performance. By analogy with PIM, PCM encompasses metal co-injection moulding (MCM) and ceramic co-injection moulding (CCM).

3.1 The powder injection moulding process cycle

The PIM process is outlined below.

(a) Preparation of a feedstock by compounding together very fine ceramic or metal powders with a binder comprising waxes, polymers, lubricants, surfactants and additives. The binder imparts fluidity and plasticity to the powders, thus retaining the thermoplastic behaviour of the binder materials used. The resulting feedstock is then granulated.

(b) The feedstock can be treated in the same way as a typical thermoplastic polymer, by heating to temperatures of 165°C to 220°C. An injection moulding machine is used to fill a mould cavity with the feedstock under pressure. The molten feedstock is allowed to cool, solidify and become a "green" moulding. Any green mouldings that are scrapped due to moulding defects are easily recycled, leading to savings in expensive materials. The binder imparts sufficient strength to permit handling in further processing stages.

(c) After injection moulding, the binder components are removed by a process of debinding. The green moulding becomes a highly porous "brown" moulding after debinding, which has sufficient inter-particle adhesion to support the network of powder particles.

(d) The brown mouldings are sintered to an elevated temperature. The brown parts typically sinter to more than 95% theoretical density. The brown parts shrink during sintering, but the net shape is retained throughout.

(e) Further treatment of the sintered parts, such as shot peening or hot isostatic pressing.

Figure 3.1 shows schematically the PIM and PCM process, as the principles behind the two processing methods are largely similar.

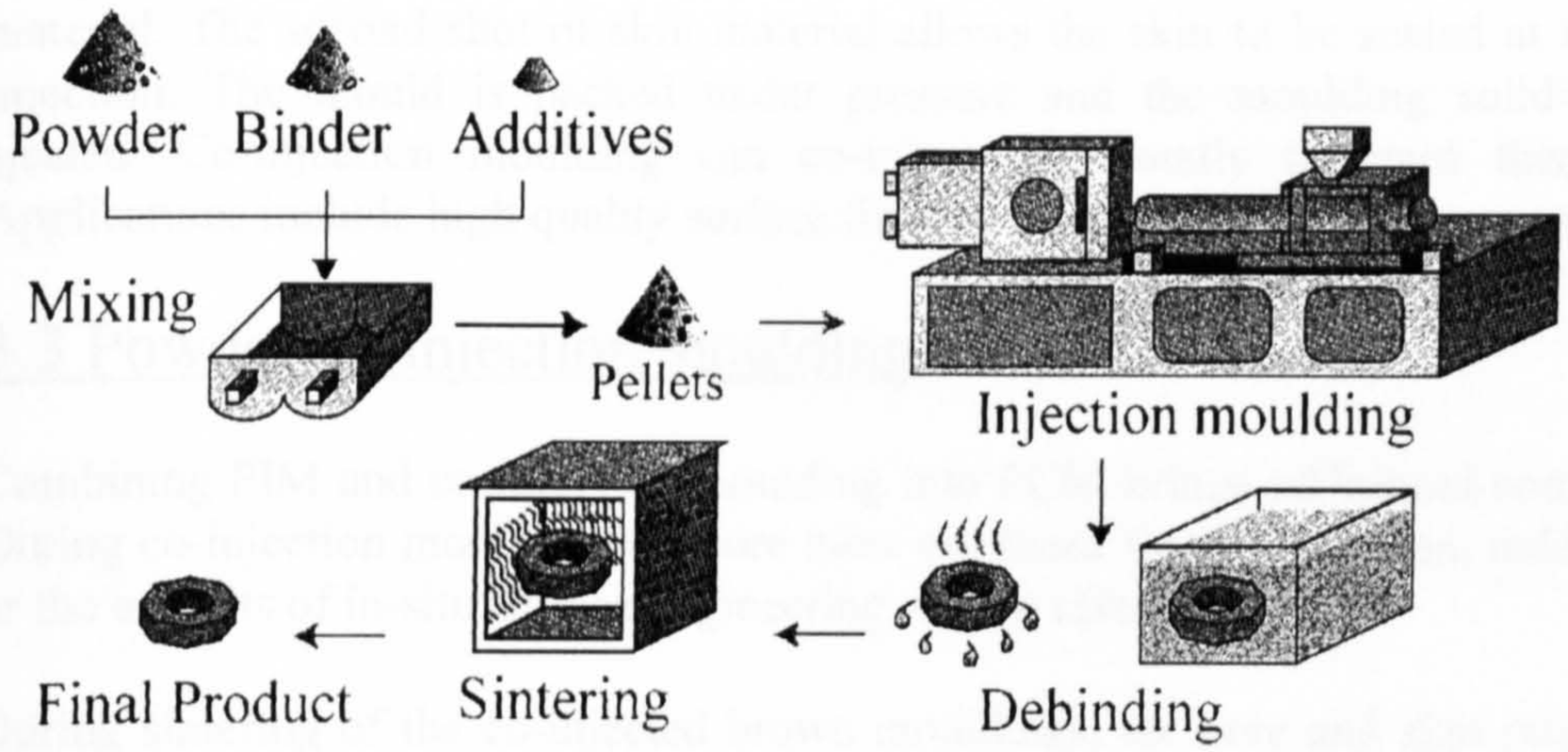

Figure 3.1 The PIM/PCM cycle

3.2 The co-injection moulding technique

Sandwich moulding[4] was first developed by ICI in the 1970's for the manufacture of laminated polymer components using injection moulding. Sandwich moulding involves the simultaneous or sequential injection moulding of two thermoplastics into a mould cavity. One of the thermoplastics forms the skin and the other forms the core. Figure 3.2 shows in greater detail the sequence of co-injection moulding:

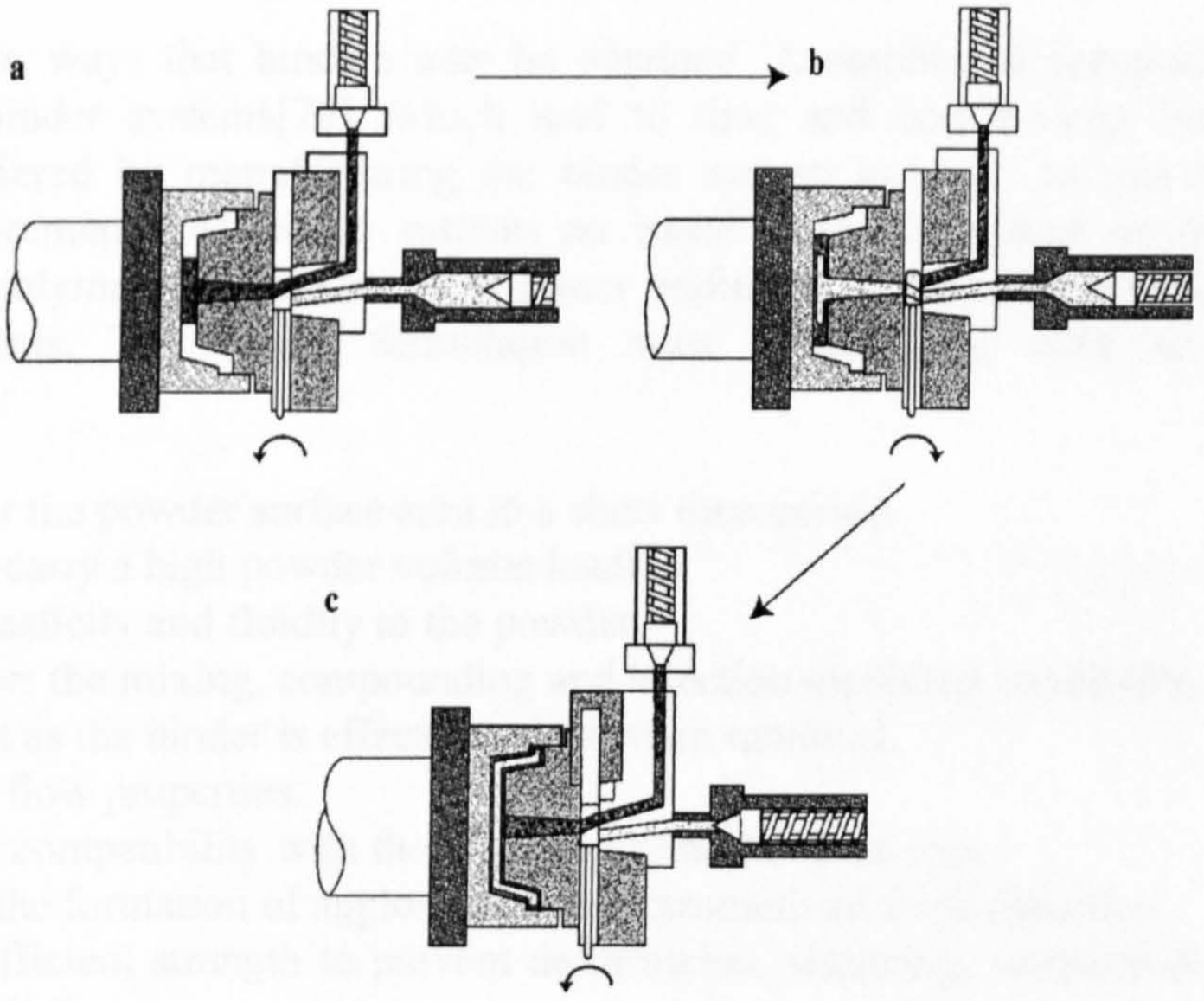

Figure 3.2 Sequence of co-injection moulding steps[25]

The co-injection sequence starts with an injection of skin material. Part-way through the mould filling phase, a changeover valve switches from the skin material to the core material, and the mould cavity continues to fill. Shortly before the mould cavity is

completely filled, the changeover valve switches from the core material to the skin material. The second shot of skin material allows the skin to be sealed at the point of injection. The mould is packed under pressure and the moulding solidifies and is ejected. Co-injection moulding can co-inject two totally different thermoplastics. Applications include high quality surface finishes on foamed or lower cost cores.

3.3 Powder co-injection moulding

Combining PIM and co-injection moulding into PCM brings additional considerations. During co-injection moulding, the core must not break through the skin, unless required or the benefits of in-situ surface engineering will be affected.

During sintering of the co-injected brown mouldings, the core and skin must have the same shrinkage rate and the same volume shrinkage percentage. If the core shrinks more than the skin, delamination of the core/skin interface will occur or the core will crack. If the skin shrinks more than the core, then the skin will crack, due to internal stressing and volume constraints.

PCM permits the manufacture of mouldings, where the core material is encapsulated by a different skin material. The aim of this project is to investigate the feasibility of PCM, permitting further exploitation of PIM.

3.4 Binder formulation

There are two ways that binders may be obtained. A number of companies produce proprietary binder systems[26], which lead to time and cost savings but deny the flexibility offered by manufacturing the binder system in-house to suit individually tailored requirements. All binder systems are based on two important major groups of ingredients, polymers and waxes with minor additions of lubricants, surfactants and coupling agents. The binder formulation must be designed with the following attributes[27]:

(a) must cover the powder surface area in a short time period.
(b) be able to carry a high powder volume loading.
(c) provide plasticity and fluidity to the powder.
(d) stable under the mixing, compounding and injection moulding conditions.
(e) low in cost as the binder is effectively lost when removed.
(f) have good flow properties.
(g) have good compatibility with the other components of the mix.
(h) minimise the formation of agglomerates and promote uniform densities.
(i) possess sufficient strength to prevent deformation, slumping, warpage and cracking during debinding.
(j) the binder must be easily removable without adversely affecting the moulding.
(k) any binder residues left in the moulding should not affect the resulting properties after sintering.

Polymers are used to give the mouldings a "backbone", which provides "green strength" between injection moulding and debinding. Amaya[28] pointed out that as the powder particle diameter decreases, the feedstock viscosity will increase. Waxes are used to counteract the effect of decreasing powder particle size, and permit higher powder loadings to be used.

As the powder volume loading increases, the average separation distance between powder particles decreases. The quantity of particle to particle contacts increases, and there is a greater resistance to gravity driven distortion during debinding and sintering. The ease of removing the binders is reduced due to the closer packing of the powder particles, hence increasing the risk of defects forming. Thus a compromise is necessary between the desired powder loading and the ease of binder removal.

3.5 Powder systems

There are many advantages in developing and optimising a composite powder system, as this permits the further exploitation of materials to achieve lower cost, and/or improved material performance. Example properties that can be improved include corrosion resistance, wear resistance and toughness. Furthermore, powder co-injection moulding offers the opportunity to carry out in-situ surface engineering. Additions are made to the skin material powder system before compounding. This will then achieve the desired material properties after sintering.

One example of surface engineering would be the addition of rigid non sinterable hard ceramic particles such as alumina to a sinterable metal powder such as iron before densification. This would improve the wear properties of the final sintered mouldings. Since alumina and iron do not alloy together, a two phase composite material is formed during sintering. A material that comprises both ceramic and metal is called a cermet.

Another example of surface engineering would be the addition of zirconia particulates to an alumina matrix. This would improve the toughness properties of the bulk material by a mechanism of limiting crack growth in the alumina matrix, as reported by Stevens[29]. Commercially available powder mixtures of alumina and zirconia are readily available, along with monolithic alumina and monolithic zirconia powders from Dynamic Ceramic.

Another example of surface engineering would be the addition of alloying metal particles to a metal matrix system. For example, chromium, nickel and molybdenum particles to an iron matrix powder to produce a corrosion resistant material. This method permits control of the metal alloy's composition. There has been a recorded attempt at injection moulding a metal powder that had a masteralloy added to the feedstock[30].

The important criterion for successful injection moulding of a composite powder system is that the addition of rigid non-sinterable or alloying particulates must have a negligible effect on the sintering rate. If the sintering rate is compromised, differential sintering will occur, leading to delamination, cracking or distortion.

Once the optimum powder system has been designed, this makes sintering of the co-injection moulding feasible as the same skin powder matrix material could be used on its own for the core powder material. The skin powder system and core powder system would sinter at equal rates and shrinkage. Such a model co-injected moulding could comprise an iron core and an iron-alumina cermet skin or an iron core with an iron and masteralloy skin.

The two main controllable factors that may affect the sintering rate and sintered density in a binary powder system are the relative volume loadings and relative powder diameters of the two chosen powders. The sintering of composites is examined further in the literature review of sintering.

3.6 Compounding

Compounding[31] is a processing technique used to mix the required ratios of the binder components and powders into a feedstock. Compounding is required to achieve the following objectives:

(a) to break up any powder agglomerates present
(b) to ensure full and uniform dispersion of the powder into the binder system
(c) to ensure full homogeneity of the binder components

Chung[32] describes several stages in the compounding process. The stages are:

(a) metered feeding of the feedstock components into the compounder's feed port
(b) conveying the feedstock components to the heated zones
(c) heating the feedstock until the binder components are molten
(d) conveying the heated materials towards the compounding elements of the screws
(d) mixing together the binder components and powders
(e) removing any entrapped gases and volatiles
(f) extruding (ejecting) the homogenised feedstock for cooling to a solid state by air or water
(g) chopping the extrudate into small pellets using a pelletiser machine

Ebenhoch and Krueger[33] and Hens and Kupp[34] report that one of the many causes of shrinkage variations and cracking during debinding and sintering of PIM products is incorrect compounding conditions. Shrinkage variations and cracking arise as a result of powder to binder volume ratio variations during compounding. It has been reported by Edirisinghe and Evans[35] and Hogan and Bradley[36] that poor dispersion of powder and the survival of agglomerates during compounding can affect the final sintered product microstructure, shrinkage uniformity and other defects. Agglomerates and/or poor powder dispersal will ultimately affect the homogeneity of the feedstock, leading to other additional effects such as non-uniform rheology.

Ess and Hornsby[37] discuss the mechanisms involved for both agglomerate formation and breakdown. Thus it is important to ensure suitable compounding conditions are achieved. Hunt and Evans[38] have investigated the influence of two different mixing

methods on the feedstock quality and concludes that a twin screw extruder produces better dispersed feedstocks and less degradation compared to double blade mixers. In addition, Buerkle[39] and Martin[40] state that the design of the screw geometry is significant in ensuring the homogeneity of the feedstock. Careful design of the screw profile is required to achieve high shear conditions. High shear is favourable towards feedstock homogeneity. Rios et al.[41] have developed a computer simulation technique to design a suitable screw geometry profile to achieve optimal mixing conditions.

Appello[42] has investigated the use of dielectric analysis as a means of characterising the dispersion of carbon black in high density polyethylenes. The conclusion was that the electrical resistivity decreased as the distance between the carbon black aggregates decreased. This implies that the filler was more uniformly dispersed. This method could have potential applications for characterising the metal or ceramic powder dispersion level in the binder system. It is thought that this method will not characterise the degree of mixing within the binder components.

Kalyon et al.[43] have demonstrated the use of wide angle X-ray diffraction to characterise the dispersion of hollow glass spheres and poly(dimethyl siloxane) polymer. It is concluded that specialised techniques are necessary to quantitatively analyse the dispersive and distributive degree of mixing between the filler and matrix materials. This method could have applications in determining the homogeneity of the binder components.

Since the feedstocks being produced for PCM could contain highly abrasive powder particles such as alumina, there is a significant problem of excessive wear on the compounding equipment, considering that high shear rates are needed to ensure maximum homogeneity. Shorr[44] states that pre-heating the materials used before compounding offers a way of reducing this wear problem and that the compounding quality would increase.

3.7 Injection moulding

Injection moulding[12] is a cyclic process of forming polymers into a desired shape by heating the plastic to its molten state. Pressure is applied to force the molten polymer into a mould cavity. The polymer is allowed to solidify to the desired shape, which is dictated by the mould cavity geometry. Injection moulding is an accepted and common manufacturing process and allows the mass production of intricately shaped parts. Often there are no further post processing procedures required on the final injection moulded polymer parts. Figure 3.3 illustrates the basic construction of an injection moulding machine.

The hopper is filled with the material to be injection moulded. The material is heated to a molten state. The heat energy is supplied by the barrel heaters and by shear heating. Shear heating occurs between the rotating screw and barrel, and the shear forces acting on the material as it is conveyed along by the rotating screw. The molten material is conveyed along the screw to the shot zone, which is the region between the nozzle and the screw tip. The volume of the shot is dependent upon the piston travel.

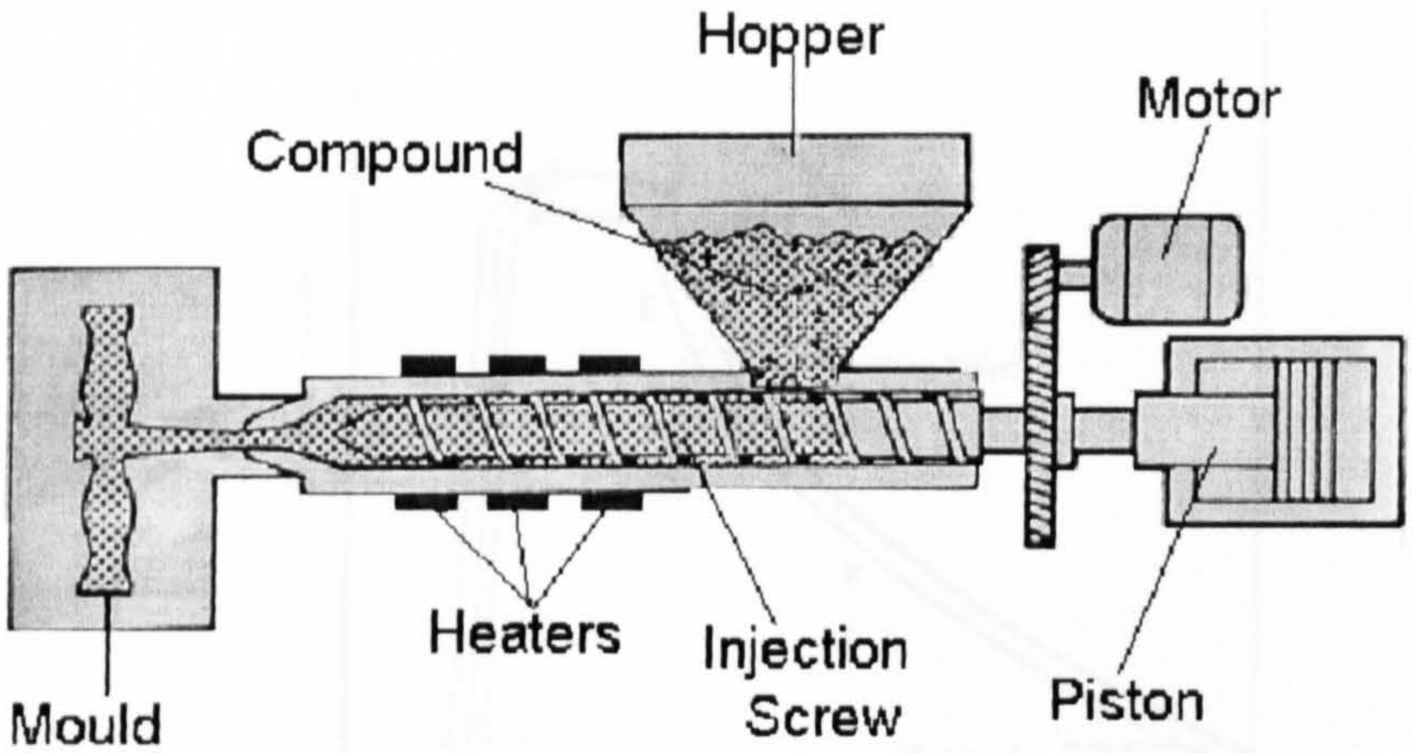

Figure 3.3 Schematic of a basic injection moulding machine[12, pp191-194].

Figure 3.4 shows the injection moulding cycle schematically. In terms of the injection moulding cycle, this can be broken down into the following sequence[12, pp191-194]:

(a) The mould tooling closes and is clamped with a clamping force
(b) Period A is the dead time period between the injection screw starting to move forward until the material starts to flow into the runner system of the mould.
(c) Period B is the mould filling period, during which time the mould cavity is being filled with the material
(d) Period C is the pressure build up period, from the point of a completely filled mould cavity to where the mould cavity pressure rises to the injection pressure
(e) Period D occurs simultaneously with period C. Period D is the packing period. As the material cools, it volumetrically contracts. More material must be injected into the mould cavity to accommodate the shrinkage or sink marks will occur. The material flows at a relatively slow rate. When the packing period ends, so does the injection cycle, and the injection screw retracts.
(f) Period E, is the discharge period. At this point, the material at the gate is still fluid. The applied runner pressure is now zero, and the cavity pressure is now slightly lower than the holding pressure and the material flow reverses. The material continues to cool until the gate freezes off, and this is known as the sealing point.
(g) Period F is the cooling period, during which the material in the mould cavity continues to cool. There is no further material flow through the gate in either direction.
(h) At the end of the cooling period F, there is still some residual mould cavity pressure. The mould cavity opens, the moulding is ejected and the mould closes for the injection cycle to start again for the next moulding.

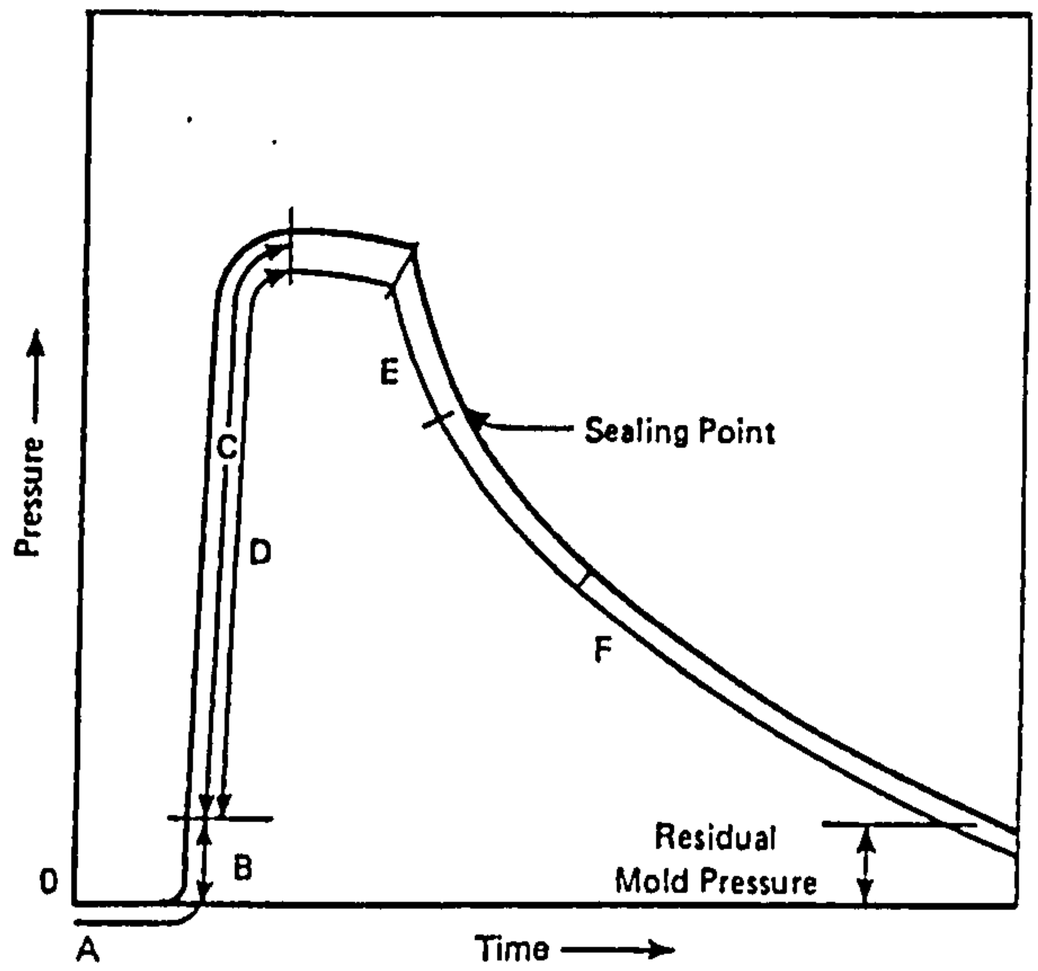

Figure 3.4 Pressure profile chart for one moulding cycle[45]

Many moulding defects can develop during injection moulding. The injection moulding process parameters have to be optimised in order for high quality mouldings to be made to a high degree of reproducibility. Different materials require different sets of optimum process values for successful moulding. The properties of the material have an influence on the time, temperature and pressure profiles required for successful moulding.

The list below shows the defects that can occur as a result of incorrect moulding conditions.

(a) weld lines
(b) flashing
(c) thermal stresses
(d) frozen in stresses
(e) short shots
(f) sink marks
(g) warpage after ejection from the mould
(h) flow lines
(i) shrinkage
(j) entrapped gases
(k) cracking
(l) sticking
(m) jetting
(n) delamination
(o) density gradients in particulate filled polymer systems
(p) breakthrough of core material through the skin (for co-injection only)

Figure 3.5 shows the relationship between incorrect parameter values and defects in injection moulding. In PIM or PCM, any of the above defects will be carried through to

the final product. There are few techniques available for eliminating any of the above defects after injection moulding has taken place.

Any of these faults can be caused by incorrect mould design or by incorrect injection moulding parameters. Traditionally, the moulding process was optimised by a "trial and error" approach. In the case of incorrect mould design, a new mould would have to be designed at great expense. In the case of incorrect process parameters, optimising the process parameters was time consuming.

Legend
A = Major
B = Secondary
C = Related

			Problems								
			Jetting	Flowlines	Skin	Cracks	Shot Short	Sink Mark	Laminations	Sticking	Flashing
Causes	Process Adjustable	Cavity Pressure				A	A	C	B		B
		Injection Pressure	B	A		B			A		C
		Hold Pressure			C	A		C	B	A	B
		Back Pressure		C			C		C	C	
		Melt Condition	B	B	C	C			C		
		Cushion					A	C			
		Injection Profile	B	A	B	C		C			C
		Injection Speed	B	A	B	A	C	C			C
		Cool Time	C	C		C		B		A	
		Hold Time			C	B	C	C			
		Shot Size		B			A	C	B		
		Barrel Nozzle Temperature	A	B		A		A	B		A
	Mold	Mould Temperature		A	B	A	C	A	B	A	B
		Runner System	C	C			C	C	C		
		Gate System	A	A	B	C	C	C	C		
	Material and Machine	Clamp Pressure									C
		Ejector System				A					
		Material Characteristics	A	A	A	B		A	B	B	

Figure 3.5 Matrix illustrating the relationship between incorrect parameter values and defects in injection moulding [12, pp211]

There is a manual methodology[12, pp191-194]. available for the determination of optimal moulding parameters for a given compound. One of the considerations in PIM and PCM is the inherently different thermal properties of the feedstocks compared to polymers. This leads to potential effects on cooling times and hence a smaller time window to complete the mould filling and packing process before solidification.

3.8 Debinding

After co-injection moulding, the green mouldings contain binders such as polypropylene, paraffin wax, carnauba wax and stearic acid. The binders in the co-injection moulded parts must be removed before sintering to maximum density can take place. If the green mouldings are not debound, they will crack, distort, blister and break up during sintering.

The purpose of debinding is to remove these binder components, without disturbing the shape of the green mouldings and the metal/ceramic particles. There are many techniques available for binder removal. The choice of technique used depends upon the composition of the binder system and the powder characteristics. Each debinding method has its advantages and disadvantages. Examples include:

(a) Thermal debinding [46]
(b) High pressure thermal debinding[46] [47] [48]
(c) Thermal wicking [46]
(d) Solvent debinding[28] [46]
(e) High pressure solvent debinding
(f) Thermally assisted solvent debinding[49]
(g) Microwave thermal debinding[11] (applicable to ceramics only)
(h) Supercritical carbon dioxide fluid extraction [50][51][52]
(i) Vacuum debinding[46] [53]
(j) Catalytic debinding[46] [54]

A multi-step debinding process is far more suitable than a single step debinding process. This permits the binder removal in several smaller steps and reduces the risk of defect formation. Defect formation can be caused by excessively high binder removal rates or high heating rates. Only two debinding techniques will be discussed further in the literature survey, as they were the only two methods used in the experimental phase of the project.

3.9 Solvent debinding

If the binder system contains some components that are soluble in known solvents and are immiscible with the rest of the binder system used, then solvent debinding can be used. This comprises immersing the green mouldings into either a solvent vapour or solvent liquid. The solvent debinding is often thermally assisted at a temperature around the solvent's boiling point.

Solvent debinding is a very common method of removing the wax component in a wax and polymer binder system. Removing the waxes forms a porous network, channels and pathways, which aids the removal of the polymer in the next debinding step. The key to solvent debinding is to use a solvent that will dissolve the waxes, and does not affect the polymer binder component. The polymer binder component imparts green strength to the green mouldings. This essential for further handling in the next processing stage, thermal debinding and sintering.

As the waxes are organic, organic solvents such as pentane, hexane, heptane, ethylene chloride, ethanol, or acetone are used in solvent debinding. The use of chlorofluorocarbons (CFC's) as debinding solvents has been phased out as a consequence of the Montreal protocol.

3.9.1 Mechanism of solvent debinding of the green mouldings

Figure 3.6 illustrates in greater detail the mechanism for wax removal from the green mouldings during solvent debinding. The waxes escape out of the green mouldings by two mechanisms. In the first, the waxes melt and flow out of the green mouldings into the porous substrate. In the second, the evaporated solvent condenses within the Liebig condenser and falls down onto the green mouldings, dissolves the waxes and transports the dissolved waxes into the porous substrate. Alvain et al.[21, pp56-60] report that wax removal percentages in solvent debinding can typically reach 95% to 96%.

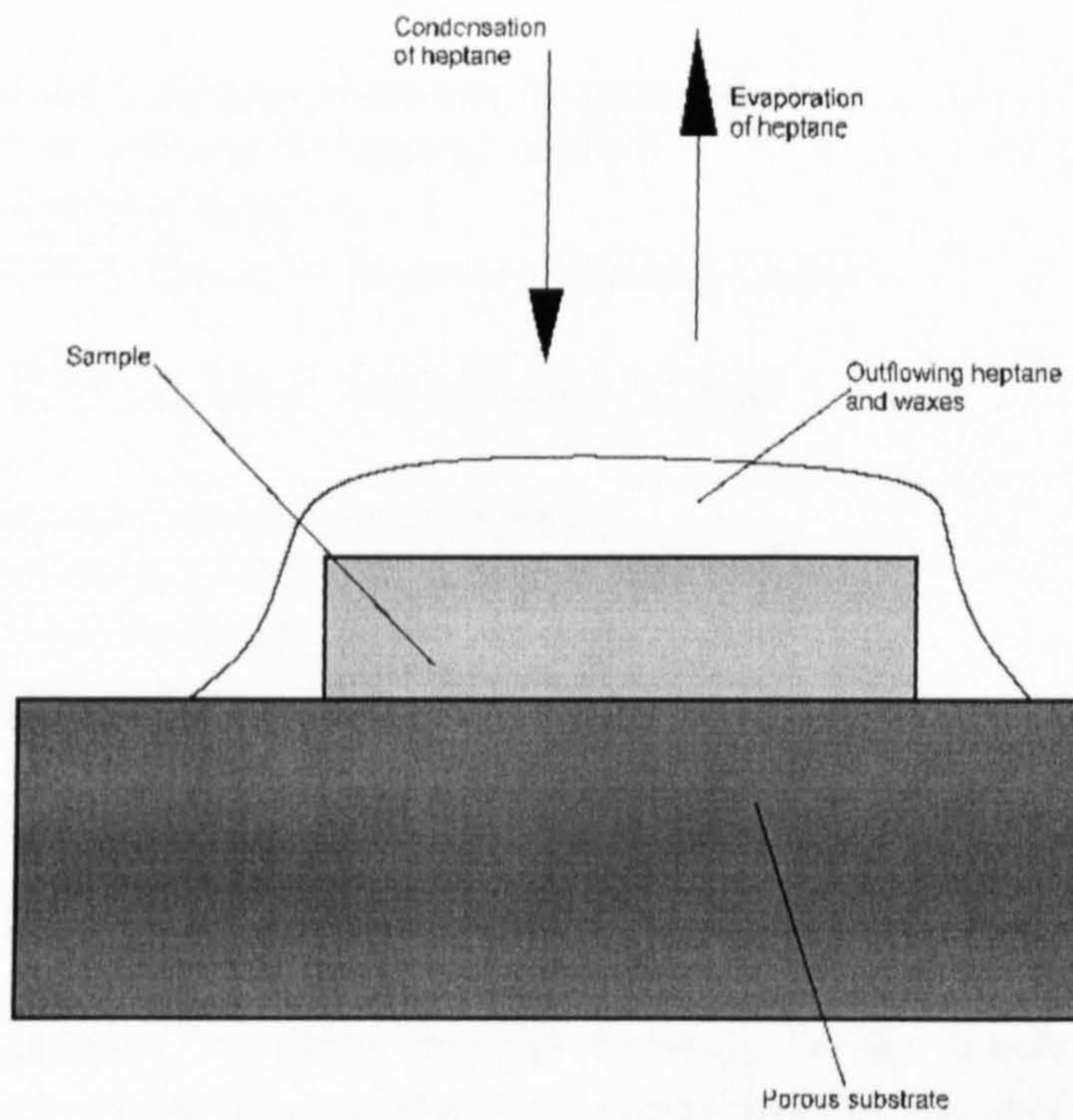

Figure 3.6 Schematic of the process of wax removal during solvent debinding

Tsai and Chen[49] have shown that during solvent debinding, the binder is removed from the outside in, and this results in a shrinking core of binder waxes. They also point out that if there is a small region of binder waxes left in the centre of the green moulding after solvent debinding, this will be a potential cause of defect formation during subsequent thermal debinding and sintering. This indicates that the major mechanism for binder removal is the dissolution of the binder components into the solvent rather than gravity driven flow.

After debinding, the green mouldings are saturated with solvent. The solvent must be allowed to freely evaporate before any subsequent thermal debinding and sintering. If any solvent remains within the green mouldings, this is a potential cause of defect formation.

3.9.2 Modelling solvent debinding

Various attempts [55][56] have been made to develop general mathematical equations to model the binder removal process and to develop pore structure evolution during solvent and wick debinding. Equations 3.1 and 3.2 have been postulated to calculate the amount of waxes removed during solvent debinding:

$$W = 2\left(\frac{D_x t}{\pi L^2}\right)^{\frac{1}{2}} \qquad \text{Eqn (3.1)}$$

$$D_x = D_o . e^{\left(\frac{-E}{kT}\right)} \qquad \text{Eqn (3.2)}$$

Where W = weight fraction of the binder removed
D_x = interdiffusion diffusivity (cm^2s^{-1})
t = debinding time, (s)
L = half-thickness of the green mouldings. (cm)

The value of D_x is calculated from equation 3.2 and:

D_o = pre-exponential frequency factor
k = Boltzmann's constant (1.3805×10^{-23} JK^{-1})
E = activation energy (J)
T = temperature in degrees Kelvin. (K)

It is pointed out that the value of D_0 is different for different solvents. There are some assumptions made with equations 3.1 and 3.2. Equation 3.2 assumes that the temperature is totally uniform throughout the debinding apparatus and does not take into account the waxes removed during the heating up and cooling down periods of solvent debinding (necessary to avoid thermal stressing of the green mouldings). During debinding, the concentration of dissolved binder rises in the solvent, and equation 3.2 does not allow for the possible re-deposition of binder onto the green mouldings by the binder containing solvent. There may also be a binder concentration gradient throughout the green mouldings due to temperature gradients. Equation 3.1 assumes a uniform thickness throughout the green mouldings.

Equation 3.1 implies that the debinding time is proportional to the square of the half thickness, and thus a doubling in the cross-sectional thickness in the green mouldings leads to a four-fold increase in the solvent debinding time required.

3.9.3 Thermal debinding

Thermal debinding is a very commonly used technique to remove the polymer binder, leaving behind a very fragile and weak structure of powder particles, held together by a combination of inter-particle friction and pre-sintering, (stage 1 sintering, neck growth). The removal of all of the binder components from a green moulding produces a brown moulding.

Thermal debinding uses the application of heat to remove the polymer binder. The polymer binder is either removed from the green moulding in its liquid or gaseous state, or the binder thermally decomposes into the gaseous state, with carbonaceous residues being left in the brown moulding. The carbon residues may or may not be beneficial to the brown moulding when sintered.

Moore et al.[57] have shown that the process gases used during debinding and sintering can influence the final carbon concentration in the brown moulding. The carbon residues produced from the binder decomposition and any residual carbon in the powder can be removed with the use of a highly reducing atmosphere. However, materials being sintered such as stainless steels may require fixed amounts of carbon to achieve the desired properties.

Shuquan et al.[58] have attempted to develop equations that model binder removal as a result of thermal debinding and suggest that the kinetics for the thermal debinding process can be described by equation 3.3:

$$\frac{da}{dt} = K(1-a)^n \qquad \text{Eqn (3.3)}$$

Where

a	= weight loss fraction
T	= reaction time
K	= reaction rate constant
n	= reaction order

The dependence of K, the reaction rate constant on temperature could be expressed by the Arrhenius equation as equation 3.4 shows.

$$K = Ae^{\left(\frac{-E}{kT}\right)} \qquad \text{Eqn (3.4)}$$

Where

E	= debinding activation energy (J)
k	= Boltzmann's constant (1.3805×10^{-23} JK^{-1})
A	= pre-exponential factor
T	= temperature (K)

Equations 3.3 and 3.4 do not take into account that the binder can be removed by more than one mechanism. Some of the binder will flow out in the liquid phase, some will be removed in the gaseous phase, and some of the binder will be thermally decomposed into carbonaceous residues.

3.9.4 Potential defects that can occur with thermal debinding

Whenever a polymer binder is heated, it expands, softens and its yield strength is reduced. There are various ways that the mouldings can develop defects. The mouldings can distort by viscous flow, due to the effects of gravity and the mass of the mouldings. As the debinding temperature increases, the polymer becomes less viscous. The powder loading decreases due to the greater thermal volumetric expansion of the polymer, leading to an increase in the inter-particle distances with increasing temperature, typically 5% to 7%. (calculated from PVT data)

These phenomena can contribute to the formation of defects if the thermal debinding is not optimised. The mouldings must be well supported to minimise gravity driven distortion and slumping. The binder removal rates must be evenly distributed throughout the mouldings to minimise pressure build up. Thermal gradients must be kept to a minimum as hotter surfaces lose binder material at a faster rate than cooler surfaces. This underlines the importance of dwell times to allow the thermal gradients within the mouldings to be eliminated. The temperature ramp rate must be well controlled to avoid excessive binder removal rates. There is a lower limit placed on the powder volume loading, as if the inter-particle spacing is too high, there will not be sufficient inter-particle friction to hold the particles together. If the powder volume loading is too high, debinding becomes more difficult.

Angermann and Van Der Biest[46] state that defects forming during thermal debinding include cracking, blistering, delamination, vapour blow-holes and warping. These defects are due to incorrect binder removal conditions. Defects during thermal debinding are usually caused by:

(a) High heating rates leading to high binder removal rates
(b) Too rapid evolution rate of decomposition gases
(c) Incorrect binder compositions
(d) Injection moulding defects

The easiest way to minimise defects is to reduce the debinding rate. This leads to increased processing times and hence makes the debinding process less cost effective. However, the rate of debinding can generally increase with the increasing porosity of the moulding being debound.

There have been several approaches used to optimise the thermal debinding technique to eliminate the formation of defects but to minimise the time and costs involved:

- Angermann and Van Der Biest[59] have demonstrated a methodology to optimise the debinding temperature versus time profiles. The binders are subjected to differential thermal analysis, (DTA), differential scanning calorimetry (DSC), and thermo-gravimetric analysis (TGA). This permits the determination of the appropriate dwell temperatures, dwell durations and temperature ramp rates.

- Angermann and Van Der Biest[60] developed novel binder systems that permit distortion free conventional thermal debinding using higher heating rates than is normally possible. Currently the exact details of the novel binder formulation have not been revealed.

- Trunec and Cihlar[47] developed a methodology of controlling the debinding temperature-time profile as a function of the binder removal rate. A weight measuring system coupled to the furnace temperature controller has been developed and permits the control of the binder removal rate by controlling the heating of the furnace.

- Controlled decomposition rate control (CDRC)[61], where the evolved gases from the green moulding being debound are analysed by a gas analyser and the information obtained is used to dynamically control the furnace temperature.

A combination of several debinding processes is preferable to using only one, as the binder can be removed in several small stages reducing the risk of defects. Generally speaking, the first debinding process allows a faster rate of binder removal in the second debinding process due to the porosity network created by the first debinding process.

Temperature ramp rates during thermal debinding typically range from $1°Cmin^{-1}$ to $5°Cmin^{-1}$, with typical dwell times of 2 hours. Two dwell temperatures are typically used. One is above the melting point of the polymer, and the other permit the polymer to either escape in the gaseous state or thermally degrade into simpler hydrocarbons. A reducing hydrogen atmosphere is typically used.

As stated earlier, carbon control can be achieved by atmosphere control within the furnace. However, there are particular considerations with stainless steel powders as used in this project. The problem with debinding and sintering powders that contain chromium is chromium's susceptibility to the formation of chromium oxides, chromium carbides, chromium nitrides and chromium evaporation. This formation of chromium compounds can lead to impaired densification, and reduces the corrosion resistance of stainless steel. Duncavage and Finn[62] suggests that 95% argon + 5% hydrogen would prevent the formation of these chromium compounds.

PCM is a novel technique, and it is important to demonstrate that both solvent and thermal debinding used in PIM can be used on PCM with little modification.

3.10 Sintering

Sintering is the final stage of powder co-injection moulding. It is the process whereby the brown mouldings must reach their desired properties, which are those of the typical bulk materials. This is the process of reduction of porosity and the maximising of density by heating the brown moulding in a controlled atmosphere furnace to a temperature below its melting point, but sufficiently high enough to allow the metal

particles to bond together and the consequent removal of porosity. Thus shrinkage of the brown mouldings also occurs.

Sintering is a term used to describe an operation involving the use of heat with or without applied pressure to consolidate the debound moulding. During the preceding debinding stage, the binder components were removed, leaving behind a network of pores, and channels. The debound moulding is held together by interparticle friction and/or by presintering. The debound moulding is very brittle and low in strength. The objectives of sintering is to densify the fragile brown moulding, with the intrinsic improvement of its mechanical properties such as wear resistance, corrosion resistance, strength, and hardness.

3.10.1 Theory of sintering

Sintering is the bonding together of powder particles when heated to elevated temperatures. The driving force that promotes sintering is the reduction in the surface energy of the particles in the debound moulding. Surface energy is inversely proportional to the particle size. Particles sinter by atomic motions that act to reduce the high surface energies associated with un-sintered powders.

The ratio of activated atoms with the required activation energy to total atoms can be calculated from the Arrhenius equation as illustrated by equation 3.5.

$$\frac{N}{N_0} = e^{\left(\frac{-E}{kT}\right)} \qquad \text{Eqn (3.5)}$$

Where
- N = Number of activated atoms with the required activation energy.
- N_0 = Total number of atoms.
- E = Activation energy (J)
- k = Boltzmann's constant (1.3805×10^{-23} JK^{-1})
- T = Temperature in Kelvin (K)

Equation 3.5 implies that as the sintering temperature increases, so does the ratio of activated atoms to total atoms and implies a higher sintering rate.

There are four stages to sintering. Figure 3.7 illustrates a model of two spherical particles in intimate contact with each other. Figure 3.8 illustrates the changes in the microstructure of the debound mouldings. Figure 3.9 illustrates in greater detail what happens when more than two particles are considered.

The point contact stage is characterised by the high number of particle to particle point contacts. The initial stage of sintering is characterised by the small neck to particle diameter ratio and shrinkage of the mouldings. The grain size is smaller than the particle size. Rapid growth of the interparticle necks occurs during initial sintering. The pore structure at this stage is typically an open structure.

The intermediate stage is the most critical in the determination of the properties of the sintered moulding. In this stage, densification, grain growth and pore rounding take place. The pore structure becomes smoother but remains interconnected, and the pores are generally located at the grain boundary intersections. As sintering progresses, the pores tend towards cylindrical geometries. In the final stage of sintering, the pores shrink by diffusion. The rate of densification falls as a result. The pores collapse into spherical pores and interconnecting network disappears. The open pores become closed pores as a result.

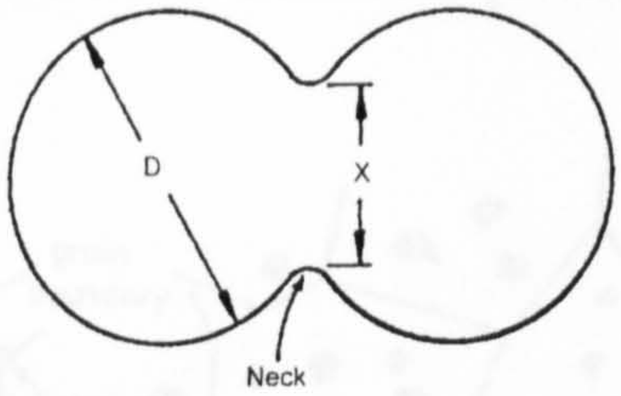

Figure 3.7 Two particles in the process of sintering[63, pp252] (D is the particle diameter, and x is the neck diameter)

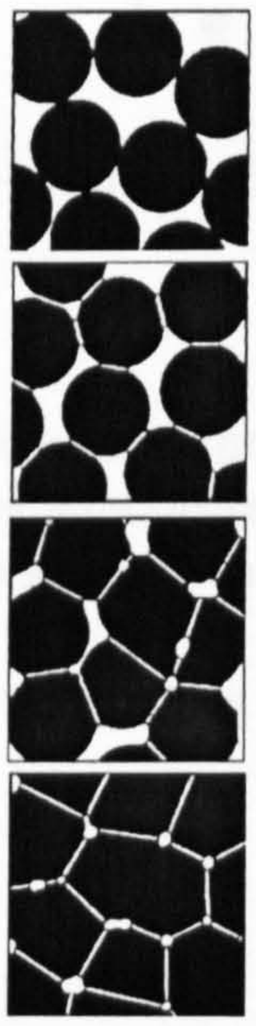

Figure 3.8 Sintering of the debound mouldings[63, pp253].

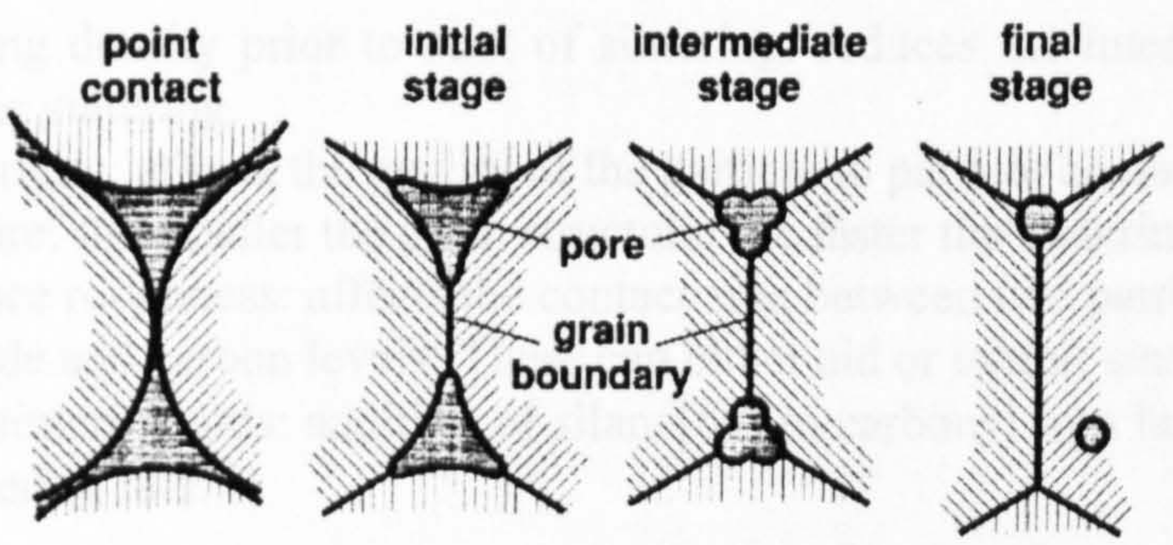

Figure 3.9 The 3 stages of sintering[5, pp261].

The closed pores that form during sintering may occur within grains or at grain boundaries. If a pore forms within a grain, very little further pore reduction will occur and subsequent further densification is difficult. If the pore is on a grain boundary, then further densification and further sintering can continue. Figure 3.10 illustrates the two possible pore-grain configurations. Pores within grains are undesirable as the theoretical maximum sintered density is reduced. This phenomenon is minimised by careful processing control. The sintering cycles are often optimised using a trial and error approach despite many recorded attempts in the literature at developing sintering theory that can usually predict the effects of material and process variables.

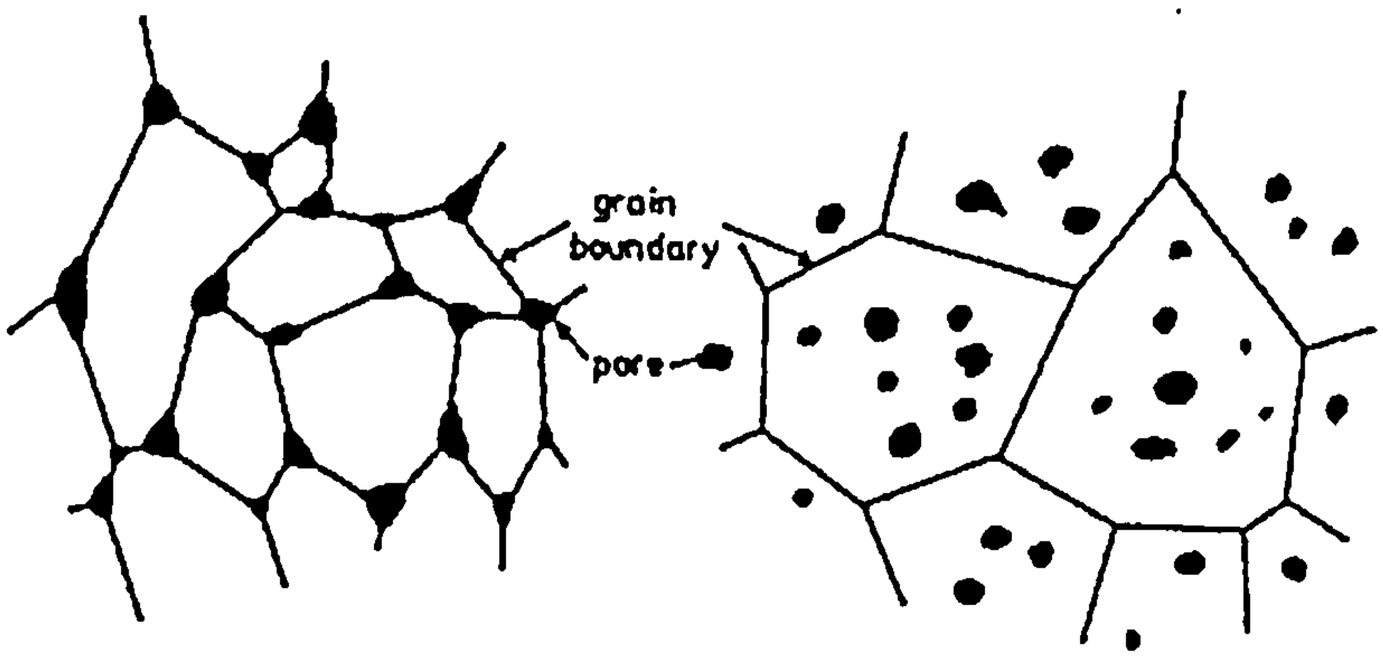

Figure 3.10 The two possible pore - grain configurations [5, pp263].

3.10.2 Process variables

(a) Pressure: increasing the pressure increases the sintering rate.
(b) Temperature: increasing the temperature increases the sintering rate.
(c) Time: increasing the time leads to greater densification until grain growth dominates, but increases processing costs.
(d) Atmosphere used: different process gases influence the sintering behaviour of different powders.

3.10.3 Material factors

(a) Powder diameter: reducing the diameter increases the sintering rate as the surface energy is higher.
(b) Initial packing density prior to start of sintering: reduces the interparticle distance and speeds up the sintering.
(c) Powder sphericity: affects the quality of the particle to particle contacts.
(d) Grain structure: the smaller the grain structure, the faster the sintering.
(e) Particle surface roughness: affects the contact area between two particles.
(f) Levels of oxide and carbon levels: These can either aid or inhibit sintering.
(g) Addition of sintering aids: addition of silane[64] to carbonyl iron has been shown to improve the sintering rate.

However the final results will also be dependent upon the quality achieved by previous processing steps since sintering cannot correct any defects caused by previous processing steps. Calculations of theoretical linear shrinkage as a result of volume changes during sintering are shown in table 3.1 using equation 3.6.

$$V_f = V_i\left(1 - \frac{\Delta L}{L_o}\right)^3 \qquad \text{Eqn (3.6)}$$

Where V_f = final volume
V_i = initial volume
ΔL = change in length
L_o = original length

Powder volume loading (%)	Maximum volume shrinkage (%)	Maximum isotropic length shrinkage (%)
50	50	20.63
55	45	18.07
60	40	15.66
65	35	13.38

Table 3.1 Calculations of theoretical shrinkage as a result of sintering

The data in table 3.1 were generated with the assumption that all of the binder components were completely removed, and that the brown mouldings sinter to full density and hence minimum volume, which is equal to the powder volume loading. The initial volume was taken to be 100%. Full densification is rarely achieved in practice, due to grain growth.

There have been attempts by Skorokhod[65], Shinagawa[66], Zhang[67], Belen'kii[68] and Liu and Patterson[69] to mathematically model the principles behind sintering. Ashby[70] has developed computer software that produces sintering and hot isostatic pressing diagrams, based upon sintering equations for any given powder, and hence calculates an estimate of the sintering time and temperature to achieve a given density. There are assumptions made, which include the assumption that every powder particle has the same diameter and surface roughness, and equal levels of carbon, oxides and impurities. Additionally the sintering equations do not consider any sintering action that may take place during the initial heating up and the final cooling down. Most sintering models make the assumption that there is only one sintering mechanism in action. In reality there can be several mechanisms concurrently active during sintering. Different sintering mechanisms have differing sensitivities to process parameters. Thus the sintering model does not relate well to real world sintering.

There was a need to develop a sintering model that closely resembled real world sintering behaviour. Shu and Johnson[71][72] present the master sintering curve (MSC). The MSC takes into account the sintering that occurs during the heating up to sintering temperature and for the cooling down from the sintering temperature. Since the MSC curve is independent of the thermal history, this allows for non uniform particle

diameters. The only drawback with the MSC is that it can only be applied to powder mouldings made from the same powder batch and by the same green body processing route. Another particularly useful feature of the MSC is its applicability to two-phase composite powder systems, which would find applications in PCM. During sintering, the brown mouldings shrink as a consequence of densification. This requires the oversizing of the mould tooling to permit the final parts to achieve the desired size. Uniform shrinkage of the brown mouldings is vital and therefore density gradients in the green parts must be minimised. This is achieved by proper selection and mixing of the powders and binder components.

3.10.4 Sintering of composites

Another consideration that must be taken into account for the purposes of the present work is the effect the addition of particulates would have on the sintering rate of the matrix. Particulate additions fall into two main categories, alloying and rigid non-sinterable inclusions.

Many examples of alloying additions can be found in the field of powder metallurgy. Antonova and Privalov[73] have produced an intermetallic compound, titanium-iron by sintering pressed mixtures of titanium and iron powders. Chan and Lin[74] have used mixtures of nickel and iron powder to produce iron-nickel alloys. Garin and Mannheim[75] have produced molybdenum - rhenium alloys by using a powder mixture of elemental molybdenum and rhenium. Narasimhan[76] has produced alloys of iron with one or more additions of the following elements, graphite, copper, nickel, phosphorus and boron.

Wada et al.[77] have produced copper-nickel alloys by metal injection moulding. Comparisons were made between using elemental copper and nickel powders and using copper-nickel alloy powder. Wada concluded that the sintered density was higher for the powder mixture than the alloyed mixture. This is probably due to the copper particles sintering to each other preferentially before alloying with the nickel particles. This is confirmed by the literature values for the melting point of 1083°C for copper and 1450°C for nickel. This implies that densification commences before alloying. The copper-nickel alloy powder will certainly have a higher melting point than that of copper and have a different sintering profile to that of the elemental powder mixture.

During sintering, the alloying addition diffuses into the bulk matrix, forming a metal alloy or intermetallic, thus physically altering the material properties of the bulk matrix material. The alloying metal particles can be commercially bought in as masteralloys or as elemental powders. It is apparent that the use of alloying additions such as chromium and nickel to an iron matrix is feasible given the prior work reported in the literature.

Many examples of rigid non-sinterable additions can be found in the field of powder metallurgy. Li et al.[78] have produced composites comprising alumina particulates and a zirconia matrix. Nakada and Kimura[79] have produced composites comprising zirconia inclusions in a zinc oxide matrix. Both are examples of adding ceramic inclusions into a ceramic matrix. Nakada et al.[80] have produced composites

comprising yttria stabilised zirconia particulates in a silver matrix. Shinagawa and Hirashima[81] have demonstrated the cold isostatic pressing and sintering of alumina and stainless steel powders. Both are examples of adding ceramic inclusions into a metal matrix.

Lafer et al.[82], Besson and Evans[83], Taylor et al.[84], Thibault et al.[85], Zavaliangos et al.[86], Lange et al.[87], Yamaguchi et al.[88], Fan and Rahaman[89] and Turner and Ashby[90] have studied the densification of powder composites. They collectively conclude that as the inclusion/matrix particle diameter ratio decreases, the amount of densification decreased. As the volume loading of the inclusions increases, the amount of densification decreased. In addition, the morphology of the rigid inclusions in a sinterable matrix had a negligible effect on the densification of the composite. This is because the sinterable matrix forms a physical barrier between the rigid particulates. This prevents neck growth between the rigid particulates, which is the first stage of sintering.

Rahaman[91] has developed differential equations to illustrate the effect of the volume fraction of rigid inclusions on the sintering rate of the composite. They include a term for the sintering rate of the matrix material with no inclusions.

$$\frac{1}{D_m}\frac{dD_m}{dt} = \frac{1}{D_c}\frac{dD_c}{dt}\left(\frac{D_{c0}}{D_{c0}-v_{i0}D_c}\right) \qquad \text{Eqn (3.7)}$$

Where D_m = density of the matrix at time t (kgm^{-3})
D_c = density of the composite at time t (kgm^{-3})
D_{c0} = initial density of the composite at t = 0 (kgm^{-3})
v_{i0} = Initial volume fraction of the inclusions

According to equation 3.7, as the initial inclusion volume fraction v_{i0} increases, the densification rate of the composite decreases as expected. If the initial inclusion volume fraction was zero, then the densification rate of the composite is the same as the densification rate of the matrix material as expected. Equation 3.7 does not take into account other factors that could affect the densification rate. Example factors include inclusion morphology, spatial distribution, inclusion diameter distribution and nominal inclusion diameters.

Li et al.[78] suggested that as the volume loading of the inclusions increased, a constraining network would form, and act to limit the amount of densification that takes place during sintering. Delie and Bouvard[92] have proposed mechanisms to explain the effect of rigid inclusions on the densification process, and states that these mechanisms become more important when the radius ratio of rigid inclusion particles to matrix particles becomes small. This implies that the rigid inclusion diameter should be at least nominally the same or greater than the diameter of the sinterable matrix powder.

3.10.5 Sintering atmospheres

The choice of sintering atmosphere allows the control of chemical reactions that may take place in the sintering process between the brown mouldings and the furnace surroundings. The choice of sintering atmosphere is influenced by several considerations. After debinding, there will be some residual binder material left in the mouldings, as the debinding process is not 100% efficient. This residual binder must be removed before densification starts, as traces of binder material can be a source of carbon contamination.

The sintering atmosphere must not detrimentally affect the material properties of the ceramic or metal powder being sintered. This usually implies that oxidation must be avoided, so a neutral or a reducing atmosphere is used for metals. Air can be used without detrimental effect for sintering oxide ceramics. In addition, the choice of sintering atmosphere may also help in the removal of existing oxides within the powders. It is emphasised by German [5, pp402] that the complexity of sintering atmospheres arises from the many possible reactions that occur internally in the furnace chamber due to contaminants present in the mouldings, such as residual binder, oxides, entrapped gases/solvents and carbon. Proper control and manipulation of the atmosphere provides an opportunity to influence the degree of sintering and the material chemistry during sintering.

3.10.6 Thermal debinding/sintering furnaces

Often thermal debinding and sintering of mouldings are undertaken "back to back". There are two main categories of furnace used, which provide the time-temperature control of the sintering cycle while containing the atmosphere. Sintering furnaces fall into one of two distinct types, batch furnaces and continuous furnaces. A batch furnace is loaded with the brown mouldings to be sintered. The door is closed, effectively creating a sealed chamber with the exception of the gas inlets and gas exhausts. Figure 3.11 illustrates a typical batch furnace.

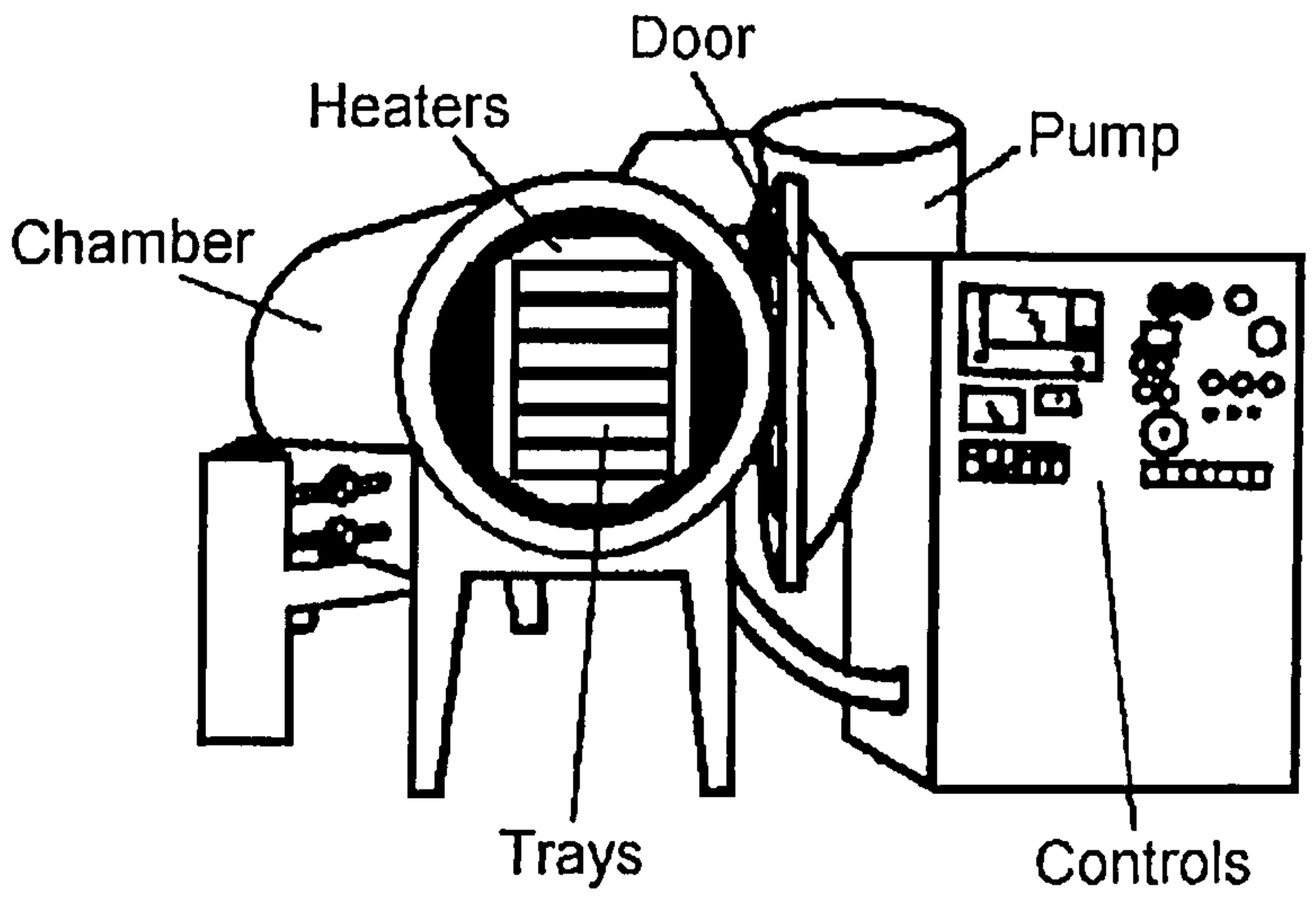

Figure 3.11 A typical batch furnace[5, pp403].

In continuous furnaces, the brown mouldings are moved by conveyor belt through a multiple temperature zone furnace. There are typically three zones in a continuous furnace. The first stage, the preheat zone removes air and binder from the mouldings that have been debound in the previous step and initiates oxide reduction. The next zone is the high heat region where the actual sintering takes place and this is where the actual time, temperature and atmosphere conditions are maintained. Cooling takes place in the last zone, the cooling zone. If necessary, the sintered mouldings may be subjected to the required cooling profile such as water or oil quenching thus effectively heat treating the sintered mouldings to their desired material properties. Figure 3.12 illustrates a typical continuous furnace.

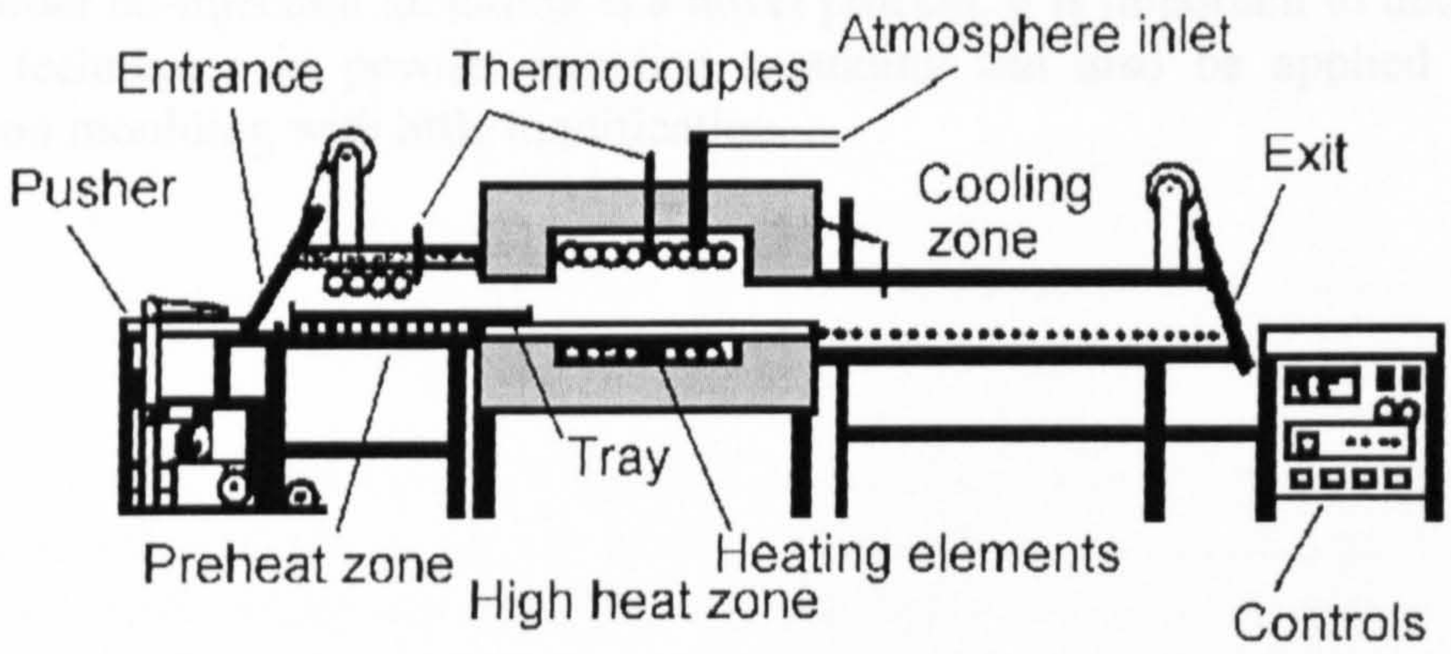

Figure 3.12 A typical continuous furnace[5, pp404].

Batch furnaces offer higher temperatures and the ability to achieve a vacuum. Continuous furnaces are open to the atmosphere at the ends of the conveyor belt, so a vacuum is impossible to achieve. The material used for the conveyor belt dictates the maximum operating temperature that continuous furnaces can run at. Continuous furnaces offer higher productivity and higher capacity. Due to the mass production ability built in, they are more energy efficient and faster than batch furnaces.

3.11 Special considerations for the sintering of powder co-injected mouldings

In the case of powder co-injection moulding, the main factors that are critical to the success of sintering co-injected mouldings are that the skin and core must not delaminate and must sinter at the same sintering rate and achieve equal volume shrinkages. Steps must be taken to equalise the sintering rate and final sintered volumes of the skin and core. Possibilities for achieving that aim include:

- addition of sintering accelerants/retardants appropriate for the skin and core
- changing the particle sizes of the skin and core powders, as the sintering rate increases with decreasing particle diameters

- use a chemical blowing agent in the core only, and hence a lower density core is achieved with the concomitant weight savings

- addition of non sintering rigid particles to either the skin or the core. Weight savings would be made if the rigid particulates had a lower density than the matrix powder

- using two identical powders for the skin and core, and adding alloying additions to either the skin or core to achieve the desired material properties, as the skin and core would have closer particulate diameters and hence match their sintering rates.

Since powder co-injection moulding is a novel process, it is important to determine that sintering techniques in powder injection moulding can also be applied to powder co-injection moulding with little modification.

4 Literature survey: Computer modelling

The traditional method of optimising injection moulded parts was by a process of trial and error. This was done by adjusting the injection moulding machine parameters until the injection moulded part quality was optimised and/or cutting expensive new moulds to eliminate processing problems. This was an inefficient use of machine time, polymer materials, and labour time.

Thus, a more efficient method of optimising the injection machine parameters was required. Mathematical models were developed as early as 1975 by Lord and Williams[93] that model the process of injecting a molten material into a mould cavity. To date, only one commercial company, Concurrent Technologies Corporation[94], Johnstown, PA, USA, has developed CAE software specifically for powder injection moulding. However, Rensslaer Polytechnic Institute[95][96], New York, have developed their own computer software for the modelling of the mould filling process for powder injection moulding.

Computer-aided engineering[23][97][98] (CAE) software have been used to model the injection moulding cycle of highly filled powder feedstocks by Najmi and Lee[95], Aksit and Lee[99], Najmi and Lee[96] and Kwon and Park[100], in order to predict the optimum mould design and optimum moulding parameters. The moulding software uses several mathematical techniques[95], such as finite element modelling (FEM), finite difference modelling (FDM), pressure and energy differential equations. This has led to substantial saving of time and money by the injection moulding companies. The literature did not reveal any previous attempts to model the co-injection of polymers or PIM feedstocks. Two of the objectives of the present work are to:

(a) verify that commercial computer modelling software can be used as a predictive tool with polymer co-injection moulding,
(b) determine whether commercial computer modelling software could be used to model the co-injection of metal or ceramic feedstocks.

The main commercial companies that produce commercial computer prediction and modelling software for injection moulding are:

1. AC Technology, Inthaca, New York, U.S.A
2. Cisigraph Corporation, Farmington Hills, Michigan, U.S.A.
3. ICAM Technology, Pointe Claire, Quebec, Canada.
4. Techanalysis, Indianapolis, U.S.A
5. Moldflow Inc, Shelton, Conn, USA.
6. CAE Services, Bloomingdale, Illinois, U.S.A.
7. Delcam International, Birmingham, England.
8. Parametric Technology, Waltham, MA, U.S.A.
9. Plastics and Computer International, Milan, Italy.
10. Structural Dynamics Research Corporation, Milford, Ohio, U.S.A.

AC Technology is the only company to date that supplies software, that is designed to simulate the process of co-injection moulding[101][102][103] of two distinctly different polymers, and was the software company of choice for the purposes of the present work. AC Technology's software product, C-MOLD was used in the present work to model the twin barrel co-injection of two different materials into a mould cavity.

Amongst the features of the C-Mold software are:

- Performance and productivity analysis and prediction
- Mould filling analysis and prediction
- Moulded part defect detection and prediction
- Post filling/Packing analysis and prediction
- Cooling analysis and prediction
- Residual stress analysis and prediction
- Part shrinkage analysis and prediction
- Warpage analysis and prediction
- Detection of weld/meld lines, air entrapment, runner balancing

One drawback of the modelling software is its high purchasing cost. Mapleston[23] states that the savings of time and money in optimising injection mould design and process parameters more than cover the initial outlay for the necessary software and hardware.

4.1 Procedure for using computer modelling software

The procedure in using C-Mold is illustrated by figure 4.1. The computer modelling process is described further.

- use C-Mold modeller to draw the desired mould geometry or to select an existing mould geometry file
- use C-Mold modeller to create a finite element mesh to the geometry generated in the previous step or select an existing FEM file
- select the injection moulding process in C-Mold control panel
- select or create the injection moulding machine being used in C-Mold rapid designer
- select or create the material(s) being injection moulded C-Mold rapid designer
- select or create mould material being used C-Mold rapid designer
- select or create the cooling fluid type in C-Mold rapid designer
- select or create the process conditions being used for the injection moulding cycle in C-Mold rapid designer
- select or create a parameter file that defines the level of precision required, number of mould layers and time steps for the analysis
- save as a design file and run design diagnostics in C-Mold control panel to execute the analysis
- use C-Mold visualiser to view the analysis results
- repeat procedure until the design goals are achieved by changing parameters, materials etc.

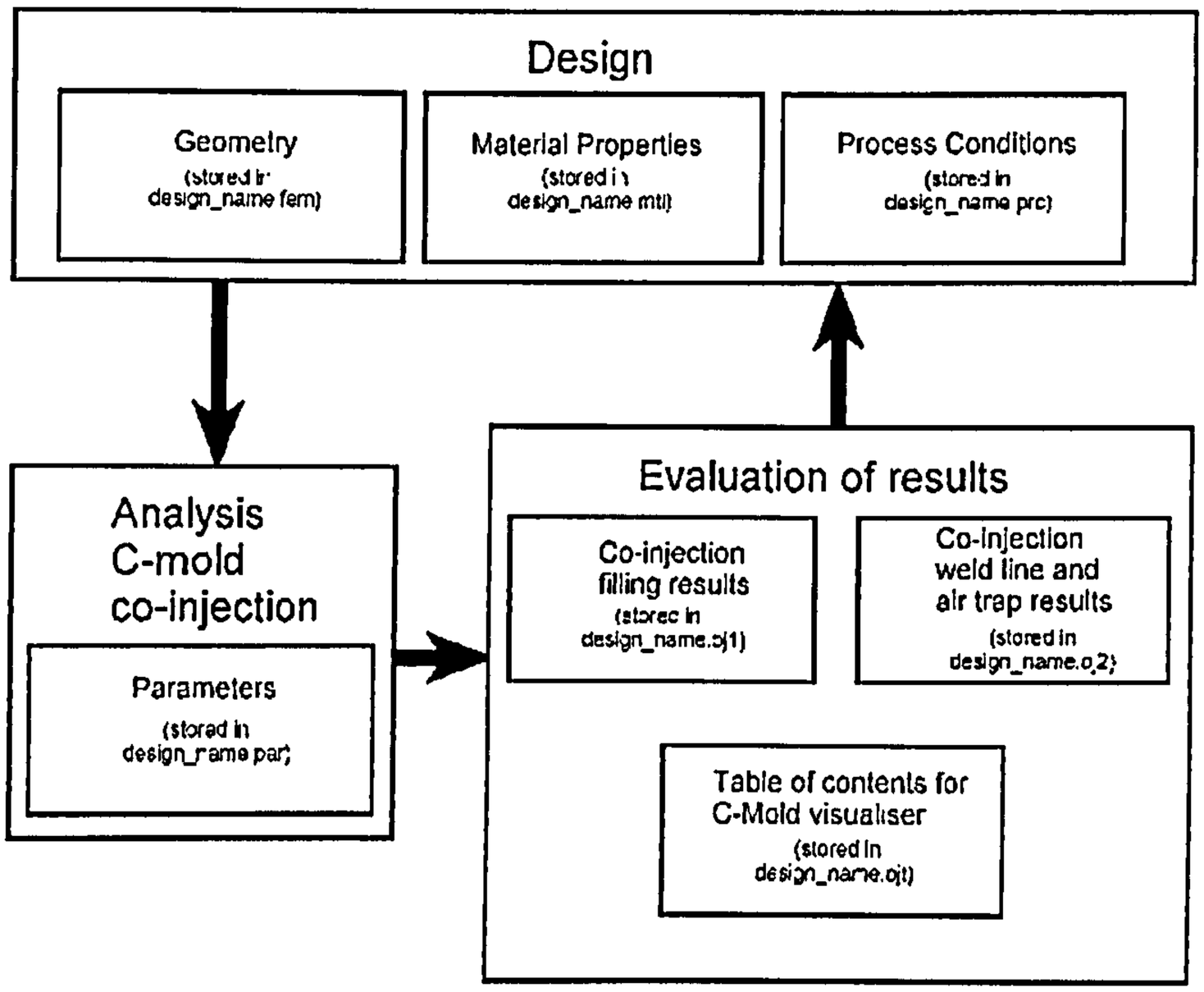

Figure 4.1 Schematic of the computer modelling process

4.2 Material property data requirements for computer modelling

The properties[104] of the materials being injection moulded are used by the C-Mold simulation software and are summarised below:

- thermal conductivity
- specific heat capacity
- melt density
- "no-flow" temperature (melting point)
- rheology
- pressure-volume-temperature profiles

C-Mold has an integrated material property database for a wide range of polymers, where typically the data has been supplied by the manufacturer or extracted from the open literature. Material property data for classes of polymers are well documented in the polymer manufacturer's product literature and in many polymer material data books. Material property data are in reasonable agreement for nominally identical polymers from different manufacturers. Figure 4.2 shows how the above material properties, geometry data and processing conditions are used by the computer software for the pressure and energy differential equations that are used in the simulation analyses.

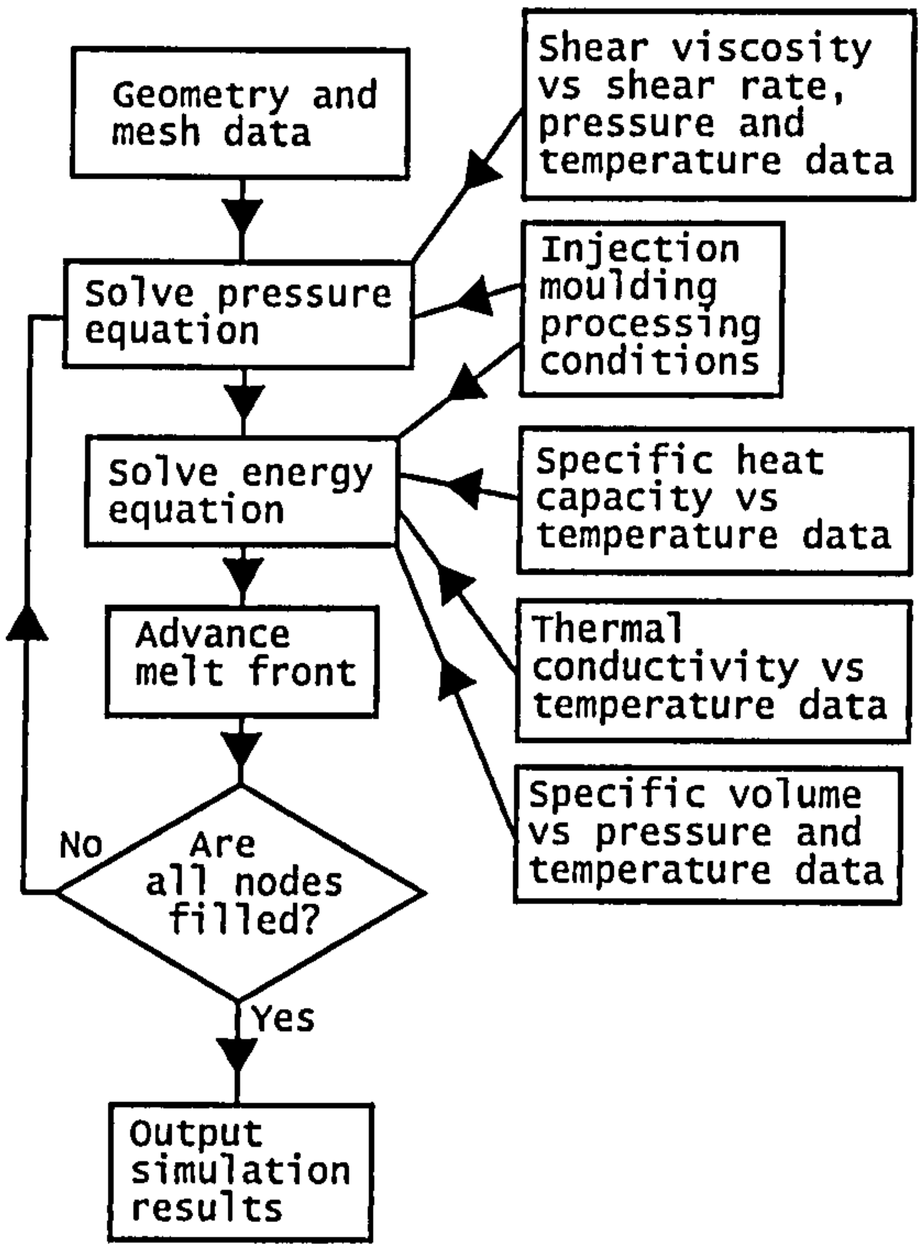

Figure 4.2 Schematic of typical computer modelling software[100] (Material properties and processing conditions boxes added by author)

The material property data for PIM feedstocks change whenever their compositions are altered. There is no generally available material property data on PIM feedstocks in the open literature or from commercial feedstock manufacturers. The material properties of feedstocks can be measured experimentally. Each time the ratios of the components in a feedstock are altered, the material properties must be experimentally re-analysed again. Since the material properties of the individual components remain unaltered, a rule of mixtures approach could be developed to reduce the need for repeated time consuming material property data determination every time the feedstock composition is altered.

From the point at which the PIM feedstock is injected into the mould cavity to the ejection of the moulding from the mould cavity, heat is exchanged from the PIM feedstock material to the mould cavity walls. The cooling rate of the PIM material is determined by several factors during the injection moulding cycle, illustrated by equation 4.1.

$$t = \frac{Fx^2}{a} \qquad \text{Eqn (4.1)}$$

Where F = Fourier number

x = moulding cross-sectional thickness (m)

t = cooling time (s)

a = thermal diffusivity (m^2s^{-1})

(if heat is being exchanged from both sides of the moulding cross-section, the section thickness is halved)

The Fourier number is a dimensionless parameter which is used for studying heat flow phenomena. The Fourier number describes the magnitude of the thermal gradients in the mouldings. A value of less than 0.1 indicates that the injection moulded material is little affected by its surroundings. If it is greater than 1.0, then the injection moulded material has come to near thermal equilibrium with its surroundings. The cooling time is defined to be the time for the moulding to cool from its processing temperature to near ambient temperature. In calculating the minimum time required, it is convenient to take the value of the Fourier number as 1. The thermal diffusivity is determined by equation 4.2.

$$a = \frac{k}{\rho c} \qquad \text{Eqn (4.2)}$$

Where a = Thermal diffusivity ($m^2\ s^{-1}$)
k = Thermal conductivity ($W\ m^{-1}\ K^{-1}$)
c = Specific heat capacity ($J\ kg^{-1}\ K^{-1}$)
ρ = Density ($kg\ m^{-3}$)

The determination of density, specific heat capacity and thermal conductivity as a function of temperature is important to allow the calculation of the PIM feedstock's diffusivity and the minimum cooling time.

PVT data is also used to permit the evaluation of shrinkage and cooling. The amount of volumetric shrinkage can be evaluated from the changes in temperature and pressure. Volumetric shrinkage is a qualitative indication of linear shrinkage. If the mouldings shrink isotropically, the linear shrinkage will be approximately a third of the volumetric shrinkage for low shrinkage levels. Anisotropic shrinkage leads to potential warpage or cracking. The major causes of non-uniform shrinkage are density gradients in the mouldings, which are either caused by incorrect compounding or injection moulding conditions.

Thermal diffusivity is inversely proportional to density. The density can be calculated from the specific volume data. This contributes to the determination of the diffusivity data of the material together with the specific heat capacity and thermal conductivity data. Thermal diffusivity influences the rate of heat exchange from the material to the mould cavity walls. The cooling time is inversely proportional to the thermal diffusivity. The material data is used by C-Mold for the simulation of the thermal and flow dynamics of filling a mould cavity with a pressurised and heated material.

4.3 Rheology

Material rheology is the most important property used in flow simulations. The viscosity of the PIM feedstock material is dependent upon its temperature and pressure. The determination of PIM feedstock thermal properties data contributes towards the calculation of viscosity as a function of temperature and allows the tracking of viscosity, and the pressure required to fill and pack the mould cavity, allowing the simulation of mould filling, fluid flow, heat transfer, and the pressure distribution.

The study of deformational and flow processes is the science of rheology. Rheology's foundations are drawn from classical mechanics[105]. There are three simple modes of deformation. In shear deformation, a force is applied tangentially to the surface of the material as shown in figure 4.3:

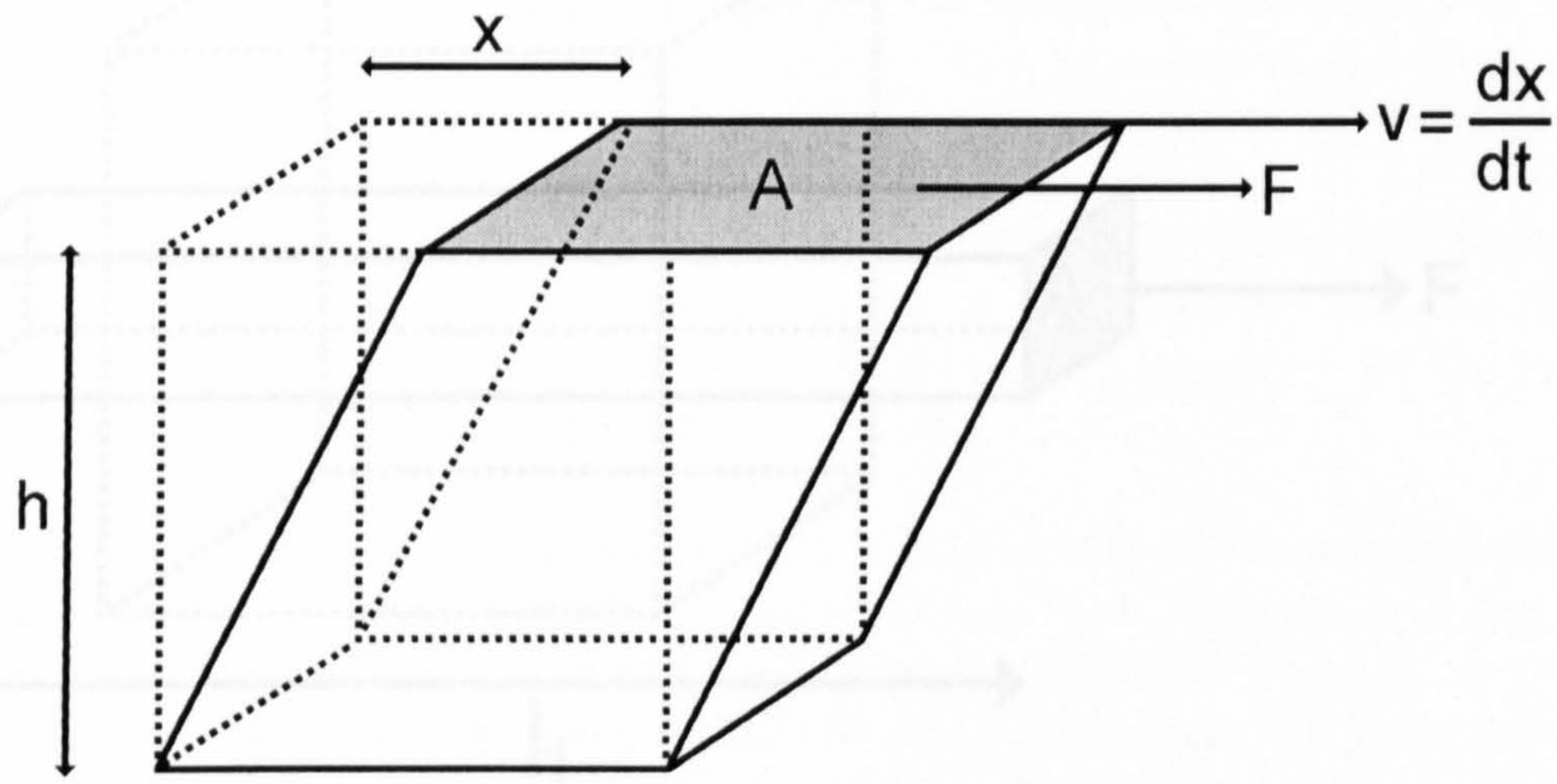

Figure 4.3 Simple shear deformation: area A and distance h remain constant during shear deformation[106]

$$\tau = \frac{F_s}{A} \qquad \text{Eqn (4.3)}$$

$$\gamma = \frac{x}{h} \qquad \text{Eqn (4.4)}$$

$$\dot{\gamma} = \frac{1}{h}\frac{dx}{dt} = \frac{v}{h} \qquad \text{Eqn (4.5)}$$

Where τ = Shear stress (Pa)
γ = Shear strain (dimensionless)
$\dot{\gamma}$ = Rate of shear strain (s^{-1})
F_s = Shear force (N)
A = Cross-sectional area (m^2)
h = Height (m)
x = Deformational horizontal distance (m)
v = Velocity (ms^{-1})

In extensional deformation, a force is applied normal to the surface of the material, as shown in figure 4.4.

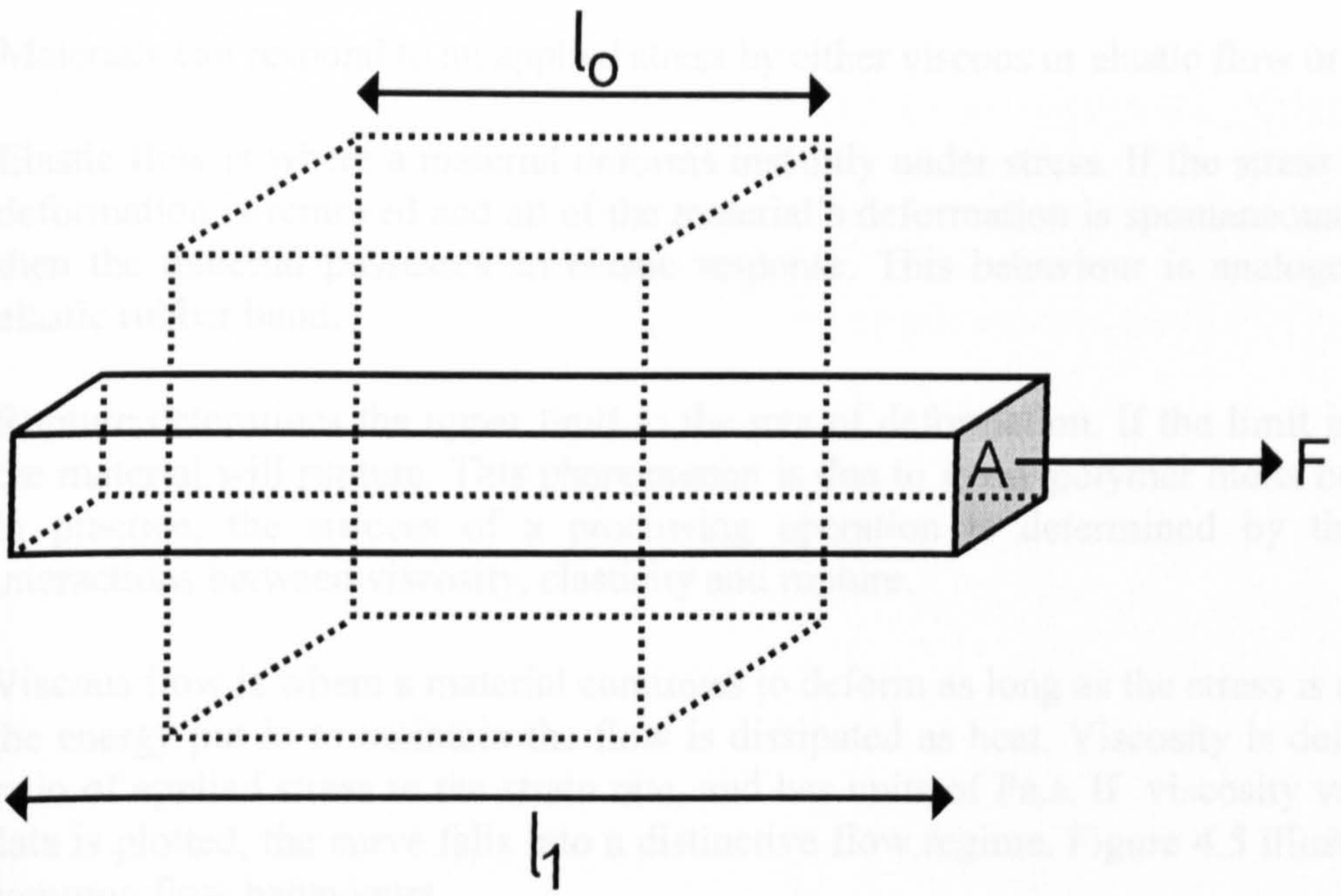

Figure 4.4 Simple extensional deformation: crossectional area A and sample length both vary during deformation.[106]

$$\sigma = \frac{F_e}{A} \qquad \text{Eqn (4.6)}$$

$$\varepsilon = \int_{l_0}^{l_1} \frac{dl}{l} = \ln \frac{l_1}{l_0} \qquad \text{Eqn (4.7)}$$

$$\dot{\varepsilon} = \frac{v}{l} \qquad \text{Eqn (4.8)}$$

Where

σ = Extensional stress (Pa)
ε = Extensional strain (dimensionless)
$\dot{\varepsilon}$ = Rate of extensional strain (s^{-1})
L_o = Initial length (m)
L_1 = Final length (m)
F_e = Extensional force (N)
A = Cross-sectional area (m^2)
v = Velocity (ms^{-1})

In bulk deformation, the applied bulk stress is applied normal to all faces. The bulk stress is the applied pressure, P, and the bulk strain is the change in volume per unit volume, and is covered by the work on PVT/specific volume.

4.3.1 Response of materials under an applied stress

Materials can respond to an applied stress by either viscous or elastic flow or by rupture.

Elastic flow is where a material deforms instantly under stress. If the stress causing the deformation is removed and all of the material's deformation is spontaneously reversed, then the material possesses an elastic response. This behaviour is analogous with an elastic rubber band.

Rupture determines the upper limit to the rate of deformation. If the limit is exceeded, the material will rupture. This phenomenon is due to many polymer melts being brittle. In practice, the success of a processing operation is determined by the complex interactions between viscosity, elasticity and rupture.

Viscous flow is where a material continues to deform as long as the stress is applied and the energy put in to maintain the flow is dissipated as heat. Viscosity is defined as the ratio of applied stress to the strain rate, and has units of Pa.s. If viscosity vs shear rate data is plotted, the curve falls into a distinctive flow regime. Figure 4.5 illustrates some common flow behaviours.

1. Newtonian flow: The viscosity remains constant and is independent of the shear rate
2. St Venant flow: The viscosity is inversely proportional to the shear rate
3. Bingham flow: The material does not start to flow until a critical shear stress value
4. Pseudoplastic flow: The viscosity decreases with increasing shear rate
5. Dilatant flow: The viscosity increases with increasing shear rate

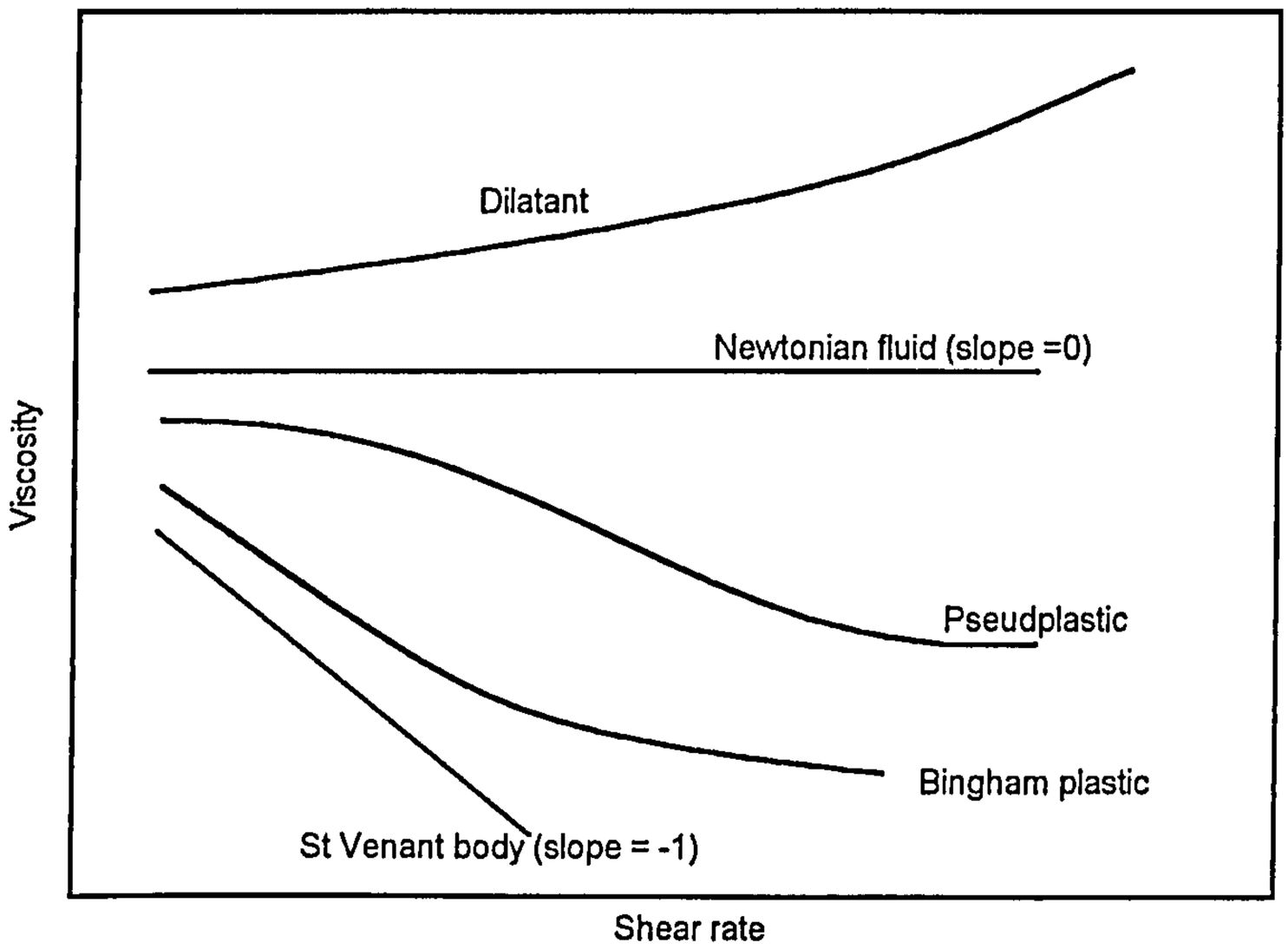

Figure 4.5 Rheological behaviour of viscous fluids[12]

Several viscosity determination techniques exists, but for the purposes of injection moulding, the capillary rheometer is the most common way of determining the viscosity

of polymer melts, as it covers the shear rate ranges and temperatures normally encountered in injection moulding.

4.3.2 Equations for apparent rheological properties and corrections for various errors

The equations for shear and extensional viscosity are derived using the Poiseuille[107][108] law for capillary flow, and are shown in equations 4.9 to 4.15.

(a) Shear Flow

Apparent shear rate	$\dot{\gamma}= \frac{4Q}{\pi R^3}$	Eqn (4.9)
Apparent shear stress	$\tau = \frac{PR}{2L}$	Eqn (4.10)
Apparent shear viscosity	$\eta = \frac{\tau}{\dot{\gamma}} = \frac{P\pi R^4}{8LQ}$	Eqn (4.11)
Pseudoplasticity index n from	$\tau \propto \dot{\gamma}^n$	Eqn (4.12)

(b) Extensional flow

Extensional stress	$\sigma = \frac{3}{8}(n+1)P_o$	Eqn (4.13)
Extensional rate	$\dot{\varepsilon}= \frac{4\eta\dot{\gamma}^2}{3(n+1)P_o}$	Eqn (4.14)
Extensional viscosity	$\lambda = \frac{\sigma}{\dot{\varepsilon}} = \frac{9(n+1)^2P_o^2}{32\eta\dot{\gamma}^2}$	Eqn (4.15)

Where

η = shear viscosity (Pa.s)
$\dot{\gamma}$ = shear rate (s^{-1})
Q = volumetric flow rate (m^3s^{-1})
R = capillary radius (m)
τ = shear stress (Pa)
P = pressure drop of the long die (Pa)
P_o = pressure drop of the orifice die (Pa)
L = length of the long die (m)
n = pseudoplasticity index (dimensionless)
σ = extensional stress (Pa)
$\dot{\varepsilon}$ = extensional rate (s^{-1})
λ = extensional viscosity (Pa.s)

There are important sources of error to consider when determining the rheology of high viscosity materials.

The Rabinowitsch[109] correction relates to the non-parabolic velocity profile, which results from the effect of pseudoplasticity of the melt, which leads to the velocity profile in the die being more plug-like than the commonly assumed parabolic form. The apparent shear rate can then be corrected using equation 4.16 instead of equation 4.9 to give the true shear rate:

True shear rate $$\dot{\gamma} = \left(\frac{3n+1}{4n}\right)\frac{4Q}{\pi R^3}$$ Eqn (4.16)

(Note: n may vary with shear rate, but is commonly assumed to be constant)

The Bagley[110] correction corrects for the pressure drop at the entry to the die and the pressure drop at the exit of the die. The pressure transducer measures the pressure in the barrel. Thus, a correction must be made to allow for the entry and exit pressure drops, allowing the calculation of the pressure drop within the die itself. This is achieved using an orifice die and using equation 4.17 instead of equation 4.10.

True shear stress $$\tau = \frac{(P-P_o)R}{2L}$$ Eqn (4.17)

A capillary rheometer may consist of two capillaries of different lengths and radii in series. During a rheology experiment, the effective length of the barrel changes. A correction[111] for the capillary flow in the barrel can be made, and the correction is not constant because the barrel length is decreasing. This effect is conveniently avoided by placing the pressure transducer to a position just above the die. The effect of piston friction becomes significant if the pressure measurement is deduced from the applied load on the piston. The use of pressure transducers avoids the effects of piston friction.

The rheological equations depend on the assumption that there is no slip at the die walls[112][113][114][115]. Slip is a phenomenon associated with particulate materials and with materials that exhibit particulate flow mechanisms such as polyvinyl chloride (PVC).

There are two types of slip, true slip and apparent slip. True slip occurs when the material does not adhere to the die walls. This implies that the material slides through the die with little or no deformation. Apparent slip occurs when there is local variation in the composition of the material, such as an excess of wax, providing a lubricating layer on the die walls. Mooney[116] states that effect of slip can be disregarded once the slip velocity is known.

Volume flow rate $$Q = \frac{\pi R^3}{4}\dot{\gamma}_{true} + \pi R^2 v$$ Eqn (4.18)

Apparent shear rate $$\dot{\gamma}_{apparent} = \frac{4Q}{\pi R^3} = \dot{\gamma}_{true} + \frac{4v}{R}$$ Eqn (4.19)

Where R = radius of die (m)
Q = volume flow rate (m^3s^{-1})
V = slip velocity (ms^{-1})
$\dot{\gamma}_{true}$ = true shear rate (s^{-1}) before Rabinowitsch correction
$\dot{\gamma}_{apparent}$ = apparent shear rate (s^{-1})

Experimental direct observation of wall slip is difficult and time consuming and provides conflicting evidence. The indirect measurement of wall slip is performed using dies of different radii and constant length to radius ratios. From equations 4.18 and 4.19, the apparent shear rate may be plotted against 1/R and an indication of the slip velocity is obtained from the gradient of the graph.

Due to the particulate nature of the feedstocks used in the course of the project, it would be useful to determine the presence of any slip and its magnitude, and its effect on the rheology of the feedstocks but the required equipment was not available. The effect of slip velocity can be included in the viscosity data that is imported into the C-Mold materials database.

The action of extruding the melt through a long, narrow die may modify the chemical or morphological structure of the extrudate. Excessive shear rates and excessively long dies should be avoided where possible.

Polymer melts are compressible, leading to variations in density. In a pressure-induced flow, there will be a pressure gradient in the die, and viscosity is dependent on pressure, leading to a viscosity gradient in the die. Shear heating takes place, leading to temperature gradients in the die and viscosity is dependent on temperature, leading to viscosity gradients in the die. Thus, the volume and viscosity are directly influenced by pressure and temperature[117].

The Bagley and Rabinowitsch corrections to the rheological data are recommended. Van Wazer[118] lists additional sources of errors in the determination of the rheology of low viscosity materials and states that these errors are mutually self-cancelling to a certain extent. The two main errors in low viscosity material rheology determination are material leakage past the piston and die seals and the accuracy of the die diameter. Smaller diameter dies have to be used for such materials, as they flow through normal sized dies under the effect of gravity.

4.3.3 Effect of powder loading, particle size and viscosity of polymer - wax-based binder systems on the feedstock viscosity

The viscosity of the compound is affected by the ratios of the binder materials used. There have been several attempts to mathematically model the combined viscosity as a function of the individual binder component ratios. All binder systems are frequently based on two important major groups of ingredients, polymers and waxes, with minor additions of lubricants, surfactants and coupling agents

The viscosity of a binder system can be measured experimentally. Each time the ratios of the constituents are changed in the binder system, the binder system has to be analysed again for its new rheological behaviour. Since the individual components remain unchanged, a method of calculating the binder system viscosity as a function of mass or volume ratios could be used to reduce the need for repeated time consuming rheological determination every time the binder composition is changed.

Attempts have been made by Shah and Nunn[119] and Kaanevskii et al. [120] to calculate the resulting viscosity of a binder system from the viscosities of the individual binder components using a logarithmic additivity rule as illustrated by equation 4.20 and 4.21.

The viscosity of the n-component binder is found by:

$$\ln \eta_{binder} = \sum_{n=1}^{n=N} \left(\frac{V_n}{V_{binder}} . \ln \eta_n \right) \qquad \text{Eqn (4.20)}$$

Rearranging equation 4.20 yields:

$$\eta_{binder} = e^{\left(\sum_{n=1}^{n=N} \left(\frac{V_n}{V_{binder}} . \ln \eta_n \right) \right)} \qquad \text{Eqn (4.21)}$$

where η_{binder} is the viscosity of the binder system (Pa.s)
η_n is the viscosity of the nth component (Pa.s)
V_{binder} is the volume of the binder system (m^3)
V_n is the volume of the nth component (m^3)

There are several difficulties with applying this equation to the actual rheology of binder and powder systems. It is very difficult in practice to determine the viscosity of say, paraffin wax, as it has a very low viscosity in the molten state and it is practically difficult to use a capillary rheometer with such a low viscosity material.

Another consideration is if any of the components are soluble or if its behaviour is altered by the presence of another component then the overall viscosity will be altered.

Additionally, the polymer viscosity is influenced by the temperature and shear rate, so equation 4.21 would only be valid for fixed temperatures and fixed shear rates.

Every time the powder volume loading is changed, the feedstock viscosity is altered. Since the individual components remain unchanged, a method of calculating the feedstock viscosity as a function of powder volume loading could be used to reduce the need for repeated time consuming rheological determination every time the powder volume loading is changed.

Metzner[121] and Mutsuddy and Ford[12, pp 128-135] have attempted to model the resulting viscosity of a feedstock as a function of the viscosity of the binder system and the powder solids loading fraction using mathematical models. To illustrate, the Metzner model is considered further.

$$\eta_{feedstock} = \eta_{binder} . \left(1 - \frac{\Phi}{\Phi_c}\right)^{-2} \qquad \text{Eqn (4.22)}$$

Where:

$\eta_{feedstock}$ = viscosity of the particulate filled system (Pa.s)
η_{binder} = viscosity of the binder system (Pa.s)
Φ = fractional solids loading in the feedstock
Φ_c = critical solids loading

The critical solids loading can be calculated from the tap density and true density of the powder. However, the assumptions made are that all the powder particles have identical shapes and diameters. Since the viscosity of the binder system varies with temperature and shear rate, it is necessary to state what shear rate and temperature the calculation is being made at. Equation 4.22 does not take into account that segregation of the binder components may occur or that the powder may agglomerate, hence affecting the viscosity. Equation 4.22 also does not take into account that as the powder volume loading increases, the number of particle to particle contacts increases, implying a greater degree of mechanical interlocking.

Equations 4.21 and 4.22 can be combined to give a first pass mathematical model to permit the calculation of the feedstock viscosity as a function of the powder loading and the individual binder component viscosities. Equation 4.23 represents an example of a first pass model.

$$\eta_{feedstock} = \left(1 - \frac{\Phi}{\Phi_c}\right)^{-2} . e^{\left(\sum_{n=1}^{n=N} \left(\frac{V_n}{V_{binder}} . \ln \eta_n\right)\right)} \qquad \text{Eqn (4.23)}$$

4.3.4 Mathematical modelling of rheological behaviour

The C-Mold software is able to use several mathematical equations to model the shear viscosity as a function of temperature and shear rate. There are limitations to each model as discussed below.

The power law-exponential model is only sufficiently accurate at high shear rates as it is mathematically unable to model the Newtonian domain of the shear viscosity curves. Pressure effects are not taken into account in the model and the model is not recommended where accuracy is important.

The Cross-exponential model and the Carreau-exponential model take into account the effects of temperature, shear rate and pressure on the viscosity. They are also able to model the Newtonian and shear thinning regimes which are typical of many pseudoplastics. However, these models do not take into account the glass transition temperature, so these models are not appropriate for post filling analyses. Their usefulness is limited to the mould filling stage, as the bulk of the polymer is in the vicinity of the processing temperature, which in most cases is more than 100°C away from the glass transition temperature.

The Carreau-WLF model and the Cross-WLF model take into account the effects of temperature, pressure and shear rate on the viscosity. They are also able to model Newtonian and shear thinning regimes which are typical of many pseudoplastics. In addition, the models take into account the effects of pressure on the zero shear rate viscosity, the glass transition temperature and lend themselves to post-filling simulations.

The melt flow index (MFI) is a single value parameter, which provides an approximate measure of viscosity at one temperature and a single shear rate. The effects of temperature, pressure, shear rate and glass transition temperature are ignored and it is unable to model Newtonian or shear thinning regimes.

The most preferred model for use with C-Mold is the 7-constant Cross-WLF model, which is used to mathematically describe the viscosity as a function of shear rate, temperature and pressure. The equation also allows for the two most common flow behaviours typical of most polymers, Newtonian and shear thinning regimes. Viscosity data at different temperatures are easily obtained from a capillary extrusion rheometer.

For the purposes of the project, only the Cross-WLF model will be studied in greater detail. The Cross-WLF equation combines the Cross equation and the WLF equation. Williams et al.[122] present the derivation of the WLF equation from the Doolittle equation. Equation 4.24 illustrates the general WLF equation.

$$\log\left(\frac{\eta}{\eta_g}\right) = \frac{-C_1(T-T_g)}{C_2+T-T_g} \qquad \text{Eqn (4.24)}$$

Where η = Viscosity at temperature T (Pa.s)

η_g = Viscosity at the glass transition temperature T_g (Pa.s)
T_g = Transition temperature (°C)
T = Temperature (°C)
C_1 = WLF constant approximated to 17.44 for most polymers (dimensionless)
C_2 = WLF constant, approximated to 51.6 for most polymers (°C)

The WLF equation can be used to calculate viscosity as a function of temperature, as long as the transition temperature, and the viscosity at the transition temperature are known for the material. Cross[123] presented an equation to model the non-Newtonian viscosity curve for the shear rate range of zero to infinity.

$$\eta(\dot{\gamma}) = \eta_\infty + \frac{\eta_o - \eta_\infty}{1+\left(\frac{\dot{\gamma}}{\tau^*}\right)^{(1-n)}} \qquad \text{Eqn (4.25)}$$

Where $\eta(\dot{\gamma})$ = Viscosity at shear rate $\dot{\gamma}$ (Pa.s)
η_o = Viscosity at zero shear rate (Pa.s)
η_∞ = Viscosity at infinite shear rate (Pa.s)
$\dot{\gamma}$ = Shear rate (s^{-1})
τ^* = Critical shear stress at which pseudoplasticity starts. (Pa)
n = Pseudoplasticity index (dimensionless)

The basic Cross equation does not take into account the effect of temperature or pressure on the shear viscosity and a general function, $\eta_o(T,p)$ is substituted into the Cross equation, which yields equation 4.26. The function, $\eta_o(T,p)$ describes the zero shear viscosity as a function of temperature and pressure.

$$\eta(T,\dot{\gamma},p) = \frac{\eta_o(T,p)}{1+\left(\frac{\eta_o(T,p)\dot{\gamma}}{\tau^*}\right)^{(1-n)}} \qquad \text{Eqn (4.26)}$$

The Cross model does not take into account the transition temperature, and the WLF equation does not take into account the effect of pressure or shear rate on the viscosity. It is mathematically advantageous to combine equation 4.24 and equation 4.26 to obtain the Cross-WLF equation:

$$\eta(T,\dot{\gamma},p) = \frac{\eta_o(T,p)}{1+\left(\frac{\eta_o(T,p)\dot{\gamma}}{\tau^*}\right)^{(1-n)}} \qquad \text{Eqn (4.27)}$$

$$\eta_o(T,p) = D_1 e^{\left[-\frac{A_1(T-T^*)}{A_2+T-T^*}\right]}$$ Eqn (4.28)

$$T^* = D_2 + D_3 p$$ Eqn (4.29)

$$A_2 = \tilde{A}_2 + D_3 p$$ Eqn (4.30)

Where

n = pseudoplasticity index of the shear thinning region (dimensionless)
$\eta(T,\dot{\gamma},p)$= viscosity at temperature T, pressure p and shear rate $\dot{\gamma}$ (Pa.s)
$\eta_o(T,p)$ = viscosity at zero shear, at temperature T and pressure p (Pa.s)
$\dot{\gamma}$ = shear rate (s^{-1})
T = temperature (K)
P = pressure (Pa)
T^* = glass transition temperature as a function of pressure (K)
D_1 = normalisation constant (Pa.s)
D_2 = glass transition temperature at zero pressure (K)
D_3 = glass transition temperature dependency on pressure constant (KPa^{-1})
A_1 = WLF constant (dimensionless)
$\tilde{A}_2$ = WLF constant (K)

Substituting equations 4.29 and 4.30 into 4.28 yields:

$$\eta_o(T,p) = D_1 e^{\left[\frac{-A_1(T-D_2-D_3p)}{\tilde{A}_2+T-D_2}\right]}$$ Eqn (4.31)

Substituting equation 4.31 into equation 4.27 yields equation 4.32, which is the full Cross-WLF equation for modelling the viscosity as a function of temperature and pressure, using 7 constants.

$$\eta(T,\dot{\gamma},p) = \frac{D_1 e^{\left[\frac{-A_1(T-D_2-D_3p)}{\tilde{A}_2+T-D_2}\right]}}{1+\left(\frac{D_1 e^{\left[\frac{-A_1(T-D_2-D_3p)}{\tilde{A}_2+T-D_2}\right]}\dot{\gamma}}{\tau^*}\right)^{(1-n)}}$$ Eqn (4.32)

The Cross-WLF equation is the preferred rheological model for the purposes of computer modelling. If the effect of pressure on viscosity is not taken into account, then it is convenient to set $D_3 = 0\ KPa^{-1}$.

4.3.5 Experimental determination of rheology

There are many techniques for the determination of the rheological behaviour of materials. The most popular technique is capillary rheometry, illustrated in figure 4.6. The capillary rheometer is used to measure pressure as a function of piston speed at a set temperature, as the volumetric flow rate can be determined from the piston's speed and cross-sectional area. The volumetric flow rate can be used along with the capillary die's length and diameter to calculate the shear rate, and the pressure can be used to calculate the shear stress. Hence the viscosity as a function of shear rate can be determined for a selection of test temperatures.

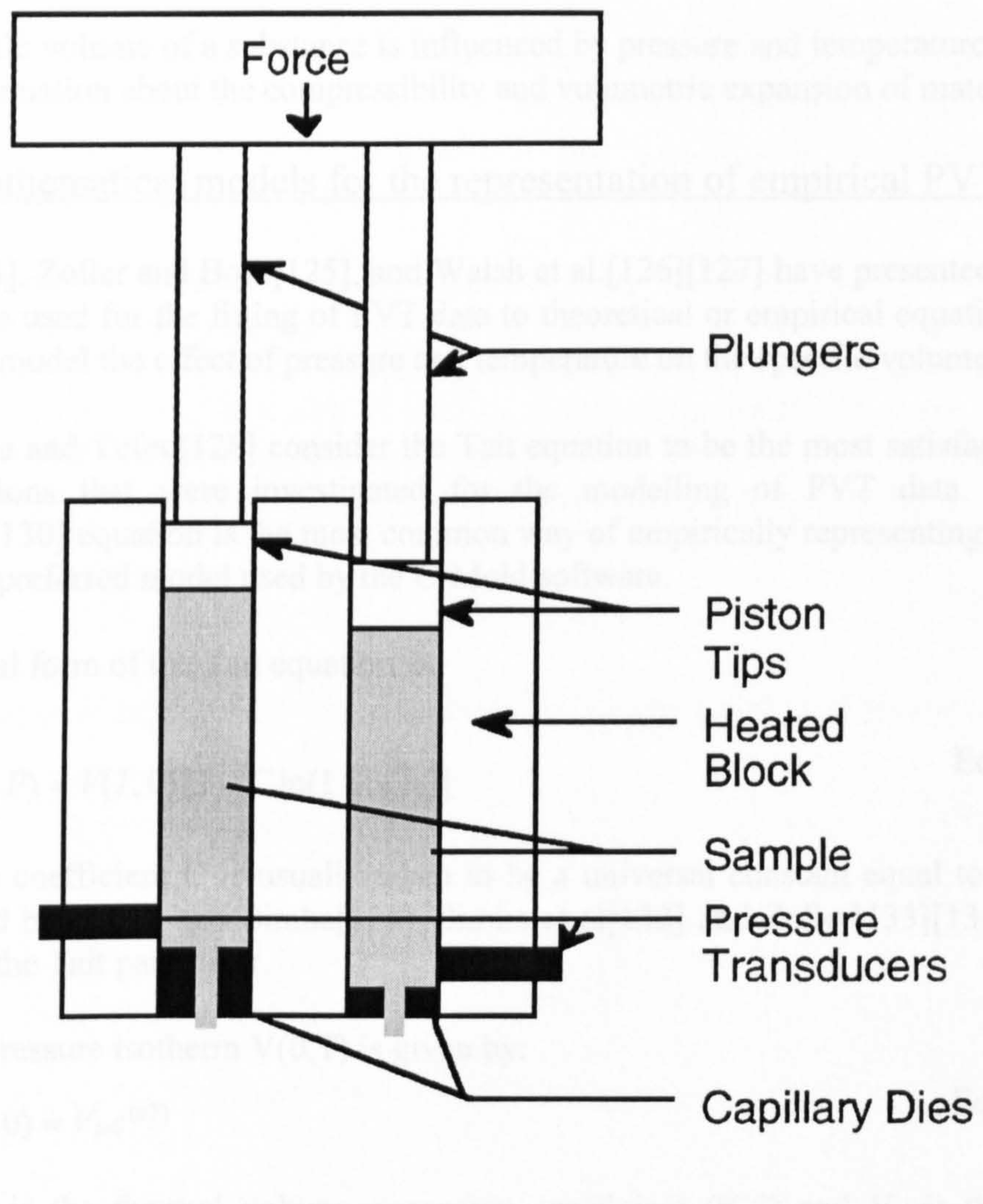

Figure 4.6 A twin barrelled capillary rheometer

4.4 Pressure - volume - temperature (PVT)

The specific volume of a substance is defined to be the volume per unit mass, whereas density is defined to be the mass per unit volume. The specific volume of a substance is the reciprocal of its density, shown by equation 4.33.

$$s_v = \frac{v}{m} \qquad \text{Eqn (4.33)}$$

Where s_v = Specific volume (m^3kg^{-1})
m = Mass (kg)
v = Volume (m^3)

The specific volume of a substance is influenced by pressure and temperature. PVT data gives information about the compressibility and volumetric expansion of materials.

4.4.1 Mathematical models for the representation of empirical PVT data

Zoller[124], Zoller and Bolli[125], and Walsh et al.[126][127] have presented equations that can be used for the fitting of PVT data to theoretical or empirical equations. These equations model the effect of pressure and temperature on the specific volume.

Le Neindre and Tufeu[128] consider the Tait equation to be the most satisfactory of all the equations that were investigated for the modelling of PVT data. Thus, the Tait[129][130] equation is the most common way of empirically representing PVT data, and is the preferred model used by the C-Mold software.

The general form of the Tait equation is:

$$V(T,P) = V(T,0)\{1 - C\ln(1 + \frac{P}{B(T)})\} \qquad \text{Eqn (4.34)}$$

Where the coefficient C is usually taken to be a universal constant equal to 0.0894 as determined by Nanda and Simha[131], Simha et al[132] and Zoller[133][134]. B(T) is known as the Tait parameter.

The zero pressure isotherm V(0,T) is given by:

$$V(T,0) = V_0 e^{(aT)} \qquad \text{Eqn (4.35)}$$

Where a is the thermal volume expansion coefficient ($^oC^{-1}$) and V_0 is the specific volume at 0°C.

The Tait parameter B(T) is usually given by:

$$B(T) = b_0 e^{(-b_1 T)} \qquad \text{Eqn (4.36)}$$

Where b_o is the compressibility at 0°C, and b_1 is a constant relating compressibility to temperature.

The Tait equation is normally a four parameter representation of the experimental PVT data, (V_0, a, b_0, b_1). Alternatively, if it is found that equations 4.35 and 4.36 do not model the experimental data accurately, then polynomial expressions, equations 4.37 and 4.38 could be substituted for equations 4.35 and 4.36.

$$V(T,0) = a_0 + a_1 T + a_2 T^2 \qquad \text{Eqn (4.37)}$$

$$B(T) = b_0 + b_1 T + b_2 T^2 \qquad \text{Eqn (4.38)}$$

The Tait equation has two major shortcomings. Firstly, it makes no allowance for any volume change that may occur at a change of state or at what temperature the change of state occurs. Secondly, it assumes that the thermal expansivities and compressibilities are exactly the same either side of a change of state. (eg for both the solid domain and molten domain.) This is often not the case experimentally.

In the computer simulation of the injection moulding cycle, the specific volume varies with temperature and pressure. The C-Mold software uses a 13 constant, 2-domain modified Tait equation, which addresses the shortcomings of the Tait equation. The 2-domain modified Tait equation is used to calculate the specific volume for a given temperature and pressure. Each element in the finite element mesh can have its own specific volume calculated from that element's pressure and temperature.

$$S_v(T,P) = S_v(T,0)\left(1 - C\ln\left(1 + \frac{P}{B(T)}\right)\right) + S_{v_t}(T,P) \qquad \text{Eqn (4.39)}$$

The transition temperature $T_t(p)$ is assumed to be a linear function of pressure:

$$T_t(P) = b_5 + b_6 P \qquad \text{Eqn (4.40)}$$

If $T<T_t(p)$

$$S_v(T,0) = b_{1_s} + b_{2_s}\bar{T} \qquad \text{Eqn (4.41)}$$

$$B(T) = b_{3_s}.e^{(-b_{4_s}\bar{T})} \qquad \text{Eqn (4.42)}$$

$$S_{v,t}(T,P) = b_7 e^{(b_8\bar{T} - b_9 P)} \qquad \text{Eqn (4.43}$$

If $T>T_t(p)$

$$S_v(T,0) = b_{1_m} + b_{2_m}\bar{T} \qquad \text{Eqn (4.44)}$$

$$B(T) = b_{3_m} e^{(-b_{4_m}\bar{T})} \qquad \text{Eqn (4.45)}$$

$$S_{v,t}(T,P) = 0 \qquad \text{Eqn (4.46)}$$

With

$$\bar{T} = T - b_5 \qquad \text{Eqn (4.47)}$$

Where

b_{1_s} = Solid domain specific volume at the transition temperature (m^3kg^{-1})
b_{2_s} = Solid domain thermal expansion coefficient (m^3kg^{-1} K^{-1})
b_{3_s}= Solid domain compressibility at transition temperature (Pa)
b_{4_s} = Solid domain dependency of compressibility on temperature (K^{-1})
b_{1_m}= Molten domain specific volume at the transition temperature (m^3kg^{-1})
b_{2_m}= Molten domain thermal expansion coefficient (m^3kg^{-1} K^{-1})
b_{3_m}= Molten domain compressibility at transition temperature (Pa)
b_{4_m}= Molten domain dependency of compressibility on temperature (K^{-1})
b_5= Transition temperature at zero pressure (K)
b_6 = Pressure sensitivity on the transition temperature ($K\ Pa^{-1}$)
b_7= Specific volume change at transition temperature at zero pressure (m^3kg^{-1})
b_8= Specific volume change temperature sensitivity at the transition point (K^{-1})
b_9 = Specific volume change pressure sensitivity at the transition point (Pa^{-1})

Substituting equation 4.47 into equations 4.41, 4.42 and 4.43 and then substituting the resulting equations into equation 4.39 yields for the condition $T_t(p) < b_5 + b_6P$:

$$S_v(T,P) = (b_{1_s} + b_{2_s}(T - b_5)).(1 - 0.0894\ln(1 + \frac{P}{b_{3_s}.e^{(-b_{4_s}(T-b_5))}})) + b_7.e^{(b_8(T-b_5)-b_9P)}$$

Eqn (4.48

Substituting equation 4.40 into equations 4.44 and 4.45, then substituting the resulting equations and equation 4.46 into equation 4.39 yields for the condition $Tt(p) > b_5 + b_6P$:

$$S_v(T,P) = (b_{1_m} + b_{2_m}(T - b_5)).(1 - 0.0894\ln(1 + \frac{P}{b_{3_m}.e^{(-b_{4_m}(T-b_5))}}))$$

Eqn (4.49

Equations 4.48 and 4.49 represent the modified 2-domain Tait model used within C-Mold to model the PVT behaviour of the materials being injection moulded.

It is pointed out that the transition temperature is influenced by pressure, temperature ramp rate and the direction of the temperature change. Matveyev and Askadskii[135] have demonstrated that the transition temperature is dependent on the cooling. Oehmke and Wiegmann[136] carried out experiments that show that the cooling rate influenced the shape and level of the PVT curves and the transition temperature is a function of cooling rate. Toratani and Takamizawa[137] have demonstrated that the transition temperature is influenced by pressure. It is pointed out that the presence of other components such as the waxes or powders may act as nucleating agents and affect the transition temperature of the polymer. Benediktov et al.[138] state that nucleating fillers raise the glass transition temperature. The modified 2-domain Tait equation does not take into account the effects of temperature ramp rate, the temperature change direction or the effect that any nucleating agents have if they are present in the material.

4.4.2 PVT rule of mixtures

Zoller and Hoehn[139] and Jain et al.[140] have carried out research into the PVT properties of polymer binary blends. A rule of mixtures approach was used. They reported that the specific volume of the molten blends at constant pressure showed a virtually linear dependence on the composition ratio of the components. In addition, the properties of the solid blends could not be modelled by simple functions of composition. There are no reported instances in the open literature of the determination of the PVT behaviour of PIM feedstocks, although this is an important material property from the computer modelling point of view. However, the PVT curves for polymers are widely available in the open literature. For example, a paper by Rodgers[141] presents the PVT relationships for 56 polymers.

4.4.3 Experimental determination of PVT

Two scientific techniques are available to measure experimentally the specific volume of a material as a function of temperature and pressure. Figure 4.7 illustrates the direct method of determining PVT behaviour, and comprises a piston and cylinder system, which is used to apply the pressure directly to the sample under test, surrounded by a controllable heating system. Piston deflections are used to measure the magnitude of the volumetric change. Since the volume of the cell and the mass of the sample are known, the absolute specific volume can be measured as a function of applied pressure and temperature.

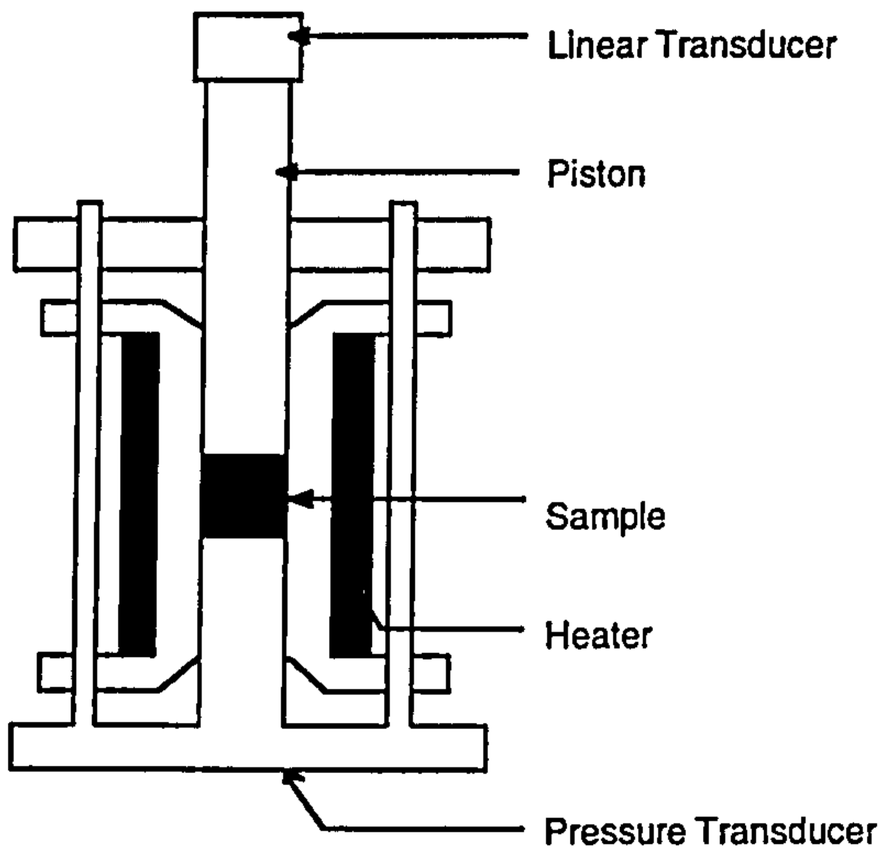

Figure 4.7 Schematic of direct PVT piston and barrel measuring equipment [142]

Figure 4.8 illustrates the indirect method of PVT determination, which comprises a confining fluid such as mercury. The confining fluid is used to apply the pressure hydrostatically to the test sample. The confining fluid and sample are enclosed in a chamber fitted with a bellows. The apparatus is surrounded by a controllable heating system. The bellows allow applied pressure to be transmitted through to the confining fluid. The deflection of the bellows is used to calculate the change in volume. Since this

method measures volume changes, a reference density at atmospheric pressure and at a known temperature, measured by an independent method such as Archimedes principle is needed. A correction for the thermal expansion and compressibility of the confining fluid must be made.

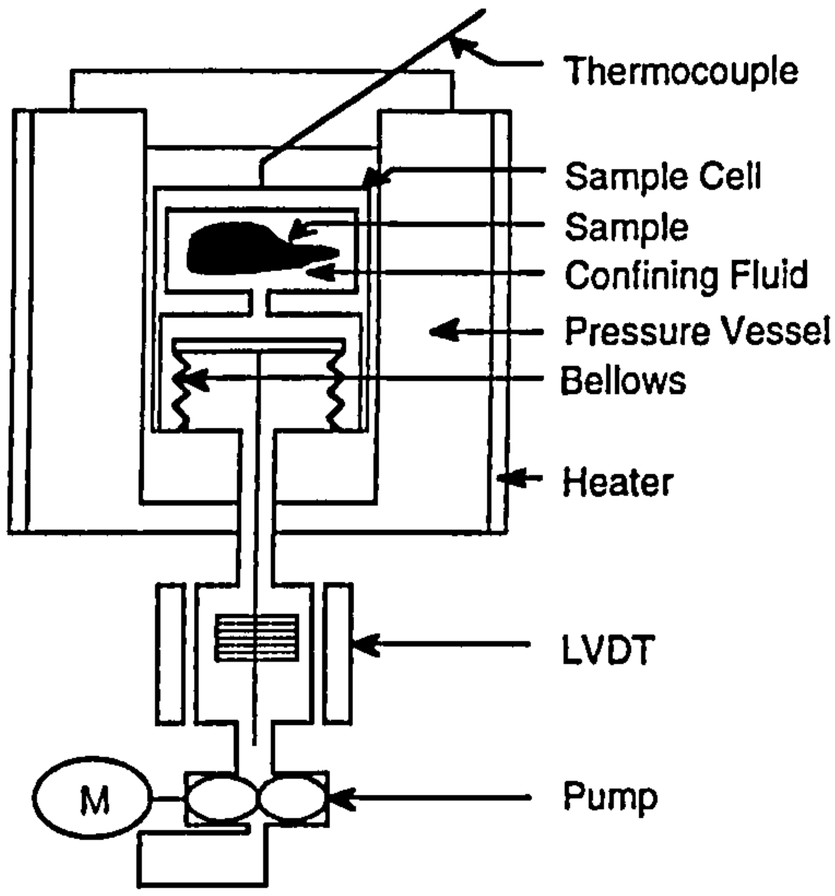

Figure 4.8 Schematic diagram of indirect PVT confining fluid measuring equipment [142]

There are four main problems with the piston and cylinder method for the determination of PVT, reported by Zoller and Fakhreddine[143] in their critique of PVT measuring equipment. The first is the leakage of the test sample past the piston tip seals. This implies a reduction of the test volume under pressure. The likelihood of such an occurrence increases with decreasing test sample viscosity. Secondly, the state of stress for a sample in the solid state is not hydrostatic, as it is for the molten or liquid state, leading to potentially misleading results. This limits all experiments to the molten/liquid domain. Thirdly, if the sample solidifies in the barrel, adhesion may occur between the barrel walls and the sample or freezing the piston to the barrel wall, leading to uncertainties in the applied pressure. Fourthly, if the piston tip seal to barrel wall friction is significant, uncertainties will be introduced in the applied pressure on the test sample. This can be overcome by fitting a pressure transducer to the barrel wall, in intimate contact with the test sample, as in the Rosand RH7-2 capilliary rheometer. More recently, Chiu and Liu[144] have presented a method of determining PVT data in the molten domain, using an injection moulding machine, where the barrel is used as a pressure chamber, and using barrel temperature, hydraulic pressure, and injection screw position data for calculating the PVT data for the polymer under test.

4.5 Specific heat capacity vs. temperature

The specific heat capacity is defined as the amount of heat energy required to raise the temperature of 1 kilogram of substance by 1 Kelvin. This allows C-Mold to evaluate the amount of heat energy that is removed per unit mass per unit temperature during the cooling part of the injection moulding cycle. The definition of specific heat capacity leads to equation 4.50:

$$c = \frac{Q}{m(T_2 - T_1)} \qquad \text{Eqn (4.50)}$$

where c is the specific heat capacity in J kg^{-1} K^{-1}
Q is the amount of heat energy in joules (J)
m is the mass of the substance in kilograms (kg)
T_1 is the final temperature in Kelvin (K)
T_2 is the initial temperature in Kelvin (K)

4.5.1 Mathematical models for specific heat capacity

The specific heat capacity of a feedstock can be measured experimentally. Each time the ratios of the constituents are changed in the feedstock, it has to be analysed again for its new specific heat capacity, even though the components remain the same. Since the specific heat capacity of the individual components remain unchanged, a rule of mixtures approach could be developed to reduce the need for repeated time consuming specific heat capacity determination each time the feedstock composition is modified.

The open literature revealed many studies into the specific heat capacity of filled composite systems. Ishida and Rimdusit[145] have studied the effect of particle morphology, loading, surface area, and size on the composite specific heat capacity. They report that the powder loading was the only factor to affect the specific heat capacity of the filled system. Additionally, they also reported that the specific heat capacity of the filled system can be predicted by the rule of mixtures with an error within $\pm$ 1%. Krupa and Chodak[146] observed that there was a non-additive dependence of specific heat capacity on the concentration of the filler powder.

4.5.2 Determination of specific heat capacity

There are various experimental methods for the determination of specific heat capacity. For the purposes of the present work, only the method that was used during the experimental work phase will be described further.

The specific heat capacity of a material is determined using differential scanning calorimetry, (DSC) as set out in ASTM E1269. In DSC, the heat flow difference between the test sample and an inert reference is measured as a function of time and temperature, in a controlled environment. The heat flux cell design, shown in figure 4.9, is used by TA instruments to determine specific heat capacity.

In the heat flux cell, the sample is encapsulated in an aluminium pan, and is placed along with an inert reference (an empty encapsulated aluminium pan) on two raised platforms on a constantan alloy disc. The constantan alloy disc is the primary means of heat transfer to and from the aluminium pans. The temperature of the sample and the inert reference are measured by area thermocouples formed by the junction of the constantan disc and chromel wafers which cover the bottom of the raised portions of the constantan disc. The thermal equivalent of Ohm's law is used to determine the differential heat flow as shown by equation 4.51.

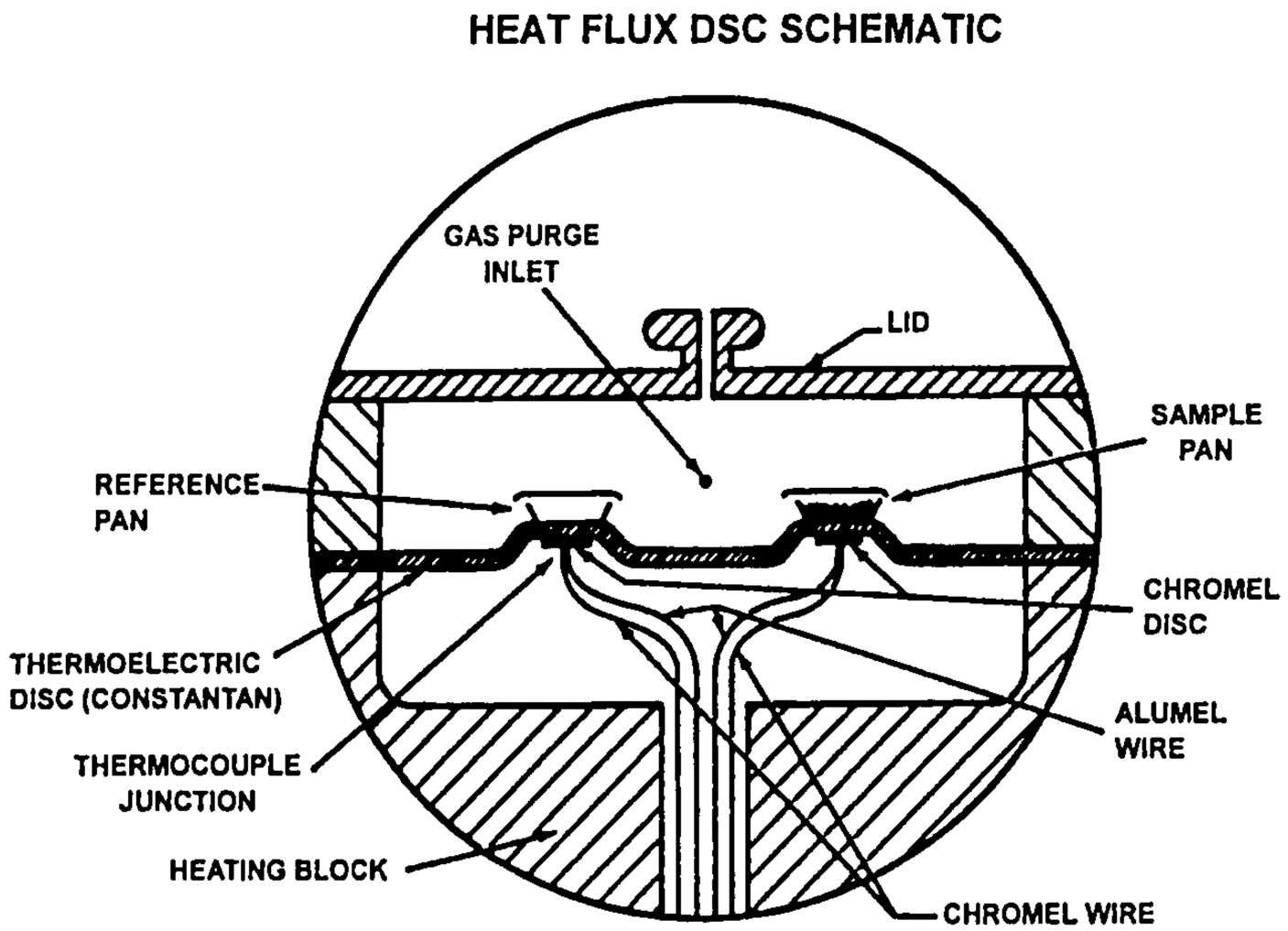

Figure 4.9 Schematic of the heat flux cell[147]

$$\frac{\Delta Q}{\Delta t} = \frac{T_s - T_r}{R_D} \qquad \text{Eqn (4.51)}$$

Where $\frac{\Delta Q}{\Delta t}$ is the differential heat flow rate in Joules per second (Js^{-1})
R_D is the thermal resistance of the constantan disc ($J^{-1}s.K$)
T_s is the temperature of the test sample in Kelvin (K)
T_r is the temperature of the reference sample in Kelvin (K)

The difference in heat flow between a sample and an inert reference is calculated and recorded as a function of time and temperature. A purge gas, usually nitrogen or argon is used to maximise thermal stability within the heat flux cell. The general equation that describes the heat flow at any point in DSC is:

$$\frac{\Delta Q}{\Delta t} = C_p\beta + f(T, t) \qquad \text{Eqn (4.52)}$$

Where C_p is the heat capacity, ($J.°C^{-1}$)
β is the heating rate, ($°Cs^{-1}$)
$\frac{\Delta Q}{\Delta t}$ is the total heat flow, (Js^{-1})

$f(T,t)$ is an equation describing the heat flow from kinetic processes (absolute temperature and time dependent processes such as melting/freezing etc). Since the mass of the sample is known, the heat capacity data obtained can be divided by the sample mass to obtain the specific heat capacity of the sample.

The main disadvantage with DSC is that the sensitivity and resolution are both affected by the linear heating/cooling rate, and that there is a trade-off between the required resolution and required sensitivity. This implies that the determination of heat capacity using standard DSC requires multiple experiments with different heating rates and considerable operator expertise to achieve results with sufficient sensitivity and resolution.

A further extension of DSC, is modulated DSC (MDSC)[148]. In DSC experiments, a constant linear heating or cooling rate is used, whereas in MDSC the linear heating or cooling rate is modulated by some form of perturbation. A mathematical treatment[149] is performed to separate the calorimetric responses to the perturbation and the underlying linear thermal ramp rate. In MDSC the perturbation is of a sinusoidal form, as it is the simplest modulation achievable in practice and is the easiest to treat mathematically for the purposes of the separation of the individual calorimetric responses to the linear and modulating temperature profile.

MDSC allows the sample to be subjected to two essentially different heating/cooling rates simultaneously, allowing good resolution and good sensitivity to be achieved in the same experiment. This means that only one experiment is required for the determination of specific heat capacity[150] vs temperature for the test sample. It is recommended[147, pp15-17] that the underlying heating rate used should be between 1 to $5°Cmin^{-1}$, the modulation amplitude used should be between 0.5°C to 3°C and the modulation period should be between 40 to 100s.

The TA Instrument produces complex specific heat capacity data, which is the net result of real and imaginary components. The real component is directly attributable to the true specific heat capacity of the sample. The imaginary component arises from the other kinetic processes occurring within the sample such as crystallisation, melting and latent heat of fusion.

Care must be taken to avoid the production of volatiles or gaseous degradation products from the sample being subjected to the temperature profile. The presence of volatiles could contaminate the MDSC cell and introduce experimental errors. Care must be taken in selecting a suitable temperature profile that minimises potential for the production of volatiles or gaseous degradation products.

4.6 Thermal conductivity

The thermal conductivity of a substance is defined as the rate of flow of thermal energy through the cross-sectional area of the substance in the presence of a thermal gradient. This definition leads to equation 4.53:

$$k = -\frac{1}{A} \cdot \frac{\partial Q}{\partial t} \cdot \frac{\Delta x}{\Delta T} \qquad \text{Eqn (4.53)}$$

Where

A = crossectional area (m^2)
$\frac{\partial Q}{\partial t}$ = rate of flow of thermal energy (W)
$\frac{\Delta x}{\Delta T}$ = temperature difference T across thickness x (mK^{-1})
k = thermal conductivity ($Wm^{-1}K^{-1}$)

4.6.1 Feedstock thermal conductivity

The open literature revealed many attempts at the determination of thermal conductivity of highly filled polymer systems as a function of filler volume loading. Sharkawy[151] investigated the effect of adding calcium carbonate to polyvinyl chloride. Wong[152] investigated the effect of adding silica, alumina or aluminium nitride to epoxy resin. Tavman[153][154] investigated the effect of adding tin or aluminium powder to polyethylene. Maiti and Ghosh[155] investigated the effect of adding silver powder to polypropylene. Agari and Uno[156] investigated the effect of adding carbon to polyethylene and polyvinyl chloride. They collectively conclude that as the filler volume loading increases, so does the thermal conductivity. At low volume loadings, the thermal conductivity increase was very gradual. At higher filler fractions, the filler particles tend to form agglomerates and conductive chains in the direction of heat flow, resulting in a rapid increase in thermal conductivity.

Kowalski et al.[157] indirectly measured the thermal conductivity of a 60% by volume of a stainless steel 316L feedstock, by using the laser flash method which produces thermal diffusivity data. The thermal conductivity was calculated from the thermal diffusivity data, the feedstock density, and the feedstock's specific heat capacity. Kowalski et al. assumed that the density of the feedstock was constant over the temperature range of 100°C to 200°C. This is not the case as the feedstock's volume loading (and hence its density) will change as a function of temperature, because the binder system's thermal expansivity is higher than the powder thermal expansivity. There is also a change in volume when a material undergoes a change of state. Kowalski et al. also assumed that the specific heat capacity was constant over the test temperature range of 100°C to 200°C. Specific heat capacity varies with temperature and with changes of state. Many binder systems have several melting points from ambient temperature to the processing temperature due to their multi-component nature.

4.6.2 Thermal conductivity models

Many thermal conductivity models are available in the literature that allow the calculation of the thermal conductivity of a composite, based on the thermal conductivity of the individual components. All of the theoretical models are based on a particulate - matrix system, and for ease of comparison, the symbols used by the various models have been changed to use a common symbol set as follows:

Matrix (binder) thermal conductivity:	K_b	$(Wm^{-1}K^{-1})$
Particulate (powder) thermal conductivity:	K_p	$(Wm^{-1}K^{-1})$
Feedstock thermal conductivity:	K_f	$(Wm^{-1}K^{-1})$
Powder volume loading ratio	ε'	
Binder volume loading ratio	ε	
Ratio of K_p/K_b	ν	

Note that $\varepsilon' + \varepsilon = 1$

The models and their equations are listed below. Each model was tested for the value of the composite thermal conductivity for two powder volume loadings, 0% and 100%. The models should evaluate to the same thermal conductivity values of the binder system and powder system respectively.

(a) Imura and Takegoshi [158]

$$\frac{K_f}{K_b} = p + \frac{1-p}{\Phi + \frac{1-\Phi}{\nu}} \qquad \text{Eqn (4.54)}$$

Where $p = \frac{\varepsilon - \phi}{1-\Phi}$ Eqn (4.55)

and $\Phi = 0.3\varepsilon^{1.6}\nu^{-0.0044}$ Eqn (4.56)

Imura and Takegoshi developed their thermal conductivity model in connection with their investigation of the effect of gas pressure and different gases in packed beds. Their experimental work consisted of using glass spheres, bronze spheres and copper spheres in a choice of three gases, air, helium and freon 12. For the purpose of this work, the effect of pressure was removed from the Imura-Takegoshi model, as there are no gases in the feedstocks and hence they can be assumed to be incompressible.

(b) Kampf and Karsten [159]

$$\frac{K_f}{K_b} = 1 - \frac{(1-\varepsilon)(\frac{1}{\nu}-1)}{1+(1-\varepsilon)^{\frac{1}{3}}(\frac{1}{\nu}-1)} \qquad \text{Eqn (4.57)}$$

Kampf and Karsten developed their model in connection with their work on nuclear reactor fuel pins, and carried out an analysis of the thermal effects of different porosity fractions within the uranium dioxide.

(c) Flinta [160]

$$\frac{K_b}{K_t} = \frac{1}{(1-\varepsilon)^{\frac{1}{3}}} \cdot \frac{1}{\frac{\sqrt{2}}{(1-\varepsilon)^{\frac{1}{3}}(1-0.92(1-\varepsilon)^{\frac{1}{3}}} + \frac{K_b}{K_c}} + \frac{1}{v} \qquad \text{Eqn (4.58)}$$

Flinta carried out an investigation into the thermal conductivity of uranium dioxide nuclear fuel pins. Flinta investigated the effect of porosity within the fuel pins on the effective thermal conductivity, and developed the Flinta model. The Flinta equation was rejected as a suitable model as the values of K_t did not agree with the expected thermal conductivity values at the powder volume loading of 0% and 100% respectively.

(d) Russell[161]

$$\frac{K_t}{K_b} = \frac{(1-\varepsilon)^{\frac{2}{3}} + \frac{1}{v}(1-(1-\varepsilon)^{\frac{2}{3}})}{(1-\varepsilon)^{\frac{2}{3}} - 1 + \varepsilon + \frac{1}{v}(2-(1-\varepsilon)^{\frac{2}{3}} - \varepsilon)} \qquad \text{Eqn (4.59)}$$

Russell developed his thermal conductivity model for porous refractories, based on the thermal conductivity of air along with the thermal conductivity of the bulk non-porous refractory material and the porosity percentage as the thermal conductivity of building/construction/structural materials is an important property.

(e) Eucken [162]

$$\frac{K_t}{K_b} = \frac{1+\frac{2(1-\varepsilon)(v-1)}{2+v}}{1-\frac{(1-\varepsilon)(v-1)}{2+v}} \qquad \text{Eqn (4.60)}$$

Eucken modified Maxwell's equations for the modelling of the thermal conductivities of glass matrix and ceramic powder composites, and gave the same results as Maxwell's equations for the same thermal conductivities encountered in feedstocks.

(f) Bruggeman[163] and Kanari[164]

$$\varepsilon = \frac{K_t - K_p}{K_b - K_p}\left(\frac{K_b}{K_t}\right)^{\left(\frac{1}{1+x}\right)} \qquad \text{Eqn (4.61)}$$

Bruggeman set the value of x to 2, and Kanari suggested that the value of x is determined by the sphericity of the filler used and the ratio of the thermal conductivity of the filler and matrix materials, and that x=2 is suggested to be valid for spherical powder morphologies.

(g) Lichtenecker/Geometric mean model [165]

$$K_t = K_p^{\varepsilon'} . K_b^{\varepsilon} \qquad \text{Eqn (4.62)}$$

Lichtenecker's model is mathematically the geometric analogue of the arithmetic mean model used for finding averages. Mitoff[166] states that Lichtenecker's method has been reported to be fundamentally flawed several times in the literature, and that Lichtenecker's model yields essentially the same results as Maxwells model provided that the powder and matrix thermal conductivities are within an order of magnitude of each other. Lichtenecker's model was not pursued further for the purpose of this work as the thermal conductivities of the powder and binder system were more than one order of magnitude apart from each other.

(h) Maxwell's model and Rayleigh's model

Maxwell[167] developed the theoretical model using Laplace equations in the form of Legendre functions to permit the calculation of a composite's material property in connection with the known individual component's material properties. The property of interest can be permeability, permittivity, electrical resistance or thermal conductance. Equation 4.63 shows one of the Maxwell equations (lower bound).

$$k = k_b\left(\frac{k_p+2k_b+2\varepsilon'(k_p-k_b)}{k_p+2k_b-\varepsilon'(k_p-k_b)}\right) \qquad \text{Eqn (4.63)}$$

Rayleigh[168], Runge[169] and De Vries[170] took Maxwell's equations and applied it to cubic lattices of spheres. This is a special case of where the sphere volume loading is 52.36% and yielded equation 4.64. Equation 4.64 was not used as it applies only to one volume loading value and for a simple cubic lattice of spheres. Such a geometrical cubic lattice of spheres is not encountered in practice and higher powder volume loadings are typically used. There is some disagreement over the value of a, which is a constant. Rayleigh set the value of a as 1.65, Runge set the value of a as 0.523 and De Vries set the value of a as 1.31.

$$k = k_b\left[3\varepsilon'\left(\frac{k_p+2k_b}{k_p-k_b}-\varepsilon'+\frac{a(k_p-k_b)\varepsilon'^{\frac{10}{3}}}{k_p+(\frac{4k_b}{3})}\right)^{-1}+1\right] \qquad \text{Eqn (4.64)}$$

In appendix B, the Maxwell model and the Rayleigh, Runge and De Vries models are compared with the SPBM model developed later on.

(i) Deissler and Eian[171][172]

$$\frac{K_f}{K_b} = \frac{\pi}{2(\frac{1}{v}-1)^2}[(\frac{1}{v}-1)-\ln\frac{1}{v}]+1-\frac{\pi}{4} \qquad \text{Eqn (4.65)}$$

Deissler-Eian's model does not contain any connection to the volume ratios of the binder and powder. The Deissler-Eian model is considered to be very limited in its applications, as far as powder injection moulding feedstocks were concerned and was rejected.

(j) Swift[173]

$$\frac{K_t}{K_b} = 0.577\pi[(\tfrac{1}{\upsilon} - 1)^{-1} - (\tfrac{1}{\upsilon} - 1)^{-2}.\ln\tfrac{1}{\upsilon}] + 0.093 \qquad \text{Eqn (4.66)}$$

Swift's model does not contain any connection to the volume ratios of the binder and powder. Swift's model is considered to be very limited in its applications and was rejected.

(k) Parallel model[174]

The feedstock system is assumed to be bars of materials connected in parallel.

$$k_t = \varepsilon k_b + \varepsilon' k_p \qquad \text{Eqn (4.67)}$$

(l) Series model[174]

The feedstock system is assumed to be plates of materials connected in series.

$$k_t = \left(\frac{\varepsilon}{k_b} + \frac{\varepsilon'}{k_p}\right)^{-1} \qquad \text{Eqn (4.68)}$$

The parallel heat energy flow model and the series heat energy flow model can be considered to be the upper and lower thermal conductivity limits for a particulate-matrix feedstock system with the actual feedstock system's thermal conductivity lying somewhere in between. The derivation of the series and parallel models (equations 4.67 and 4.68) may be found in appendix A.
The literature revealed at least seventeen more thermal conductivity models, which were compared by Progelhof et al.[175]. All of these models were developed for use with elliptical powder particulates or for polymer foams. These models were rejected because the powder particulates used in the Cranfield feedstocks were spherical and have higher thermal conductivities than the gas filled cells found in foams.

4.6.3 Thermal conductivity determination techniques

There are several methods for determining thermal conductivity.

1. Guarded hot plate method[176, sections 2.1 and 2.5]
2. Unguarded hot plate method [176, section 2.2.]
3. Heat disc method (for sheet materials) [176, section 2.3]
4. Heat flow meter method [176, section 2.4]
5. Water calorimeter method [176, section 2.6]
6. Hot pipe method [176, section 2.7]
7. Modulated differential scanning calorimetry (MDSC) [177]
8. Transient line source technique[178][179][180][181][182][183]

Table 4.1 shows a comparison of direct thermal conductivity measurement techniques. The feedstock being injection moulded typically encounters a processing temperature

range of ambient to 200°C and thermal conductivity data is required for both the solid and molten states. Polymer thermal conductivities generally range from 0.01 to 0.3 $Wm^{-1}K^{-1}$, and the addition of metal or ceramic powders increases the thermal conductivity. These considerations indicate that the transient line source technique in table 4.1 is a suitable method for the direct determination of thermal conductivity of the materials being injection moulded.

Method	Thermal conductivity range ($Wm^{-1}K^{-1}$)	Test volume range (cm^{-3})	Test temperature range (°C)	Test solids	Test liquids	Test gases
Guarded hot plate	Up to 2.0	75	-20 to 100	yes	no	no
Unguarded hot plate	0.15 to 2.0	75-150	-20 to 100	yes	no	no
Hot disc	0.15 to 2.0	20	dependent on design	yes	no	no
Heat flow meter	Up to 0.15	more than 75	-20 to 100	yes	no	no
Water calorimeter	Up to 1.5	140 to 175	400 to 1250	yes	no	no
Hot pipe	Up to 1.0	not known	up to 1000	yes	no	no
MDSC	0.1-1.5	0.01	up to 100	yes	no	no
Transient line source	0.01 to 10	50 to 100	-40 to 400	yes	yes	yes

Table 4.1 Comparison of thermal conductivity determination techniques.

There are other methods available such as the laser flash method[184][185]. The laser flash method determines the thermal diffusivity of the test sample. Before the thermal conductivity can be determined, the specific heat capacity and density of the sample must be known. Temperature influences the density and the specific heat capacity of the test sample and may introduce errors into the determination of thermal conductivity. It has been reported by Taylor and Clark[186] that thermal diffusivity values obtained by this method can be in error by more than 20%. Taylor offers corrective techniques to reduce the error to 3%. Kumada and Kobayasi[187] reports that much of the existing thermal diffusivity material data is not very reliable. Kumada suggests that imposing severe restrictions on the sample dimensions would reduce the measurement errors. Gao et al.[188] reports that using the laser flash method to determine the thermal conductivity of materials is prone to significant error. The magnitude of the error increases with decreasing sample thermal conductivity. It has been independently confirmed by Kestin and Paul[189], Assael et al.[190], Clifford et al.[191], Nieto de Castro and Roder[192] and Maitland et al.[193] that the transient line source probe is capable of producing thermal conductivity data to an accuracy of ±0.3%, when carried out in near ambient temperatures.

For the purposes of the project, only the transient line source probe will be considered further. In the transient line source technique, as illustrated by figure 4.10, a sample is heated up to the test temperature by the block's heater. The probe contains another heater and thermocouple. When thermal equilibrium is achieved, a voltage is applied to the probe heater, and the current and temperature rise is recorded over time. The value of the test voltage is determined by the requirement that the temperature rise during the test is less than 5°C, to minimise the effect of variation of thermal conductivity vs temperature and to minimise any change of the probe heater's resistance with temperature. This minimises any change in the probe heater's current. A variation of this method is to use a coolant probe instead of a heating probe. This permits the determination of thermal conductivity under a cooling regime instead of a heating regime. Only the heater probe was available at Cranfield.

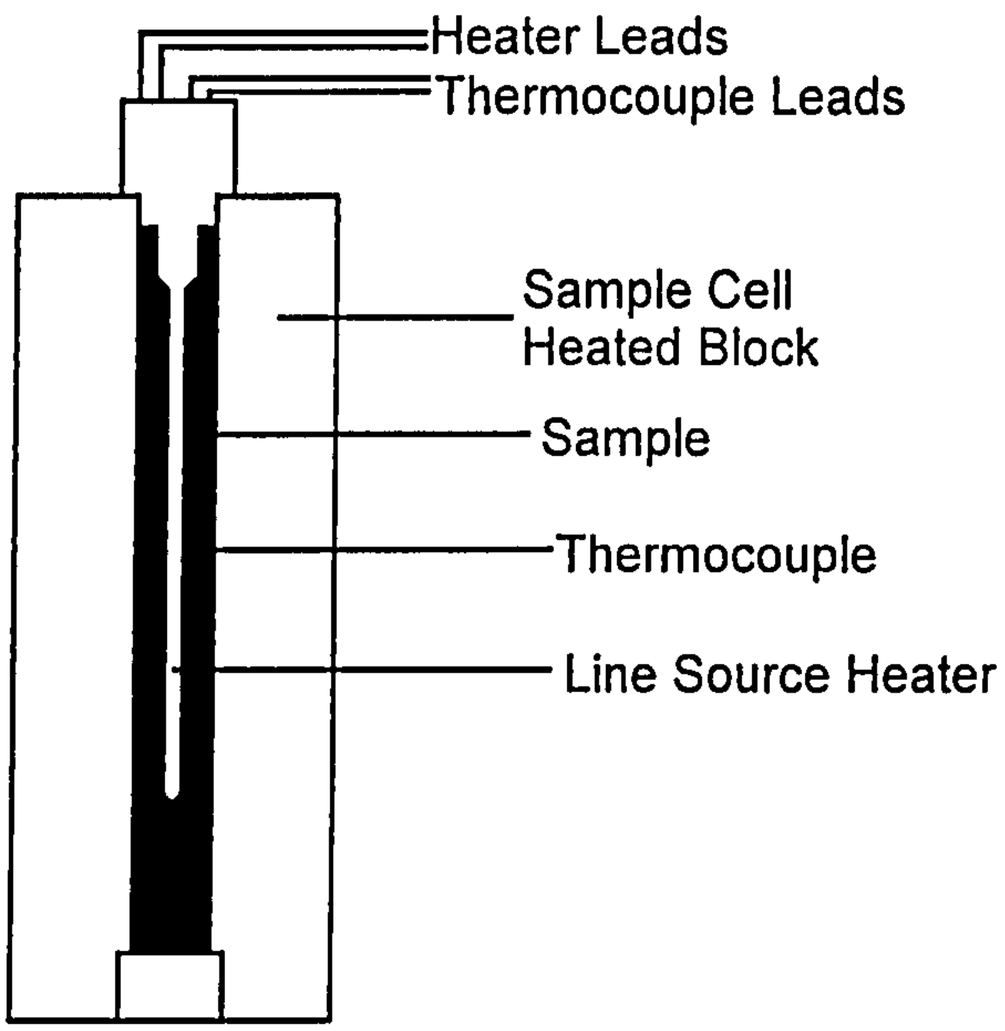

Figure 4.10 Schematic of the transient line source probe and heated block

The thermal conductivity can then be obtained from equation 4.69:

$$k = \frac{VIp \ln\left(\frac{t_2}{t_1}\right)}{4\pi(T_2 - T_1)} \qquad \text{Eqn (4.69)}$$

Where k= Thermal conductivity ($Wm^{-1}K^{-1}$)
V = Voltage across the probe heater (V)
I = Current flow through probe heater (A)
T_1 = Initial temperature (K)
T_2 = Final temperature (K)
t_1 = Initial time (s)
t_2 = Final time (s)
p = probe constant (m^{-1})

The probe constant is determined by first calibrating the system with materials of known thermal conductivity.

4.7 Solid density, melt density, thermal expansion coefficients and transition temperature

These parameters are used in the simulation of polymer flow dynamics during the filling and post filling stage and are obtained from the PVT and rheology experimental work.

Commercial computer modelling software is widely accepted for polymer injection moulding. However, there is very scant literature comparing the predicted data produced by the injection moulding modelling software against actual data obtained experimentally during the co-injection of a skin polymer and a core polymer. There are no recorded attempts to use computer modelling software for the prediction of the skin profile during the co-injection of two highly filled powder feedstocks.

5 Experimental technique: Powder co-injection moulding

This section describes the experimental work that was undertaken to demonstrate the feasibility of producing samples of three different model powder co-injection moulded systems.

5.1 Characterisation of the sintering behaviour of cermet composites

Experimental work was undertaken to investigate the effect that particle size and the volume loading of the rigid non-sinterable inclusions had on the final sintered densities of the cermet composites, as this would allow the design of a suitable core and skin powder system that have well matched sintering characteristics.

BASF iron OM of nominal diameter of 4 – 6μm was chosen for the matrix material, and three different nominal diameter sizes of alumina powder were chosen, 0.5μm, 4.0μm and 13.0μm. These powders were used in the co-injection of model wear resistant surface engineered mouldings.

The BASF carbonyl iron OM powder and the three grades of Alcan alumina were subjected to particle size determination using a Micromeritics 5100 sedigraph. This was used to confirm the manufacturer specifications for the given powders and to determine the cumulative mass and mass population distributions versus particle diameters of the iron and alumina powders.

	alumina diameter (μm)	volume of iron (%)	mass of iron (%)	volume of alumina (%)	mass of alumina (%)
A	-	100	100	0	0
B	0.5	95	97.51	5	2.49
C	0.5	90	94.89	10	5.11
D	0.5	85	92.12	15	7.88
E	0.5	80	89.19	20	10.81
F	4	95	97.51	5	2.49
G	4	90	94.89	10	5.11
H	4	85	92.12	15	7.88
I	4	80	89.19	20	10.81
J	13	95	97.51	5	2.49
K	13	90	94.89	10	5.11
L	13	85	92.12	15	7.88
M	13	80	89.19	20	10.81

Table 5.1 Compositions of the cermet die pressing feedstocks.

A binder solution was made up with 25% by mass polyethylene glycol (PEG) and 25% by mass polyvinyl acetate (PVA). A magnetic stirrer was used to mix the PEG and PVA

using 50% by mass acetone. A batch of iron and twelve batches of cermet powder mix were prepared. Their compositions are presented in table 5.1. The batches were mixed with the binder solution using a Turbula mixer. The acetone was allowed to evaporate at ambient temperature and pressure after mixing. Die pressing was used to produce small green cylinders at room temperature, with nominal dimensions of 10 mm diameter and height of 10 mm. The die pressed cylinders had sufficient green strength to permit handling into the thermal debinding and sintering stages.

The thermal debinding and sintering schedule is presented in figure 5.1 and table 5.2.

Stage	Atmosphere	Ramp rate ($^oCmin^{-1}$)	Initial temperature (^oC)	Final temperature (^oC)	Dwell time (hours)
thermal debinding	hydrogen	2	ambient	200	2
thermal debinding	hydrogen	2	200	500	2
sintering	hydrogen	4	500	850	2
sintering	hydrogen	4	850	1,050	2
cooling	hydrogen	natural	1,050	ambient	natural

Table 5.2 Description of the thermal profile used in thermal debinding and sintering.

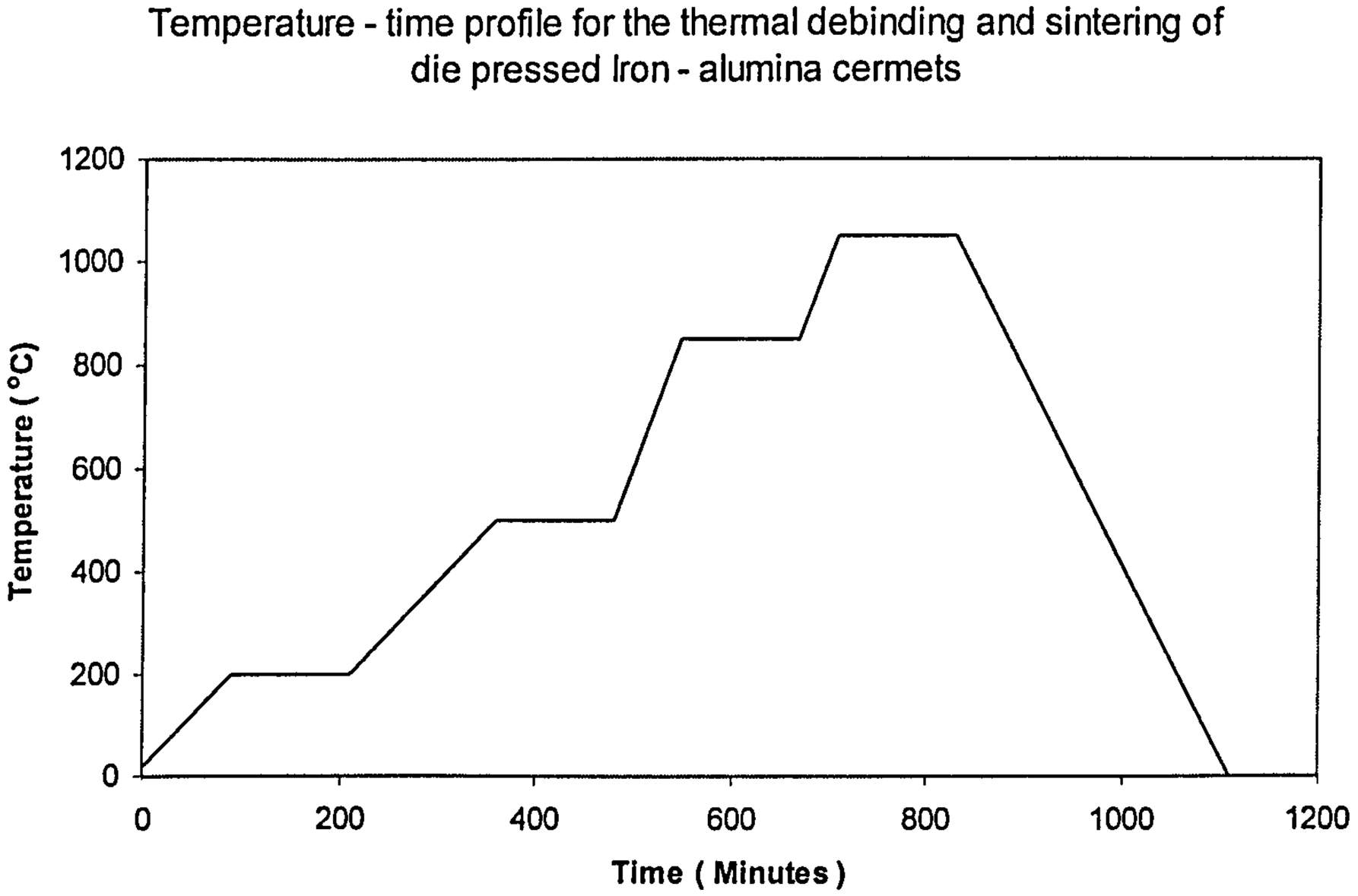

Figure 5.1 Temperature-time profile for the thermal debinding and sintering of the die pressed cermet samples

A Cambridge Instruments scanning electron microscope was used to examine the die-pressed samples after thermal debinding and sintering.

Archimede's principle was used to determine the final sintered bulk and true densities of the sintered cylinders, and graphs of sintering shrinkage vs alumina powder volume loading and alumina particle size were produced.

5.2 Powder and binder formulation for the model PCM feedstocks

The three model PCM systems required the following different feedstocks, indicated in table 5.3 and their feedstock compositions before compounding are detailed in tables 5.5 and 5.6. A binder system comprising BDH paraffin wax, BDH carnauba wax, BDH stearic acid and Exxon Escorene PP3635F1 low molecular weight polypropylene was used for the binder system for all of the model PCM feedstocks. The composition of the binder system was based on the previously used Cranfield formulation, details in table 5.4. Six feedstocks were made and their mass and volume compositions are given in tables 5.5 and 5.6.

PCM system	skin	core
corrosion resistance	stainless steel	iron
wear resistance	iron-alumina cermet	iron
higher toughness	zirconia toughened alumina	alumina

Table 5.3 Description of the three model PCM systems

	Mass (%)	Volume (%)	Density (gcm^{-3})	Specific volume (cm^3g^{-1})
LMWPP	59.7	60.01	0.9	1.11
Paraffin wax	31.85	32.02	0.9	1.11
Carnauba wax	6.95	6.35	0.99	1.01
Stearic acid	1.5	1.62	0.84	1.19

Table 5.4 Mass and volume compositions (before compounding) of the binder system used (Densities quoted are for standard temperature and atmospheric pressure.)

Feedstock	iron (%)	SS316L MA (%)	Al_2O_3 (%)	ZTA (%)	LMWPP (%)	PW (%)	CW (%)	SA (%)
60% vol iron	92.8				4.3	2.29	0.5	0.11
60% vol cermet iron and alumina	85.05		7.28		4.58	2.45	0.53	0.11
60% vol SS316L MA	62.02	31.01			4.16	2.22	0.48	0.11
50% vol alumina			80.81		11.46	6.11	1.33	0.29
55% vol alumina			83.73		9.71	5.18	1.13	0.24
55% vol ZTA				85.26	8.8	4.69	1.02	0.22

Table 5.5 Mass percentages of the feedstocks before compounding (Key to follow)

Feedstock	iron (%)	SS316L MA (%)	Al_2O_3 (%)	ZTA (%)	LMWPP (%)	PW (%)	CW (%)	SA (%)
60% vol iron	60				24	12.8	2.54	0.65
60% vol cermet iron and alumina	45		15		24	12.8	2.54	0.65
60% vol iron and SS316L MA	40	20			24	12.8	2.54	0.65
50% vol alumina	50		30		16	3.17	0.81	
55% vol alumina	55		27		14.4	2.86	0.73	
55% vol ZTA		55	27		14.4	2.86	0.73	

Table 5.6 Volume percentages of the feedstocks before compounding

Key:		
	iron	BASF 4-6μm carbonyl iron OM powder
	SS316LMA	Osprey SS316L 13.0μm masteralloy powder
	Al_2O_3	Alcan 13.0μm alumina powder
	ZTA	Dynamic Ceramic 0.5μm zirconia toughened alumina
	LWMPP	Exxon PP3635F1 low molecular weight polypropylene
	PW	BDH paraffin wax
	CW	BDH carnauba wax
	SA	BDH stearic acid

The Exxon low molecular polypropylene was supplied in granulated form. The polypropylene was cooled using liquid nitrogen. This permitted the polypropylene to be milled to a powder. The paraffin wax was supplied in pastillated form. The paraffin wax was cooled using liquid nitrogen before being milled to a fine powder. The carnauba wax and stearic acid were supplied as a powder. The feedstocks were made up by pouring the required amounts into a polyethylene bag, which was then agitated by hand. Hand agitation continued until visual inspection confirmed that all of the individual colours of the components had appeared to homogenise into a single colour.

5.3 Compounder processing conditions

The hand mixed batches were transferred into a hopper attached to a K-Tron Soder volumetric feeder. The hopper contained a motor driven mixing blade. The feedstock volumetric flow-rates were controlled using a K-Tron Soder volumetric feeder with open flight screws. The five feedstock batches were compounded on a APV MPF19 19mm co-rotating twin screw compounder with the following processing conditions:

Compounder screw speed	300 rpm
Barrel nozzle temperature	170 °C
Barrel front zone temperature	170 °C
Barrel middle zone temperature	170 °C
Barrel rear zone temperature	165 °C

K-tron volume flow rate 8.5 cm^3min^{-1}

Samples were taken at several points during the compounding of each feedstock batch. Each sample was weighed before heating to 500°C and holding at this temperature for 1 hour in a crucible in flowing hydrogen gas, cooled to room temperature and weighed again. This permitted the determination of the powder mass loading as a quality control check of the mixing and compounding process, and the burn-offs confirmed the powder volume loading was consistent throughout the compounding stage. The extrudate was collected on metal trays and was initially crushed up by hand into coarse pellets. A pestle and mortar was used to break up the coarse pellets into finer pellets of nominal lengths of typically 3 mm. The nominal diameters ranged from 0.5 to 1.0 mm.

5.4 Co-injection moulding of the 3 model PCM systems

Three model PCM systems were injection moulded on a Dassett DM30 30 tonne co-injection moulding machine and are tabulated in table 5.7.

	Skin			Core		
Run No	Manufacturer	Feedstock	Material class	Manufacturer	Feedstock	Material class
a	Cranfield	carbonyl iron and SS316L masteralloy	metal	Cranfield	carbonyl iron	metal
b	Cranfield	carbonyl iron and alumina	cermet	Cranfield	carbonyl iron	metal
c	Cranfield	zirconia toughened alumina	ceramic	Cranfield	55% alumina	ceramic

Table 5.7 Summary of the three co-injected model PCM systems

The total injection time was 1.1s (this includes both the skin and core shots). The injection moulding conditions are tabulated in tables 5.8, 5.9, 5.10, 5.11 and 5.12. The mode of operation for injection moulding on the Dassett DM30 is summarised further. There are three main phases during injection moulding. They are: filling, post filling and cooling.

In the filling phase, the Dassett DM30 injection moulding machine was operated under a controlled displacement rate profile. In this mode of operation, the injection linear screw speed profile can be programmed into the injection process controller by the operator. An example injection screw speed profile is illustrated by table 5.11. Since the cross-sectional areas of the injection barrels are constant along their full length, it follows that the volume of material injected into the mould cavity is related to the linear screw displacement. The linear screw speed profile gives a means of controlling the

volumetric injection flow rate into the mould cavity, and thus the actual injection time taken for the mould cavity to fill completely with molten material.

In the post-filling phase, after the mould cavity has been filled, the molten material starts to cool, contract in volume and solidify. The volume contraction could lead to gross defects in the ejected mouldings. To counteract this, the post filling phase is used to inject a further small amount of molten material into the mould cavity under low pressure. The duration of post filling is set as the injection low time parameter on the Dassett DM30. During the injection low time period, a low pressure is applied to the material and an example injection low pressure profile is given by table 5.10.

However there is an upper limit to the time period chosen for the duration of the pack/hold phase. This is because the extra molten material must be injected into the mould cavity before the sprue/gate has totally solidified. If the sprue/gate has totally solidified, it is no longer possible to inject any more material into the mould cavity. A suitable method for determining the sprue/gate freeze off time is by weighing the as ejected mouldings. The pack/hold time duration is gradually increased until the weight of the ejected mouldings reach an upper limit. The minimum time duration required to achieve maximum moulding weight is the time at which switch-over from hold/pack to cooling can commence.

The cooling phase is necessary because the moulding still has a reducing molten core even though the sprue and/or gate has totally frozen off at this point. The cooling time can be calculated using the mould material properties and equations 4.1 and 4.2 and programmed into the machine as the cooling time. After the cooling period has elapsed, the mould tooling opens, and the moulding is ejected. As a rule of thumb[194, chapter 4, pp4-5] the filling time is chosen to be between one tenth to one fifth of the estimated cooling time.

In co-injection moulding, three settings are required. The first is the total skin material shot size, in mm, which is the linear screw displacement for the skin material for the entire injection moulding cycle. This includes the first skin shot volume and the second small skin shot volume (used to seal off the skin at the sprue). The second setting is the total core material shot size, in mm which is the total linear displacement of the core material screw. The third setting defines the end first injection. This is the distance at which the skin material screw will stop, and is less than the skin shot size value. It is at this point that the core material is then injected. When the required volume of the core material is injected, the skin screw will then travel the remaining screw displacement to its final end position. The changeover valve is fitted with microswitches and controlled pneumatically. The injection screws are fitted with linear displacement sensors.

This sequence is illustrated using some example shot size settings:

Skin shot size = 25 mm, core shot size = 28 mm, end first injection 20 mm.

First, the injection screws are screwed back and charged up with material from the feed hoppers. At the start of the mould cavity filling phase, the skin injection screw will

advance from its starting position at constant speed until a displacement of 20 mm is reached as set as the end first injection parameter. The skin screw stops at this position. At this point, an electronically controlled pneumatic valve is actuated and releases compressed air to the changeover valve, causing it to operate. A microswitch is used to detect when the changeover valve has fully operated. This permits the core screw to move with constant speed until a linear displacement of 28 mm has been achieved as defined by the core shot size parameter. When the displacement of the core screw is completed, the electronically controlled pneumatic valve releases air to the changeover valve to return it back to its original position. As soon as the changeover valve returns to its original position, a microswitch signals the skin screw to complete the rest of its displacement, which in this example is a displacement of 5 mm. This will produce the required total displacement of 25 mm for the skin screw. The time duration of the changeover valve operating is of the order of hundredths of a second and has negligible effects on the thermodynamics of filling of the mould cavity. This is because the time taken for the changeover valve is significantly smaller than the total injection time. This entire sequence occurs inside the selected injection time set on the machine. It is not possible to alter the time taken for the changeover valve to operate.

Injection moulding machine conditions

Variable	Actual value	Units
Clamp force	300	kN
Clamp open stroke	131	mm
Start mould protect	54	mm
Mould protect pressure	3	MPa
Cooling time	10	s
Clamp open time	1.5	s
Clamp time limit	200	s

Table 5.8 Mould and clamp settings

Variable	Actual setting	Units
Skin barrel front zone	170	°C
Skin barrel middle zone	160	°C
Skin barrel rear zone	150	°C
Core barrel front zone	170	°C
Core barrel middle zone	160	°C
Core barrel rear zone	150	°C
Nozzle zone	175	°C

Table 5.9 Injection moulding machine heating settings

Table 5.10 refers to the maximum hydraulic pressure allowed during injection of the material. There are no mould cavity pressure sensors on the Dassett DM30. This limitation prevented the determination of the actual material pressures encountered during mould filling, packing, hold and cooling phases.

Variable	Skin pressure	Core pressure	Units
Injection pressure 1	0.9	1	MPa
Injection pressure 2	0.9	1	MPa
Injection pressure 3	0.9	1	MPa
Injection pressure 4	0.9	1	MPa
Injection pressure 5	0.9	1	MPa

Table 5.10 Injection pressure low profile settings

Variable	Skin barrel speed	Core barrel speed	Units
Injection speed 1	60	40	%
Injection speed 2	60	40	%
Injection speed 3	60	40	%
Injection speed 4	60	40	%
Injection speed 5	60	40	%

Table 5.11 Injection speed profile settings (max linear screw speed = 5.8 cms^{-1})

Variable	Skin Barrel	Core barrel	Units
Shot size	25	28	mm
Injection high time	10	5	s
Injection high pressure	21	15	MPa
End 1st injection	20	Not applicable	mm
Transfer position	14	4	mm
Transfer pressure	20	15	MPa
Injection low time	30	0	s
Screw rotational speed	200	200	rpm
Screw decompression	25	28	mm

Table 5.12 Injection moulding cycle settings

The injection high time is an alarm setting on the Dassett DM30, and will sound an alarm if the injection of the material does not start and finish within the injection high time setting value. The actual injection time achieved in practice is determined by the injection screw linear speed profile. (Screw diameter = 25mm. Screw length:diameter = 20:1)

Figures 5.2 and 5.3 present the dimensions and geometry of the mould cavity that was used to produce the PCM mouldings.

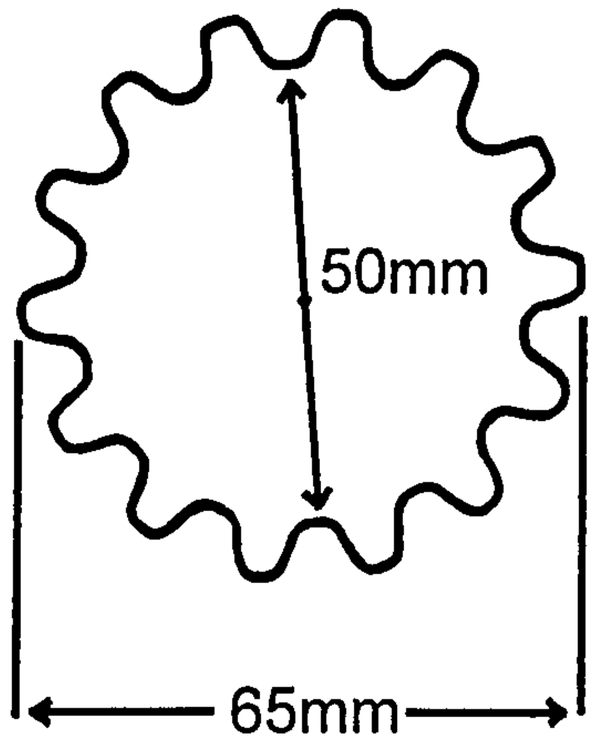

Figure 5.2 Mould cavity geometry plan view (The sprue is located at the centre)

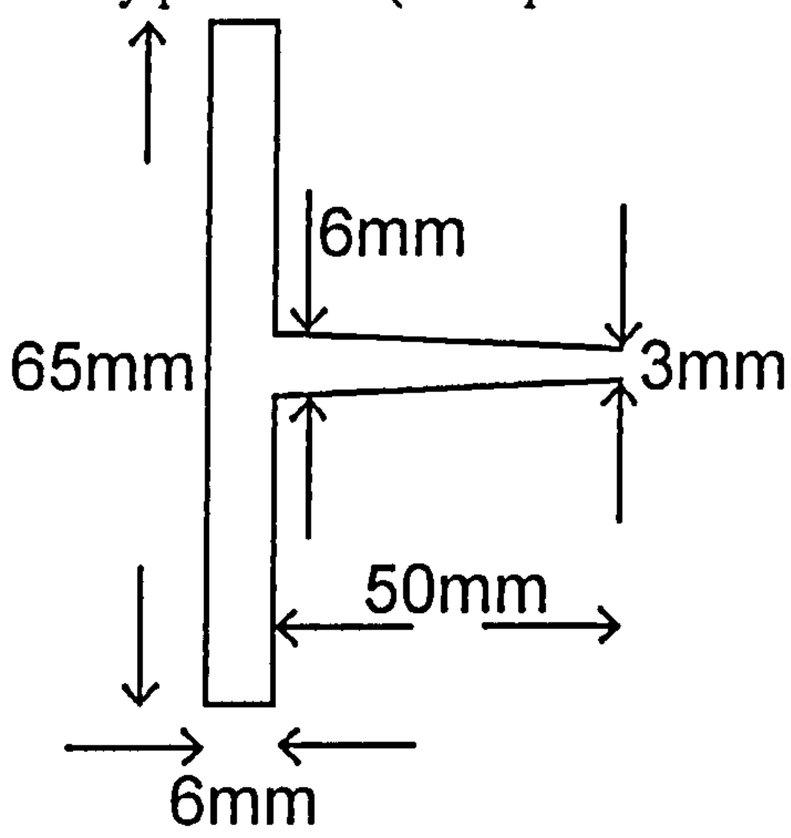

Figure 5.3 Mould cavity geometry side view.

5.5 Debinding of the powder co-injected mouldings

A two stage debinding process was used for the present work as this was determined to be most appropriate for the wax/polypropylene binder system used. The wax/polypropylene binder system had also been used at Cranfield University for a number of years. There was no scientific need to modify or improve the debinding methods. Figure 5.4 shows the solvent debinding apparatus used in the first stage of debinding.

Heptane was selected as the debinding solvent. The melting points of the waxes was 57°C for paraffin wax, 81°C for carnauba wax and 69°C for stearic acid. The binder waxes are highly soluble in heptane.

The mouldings were placed onto a porous ceramic substrate. The porous ceramic substrate was at the bottom of a glass container with a glass lid. A Liebig condenser is

attached to the centre of the glass lid and continuously supplied with chilled water from a recirculating water chiller and pump. The whole debinding assembly was suspended in a heated water bath. The glass container had a layer of an organic solvent at the bottom.

The water bath was heated to a constant temperature of 95°C, leading to a heptane vapour temperature of 80°C. The chilled water was kept at 4°C. The debinding time was 24 hours. After solvent debinding was completed, the mouldings were allowed to rest for 24 hours, allowing any entrapped heptane to evaporate freely from the mouldings. This ensured that a highly porous network was present and was followed by thermal debinding.

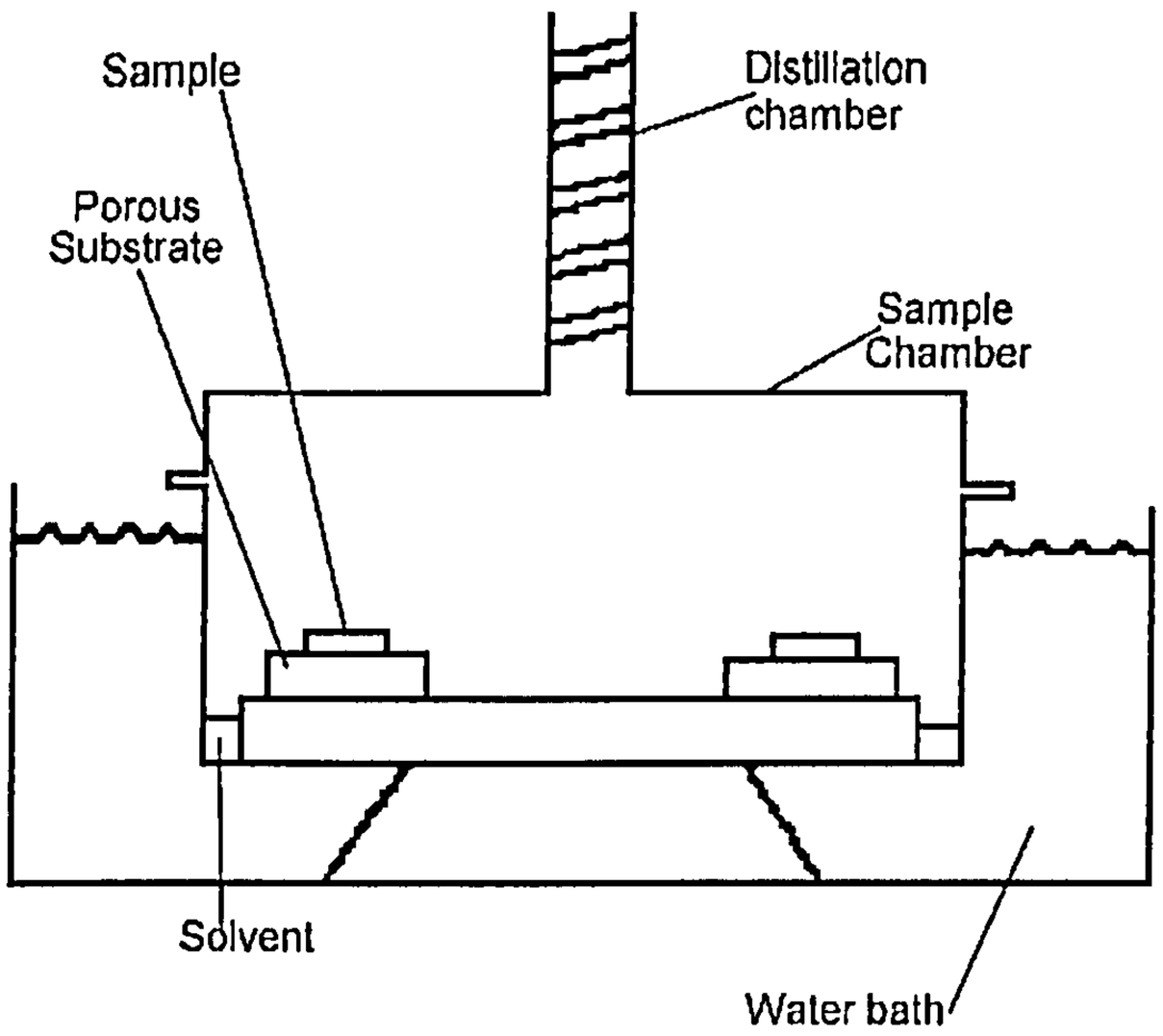

Figure 5.4 Schematic of the solvent debinding apparatus

For the metal co-injected mouldings, thermal debinding was carried out using hydrogen gas flowing at 1 $lmin^{-1}$ in a 75mm diameter tube furnace. The thermal debinding for the ceramic co-injected mouldings was carried out using a muffle furnace and the atmosphere used was air. The thermal profiles used for the thermal debinding of the metal co-injected mouldings and ceramic co-injected mouldings are tabulated in table 5.13 and graphically illustrated by figure 5.5.

Start temperature (°C)	End temperature (°C)	Heating rate (°C min^{-1})	Time taken (minutes)
Ambient	250	1	220
250	250	0	120
250	500	1	250
500	500	0	120
500	To sintering profile		

Table 5.13 Thermal debinding temperature profile

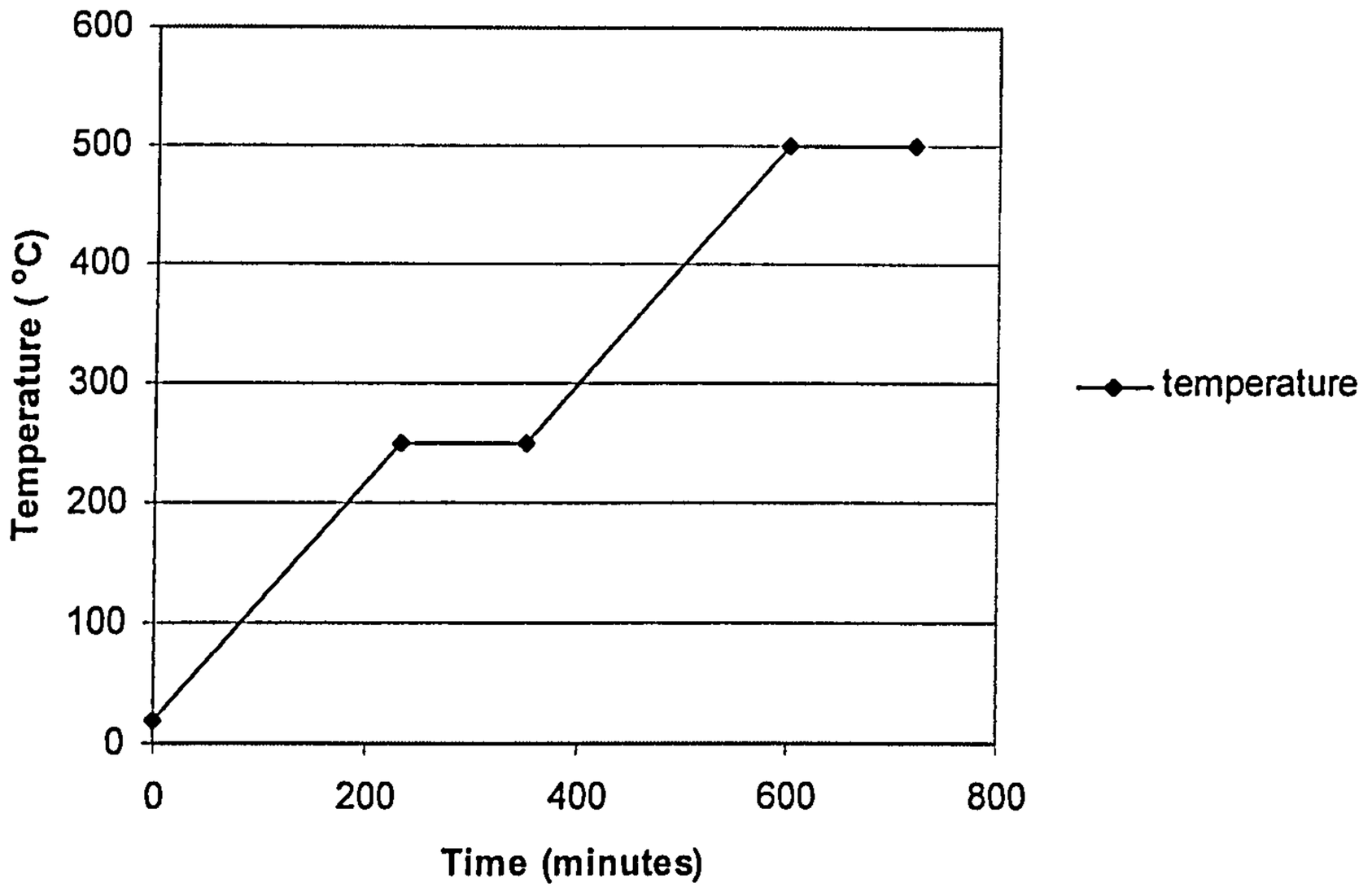

Figure 5.5 Thermal debinding temperature-time profile

5.6 Sintering of the powder co-injected mouldings

The sintering started immediately after thermal debinding finished. The same furnace was used for both thermal debinding and sintering. This avoided the need to handle the physically fragile porous debound mouldings from one furnace to another. It also dispensed with the inefficient process of cooling down to ambient temperature after thermal debinding and reheating again from ambient temperature for sintering to take place.

All of the metal co-injected mouldings were sintered in a horizontal batch tube furnace, using a reducing hydrogen atmosphere at a flow rate of 1 $lmin^{-1}$. The sintering temperature profile is illustrated by figure 5.6 and tabulated in table 5.14.

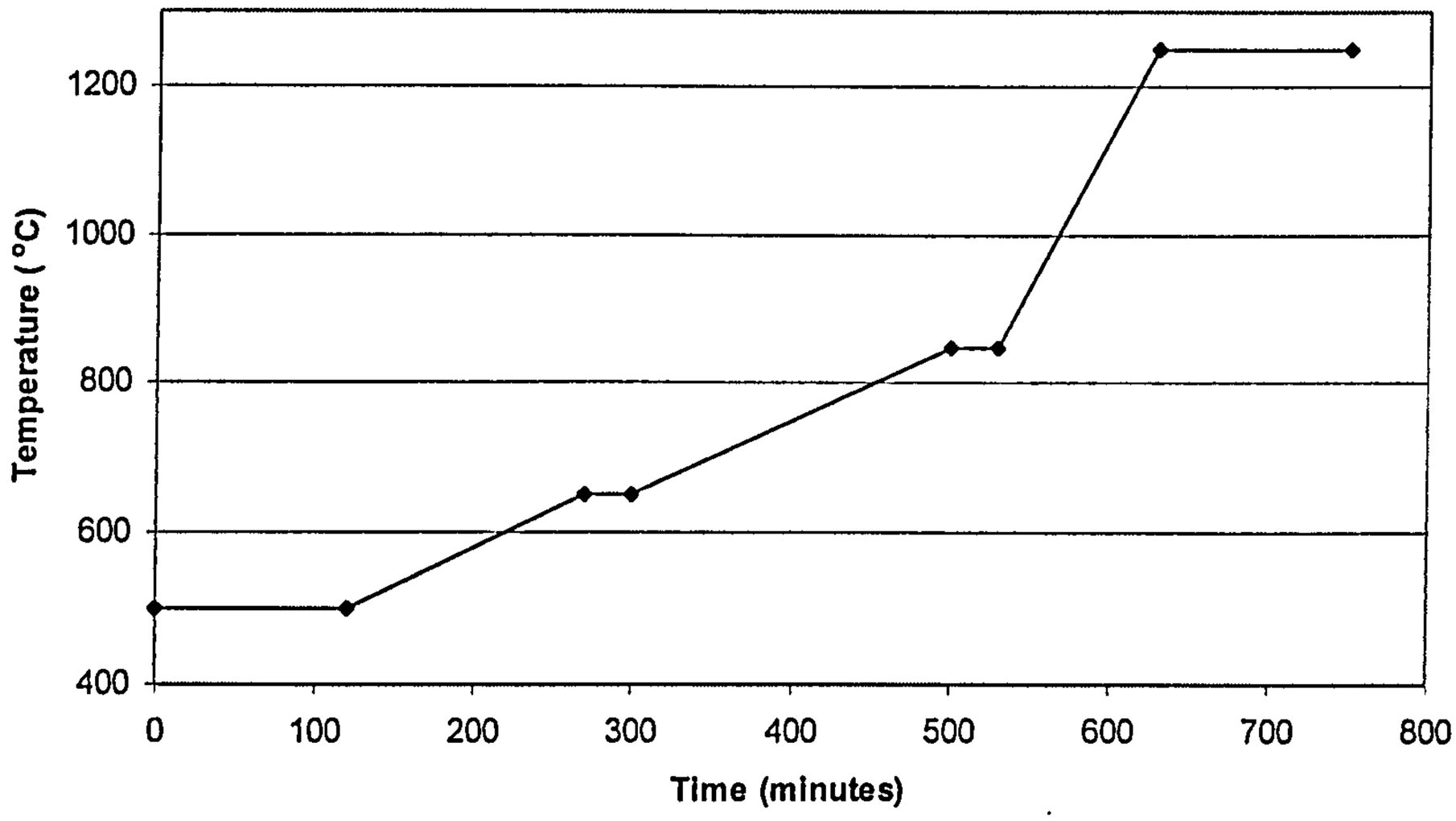

Figure 5.6 Sintering temperature profile used for the metal co-injected mouldings

Start temperature (°C)	End temperature (°C)	Heating rate (°C min^{-1})	Time taken (minutes)
(From thermal debinding)			
500	650	1	150
650	650	0	250
650	850	4	120
850	850	0	150
850	1,250	4	120
1,250	1,250	0	120
1,250	ambient	natural cooling	-

Table 5.14 Tabulated sintering profile data for the metal co-injected mouldings

All of the ceramic co-injected mouldings were sintered in a muffle furnace, under an air atmosphere. The sintering temperature profile is illustrated by figure 5.7 and table 5.15.

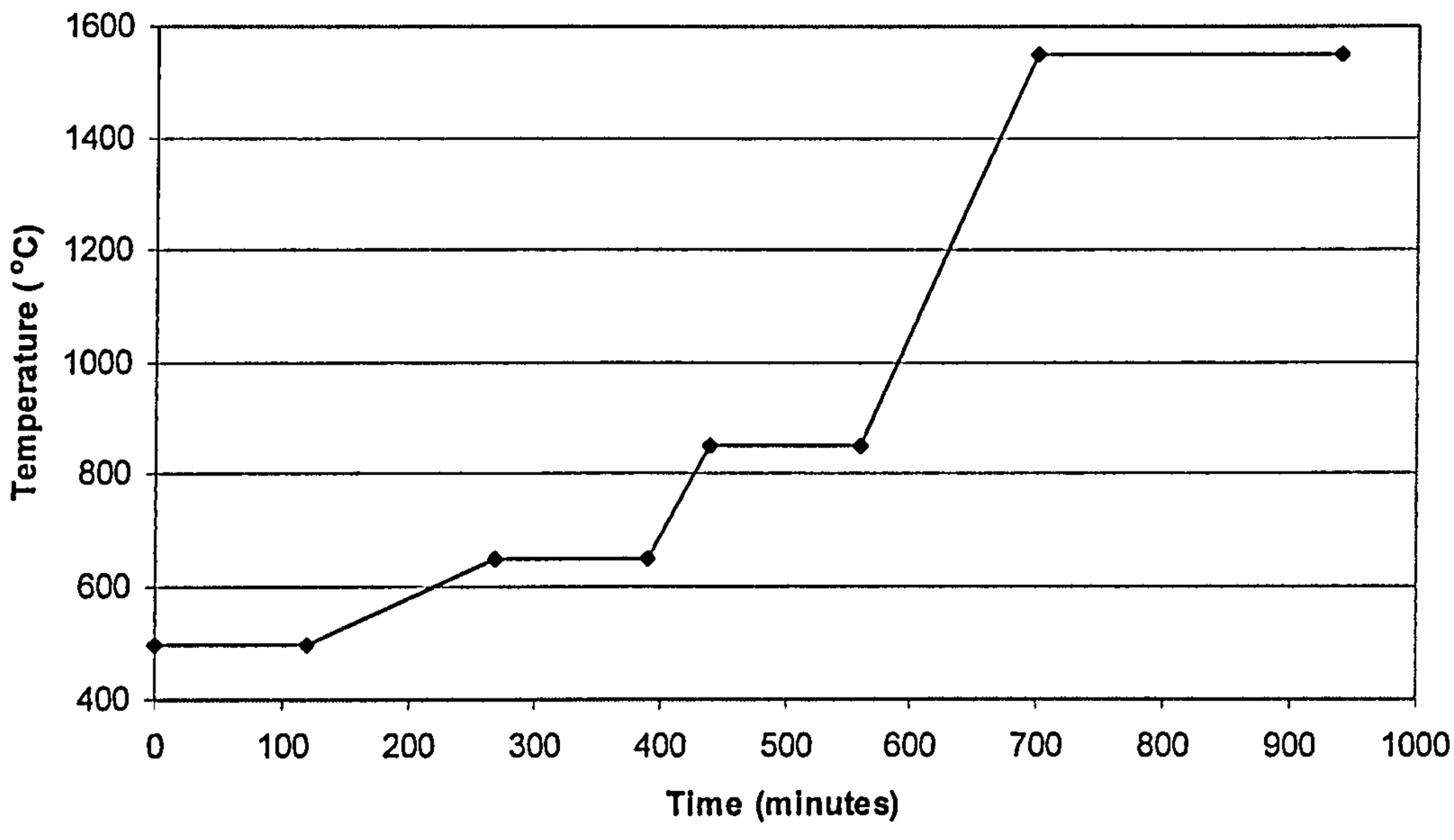

Figure 5.7 Sintering temperature profile for the ceramic co-injected mouldings

Start temperature (°C)	End temperature (°C)	Heating rate (°C min^{-1})	Time taken (minutes)
(From thermal debinding)			
500	650	1	150
650	650	0	250
650	850	4	120
850	850	0	150
850	1,550	5	140
1,550	1,550	0	240
1,550	ambient	natural cooling	-

Table 5.15 Tabulated sintering profile data for the ceramic co-injected mouldings

5.7 Metallography and ceramography of green and sintered powder co-injected mouldings

During the co-injection of the green mouldings, the first fifteen green mouldings were discarded. This was done because the first fifteen moulding may have been affected by remnants of degraded material from previous injection moulding runs. This permitted the machine to settle down into a steady state and 3 mouldings were selected at random from the next fifteen mouldings. This ensured that the sectioned mouldings were typical representations of skin profiles achieved during the co-injection of bulk quantities of green mouldings

The selected co-injected mouldings from the three model PCM systems were sectioned on a Buehler Isomet 2000 precision diamond saw rotating at 2500rpm under a 250g load. The samples were ground using silicon carbide grinding paper on a Buehler Metaserv 2000. The grit sizes used were 120 grit, 220 grit and then 1200 grit. The co-injected metal mouldings were polished on a DP-DAC cloth using diamond paste down to 3.0μm grade and finally polished on a DP-NAP cloth with 1.0μm diamond paste on a Buehler Metaserv Motopol 12. The co-injected ceramic mouldings were ground on a 70μm diamond grinding disc with water as the lubricant, followed by polishing on a Metlap disc and 6μm diamond paste and finally by a Tex-met cloth and silica colloidal suspension.

To improve the skin - core optical contrast, the sectioned and polished metal co-injected mouldings were etched with Nital (a solution of 2% nitric acid, 93% methanol and 5% distilled water).

5.8 Characterisation of the sintered skin profiles of the powder co-injected mouldings

The mouldings were positioned in a bench clamp, and a standard 300 mm ruler was aligned parallel to its sectioned face. A travelling microscope was used to determine the skin - core interface positions at a constant interval of 2mm along its radius. The absolute skin-core positions were converted to skin thickness fractions and graphs of skin fraction versus radial position were plotted.

A scanning electron microscope, Cambridge Instruments 55 was used to take secondary electron and back scattered electron micrographs of the sectioned samples to examine the interface and the skin and core materials.

6 Experimental technique: feedstock properties characterisation

This section describes the experimental work that was undertaken to characterise the feedstocks used in the 3 model PCM systems. Work was undertaken with computer modelling to demonstrate the feasibility of predicting the skin profile in co-injection moulding. This section is split into two parts, the first deals with the material characterisation and the second deals with the computer modelling of co-injection moulding. Before computer modelling can be undertaken, the input data must be prepared. C-Mold has a limited database of common machine models, mould material data and common coolant data files.

Before computer modelling could take place for the three model PCM systems, the feedstocks used had to be subjected to material property determination so that the required files could be created for each feedstock. The material property determination fell into 4 distinct groups. Rules of mixtures or models were developed to permit the calculation of feedstock material properties from those of the individual components.

The 6 compounded feedstocks were subjected to material property testing, along with their individual components to permit the determination of appropriate equations to calculate the feedstock material properties as a function of the material properties of the components and mass/volume fractions.

6.1 Specific heat capacity

This section describes the experimental work that was carried out to characterise the specific heat capacity of the PCM feedstocks. All specific heat capacity measurements were carried out using a TA instruments 2920 modulated DSC with a refrigerated cooling accessory The complex specific heat capacities as a function of temperature of the compounded feedstocks and the individual components were experimentally determined over the interval of 20°C to 170°C, which was the experimental injection moulding temperature range.

It is pointed out that if a rule of mixtures approach is being used to predict the feedstock specific heat capacity, it is not important if the experimental specific heat capacity data for the individual components are obtained under a heating or cooling regime. However, if the specific heat capacity data are to be subsequently used in computer prediction software such as C-Mold, it is important to simulate the conditions encountered by the material being injection moulded. This implies that the specific heat capacity data should be obtained under a high cooling rate thermal regime. The use of high cooling rates will reveal the presence of supercooling[194, chapter 2, pp2-15] Supercooling is an effect where the melting temperature upon heating and the solidification temperature upon cooling are not the same. Supercooling becomes more pronounced with higher temperature ramp rates. The experimental specific heat capacity data were obtained under a heating thermal profile due to the requirement to prevent the formation of

gaseous degradation products or volatiles contaminating the equipment. There were limitations imposed on the choice of underlying heating or cooling rate to less than that typically encountered in injection moulding.

6.1.1 Characterisation of the binder components, powder components and feedstock specific heat capacities

The experimental specific heat capacity vs temperature of the binder materials and powder materials in table 6.1 were determined experimentally using MDSC. The PCM feedstocks were also subjected to analysis by MDSC to determine their experimental specific heat capacity vs temperature curves.

Manufacturer	Material
Exxon	LMWPP PP3635F1 polypropylene
BDH	paraffin wax
BDH	carnauba wax
BDH	stearic acid
BASF	4.- 6 μm carbonyl iron OM powder
Osprey	13 μm stainless steel 316L powder
Osprey	stainless steel 316L masteralloy powder
Alcan	0.5 μm and 13 μm alumina powder

Table 6.1 Individual components analysed by MDSC
(Heating rate = $1^0 C min^{-1}$, modulation temperature = $\pm 1^0 C$, Modulation period = 80s)

6.1.2 Development and application of the rule of mixtures for the calculation of specific heat capacity

Appendix H shows the derivation of the rule of mixtures for calculating the feedstock specific heat capacities from the mass fractions and specific heat capacities of the individual components. The work produced equation 6.1:

$$c_{system} = \frac{m_1 c_1 + m_2 c_2 + \ldots\ldots + m_{n-1} c_{n-1} + m_n c_n}{m_{system}} \qquad \text{Eqn (6.1)}$$

Specific heat capacities vary with temperature. This implies that it is necessary to state that when using the rule of mixtures, the specific heat capacities of the individual components used must relate to the same test temperature. Equation 6.1 was used to calculate the specific heat capacity vs temperature curves for the feedstocks from the experimental specific heat capacity vs temperature curves for the individual components. The results were directly compared with experimental specific heat capacity vs temperature scans of the feedstocks as determined experimentally by MDSC.

Equation 6.1 was used to calculate the effect of varying the powder mass loading percentage on the specific heat capacity of the feedstock at 3 different temperatures for a typical metal and a typical ceramic PIM feedstock. The mass range chosen is typical of

that used in PIM. This was repeated to show the effect of varying the volume loading percentage on the specific heat capacity of the feedstock at 3 different temperatures for a typical metal and a typical ceramic PIM feedstock, as feedstocks are compounded to achieve the required powder volume loading, instead of a required mass percentage. The volume loading range chosen is typical of the volume loadings used in PIM.

6.2 Pressure-volume-temperature characterisation

This section describes the experimental work that was carried out to characterise the PVT behaviour of the powders, binders and feedstocks.

6.2.1 Development of an equation to calculate the PVT response of the powder systems from density and thermal expansivity data

For the metal and ceramic powders, the literature search revealed no PVT data for the powders used. However, the powder densities at s.t.p were found, along with either their linear or cubic expansivities. The derivation of equation 6.2 can be found in appendix J, that allows the calculation of PVT data for a given powder from its open literature density and expansivity data. The resultant equation is:

$$S_{V_f} = S_{V_0}(1 + \gamma \Delta T) \qquad \text{Eqn (6.2)}$$

Where S_{V_f} = Final specific volume ($m^{-3}kg^{-1}$)
S_{V_0} = Original specific volume ($m^{-3}kg^{-1}$)
γ = Cubic thermal expansion coefficient ($^0C^{-1}$)
ΔT = Temperature difference (^0C)

Equation 6.2 was used to calculate the specific volume as a function of temperature for all of the powders used in the feedstocks since its linear or cubic thermal expansion coefficient and its density at s.t.p were found from material data books. The thermal expansivities and densities at s.t.p for the powders used in the present study are given in table 6.2.

Powder	Linear Thermal expansion coefficient ($x10^{-6}$ $^oC^{-1}$)	Cubic Thermal expansion coefficient ($x10^{-6}$ $^oC^{-1}$)	Density at s.t.p (gcm^{-3})
iron	13	39	7.86
stainless steel 316L	16	48	8.05
alumina	7.4	22.2	3.81
zirconia	7	21	6

Table 6.2 Linear, cubic expansivities and densities for powders used in PIM

Equation 6.3 was used to calculate the specific volume vs temperature for the iron-alumina cermet powder system and for the zirconia toughened alumina powder system as their mass ratios were also known. For the iron - SS316L masteralloy powder

system, the material data was assumed to be the same as for a pre-alloyed stainless steel 316L powder.

6.2.2 Characterisation of the PVT curves of the binder components

The wax PVT curves were calculated in a similar way to that of the powders. The waxes melting points from MDSC, and thermal expansivities and densities at s.t.p from the general literature are shown in table 6.3. (The expansivities of carnauba wax and stearic acid were not found, and have been assumed to be the same as paraffin wax).

Binder material	Linear thermal expansivity ($x10^{-6}$ °C^{-1}) @ s.t.p.	Cubic thermal expansivity ($x10^{-6}$ °C^{-1}) @ s.t.p.	Density at s.t.p (gcm^{-3})	Melting point (°C)
Paraffin wax	110	330	0.9	58
Carnauba wax	110	330	0.99	81
Stearic acid	110	330	0.84	69

Table 6.3. Density and thermal expansivities of binder components

The waxes were assumed to be incompressible in both their solid and molten states. The thermal expansion coefficients for the solid and molten states were assumed to be identical. The volume change associated with the change of state at the melting temperature was also neglected, as the waxes only represent a small part of the overall formulation.

In the C-Mold material database, many different polypropylenes were found, and the vast majority of the polypropylenes listed had PVT data available, and were nominally universal for the class of polypropylenes. There was no PVT data available for any low molecular weight polypropylenes, but Ougizawa et al.[195][196] state that PVT data is independent of the molecular weights of polymers within a generic class. For the purposes of the PVT work, a typical polymer with its associated PVT data was used from the C-Mold material database, such that the melt transition of the chosen polymer matched that of the LMWPP's melt transition point as determined at MDSC. A scaling factor was applied to the PVT data to bring the specific volume at s.t.p data point to the value of $1.111cm^3g^{-1}$ as the Exxon PP3536F1 LMWPP's density at s.t.p was quoted as $0.9gcm^{-3}$ in the manufacturer's polymer data sheets.

6.2.3 Application of a rule of mixtures to calculate the PVT behaviour of feedstock and validation of the Tait equation for modelling the PVT behaviour of feedstocks

An equation was derived to allow the calculation of the specific volume of a mixture of any number of substances with known specific volumes as a function of temperature and pressure and known mass or volume. The derivation is presented in appendix I. The equation that was used for calculating the specific volume of the feedstock from the specific volumes of the n individual components is presented below:

$$m_{system}s_{v_{system}} = m_1 s_{v_1} + m_2 s_{v_2} + ... + m_{n-1} s_{v_{n-1}} + m_n s_{v_n} \quad \text{Eqn (6.3)}$$

Where v = volume (m^3)
m = mass (kg)
S_v = specific volume (m^3kg^{-1})

Equation 6.3 was used to calculate the PVT curves for the PIM feedstocks that were used in the powder co-injection moulding experiments from the PVT data for the individual components and the mass fractions of the feedstocks given in table 5.5.

The PVT data for the PIM feedstocks were submitted to AC Technology for conversion into a material data import file. The material data import file was then imported into the C-Mold software and the 13 constants for the 2-domain modified Tait equation were calculated by the C-Mold software.

The data generated using the rule of mixtures were compared with the numerical data generated by the 2-domain modified Tait equation using the 13 constants calculated for each feedstock. This permits the determination of the applicability of using the modified 2-domain Tait equation for modelling the PVT behaviour of feedstocks.

6.2.4 Characterisation of the effect of temperature and pressure on the powder loading of the feedstocks

From the data generated for the specific volume vs temperature and pressure, it was possible to calculate the effect of temperature and pressure on the volume loadings on the feedstocks, as the powder volume loading affects the flow viscosity and thermal conductivities. This data can then be used in work involving viscosity and thermal conductivity with respect to either variations in temperature or pressure.

6.3 Thermal conductivity

This section describes the thermal conductivity experimental work that was undertaken.

It is pointed out that if a rule of mixtures approach is being used to predict the feedstock thermal conductivity, it is not important if the experimental thermal conductivity data for the individual components are obtained under a heating or cooling regime.

However, if the thermal conductivity data is to be subsequently used in computer prediction software such as C-Mold, it is important to simulate the conditions encountered by the material being injection moulded. This implies that the thermal conductivity data should be obtained under a high cooling rate thermal regime. The experimental thermal conductivity data was obtained under a heating thermal profile. This is because the transient line source technique had a heater probe instead of a coolant probe. This implies that is was not possible to obtain thermal conductivity data for a cooling regime.

6.3.1 Thermal conductivity determination of the binder components and powder components

The transient line source probe was used to measure the thermal conductivity at various temperatures between ambient and maximum injection moulding temperature for the four binder system components, polypropylene, paraffin wax, carnauba wax and stearic acid. The experimentally determined thermal conductivity vs temperature data was then manipulated to produce the overall thermal conductivity vs temperature data for the binder system using the series heat flow model.

There were inherent difficulties present in the determination of the thermal conductivities of the metal or ceramic powders. This was because the test powder samples are effectively composites comprising metal or ceramic particulates in an air matrix. This would lead to serious measurement errors due to the thermal conductivity of air being several orders of magnitude lower than those of the metal or ceramic powders.

The thermal conductivities were found from the open literature data for iron, stainless steel, alumina and zirconia. The thermal conductivity of the iron-alumina cermet and the zirconia toughened alumina composite powder was estimated using the series thermal conductivity model and the literature values for the thermal conductivities of iron, alumina and zirconia.

6.3.2 Experimental characterisation and numerical calculation of the feedstock thermal conductivities

The transient line source probe was used to measure the thermal conductivity at various temperatures between ambient and maximum injection moulding temperature for all of the feedstocks used during the project. The thermal conductivity data from both the binder and powder systems was combined together using the various thermal conductivity models found in the literature. The effect of temperature on the volume loading was taken into account when using these thermal conductivity models as the volume loading changes as a result of temperature. The volume loading percentages were taken from the volume loading vs temperature and pressure work. The calculated thermal conductivities were compared with the experimentally determined thermal conductivities of the feedstocks. This permitted the determination of the best model for calculating the feedstock thermal conductivities from the individual components' thermal conductivities.

6.3.3 Development of a 'spherical particulates within a bulk matrix' model (SPBM Model)

A new model was developed using the concept of a spherical particle within a cube, where the cube was considered to be the matrix material as PIM feedstocks comprise uniformly dispersed spheres in a continuous matrix. A further equation was derived

from first principles. The full derivation can be found in appendix B, which led to equation 6.4:

$$k_{total} = \frac{1}{r^2}\int_0^{r(r^2-y^2)^{\frac{1}{2}}}\int_0^{} \frac{k_b.k_p.r}{k_p r - k_p(r^2-x^2-y^2)^{\frac{1}{2}} + k_b.(r^2-x^2-y^2)^{\frac{1}{2}}}.dxdy + k_b(1-\tfrac{1}{4}\pi) \qquad \text{Eqn (6.4)}$$

Equation 6.4 proved too mathematically difficult to integrate, so a numerical approximation technique was used. This entailed the modification of the trapezium rule for use in 3-dimensional calculations, as shown in appendix C. A computer program was written in "ANSI C" computer programming language to calculate the thermal conductivity using this model, and the full code listing appears in appendix D.

6.3.4 Characterisation of the effect of various feedstock variables on the feedstock thermal conductivity using the thermal conductivity models

The thermal conductivity models found in the literature were used to investigate the effect of varying the powder volume loading, the binder system's thermal conductivity and the powder system's thermal conductivity. This work would provide an insight on how the feedstock composition influences the thermal conductivity of the feedstock.

6.4 Characterisation of feedstock rheology

The feedstocks' rheology was characterised using an instrumented Rosand precision Rh7-2 twin barrel capillary rheometer. All of the feedstocks were tested at three different temperatures, 160°C, 180°C and 200°C using a shear rate range of 10 s^{-1} to 10000 s^{-1} with a capillary die diameter of 1mm and length 20mm and a 1mm diameter "zero length" die. The pressure at the dies was recorded and the apparent viscosity vs apparent shear rate data calculated from the recorded pressures which were subject to Bagley and Rabinowitsch corrections.

The experimental true viscosity vs true shear rate data were submitted to C-Mold for the determination of the Cross-WLF constants. The Cross-WLF constants were input into the Cross-WLF equation 4.27 to generate the viscosity vs shear rate curves for the temperatures used in the rheology experiments for use in C-Mold. The Cross-WLF generated curves and the experimental shear viscosity vs shear rate data were then plotted to permit direct comparison. This permitted the determination of whether the Cross-WLF equation was a suitable model for modelling the rheology of typical PIM feedstocks.

To permit direct comparison, the low molecular weight polypropylene's rheology was also determined. Attempts were made to compound the binder components together in order to determine the rheology of the binder system. This failed because there were problems with compounding together binder components that had significantly different viscosities. The rheology of the binder system could not be determined.

7 Experimental technique: computer modelling

This section describes the computer modelling experimental work that was undertaken.

7.1 Creation of the finite element mesh model

The C-Mold Modeller software was used to create a geometrical representation of the mould cavity, with the dimensions of the mould cavity and some polymer mouldings being recorded by use of a vernier gauge and micrometer and the dimensions were put into the C-Mold modeller software. C-Mold modeller has an automatic mesher feature, and this was used to create the required mesh for the purposes of the simulations. Figure 7.1 shows a representation of the mesh that was created in C-Mold modeller and subsequently used in the injection moulding simulations.

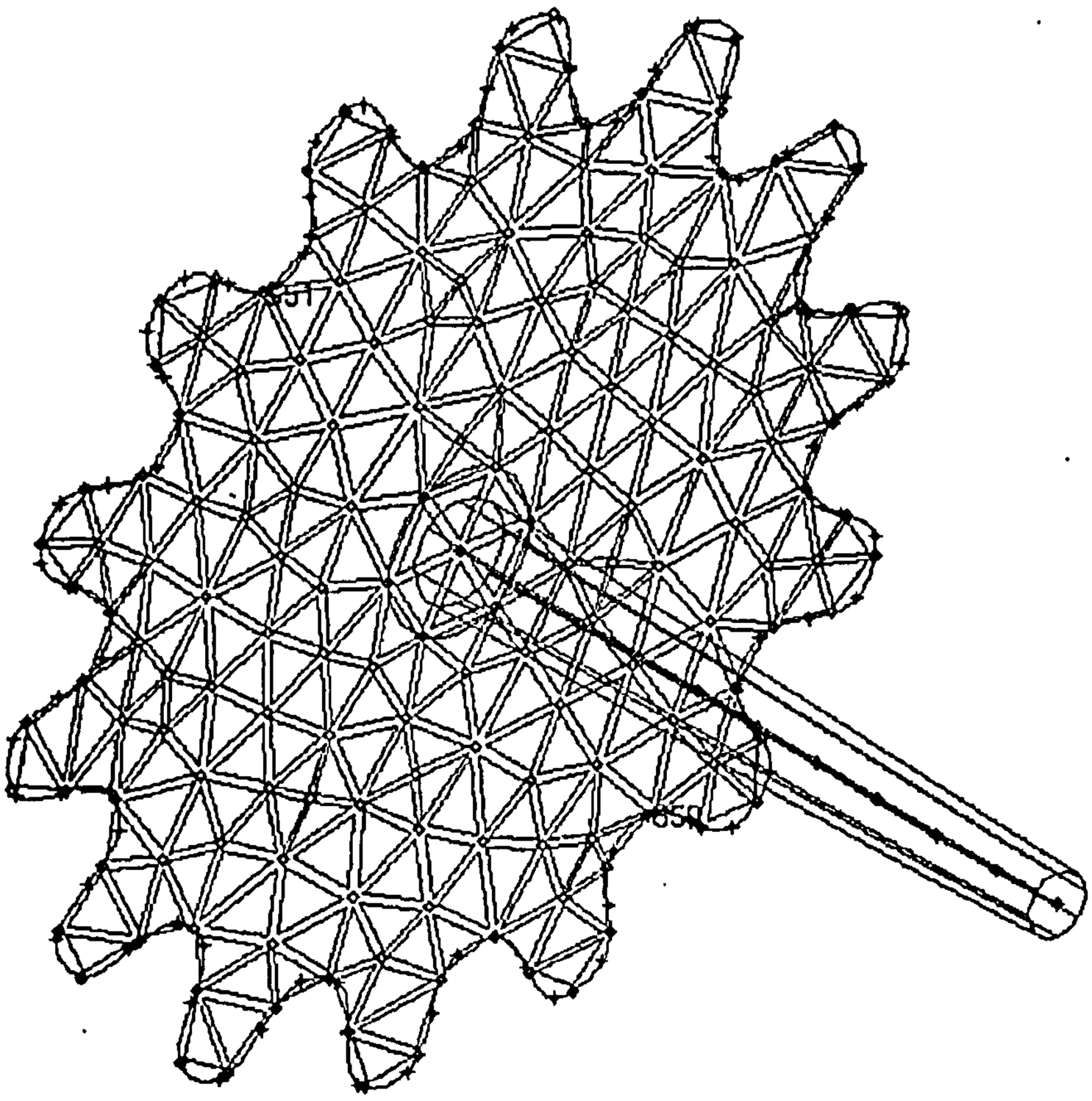

Figure 7.1 Finite element mesh representation of the mould cavity (Mesh element size = 2 mm and number of layers used in simulations = 12)

Increasing the number of layers used during the simulation of mould filling increases the accuracy of the predicted core thickness fraction. For example, if 12 layers are used across a 6mm cross-sectional thickness, each layer represents 0.5mm. This implies that the maximum error in the skin thickness prediction will be $\pm$ 0.25mm, or $\pm$ 4%. This implies that increasing the number of layers used in the simulations improves the accuracy of the skin thickness fraction. Increasing the number of layers increases the

computation time. Decreasing the mesh size decreases the maximum error in the radial position data. For example, if a 2 mm mesh element size was used, the error in the radial position would be ±1 mm for each element or ±3.2 to ±4% if the whole radius is taken into account. However, halving the mesh element size implies that the number of mesh elements are quadrupled, with a corresponding increase in the computation time needed for a mould filling simulation.

7.2 Creation of coolant data file, mould material data file, Dassett DM30 specification data file, and simulation settings data file

The material property data were found from the open literature for the coolant used in cooling the mould which was Castrol HT5 oil and a coolant file was created. The material property data of the mould material, which was tool steel P-20 was obtained from the mould manufacturers, Giffex Ltd, Luton, Bedfordshire, England. The data obtained was used to create a mould material data file. An injection machine specification file was created from the manufacturer's specifications of the Dassett DM30 injection moulding machine. The relevant data files that were created can be found in appendix E. The number of layers used during the simulations was set to 12. This implies that, for the 6 mm cross sectional thickness, the error in the core thickness would be ± 0.25 mm or ± 4.2%.

7.3 Injection moulding cycle process parameters

For all of the polymer injection moulding work and the injection moulding of the 3 model PCM systems, the C-Mold modelling process conditions and the Dassett DM 30 injection moulding process conditions were set up according to appendix K. The operation of the changeover valve was explained in section 5.4. It was stated that the time taken for the changeover valve to switch from one barrel to the other was of the order of hundredth of a second. C-Mold does not allow the possibility of investigating the effect of valve switch-over time on the skin profile. In addition, it is thought that the valve change over time was negligibly small to the injection times used. For details on the mould geometry and dimensions, the reader is directed to figures 5.2 and 5.3, in chapter 5.

7.4 Co-injection moulding and computer modelling of polymer systems

During the co-injection of the polymers, the first fifteen mouldings were discarded. This was done because the first fifteen mouldings may have been affected by remnants of degraded material from previous injection moulding runs. This permitted the machine to settle down into a steady state and 3 mouldings were selected at random from the next fifteen mouldings. This ensured that the sectioned mouldings were typical representations of skin profiles achieved during the polymer co-injection of bulk quantities of mouldings.

The actual moulding runs were carried out using polymers which had their material properties documented in the C-Mold polymers database which were also available at Cranfield. The selected polymers used did not have to have their material properties experimentally determined, and permitted computer simulation of injection moulding. This permitted the comparison of predicted and actual skin profiles for a selection of polymers. A Dassett DM30 co-injection moulding machine was used to co-inject three different polymers, as shown in table 7.1. Details of the mould cavity geometry and dimensions are presented by figures 5.2 and 5.3 in Chapter 5.

Manufacturer	Grade	Polymer classification
Solvay	A3180	polyethylene
Solvay	TUB	polyethylene
ICI	GWM213	polypropylene

Table 7.1 The three polymers used in the experiments

The predicted skin profile data was obtained by running modelling simulations of a Dassett DM30 30 tonne injection moulding machine co-injecting 2 polymers into a mould cavity. Figure 7.1 illustrates the cross-section of the mould cavity, which was 6 mm thick. The mould tooling was manufactured by Giffex, Luton, Bedfordshire, England. The mould cavity was cooled using Castrol HT5 oil supplied by a Churchill oil cooler and control unit. Data files containing machine data, mould material data, coolant data and modelling parameters were created and used in C-Mold. These files are listed in appendix E and the polymer material properties data files used in the C-Mold simulations are listed in appendix F.

All of the polymers used were colourless, with the exception of the Solvay TUB which was supplied in black. To aid visual identification of the skin-core polymer boundary in the sectioned mouldings with the travelling microscope, the colourless polymers were coloured by the addition of polymer colourants, red and black. 5% by weight of colourant was added to the bulk polymer and was considered to have negligible effect on any of the bulk polymer's overall material properties. All of the polymer moulding runs were performed at 200°C and the skin volume was 34.4% and the core was 67.6%. The ram speed profile was constant from start to end of the injection sequence. The actual linear injection screw speed was determined by the injection time specified in the control panel. The actual skin profiles were obtained by sectioning the co-injected polymers and measuring the thickness of the top and bottom skin layers at 2mm $\pm$ 0.25mm intervals along its radius using a travelling microscope, which had a resolution of $\pm$ 0.01 mm

7.5 Comparison of actual and predicted skin profiles for polymer co-injection moulding for the verification of C-Mold's use as a predictive tool

Six moulding runs were performed, using two polymers as shown in table 7.2 for three different injection filling times. The corresponding simulations were run on C-Mold. The mouldings were sectioned and their skin profiles were measured. The core

thickness fraction data were extracted from the simulation results and converted into skin thickness fractions. Graphs were plotted showing the skin thickness fractions vs radial position for the actual and predicted skin profiles.

	Skin			Core		
	Manufacturer	Grade	Polymer class	Manufacturer	Grade	Polymer class
1	ICI	GWM213	PP	ICI	GWM213	PP
2	Solvay	A3180	PE	Solvay	A3180	PE

Table 7.2 Details of co-injection moulding runs carried out

Three injection moulding runs were carried out using ICI GWM213 polypropylene for both the core and skin for three total injection times of 1.0s, 1.7s and 3.3s. This was repeated with the polypropylene substituted with Solvay A3180 polyethylene. (Total injection time includes the injection times for both the skin and core materials)

7.6 Effect of polymer rheology on the skin profile

The computer modelling software and injection moulding machine experiments were used to investigate the effect that rheology has on the skin profile and to compare the predicted and actual skin profiles. This was done by choosing a medium viscosity polypropylene, ICI GWM213, and a high viscosity polyethylene, Solvay TUB.

The moulding runs are detailed in table 7.3. Three moulding runs were performed using these two polymers. The ICI GWM213 polypropylene was coloured with the addition of 5% by weight red polymer colourant, and the Solvay TUB polyethylene was supplied in black.

	Skin			Core		
Run No	Manufacturer	Grade	Polymer class	Manufacturer	Grade	Polymer class
A	ICI	GWM213	PP	Solvay	TUB	PE
B	ICI	GWM213	PP	ICI	GWM213	PP
C	Solvay	TUB	PE	ICI	GWM213	PP

Table 7.3 Co-injection moulding details for the effects of viscosity on the skin profile

7.7 Effect of mould filling time on the skin profile

C-Mold was used to investigate the effect of varying the injection time with a constant skin to core thickness ratio, to see if this had any influence on the skin profile. 12 co-injection moulding runs were carried out as shown in table 7.4. The ejected mouldings were sectioned and their skin profiles were measured using a travelling microscope.

	Skin			Core			
Run No	Manufacturer	Grade	Polymer class	Manufacturer	Grade	Polymer class	Injection time (s)
1	ICI	GWM213	PP	ICI	GWM213	PP	1.0
2	Solvay	A3180	PE	Solvay	A3180	PE	1.0
3	ICI	GWM213	PP	Solvay	TUB	PE	1.0
4	Solvay	TUB	PE	ICI	GWM213	PP	1.0
5	ICI	GWM213	PP	ICI	GWM213	PP	1.7
6	Solvay	A3180	PE	Solvay	A3180	PE	1.7
7	ICI	GWM213	PP	Solvay	TUB	PE	1.7
8	Solvay	TUB	PE	ICI	GWM213	PP	1.7
9	ICI	GWM213	PP	ICI	GWM213	PP	3.2
10	Solvay	A3180	PE	Solvay	A3180	PE	3.2
11	ICI	GWM213	PP	Solvay	TUB	PE	3.2
12	Solvay	TUB	PE	ICI	GWM213	PP	3.2

Table 7.4 Details of injection moulding runs performed

7.8 Effect of polymer thermal properties on the skin profile

For the simulation experiments into the effect of thermal properties on the skin profile, the ICI GXM43 polypropylene data file was selected. The thermal data in the materials data file were modified to permit the investigation into the effects of thermal properties on the predicted skin profile. No moulding runs were carried out as it was practically impossible to alter the intrinsic thermal properties of typical polymers. Since there are infinite combinations of feedstock composition, this was done to provide an insight on how the feedstock composition affects the final feedstock material properties.

The material properties data of the ICI GXM43 can be found in appendix F. The simulation experiments were done in two parts. The first investigated the effect of specific heat capacity. The ICI GXM43 specific heat capacity value was 2000 $Jkg^{-1}K^{-1}$, and two test specific heat capacity values of 500 $Jkg^{-1}K^{-1}$ and 3500 $Jkg^{-1}K^{-1}$ were used. The second investigated the effect of thermal conductivity on the predicted skin profiles. The thermal conductivity value of the ICI GXM43 was 0.15 $Wm^{-1}K^{-1}$, and two test values of 0.05 $Wm^{-1}K^{-1}$ and 0.25 $Wm^{-1}K^{-1}$ were used.

7.9 Computer modelling of model PCM systems

This section describes the powder co-injection computer modelling experimental work that was undertaken. The effects of feedstock thermal properties on the skin profile and the modelling of the three model PCM systems were studied. The reader is reminded that the thermal conductivity and specific heat capacity data of the feedstocks was experimentally determined under a heating regime due to limitations imposed by the equipment. Since the material being injection moulded undergoes rapid cooling within the mould cavity, the thermal conductivity and specific heat capacity data should have been obtained under a cooling regime, as this would simulate the actual thermal behaviour of the feedstock being injection moulded.

7.9.1 Computer modelling of the effect of thermal properties on co-injection moulding of feedstocks

This was done to examine the effect of the feedstock thermal conductivity and specific heat capacity on the skin profile. Modifying the binder composition influences the feedstock thermal conductivity and altering the powder composition affects the feedstock's specific heat capacity. This was done by using the material data gathered from the material testing on the 60% iron feedstock, and the relevant material data are listed in appendix G. The simulations were run several times with different values of specific heat capacity and thermal conductivity for both the skin and core feedstocks

The thermal conductivity data was altered to a new value for both the skin and core. This allowed the comparison of predicted skin profiles for three different thermal conductivities of 0.5, 1.5 and 2.5 $Wm^{-1}K^{-1}$. The specific heat capacity data was altered to a new value for the skin and core. This allowed the comparison of predicted skin profiles for three different specific heat capacities of 200, 500 and 800 $Jkg^{-1}K^{-1}$.

7.9.2 Comparison of predicted and actual skin profiles for 3 model powder co-injected moulding systems

As stated earlier, no recorded attempt has been found for the use of modelling software for the prediction of the skin profile in the co-injection of two distinct feedstocks. Three model powder co-injection moulding systems were injection moulded, sectioned and their skin profiles measured with radial position. Simulations were also run on C-Mold to obtain the predicted skin profiles. The material property data of the 5 feedstocks used in the modelling can be found in appendix G. Three model powder co-injection moulding runs were performed as shown in table 5.7, section 5.4.

8 Results: powder co-injection moulding

The results of the powder co-injection moulding work are presented in this section.

8.1 Characterisation of selected powders

The results of the powder characterisation from the x-ray sedigraph experiments are presented for the iron and three different sizes of alumina powders. Figures 8.1 and 8.2 show the cumulative mass percentage and mass population percentage respectively as a function of the particle size of BASF 4-6μm nominal diameter carbonyl iron OM.

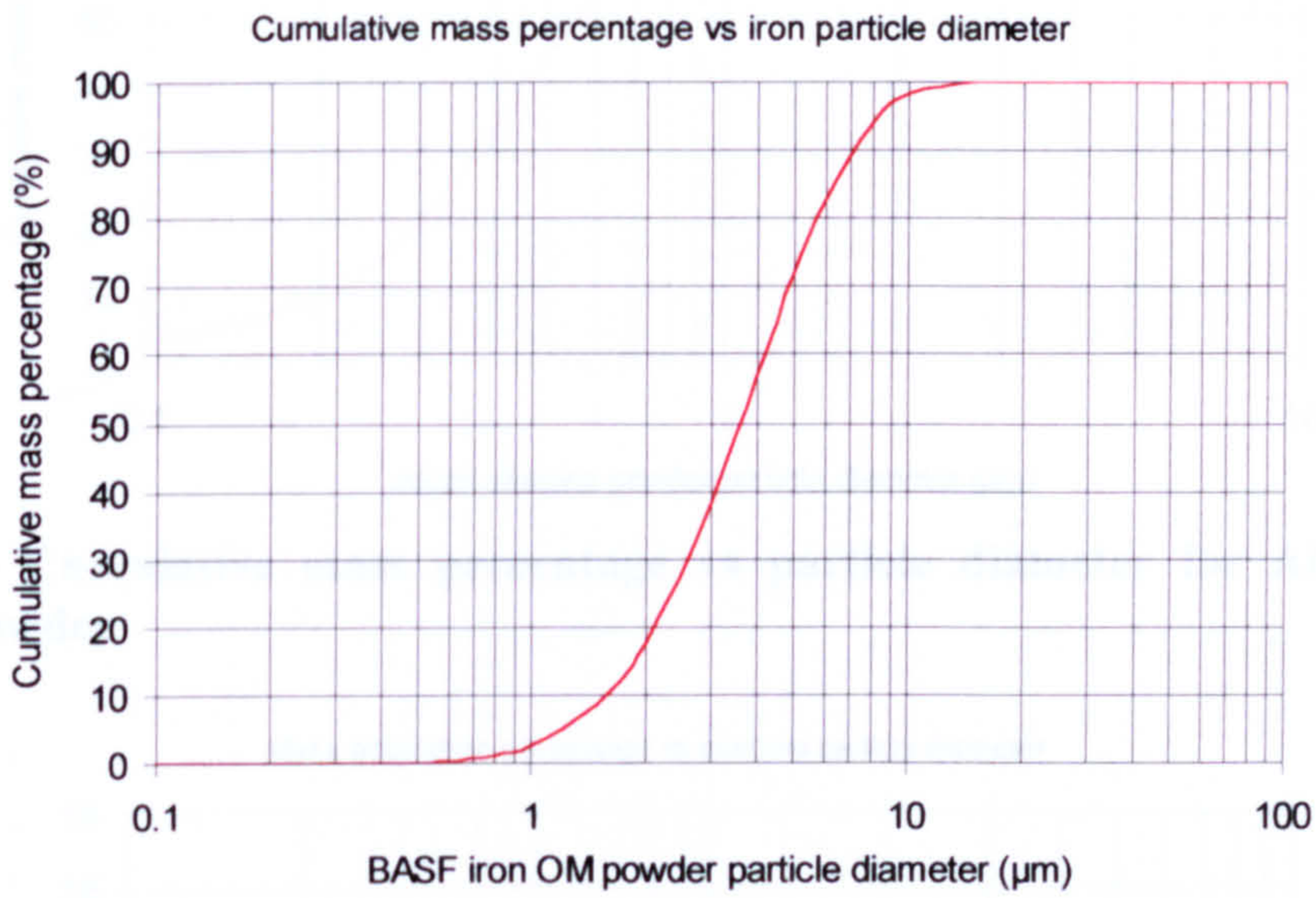

Figure 8.1 Cumulative mass percentage vs particle diameter for BASF carbonyl iron OM powder

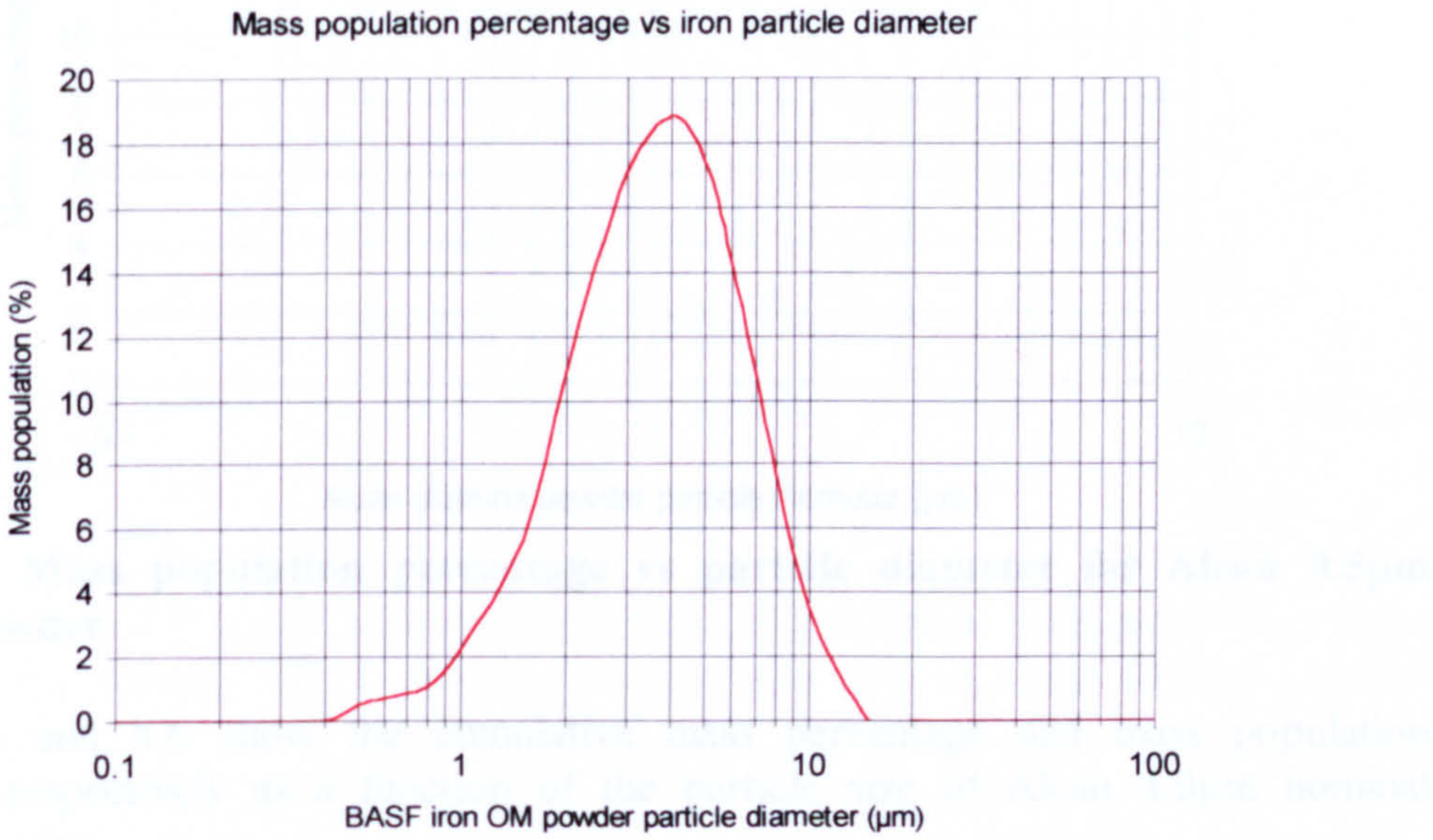

Figure 8.2 Mass population percentage vs particle diameter for BASF carbonyl iron OM powder

Figures 8.3 and 8.4 show the cumulative mass percentage and mass population percentage respectively as a function of the particle size of Alcan 0.5μm nominal diameter alumina.

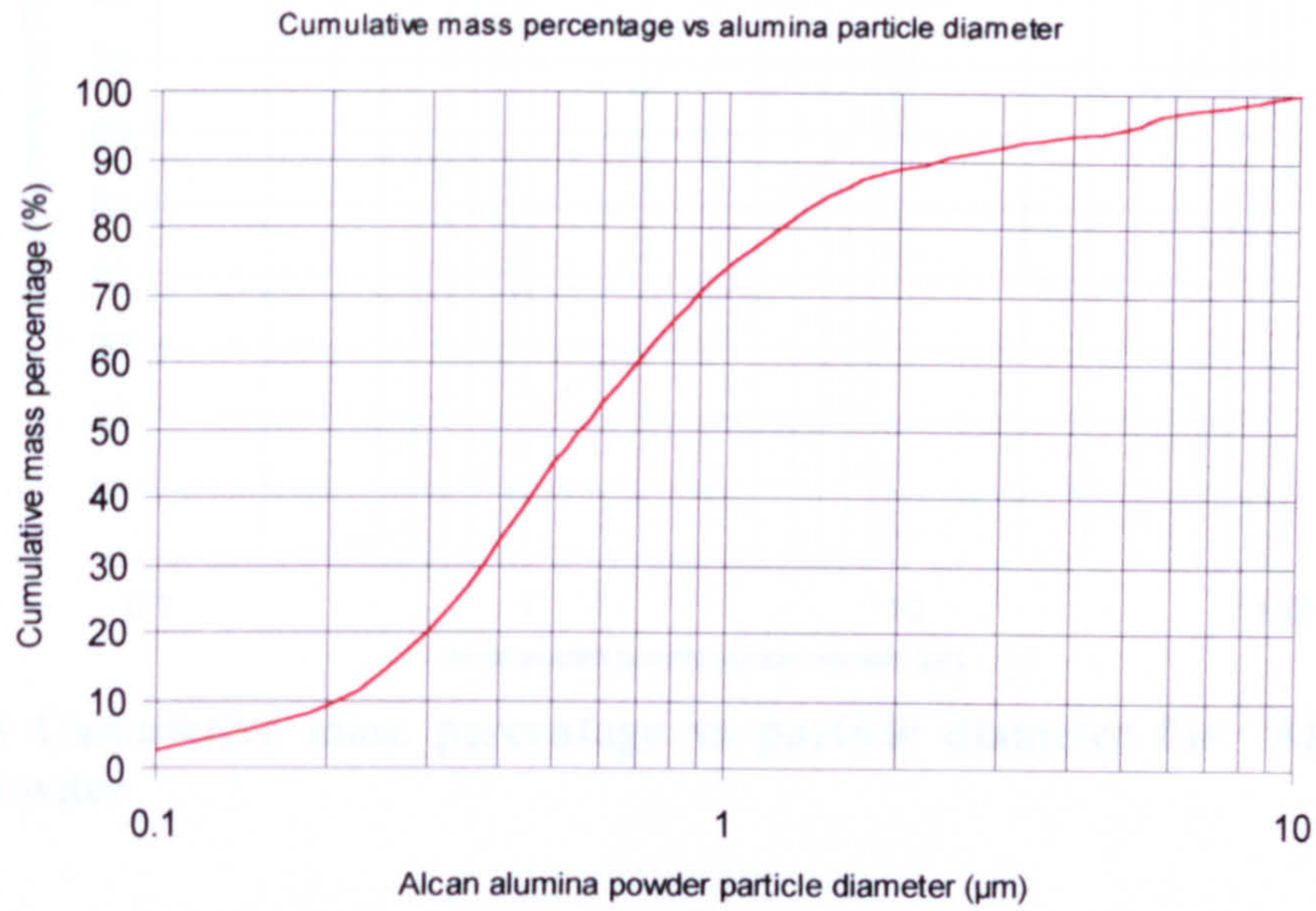

Figure 8.3 Cumulative mass percentage vs particle diameter for Alcan 0.5μm alumina powder

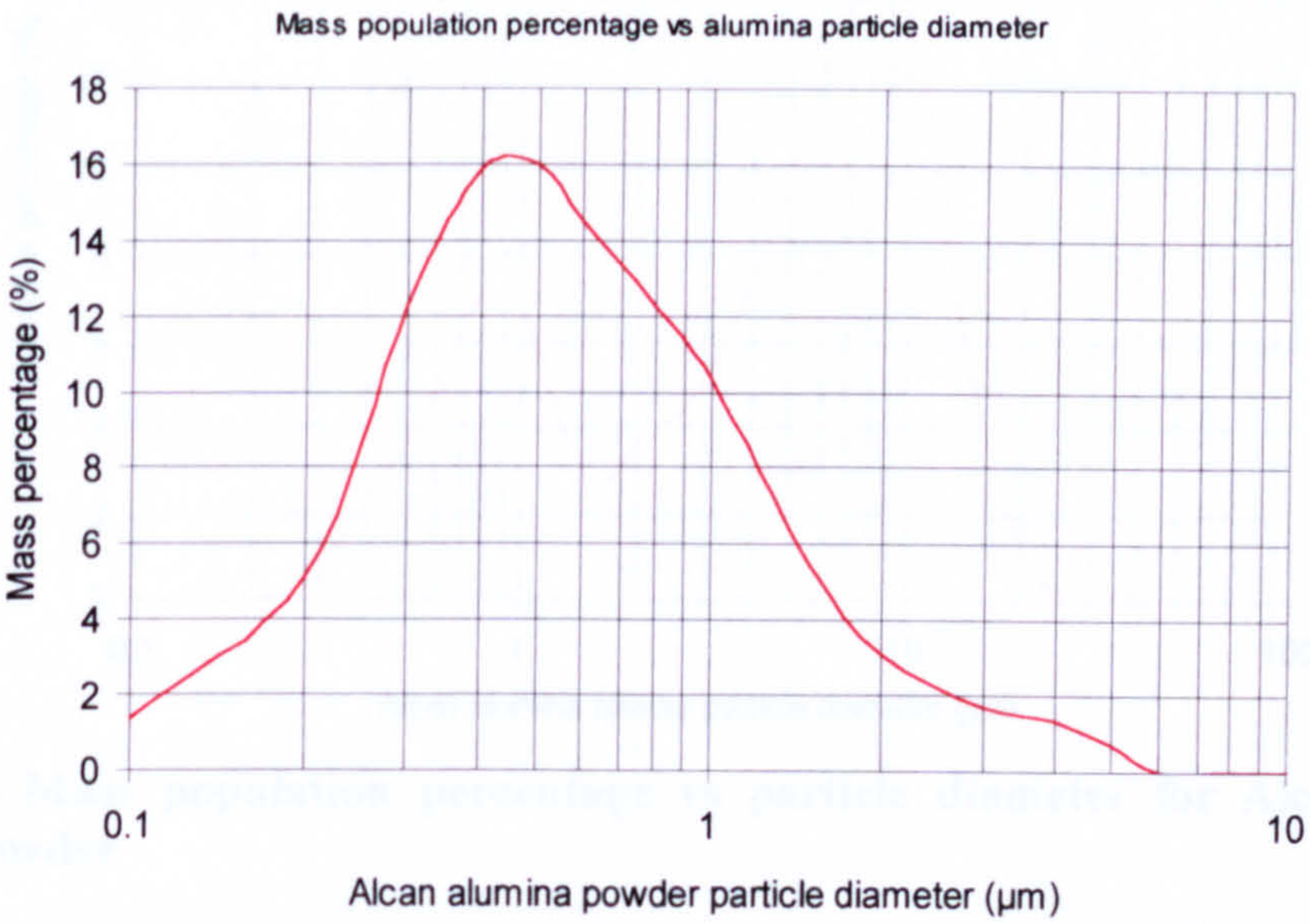

Figure 8.4 Mass population percentage vs particle diameter for Alcan 0.5μm alumina powder

Figures 8.5 and 8.6 show the cumulative mass percentage and mass population percentage respectively as a function of the particle size of Alcan 4.0μm nominal diameter alumina.

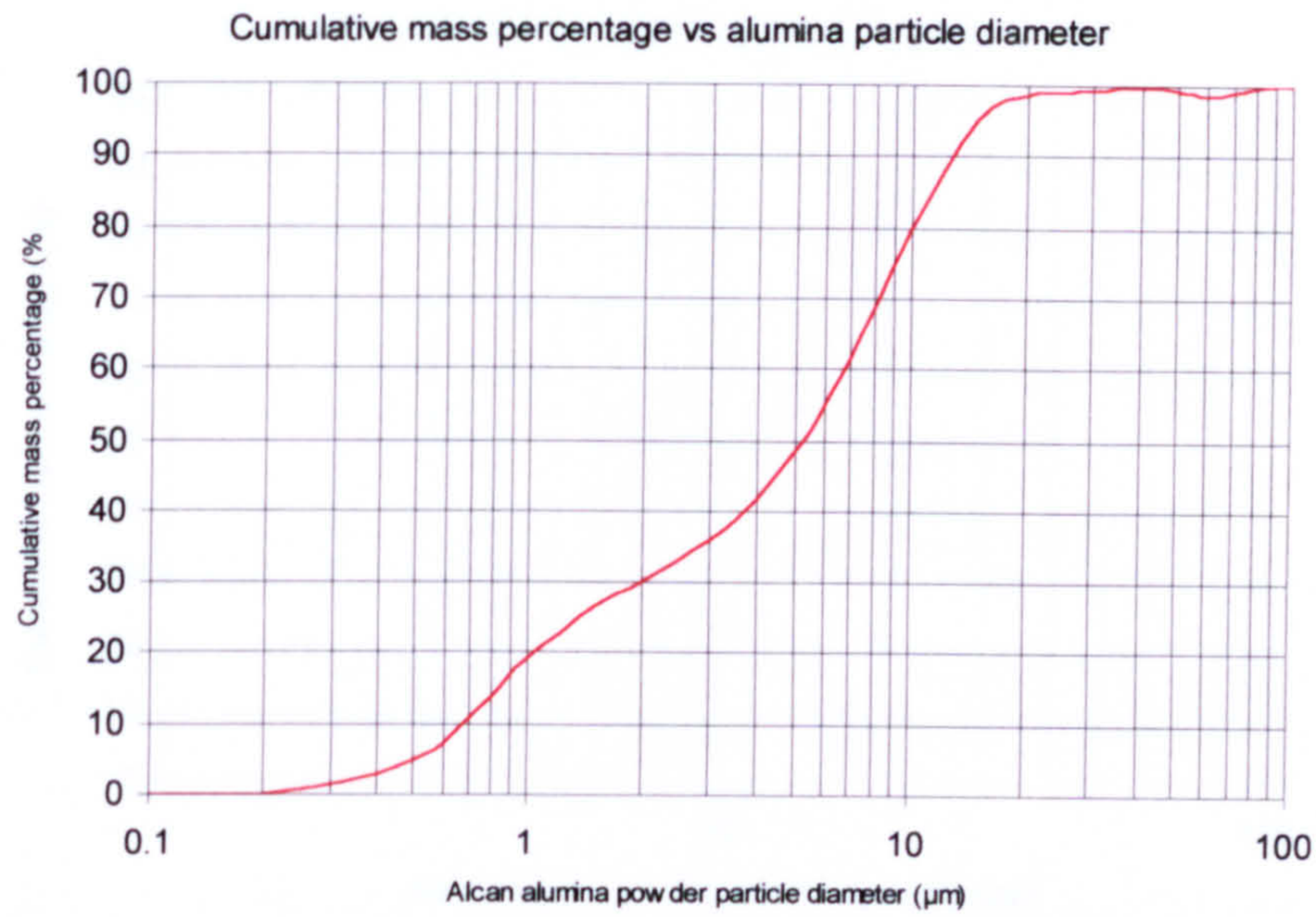

Figure 8.5 Cumulative mass percentage vs particle diameter for Alcan 4.0µm alumina powder

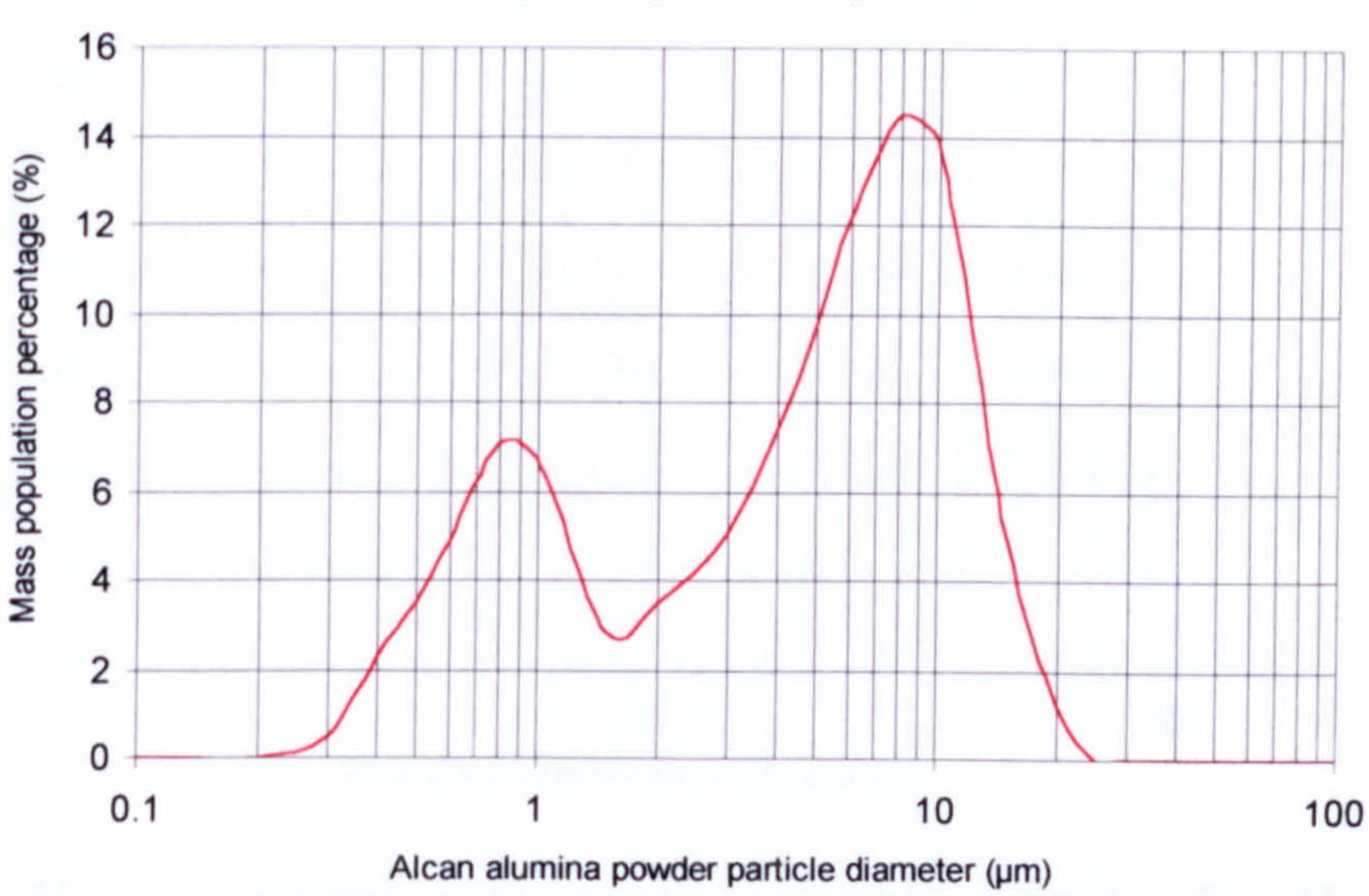

Figure 8.6 Mass population percentage vs particle diameter for Alcan 4.0 µm alumina powder

Figures 8.7 and 8.8 show the cumulative mass percentage and mass population percentage respectively as a function of the particle size of Alcan 13.0µm nominal diameter alumina.

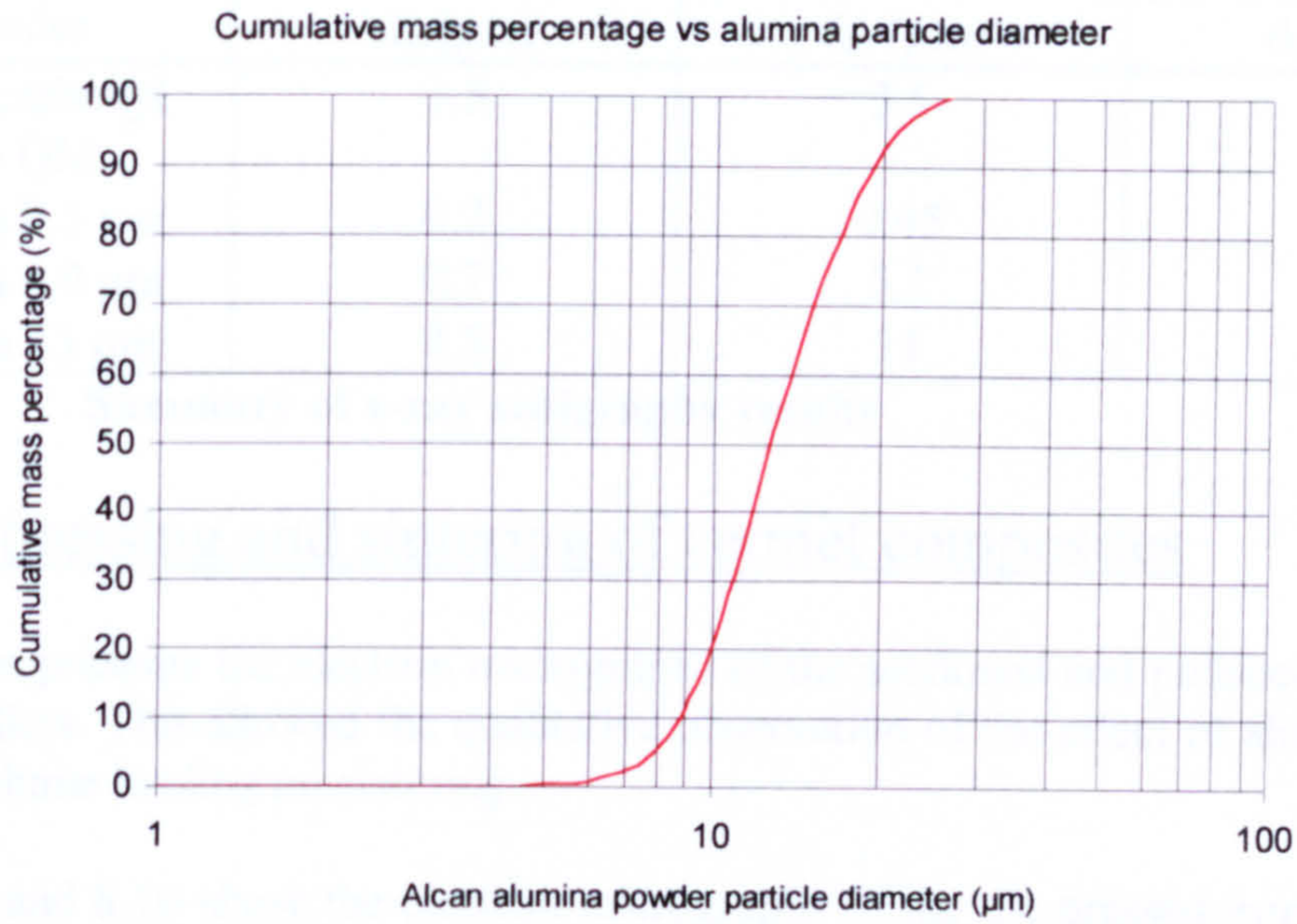

Figure 8.7 Cumulative mass percentage vs particle diameter for Alcan 13.0μm alumina powder

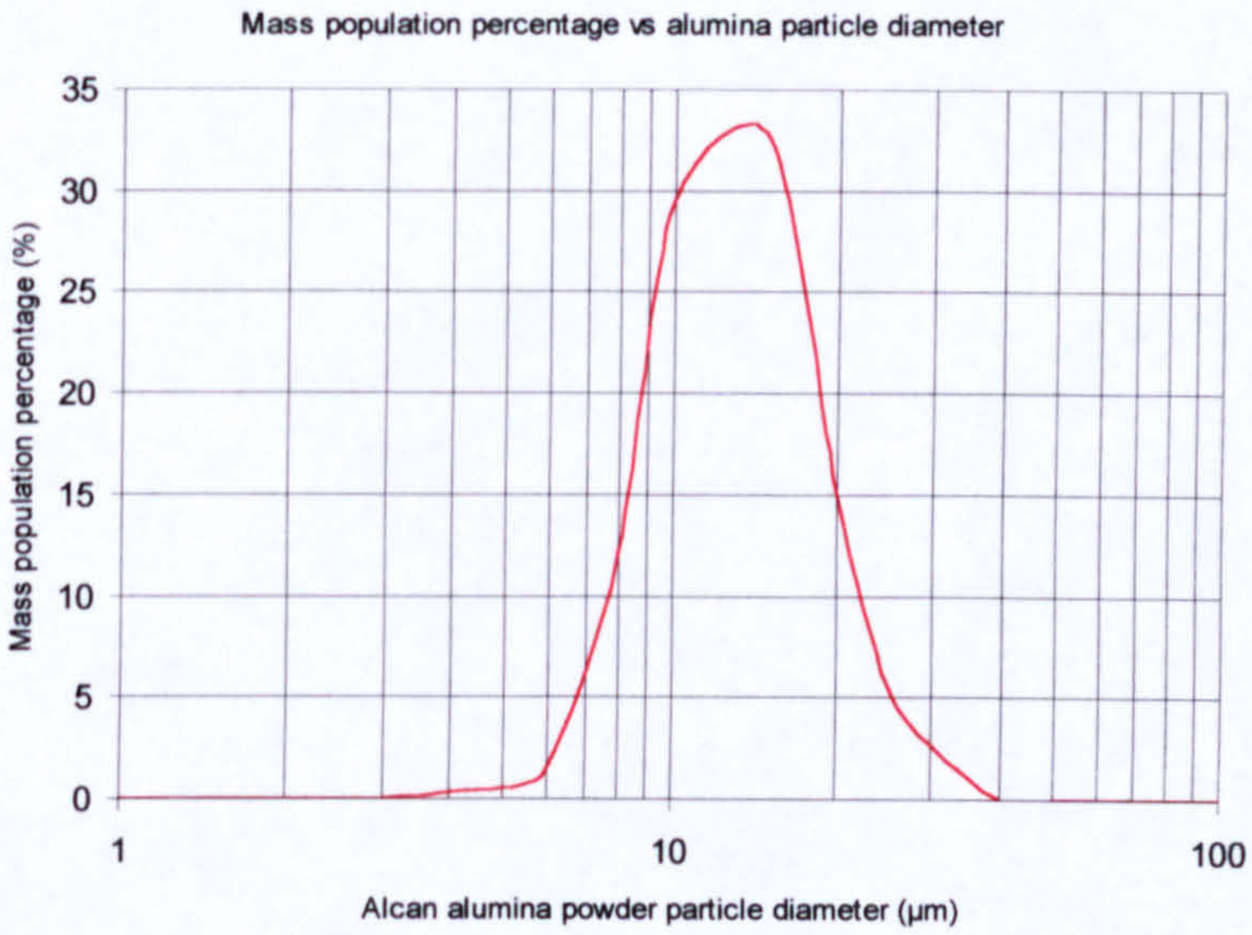

Figure 8.8 Mass population percentage vs particle diameter for Alcan 13.0μm alumina powder

Table 8.1 summarises the important points of the x-ray sedigraphy results in figures 8.1 to 8.8. The powder characterisation indicated that all of the powders specifications agreed with the manufacturer's nominal specifications with the exception of the Alcan 4.0μm alumina as figure 8.6 indicated that the alumina powder of nominal diameter 4.0μm was a bi-modal mixture of two different diameter powders, illustrated by the mass population percentage versus particle diameter. There were significant quantities of 0.8μm to 0.9μm alumina particulates. which were also evident in the SEM photos of the die pressed cermets. This was considered to be the result of poor quality control by the manufacturer.

Powder	d_{10} (μm)	d_{50} (μm)	d_{90} (μm)
BASF carbonyl iron OM	1.5	3.5	7
alumina 0.5 μm	0.2	0.45	2.1
alumina 4.0 μm	0.7	5.1	11
alumina 13 μm	8.5	11	19

Table 8.1 Summary of x-ray sedigraphy results

8.2 Die pressing and sintering of cermet composites

This section presents the electron micrographs of the sectioned and polished sintered die pressed pellets. This allowed the qualitative observation of the effect of alumina particle size and volume loading on sintering.

Figure 8.9 and 8.10 show the electron micrographs of the die pressed iron pellets after sintering. Both figures 8.9 and 8.10 show considerable sintering of the iron particles. Typical pore diameters were 1μm to 2μm.

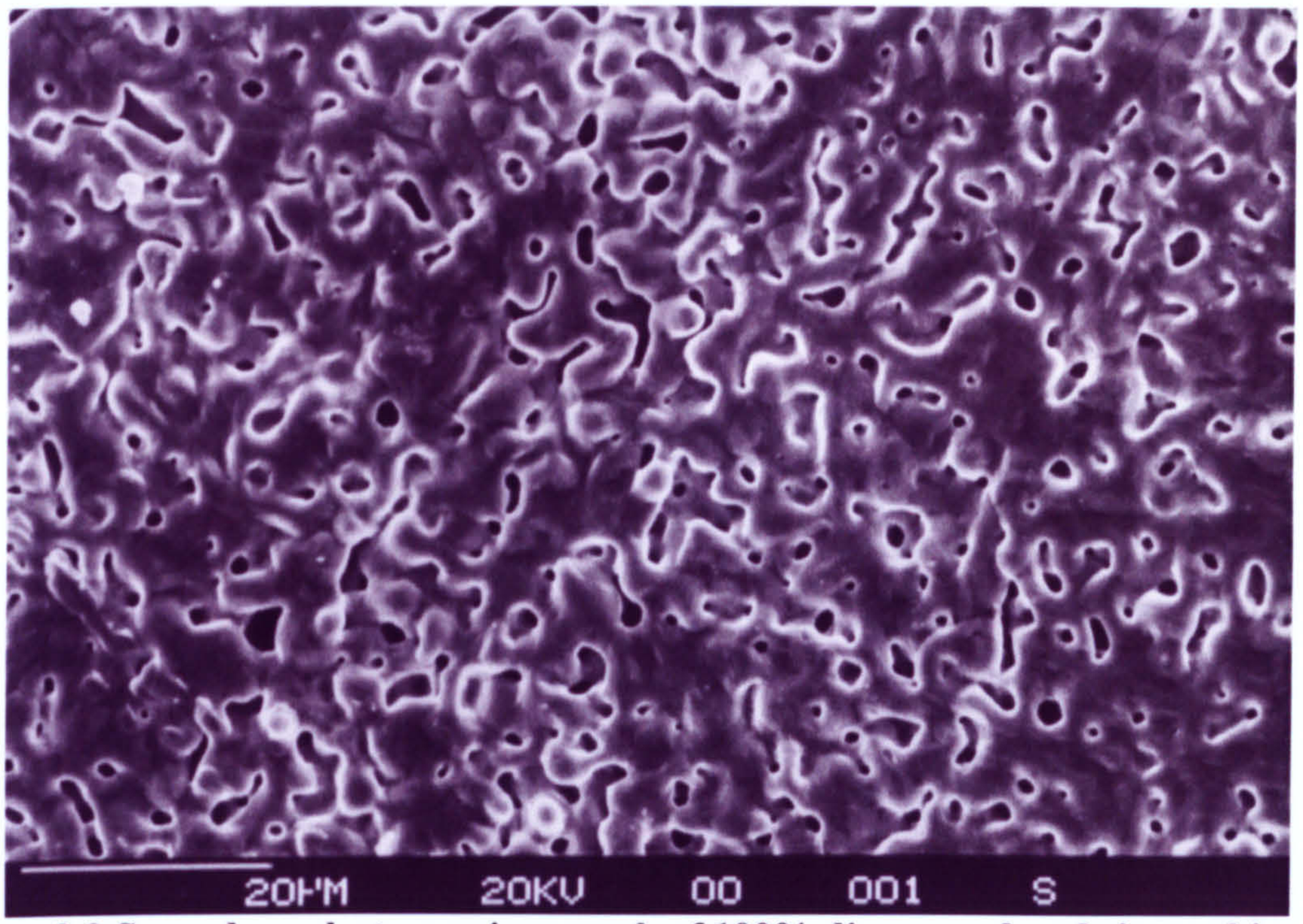

Figure 8.9 Secondary electron micrograph of 100% die pressed and sintered iron

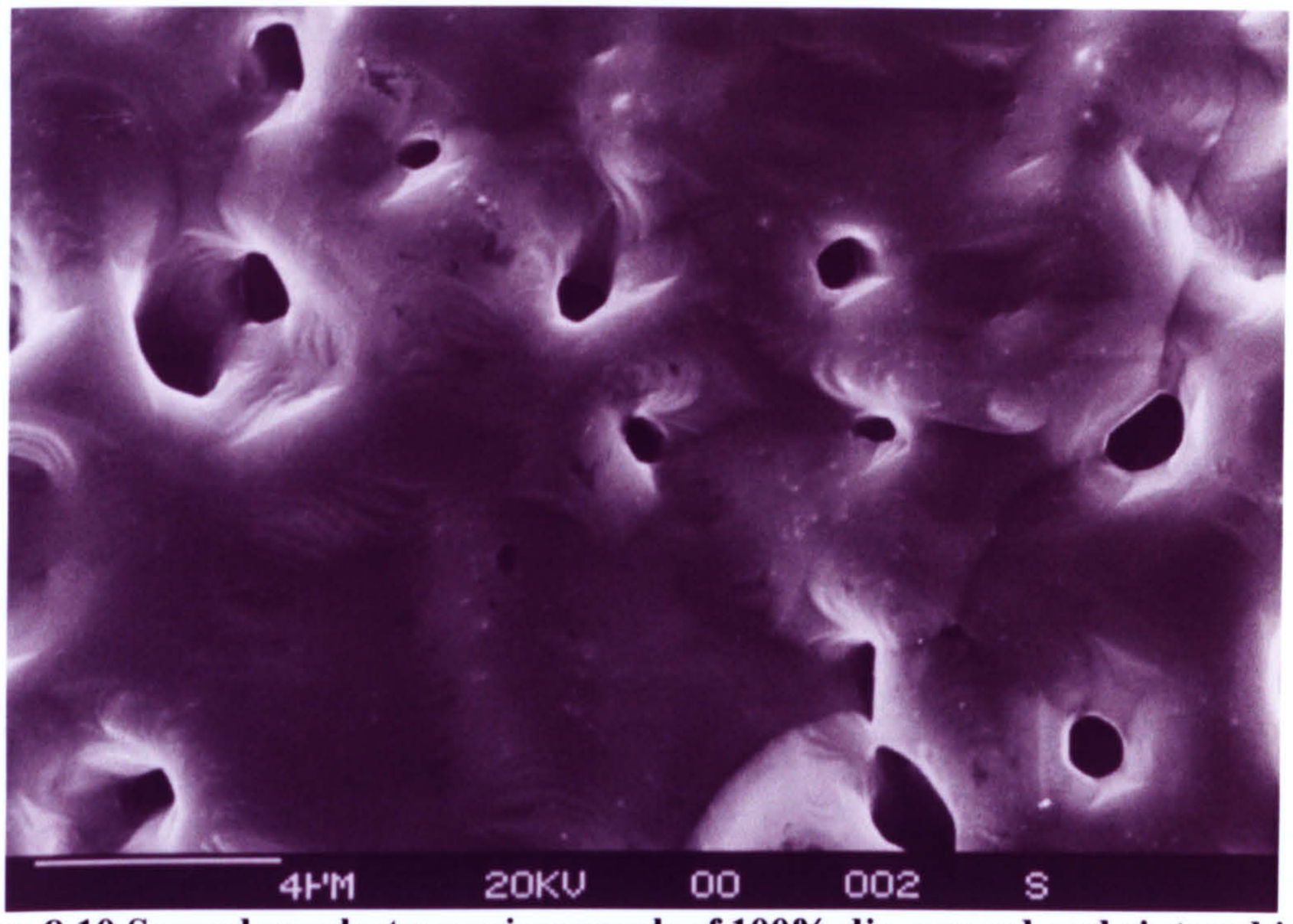

Figure 8.10 Secondary electron micrograph of 100% die pressed and sintered iron

Figure 8.11 shows an electron micrograph of iron with 15% by volume of 0.5μm alumina. It shows very little apparent sintering. Some neck formation between neighbouring iron particles is apparent. It is apparent that there are a substantial number of alumina particles in between two adjacent iron particles and inhibiting neck formation, which is essential for sintering to take place.

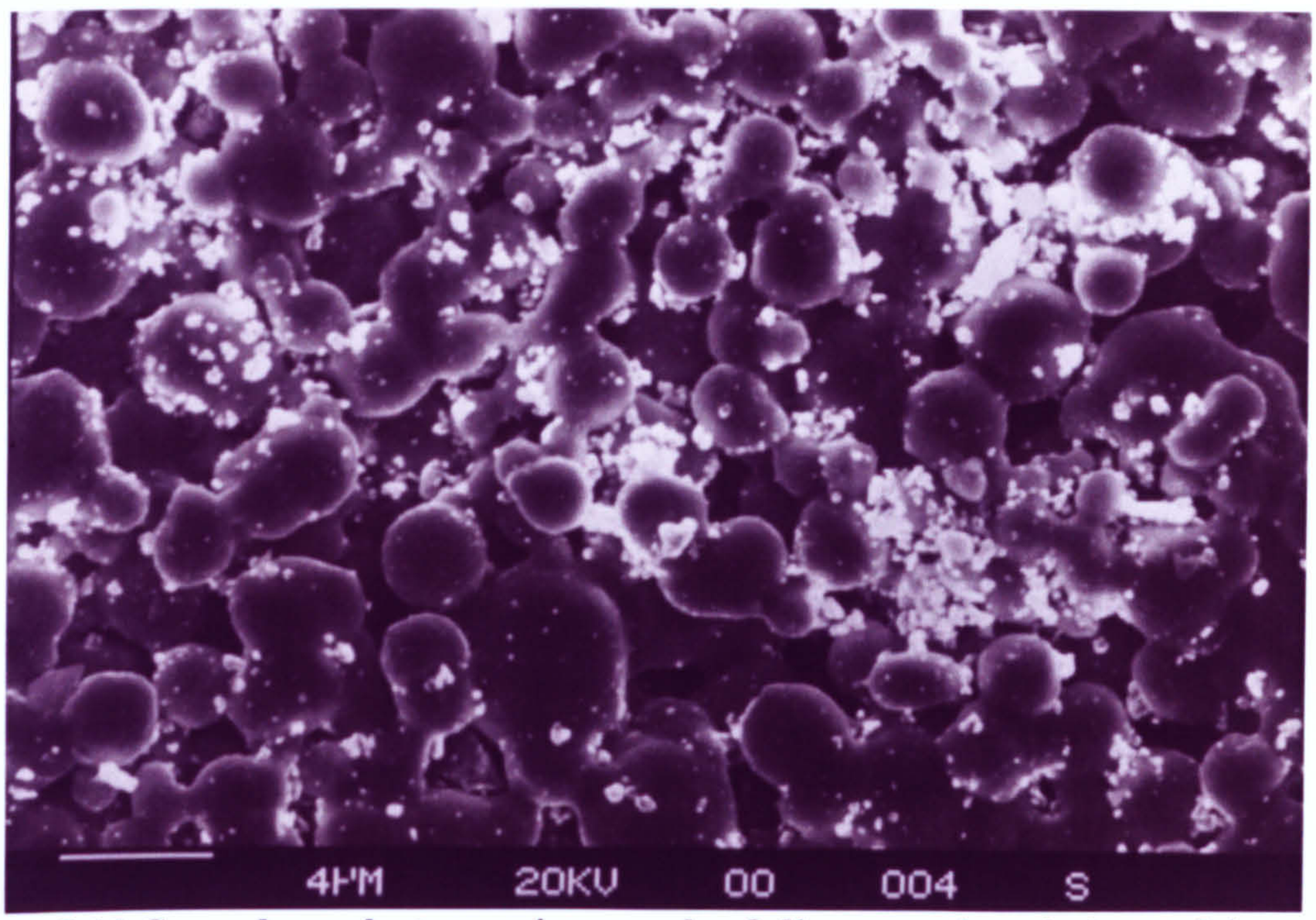

Figure 8.11 Secondary electron micrograph of die pressed and sintered iron and 15% vol 0.5μm alumina cermet

Figure 8.12 shows an electron micrograph of iron with 15% by volume of 4.0μm alumina. Significant sintering has taken place. Substantial necks can be seen between adjacent iron particles. Iron particles can be observed to sinter around the central alumina particle (white). There is a light scattering of sub-micron sized alumina particles (white). Figure 8.13 illustrated graphically that there was significant sintering of the matrix when the amount of sub-micron alumina was low. In areas of significant sub-micron alumina particle quantities, little iron to iron particle sintering was apparent.

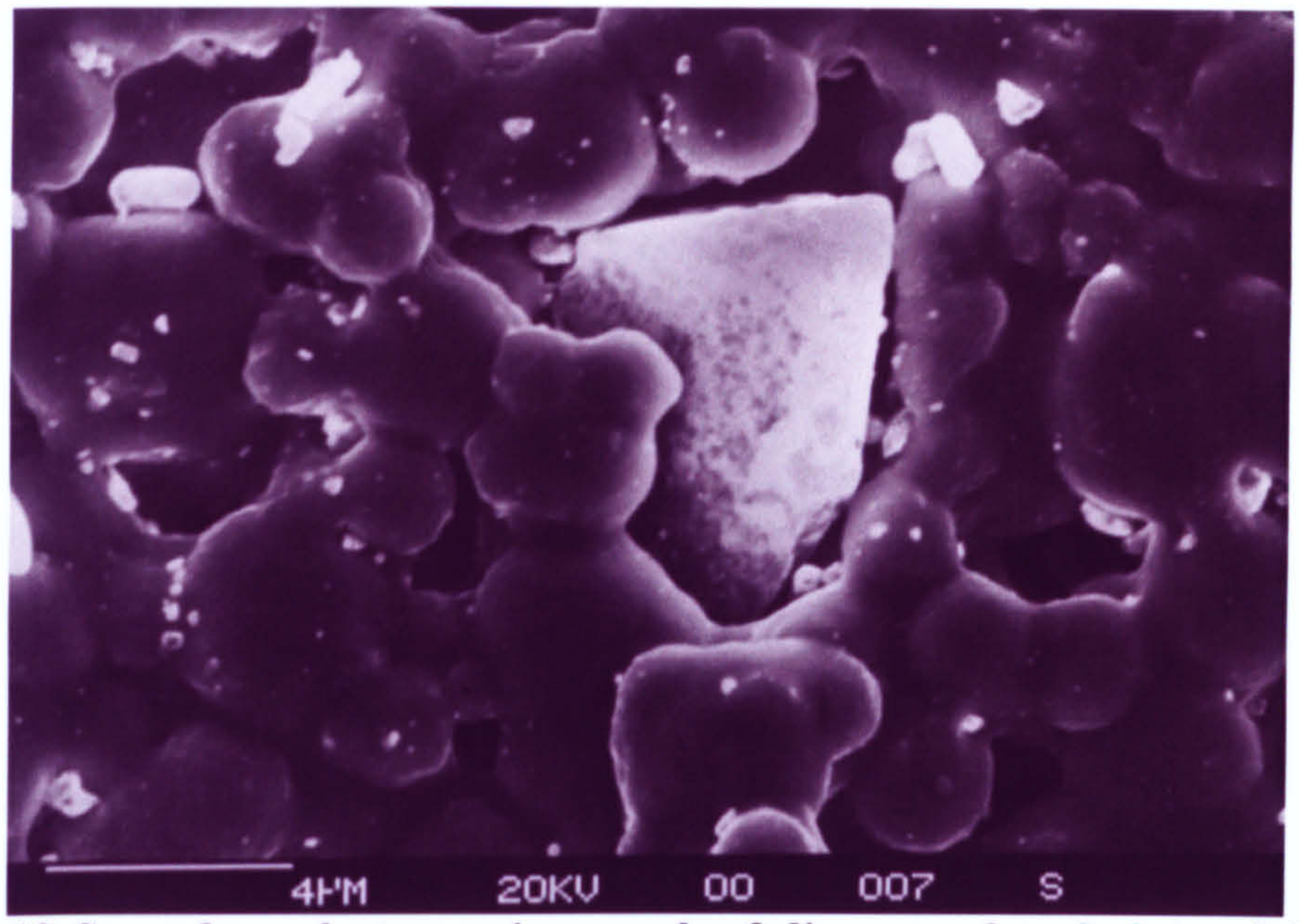

Figure 8.12 Secondary electron micrograph of die pressed and sintered iron and 15% vol 4.0μm alumina cermet

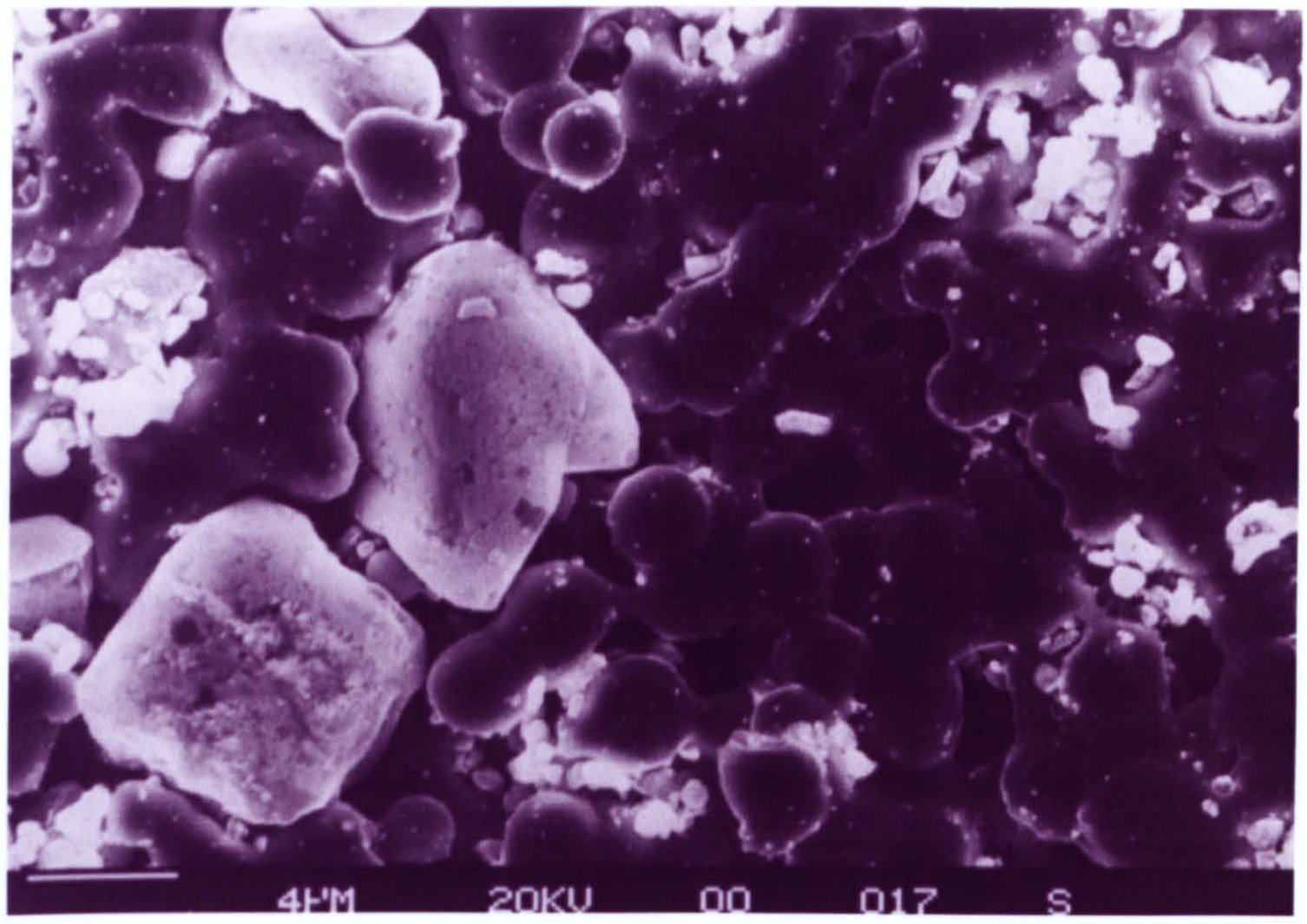

Figure 8.13 Secondary electron micrograph of die pressed and sintered iron and 15% vol 4.0μm alumina cermet

Figures 8.14 to 8.16 are electron micrographs of iron with 15% by volume of 13.0μm alumina at different magnifications. Figure 8.14 shows substantial iron particle sintering and the white alumina particulates are surrounded by a network of connected iron particles. Figure 8.15 shows that considerable sintering has occurred to the point of closed pores forming and has nominally identical porosity levels as the 100% die pressed iron samples. Figure 8.16 shows in greater detail the formation of the iron matrix around a single white alumina particle.

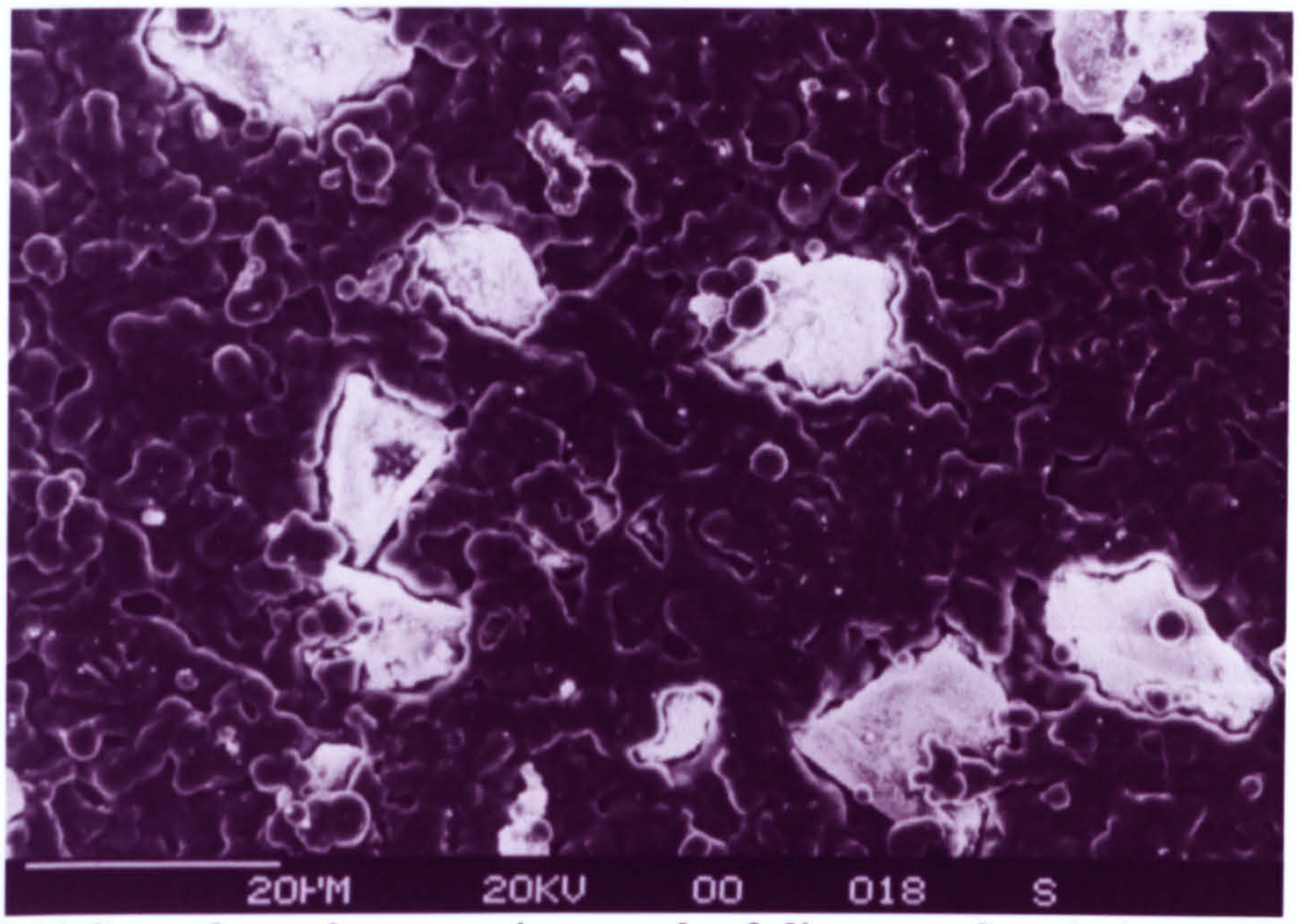

Figure 8.14 Secondary electron micrograph of die pressed and sintered iron and 15% vol 13μm alumina cermet

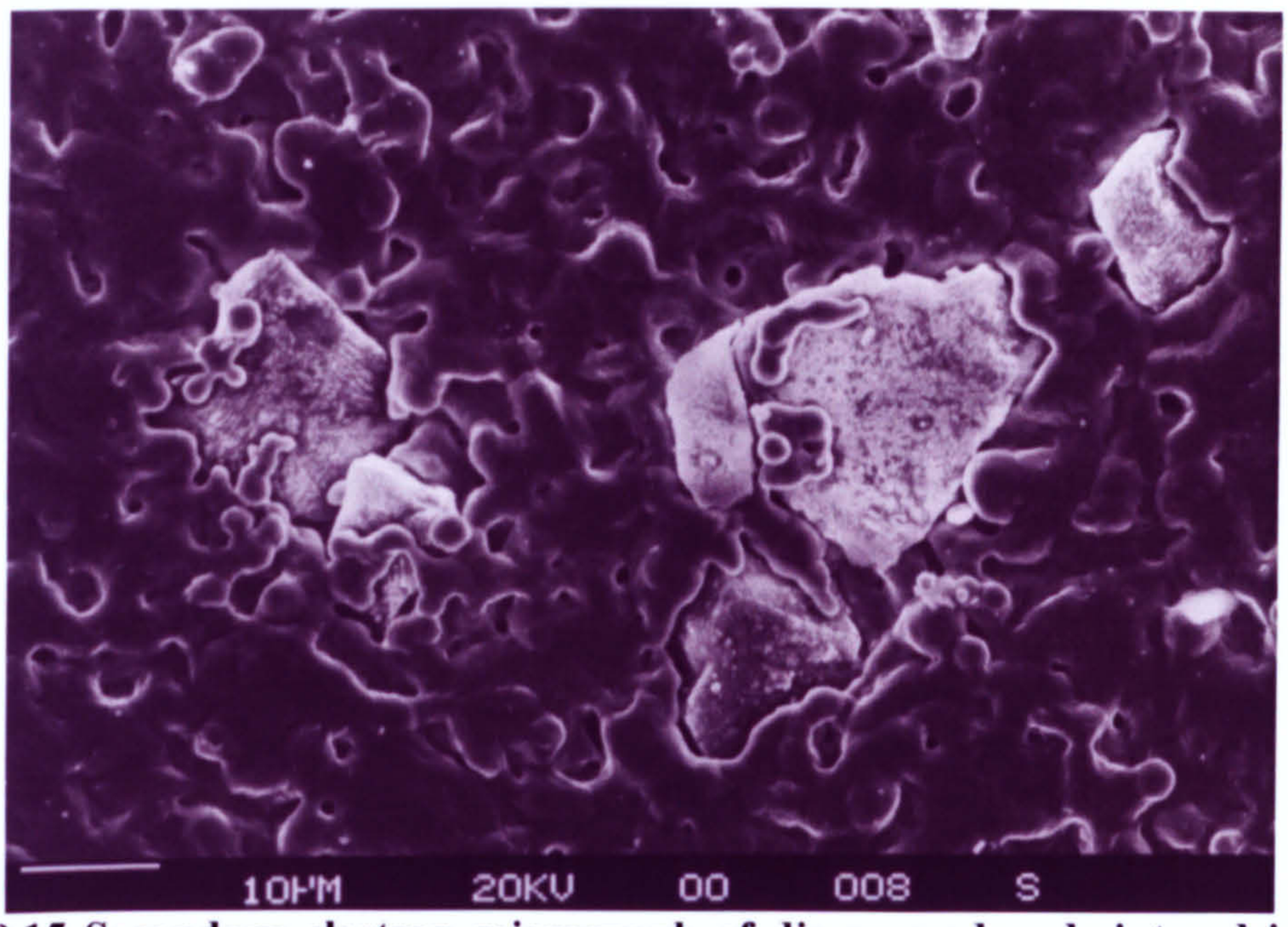

Figure 8.15 Secondary electron micrograph of die pressed and sintered iron and 15% vol 13μm alumina cermet

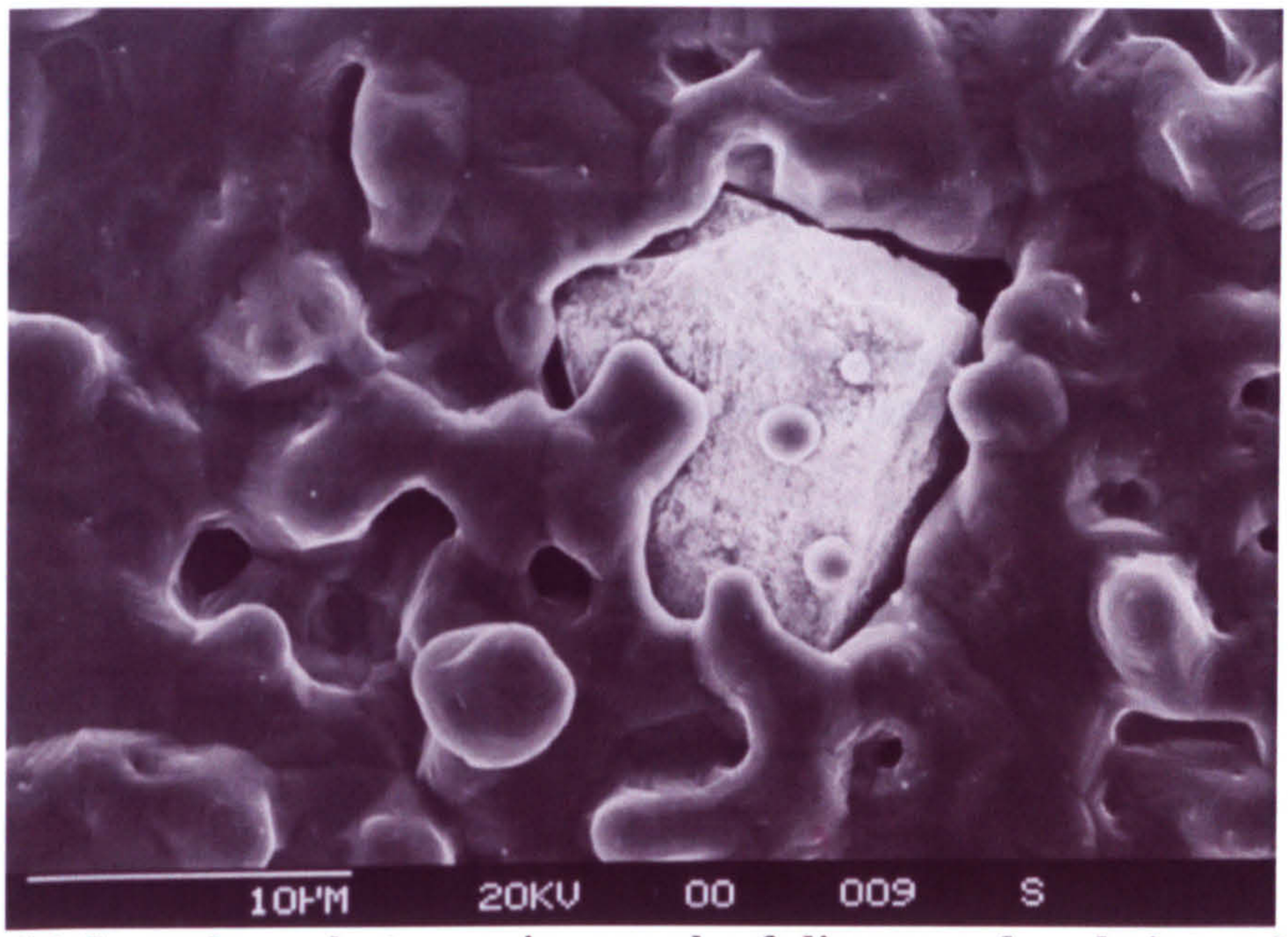

Figure 8.16 Secondary electron micrograph of die pressed and sintered iron and 15% vol 13µm alumina cermet

8.3 Effect of alumina volume loading and alumina particle size on shrinkage

Figure 8.17 illustrates that the sintered density decreases dramatically with decreasing rigid alumina inclusion diameters and that with increasing rigid alumina inclusion diameters, the sintered density of the composite cermet approaches that of the sintered density of 100% volume iron matrix powder.

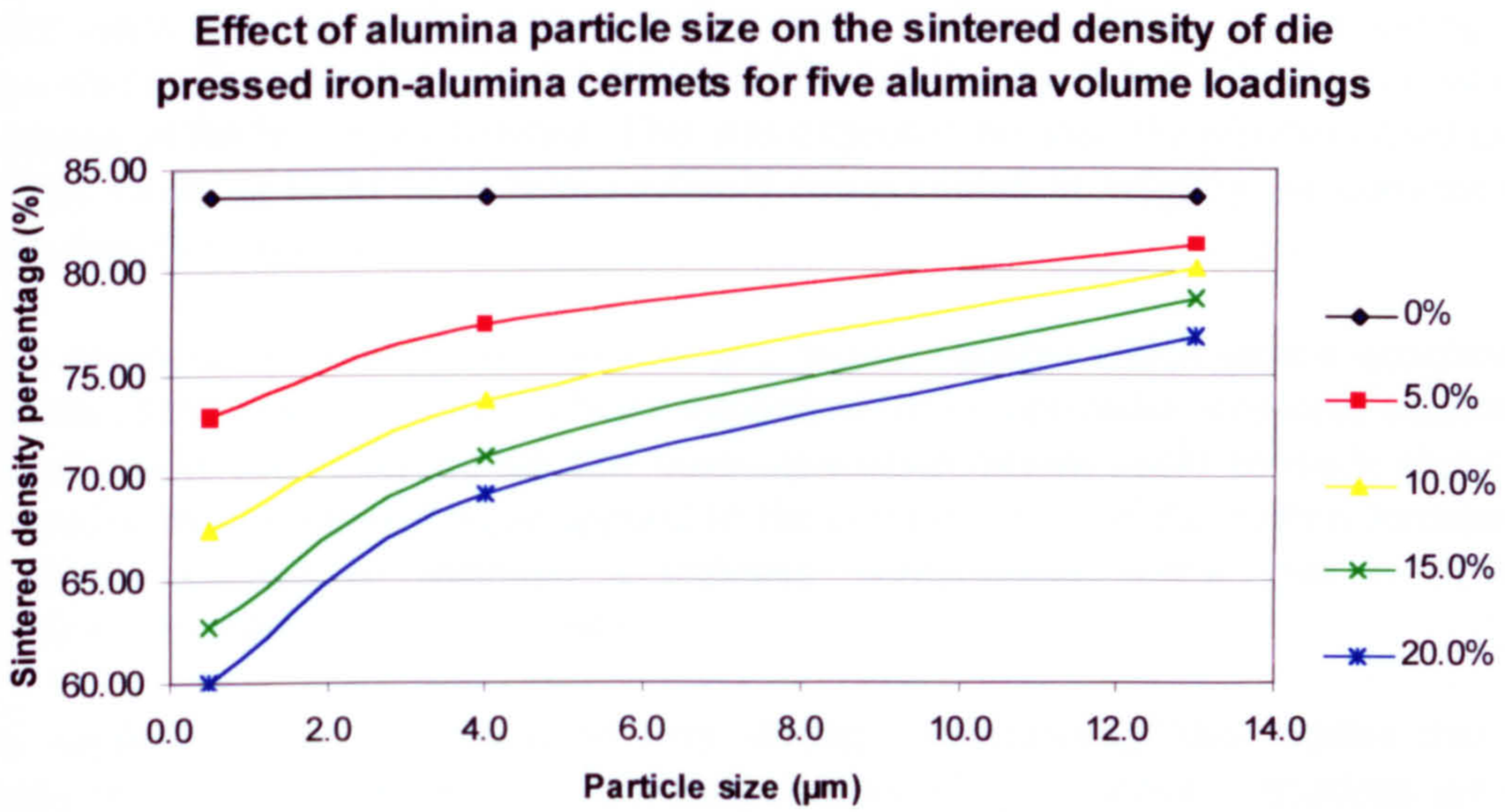

Figure 8.17 Effect of alumina particle size on the sintered density of die pressed iron-alumina cermets (Sintered density percentage is defined as the ratio of apparent density to maximum theoretical density expressed as a percentage)

Figure 8.18 illustrates that the volume loading of the rigid inclusions affected the sintered density and that the effect of particle size of the rigid alumina inclusions determined the degree of influence that the volume loading had on the sintered density. As the particle size of the rigid alumina inclusions decreased, the effect of volume loading on the sintered density became more pronounced.

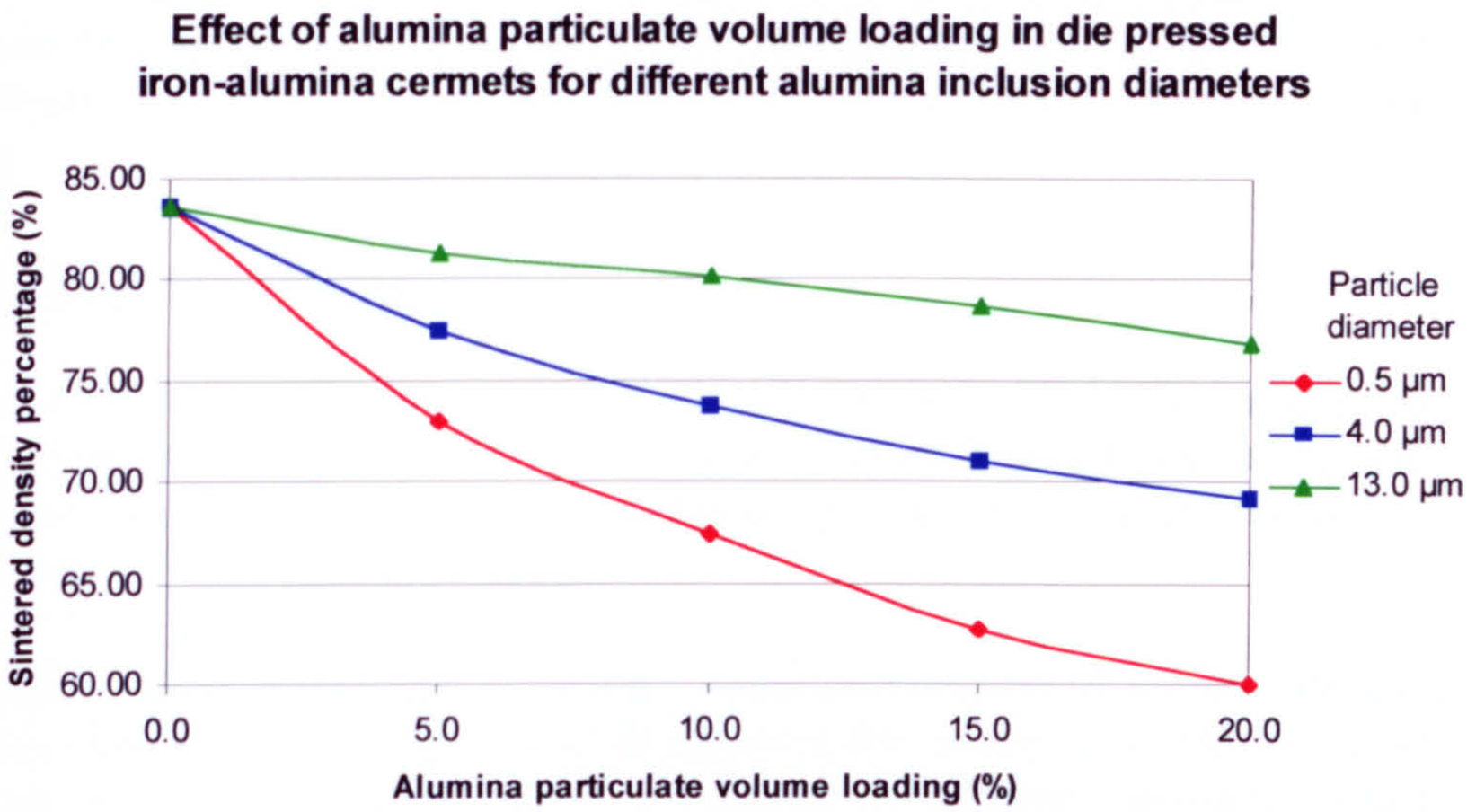

Figure 8.18 Effect of alumina particulate volume loading in die pressed iron-alumina cermets (Sintered density percentage is defined as the ratio of apparent density to maximum theoretical density expressed as a percentage)

8.4 Compounding

The mass burn-offs of extrudate samples taken during compounding indicated that the powder mass loading during compounding was consistent during compounding and comparable to the intended powder masses indicated in table 5.5 during the preparation and mixing of the feedstock batches. This was expected because the powders used in the feasibility study of PCM have been routinely compounded in industry for conventional powder injection moulding.

On the compounder used, there was a torque meter available which gave a quantitative indication of the amount of torque being applied to the compounder screws to maintain a constant rpm setting. This implies that qualitative observations could be made about the comparative magnitude of torque applied to the compounding of the molten feedstocks. The torque applied to maintain a constant compounder screw rpm is directly proportional to the feedstock viscosity.

If the applied torque was found to vary during compounding, this implies that the viscosity of the feedstock had altered during compounding. Viscosity variations are due to numerable causes such as powder agglomeration, development of binder rich regions or variations in powder loading. Negligible torque variations were observed during compounding. This together with the mass burn-offs imply that the quality of the compounded feedstocks was high. This is further supported by the lack of gross defects

during solvent debinding, thermal debinding and sintering during subsequent visual unaided and optical microscopic examination.

When the ceramic feedstocks were compounded, it was observed that the feedstock took on a grey appearance. This was thought to be due to the highly abrasive nature of the ceramic particles through the volumetric feeder screws, resulting in metal debris contaminating the ceramic feedstocks. The closed flight screws were exchanged with open flight screws, which resolved the problem satisfactorily for the duration of the project.

8.5 Injection moulding

No problems were encountered as the PCM feedstocks used in the present study were routinely injection moulded in conventional powder injection moulding and a well established technique of co-injection moulding was used for the first time at Cranfield to co-inject feedstocks instead of polymers.

Immediately after co-injection moulding, visual examination of the mouldings with the naked eye revealed that the green mouldings were free of any gross defects, as illustrated by figure 8.19. Figure 8.19a shows a polymer co-injection moulding, which is for illustrative purposes to give the reader a view of a typical core region that could reasonably be expected in powder co-injection mouldings. Figure 8.19b shows a sample ceramic co-injected moulding, where the core was alumina feedstock and the skin is zirconia toughened alumina. Figure 8.19c shows a sample metal co-injected moulding, where the core was iron and the skin was iron and stainless steel masteralloy.

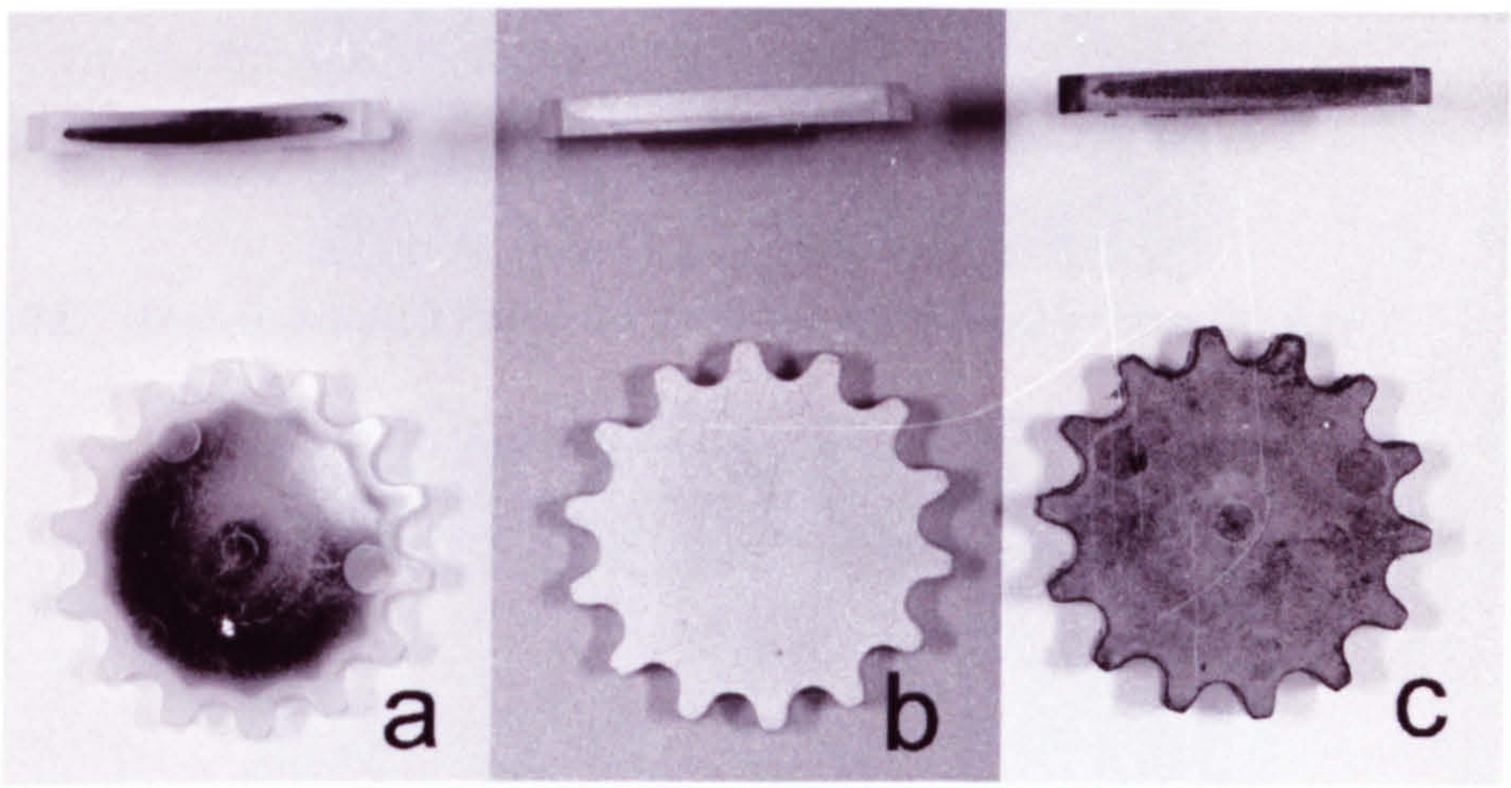

Figure 8.19 Optical photographs of the co-injected mouldings

8.6 Debinding

All of the model PCM systems were apparently debound in both the solvent and thermal debinding stages. Visual macroscopic inspection of the solvent debound mouldings did not reveal any apparent defects. It was not possible to inspect the thermally debound mouldings as the thermal debinding and sintering were carried out in the same furnace. As soon as the thermal debinding was completed, the sintering profile started at this point. This eliminated the need to cool down after thermal debinding and heating up again to start sintering.

8.7 Sintering

Figure 8.20a shows a sample metal co-injected moulding immediately after sintering had concluded and visual inspection by the naked eye and optical microscopy showed that there were no apparent gross defects. Figure 8.21a shows a sample metal co-injected moulding that has been sectioned, ground, polished and etched with Nital etchant to improve the skin - core optical contrast. The core is carbonyl iron and the skin is stainless steel alloy. Figure 8.20b shows a sample sintered ceramic co-injected moulding immediately after sintering had concluded. It was visually inspected with the naked eye and by optical microscopy, and was free of any apparent gross defects. Figure 8.21b shows a sample ceramic moulding that has been sectioned, ground and polished. The core is alumina and the skin is zirconia toughened alumina.

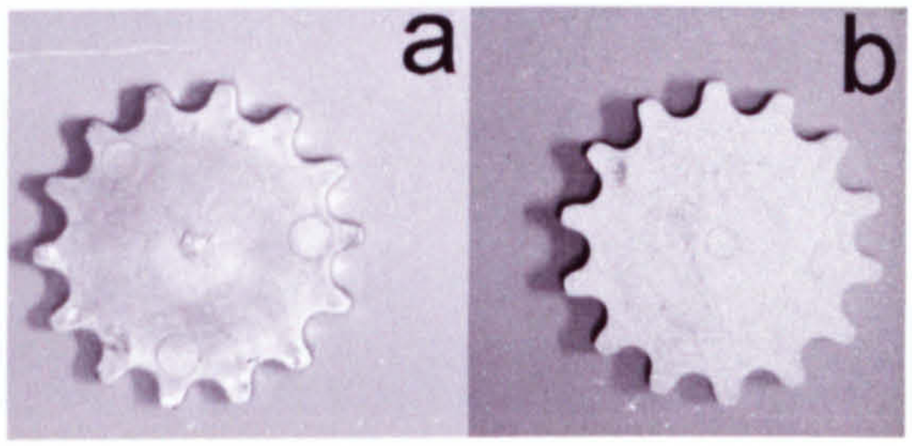

Figure 8.20 Debound and sintered powder co-injection mouldings

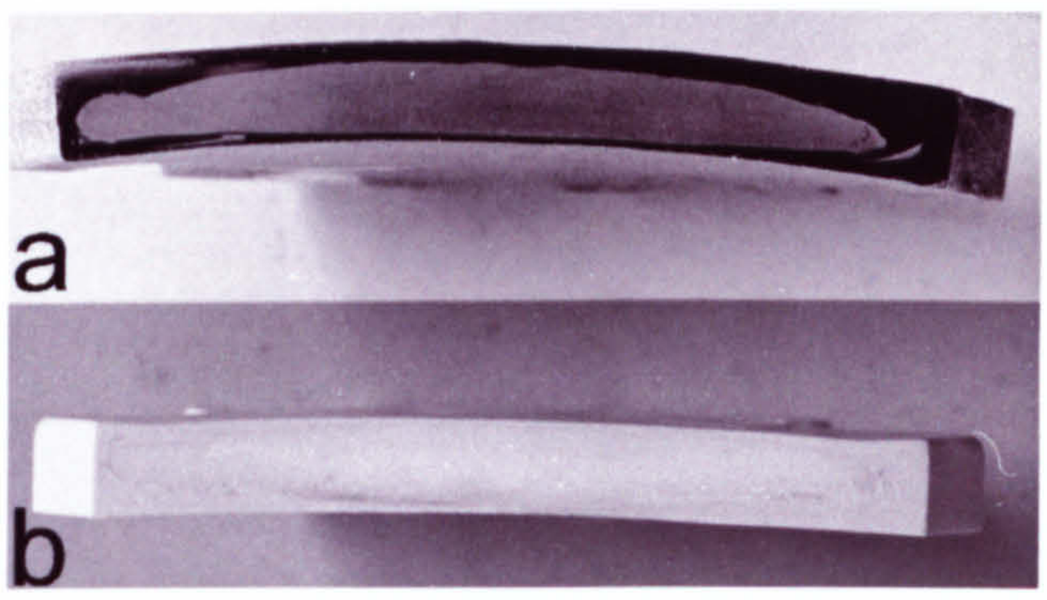

Figure 8.21 Debound and sintered sectioned powder co-injected mouldings

8.8 Metallographic/ceramographic examination of sectioned powder co-injected mouldings

Figure 8.22 shows a sectioned sample of a corrosion resistant metal co-injected moulding where the skin comprised stainless steel and the core comprised carbonyl iron. Figure 8.22a and 8.22b show the skin and core after sintering to 900°C for 2 hours. Figure 8.22a shows the iron matrix and the stainless steel masteralloy particles. An example masteralloy particle is marked with an x in figure 8.22a. No diffusion of the masteralloy particles into the iron matrix is apparent. Figure 8.22b shows the carbonyl iron core. Figure 8.22c and figure 8.22d show the final result after sintering at 1250°C for 4 hours. Figure 8.22d is a stainless steel alloy, and the masteralloy particles have totally diffused into the iron matrix. A chromium x-ray dot map of figure c/d indicated that there was an homogenous distribution of chromium through out the skin region. There was no evidence of chromium in the core region. Figure 8.22c shows the carbonyl iron core and figure 8.22 shows that there was no interfacial delamination and indicated that sintering shrinkage was nominally identical.

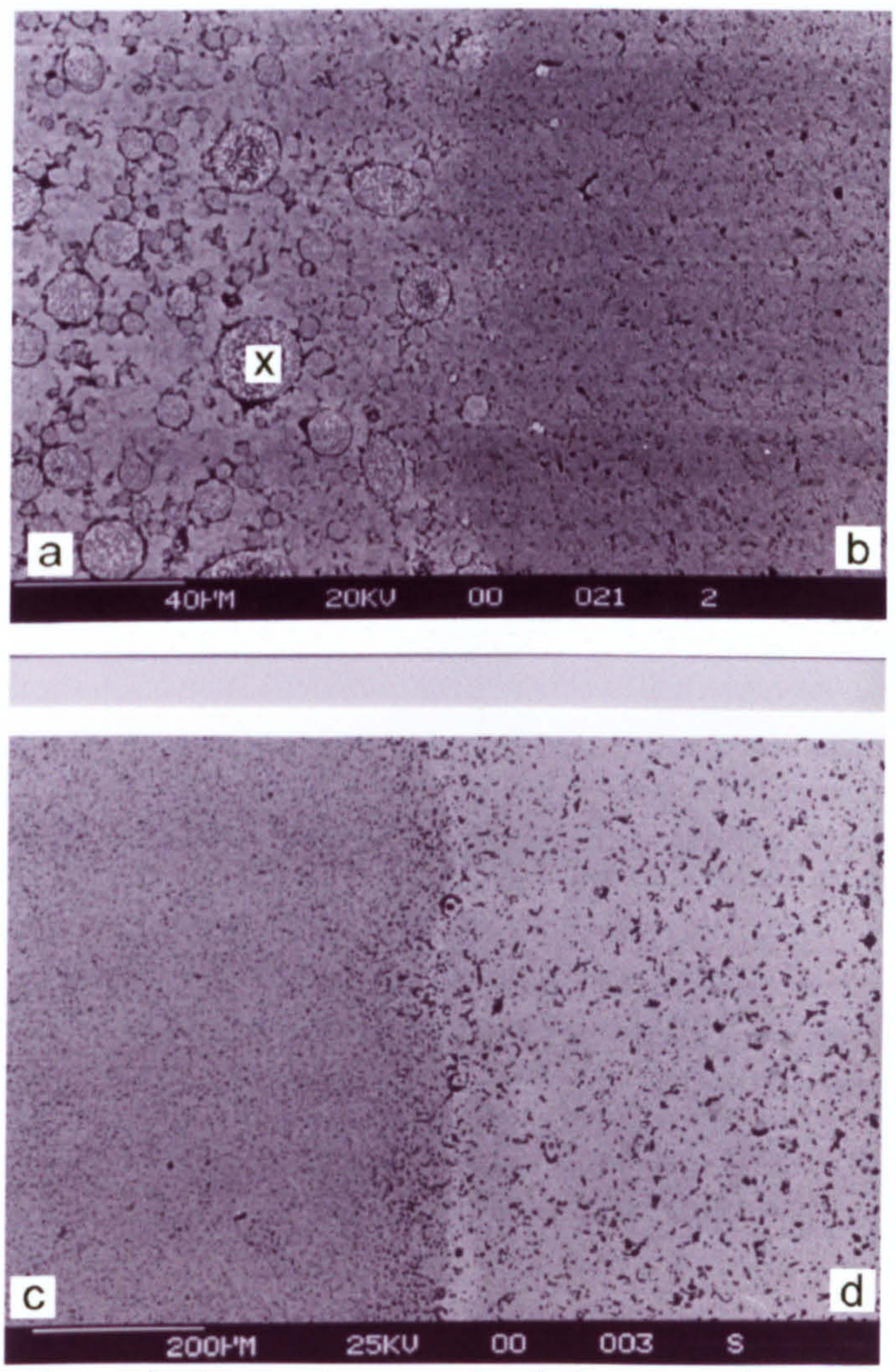

Figure 8.22 Secondary electron micrograph of the corrosion resistant co-injected moulding

Figure 8.23 illustrates a sectioned wear resistant metal co-injected moulding. The top layer in figure 8.23 is the skin, which comprised 85% vol iron and 15% vol 13μm alumina. The bottom layer is the core region, which comprised 100% iron. There is an apparent uniform distribution of alumina particulates within the iron matrix in the skin region. Figure 8.23 shows that there was no interfacial delamination and indicated that the sintering shrinkage was nominally identical for both the core and skin.

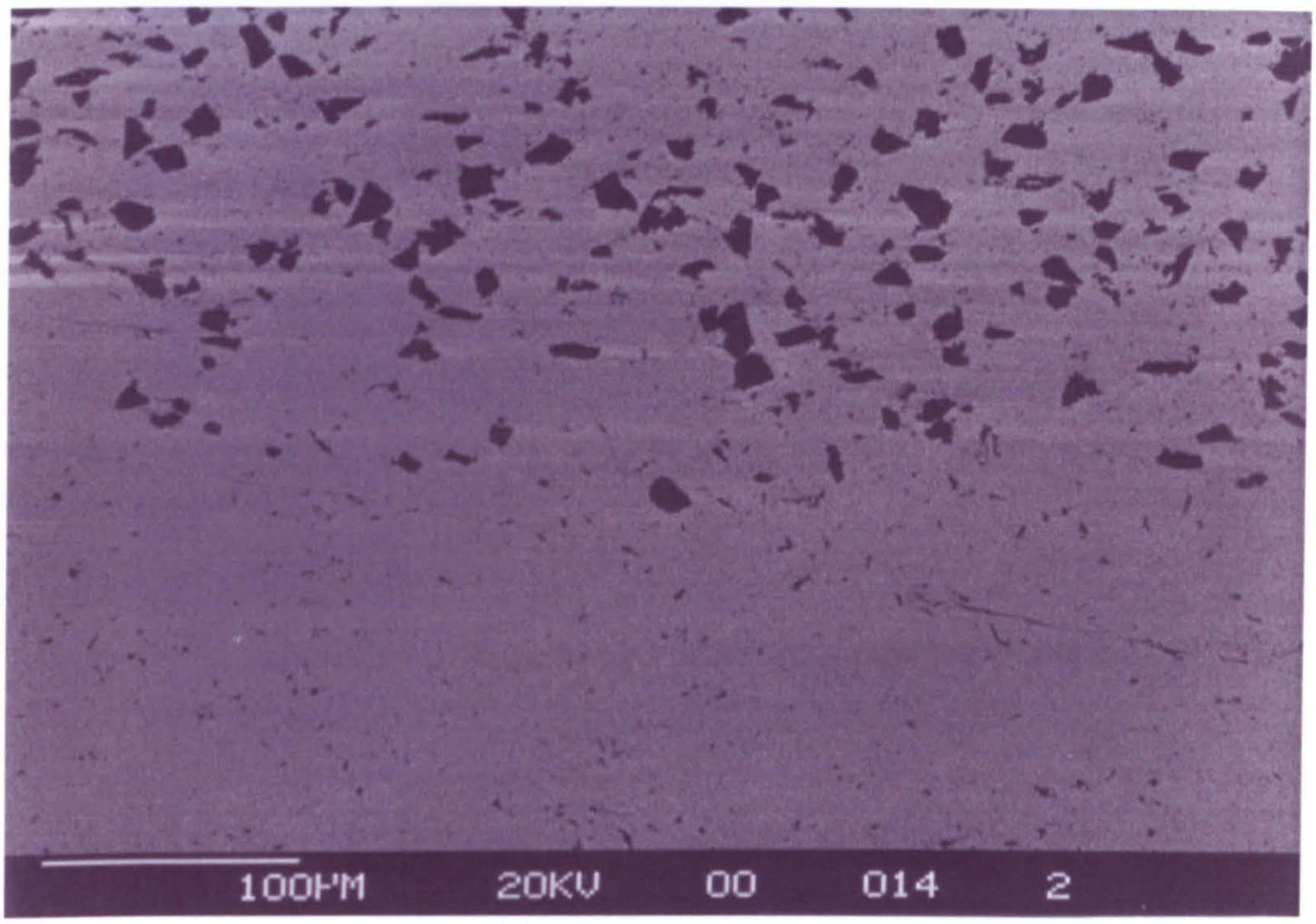

Figure 8.23 Secondary electron micrograph of the wear resistant co-injected moulding.

Figure 8.24 illustrates a sectioned ceramic powder co-injected moulding, which comprised an alumina core and the skin comprised zirconia toughened alumina. The top layer is an alumina matrix with 20% by volume of 0.5μm zirconia particulates, and the bottom layer is bulk alumina. It was evident from figure 8.24 that there was no interfacial delamination and that the sintering shrinkage was nominally identical for the zirconia toughened alumina skin and alumina core. The bonding strength between the zirconia particulates and the alumina matrix was sufficiently strong to resist particle pullout during the sectioning, grinding and polishing of the co-injection moulded ceramic samples. It was observed that there was some skin and core intermixing towards the circumference of the gear cogs during injection moulding as figure 8.25 illustrates. Figure 8.25 indicates that fingers of skin material protrude into the core region on the injection side of the gear cog. However, the skin - core boundary was sharply defined from the gate to about 18mm radially on the same face as the sprue and gate. The skin-core boundary was sharply defined up to 30mm from the sprue on the opposite side to the sprue/gate.

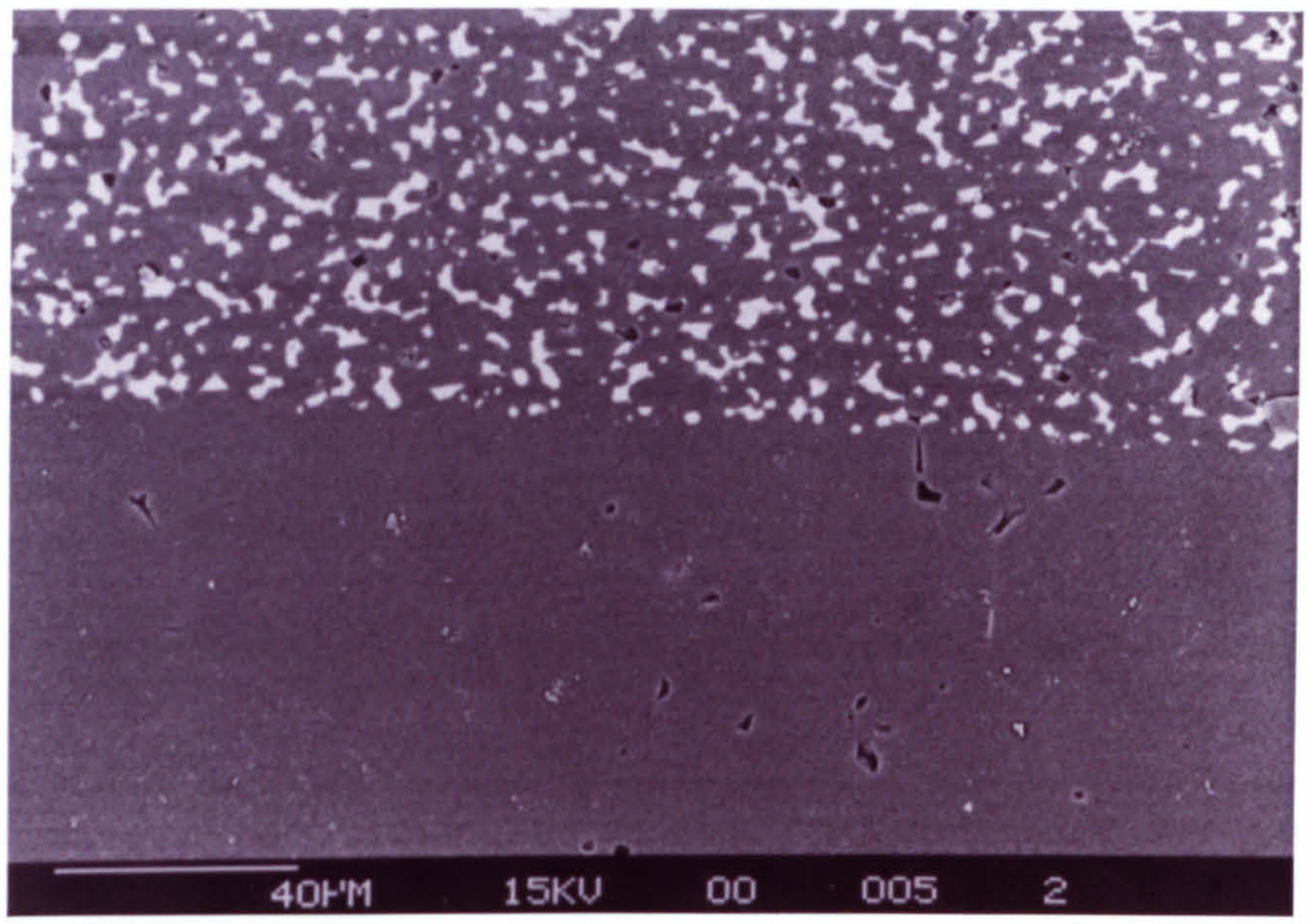

Figure 8.24 Secondary electron micrograph image of a sectioned ceramic co-injected moulding

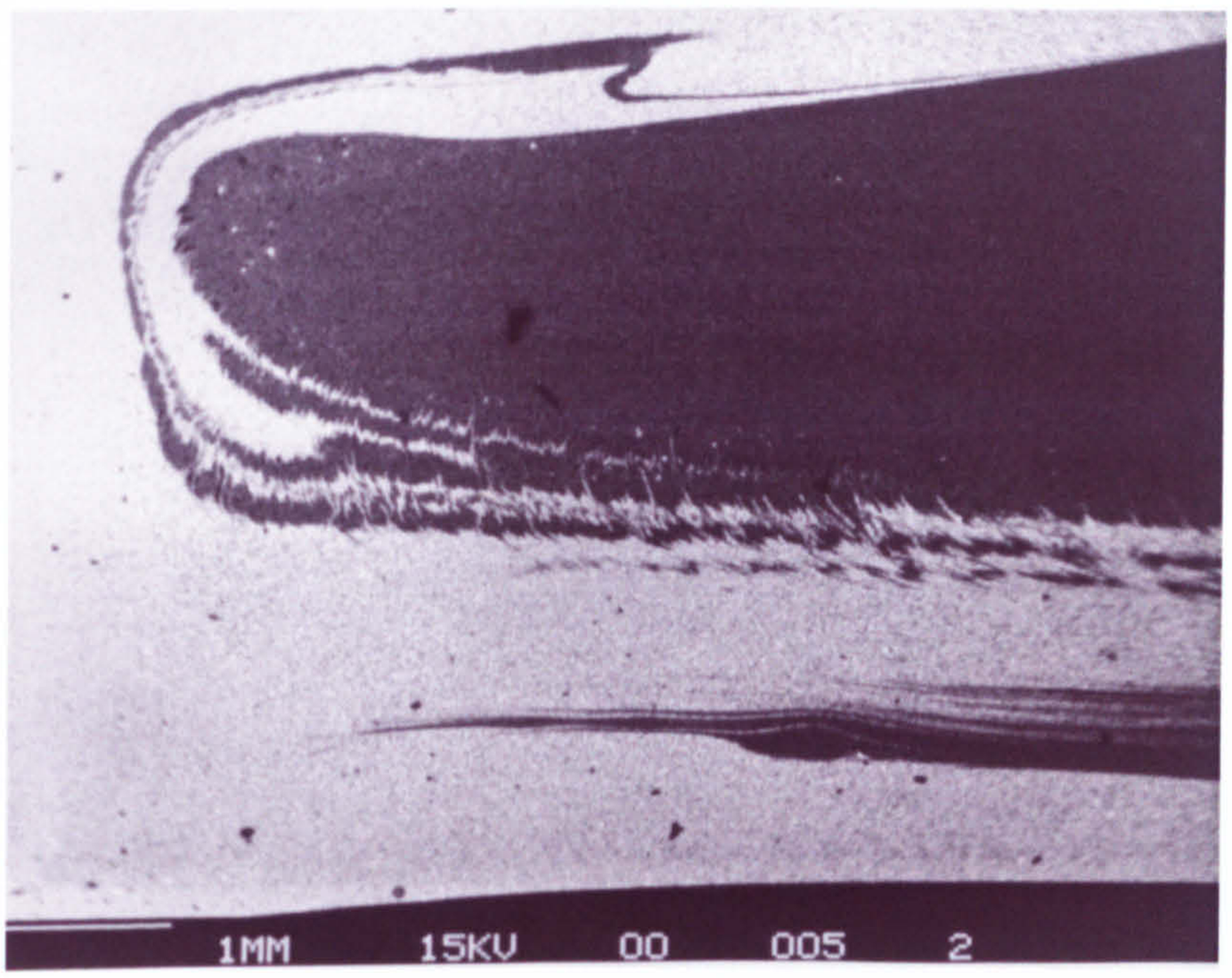

Figure 8.25 Secondary electron micrograph image of a sectioned ceramic co-injected moulding (The top skin layer is opposite to the sprue side, and the bottom skin layer is the same side as the sprue location.)

For the purposes of measuring the skin profile of the sectioned ceramic mouldings with the travelling microscope, the surface was considered to consist of three regions. The first region comprised skin material only. The second region comprised intermixed skin and core material. The third region comprised core material only. The two boundaries were measured for all three regions. The midpoint was calculated from the boundary measurements. This was considered to be a good approximation of where the true skin to core boundary would have been had there been no intermixing present.

9 Results: Polymer co-injection moulding and modelling

This section presents the results of the polymer co-injection moulding and modelling work and also the results of the validation of C-Mold as a predictive tool and the effect of rheology, injection time and thermal properties. It is pointed out to the reader that C-Mold assumes a symmetrically placed core region. It will be shown in this section, that symmetrically placed core regions may not actually occur in practice. All of the sectioned mouldings were measured experimentally for the skin profiles on both sides of the mouldings. All injection times quoted are the total time for injection of the skin and core materials.

The reader is reminded that the predicted radial position has an error of $\pm$1 mm due to the mesh element size being 2 mm. The predicted skin thickness has an error of $\pm$0.25 mm due to twelve layers being used across a 6 mm cross-sectional thickness. The actual radial position vs skin thickness data were measured to an accuracy of 0.01 mm and have an error of $\pm$0.005 mm. For details on how the sectioned mouldings were selected from the batch of mouldings produced, the reader is directed to section 7.4. The variation in skin profiles between the three mouldings selected was negligible. The three injection times reported by the Dassett DM30 injection moulding machine were the result of using three different constant ram speed profiles of 100%, 75% and 50%. Three different polymers were used for the purposes of this chapter, and their viscosities at 200°C are illustrated by figure 9.1.

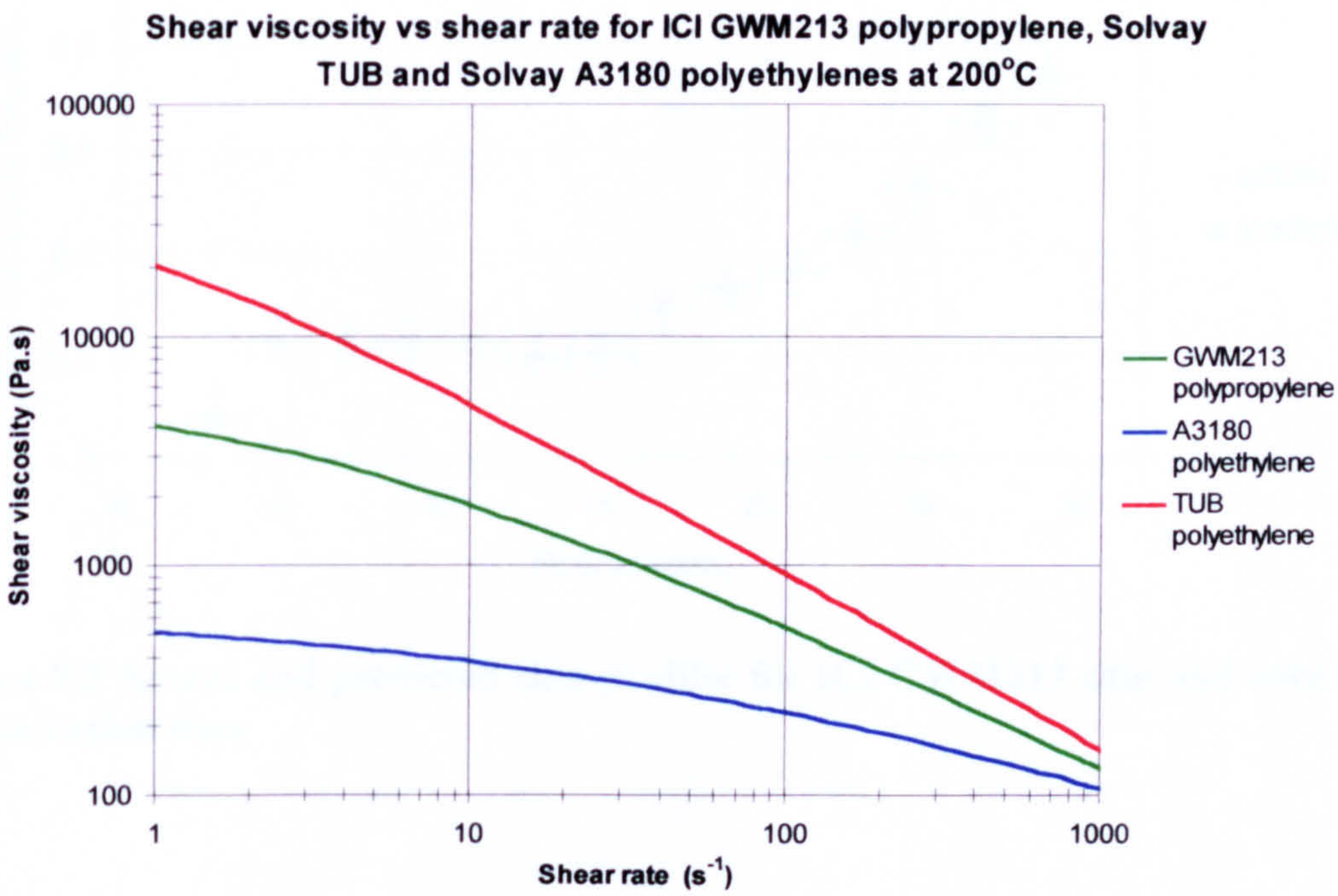

Figure 9.1. Shear viscosity vs shear rate for ICI GWM213 polypropylene, Solvay A3180 and Solvay TUB polyethylenes.

9.1 Validation of C-Mold as a predictive skin profile tool for polymer co-injection

This section presents the results of the validation of C-Mold as a predictive tool for polymer co-injection moulding. This is in two parts, the injection moulding of ICI GWM213 polypropylene for both the skin and core and the injection moulding of Solvay A3180 polyethylene for both the skin and core. It is pointed out to the reader that if only one actual skin profile is present in any of the following graphs instead of a pair of top and bottom skin profile plots, that the single actual skin profile plotted represents the total sum of the bottom and top skin profiles.

Figures 9.2, 9.3 and 9.4 show the predicted and actual skin profiles for three different injection times. They show that the predicted skin thickness fraction was slightly less than the actual skin thickness fraction for the radial positions of 13mm and 15mm. For the radial positions of 17mm, 19mm and 21mm, the actual skin profiles fell within the error bars of the predicted skin fraction data points. At the radial positions of 25mm, 27mm and 29mm, the predicted skin thickness fraction was slightly greater than the actual skin thickness fraction. The correlation between the actual and predicted skin profiles is markedly different for the injection time of 3.3s, as illustrated in figure 9.4.

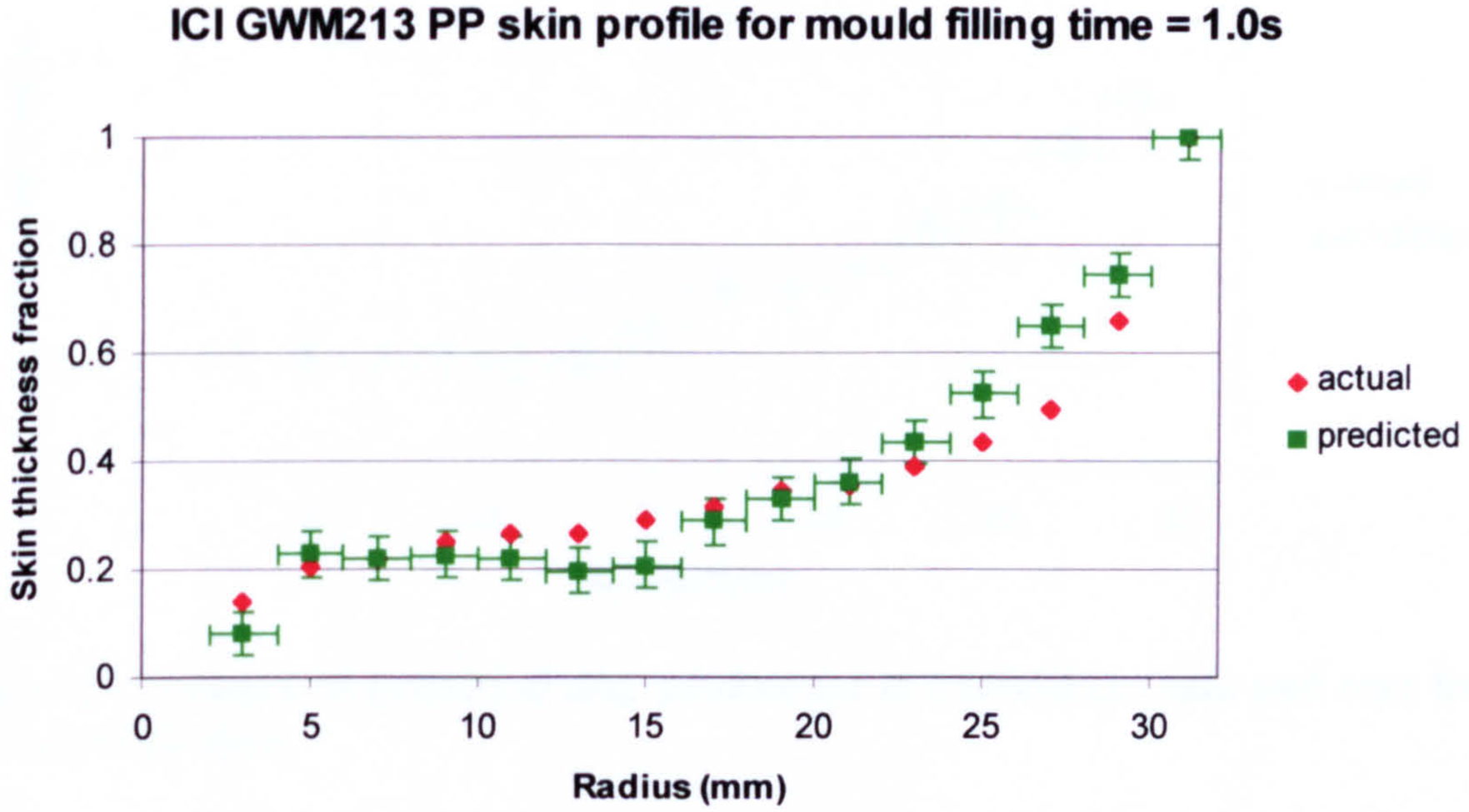

Figure 9.2 Actual and predicted skin profiles for ICI GWM213 skin and core for a 1.0s injection time

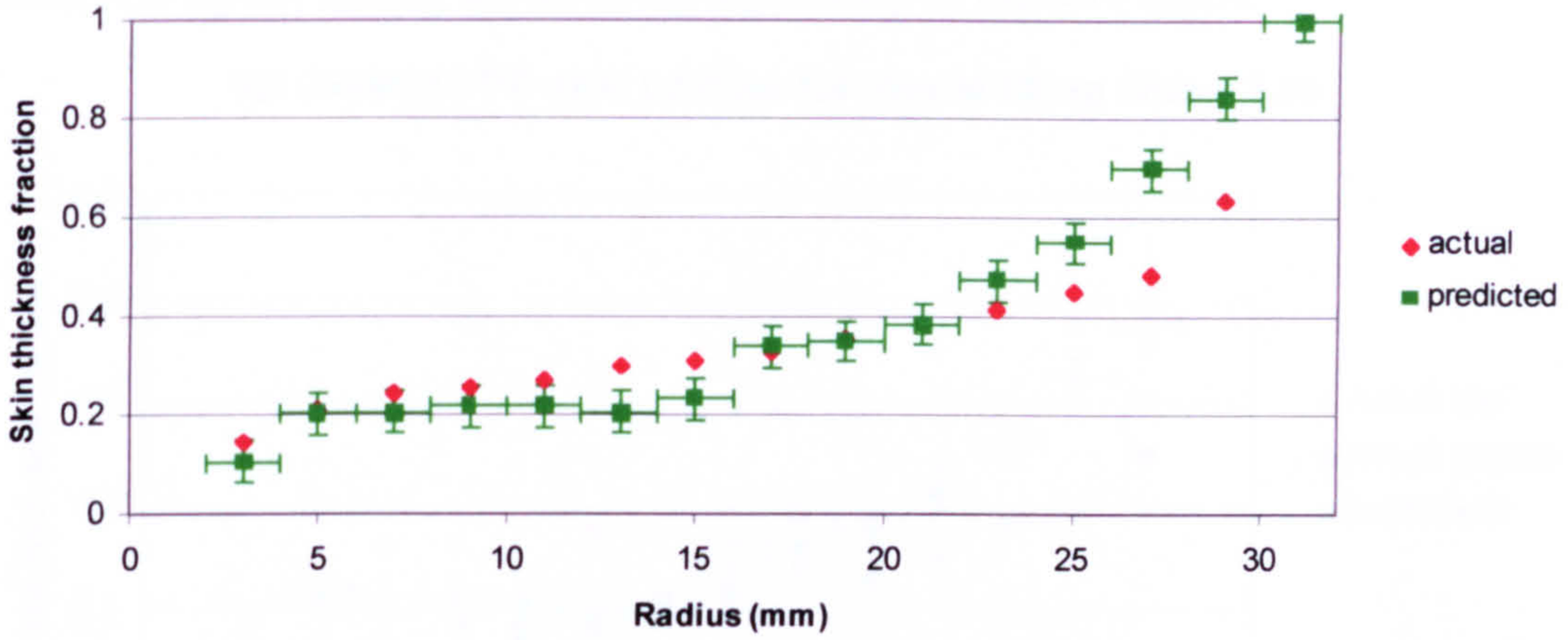

Figure 9.3 Actual and predicted skin profiles for ICI GWM213 skin and core for a 1.7s injection time

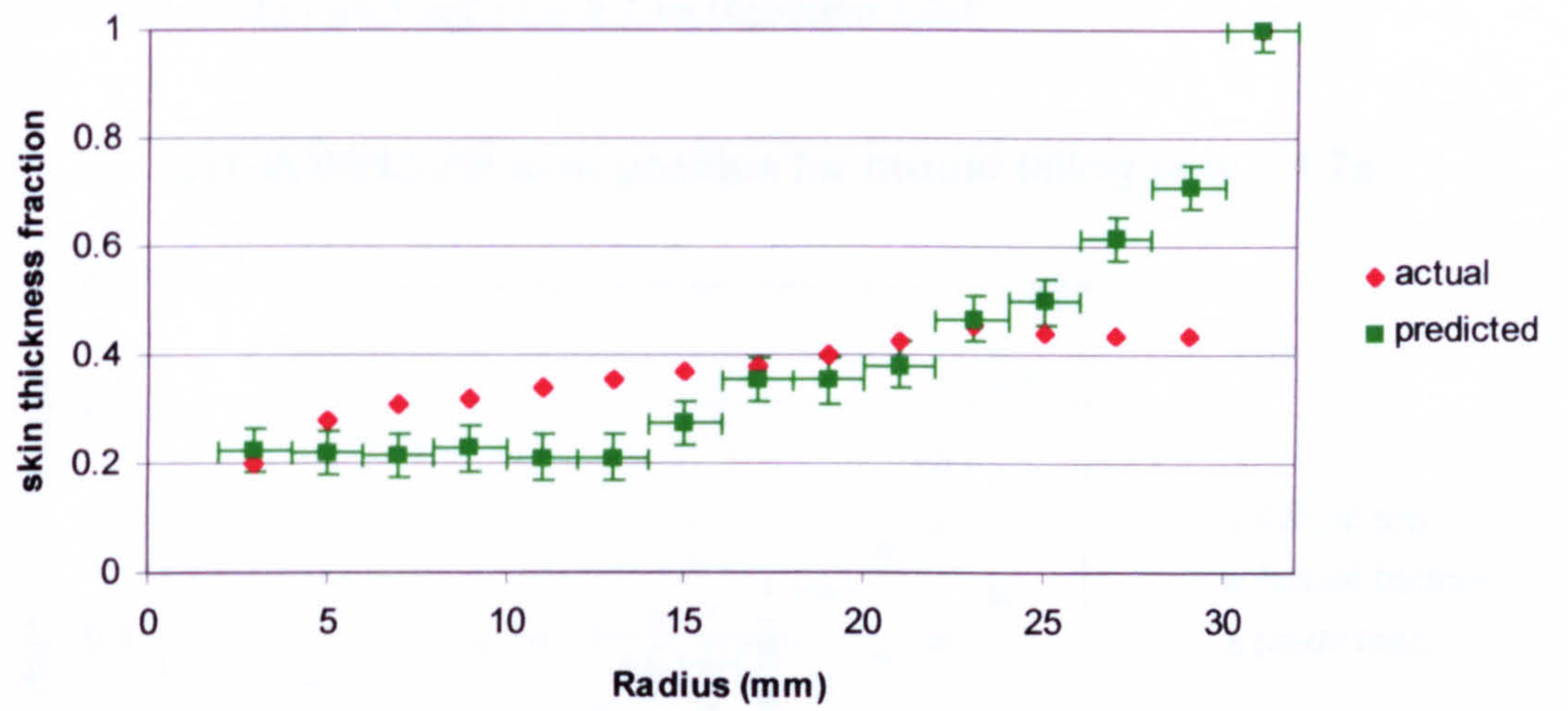

Figure 9.4 Actual and predicted skin profiles for ICI GWM213 skin and core for a 3.3s injection time

The predicted and actual skin data for figures 9.2, 9.3 and 9.4 were re-plotted. This was done to compare the top and bottom skin profiles with half the predicted skin profile thickness for all three injection times. Figures 9.5, 9.6 and 9.7 demonstrate that the actual top and bottom skin profiles were asymmetrical. This implies that the core region is not symmetrically placed. The bottom layer is opposite to the sprue side of the mouldings, and the top layer is on the same side as the sprue.

Comparing figures 9.5, 9.6 and 9.7 indicated that with increasing injection time, the top skin profile became thicker. This lead to an increased differential between the top and bottom skin layers, leading to increasing asymmetry of the core region.

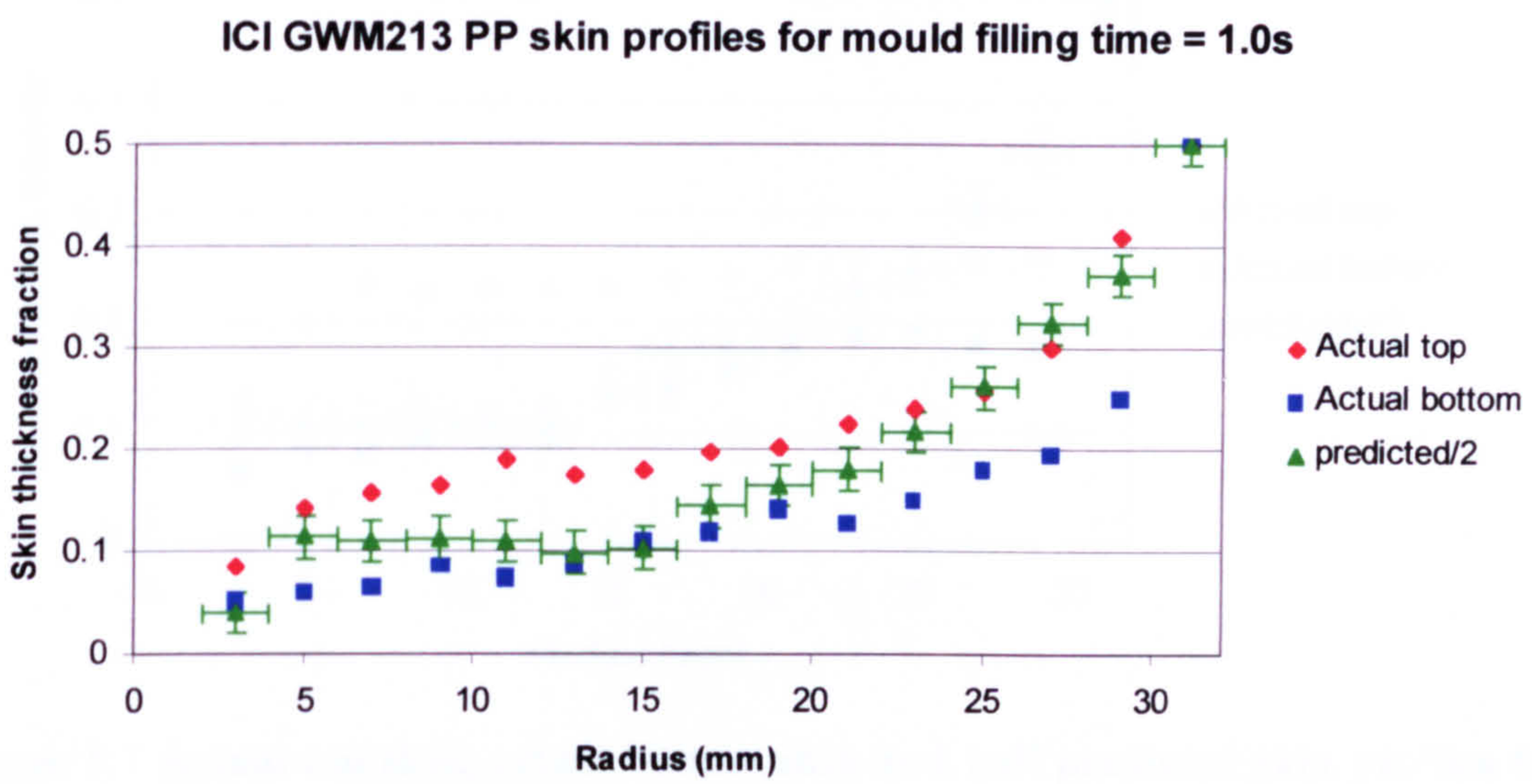

Figure 9.5 Actual top skin, actual bottom skin and half predicted skin profiles for ICI GWM213 skin and core for a 1.0s injection time

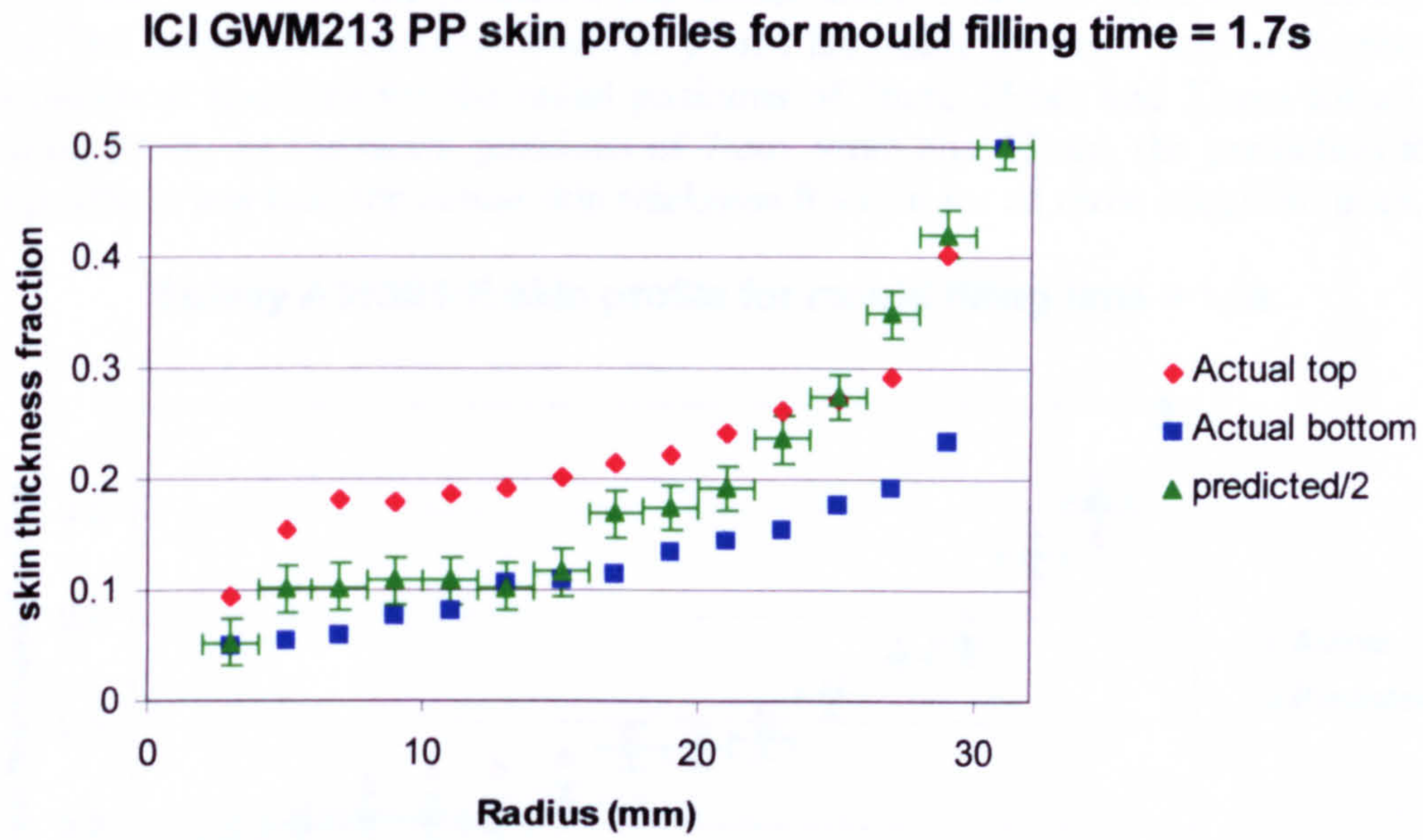

Figure 9.6 Actual top skin, actual bottom skin and half predicted skin profiles for ICI GWM213 skin and core for a 1.7s injection time

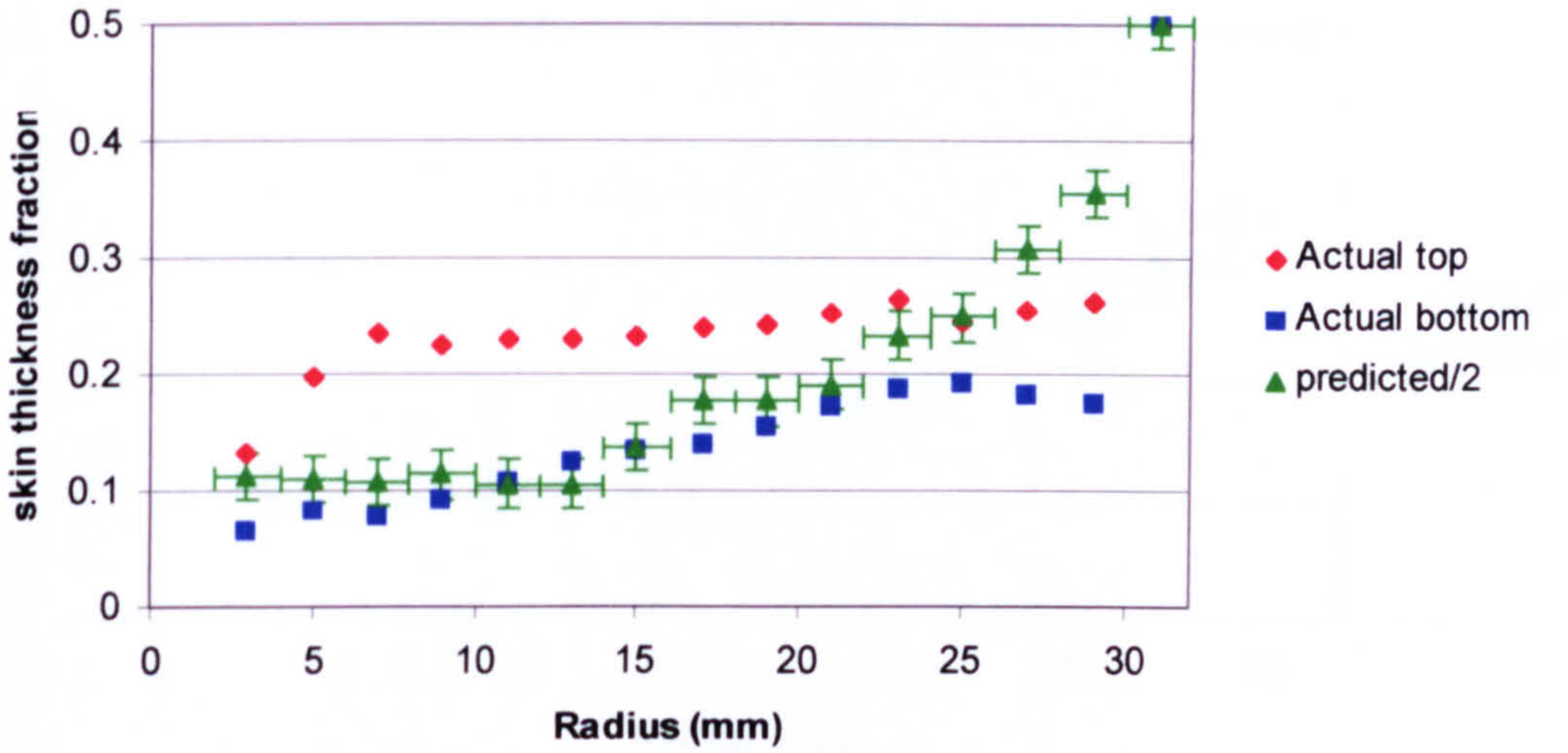

Figure 9.7 Actual top skin, actual bottom skin and half predicted skin profiles for ICI GWM213 skin and core for a 3.3s injection time

The validation work of using C-Mold as a skin profile prediction tool was repeated again, but this time using Solvay A3180 polyethylene for both the skin and core. Figures 9.8, 9.9 and 9.10 show the predicted and actual skin profiles for three different injection times. The actual skin thickness fractions points fall inside the error bars of the predicted skin thickness fractions for the radial positions of 3mm, 15mm and 23mm for all three injection times. At the radial positions of 7mm, 9mm and 15mm, the prediction for the skin profile is less than the actual skin thickness fraction for all three injection times.

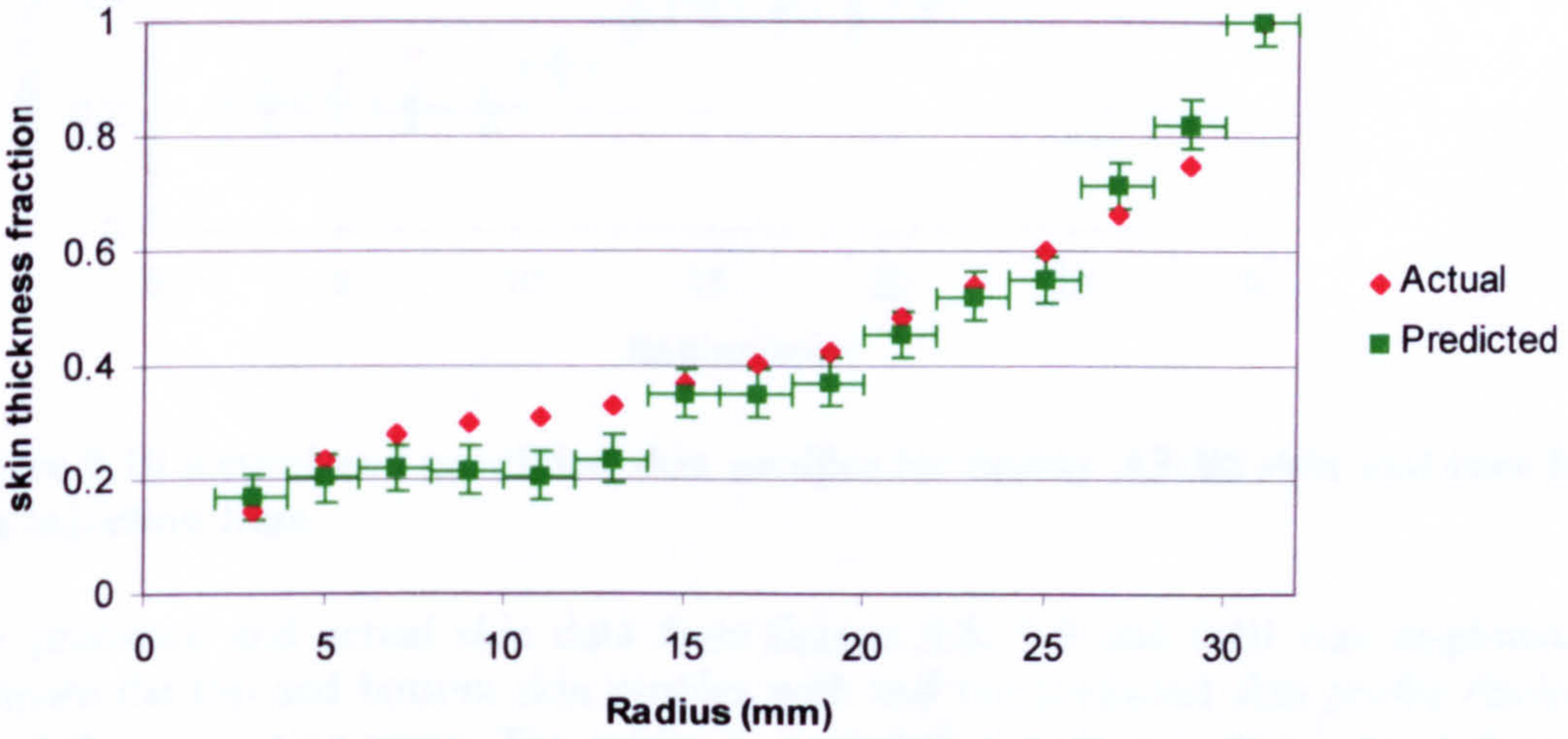

Figure 9.8 Actual and predicted skin profiles for Solvay A3180 skin and core for a 1.0s injection time

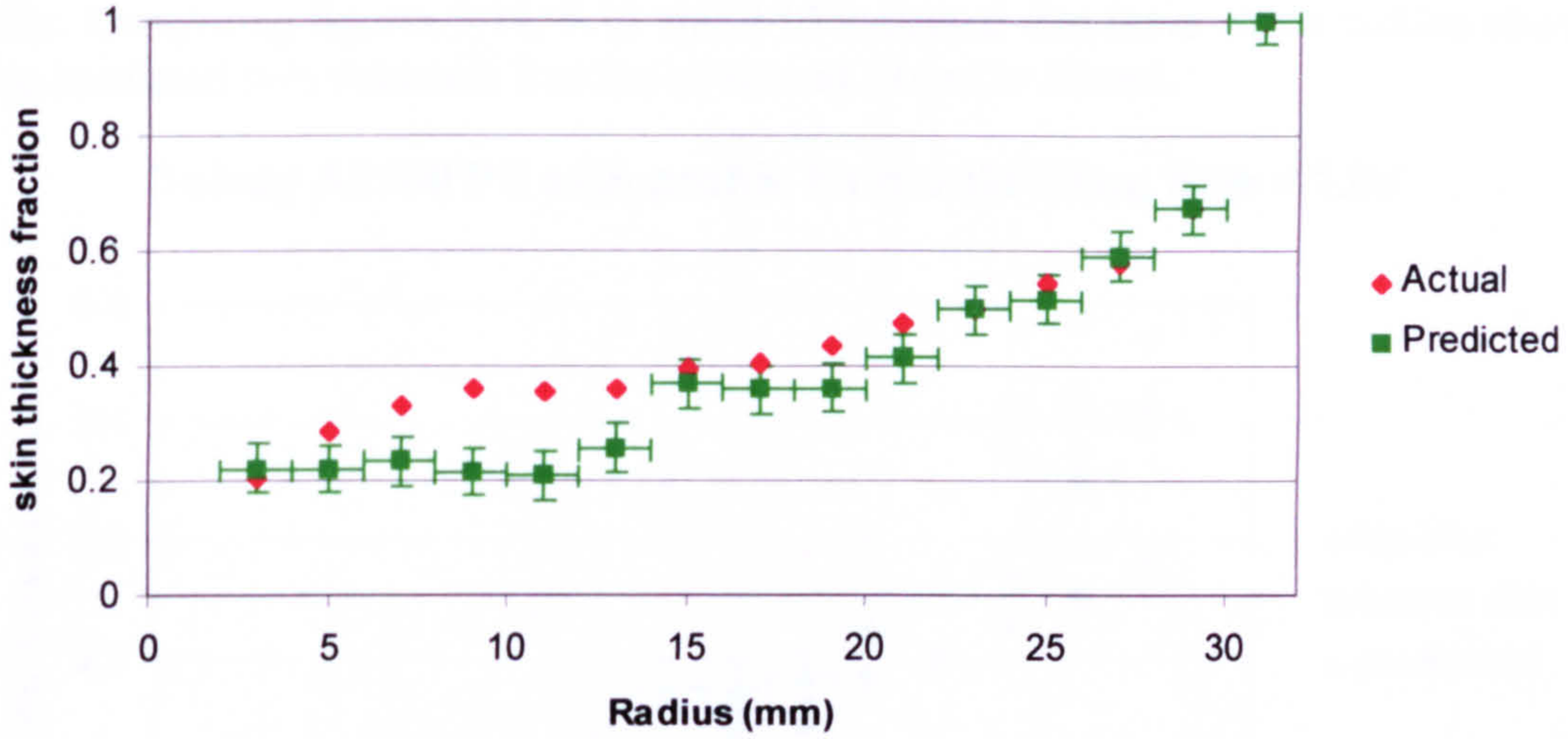

Figure 9.9 Actual and predicted skin profiles for Solvay A3180 skin and core for a 1.7s injection time

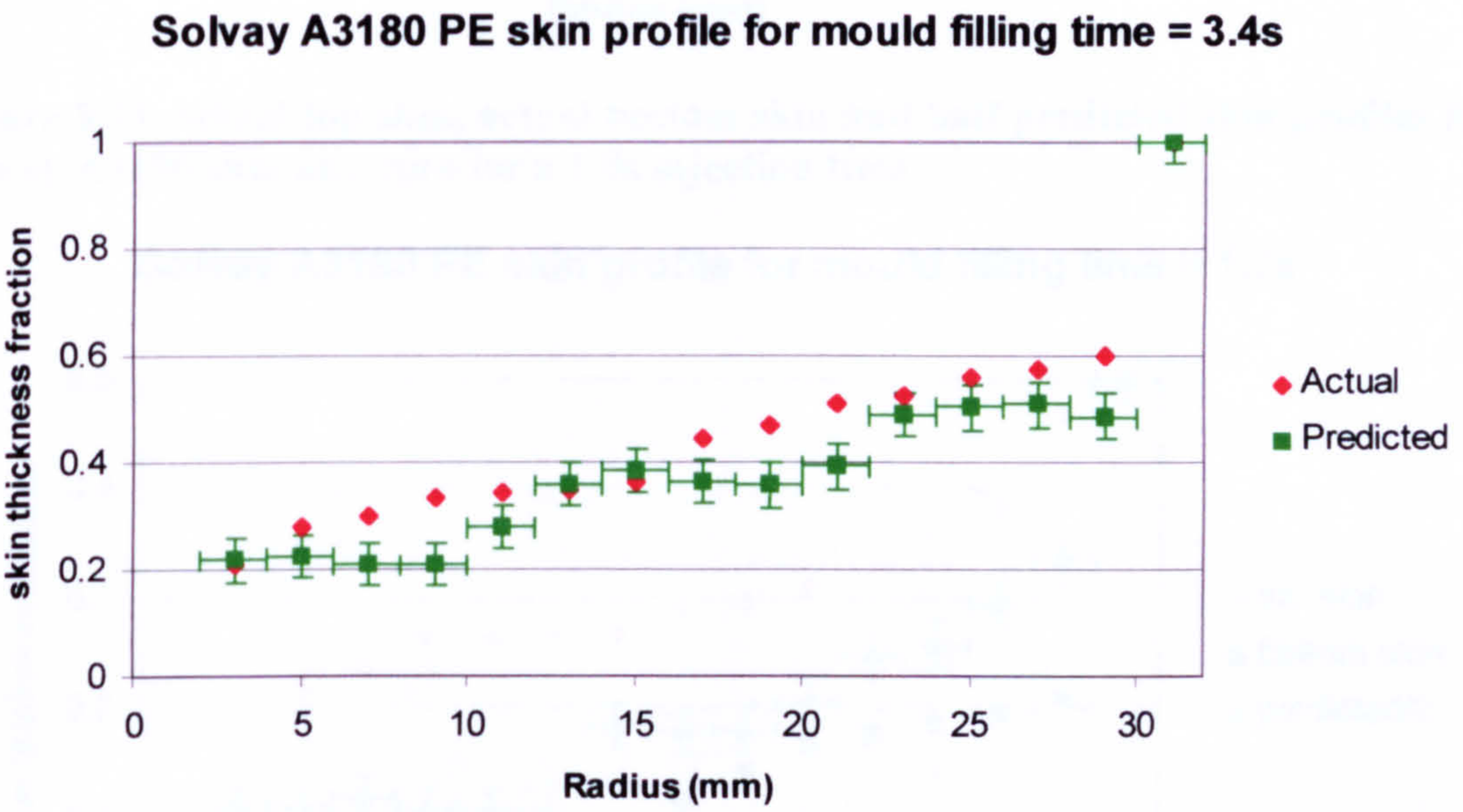

Figure 9.10 Actual and predicted skin profiles for Solvay A3180 skin and core for a 3.4s injection time

The predicted and actual skin data from figures 9.8, 9.9 and 9.10 was re-plotted to compare the top and bottom skin profiles with half the predicted skin profile thickness for all three injection times. The reader is reminded that the top skin is located on the same side of the mouldings as the sprue, and that the bottom layer is on the opposite side to the sprue. Figures 9.11, 9.12 and 9.13 show that the actual top and bottom skin profiles are not symmetrical. This implies that the core is located asymmetrically. The

actual skin thickness fractions fall outside the error bars of the predicted skin thickness fractions for the majority of the radial positions plotted. The top skin shows greater disagreement than the bottom skin when compared with the predicted skin thickness profile. Comparing figures 9.11, 9.12 and 9.13 indicated that there was a sudden change in the predicted skin thickness fraction at around 11mm to 13mm.

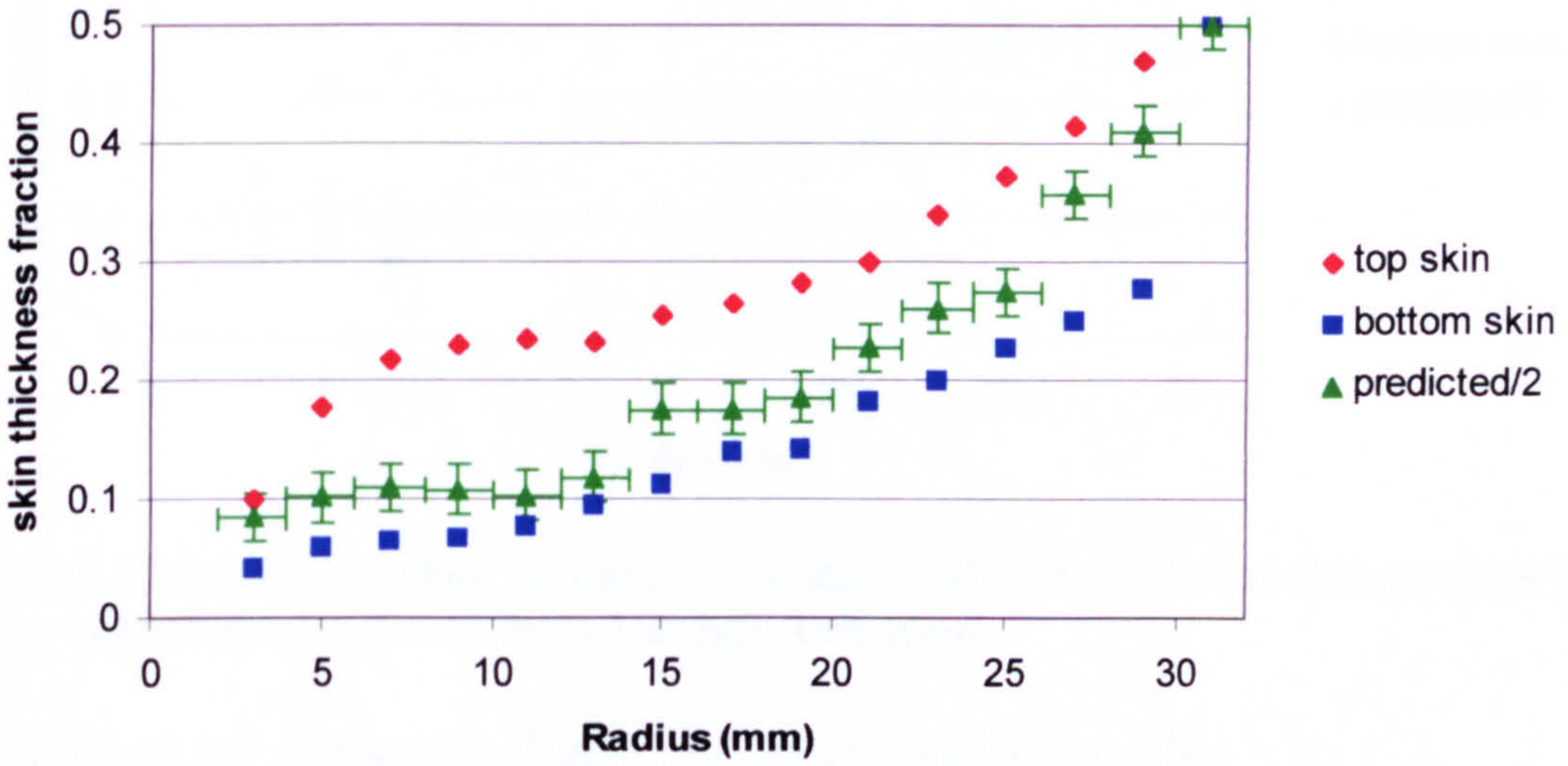

Figure 9.11 Actual top skin, actual bottom skin and half predicted skin profiles for Solvay A3180 skin and core for a 1.0s injection time

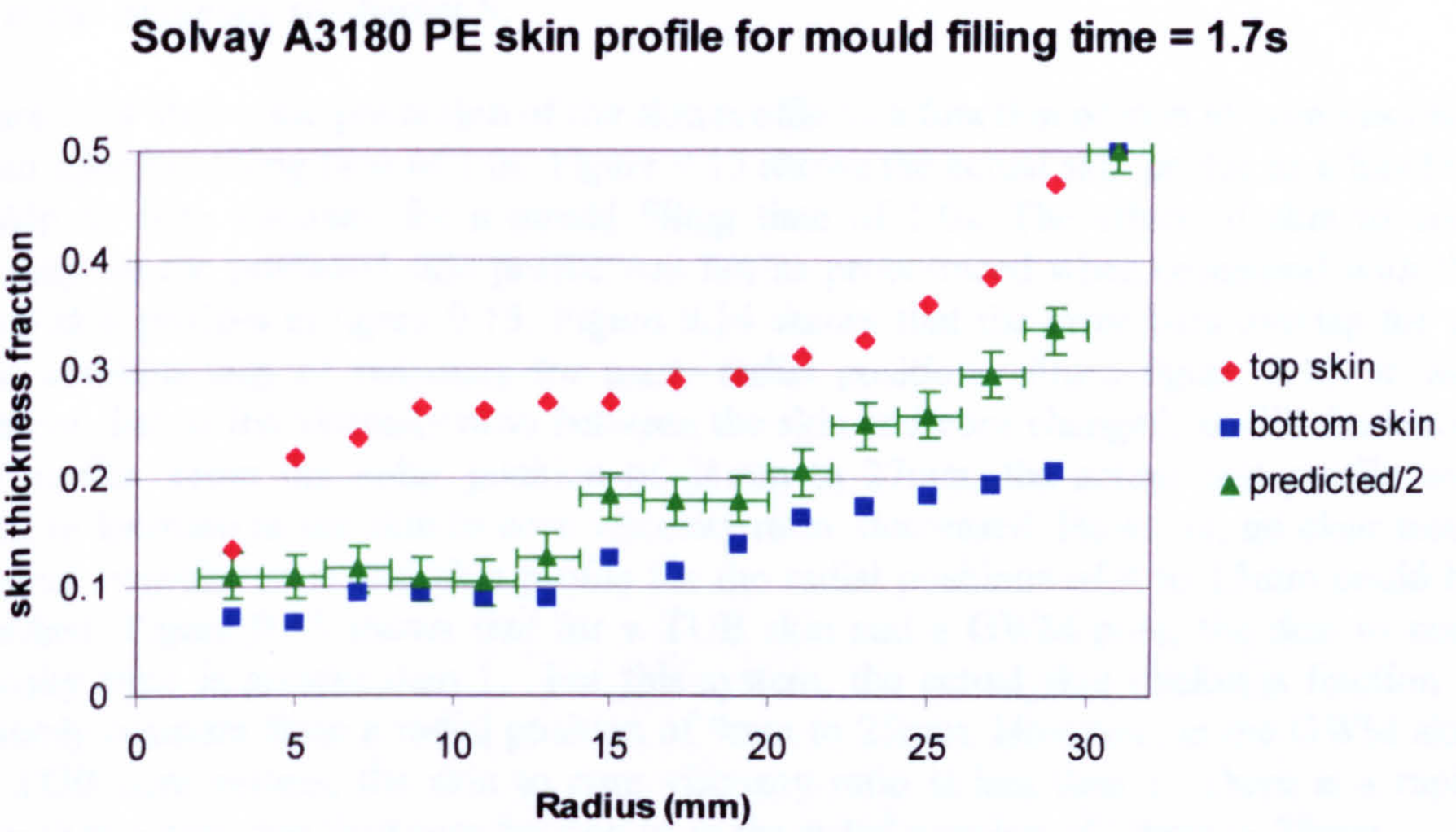

Figure 9.12 Actual top skin, actual bottom skin and half predicted skin profiles for Solvay A3180 skin and core for a 1.7s injection time

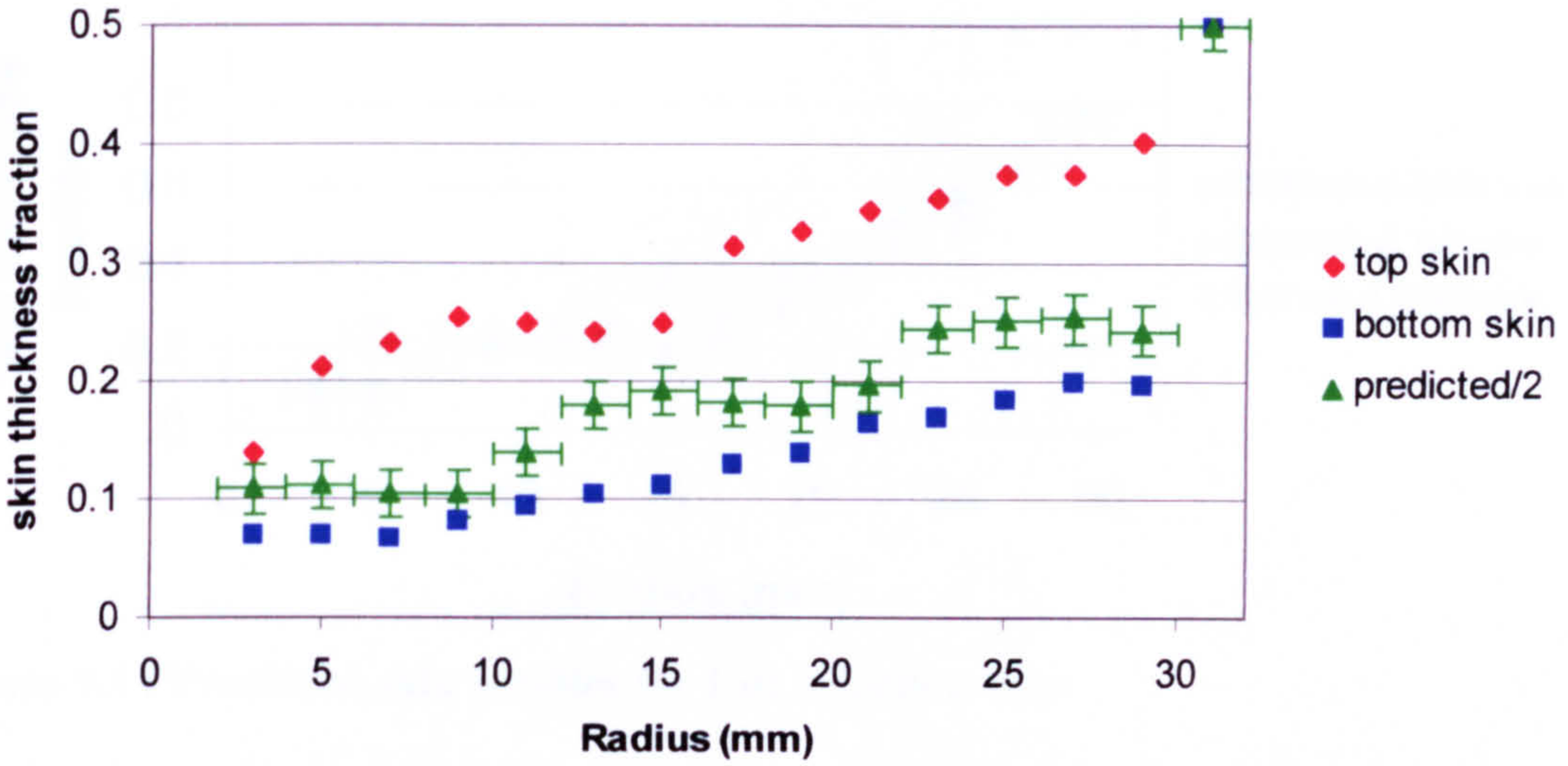

Figure 9.13 Actual top skin, actual bottom skin and half predicted skin profiles for Solvay A3180 skin and core for a 3.4s injection time

9.2 Effect of polymer rheology on the skin profile

For details of how the shear viscosity varies with shear rate at 200°C for the ICI GWM213 polypropylene and Solvay TUB polyethylene, the reader is directed to figure 9.1 at the beginning of chapter 9.

Figure 9.14 shows the prediction of the skin profile as a function of skin to core viscosity for an injection filling time of 1.0s. Figure 9.15 shows the actual skin profile as a function of skin to core viscosity for a mould filling time of 1.0s. The effect of skin to core viscosity on the predicted skin profile was not as pronounced when compared with the actual skin profiles in figure 9.15. Figure 9.14 shows that the error bars overlap for all three combinations of polymers for many radial positions. From figure 9.15, it was apparent that as the viscosity ratio between the skin and core changed, so did the actual skin profile. From the radial position of 21mm to 27mm, the actual skin profile was found to increase as the skin to core viscosity ratio decreased. However, no clear trend between viscosity ratio and skin profile for the radial positions of 9 to 15mm could be identified. Figure 9.15 shows that for a TUB skin and a GWM core, the skin to core viscosity ratio is greater than 1. For this system, the actual skin thickness fraction is relatively constant from a radial position of 9mm to 25mm. However, in the GWM skin and TUB core system, the skin to core viscosity ratio is less than 1. There is a rapid increase in actual skin thickness fraction from the radial position of 19mm to 23mm.

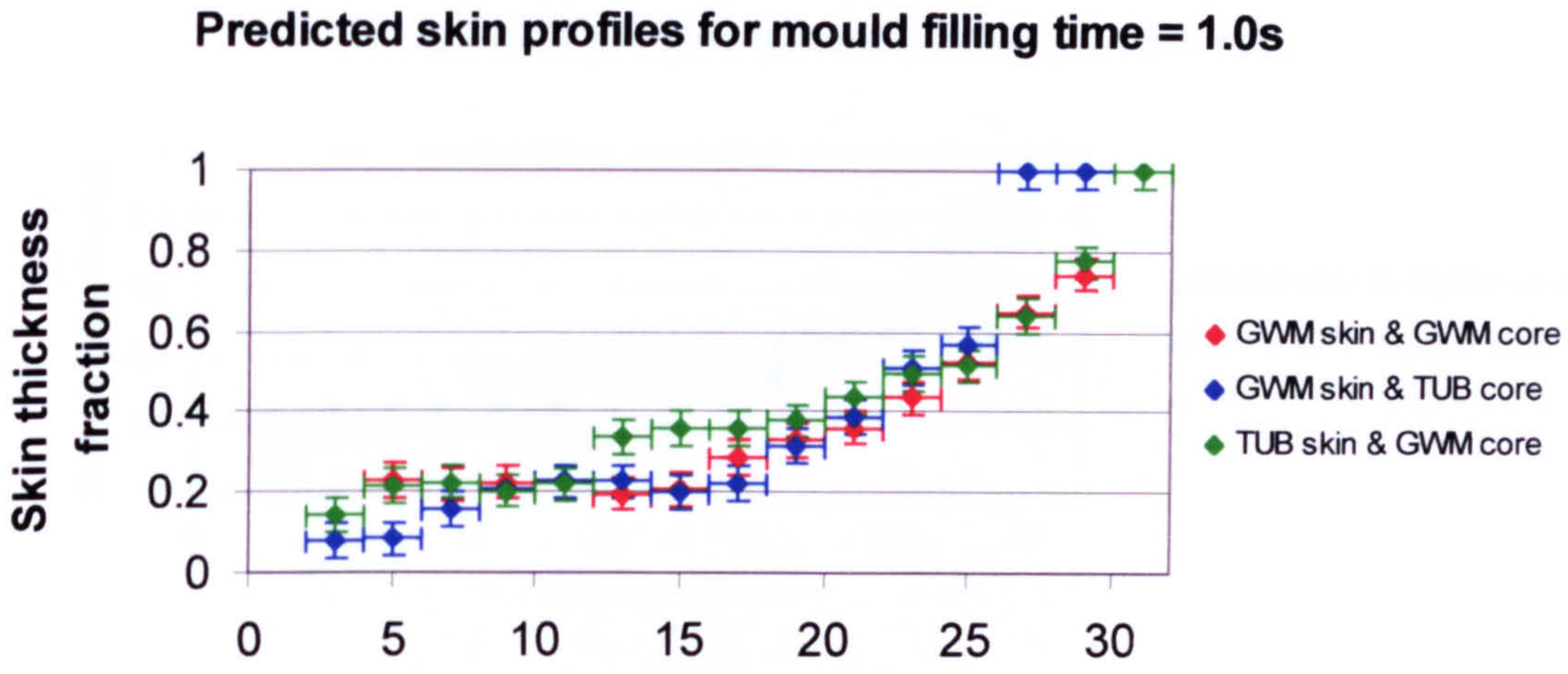

Figure 9.14 Predicted skin profiles for 1.0s injection time

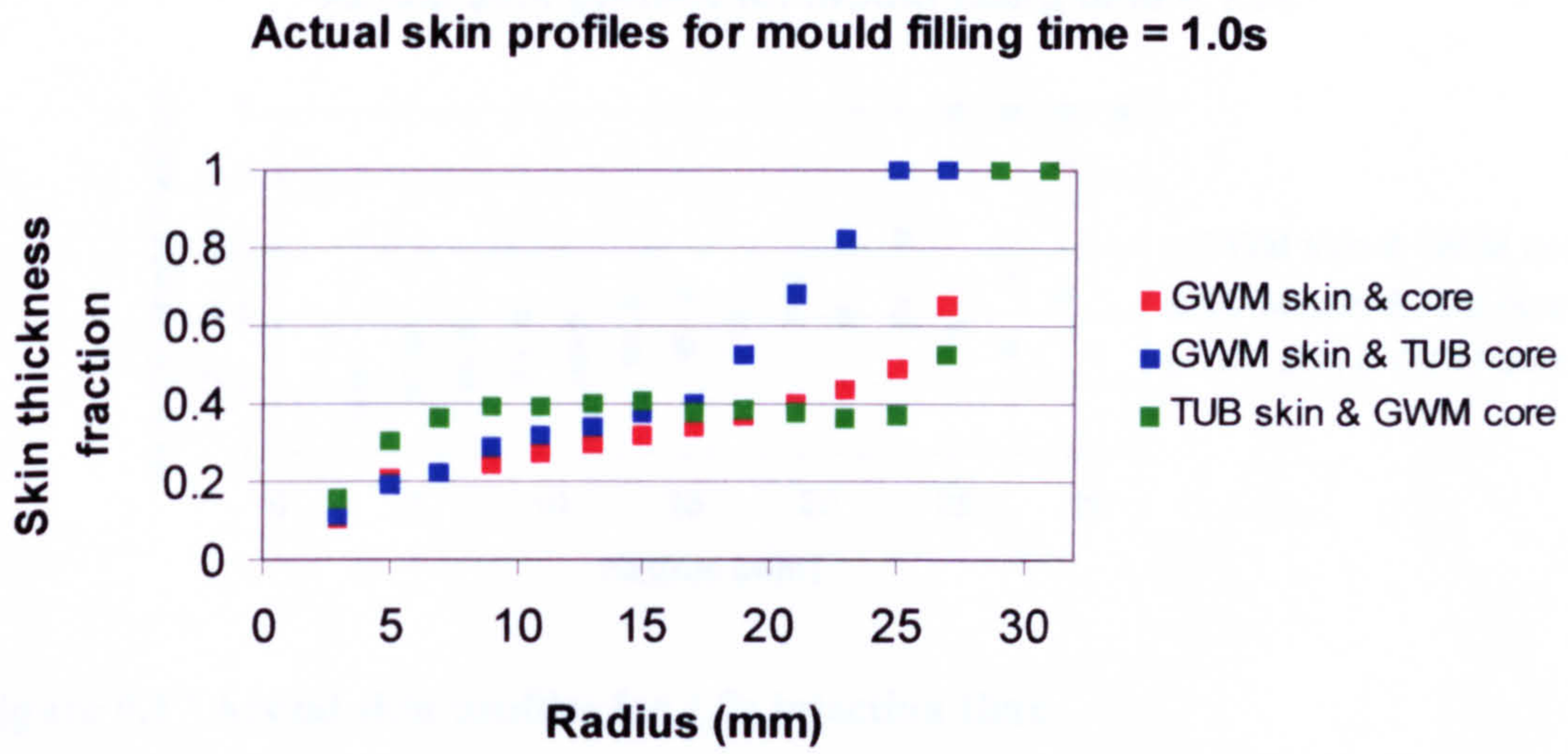

Figure 9.15 Actual skin profiles for 1.0s injection time

Figure 9.16 illustrates the prediction of the skin profile as a function of skin and core viscosity for a mould filling time of 1.7s. Figure 9.17 illustrates the actual skin profile as a function of skin and core viscosity for a mould filling time of 1.7s. The predicted effect of viscosity on the skin profile was not as pronounced when compared to figure 9.17 and may of the error bars overlap for each radial position. Varying the viscosity ratio between the skin and core resulted in little apparent change in the predicted skin profile. Figure 9.17 shows that varying the skin to core viscosity ratio did result in a change in the actual skin profile. For the radial positions of 3mm to 15mm, the actual skin thickness fraction increased with increasing skin to core viscosity ratio. For the radial positions of 21mm to 29mm, the actual skin thickness fraction decreased with increasing skin to core viscosity ratio.

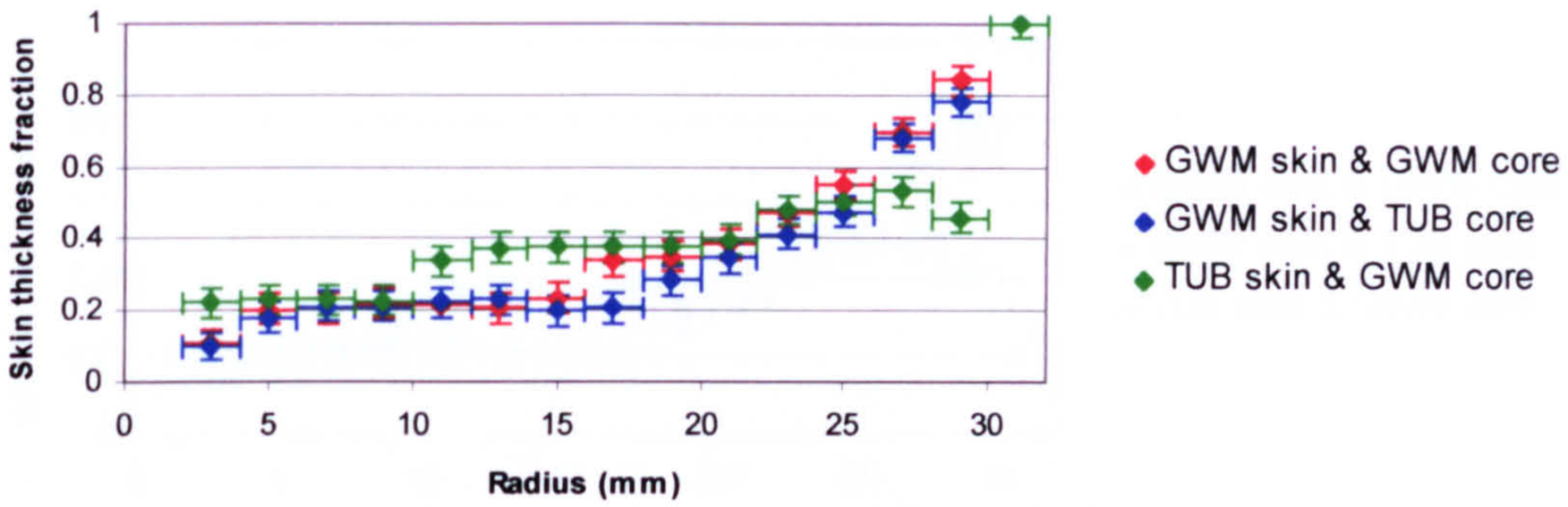

Figure 9.16 Predicted skin profile for 1.7s injection time

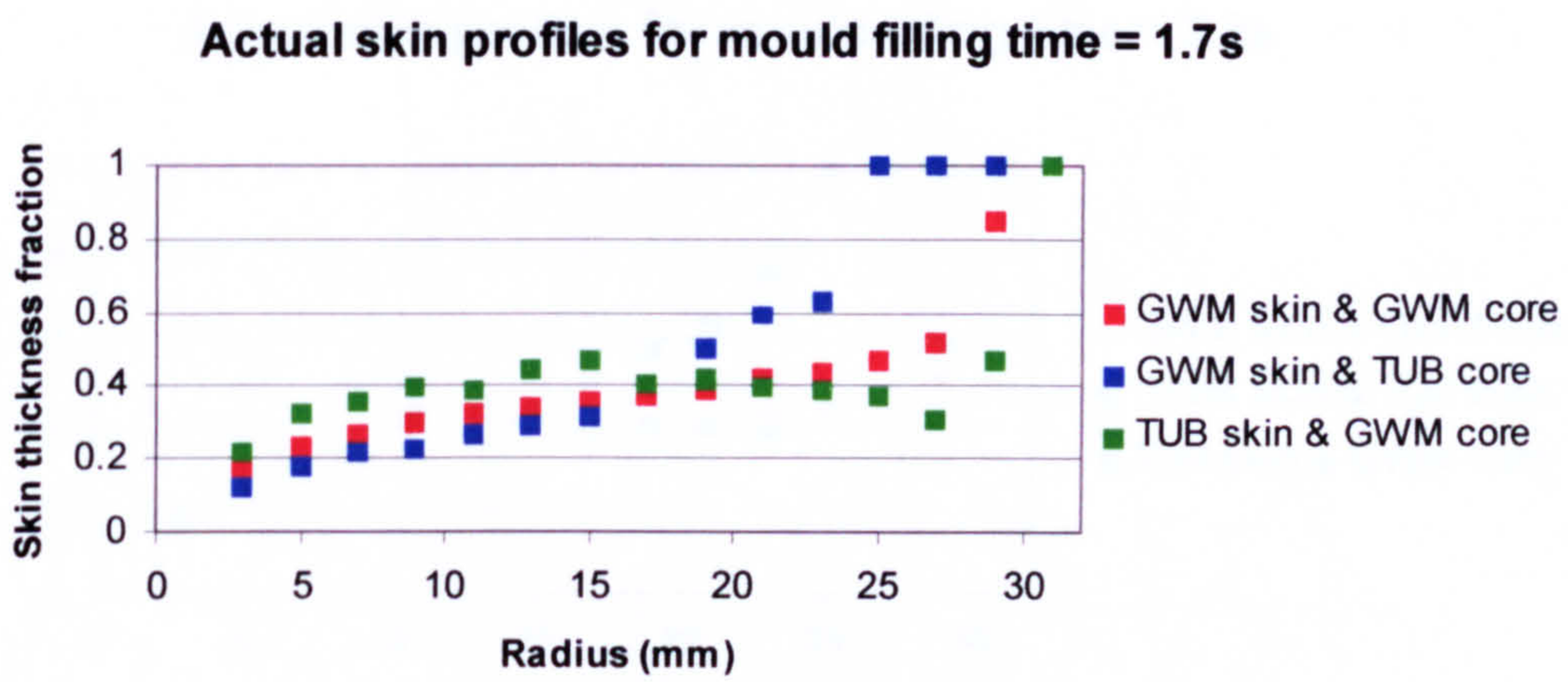

Figure 9.17 Actual skin profiles for 1.7s injection time

Figure 9.18 illustrates the prediction of the skin profile as a function of skin and core viscosity for a mould filling time of 3.2s. The effect of viscosity on the predicted skin profile in figure 9.18 was negligible as many of the error bars overlapped at many of the radial positions. Figure 9.19 illustrates the actual skin profile as a function of skin and core viscosity for a mould filling time of 3.2s. The skin profile for the GWM skin and TUB core was markedly different to the other two skin profiles, which were in close agreement with each other. The skin profiles for all three combinations were similar up to the radial position of 13mm. For the ICI GWM skin and Solvay TUB core the actual and predicted skin profiles in figures 9.18 and 9.19 showed the greatest differences.

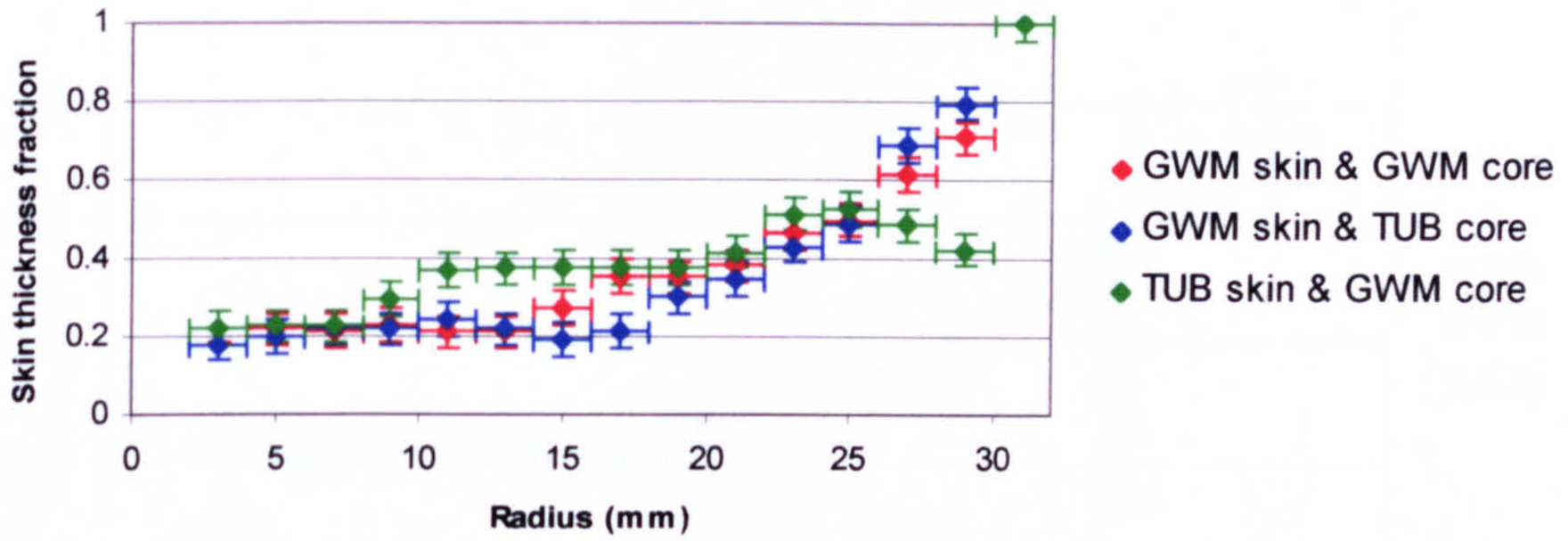

Figure 9.18 Predicted profile for 3.3s injection time

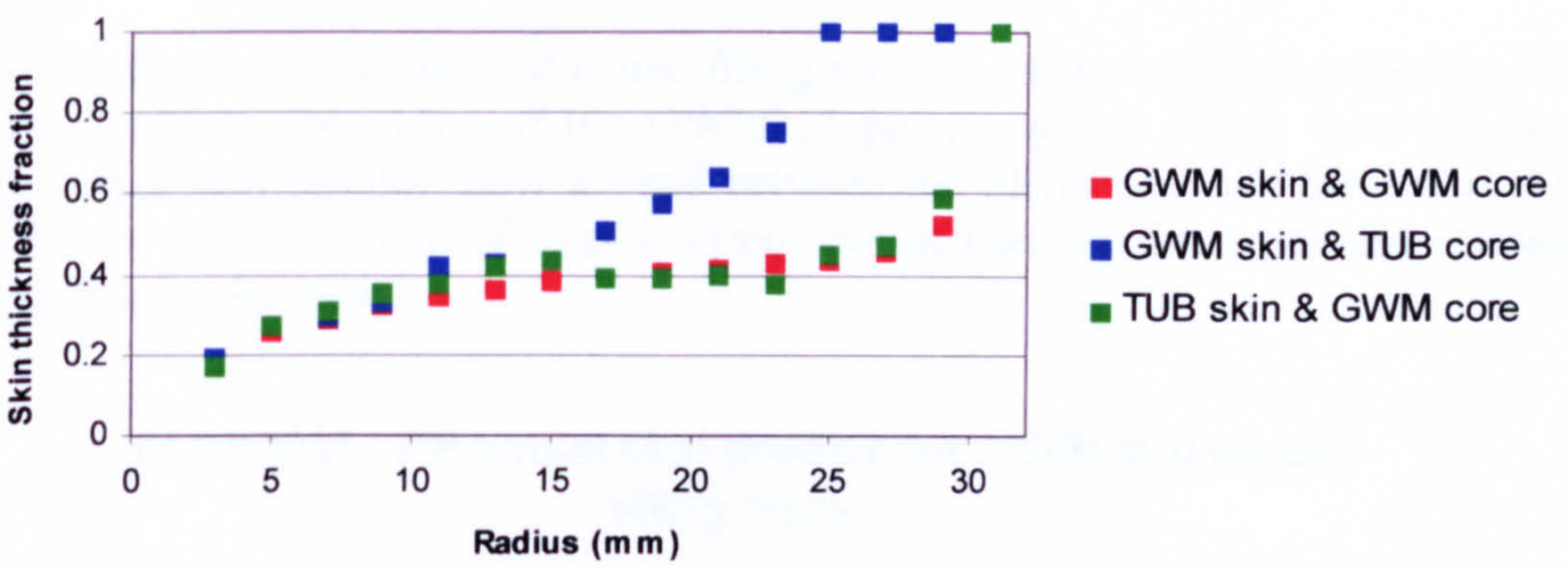

Figure 9.19 Actual skin profiles for 3.3s injection time

9.3 Effect of mould cavity filling time on the skin profile

Figure 9.20 illustrates the effect of different mould filling times on the predicted skin profiles of ICI GWM213 polypropylene skin and core polymers. Figure 9.20 indicates that no clear trend could be identified between the filling time and the predicted skin profiles. Many of the data-point's error bars overlap and implies that the effect of filling time on the skin profile was negligible. This is thought to be down to the mesh element size of 2mm, leading to a $\pm$1mm uncertainty in the radial positions whereas the actual profiles were measured with greater accuracy.

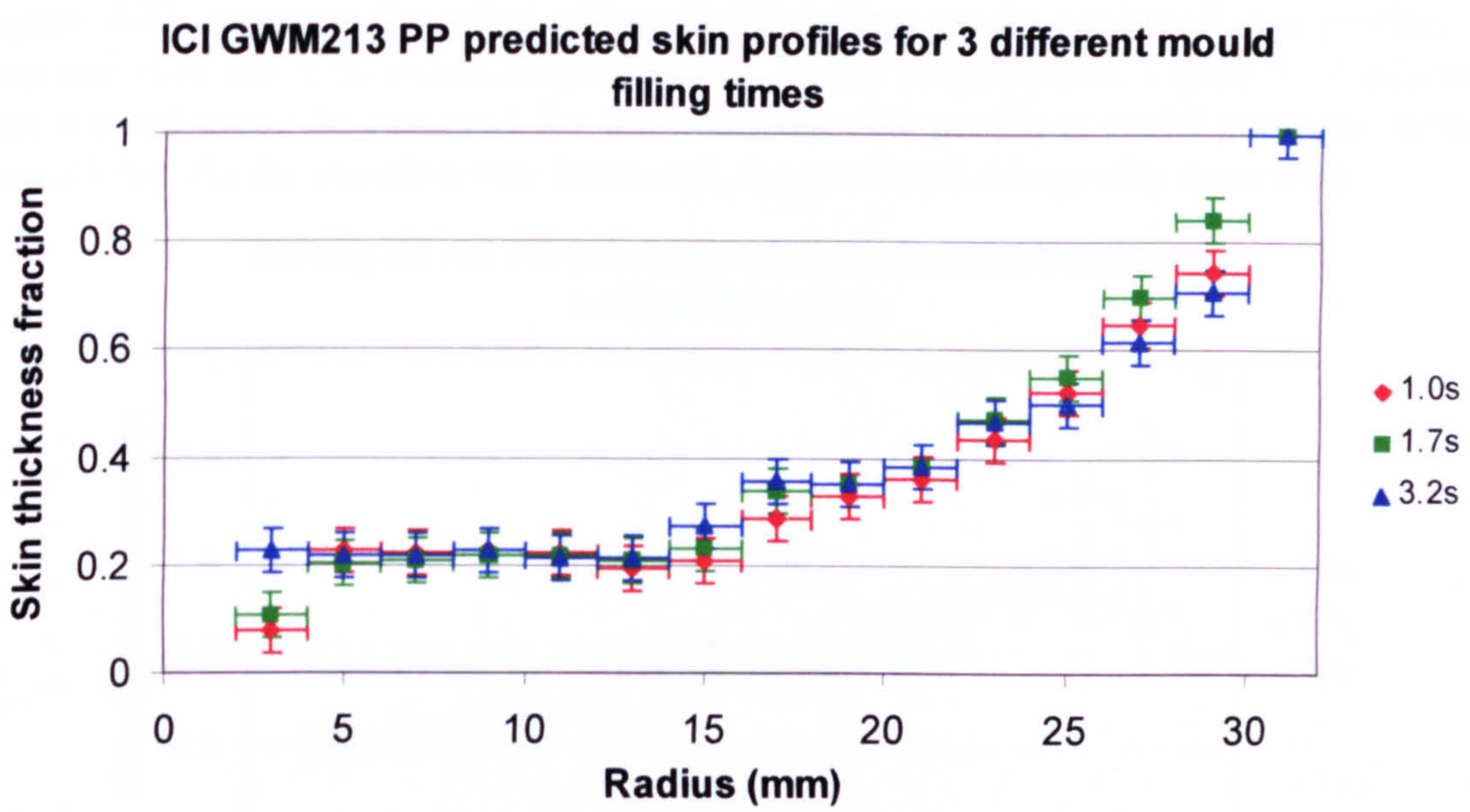

Figure 9.20 Predicted skin profiles for ICI GWM213 PP skin and core for three injection filling times

Figure 9.21 illustrates the effect of mould filling time on the actual skin profiles for skin and core materials comprising of ICI GWM213 polypropylene. Figure 9.21 indicated that the actual skin profiles show a trend between the filling time and the actual skin profile for the radial positions of 5mm to 21mm. As the injection time increased, the skin thickness fraction increased.

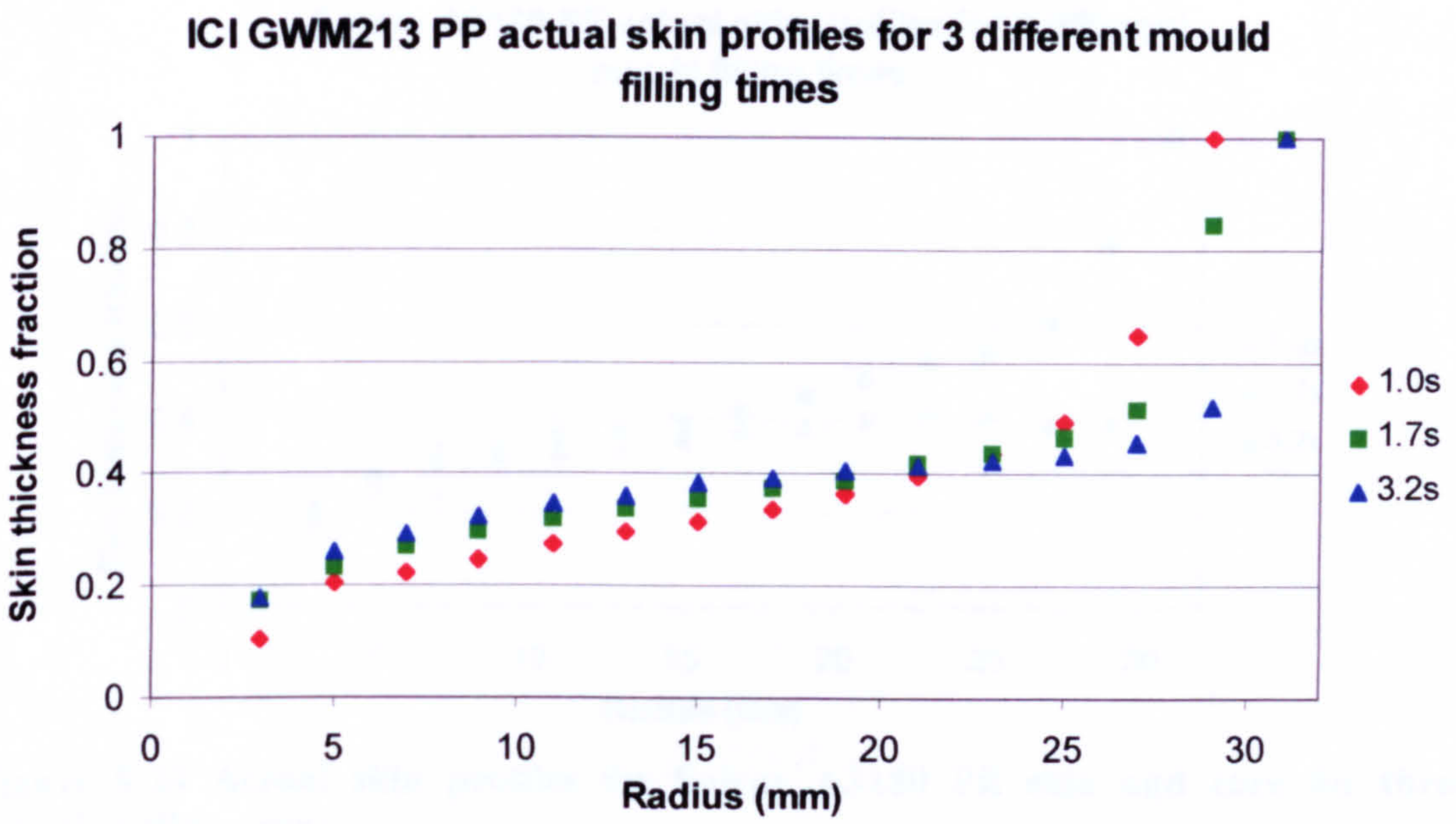

Figure 9.21 Actual skin profiles for ICI GWM213 PP skin and core for three injection filling times

Figure 9.22 illustrates the effect of mould filling time on the predicted skin profiles for skin and core materials comprising of Solvay A3180 polyethylene. Figure 9.22 indicated that a trend could be observed for the predicted skin profile at radial positions greater than 25mm. As the injection time increased, the predicted skin profile decreased.

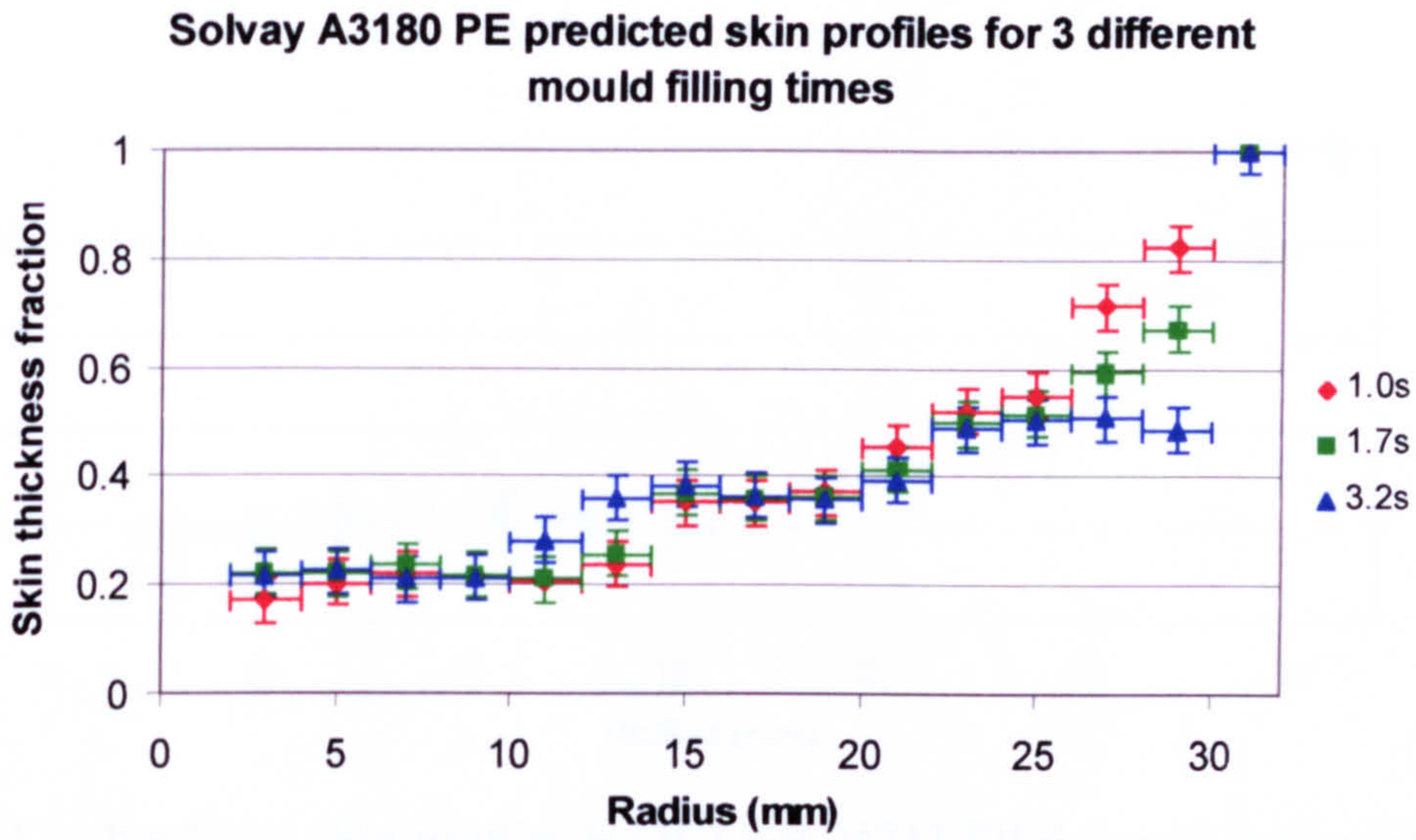

Figure 9.22 Predicted skin profiles for Solvay A3180 PE skin and core for three injection filling times

Figure 9.23 illustrates the effect of mould filling time on the actual skin profiles of skin and core materials comprising of Solvay A3180 polyethylene. No clear trend could be identified between the filling time and the actual skin profiles.

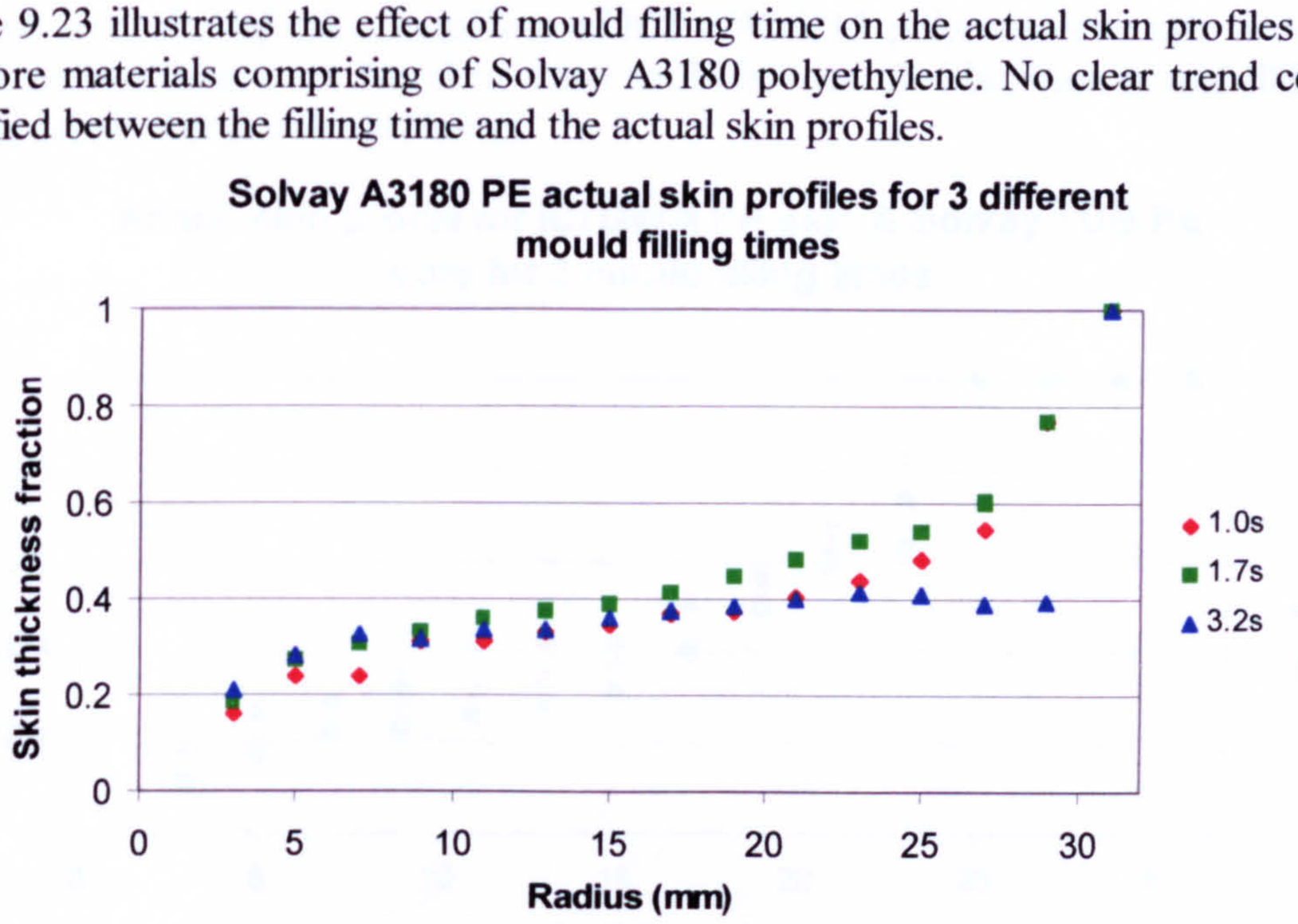

Figure 9.23 Actual skin profiles for Solvay A3180 PE skin and core for three injection filling times

Figure 9.24 illustrates the effect of varying the mould filling time on the predicted skin profiles for the simulation of injection moulding of ICI GWM213 polypropylene skin and Solvay TUB polyethylene core. No clear trend could be identified in figure 9.24 between

the filling time and the predicted skin profiles. This is thought to be down to the mesh element size of 2mm, leading to a ±1mm uncertainty in the radial positions. The actual profiles were measured with greater accuracy.

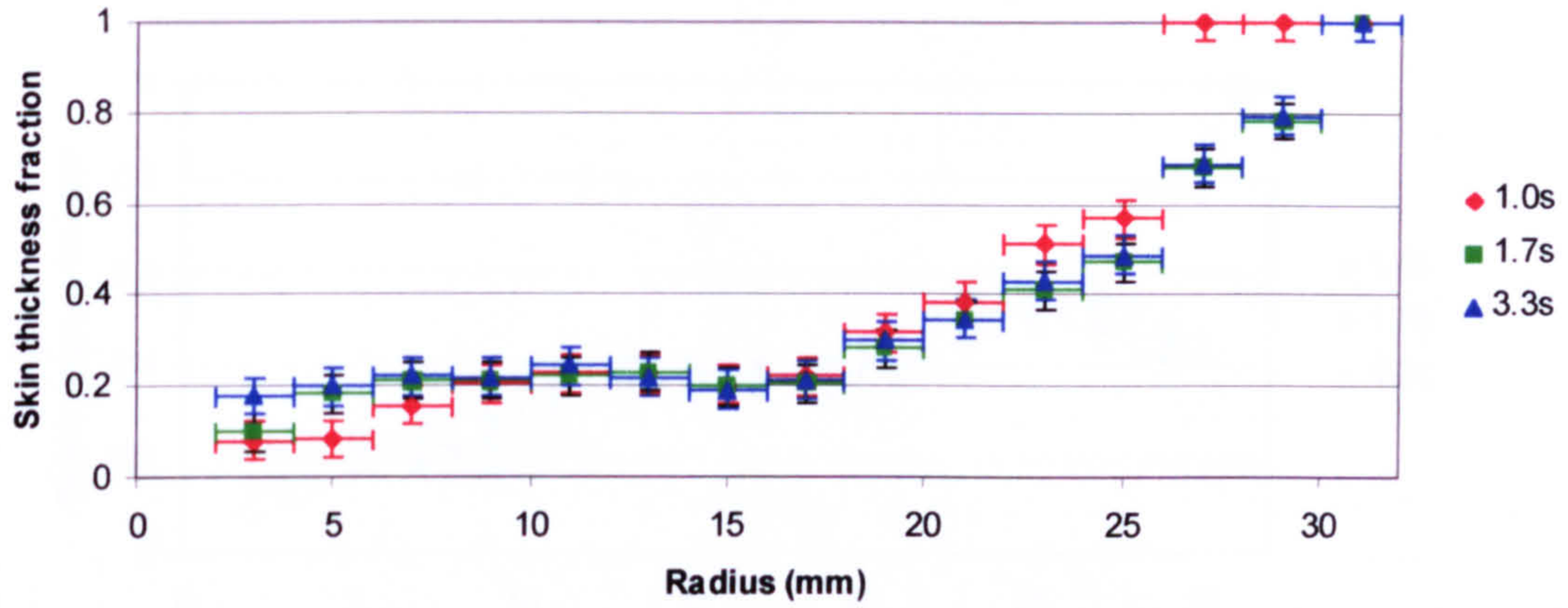

Figure 9.24 Predicted skin profiles for ICI GWM213 PP skin and Solvay TUB core for three injection filling times

Figure 9.25 illustrates the effect of varying mould filling time on the actual skin profiles obtained from the injection moulding of ICI GWM213 polypropylene skin and Solvay A3180 polyethylene core. No clear trend could be identified between mould filling time and the actual skin profiles achieved.

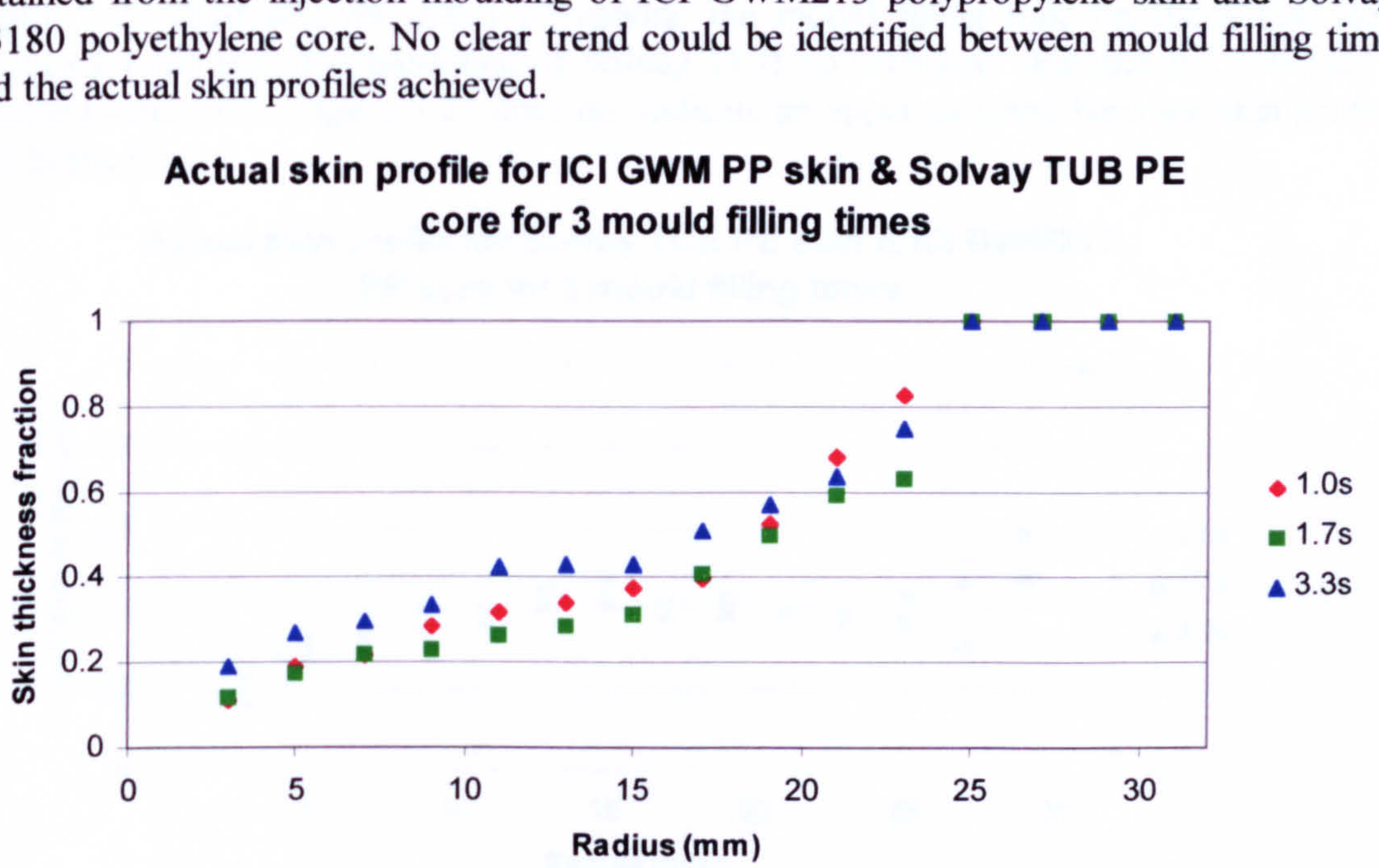

Figure 9.25 Actual skin profiles for ICI GWM213 PP skin and Solvay TUB core for three injection filling times

Figure 9.26 illustrates the effect of varying the moulding filling time on the predicted skin profiles for the simulation of injection moulding Solvay TUB polyethylene skin and ICI GWM213 polypropylene core. Figure 9.26 indicates that for radial positions greater than 25mm, the skin thickness fraction decreased as the mould filling time increased.

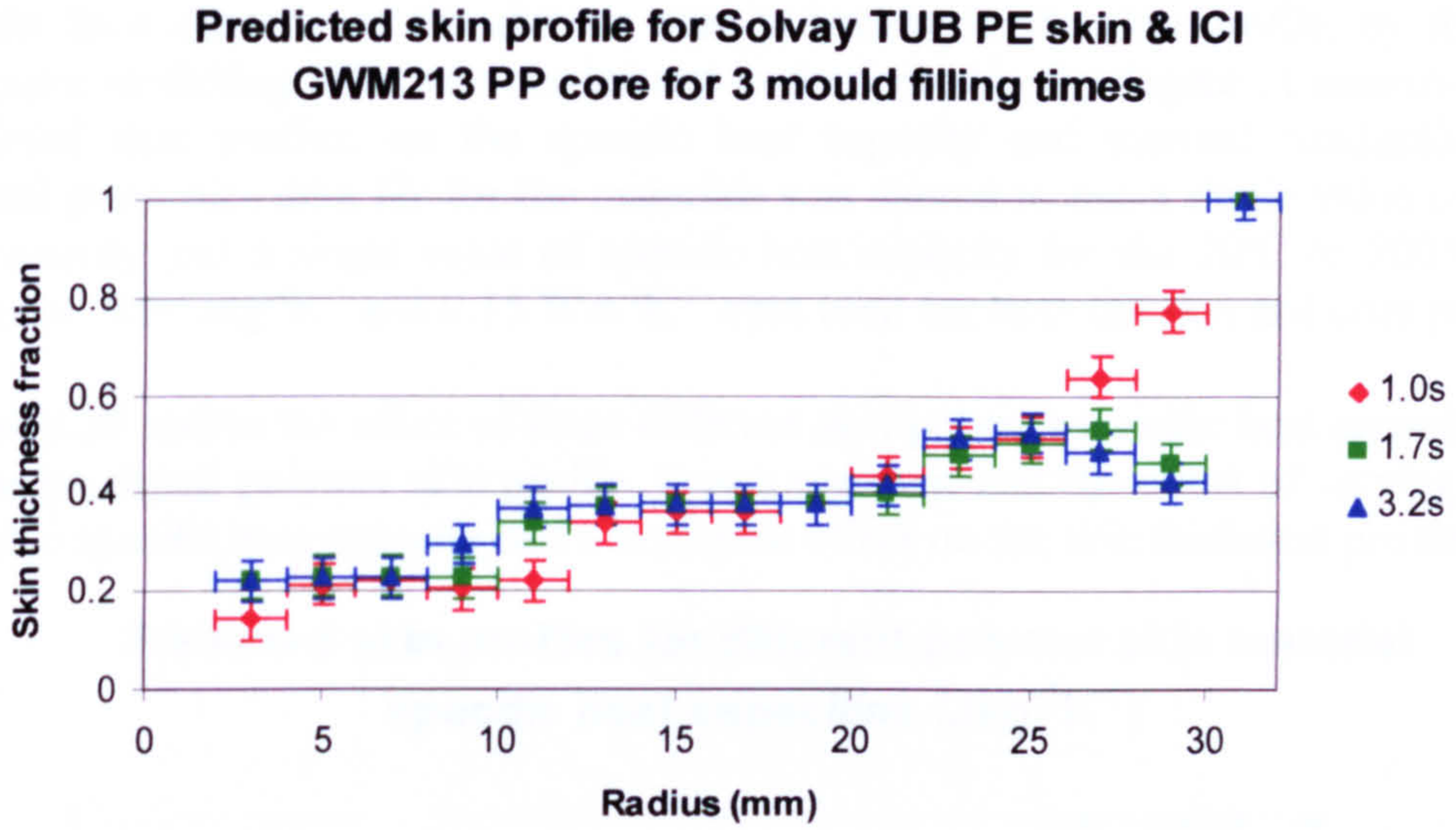

Figure 9.26 Predicted skin profiles for Solvay TUB PE skin and ICI GWM213 PP core for three injection filling times

Figure 9.27 illustrates the effect of varying the mould filling time on the actual skin profiles for the injection moulding of Solvay TUB polyethylene skin and ICI GWM213 polypropylene core. Figure 9.27 does not indicate an apparent trend between skin profile and filling time.

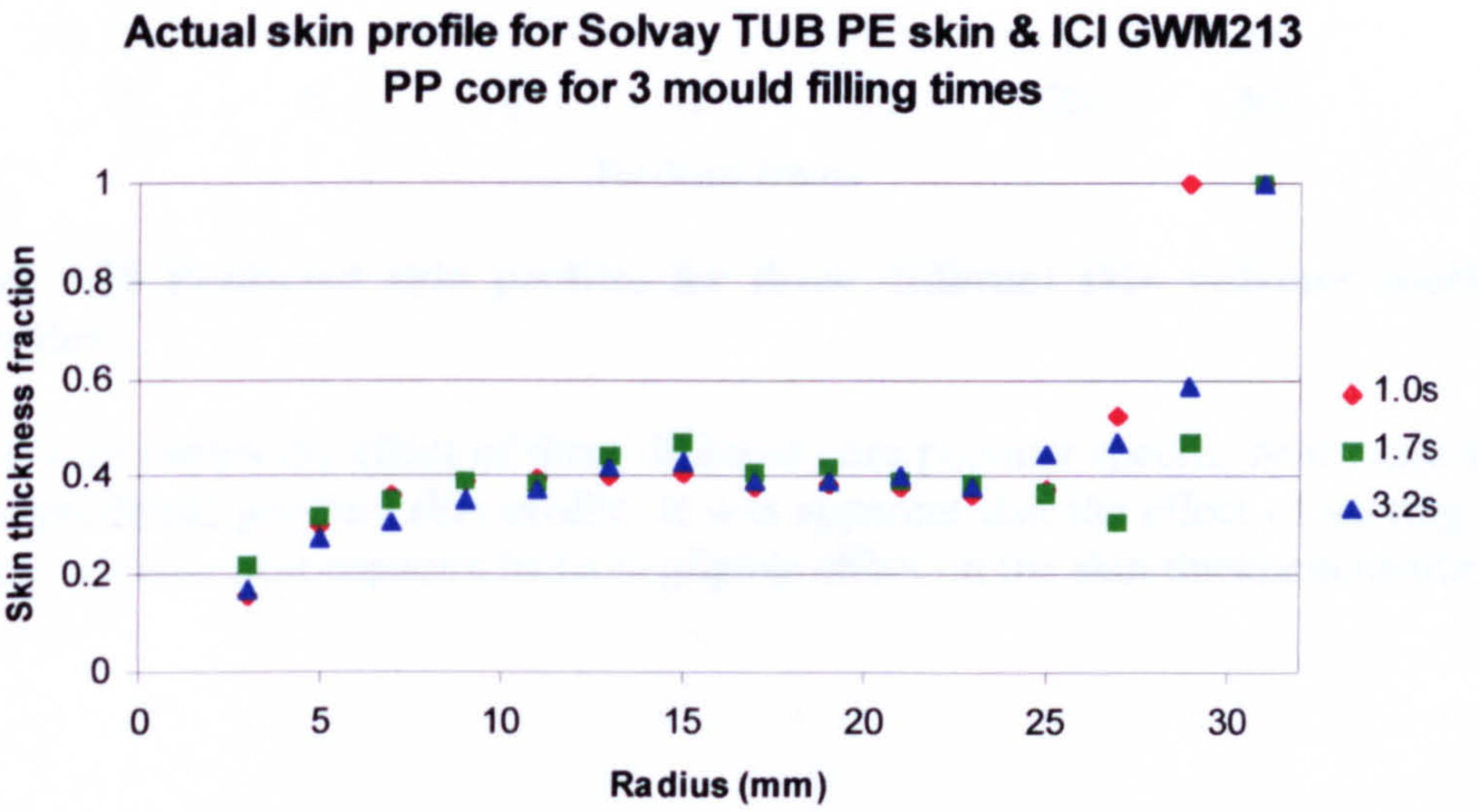

Figure 9.27 Actual skin profiles for Solvay TUB PE skin and ICI GWM213 PP core for three injection filling times

9.4 Computer modelling of the effect of thermal properties on the skin profile of two co-injected identical polymers

This section presents the results of the effect of varying the thermal conductivity or the specific heat capacity of the skin or core polymers on the skin profile, by the use of computer modelling. This was carried out to demonstrate the degree of sensitivity of the predicted skin profiles on the specific heat capacity and thermal conductivity. The thermal properties data file for the materials was altered to use a single value of thermal conductivity and a single value of specific heat capacity for the 20°C to 200°C. Initial values of 2000 $Jkg^{-1}K^{-1}$ and 0.15 $Wm^{-1}K^{-1}$ were used for both the skin and core polymers.

Figure 9.28 shows the effect of three different skin polymer specific heat capacity values on the predicted polymer skin profile. It was apparent that the effect of varying the skin polymer specific heat capacity had a negligible effect on the skin thickness profile.

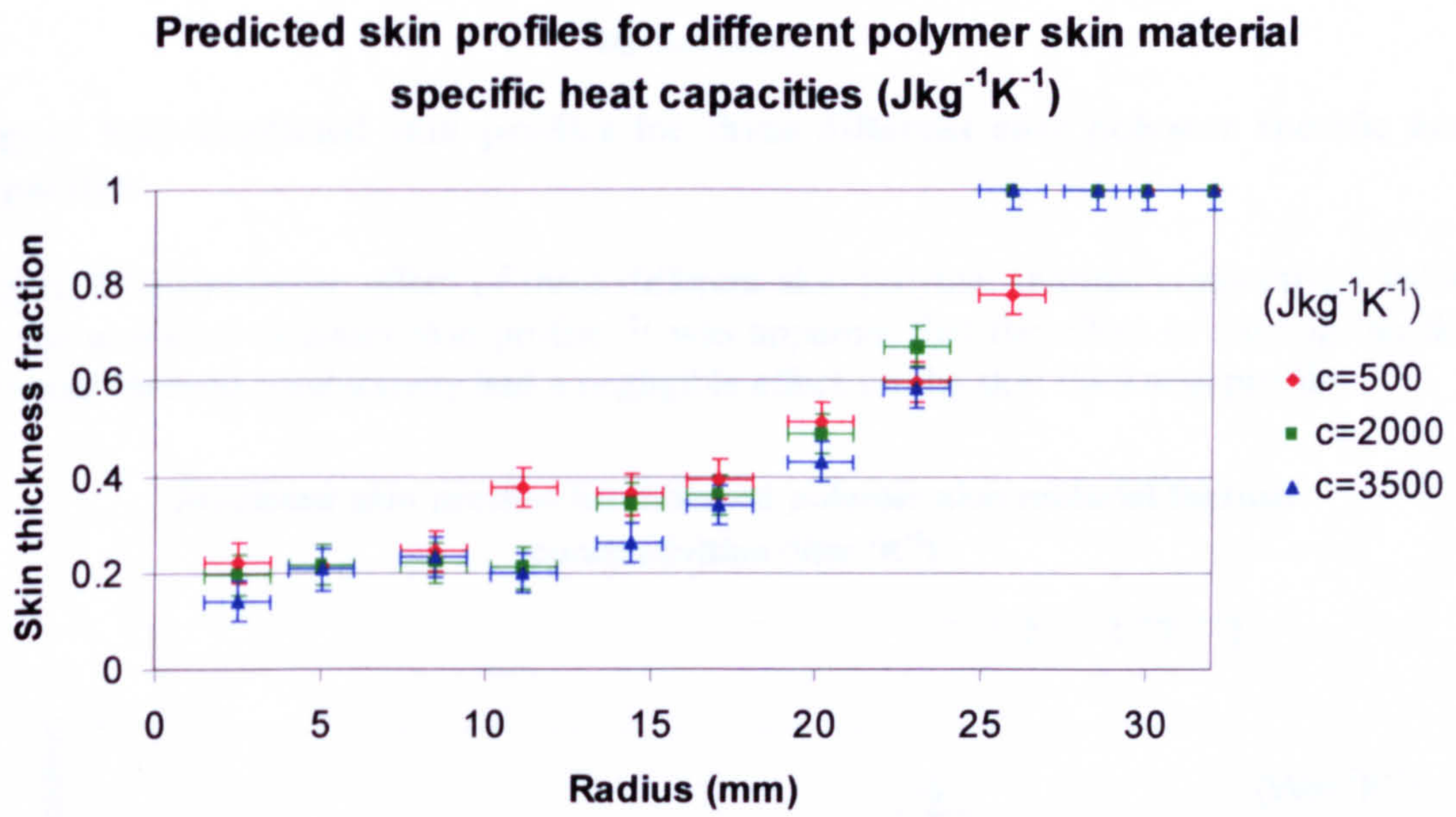

Figure 9.28 Predicted skin profiles for three different skin polymer specific heat capacities

Figure 9.29 shows the effect of three different core polymer specific heat capacity values on the predicted polymer skin profile. It was apparent that the effect of varying the core polymer specific heat capacity had a negligible effect on the skin thickness profile.

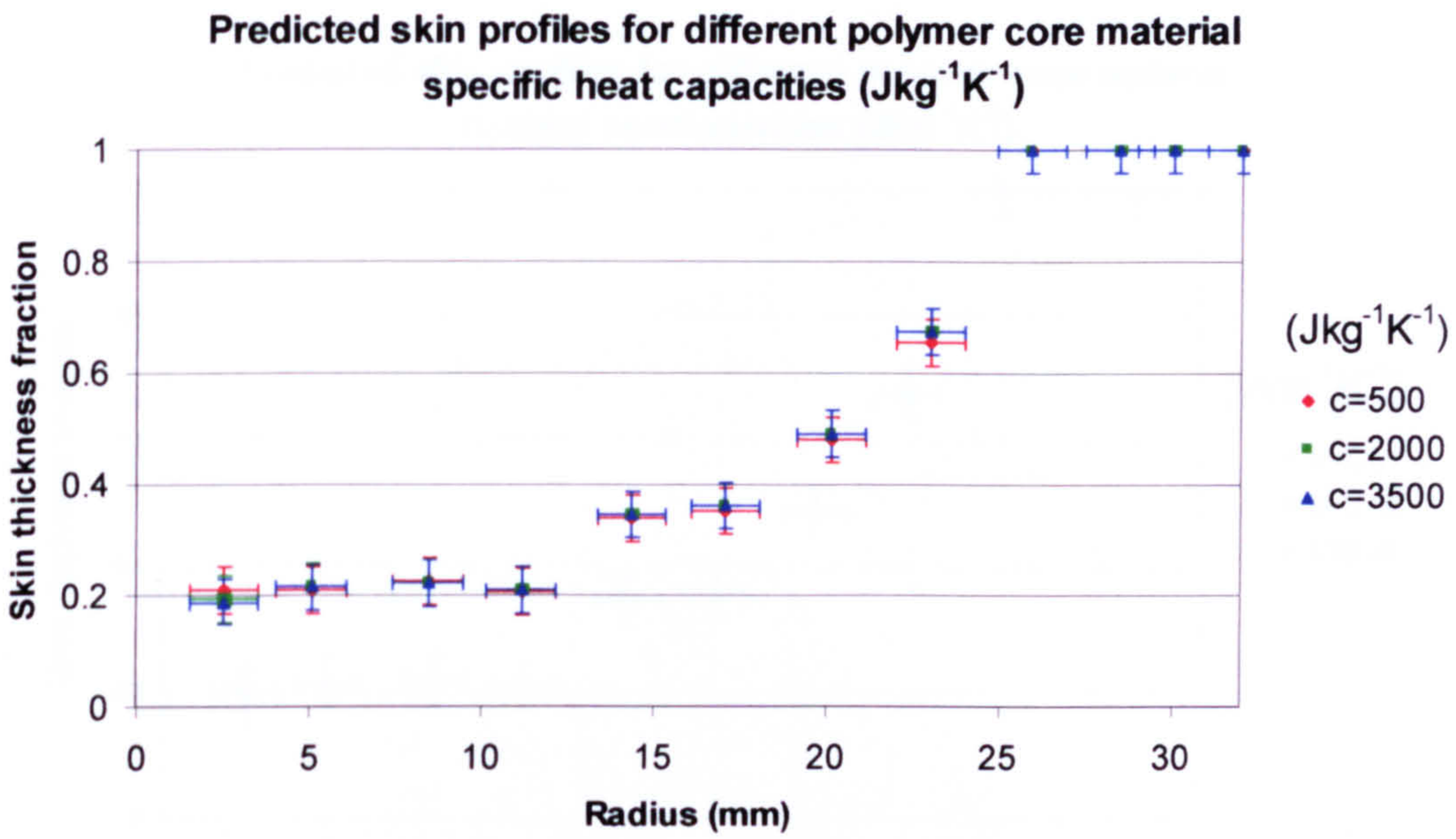

Figure 9.29 Predicted skin profiles for three different core polymer specific heat capacities

Figure 9.30 shows the effect of three different skin polymer thermal conductivity values on the predicted polymer skin profile. It was apparent that the effect of varying the skin polymer thermal conductivity had a negligible effect on the skin thickness profile.

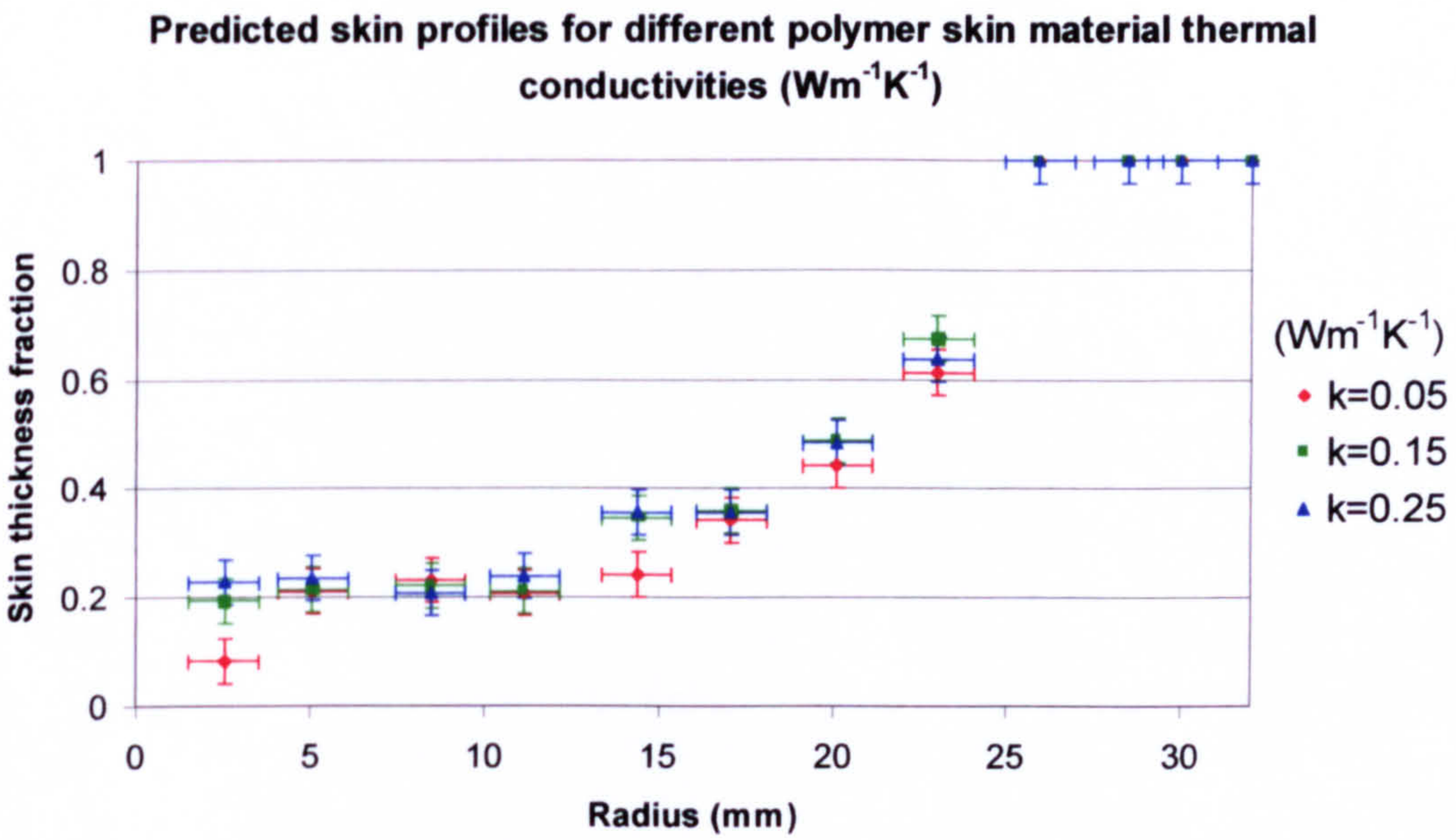

Figure 9.30 Predicted skin profiles for three different skin polymer thermal conductivities

Figure 9.31 shows the effect of three different core polymer thermal conductivity values on the predicted polymer skin profile. It was apparent that the effect of varying the core polymer thermal conductivity had a negligible effect on the skin thickness profile.

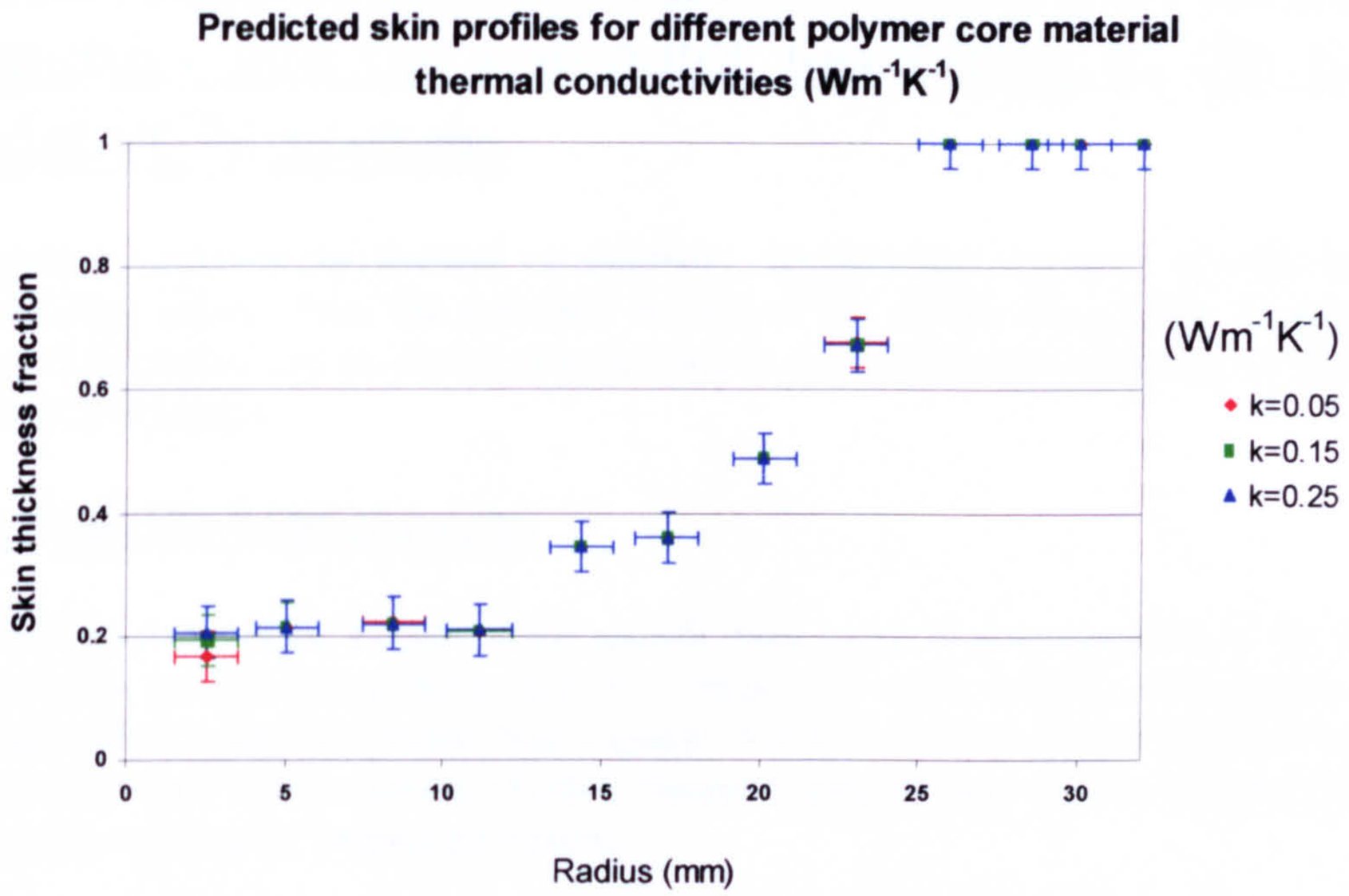

Figure 9.31 Predicted skin profiles for three different core polymer thermal conductivities

10 Results: characterisation of feedstock material properties and the computer modelling of the three model PCM systems

This section presents the thermal conductivity, specific heat capacity, specific volume and rheology results from the materials testing of the feedstocks. It also presents the results of the actual and predicted skin profiles in the co-injection moulding of the three model PCM systems.

10.1 Specific heat capacity

This section presents the results of the specific heat capacity determination of the binder components, powder components and the feedstocks using MDSC. The graphs have been plotted as complex specific heat capacity versus temperature and present the data produced by the TA Instruments MDSC. Complex specific heat capacity represents both non-kinetic and kinetic thermal processes.

The peaks represent a change of state, such as a melting or solidification. Kinetic processes such as melting will absorb thermal energy and result in a peak during heating in the determination of complex specific heat capacity. This occurs because extra heat is being absorbed into the material during the change of state from a solid to a liquid and is an endothermic process. The area of the peak represents a measure of its latent heat, which is a measure of the energy change for that transition.. The converse is also true, a trough occurs during freezing as this represents the energy released by the material during its change of state from a liquid to a solid, and is an exothermic process.

In injection moulding, latent heat is released from the molten feedstock as it solidifies. The release of latent heat influences the cooling dynamics. C-Mold is able to take the latent heat of solidification into account in its analyses provided that sufficient data are available for that material. Many of the polymers listed in the C-Mold materials database have a single specific heat capacity data value at a single molten temperature. Under these circumstances, C-Mold is not able to take the latent heat of solidification into account. The C-Mold manual[197] states explicitly that a constant value of specific heat capacity is not adequate during post filling as latent heat is released during solidification. This emphasises the importance of determining the specific heat capacity data for the entire temperature range that the feedstock encounters, permitting the effects of latent heat to be taken into account, as heat influences both viscosity and specific volume.

During the melting transition, there exists a two phase region comprising a solid and a liquid. Thus some sort of rule of mixtures applies for the specific heat capacity during the transition. The exact rule of mixtures for the specific heat capacity during the transition is unknown. This is dealt with by drawing in intersecting dashed lines from the baseline above and below the transition region. Thus, the dashed lines represent the expected specific heat capacity value during the transition.

It is pointed out that if the MDSC determinations are carried out under a heating profile from ambient to processing temperature, the melting transitions appear as peaks in the complex specific heat capacity graphs. If the same experiment was repeated, but with a cooling profile from processing to ambient temperature instead, the transitions would appear as troughs in the complex specific heat capacity graphs.

10.1.1 The specific heat capacity of the binder and powder components

This section presents the results of the MDSC work on the powder and binder components. Figure 10.1 illustrates that the Exxon PP3536F1 polypropylene has two transitions which are the solid to melt transition, and the softening point, which occur simultaneously. Melting occurs at 161°C. The specific heat capacity is 1.56 $kJkg^{-1}K^{-1}$ at s.t.p. which agrees well with literature values for this class of polypropylenes.

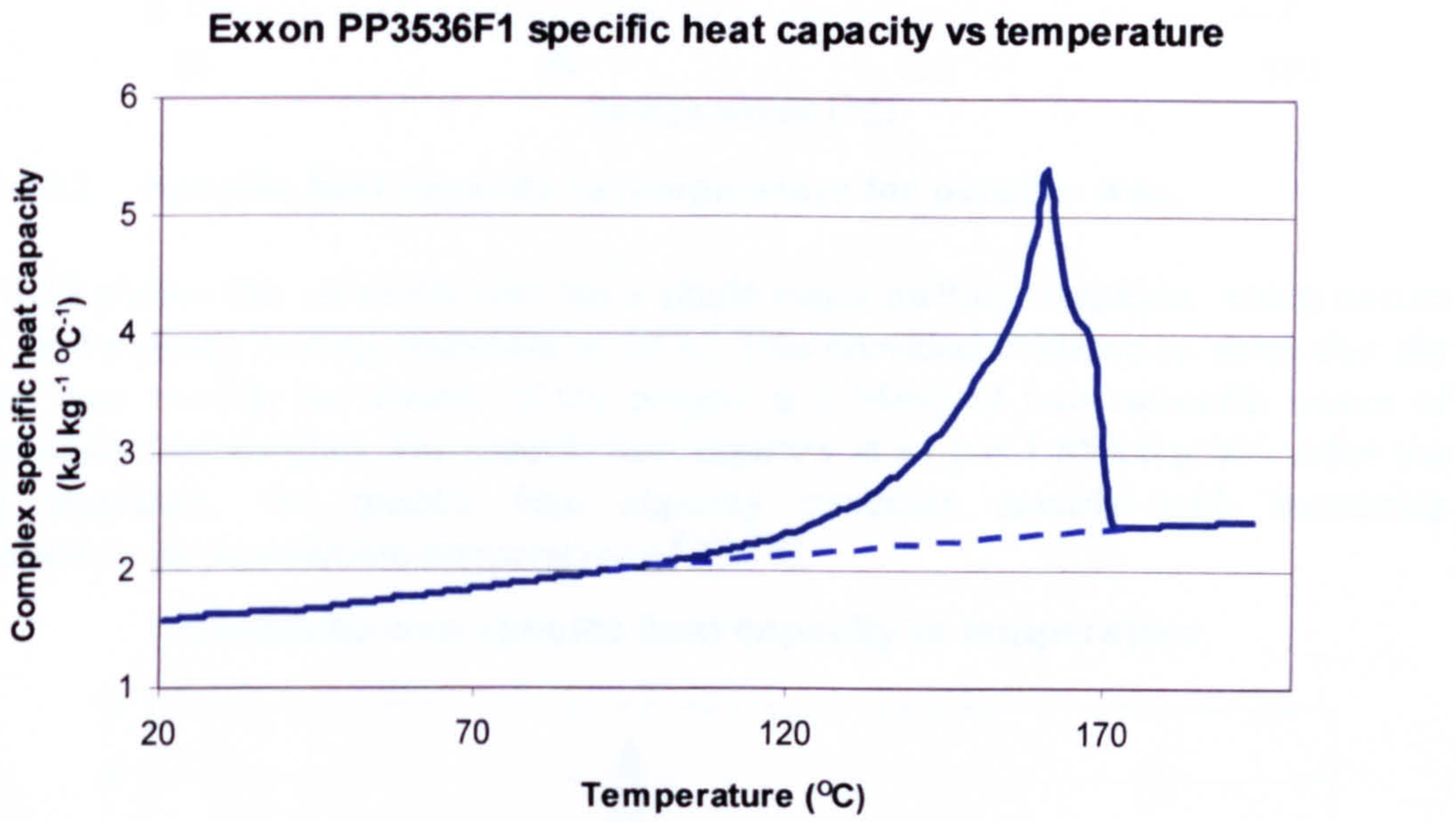

Figure 10.1 Specific heat capacity vs temperature for Exxon PP3635F1 LMWPP

Figure 10.2 shows that there are two melting points for the paraffin wax, and provided evidence to show that the paraffin wax used in the course of the project is a blend of two paraffin waxes with different molecular weights. Thus the major fraction's melting point was 58°C and the minor fraction's melting point was 43°C. The baseline value of specific heat capacity was 2.32 kJ $kg^{-1}K^{-1}$ at s.t.p. Above the melting point, the specific heat capacity shows a gradual linear increase with increasing temperature up to 165°C. The thermal degradation of paraffin wax starts at 170°C which imposed a limitation on the upper bound of the test temperature range used in MDSC.

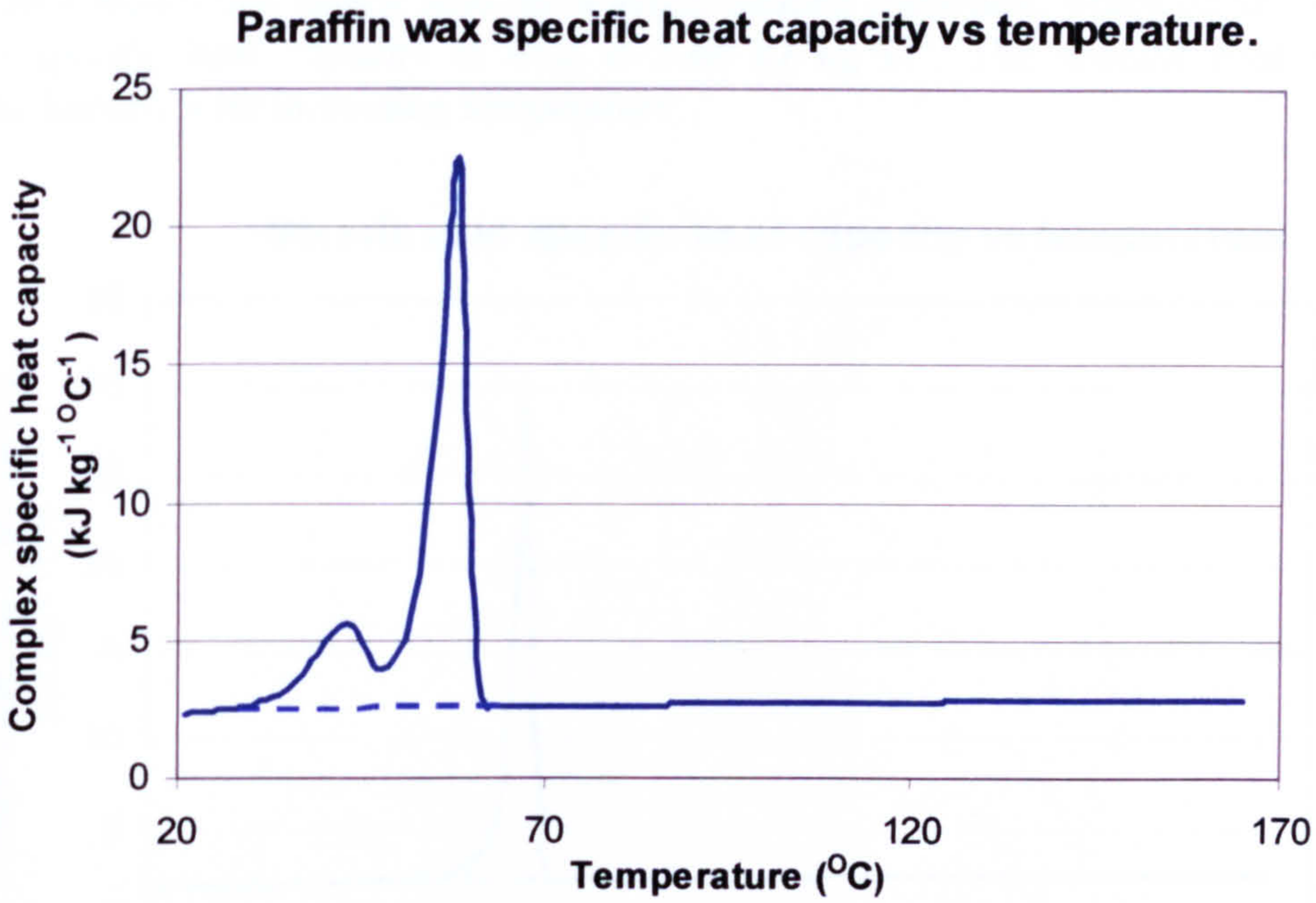

Figure 10.2 Specific heat capacity vs temperature for paraffin wax

Figure 10.3 shows that carnauba wax has a single major melting transition, which occurs at 81°C and a minor melting transition at 59°C. This provided evidence to show that the carnauba wax used in the course of the project is a blend of two carnauba waxes of different molecular weights. The specific heat capacity at s.t.p is 1.85 $kJkg^{-1}K^{-1}$. After the melting transition, the specific heat capacity increases linearly with increasing temperature to its degradation temperature of 177°C.

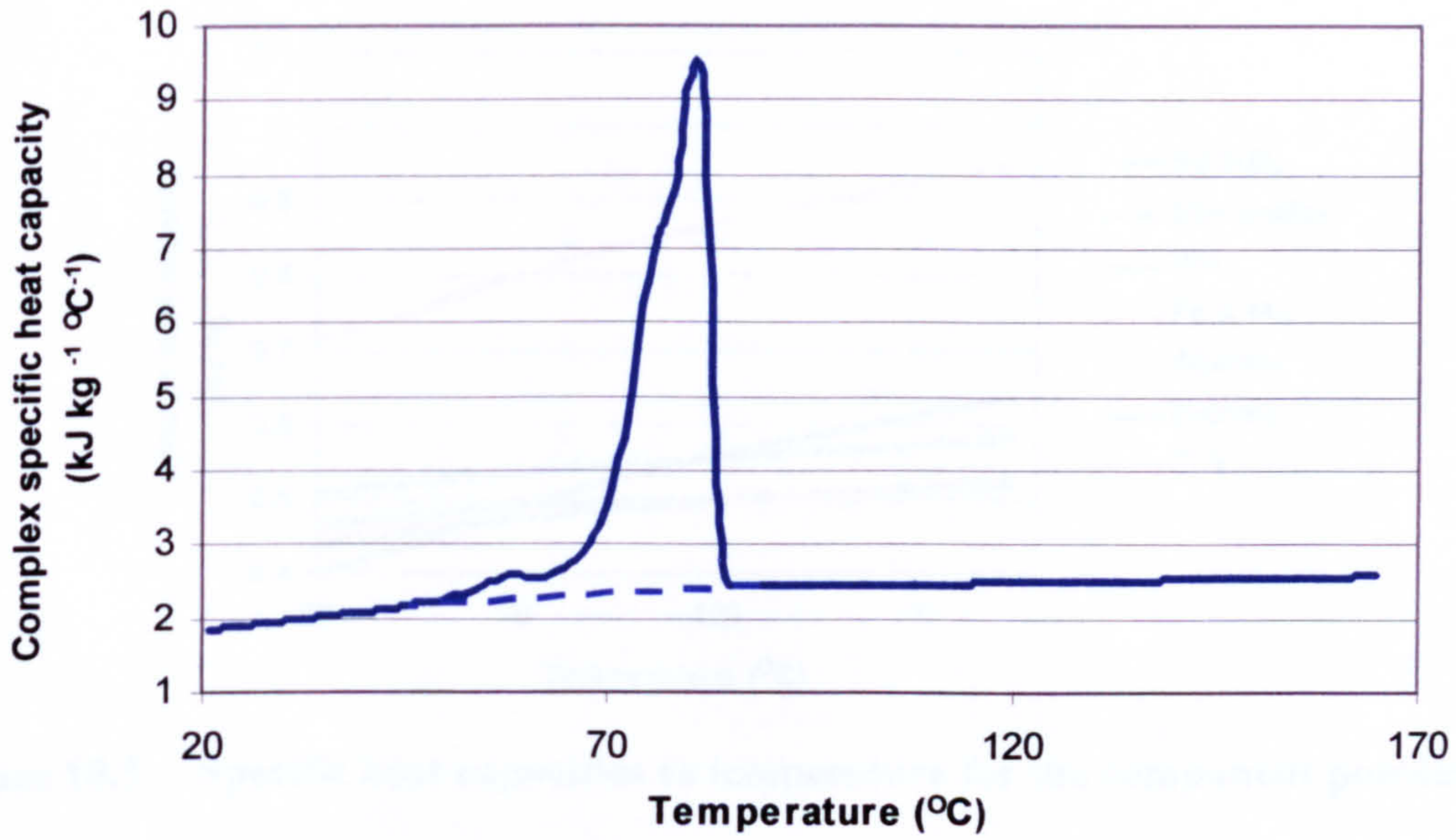

Figure 10.3 Specific heat capacity vs temperature for carnauba wax

Figure 10.4 shows that stearic acid has a single melting transition, which occurs at 69°C, and the specific heat capacity at s.t.p is 1.60 kJ $kg^{-1}K^{-1}$. The specific heat capacity increases linearly with increasing temperature.

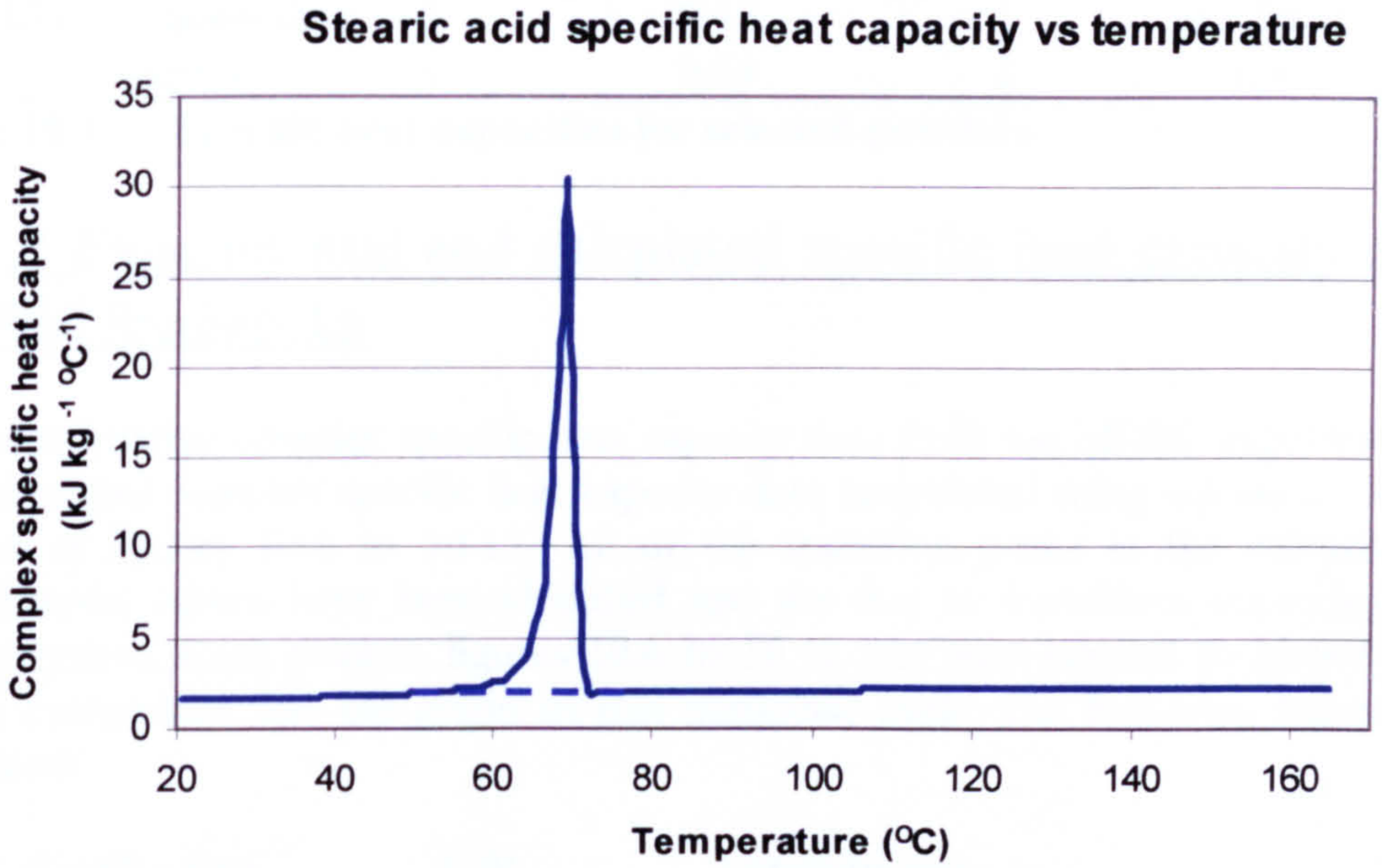

Figure 10.4 Specific heat capacity vs temperature for stearic acid

Figure 10.5 shows the specific heat capacities versus temperature for the four powders listed in table 10.1. All of the powders' specific heat capacities are observed to increase with temperature.

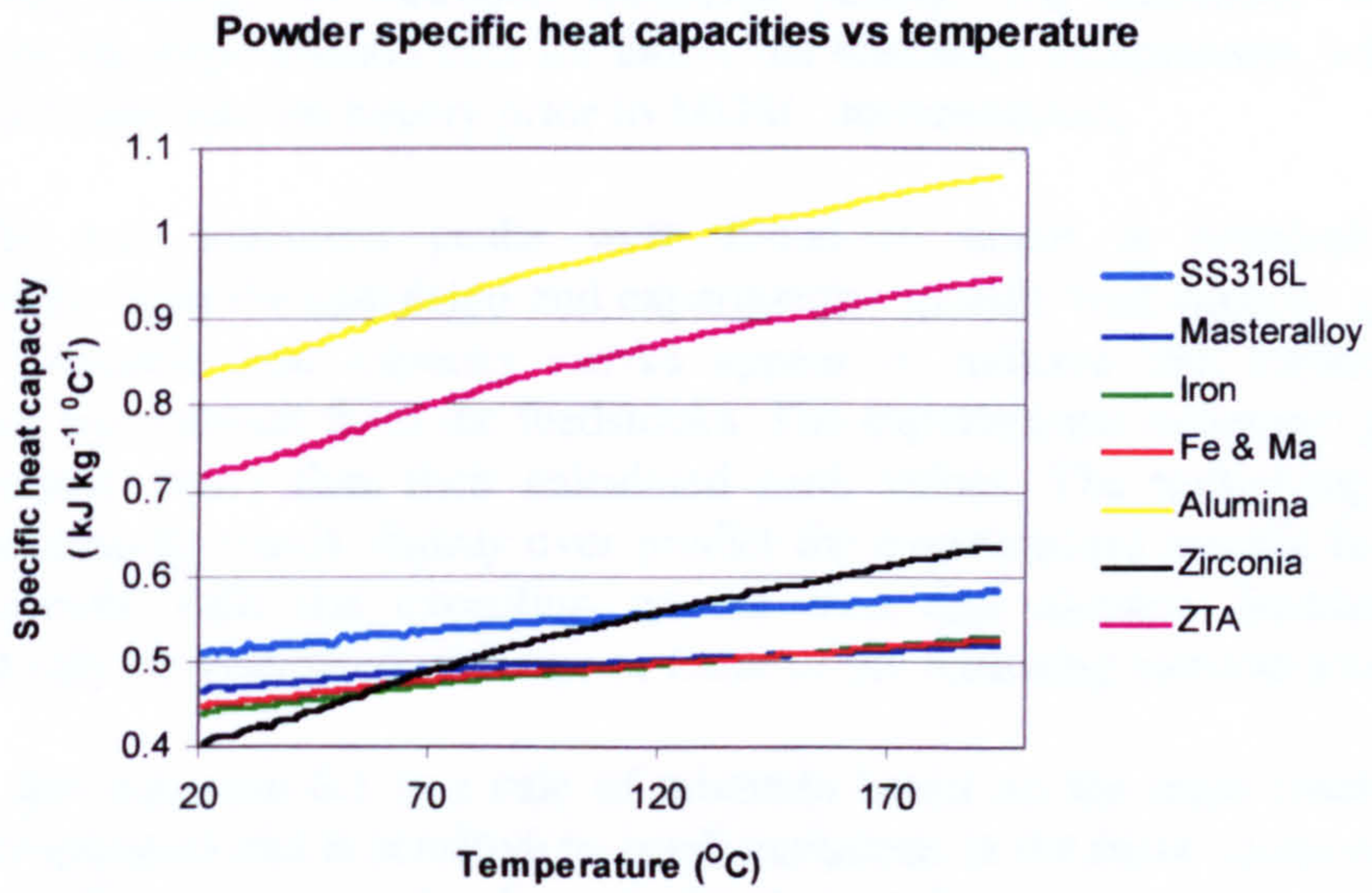

Figure 10.5 Specific heat capacities vs temperature for the component powders

Table 10.1 lists the specific heat capacities at s.t.p. of the powder components. The experimental and literature values in table 10.1 show close agreement.

Powder	Experimental S.H.C at s.t.p ($kJ\ kg^{-1}\ K^{-1}$)	Literature S.H.C at s.t.p ($kJ\ kg^{-1}\ K^{-1}$)
Carbonyl Iron	0.44	0.5
SS316L	0.51	0.51
SS316L masteralloy	0.46	not listed
Alumina	0.84	0.8

Table 10.1 Specific heat capacities for selected powders

10.1.2 Experimental and calculated specific heat capacity curves for PIM feedstocks

The experimental complex specific heat capacity data from the MDSC experiments and the calculated complex specific heat capacity data (calculated using equation 6.1) were plotted in figures 10.6 to 10.12. All of the transition peaks in the calculated and experimental curves have been identified and are due to transitions occurring in the binder system. Each peak in figures 10.6 to 10.12 has been labelled to identify which binder component was the origin of that particular peak. The following legends have been used:

PW	Paraffin wax	CW	Carnauba wax
SA	Stearic acid	LMWPP	Low molecular weight polypropylene

The experimental and calculated LMWPP peaks in figures 10.6 to 10.12 do not occur at the same nominal temperature. This is thought to be due to the thermal and mechanical history of the feedstocks being compounded as the experimental MDSC data was obtained using samples of extruded feedstock pellets. The calculated curves were obtained using the experimental data for individual feedstock components, which had no prior thermal or mechanical history prior to MDSC determination.

The paraffin wax transition peaks were found to occur at nominally identical temperatures for both the calculated and experimental specific heat capacity graphs. The experimental specific heat capacity curves appear to indicate that stearic acid and carnauba wax were absent from the feedstocks. The experimental maximum peak values were consistently lower than their calculated peak values. The underlying calculated specific heat capacity trends slightly over predict the experimental specific heat capacity underlying trends with the exception of the iron and alumina feedstock. These observations may be associated with one or more of the following considerations:

The first is that equation 6.1 is a rule of mixtures based on the mass fractions of the feedstock components and is sensitive to small variations in the mass composition of the feedstocks, leading to errors in the calculated specific heat capacity data. This is reinforced by the fact that carnauba wax and stearic acid account for 0.59% to 1.62% of the feedstock mass and the powders account for 80.81% to 93.03% of the feedstock mass. The second is due to inhomogeneities or volume loading variations occurring during the compounding of the feedstocks, leading to errors in the experimental determination of specific heat capacity of the compounded feedstocks. The third is due

to mechanical or thermal degradation of the feedstocks. The specific heat capacity determination of the individual feedstock components was carried out on samples that had no prior thermal or mechanical history. The specific heat capacity determination of the feedstocks was carried out on samples of granulated feedstock that had been compounded and hence had a thermal and mechanical history.

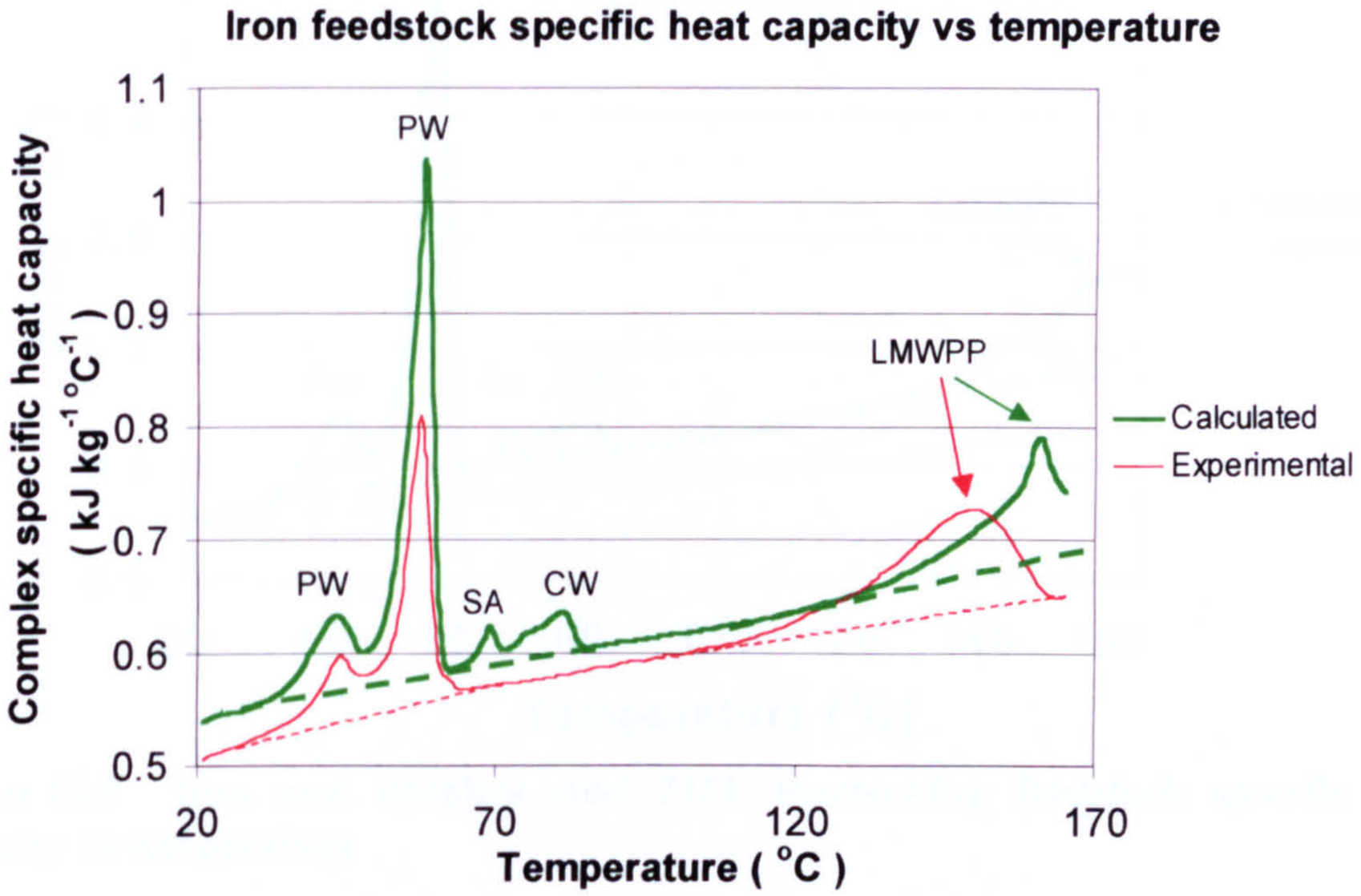

Figure 10.6 Iron feedstock specific heat capacity vs temperature

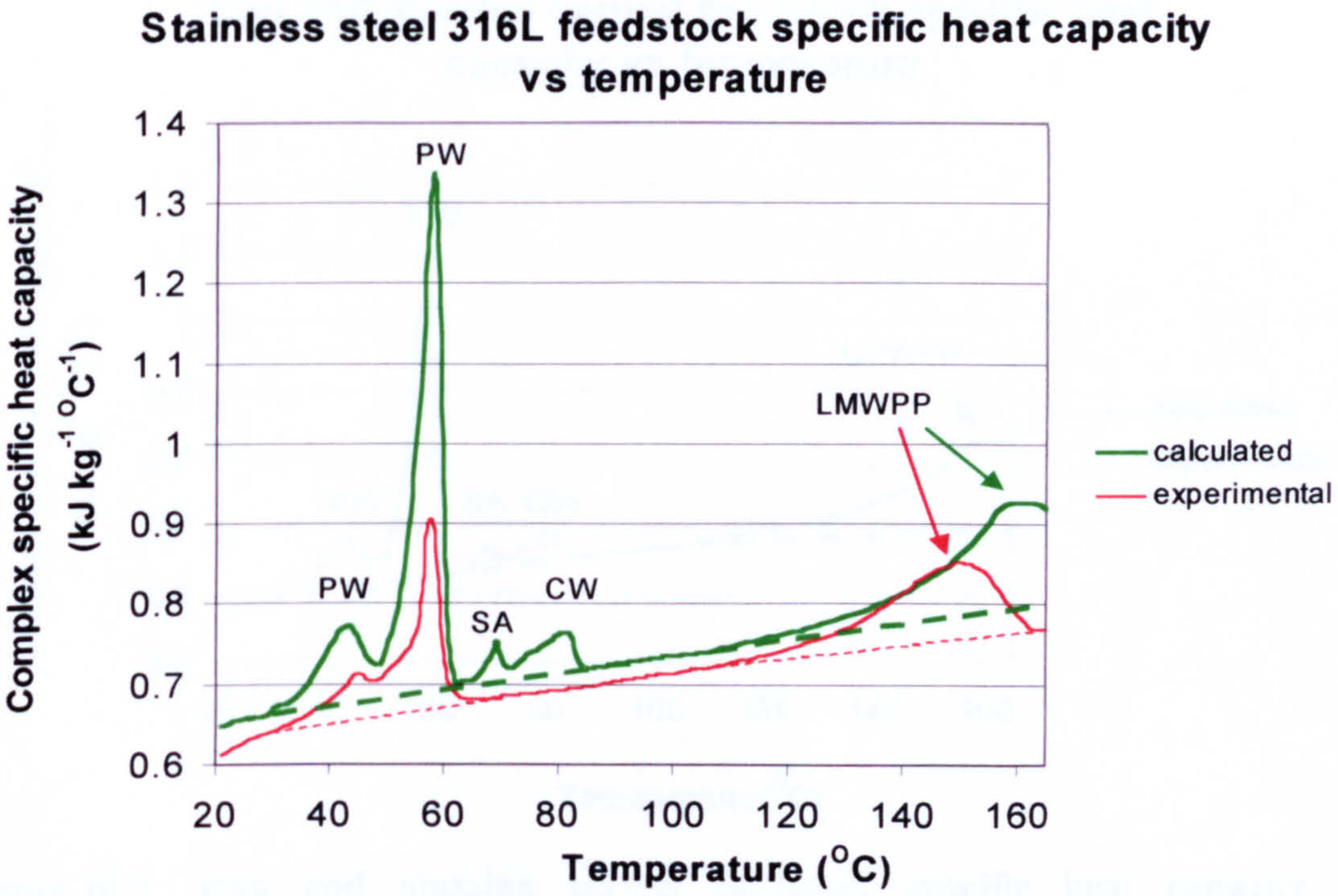

Figure 10.7 Stainless steel 316L feedstock specific heat capacity vs temperature

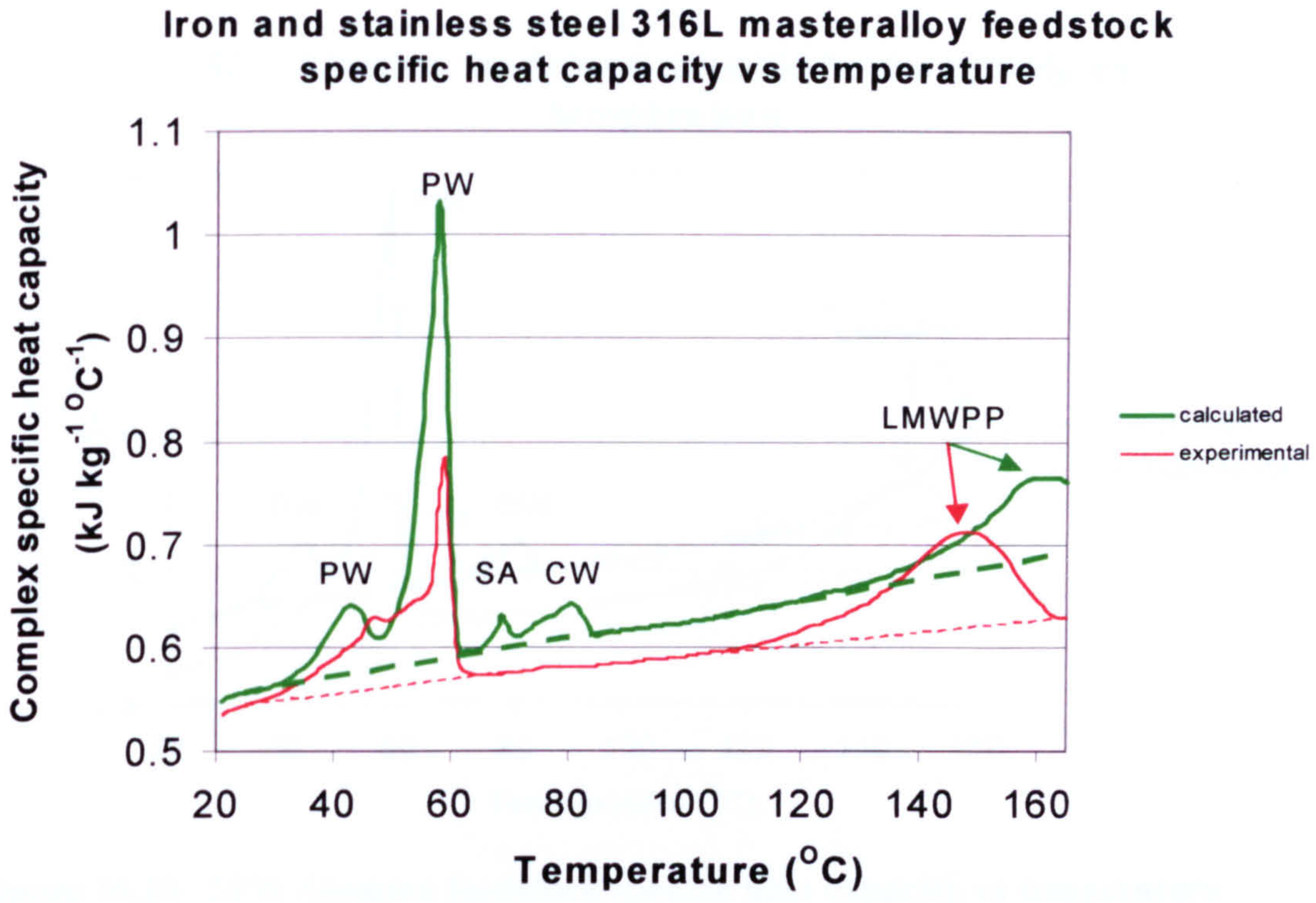

Figure 10.8 Iron and stainless steel 316L masteralloy feedstock specific heat capacity vs temperature

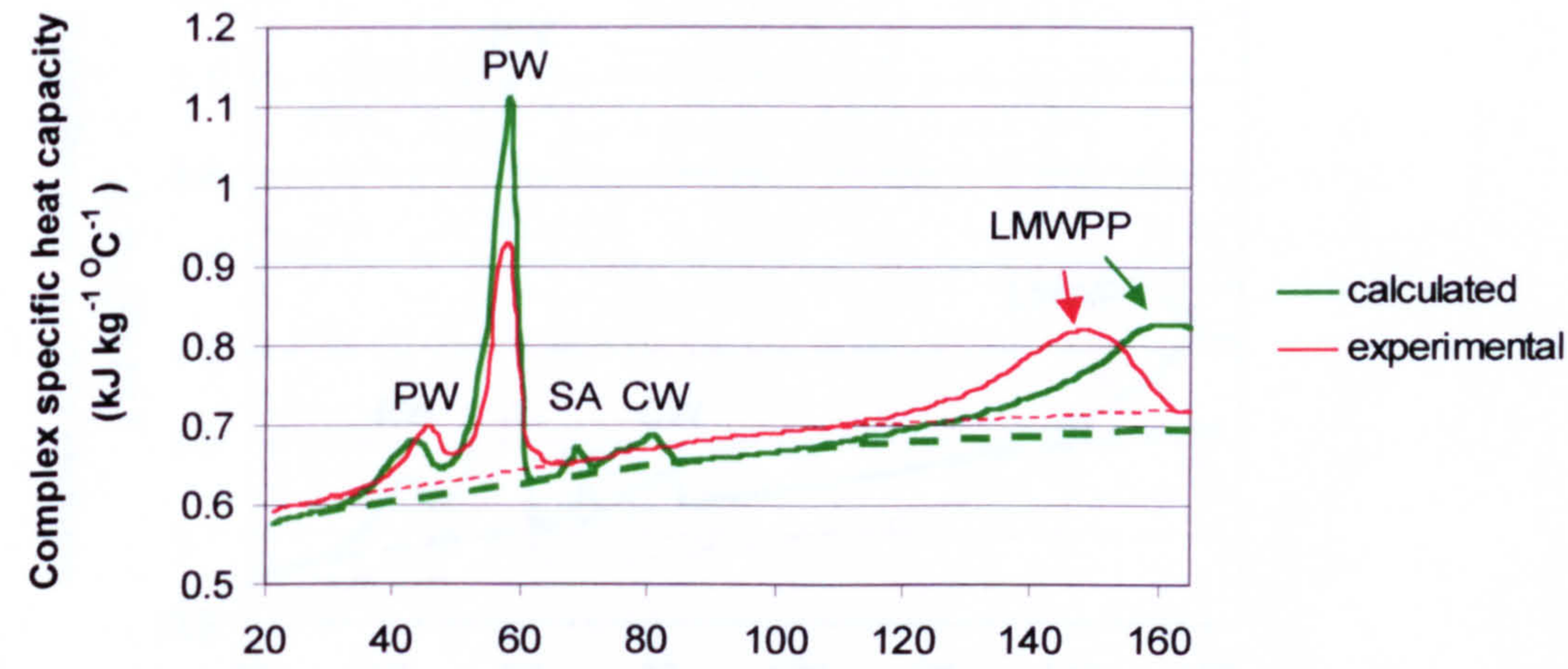

Figure 10.9 Iron and alumina cermet feedstock specific heat capacity vs temperature

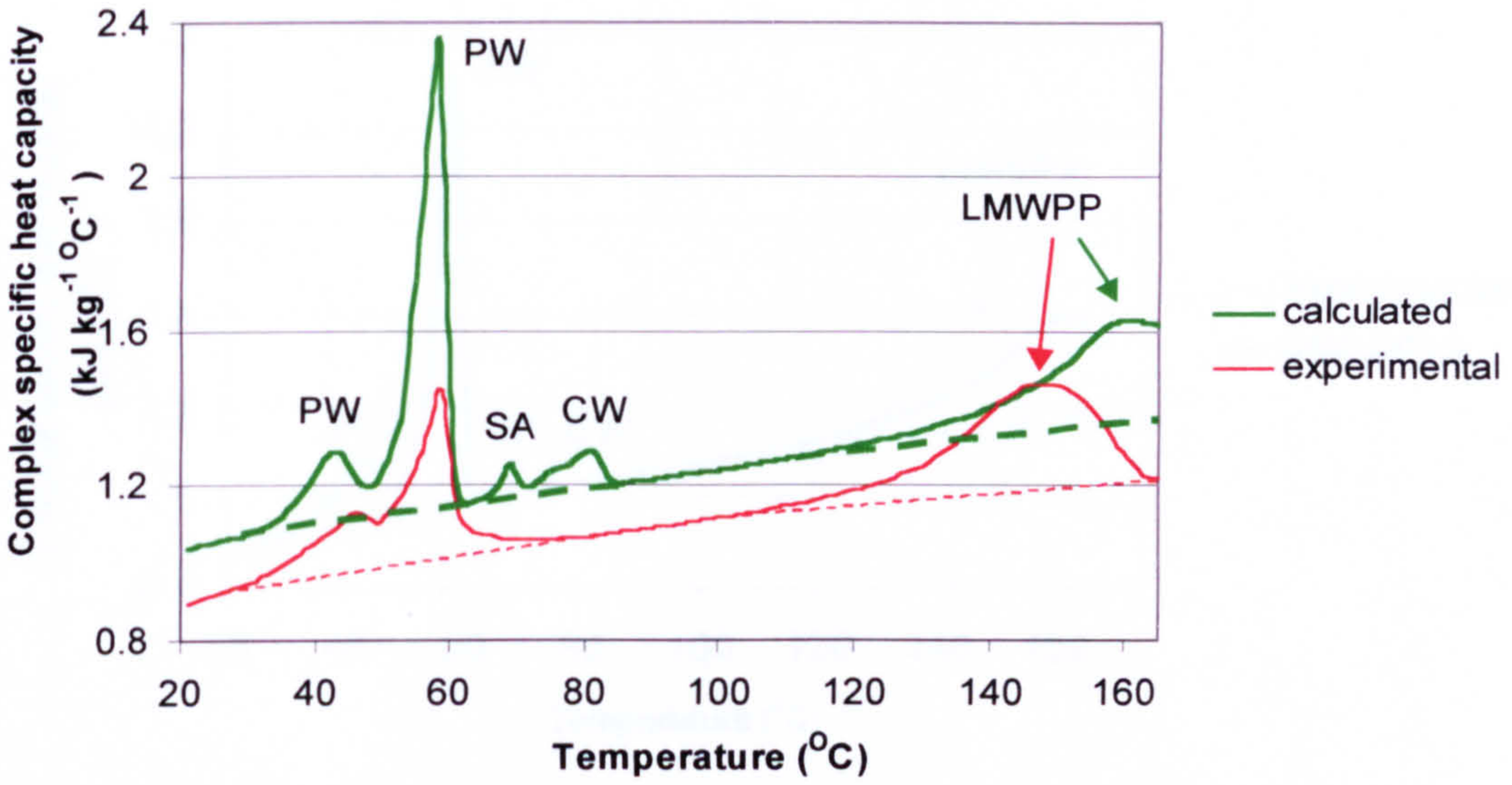

Figure 10.10 50% Alumina feedstock specific heat capacity vs temperature

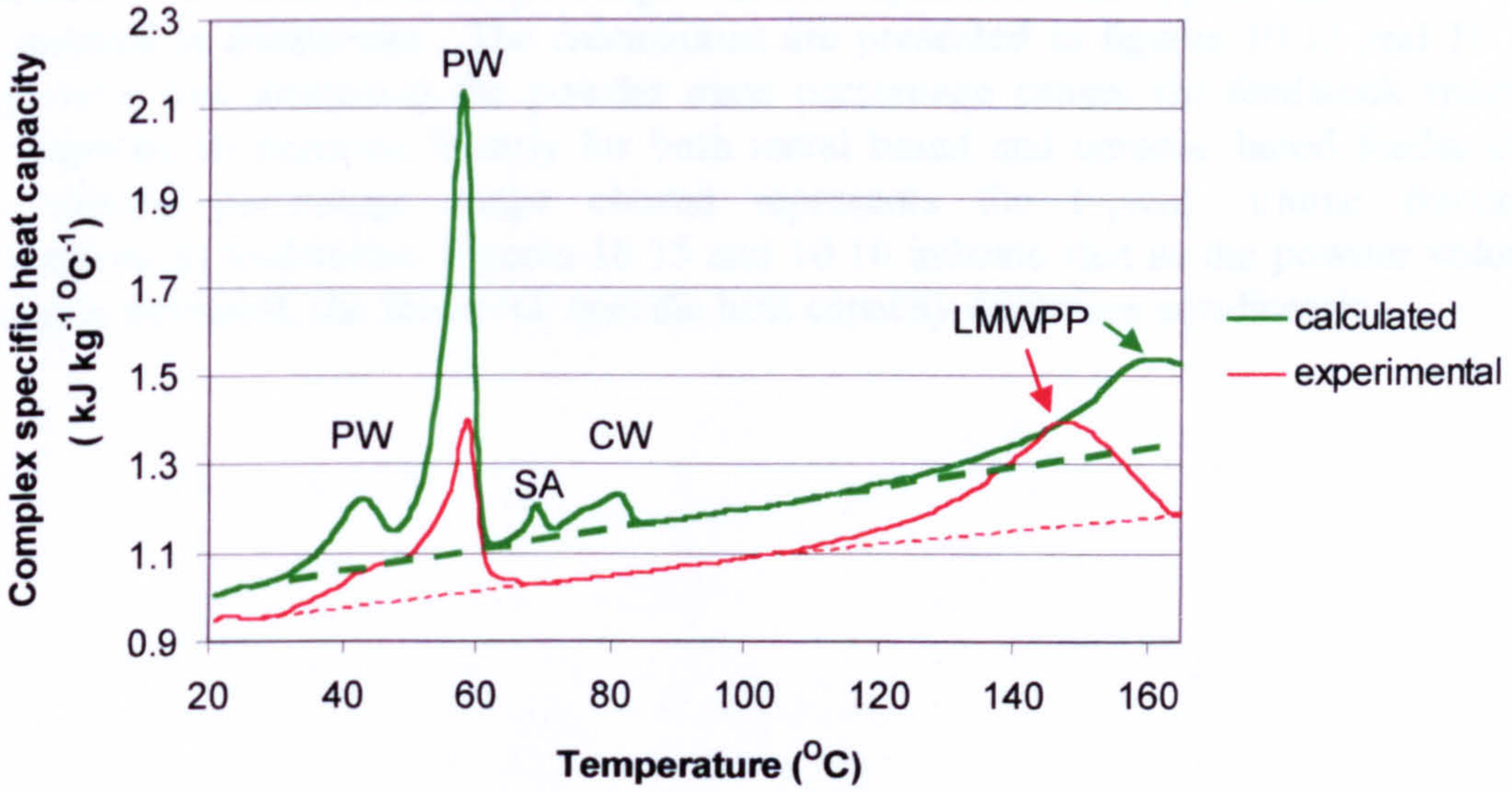

Figure 10.11 55% Alumina feedstock specific heat capacity vs temperature

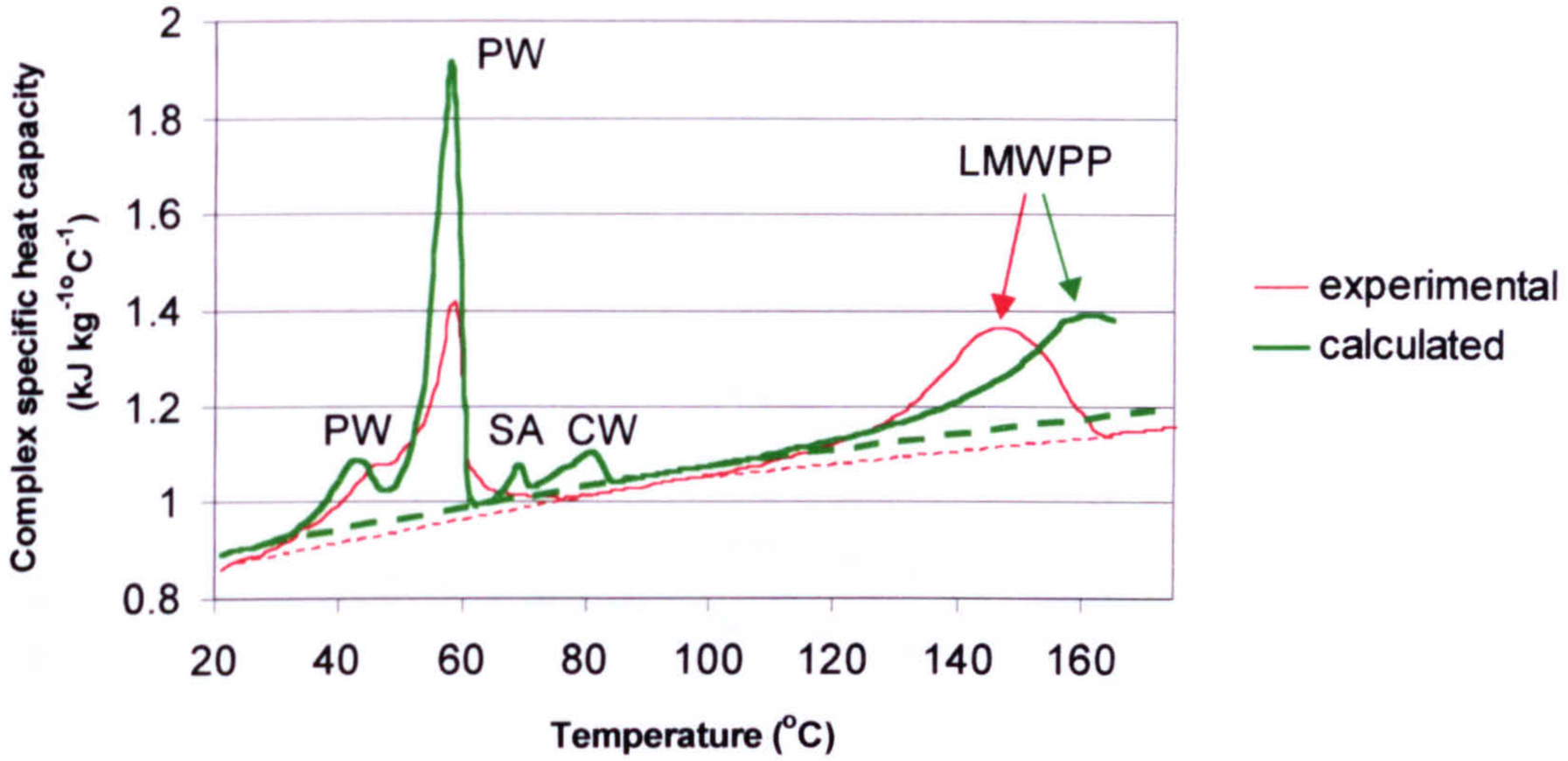

Figure 10.12 Zirconia toughened alumina feedstock specific heat capacity vs temperature

10.1.3 Effect of varying the powder loading on the feedstock specific heat capacity

Equation 6.1 was used to investigate the effect that varying either the powder mass percentage or the powder volume percentage had on the feedstock specific heat capacity at three different temperatures. This was done for a ceramic feedstock and a metal feedstock. The mass percentage range chosen represents the typical mass fractions encountered in feedstocks. The calculations are presented in figures 10.13 and 10.14. They show that increasing the powder mass percentage causes the feedstock specific heat capacity to decrease linearly for both metal based and ceramic based feedstocks. The volume percentage range chosen represents the typical volume fractions encountered in feedstocks. Figures 10.15 and 10.16 indicate that as the powder volume loading is increased, the feedstock specific heat capacity decreases non-linearly.

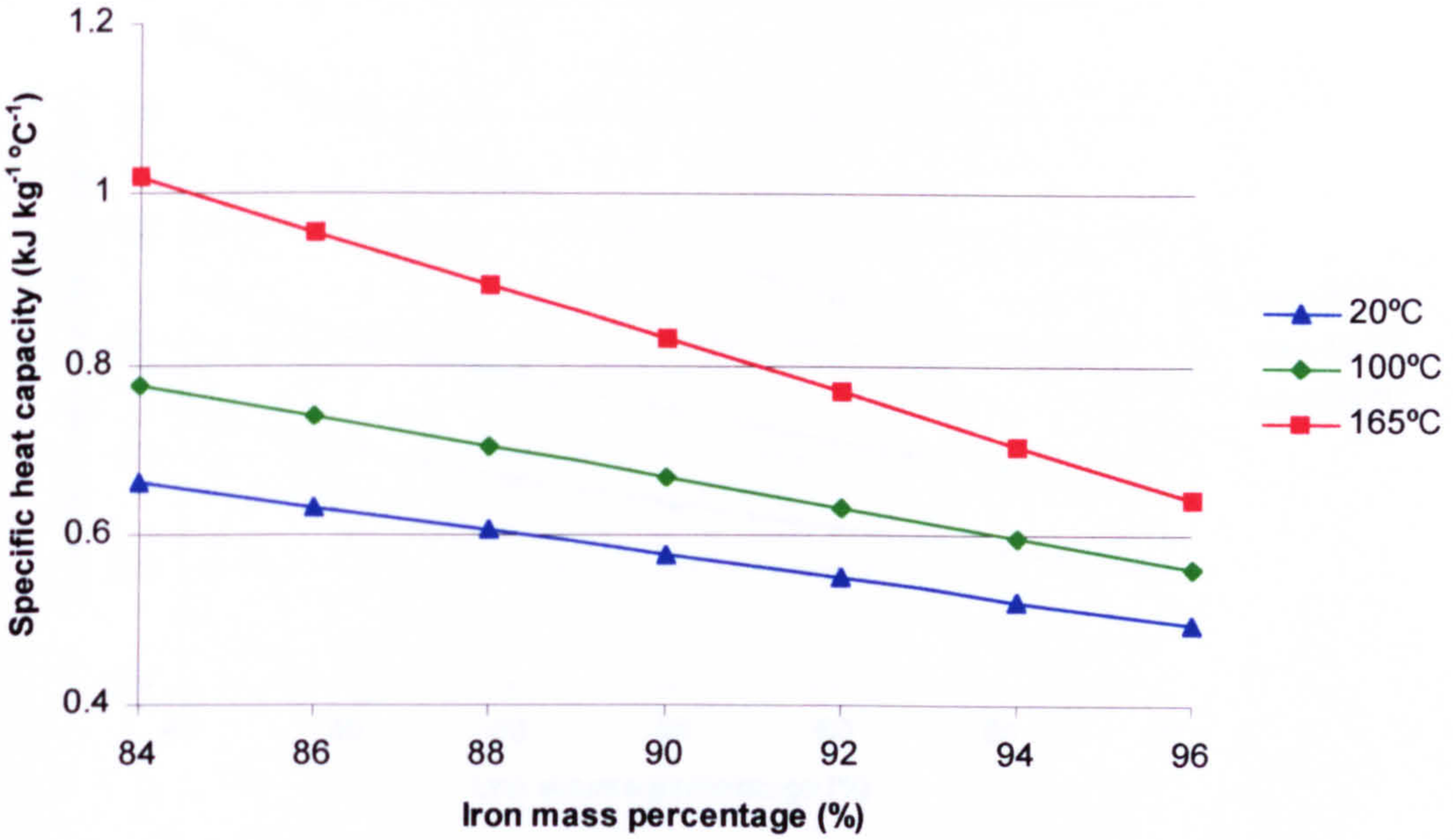

Figure 10.13 Effect of varying the powder mass loading on the specific heat capacity of a typical metal feedstock

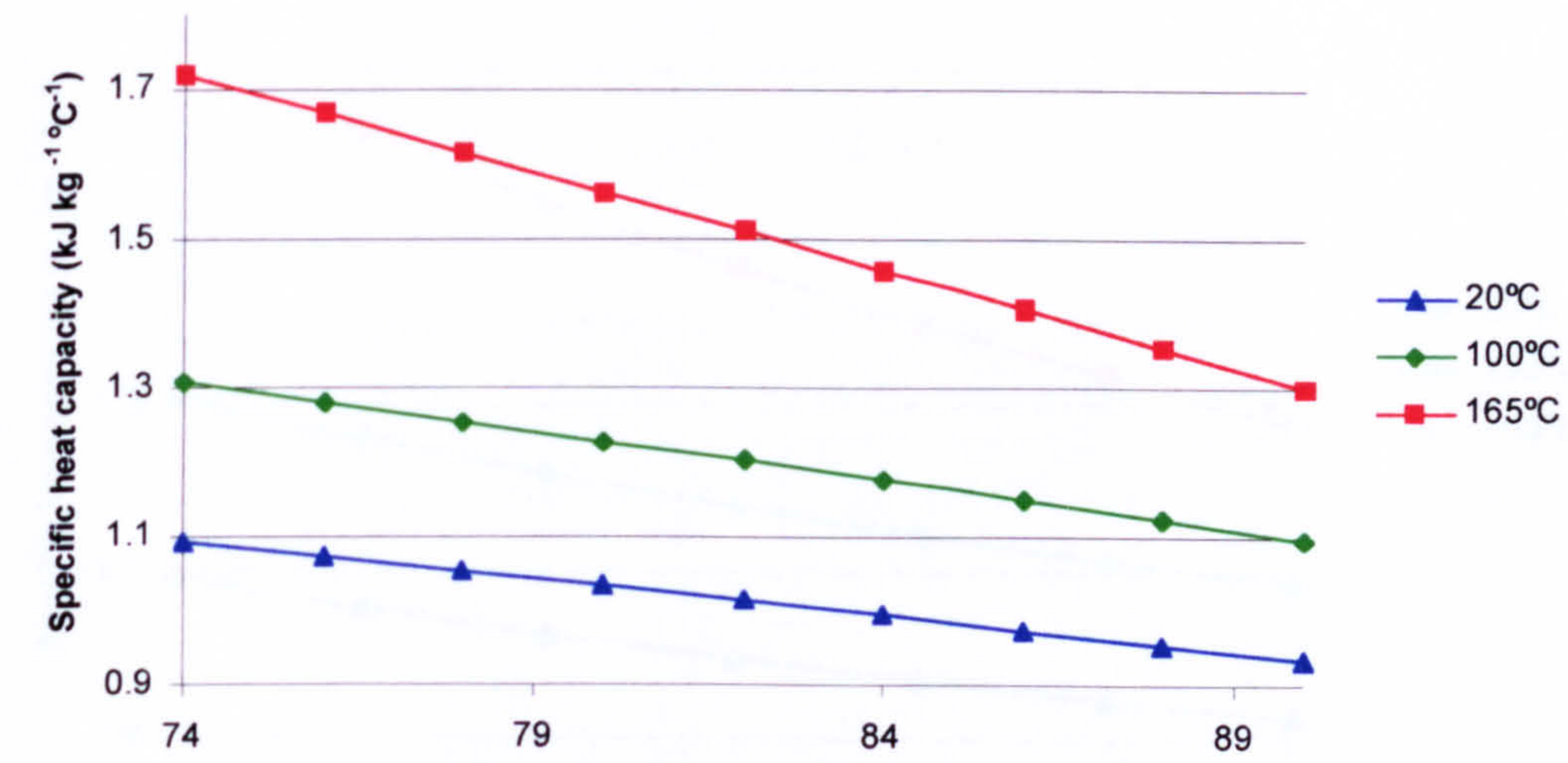

Figure 10.14 Effect of varying the powder mass loading on the specific heat capacity of a typical ceramic feedstock

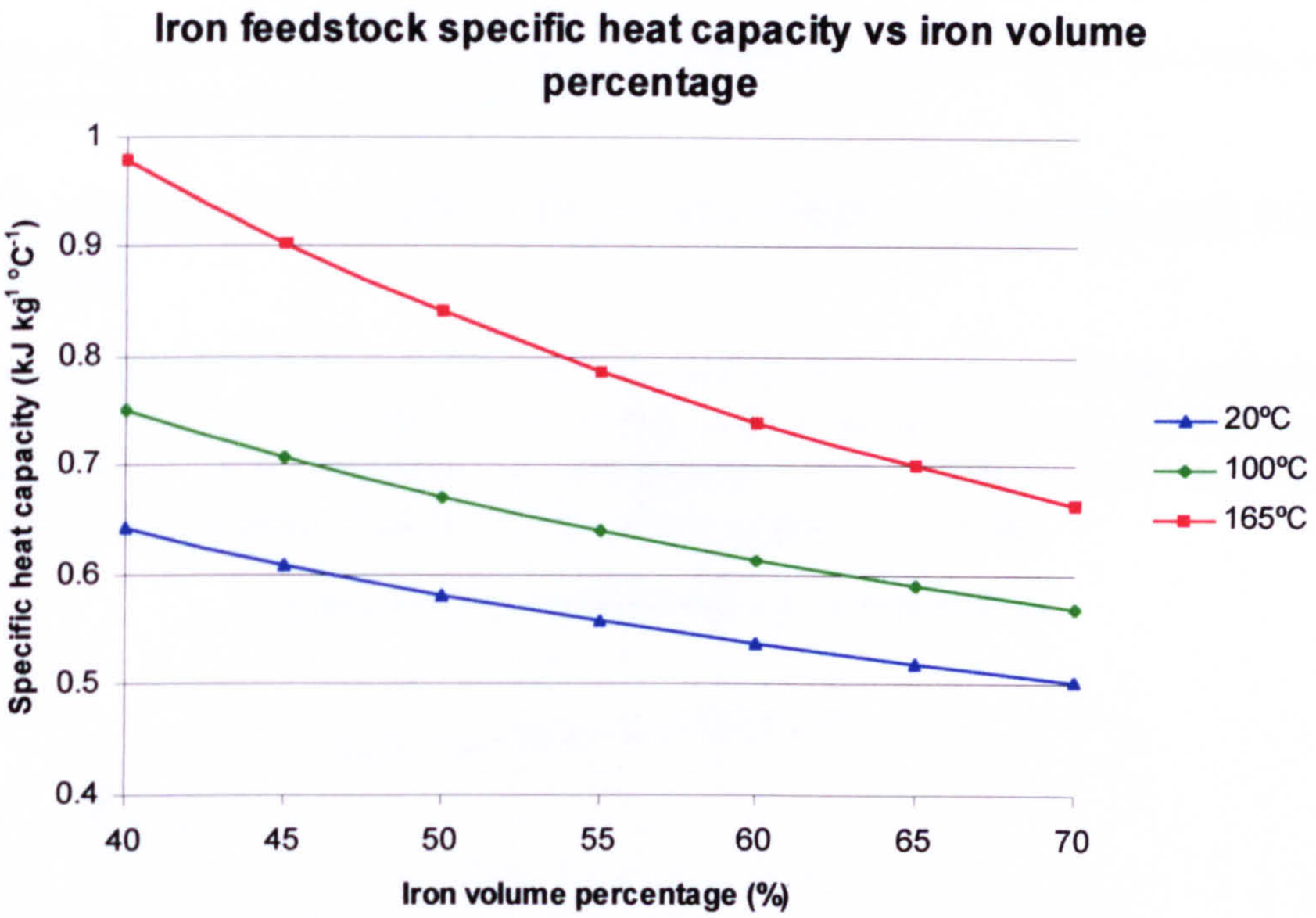

Figure 10.15 Effect of varying the powder volume loading on the specific heat capacity of a typical metal PIM feedstock

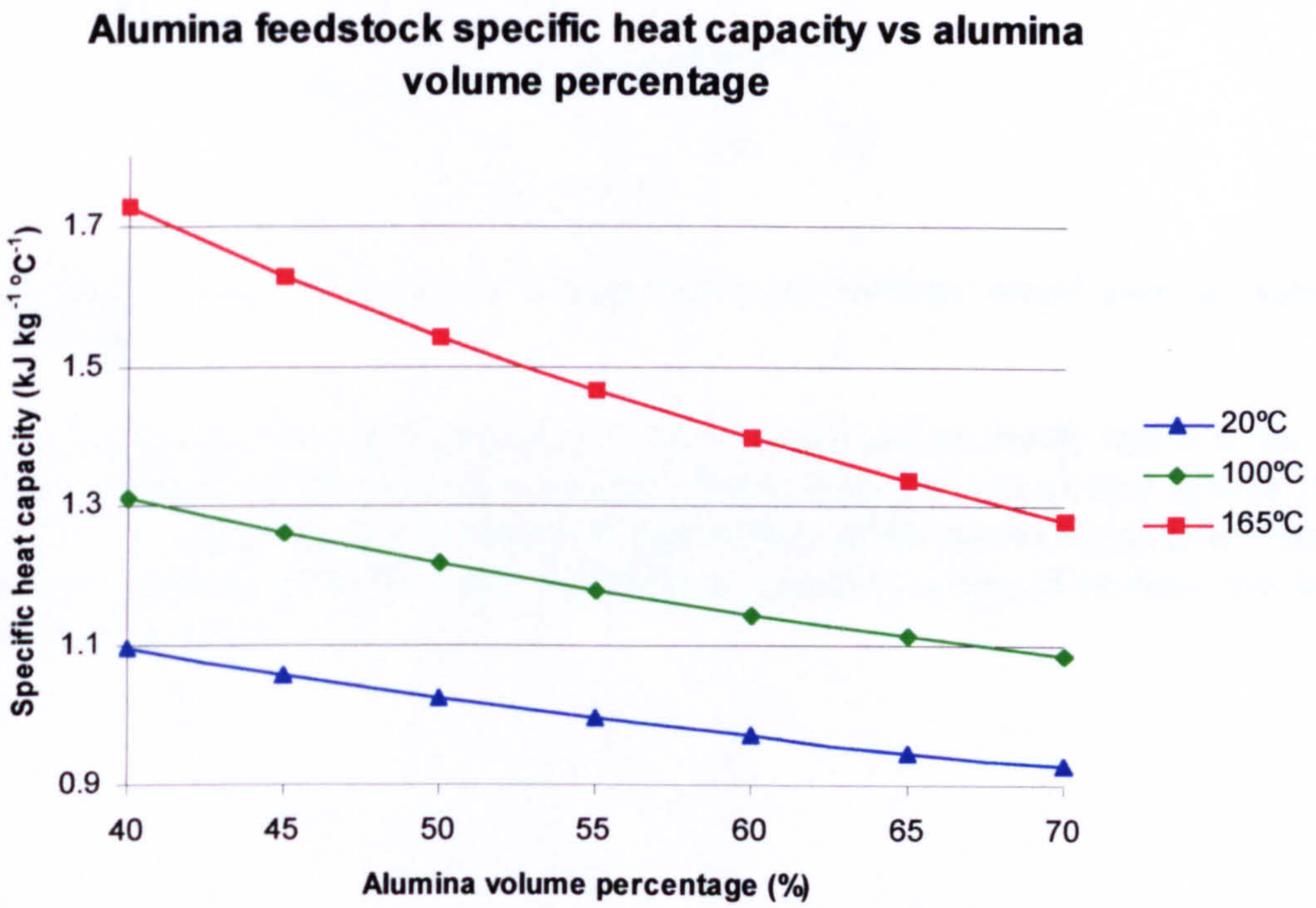

Figure 10.16 Effect of varying the powder volume loading on the specific heat capacity of a typical ceramic PIM feedstock

10.2 Pressure, volume and temperature (PVT)

This section presents the results of the experimental PVT work on the powders, binder components, binder system and feedstocks.

10.2.1 Calculated PVT behaviour for the binder components and powder components

The results of the calculations for the powder system components are presented in figures 10.17 and 10.18. Figure 10.17 indicates that the metal based powders expand uniformly as a linear function of temperature. The powders have very similar expansivities but different densities, hence different specific volumes.

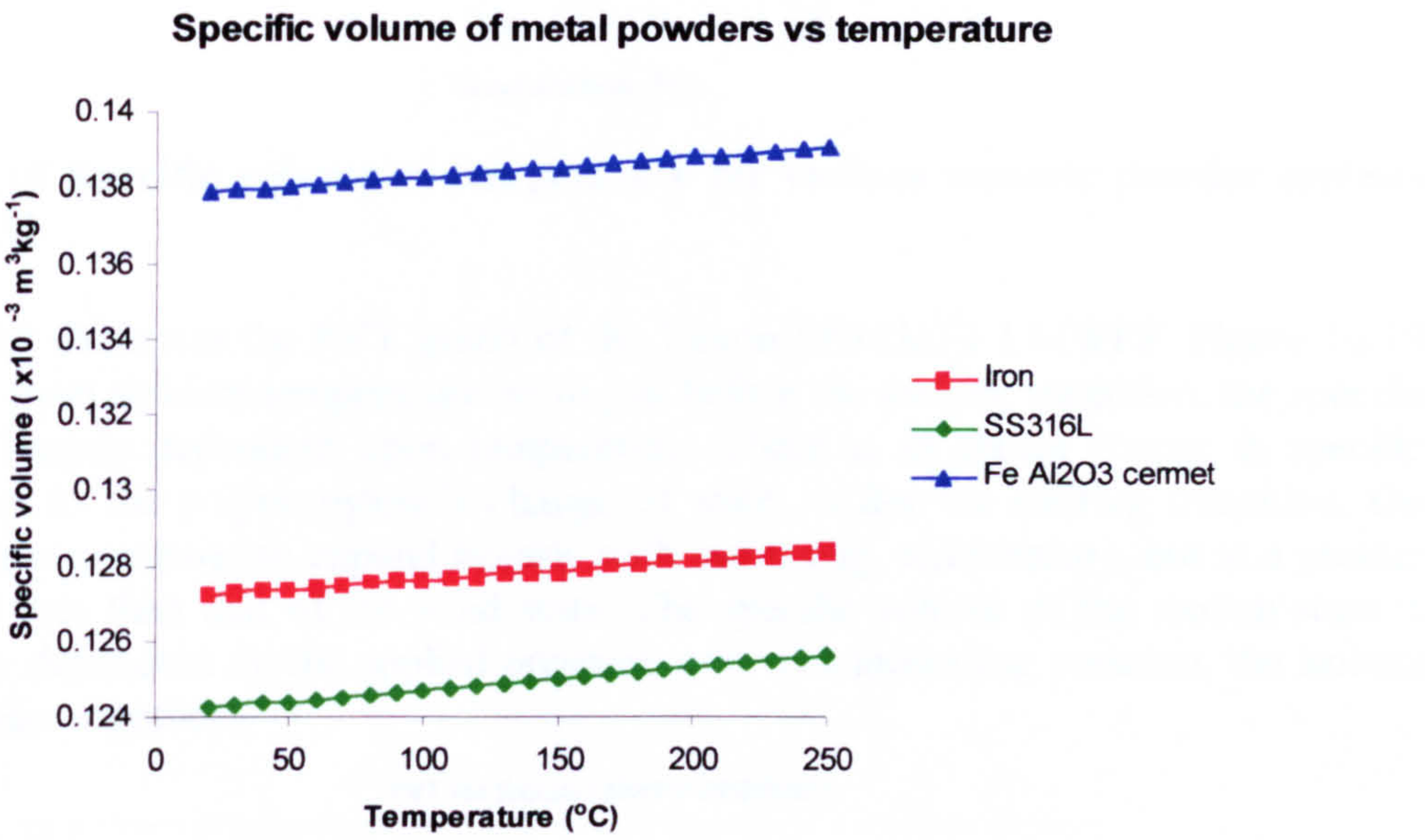

Figure 10.17 Specific volume vs temperature for various metal powder systems used in PIM

Figure 10.18 shows that the expansivity of the ceramics are nominally identical and that they have different specific volumes, hence different densities. Comparing figures 10.17 and 10.18, it is apparent that the thermal expansivities of the metals are greater than the thermal expansivities of the ceramics and that the specific volumes of ceramics are lower than those of metals.

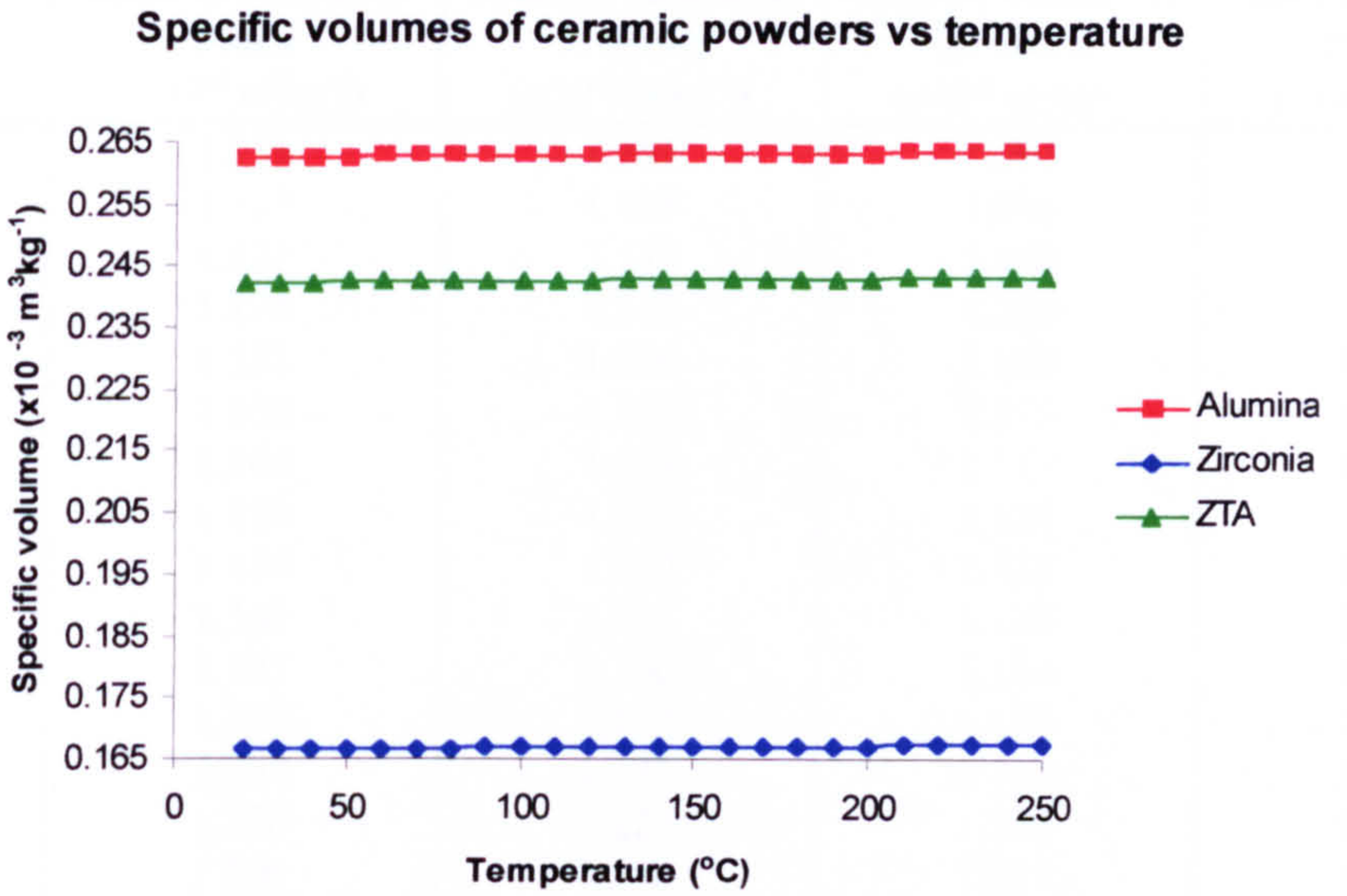

Figure 10.18 Specific volume vs temperature for various ceramic powder systems used in PIM

Figure 10.19 illustrates the PVT graph of the Exxon PP3536F1 LMWPP. Figure 10.19 shows that from ambient temperature up to just before the melting transition, the specific volume is linearly dependent upon temperature. There is an abrupt change in specific volume, due to the polypropylene's change of state. After the melting transition, the polypropylene continues to expand linearly with increasing temperature, but at a greater expansivity rate than that of the solid state. The specific volume of the molten state is non-linearly dependent on the applied pressure, and with increasing pressure, the isobars become closer together.

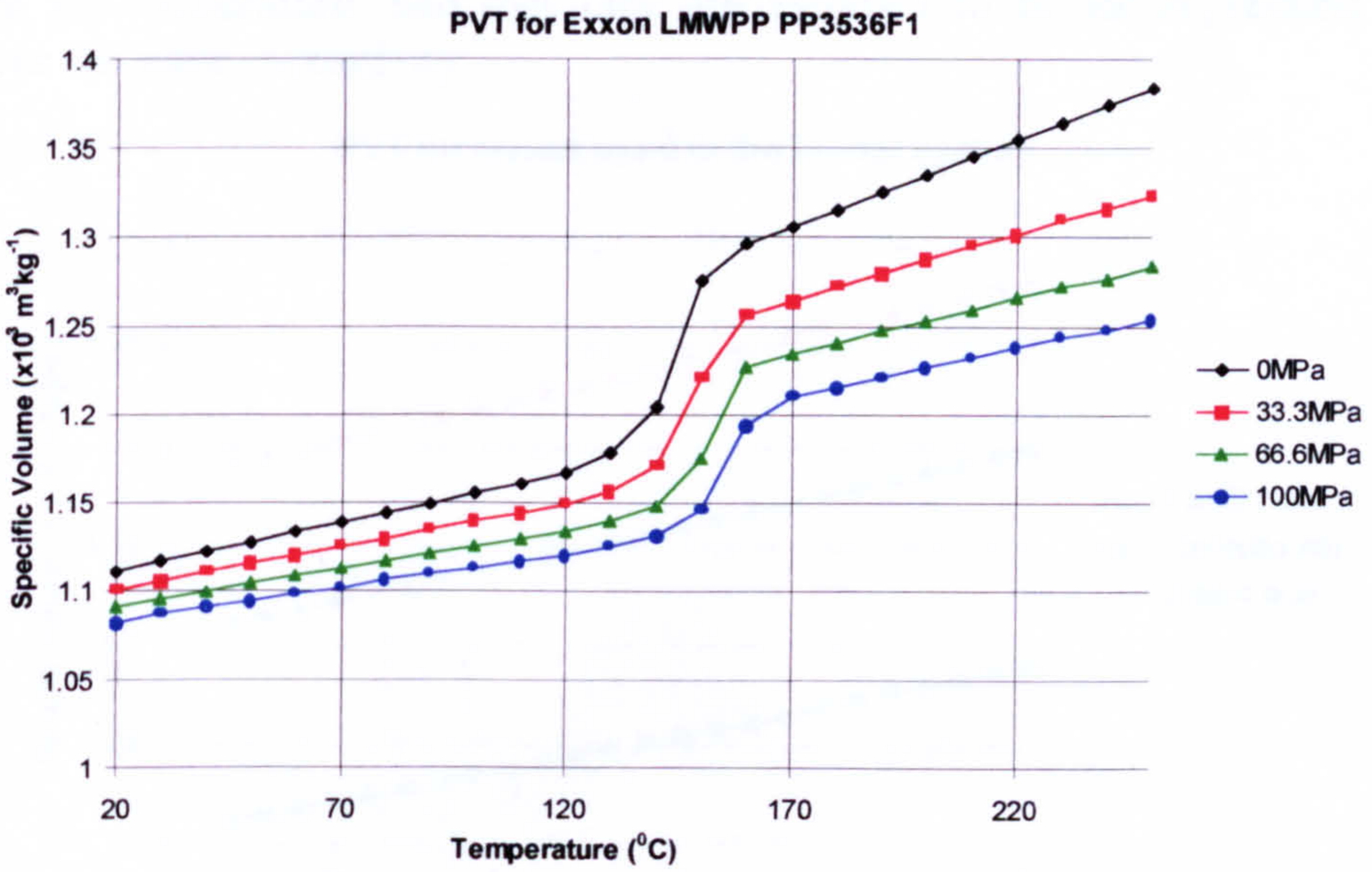

Figure 10.19 PVT graph for the Exxon PP3536F1 LMWPP with scaling factor applied

The numerical PVT data for the Exxon PP3536F1 LMWPP is presented in table 10.2.

Temperature (°C)	Specific volume at 0MPa ($x10^{-3}$ m^3kg^{-1})	Specific volume at 33.3MPa ($x10^{-3}$ m^3kg^{-1})	Specific volume at 66.6MPa ($x10^{-3}$ m^3kg^{-1})	Specific volume at 100MPa ($x10^{-3}$ m^3kg^{-1})
20	1.111	1.101	1.091	1.082
30	1.117	1.106	1.096	1.087
40	1.122	1.111	1.100	1.091
50	1.128	1.116	1.105	1.094
60	1.133	1.120	1.109	1.099
70	1.138	1.125	1.113	1.102
80	1.144	1.129	1.117	1.107
90	1.150	1.135	1.121	1.110
100	1.155	1.139	1.126	1.113
110	1.160	1.144	1.130	1.117
120	1.167	1.150	1.134	1.121
130	1.178	1.157	1.139	1.125
140	1.204	1.171	1.149	1.132
150	1.276	1.221	1.175	1.146
160	1.296	1.256	1.227	1.194
170	1.305	1.264	1.234	1.210
180	1.315	1.272	1.240	1.216
190	1.325	1.280	1.247	1.221
200	1.335	1.288	1.253	1.227
210	1.345	1.295	1.259	1.233
220	1.354	1.302	1.266	1.238
230	1.364	1.310	1.272	1.244
240	1.374	1.317	1.277	1.248
250	1.383	1.323	1.284	1.254

Table 10.2 Specific volume of Exxon PP3536F1 LMWPP for temperature and pressure

Figure 10.20 illustrates that the specific volumes of the binder waxes are linearly dependent on temperature, and that they are assumed to be incompressible. All the waxes have the same expansivity.

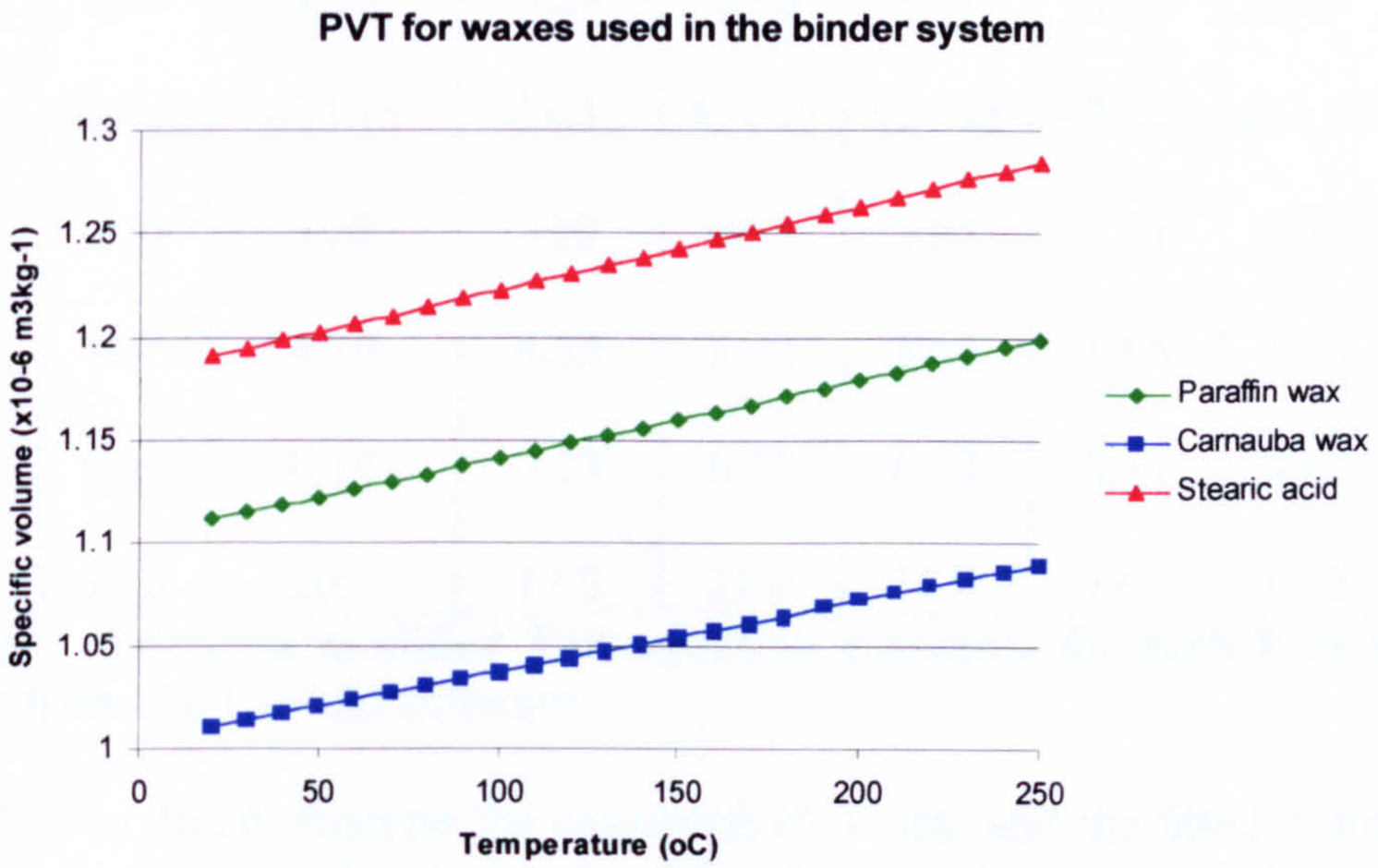

Figure 10.20 Specific volume vs temperature for three binder components

10.2.2 Calculation of feedstock PVT behaviour and comparison of the calculated PVT data to the 2-domain Tait models of PVT data

Equation 6.3 was used to calculate the resultant PVT data for the PCM feedstocks. This data was sent to C-Mold for determination of the 13 Tait model constants for subsequent use in the Tait model (equations 4.48 and 4.49). The 13 Tait equation parameters were input into the Tait equation to obtain the fitted lines. The Tait model data was then compared with the calculated PVT data. The Tait parameters for the model powder feedstocks are tabulated in table 10.3.

	Iron	SS316LMA	SS316L	Cermet	50% Alumina	55% Alumina	55% ZTA	Exxon LMWPP
B1s $x10^{-3}$ (m^3kg^{-1})	0.202	0.198	0.198	0.217	0.437	0.410	0.379	1.18
B2s $x10^{-9}$ ($m^3kg^{-1}\,K^{-1}$)	38.0	38.1	38.2	40.6	94.8	81.2	73.7	551.0
B3s $x10^{+9}$ (Pa)	0.763	0.792	0.763	0.761	0.606	0.674	0.687	0.161
B4s $x10^{-3}$ (K^{-1})	4.57	4.15	4.58	4.57	4.61	4.60	4.59	4.70
B1m $x10^{-3}$ (m^3kg^{-1})	0.206	0.202	0.202	0.222	0.449	0.420	0.388	1.29
B2m $x10^{-9}$ ($m^3kg^{-1}\,K^{-1}$)	57.2	59.7	55.3	60.6	142.0	121.0	110.0	978.0
B3m $x10^{+9}$ (Pa)	0.411	0.453	0.424	0.407	0.334	0.374	0.382	0.0866
B4m $x10^{-3}$ (K^{-1})	3.56	4.90	3.24	3.32	3.37	3.35	3.32	4.82
B5 (K)	424.15	423.15	424.15	424.15	424.15	424.15	424.65	422.15
B6 $x10^{-9}$ ($K\,Pa^{-1}$)	110	100	110	92.5	110	110	105	118
B7 $x10^{-6}$ (m^3kg^{-1})	4.65	4.79	4.55	5.02	12.5	10.6	10.3	95.9
B8 (K^{-1})	0.13	0.14	0.13	0.13	0.13	0.13	0.13	0.15
B9 $x10^{-9}$ (Pa^{-1})	17.0	20.5	17.0	17.0	17.0	17.0	17.0	19.8

Table 10.3 2-domain modified Tait equation constants for each PIM feedstock calculated from the C-Mold software

Figures 10.21 to 10.26 illustrate the calculated PVT data and the fitted 2 domain Tait curves for the PCM model feedstocks. The data points represent the data-points obtained from equation 6.3. The solid lines represent the data produced from the Tait model using the constants listed in table 10.3. There are many similarities in figures

10.21 to 10.26. They all illustrate that the feedstock's specific volume is linearly dependent on the temperature for both the solid state and the liquid state. The feedstock's specific volume is non-linearly dependent on the pressure for both the solid and molten state, and the amount of volume change at a constant pressure increased with increasing temperature. There is an abrupt volume change between the solid and the molten states, which is due to the LMWPP's change of state. Figures 10.21 to 10.26 indicate good agreement between the Tait model generated fitted plots and the data-points produced by equation 6.3.

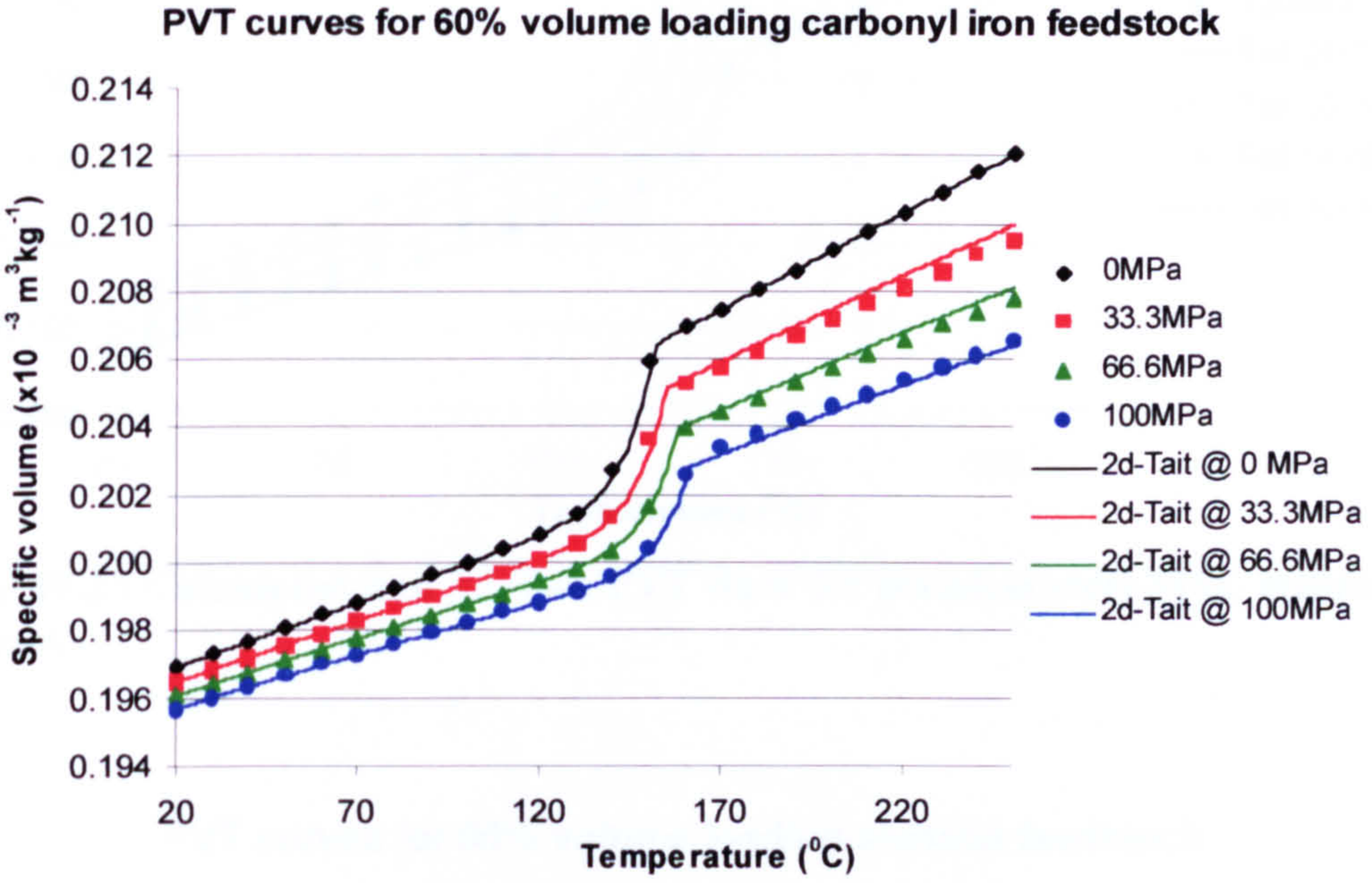

Figure 10.21 Calculated PVT data and 2d-Tait generated data for carbonyl iron feedstock

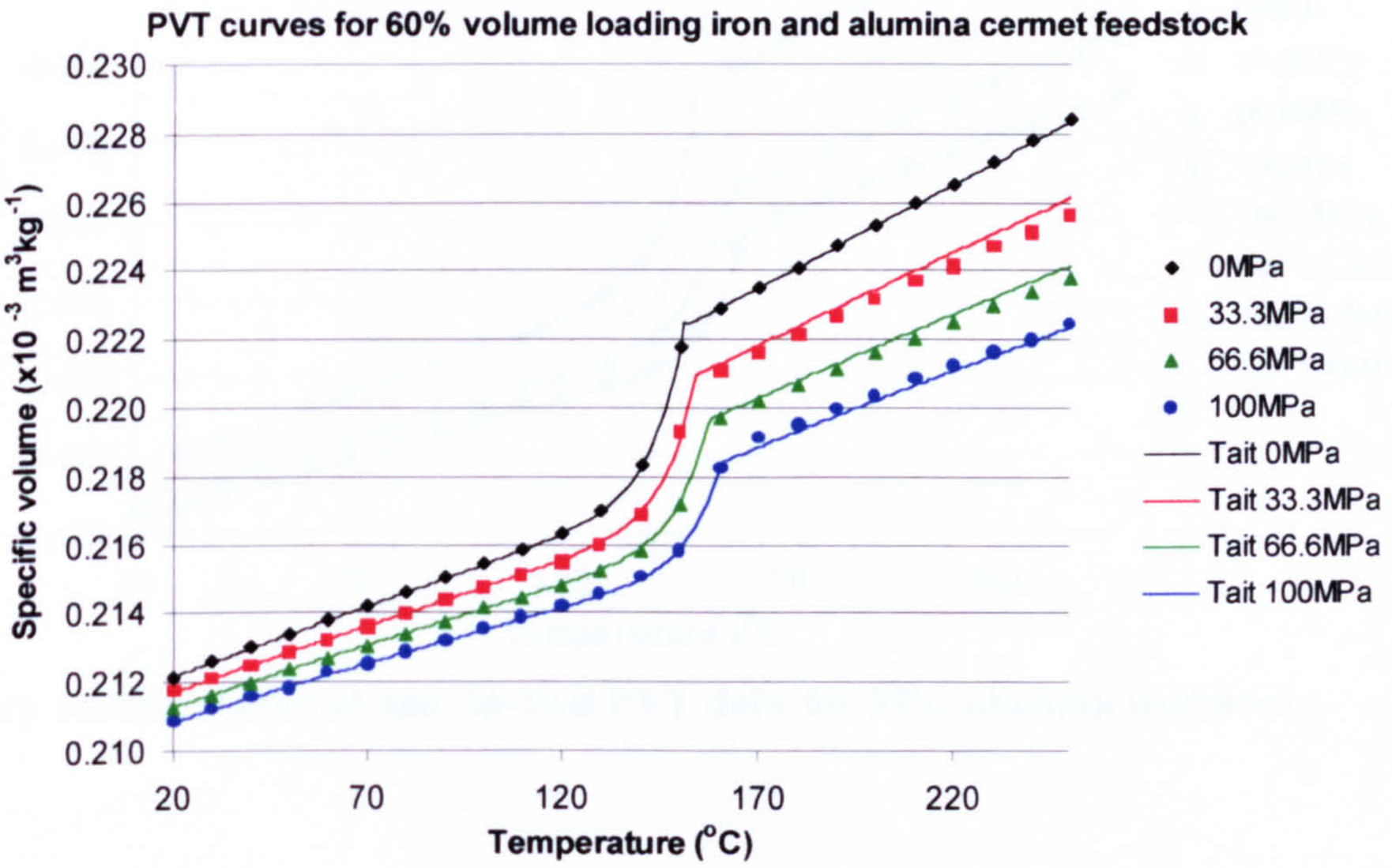

Figure 10.22 Calculated and 2d-Tait PVT data for iron-alumina cermet feedstock

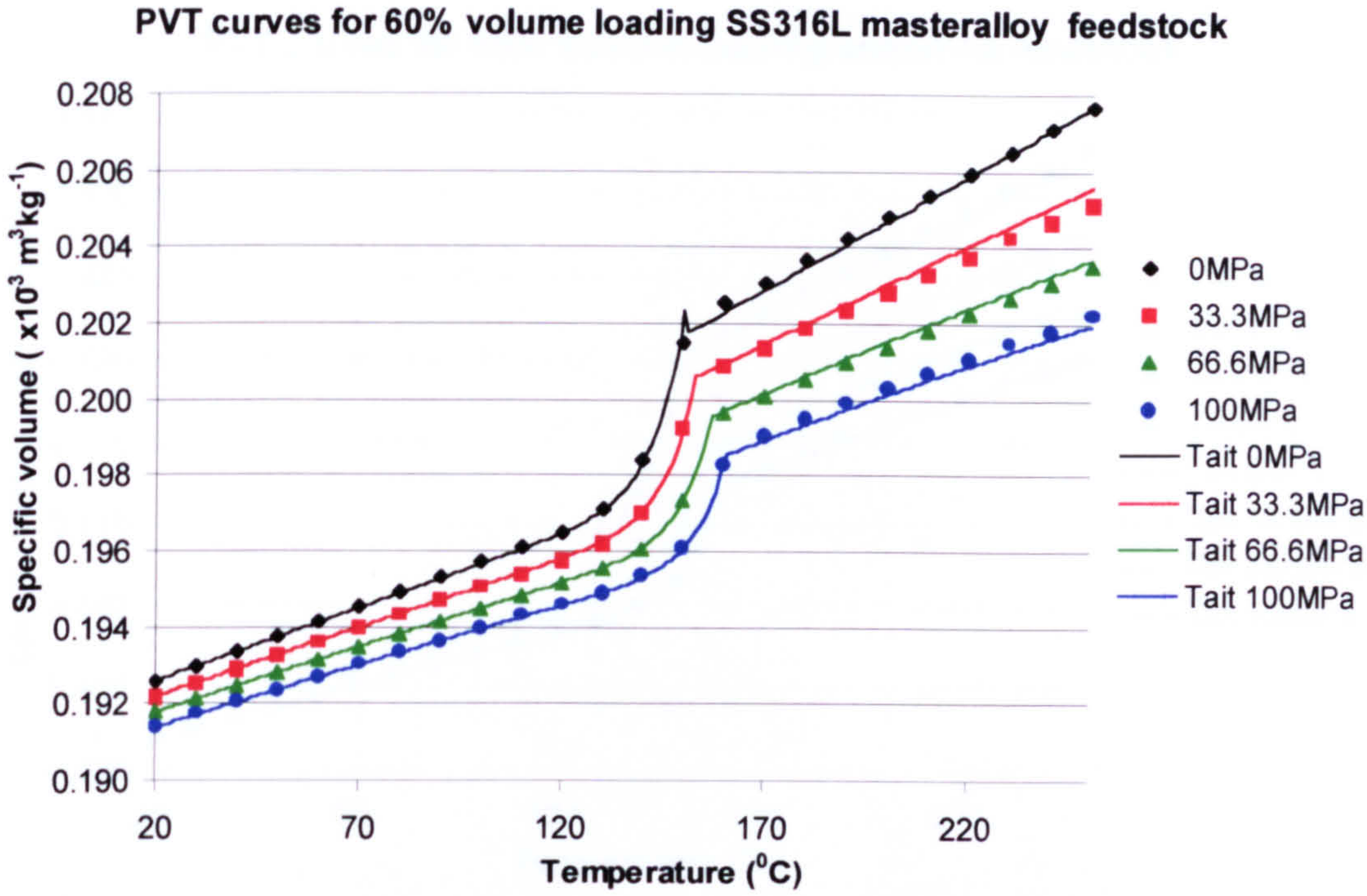

Figure 10.23 Calculated and 2d-Tait PVT data for stainless steel 316L masteralloy feedstock

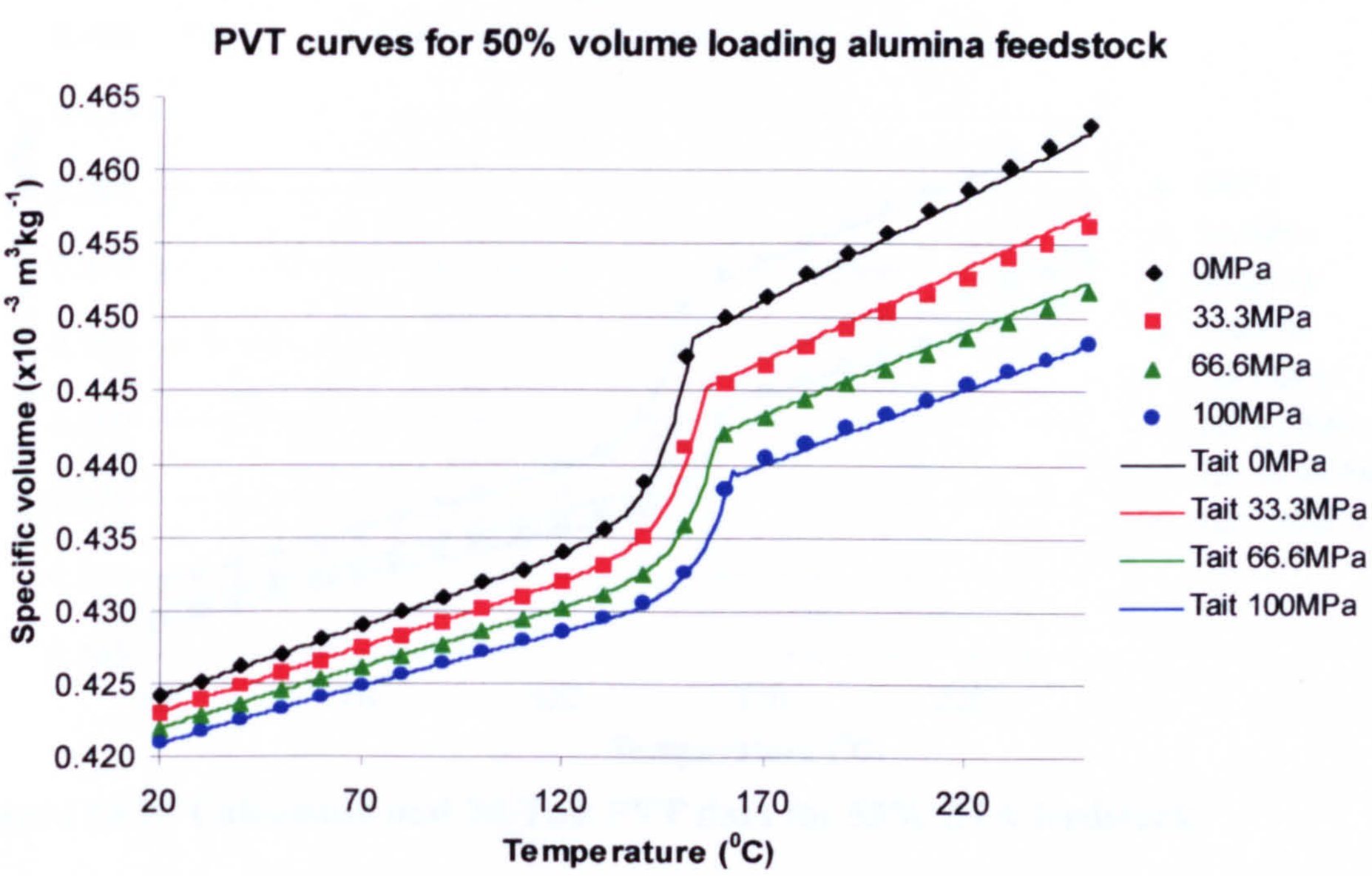

Figure 10.24 Calculated and 2d-Tait PVT data for 50% alumina feedstock

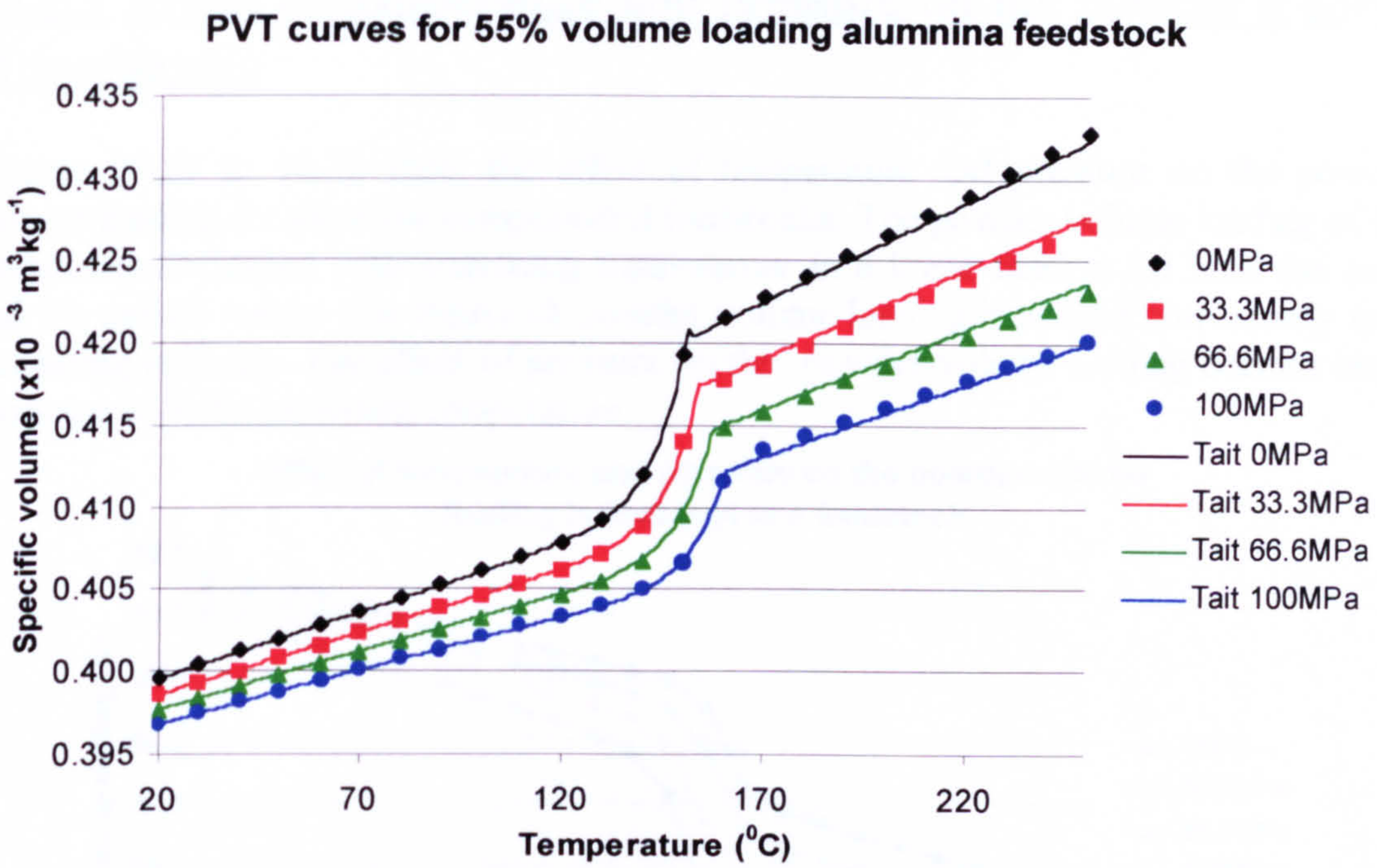

Figure 10.25 Calculated and 2d-Tait PVT data for 55% alumina feedstock

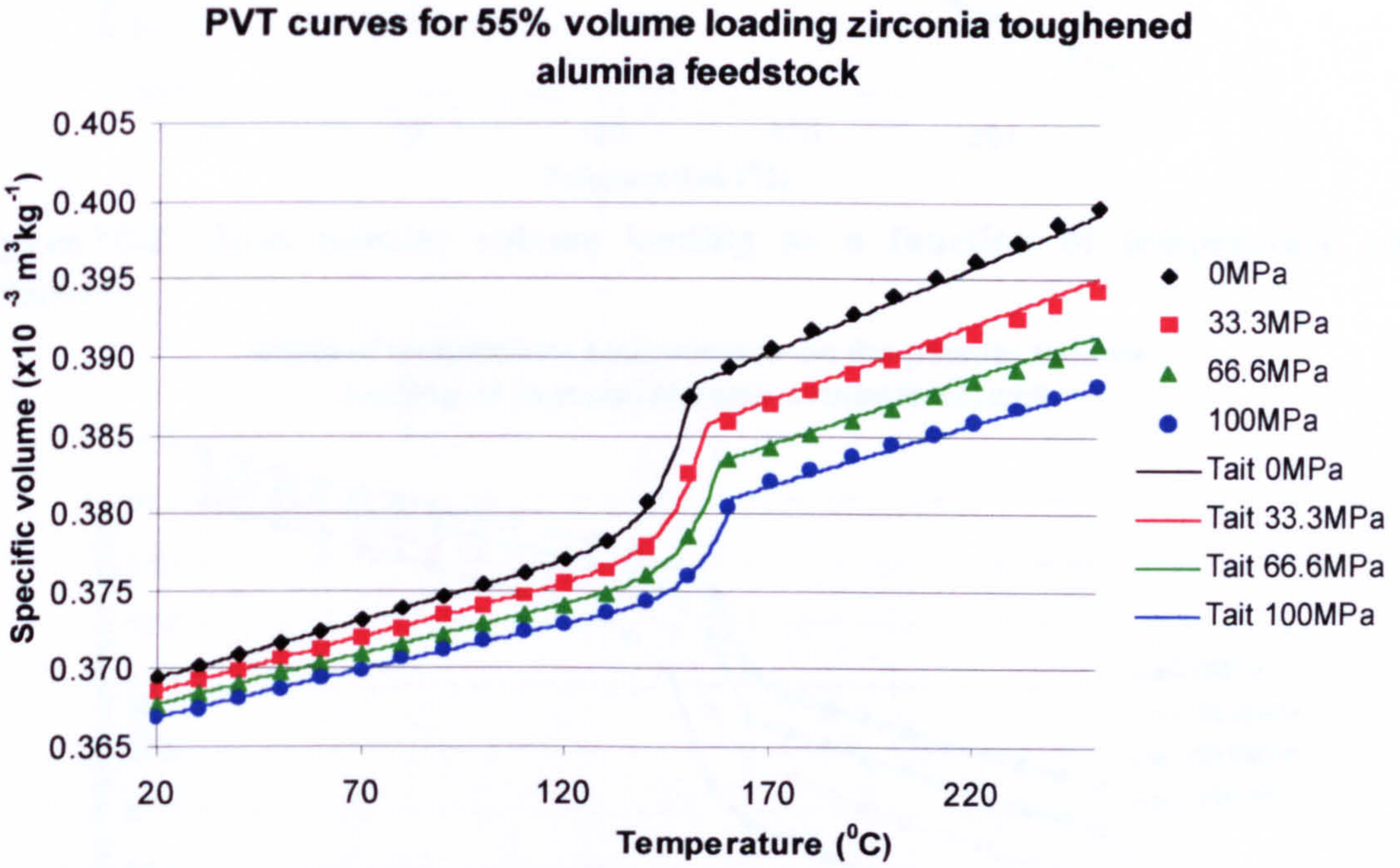

Figure 10.26 Calculated and 2d-Tait PVT data for 55% ZTA feedstock

Figures 10.21 to 10.26 shows good agreement between the fitted 2 domain Tait model data and the calculated PVT data. This offers evidence for the applicability of the 2 domain Tait model for modelling the PVT data.

10.2.3 Effect of temperature and pressure on the powder loading of feedstocks

Figures 10.27 to 10.32 show the effect of temperature and pressure on the powder volume loading for all of the compounded feedstocks. The powder volume loading of the feedstocks decreased with increasing temperature in a linear fashion for both the solid and the molten states. The feedstock powder volume loading increased non-linearly with increasing pressure. The effect of pressure on the powder volume loading became more pronounced with increasing temperature.

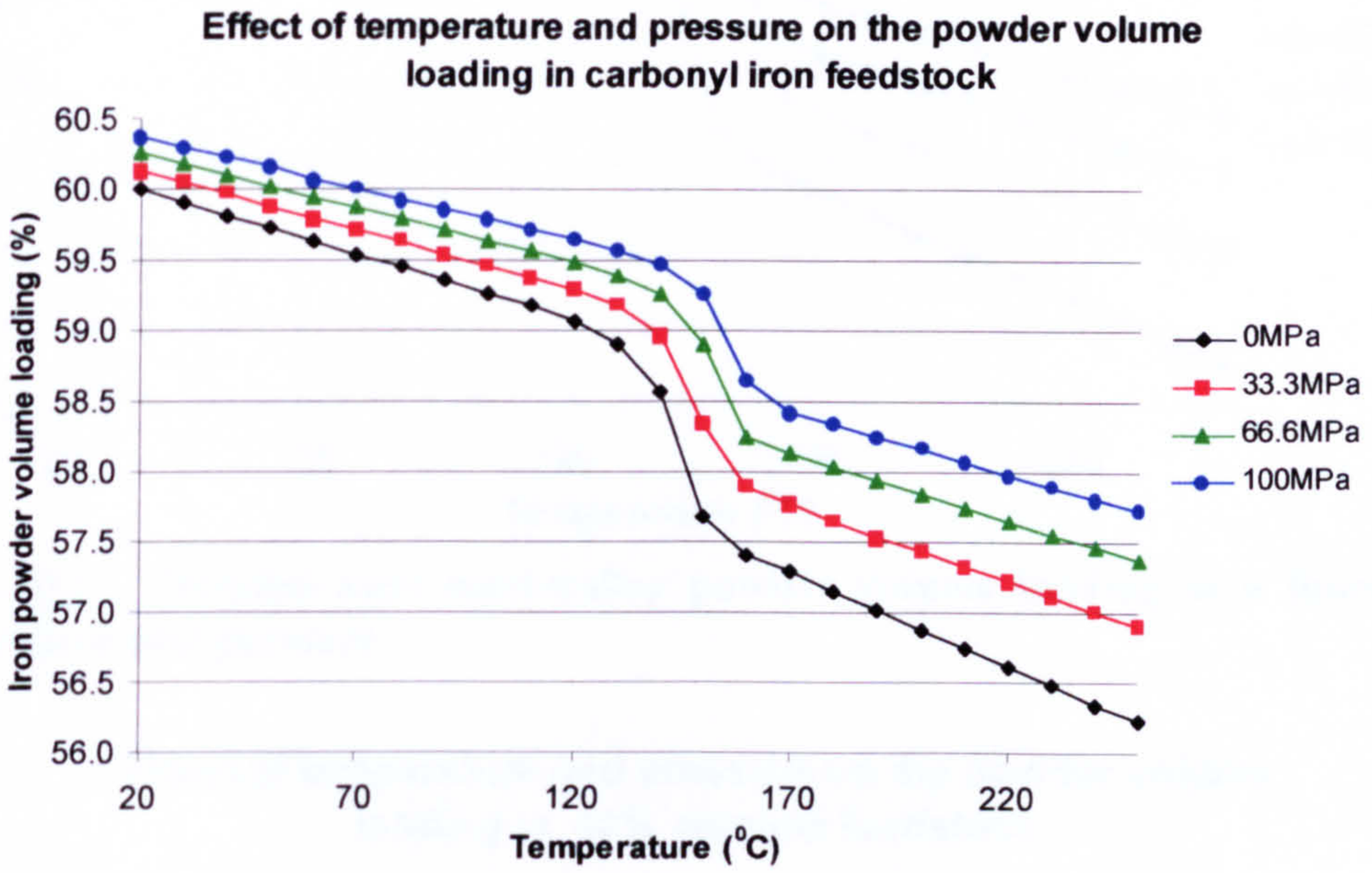

Figure 10.27 Iron powder volume loading as a function of temperature and pressure

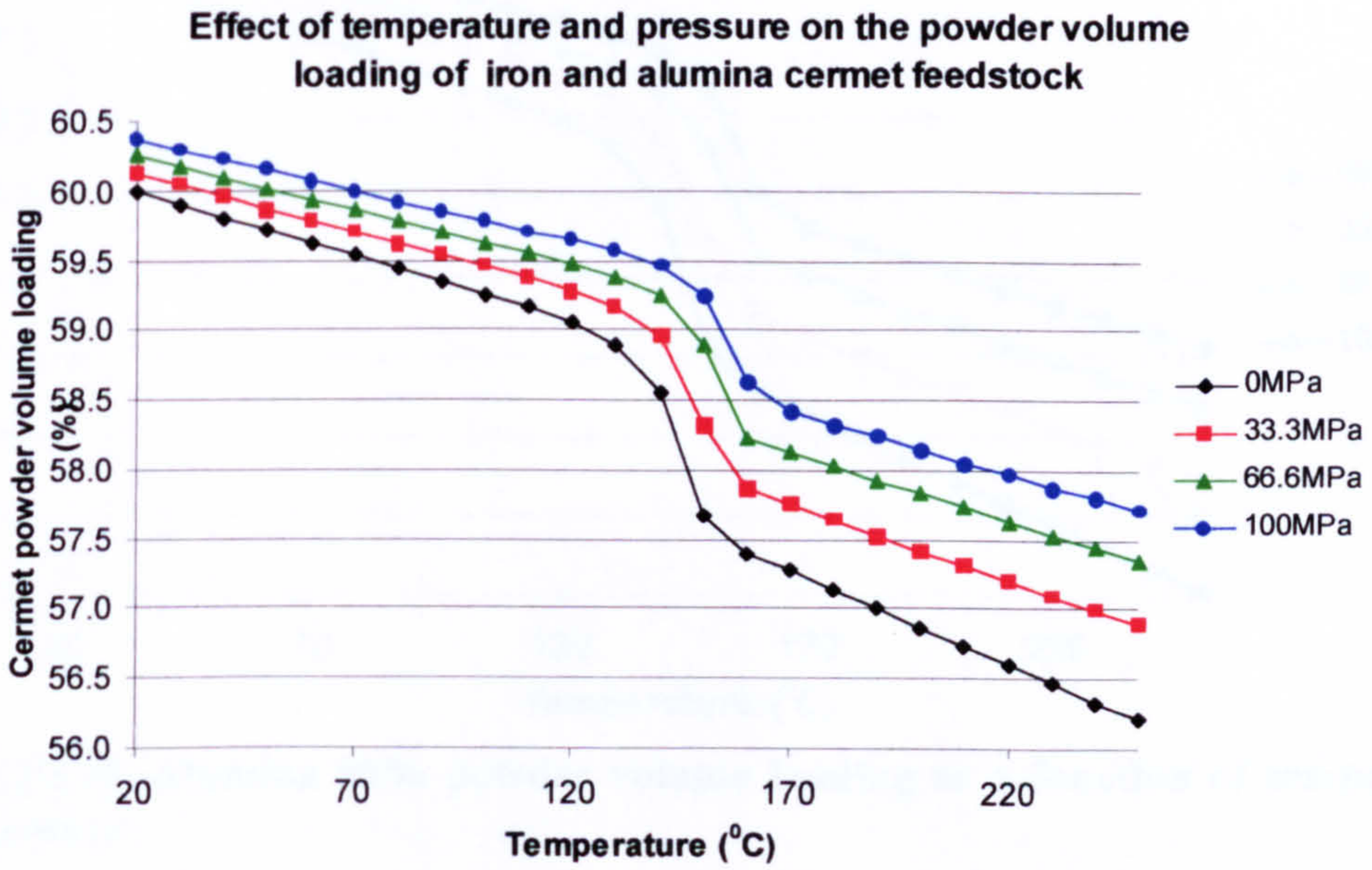

Figure 10.28 Cermet powder volume loading as a function of temperature and pressure

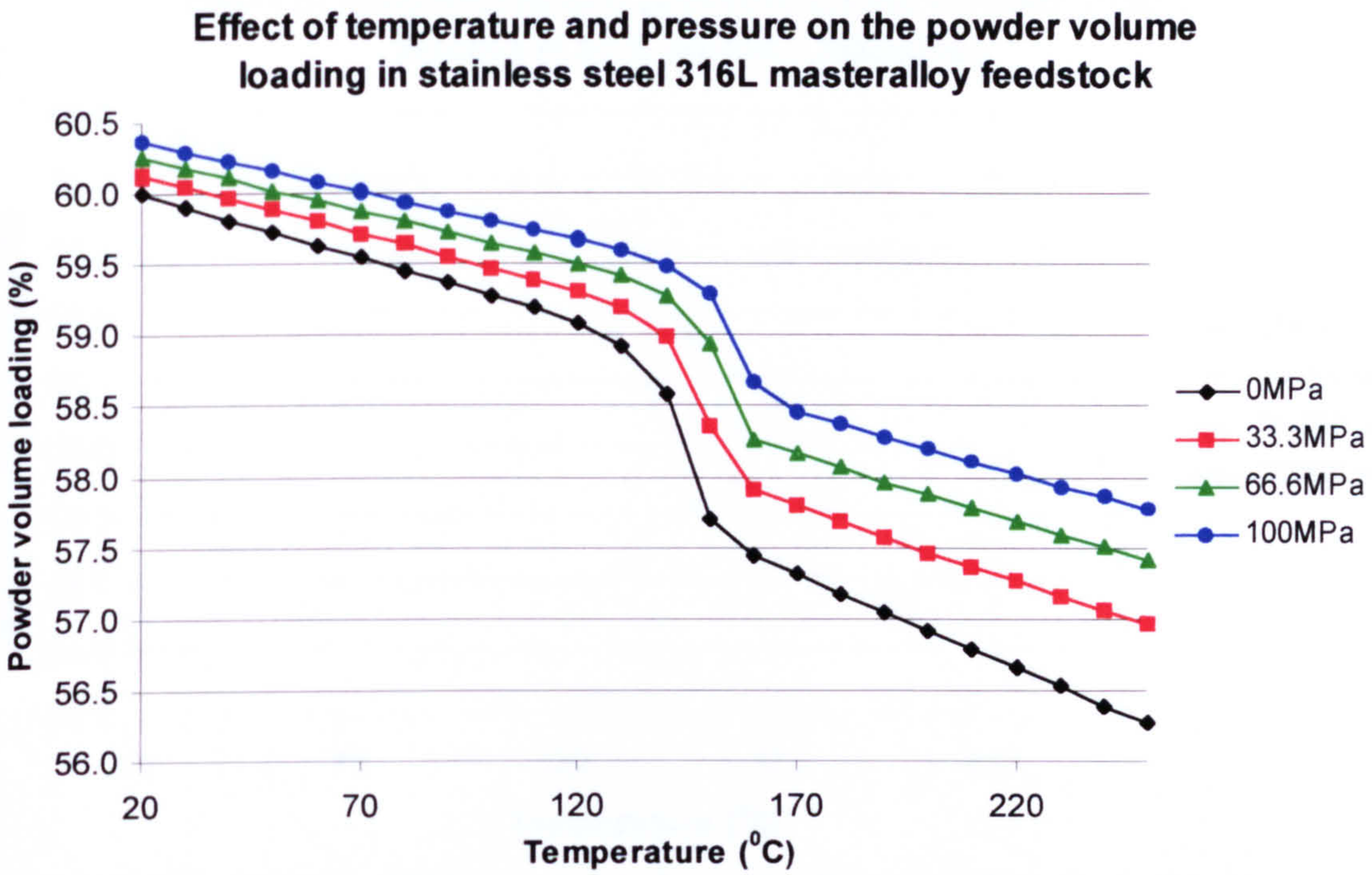

Figure 10.29 Stainless steel masteralloy powder volume loading as a function of temperature and pressure

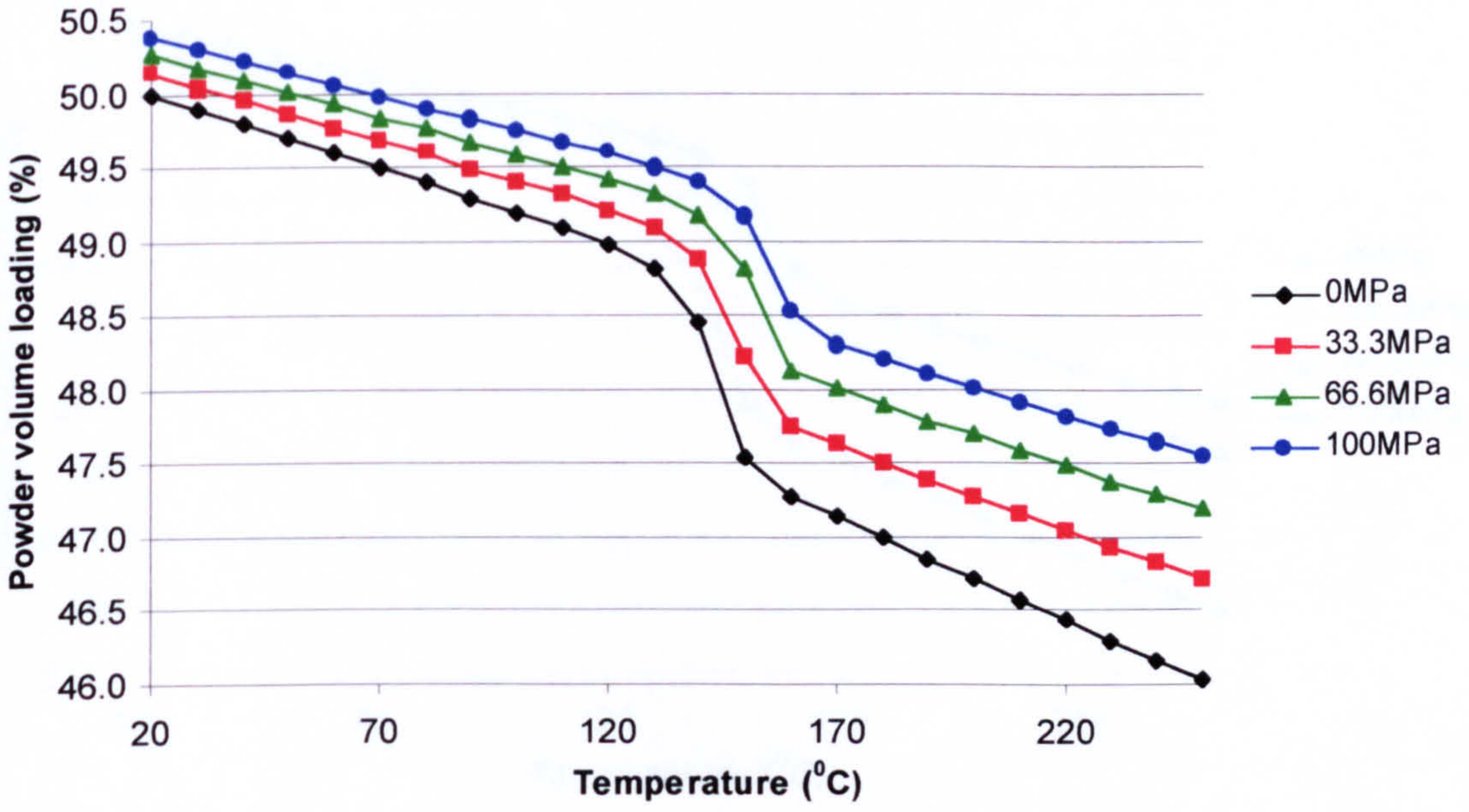

Figure 10.30 Alumina 50% powder volume loading as a function of temperature and pressure

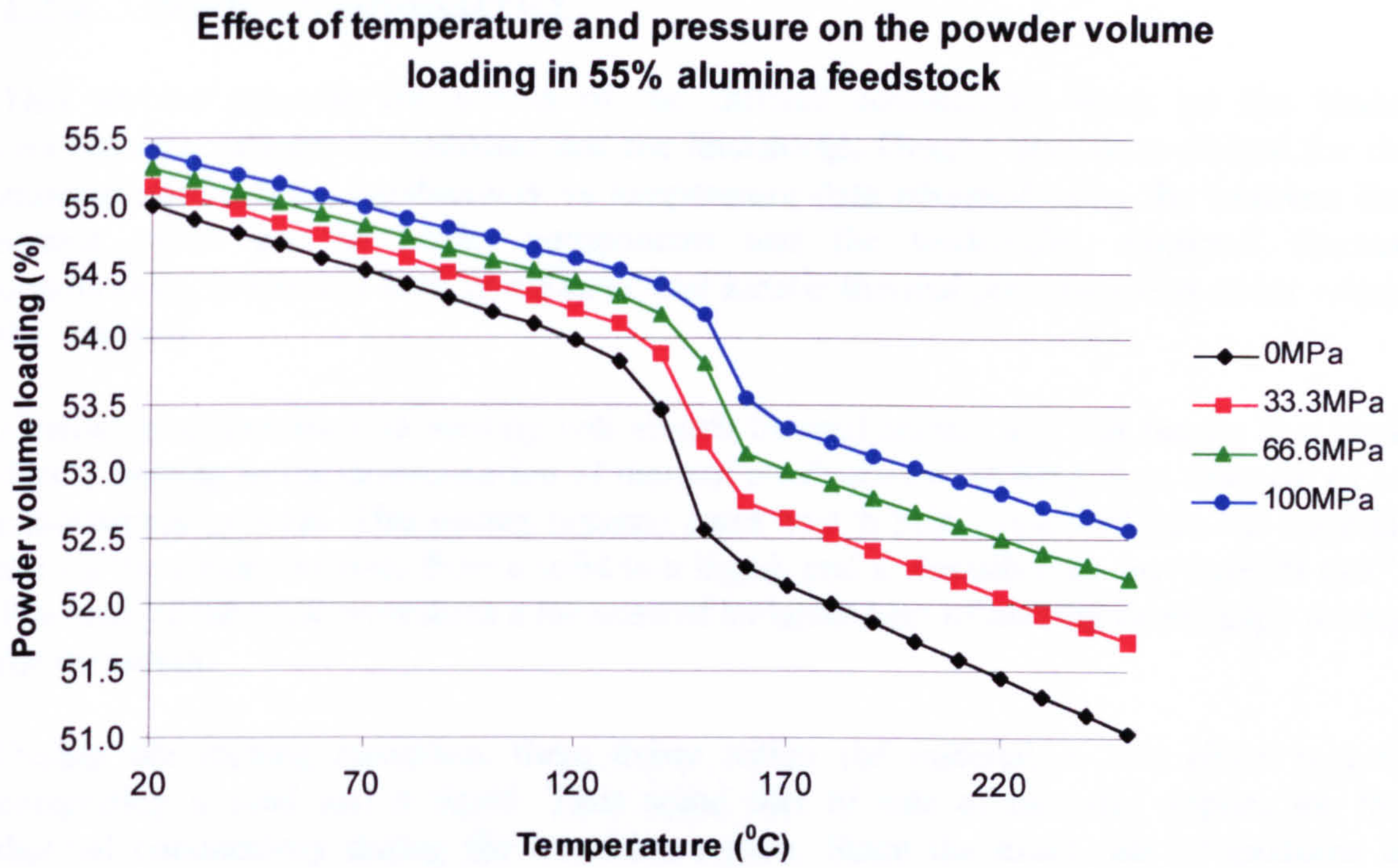

Figure 10.31 Alumina 55% powder volume loading as a function of temperature and pressure

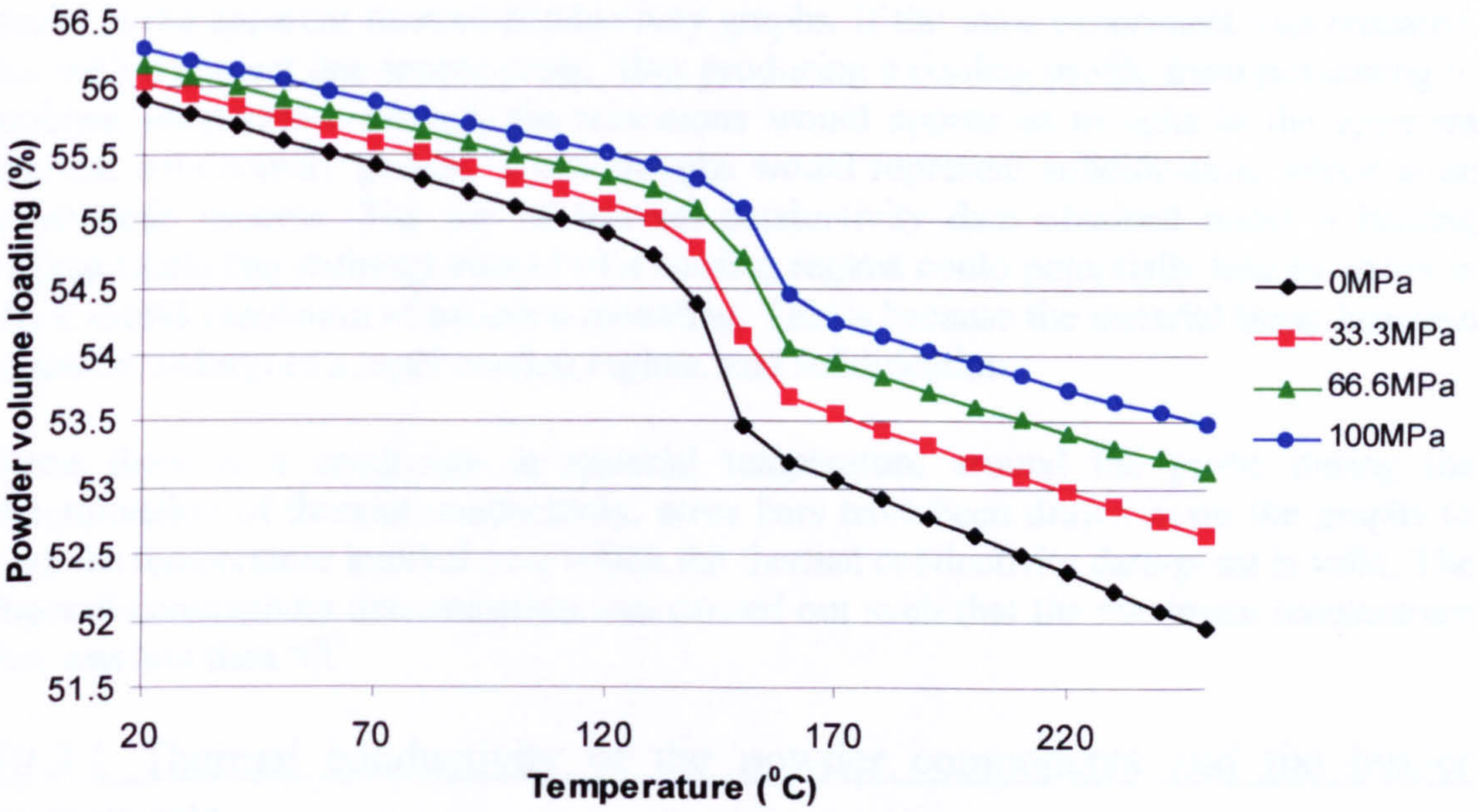

Figure 10.32 Zirconia toughened alumina 55% powder volume loading as a function of temperature and pressure

10.3 Thermal conductivity

This section presents the results of the thermal conductivity work on the binder components, powder components and the feedstocks. Graphs have been plotted for the experimental thermal conductivity vs temperature data obtained using the transient line source probe on the binder components and the feedstocks. Apparent thermal conductivity represents both non-kinetic and kinetic thermal processes that occur within the material.

Kinetic processes such as melting will absorb thermal energy and this results in a peak during heating in the determination of thermal conductivity. Melting is an example of an endothermic process. This occurs because extra heat is being absorbed into the material during the change of state from a solid to a liquid, and is described as an "internal sink". The area of the peak represents a measure of its latent heat of melting or enthalpy during the transition.

During the melting transition, there exists within the material, a two phase region, comprising a solid and a liquid. Thus some sort of rule of mixtures applies for the thermal conductivity during the transition region. Since the exact rule of mixtures is unknown, this is dealt with by drawing in intersecting dashed lines from the baseline above and below the transition region. Thus, the dashed lines offers a guide to the expected thermal conductivity of the two phase mixture during the transition.

It is pointed out that if the thermal conductivity determinations are carried out under a heating profile from ambient to processing temperature, the melting transitions appear as peaks in the apparent thermal conductivity graphs. If the same experiment was repeated, but with a coolant line source probe, thus producing a cooling profile from processing to ambient temperature instead, the transitions would appear as troughs in the apparent thermal conductivity graphs. These troughs would represent solidification, which is an exothermic process. The use of thermal conductivity data obtained under a heating regime (including melting) instead of a cooling regime could potentially lead to errors in the C-Mold simulation of injection moulding. This is because the material being injection moulded undergoes a rapid cooling regime, and solidification.

Since there is a small rise in material temperature around the probe during the determination of thermal conductivity, error bars have been drawn in on the graphs to give the temperature interval over which the thermal conductivity data-point is valid. The thermal conductivity determination was carried out such that the maximum temperature rise was less than 5^0C.

10.3.1 Thermal conductivity of the powder components and the binder components

The thermal conductivity of the powder components was obtained from the open literature and the data are presented in tables 10.4 to 10.9.

Carbonyl iron [198]

Temperature (°C)	Thermal conductivity ($Wm^{-1}k^{-1}$)
0	83.56
20	80.99
40	78.58
60	76.31
80	74.17
100	72.15
120	70.24
140	68.43
160	66.72
180	65.09
200	63.54

Table 10.4 Thermal conductivities for bulk high purity Iron (BASF Iron OM powder is 99.5% iron.)

Stainless steel [199]

Temperature (°C)	Thermal conductivity ($Wm^{-1}k^{-1}$)
20	15.14
40	15.41
60	15.67
80	15.94
100	16.21
120	16.47
140	16.74
160	17.00
180	17.27
200	17.54

Table 10.5 Thermal conductivity values for bulk stainless steel 316L

Both the Osprey stainless steel powders and the BASF iron - Osprey stainless steel masteralloy powder system were considered to have the same thermal conductivity data, so the same data was therefore used for the stainless steel masteralloy system.

Alumina[200, pp752.]

Temperature (°C)	Thermal conductivity ($Wm^{-1}k^{-1}$)
20	38.99
40	35.93
60	33.03
80	30.28
100	27.70
120	25.28
140	23.02
160	20.92
180	18.97
200	17.19

Table 10.6 Thermal conductivity values for bulk alumina (alpha form)

Zirconia[200, pp776]

Temperature (°C)	Thermal conductivity ($Wm^{-1}k^{-1}$)
20	1.65
40	1.65
60	1.66
80	1.66
100	1.67
120	1.68
140	1.68
160	1.69
180	1.69
200	1.70

Table 10.7 Thermal conductivity values for bulk zirconia

Iron - alumina cermet

This was generated by combining the alumina data and the iron data, using the series heat flow equation 4.68. The volume percentages were 15% alumina and 85% iron.

Temperature (°C)	Thermal conductivity ($Wm^{-1}k^{-1}$)
20	69.73
40	66.70
60	63.77
80	60.92
100	58.15
120	55.45
140	52.80
160	50.22
180	47.70
200	45.24

Table 10.8 Thermal conductivity values for bulk iron - alumina cermet

Zirconia toughened alumina

This was generated by combining the alumina data and the zirconia data together using the series heat flow equation 4.68. The volume percentages were 80% alumina and 20% zirconia.

Temperature (°C)	Thermal conductivity ($Wm^{-1}k^{-1}$)
20	7.04
40	6.98
60	6.90
80	6.82
100	6.73
120	6.62
140	6.51
160	6.38
180	6.24
200	6.09

Table 10.9 Thermal conductivity values for bulk zirconia toughened alumina

Figure 10.33 shows graphically the thermal conductivity of the five model powder systems used in PCM over the temperature range encountered in injection moulding. Figure 10.33 shows that the thermal conductivity of the iron, iron-alumina cermet and the alumina decreased with increasing temperature. The thermal conductivity of the stainless steel increased slightly with increasing temperature. The thermal conductivity of the zirconia toughened alumina remained reasonably constant for the temperature range.

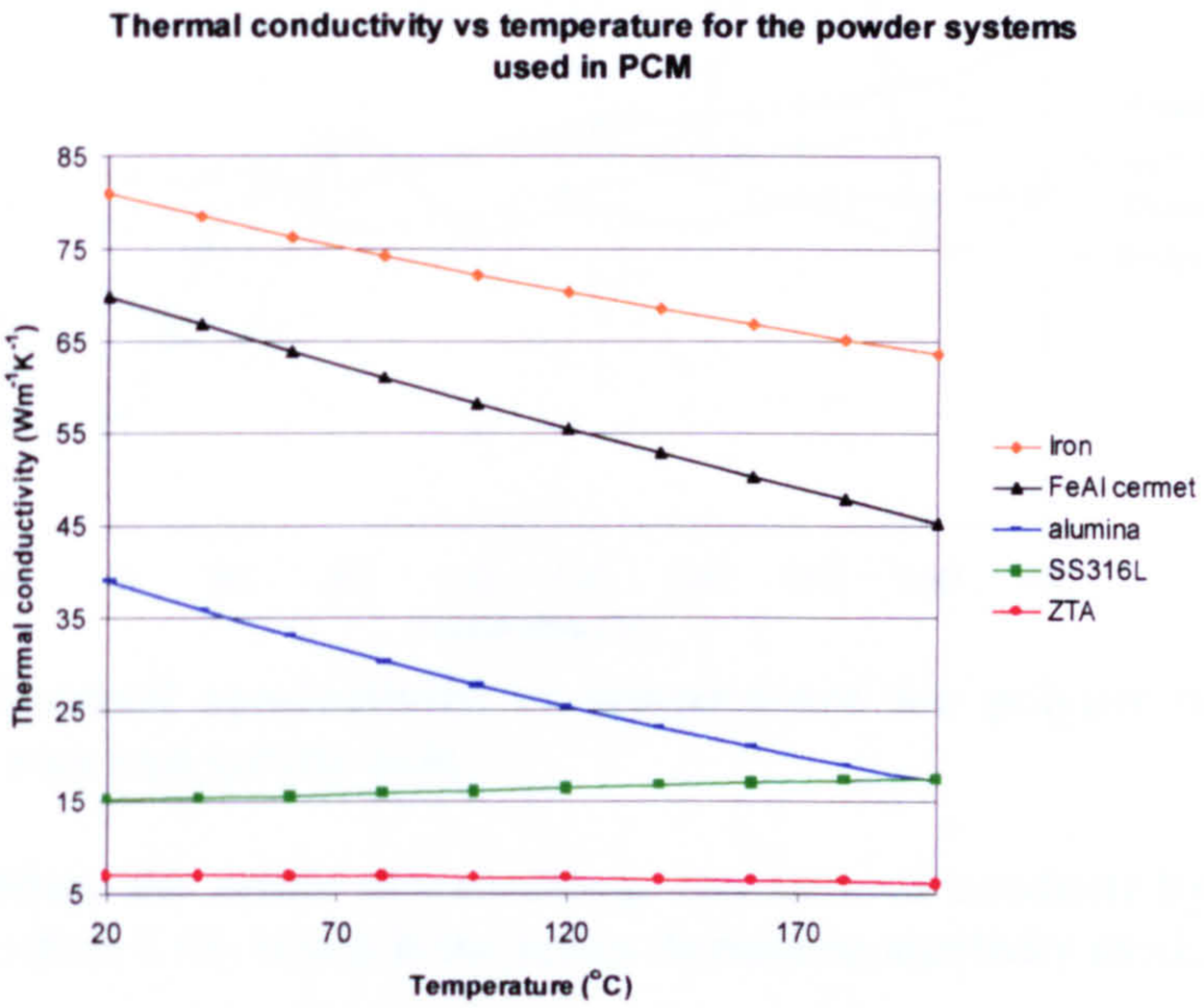

Figure 10.33 Powder systems thermal conductivity vs temperature

Figure 10.34 shows the results of the thermal conductivity determination of the individual binder components. The polypropylene had a thermal conductivity of about 0.2 $Wm^{-1}K^{-1}$ and a peak, which is due to the solid to melt transition, which agrees well with the findings in the specific heat capacity work. The paraffin wax has a solid state thermal conductivity of about 0.13 $Wm^{-1}K^{-1}$ and changed to a liquid state thermal conductivity, which increased gradually with increasing temperature. The carnuaba wax had a solid state thermal conductivity of 0.15 $Wm^{-1}K^{-1}$, which increased to 0.2 $Wm^{-1}K^{-1}$ in the liquid state, gradually increasing with increasing temperature. The peaks are due to the changes of state, which is confirmed by the specific heat capacity experiments on the same binder components.

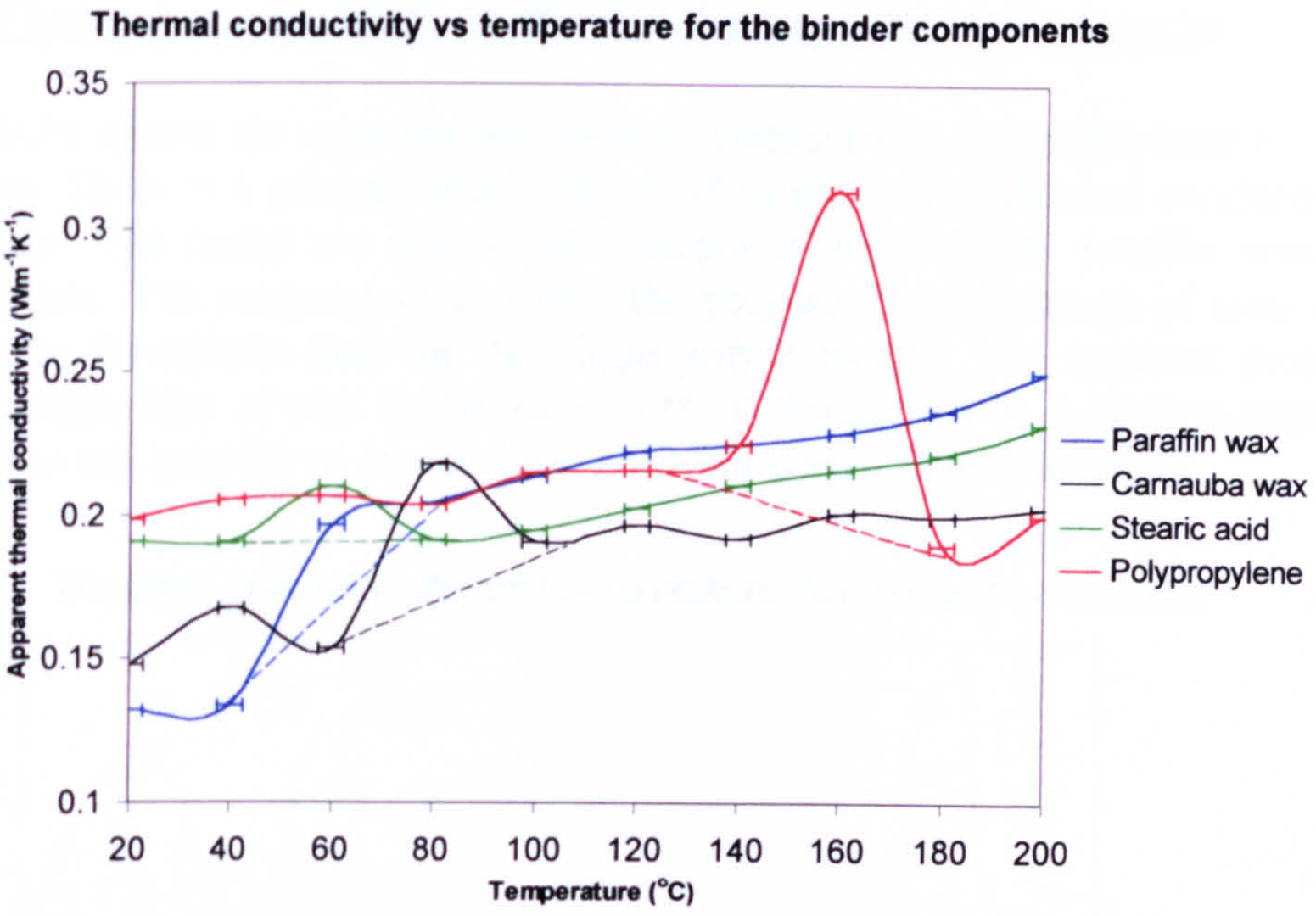

Figure 10.34 Thermal conductivity vs temperature for polypropylene, paraffin wax, carnauba wax and stearic acid

Figure 10.35 shows the result of calculating the thermal conductivity of the binder system using equation 4.68, which is the series thermal conductivity model.

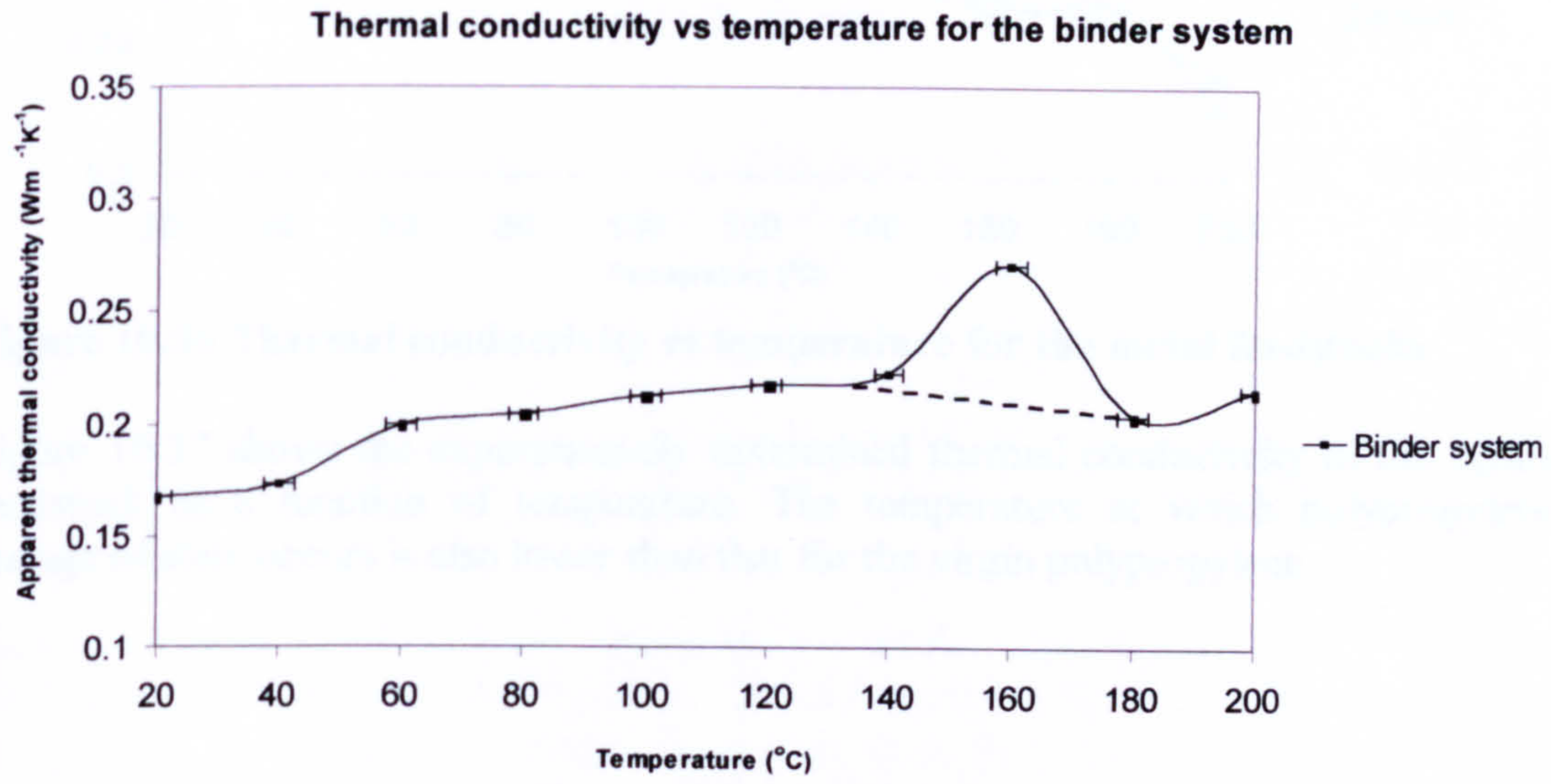

Figure 10.35 Thermal conductivity vs temperature for the binder system

10.3.2 Thermal conductivity of the metal and ceramic feedstocks

Figure 10.36 shows the experimental thermal conductivity vs temperature of the metal feedstocks. There is a general underlying trend of decreasing thermal conductivity with temperature. The peaks are due to the changes of state of the paraffin wax and the polypropylene. The temperature at which the polypropylene's change of state occurs is lower in the feedstocks than for the virgin polypropylene. The apparent peak for the thermal conductivity of iron feedstock at 40°C is thought to be a random experimental error. It was not possible to repeat the experiment due to time constraints.

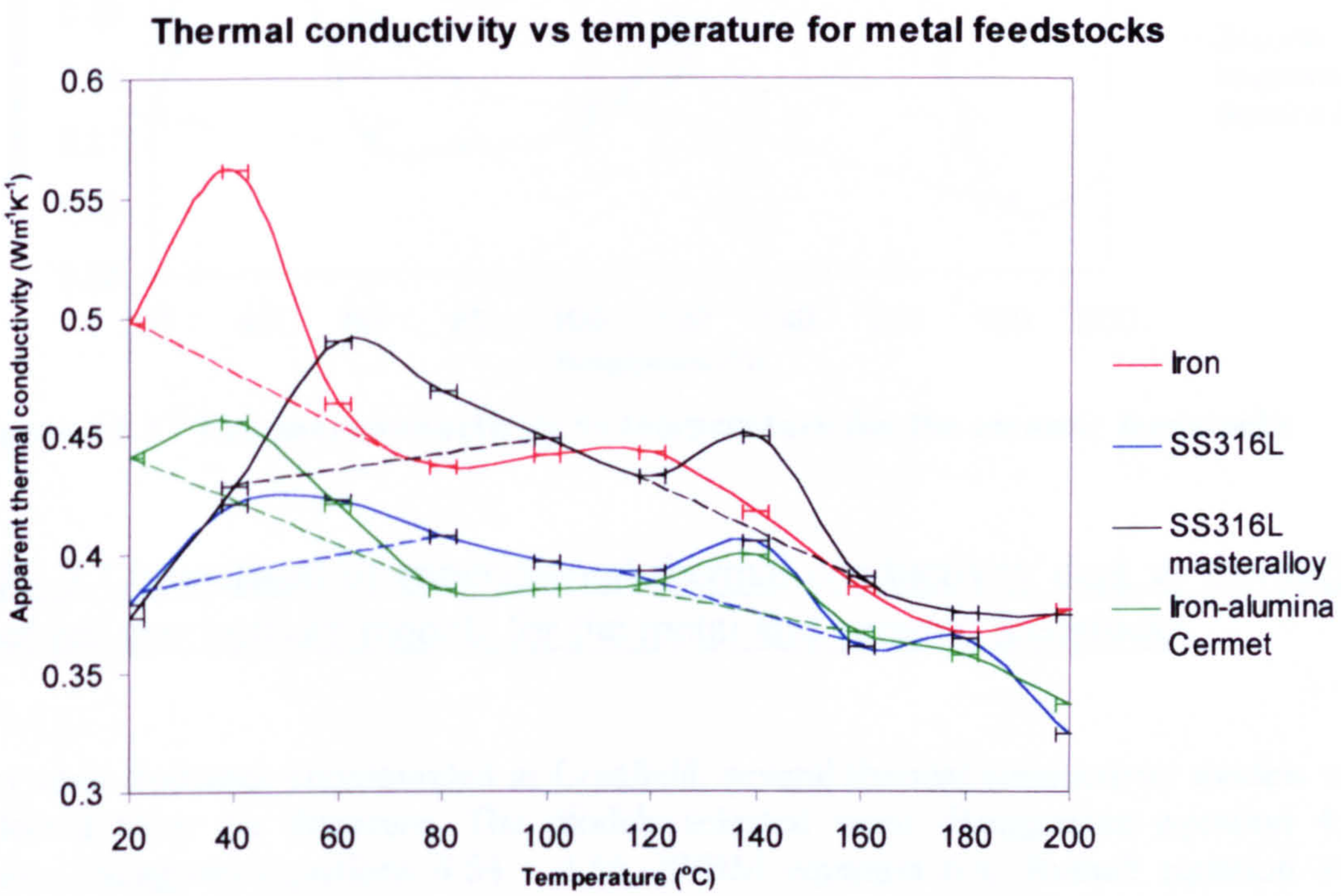

Figure 10.36 Thermal conductivity vs temperature for the metal feedstocks

Figure 10.37 shows the experimentally determined thermal conductivity of the ceramic feedstock as a function of temperature. The temperature at which polypropylene's change of state occurs is also lower than that for the virgin polypropylene.

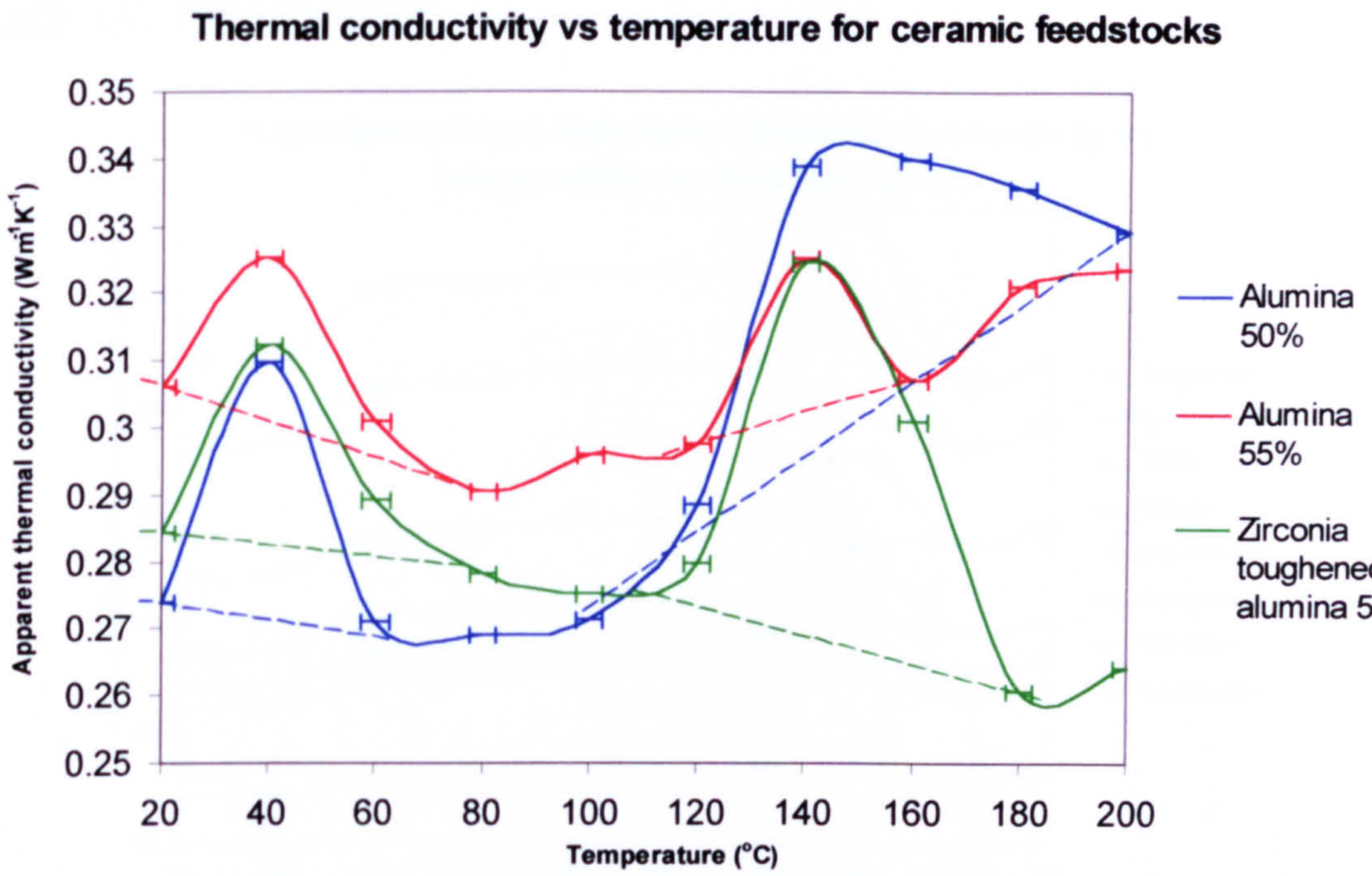

Figure 10.37 Thermal conductivity vs temperature for the ceramic feedstocks

10.3.3 Comparison of experimental thermal conductivity data vs theoretical thermal conductivity models for the metal and ceramic feedstocks

For each feedstock compounded at Cranfield, several thermal conductivity models were selected from the literature. The models selected were: Bruggeman equation 4.61, Imura-Takegoshi equations 4.54 - 4.56, SPBM equation 6.4, Russell equation 4.59, Maxwell equations 4.63 - 4.64, Kampf-Karsten equation 4.57 and the series flow equation 4.68. The selected equations were used to calculate the thermal conductivity vs temperature of each feedstock from the individual components experimentally determined thermal conductivity vs temperature data and volumetric composition data of the feedstock.

Figures 10.38 to 10.44 show the comparison of the feedstock experimentally determined thermal conductivity against the selected thermal conductivity models from the literature for all of the compounded feedstocks. It was clear that the most suitable model for predicting the thermal conductivity of the feedstock was the series flow model, which was consistent in its slight over prediction of the experimental thermal conductivity.

Carbonyl iron feedstock

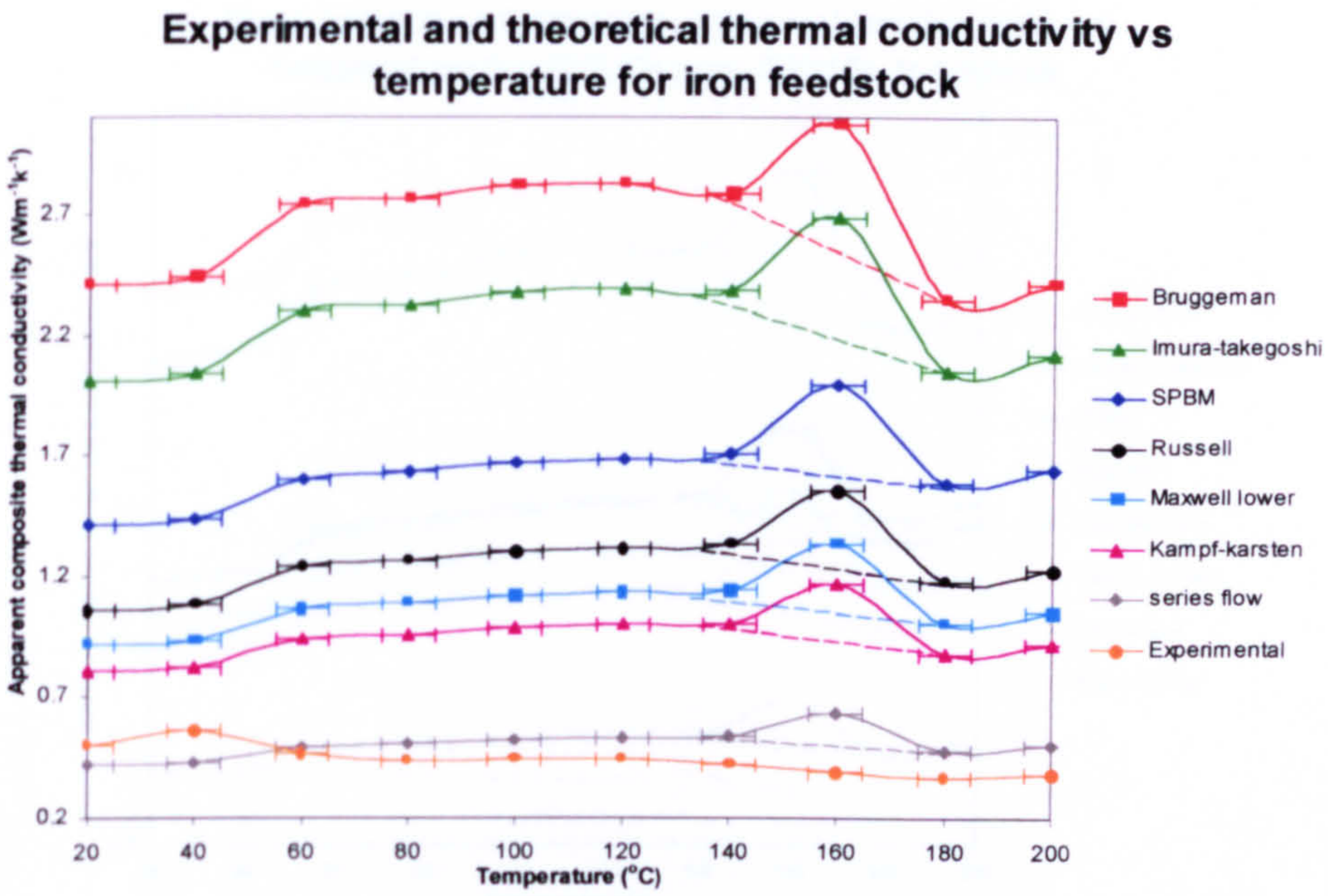

Figure 10.38 Theoretical and experimental thermal conductivity data for the iron feedstock

Iron and alumina feedstock

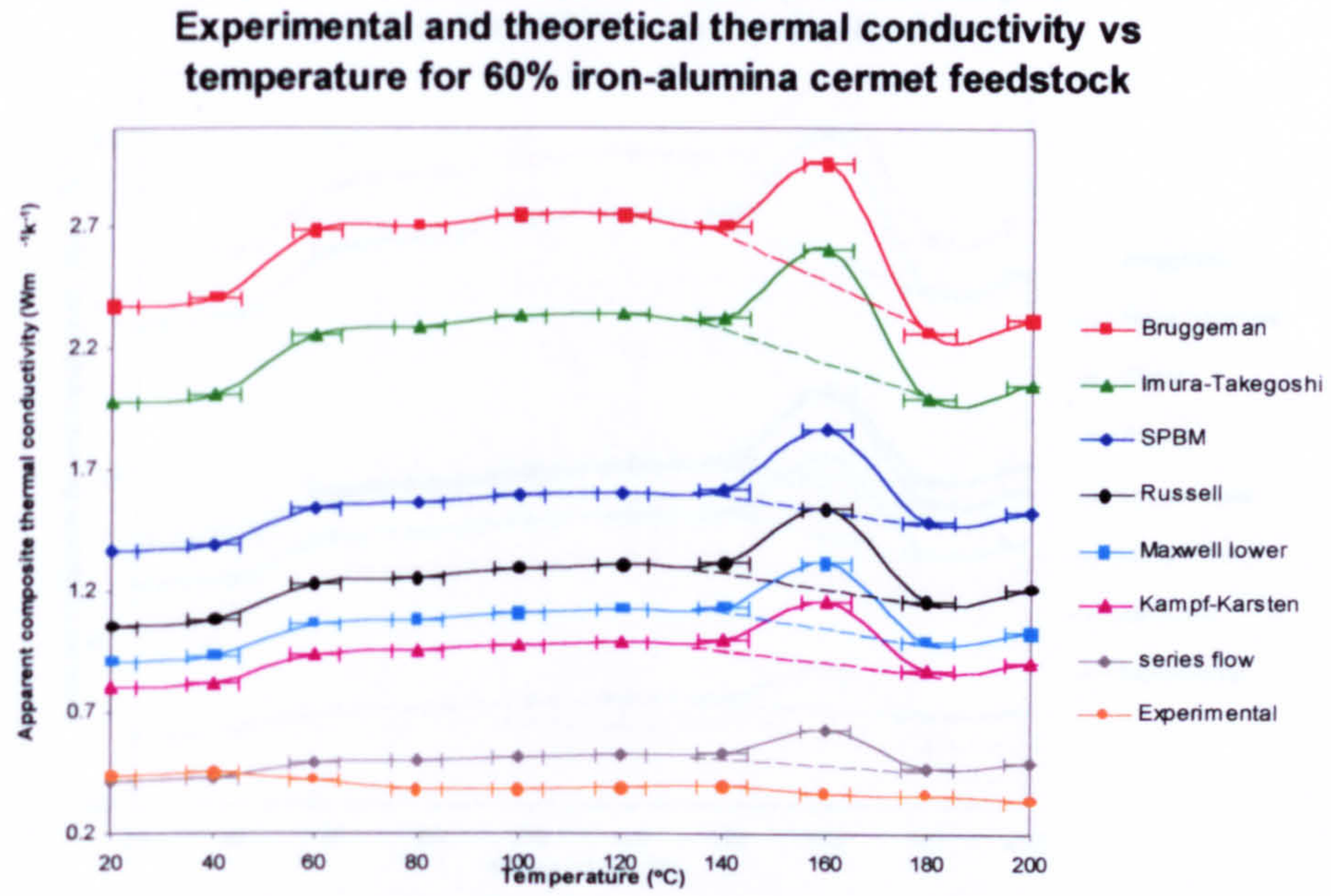

Figure 10.39 Theoretical and experimental thermal conductivity data for the iron-alumina cermet feedstock

Stainless steel 316L feedstock

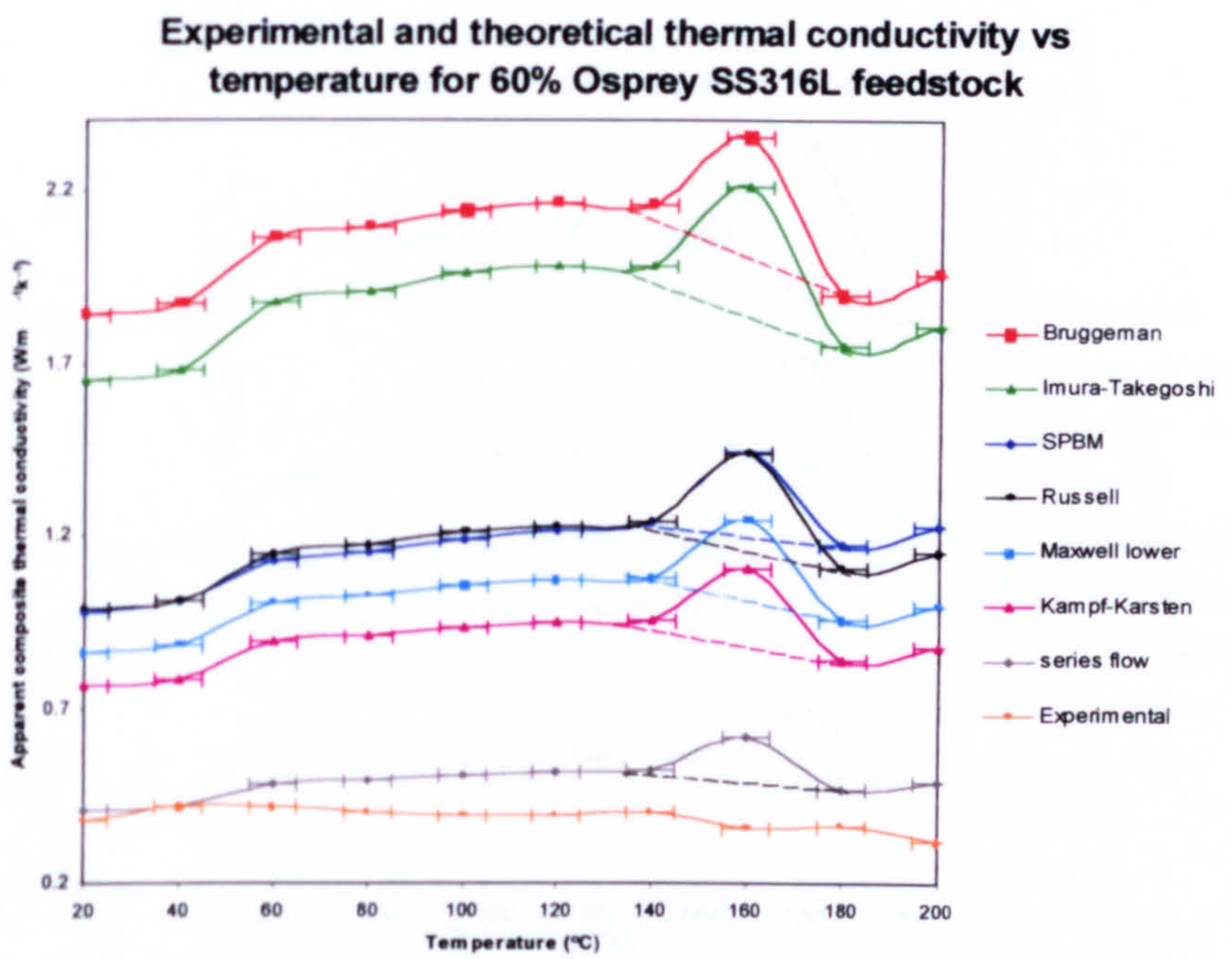

Figure 10.40 Theoretical and experimental thermal conductivity data for the Osprey stainless steel 316L feedstock

Stainless steel masteralloy 316L

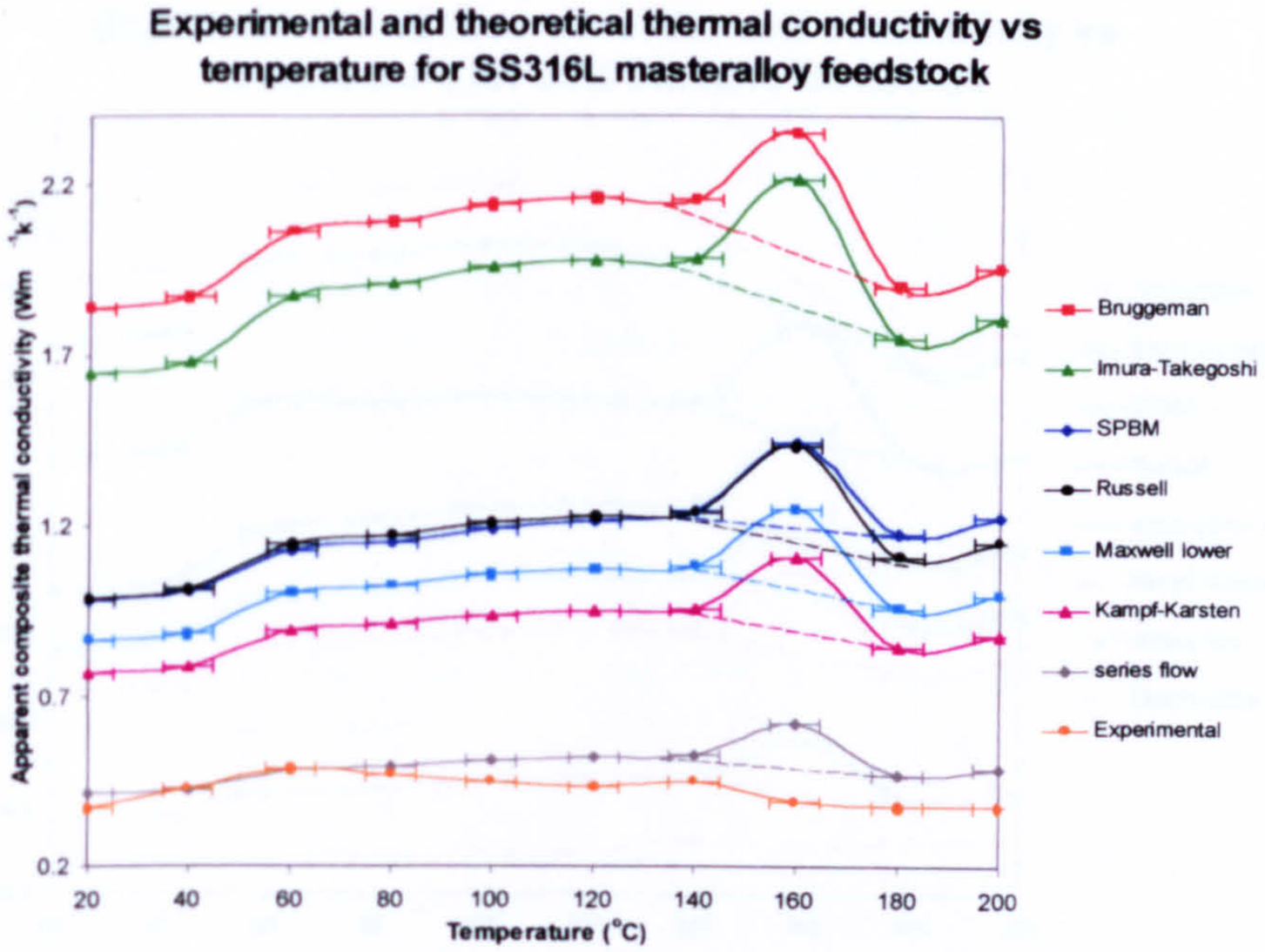

Figure 10.41 Theoretical and experimental thermal conductivity data for the stainless steel 316L masteralloy feedstock

Alumina 50% vol feedstock

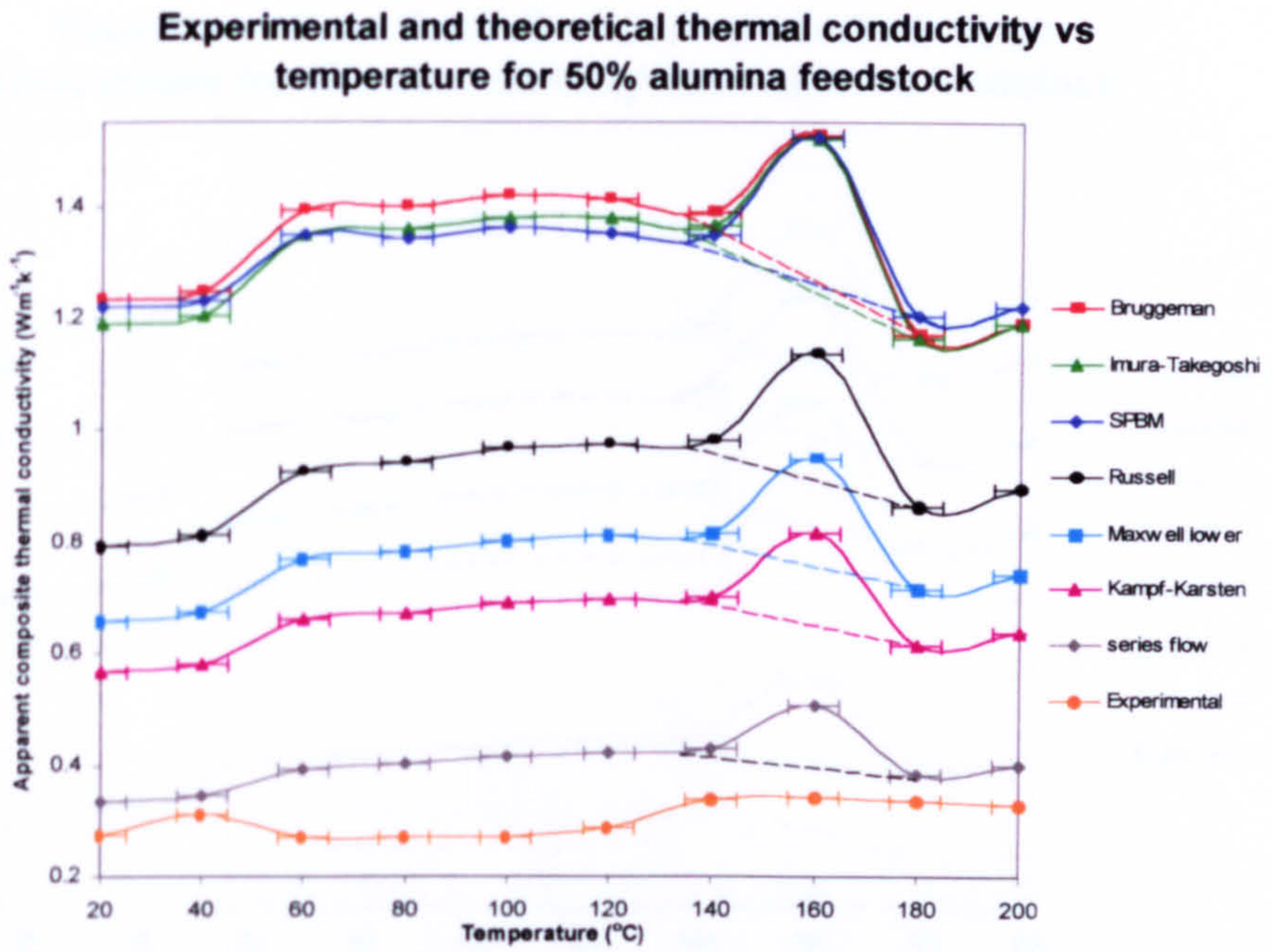

Figure 10.42 Theoretical and experimental thermal conductivity data for the 50% alumina feedstock

Alumina 55% vol feedstock

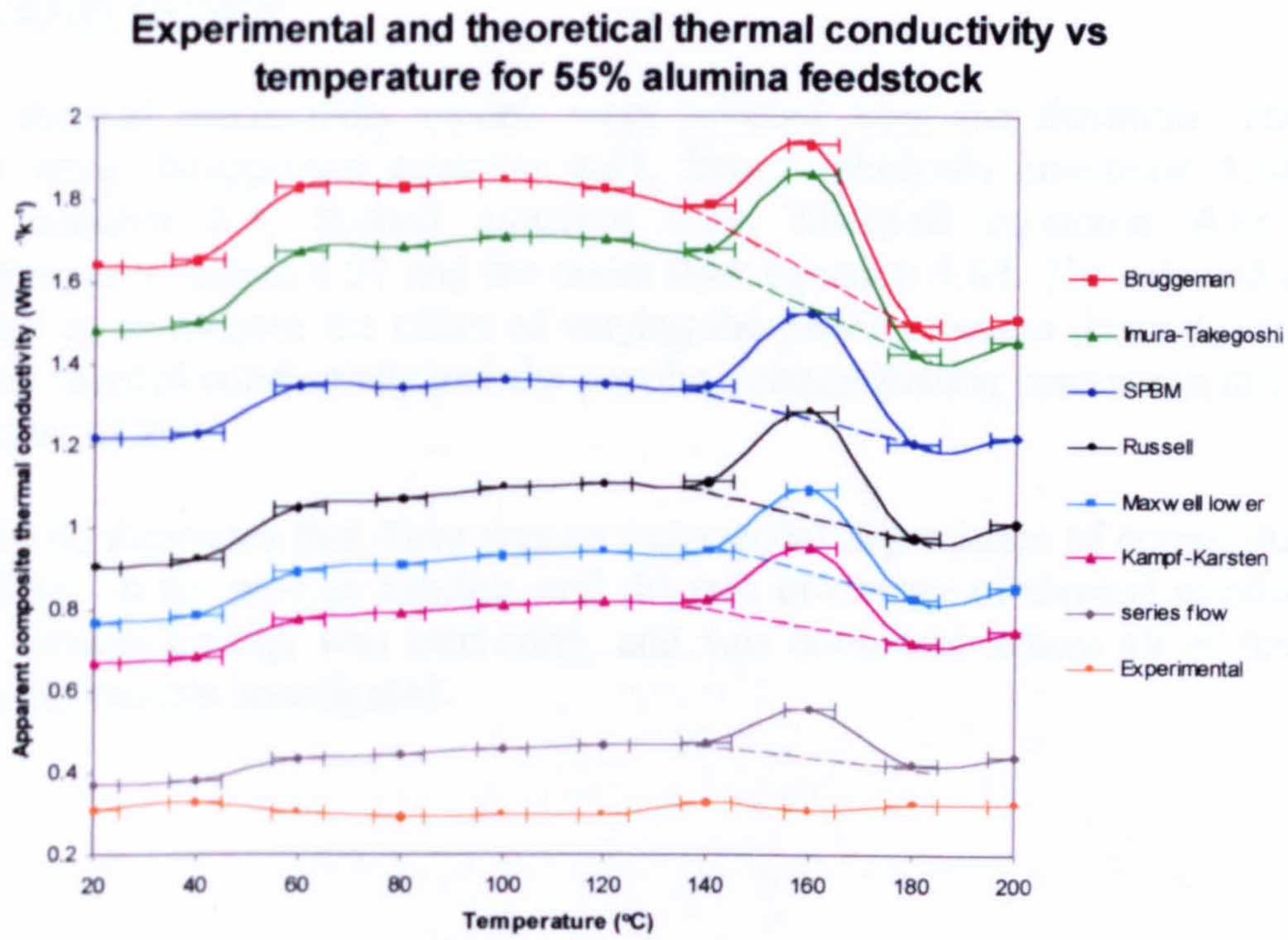

Figure 10.43 Theoretical and experimental thermal conductivity data for the 55% alumina feedstock

Zirconia toughened alumina feedstock

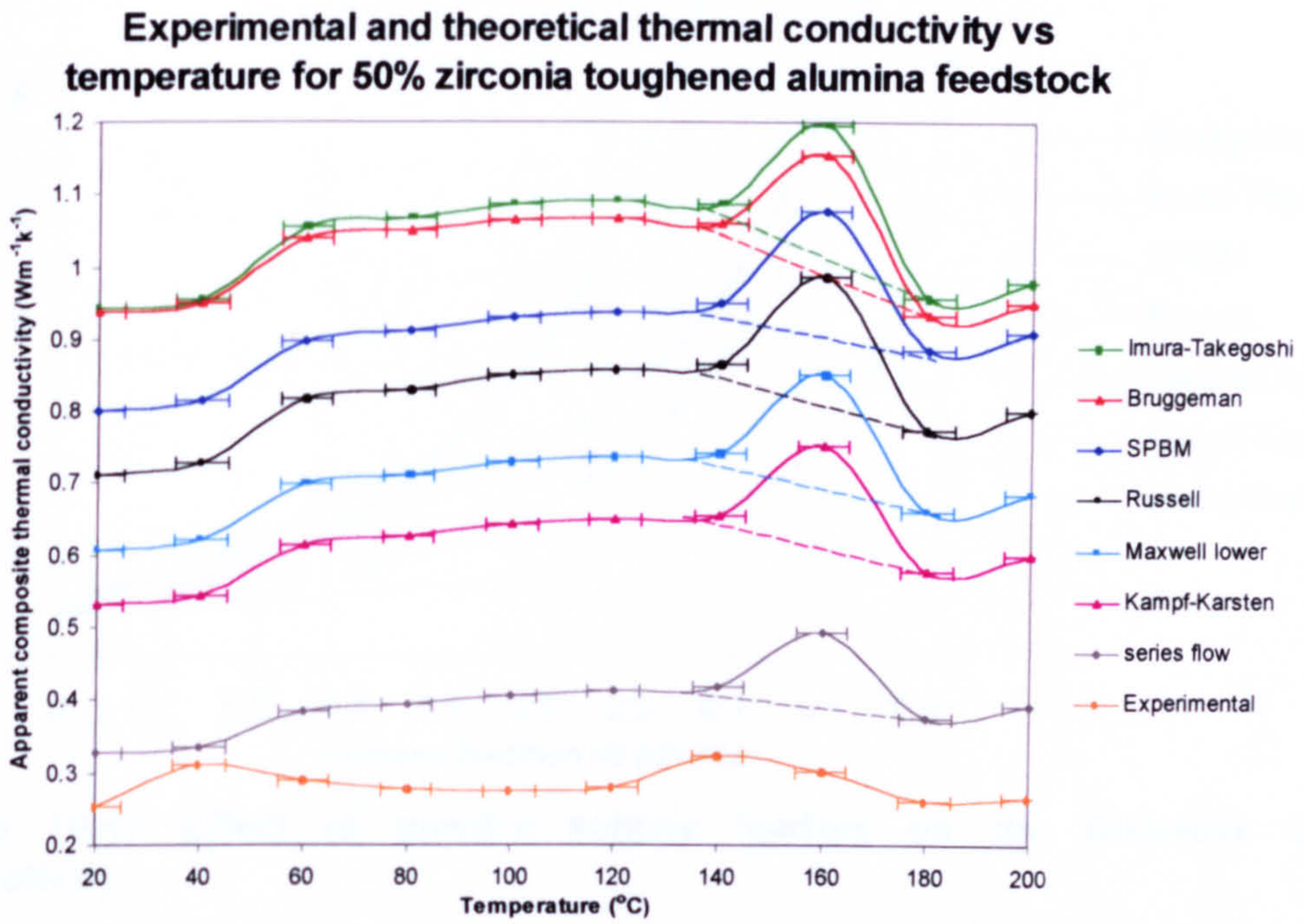

Figure 10.44 Theoretical and experimental thermal conductivity data for the zirconia toughened alumina feedstock

10.3.4 Investigation of various material properties using the thermal conductivity models

Several thermal conductivity models were selected from the literature. The models selected were: Bruggeman equation 4.61, Imura-Takegoshi equations 4.54 - 4.56, SPBM equation 6.4, Russell equation 4.59, Maxwell equations 4.63 - 4.64, Kampf-karsten equation 4.57 and the series flow equation 4.68. The selected equations were used to investigate the effect of varying the powder system thermal conductivity, the binder thermal conductivity and the powder volume loading percentage at a constant temperature of 20°C.

Figure 10.45 illustrates that there was an exponential dependence of composite thermal conductivity on the powder loading, and the rate of change of thermal conductivity vs powder volume loading was increasing, and was consistent across all of the thermal conductivity models investigated.

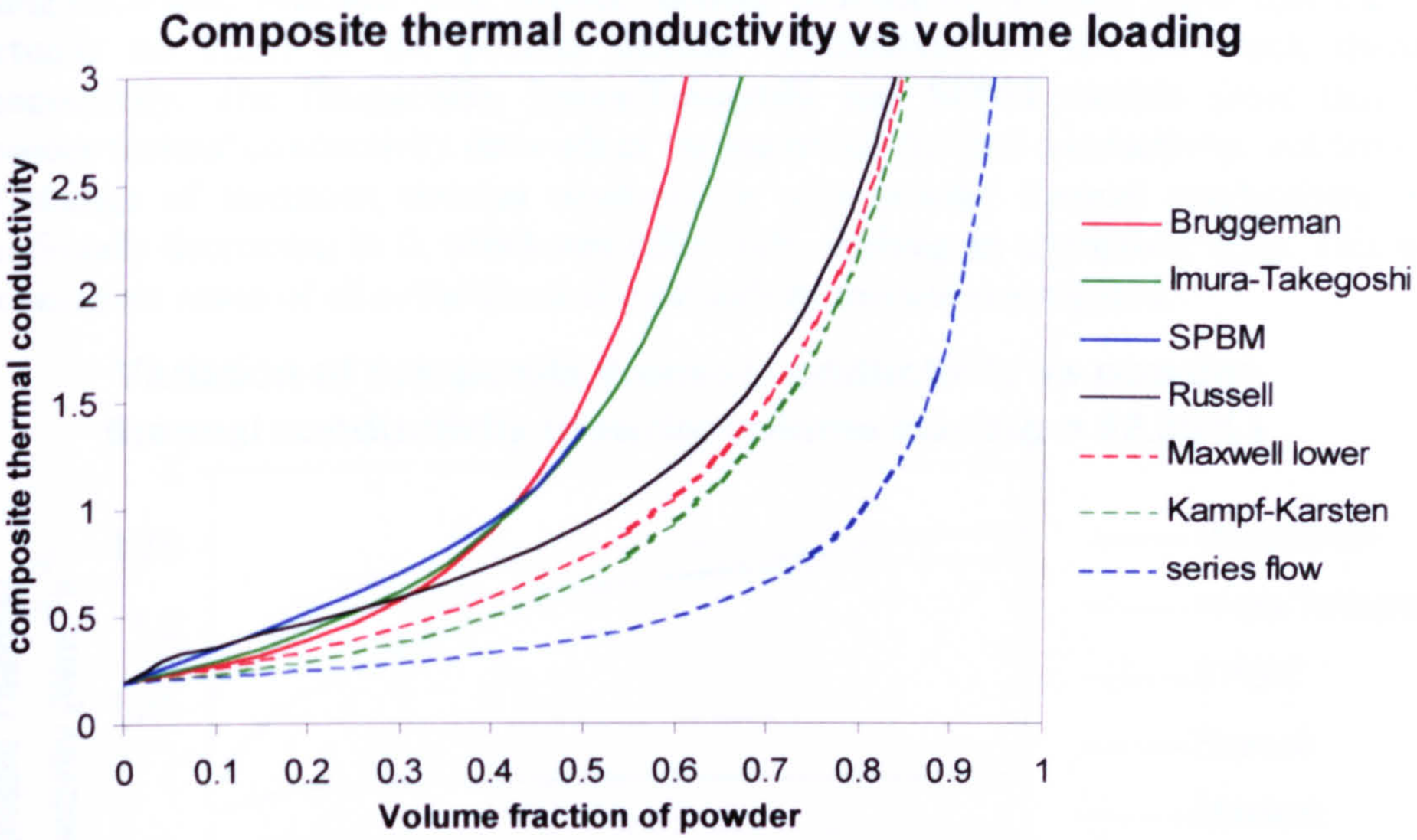

Figure 10.45 Effect of powder volume loading on the feedstock thermal conductivity

Figure 10.46 illustrates the effect of the binder thermal conductivity on the feedstock thermal conductivity for a constant powder volume loading of 52.36%. All of the models illustrated that the feedstock thermal conductivity was virtually linearly dependent on the binder thermal conductivity. This was consistently predicted by all of the thermal conductivity models.

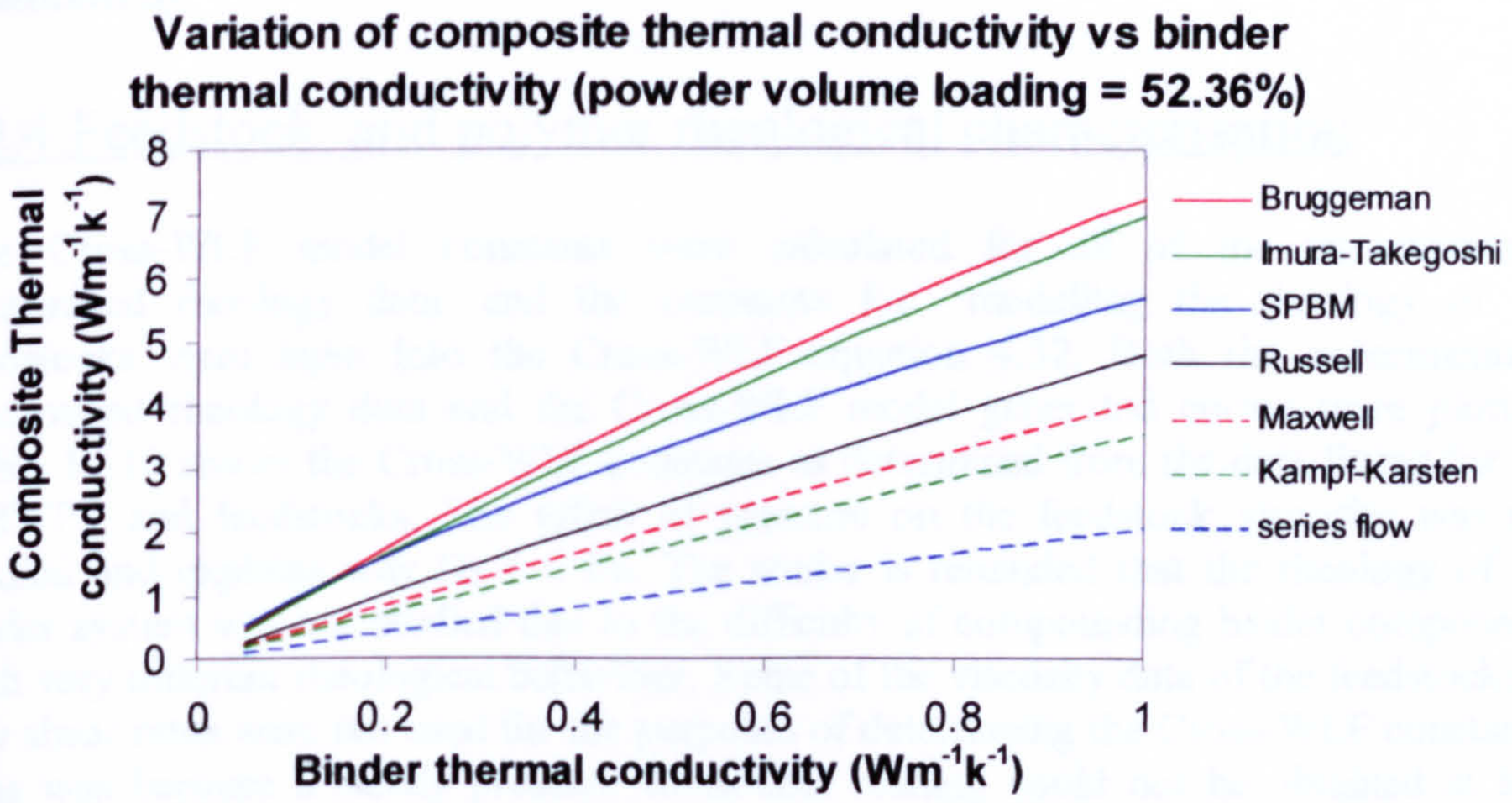

Figure 10.46 Effect of binder thermal conductivity on the feedstock thermal conductivity

Figure 10.47 illustrates the effect of the powder thermal conductivity on the feedstock thermal conductivity for a constant powder volume loading of 52.36%. The series flow,

Kampf-Karsten, Maxwell and Russell thermal conductivity models show that there is virtually no effect of the powder thermal conductivity on the feedstock thermal conductivity. The Bruggeman, Imura-Takegoshi and SPBM models show that the powder thermal conductivity does affect the feedstock thermal conductivity, but the rate of change of feedstock thermal conductivity with powder thermal conductivity was continually decreasing to 0, which was effectively reaching an asymptotic state. This was a consistent result of all of the thermal conductivity models investigated.

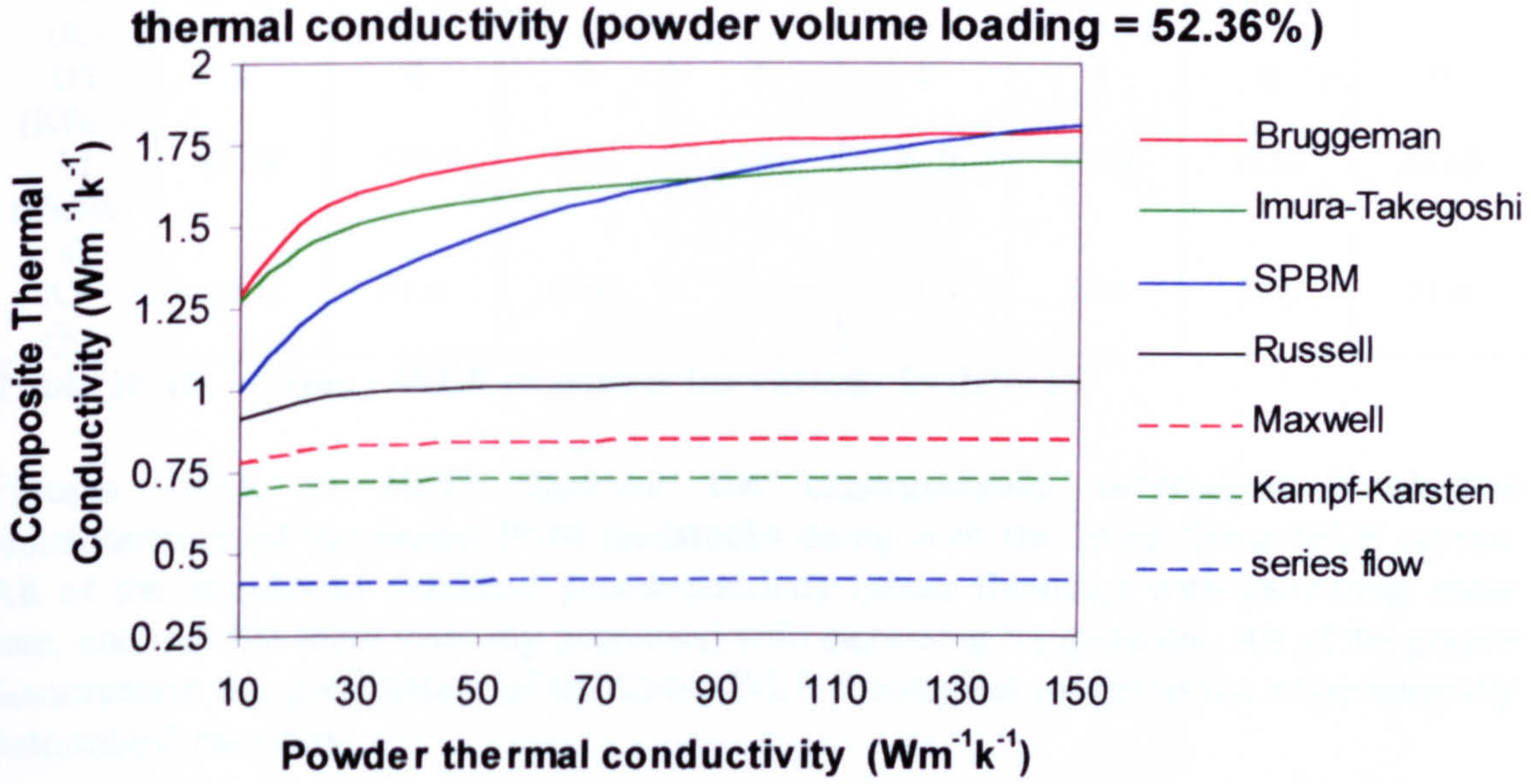

Figure 10.47 Effect of powder thermal conductivity on the powder thermal conductivity

10.4 Feedstock and polymer rheological characterisation

The Cross-WLF model constants were calculated for all of the experimentally determined rheology data, and the constants for modelling the rheology of the feedstocks were input into the Cross-WLF equation 4.32. Both the experimentally determined rheology data and the Cross-WLF model generated curves were plotted. Table 10.10 shows the Cross-WLF constants as determined from the data fitting for the LMWPP and feedstocks. The effect of pressure on the feedstock viscosity was not studied and explains why $D_3 = 0$ Pa. The reader is reminded that the rheology of the binder system was not studied due to the difficulty of compounding binder components with very different rheological behaviour. Some of the viscosity data of the feedstocks at low shear rates were not used for the purposes of determining the Cross-WLF constants. This was because a steady pressure transducer reading could not be obtained at low shear rates. This was thought to be the consequence of high inter-particle friction between the particles or the consequence of slip stick.

	Iron	SS316L MA	SS316L	Cermet	50% Alumina	55% Alumina	55% ZTA	Exxon LMWPP
η (unitless)	0.2650	0.3851	0.2664	0.2248	0.4165	0.4085	0.4653	0.2319
T^* (Pa)	53,578	25,759	60,174	68,813	3,824.5	1,009.6	2,031.6	55,075
D1 (Pa.s)	$3.97x10^{+18}$	$9.51x10^{+13}$	$3.58x10^{+12}$	$1.26x10^{+13}$	$1.22x10^{+15}$	$1.92x10^{+18}$	$2.67x10^{+19}$	$2.70x10^{+11}$
D2 (K)	263.15	263.15	263.15	263.15	263.15	263.15	263.15	263.15
D3 (KPa^{-1})	0	0	0	0	0	0	0	0
A1 (Unitless)	43.59	32.59	29.31	29.46	34.76	40.39	47.01	25.45
A2~ (K)	51.6	51.6	51.6	51.6	51.6	51.6	51.6	51.6

Table 10.10 Cross - WLF constants for various feedstocks

Figures 10.48 to 10.55 illustrate the experimentally determined rheological characteristics of the model PCM feedstocks along with the fitted Cross-WLF curves. All of the feedstocks exhibited psuedoplasticity (shear thinning) with increasing shear rate, and that the shear viscosity decreased with increasing temperature. All of the graphs demonstrate the good fitting of the Cross-WLF rheological model to the experimentally determined rheology.

60% Carbonyl iron feedstock

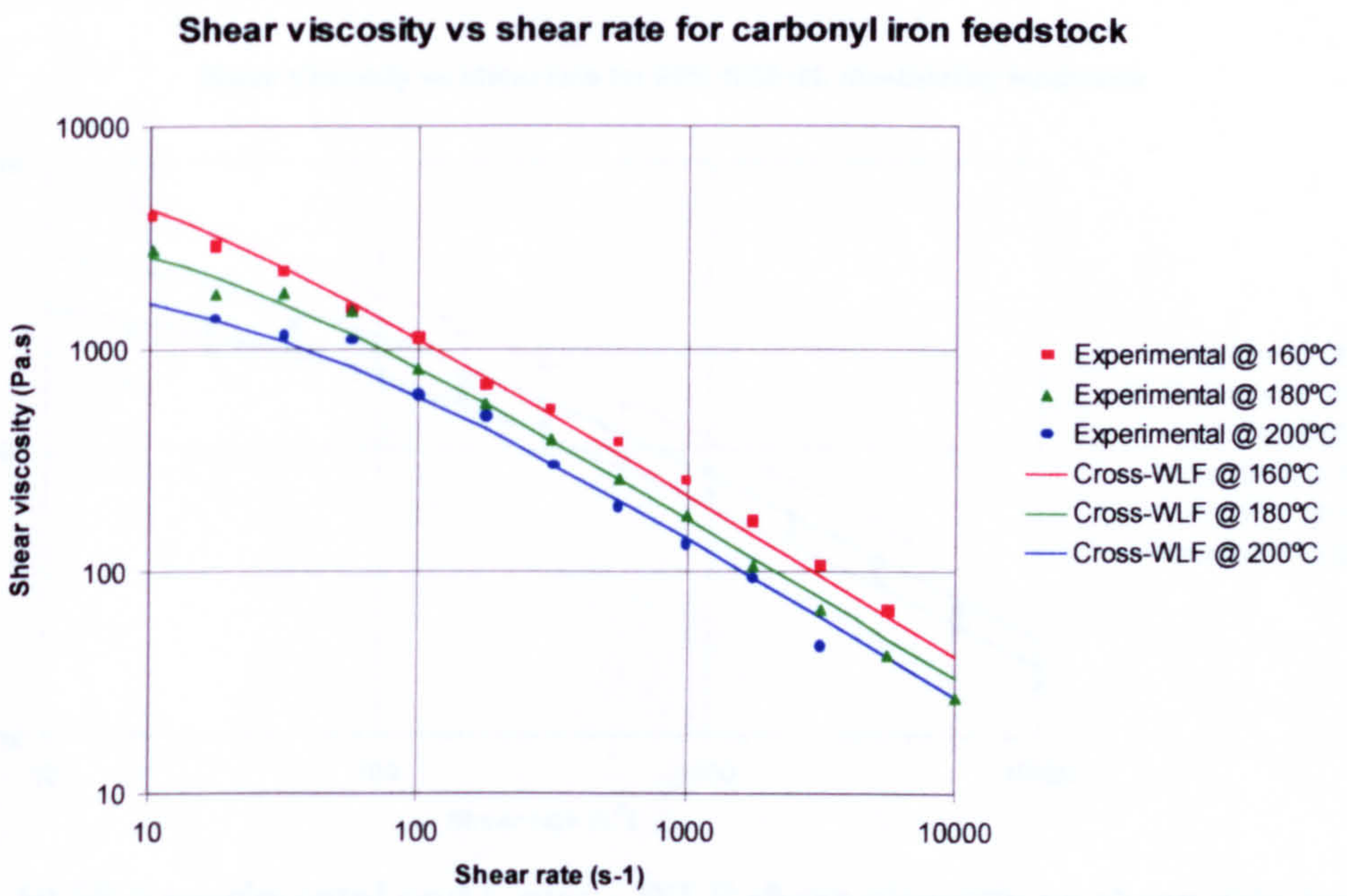

Figure 10.48 Experimental and Cross - WLF shear viscosity vs shear rate for 60% carbonyl iron feedstock

60% SS316L feedstock

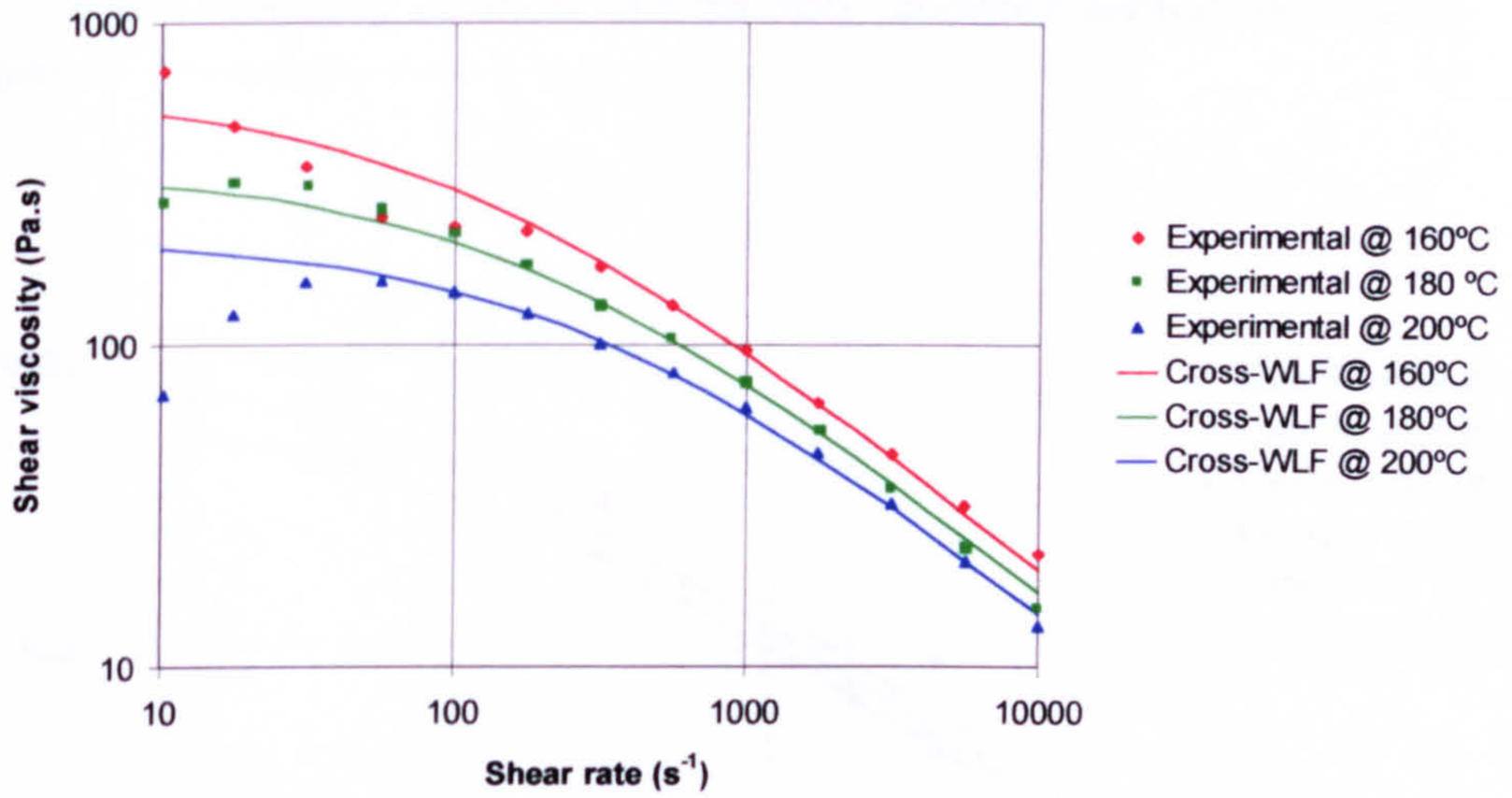

Figure 10.49 Experimental and Cross - WLF shear viscosity vs shear rate for 60% stainless steel 316L feedstock

It is apparent in figures 10.49 and 10.50 that the experimental viscosity falls at low shear rates. This is thought to be due to the presence of a slip layer. The viscosity data at low shear rates was not used for the determination of the Cross-WLF constants.

60% SS316L masteralloy feedstock

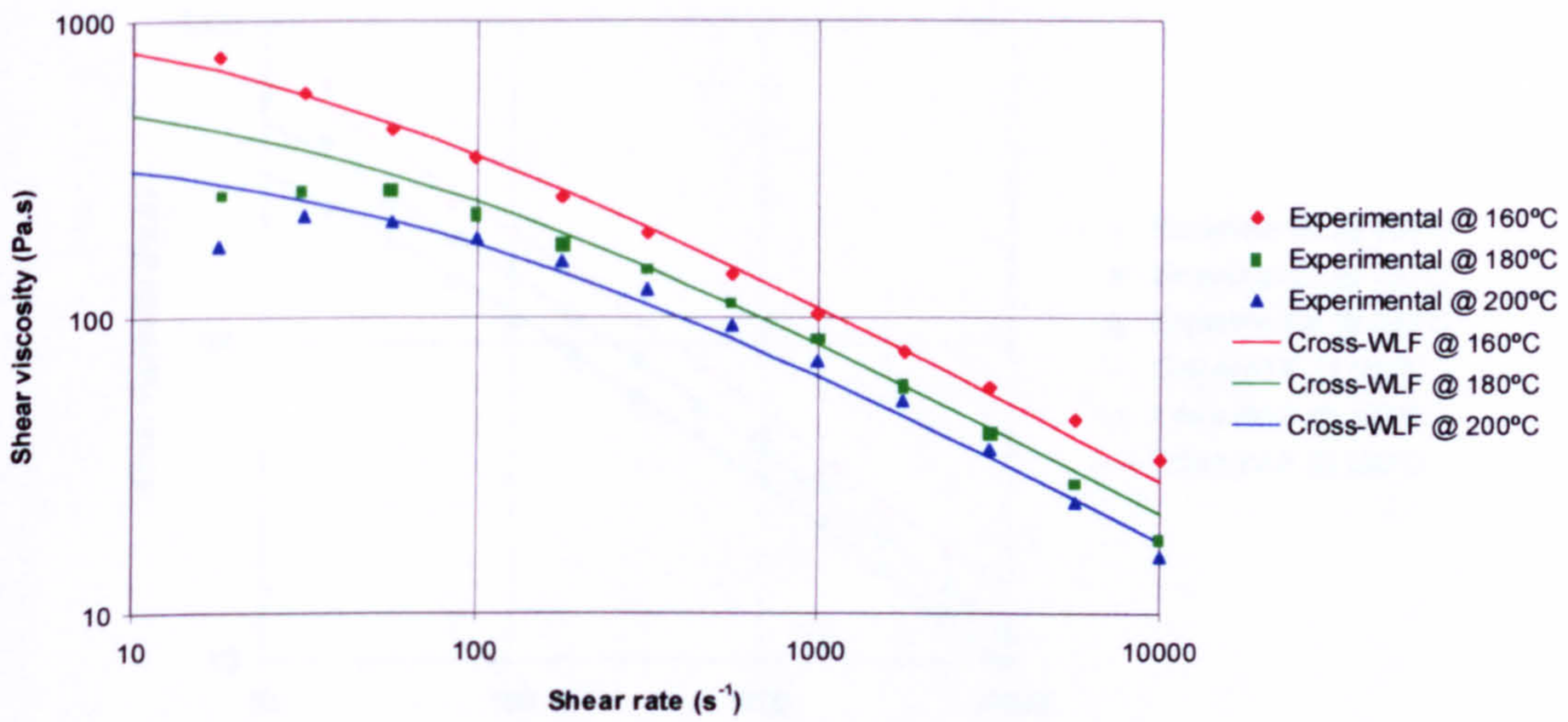

Figure 10.50 Experimental and Cross - WLF shear viscosity vs shear rate for 60% stainless steel 316L masteralloy feedstock

60% Iron - alumina cermet feedstock

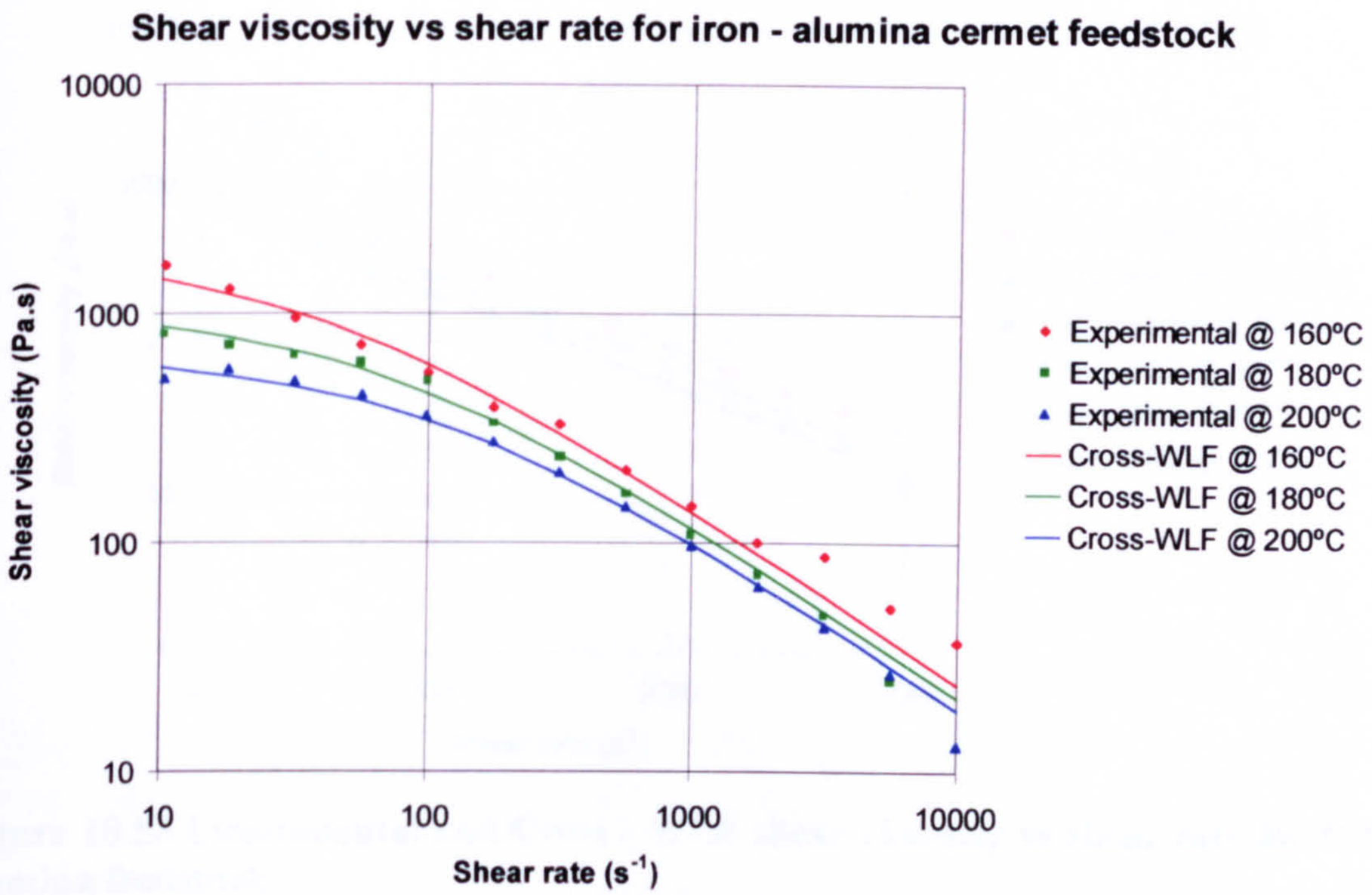

Figure 10.51 Experimental and Cross - WLF shear viscosity vs shear rate for 60% carbonyl iron and alumina cermet feedstock

50% Alumina feedstock

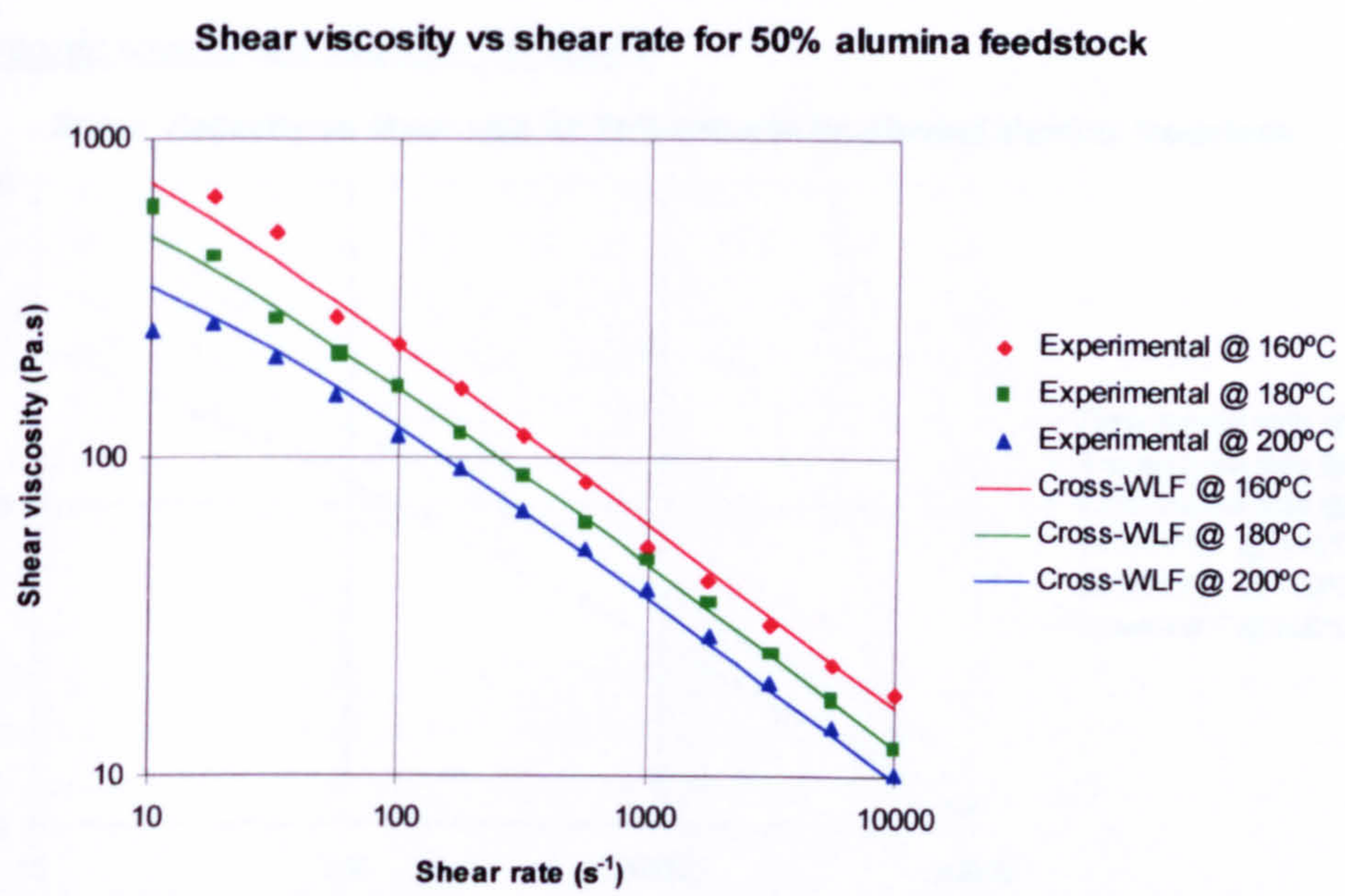

Figure 10.52 Experimental and Cross - WLF shear viscosity vs shear rate for 50% alumina feedstock

55% Alumina feedstock

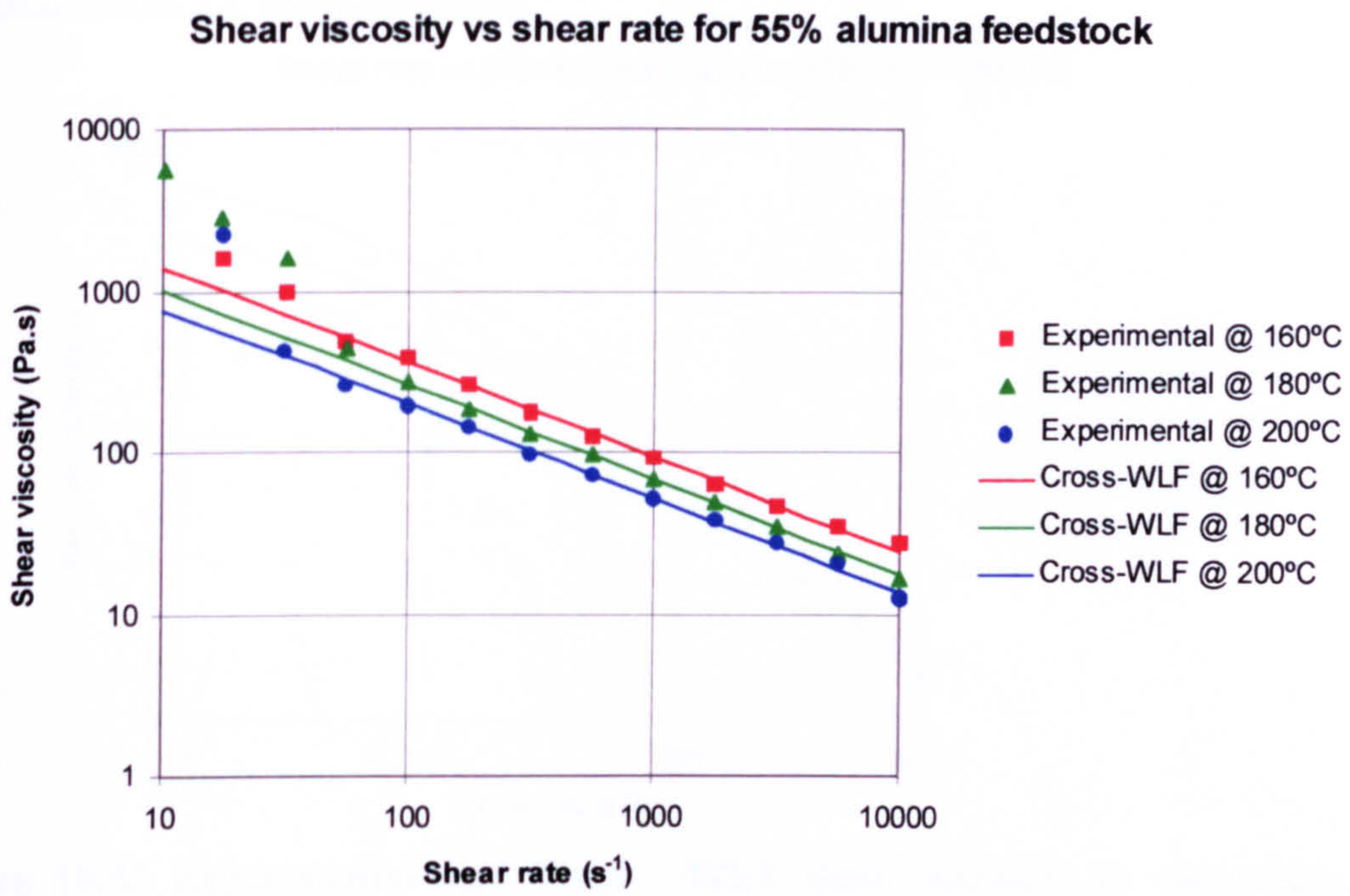

Figure 10.53 Experimental and Cross - WLF shear viscosity vs shear rate for 55% alumina feedstock

The viscosity at low shear rates in figure 10.53 was observed to be higher than expected. This is thought to be the result of interparticle and particle to barrel wall frictional effects.

55% Zirconia toughened alumina feedstock

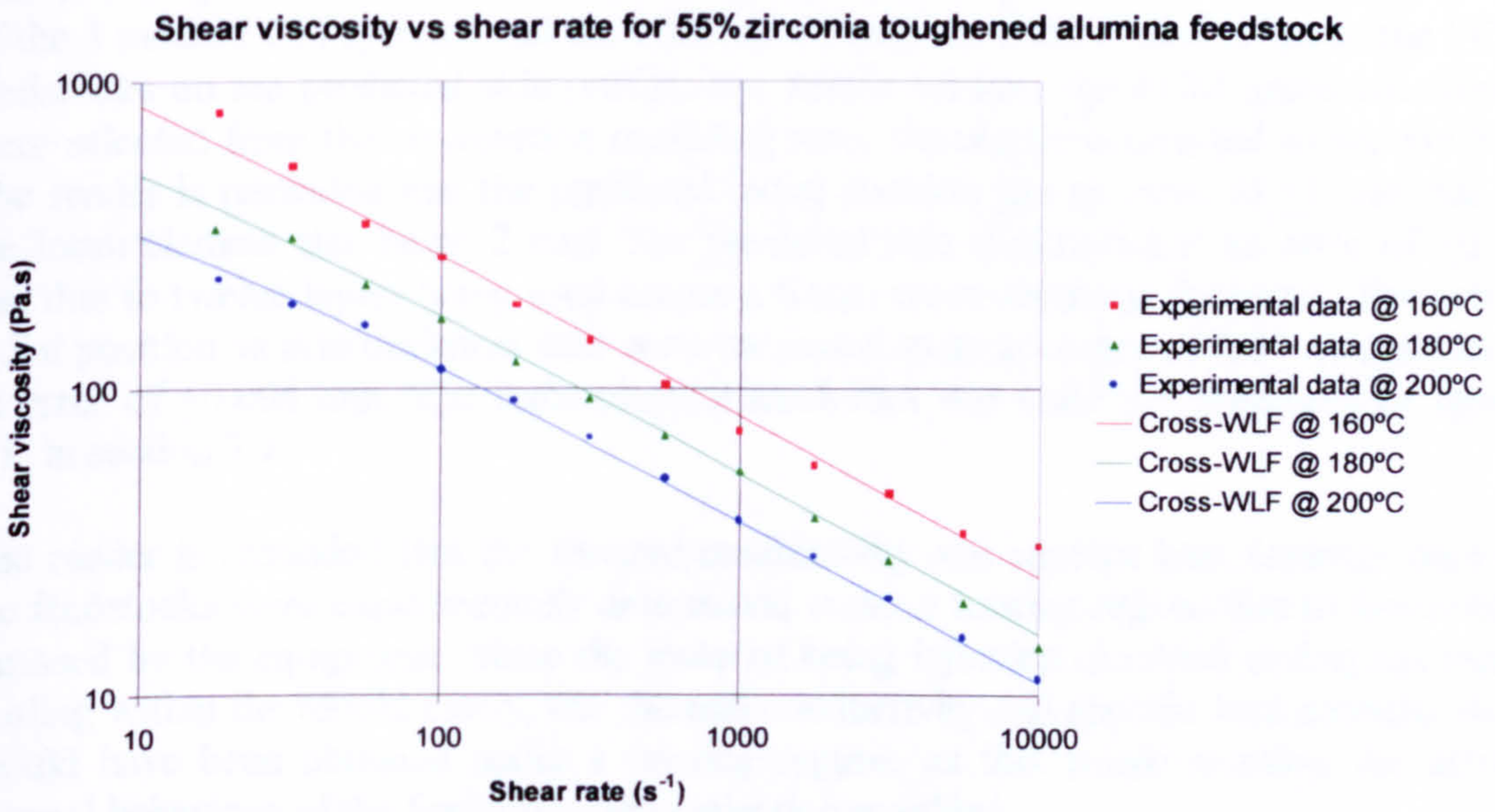

Figure 10.54 Experimental and Cross - WLF shear viscosity vs shear rate for 55% zirconia toughened alumina feedstock

Exxon LMWPP PP3536F1 polymer

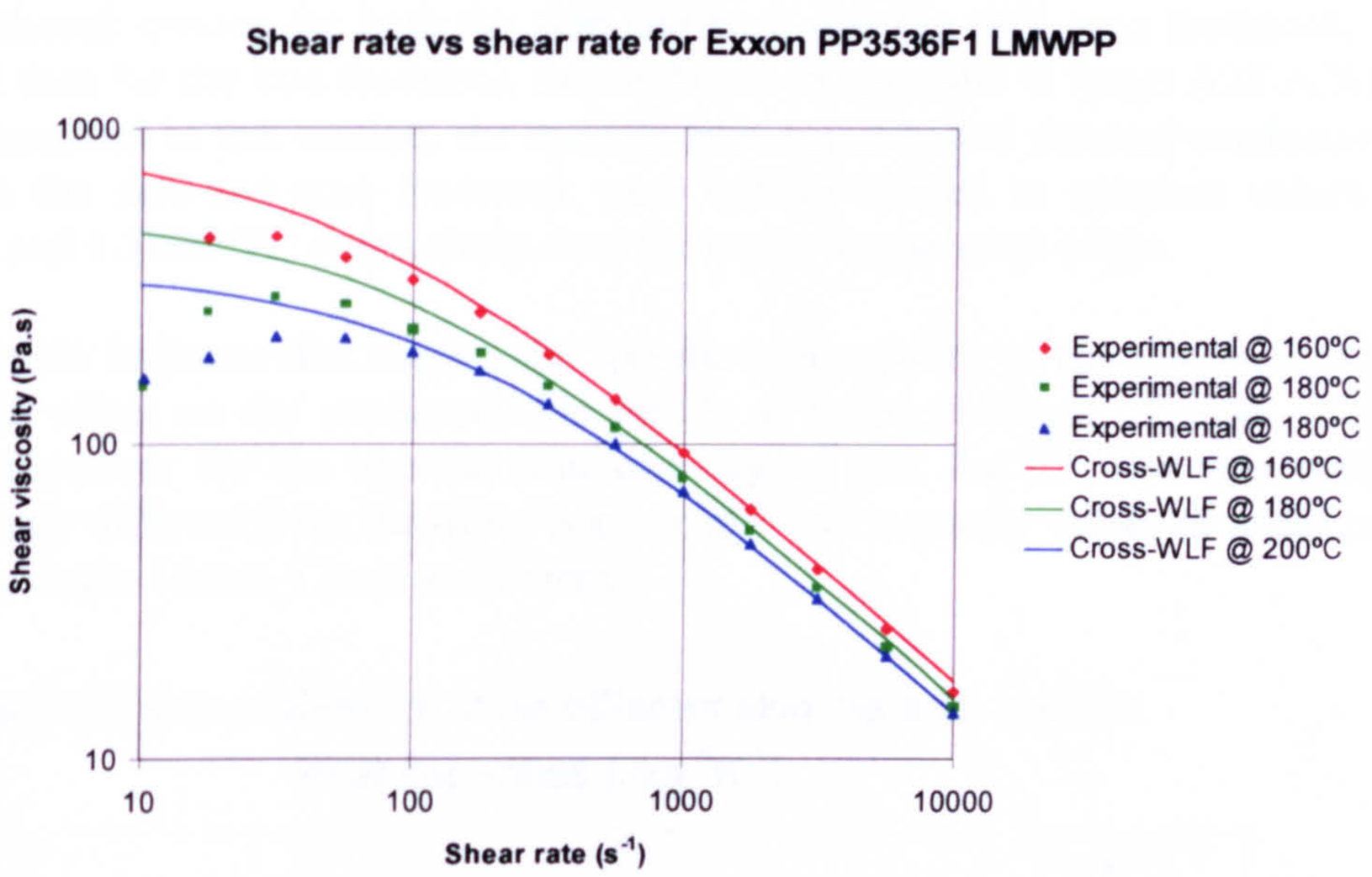

Figure 10.55 Experimental and Cross - WLF shear viscosity vs shear rate for Exxon PP3536F1 low molecular weight polypropylene

For the Exxon polypropylene, it was apparent that the viscosity falls at low shear rates. This is thought to be due to the presence of a slip layer. The viscosity data at low shear rates was not used in the determination of the Cross-WLF constants.

10.5 Powder co-injection computer modelling

This section presents the results of the computer modelling of the co-injection moulding of the 3 model PCM systems and the effect of varying the thermal properties of the PCM feedstocks on the predicted skin profile. For details on how the PCM green mouldings were selected from the co-injection moulding runs, the reader is directed to section 5.7. The reader is reminded that the predicted radial position has an error of $\pm$1 mm due to the mesh element size being 2 mm. The predicted skin thickness has an error of $\pm$0.25 mm due to twelve layers being used across a 6 mm cross-sectional thickness. The actual radial position vs skin thickness data were measured to an accuracy of 0.01 mm and have an error of $\pm$0.005 mm. The finite element mesh that was used is represented by figure 7.1, in section 7.1.

The reader is reminded that the thermal conductivity and specific heat capacity data of the feedstocks were experimentally determined under a heating regime due to limitations imposed by the equipment. Since the material being injection moulded undergoes rapid cooling within the mould cavity, the thermal conductivity and specific heat capacity data should have been obtained under a cooling regime, as this would simulate the actual thermal behaviour of the feedstock being injection moulded.

10.5.1 Effect of feedstock thermal properties on the predicted skin profile

The feedstock chosen for both the skin and core was the 60% iron feedstock, and the material data for the iron feedstock can be found in appendix G (page A25-A26). In the study described in this section, the specific heat capacity and thermal conductivity data for both the skin and core feedstock were initially altered to constant values of 500 $Jkg^{-1}K^{-1}$ and 1.5$Wm^{-1}K^{-1}$ respectively over the entire temperature range.

Figure 10.56 indicates that varying the specific heat capacity of the skin feedstock had a negligible effect on the predicted skin profile at radial positions of 9mm, 11mm and 23mm. However for the specific heat capacity of 200 $Jkg^{-1}K^{-1}$, the skin profile was significantly different from the other two specific heat capacity values at radial positions of 3mm, 5mm, 15mm, 17mm and 28mm.

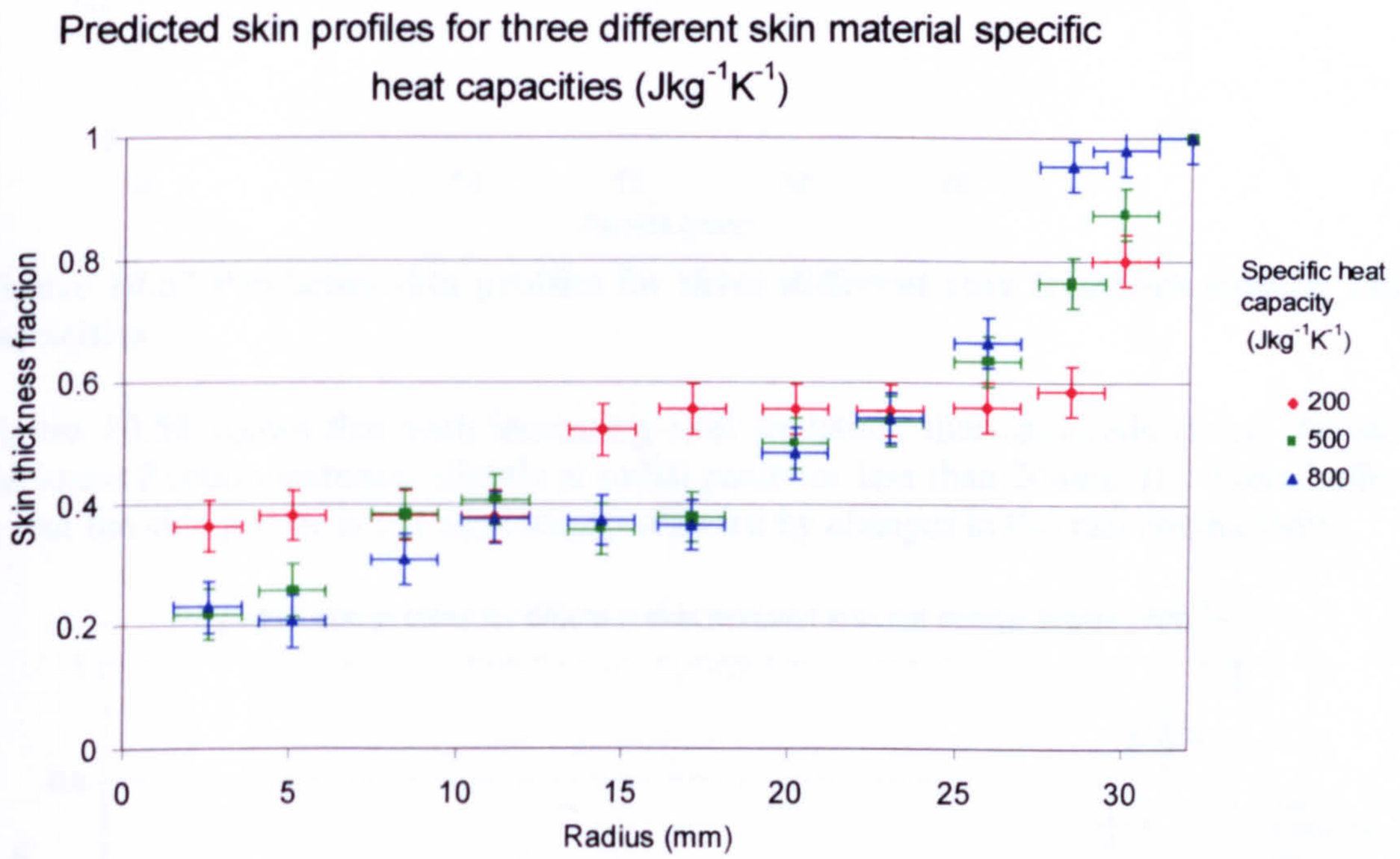

Figure 10.56 Predicted skin profiles for three different skin feedstock specific heat capacities

Figure 10.57 illustrates that altering the specific heat capacity of the core PCM feedstock had a negligible effect on the skin profile.

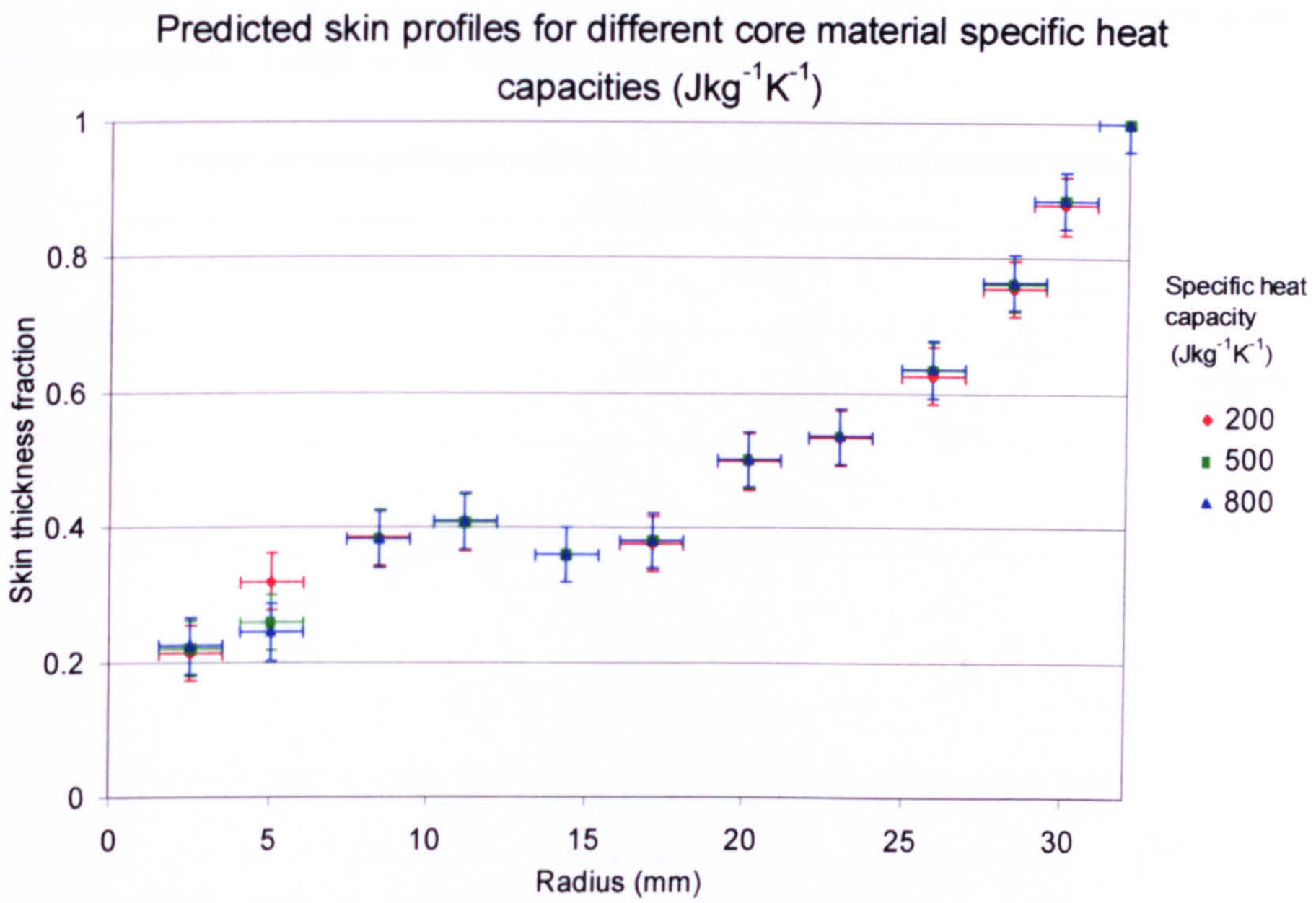

Figure 10.57 Predicted skin profiles for three different core feedstock specific heat capacities

Figure 10.58 shows that with increasing skin feedstock thermal conductivity, the skin thickness fraction increases slightly at radial positions less than 20mm. The overall effect is that the skin profile is not significantly affected by changes in thermal conductivity.

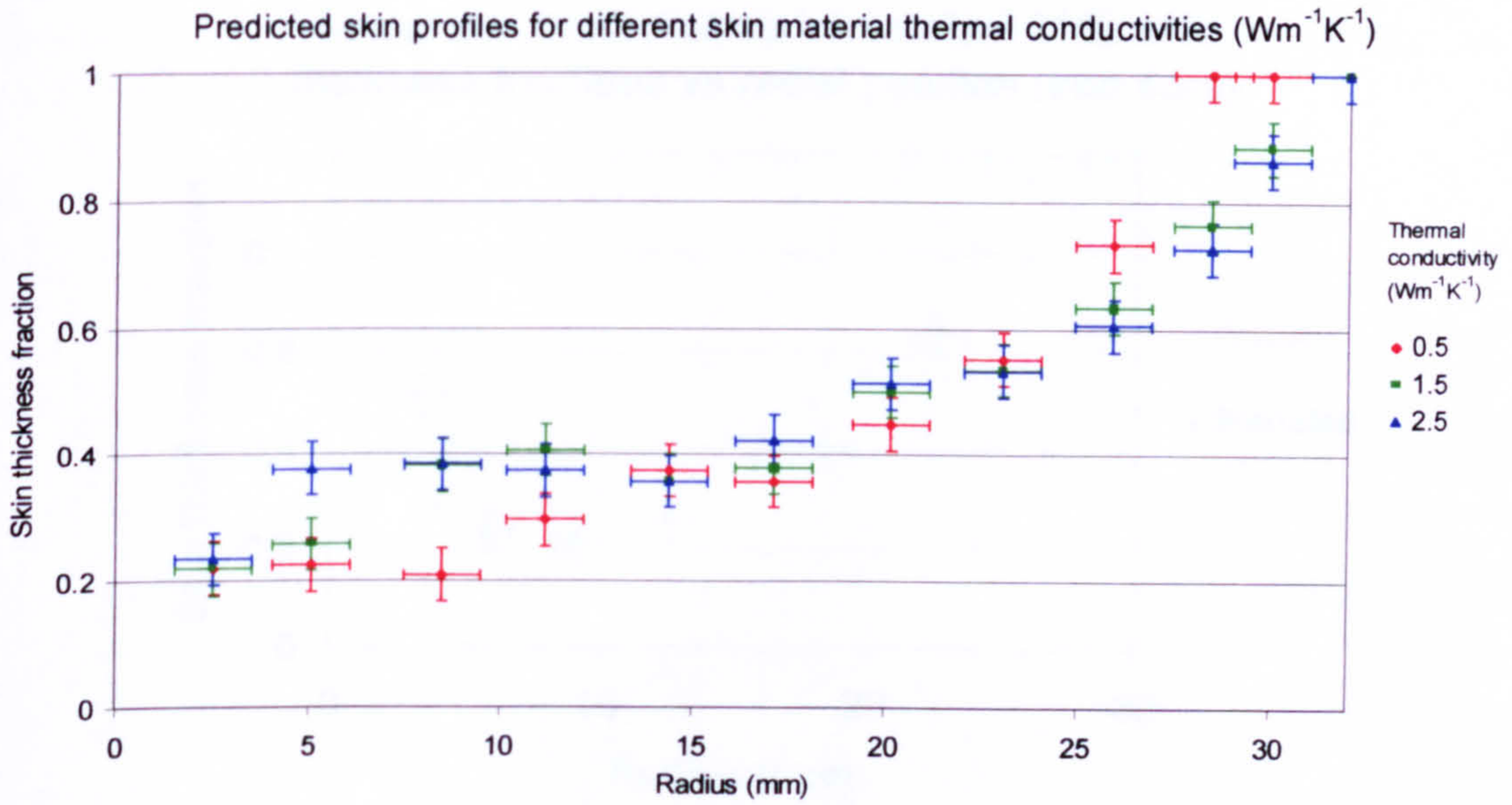

Figure 10.58 Predicted skin profiles for three different skin feedstock thermal conductivities

Figure 10.59 shows that when the thermal conductivity of the core feedstock is altered, there is negligible change in the predicted skin profile.

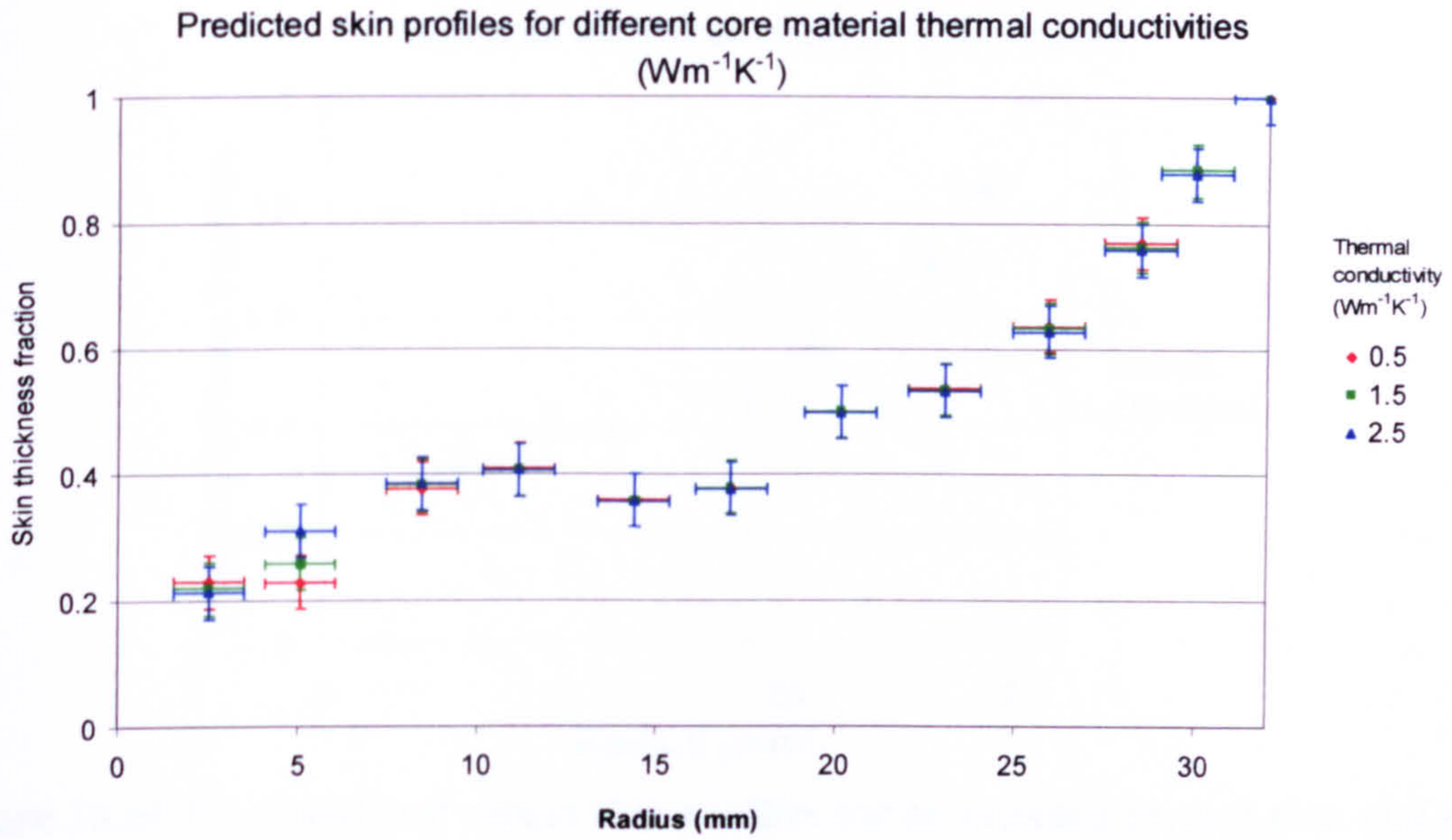

Figure 10.59 Predicted skin profiles for three different core feedstock thermal conductivities

10.5.2 Actual and predicted skin profiles for the three model PCM systems

The predicted and actual skin profiles for the co-injected stainless steel skin and iron core show reasonable agreement in figure 10.60.

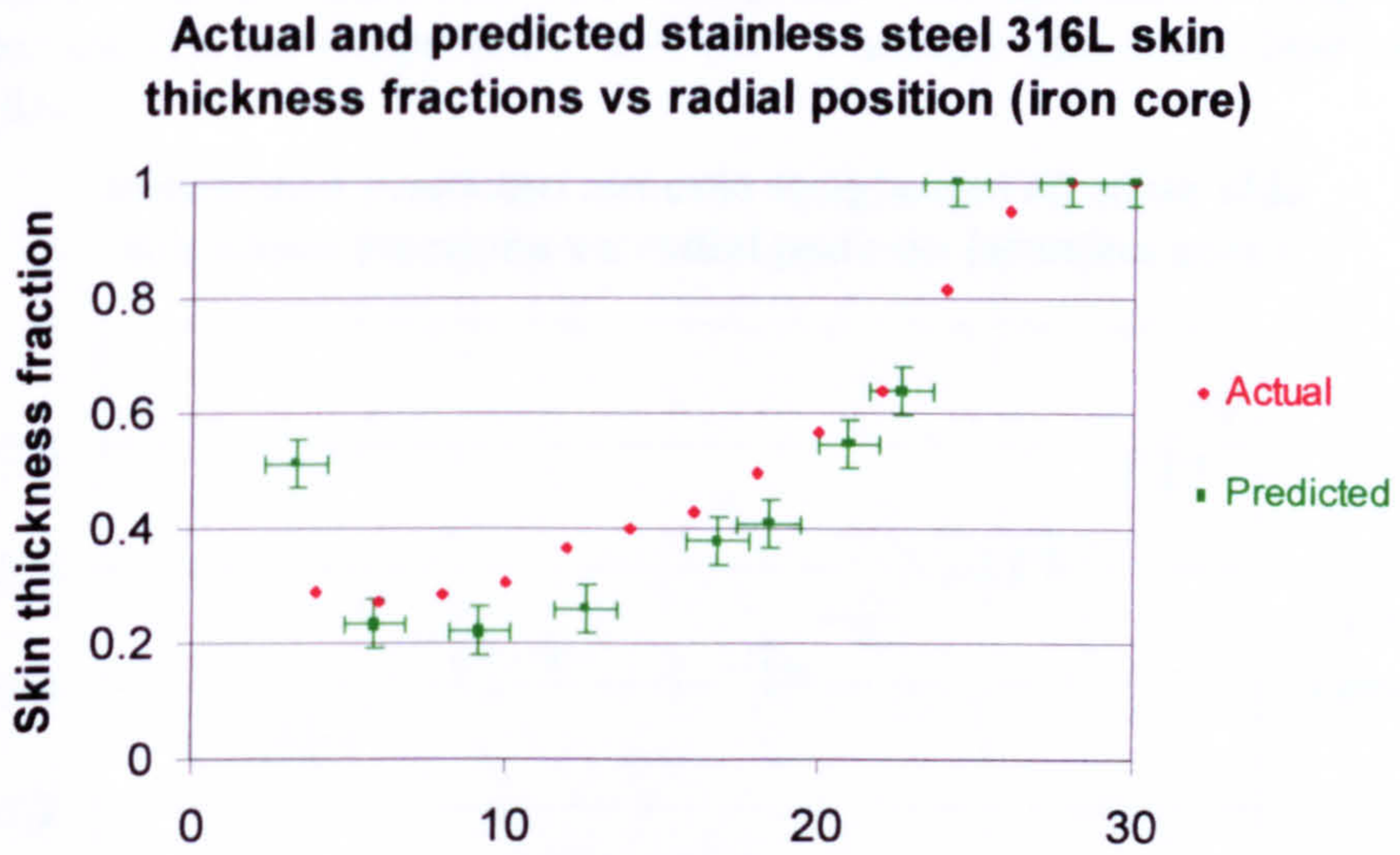

Figure 10.60 Predicted and actual skin profiles for co-injected stainless steel skin and iron core

The predicted and actual skin profiles for the cermet skin and iron core show reasonable agreement, as illustrated by figure 10.61.

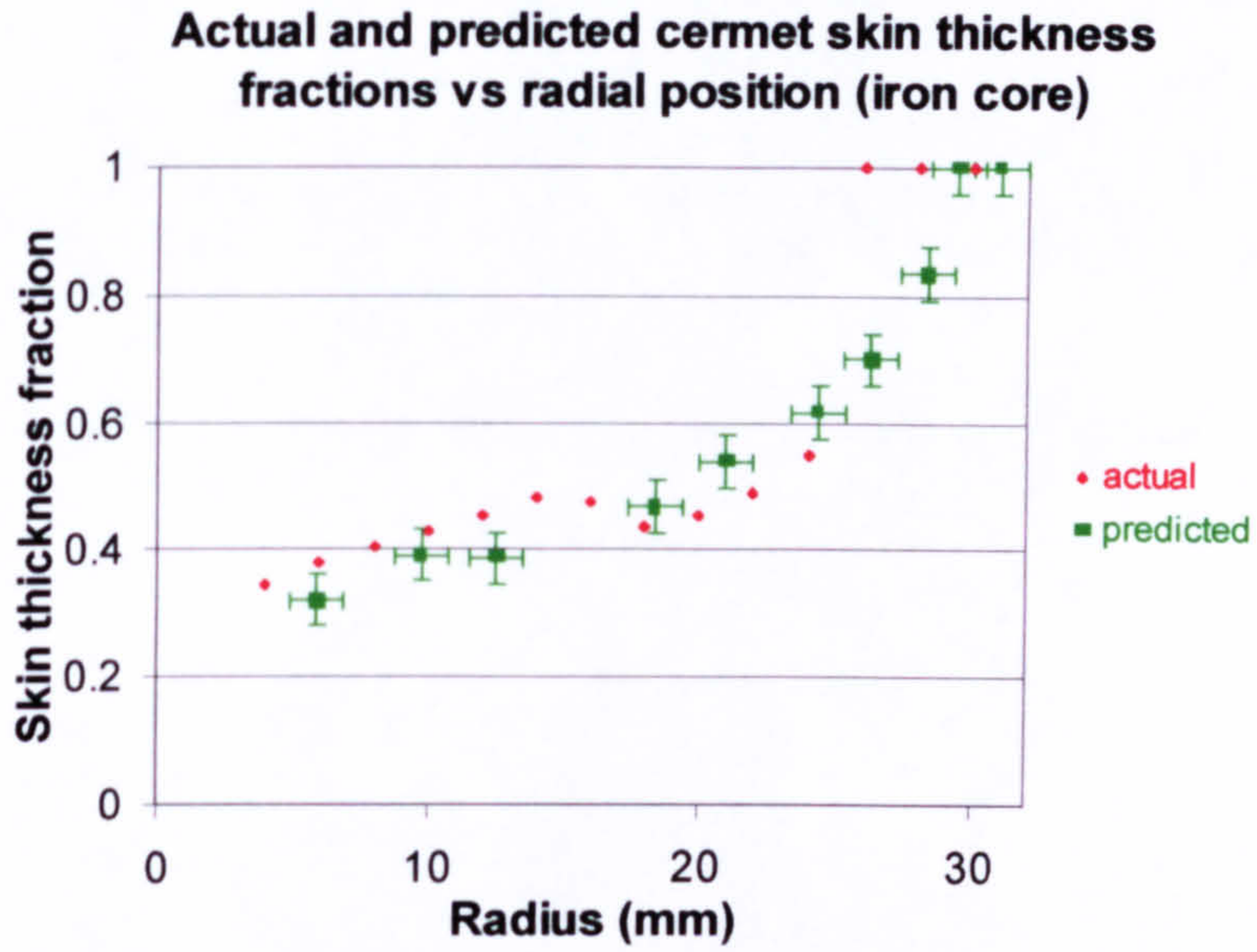

Figure 10.61 Predicted and actual skin profiles for co-injected cermet skin and iron core

The predicted and actual skin profiles for the zirconia toughened alumina feedstock skin and alumina feedstock core show reasonable agreement up to a radial position of 21 mm. After a radial position of 21mm, the predicted skin profile diverges significantly from the actual skin profile, for the remainder of the radial profile as illustrated by figure 10.62. As mentioned previously in section 8.8, there was evidence of intermixing between the skin and core ceramic feedstocks. The skin profile was determined using a travelling microscope, and the most appropriate skin-core boundary was determined as described in section 8.8.

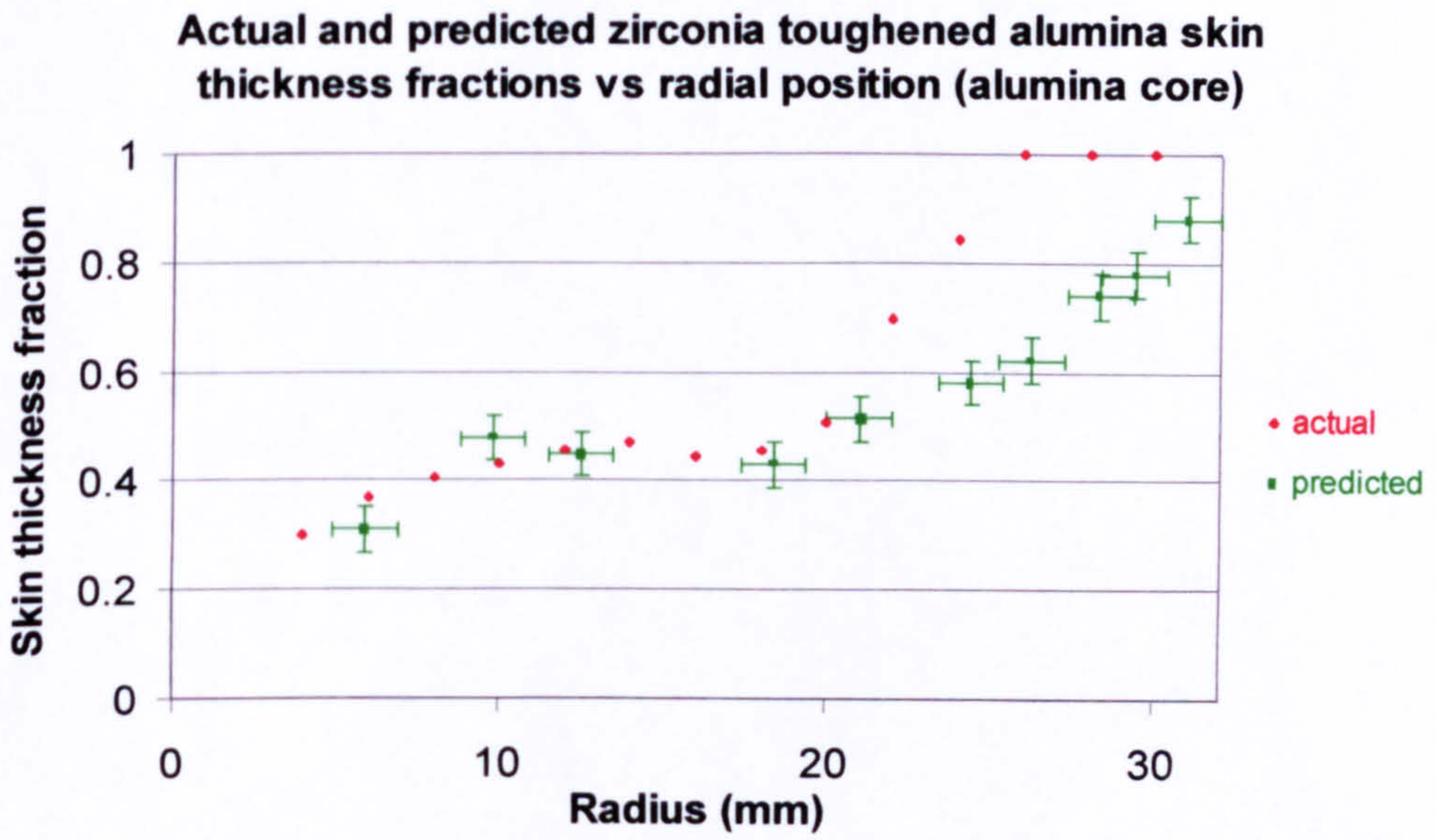

Figure 10.62 Predicted and actual skin profiles for co-injected zirconia toughened skin and alumina core

The skin profile disagreement for the latter half of the radial distribution is considered to be the consequence of a flow instability, which occurred during the mould filling stage of injection moulding. The sectioned sintered ceramic mouldings showed the presence of ears of skin material protruding into the core material, and indicated that during injection moulding, there was a flow instability, best described as turbulence. The origin of the flow instability is unclear, and merits further investigation. In addition, an investigation could be undertaken to ascertain whether the core region was symmetrical within the powder co-injected mouldings.

The reader is reminded that the asymmetry of the core material regions has been ignored in these comparisons

11 Discussion

This section discusses the results obtained from the experimental work and their implications for the PCM process.

11.1 Design flowchart of the PCM process

The conclusions drawn from the experimental work and the results were used to draw up a list of critical design steps for feasible PCM. The list of design steps was rearranged in order of descending importance. This was then incorporated into the standard PIM methodology as illustrated by figure 1.3 and converted into a flow chart with several decision points. The decision points were tailored to cater for the material processor's desired requirements. Figures 11.1, 11.2 and 11.3 illustrate the entire design process for PCM with a skin profile control methodology built in as determined by the experimental results. Each stage of the flow chart will be discussed in greater detail in this chapter. Figure B in figure 11.1 refers to figure 11.2. Figure C in figure 11.1 refers to figure 11.3.

The most important criteria for successful PCM is governed by the requirement that there are no gross defects in the finished final components. PCM components contain a skin and a core, that were initially distinctly separate powders. These powders densify during sintering and form bulk components. If the sintering profiles of the skin and core are not compatible, it will not be possible to correct powder incompatibilities anywhere else in the PCM process. It is considered that work should be carried out to check for sintering compatibility between the skin and core powder before proceeding further into the PCM process. This is the first decision point in the flowchart illustrated by figure 11.1. A whole flowchart, figure 11.2, deals with techniques available to achieve sintering compatibility between the skin and core powders. The second decision point, in figure 11.1 caters for the scenario where skin profile control is a key requirement. The methodology for achieving skin profile control is outlined in figure 11.3. Once the feedstocks required are compounded, the rest of the flowchart, in figure 11.1 is nominally identical to conventional PIM.

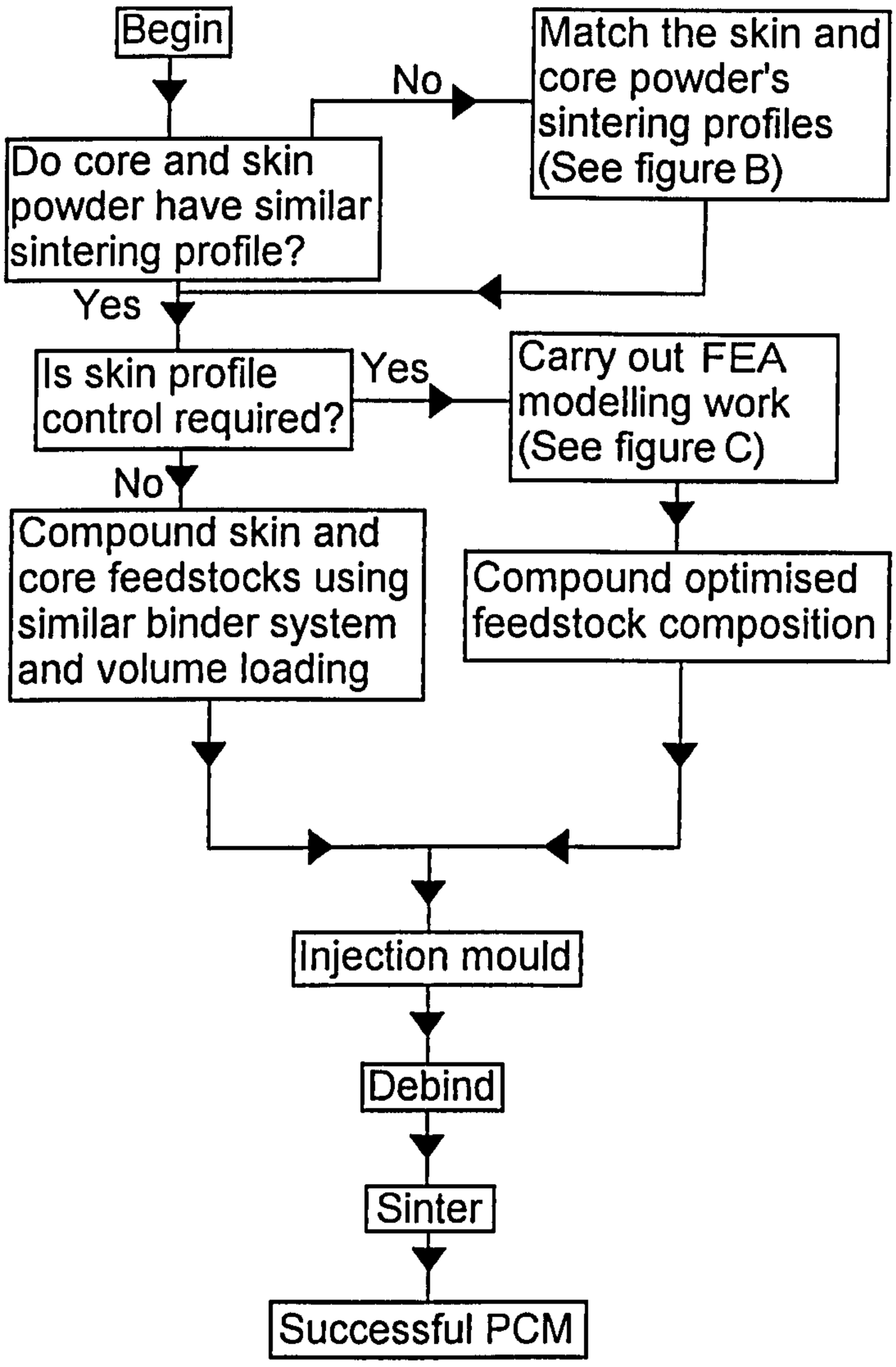

Figure 11.1 Flow chart of the complete powder co-injection moulding process

The flowchart in figure 11.2 has a three-way decision point to identify the nature of the powders being injection moulded. It offers tailored techniques for matching the sintering profile and has two possible outcomes. If the sintering profiles are compatible, then the materials processor can continue on with the PCM process. If sintering compatibility is not achievable, then there is little point in proceeding any further. The rest of the PCM process will be successful except for the final stage of sintering.

The technique of using a masteralloy powder with a base powder is useful where the alloy sinters at a different rate to the non-alloy powder. If the alloy can be made from a mixture of base powder and alloying additions, then further opportunities for sintering equalisation exist.

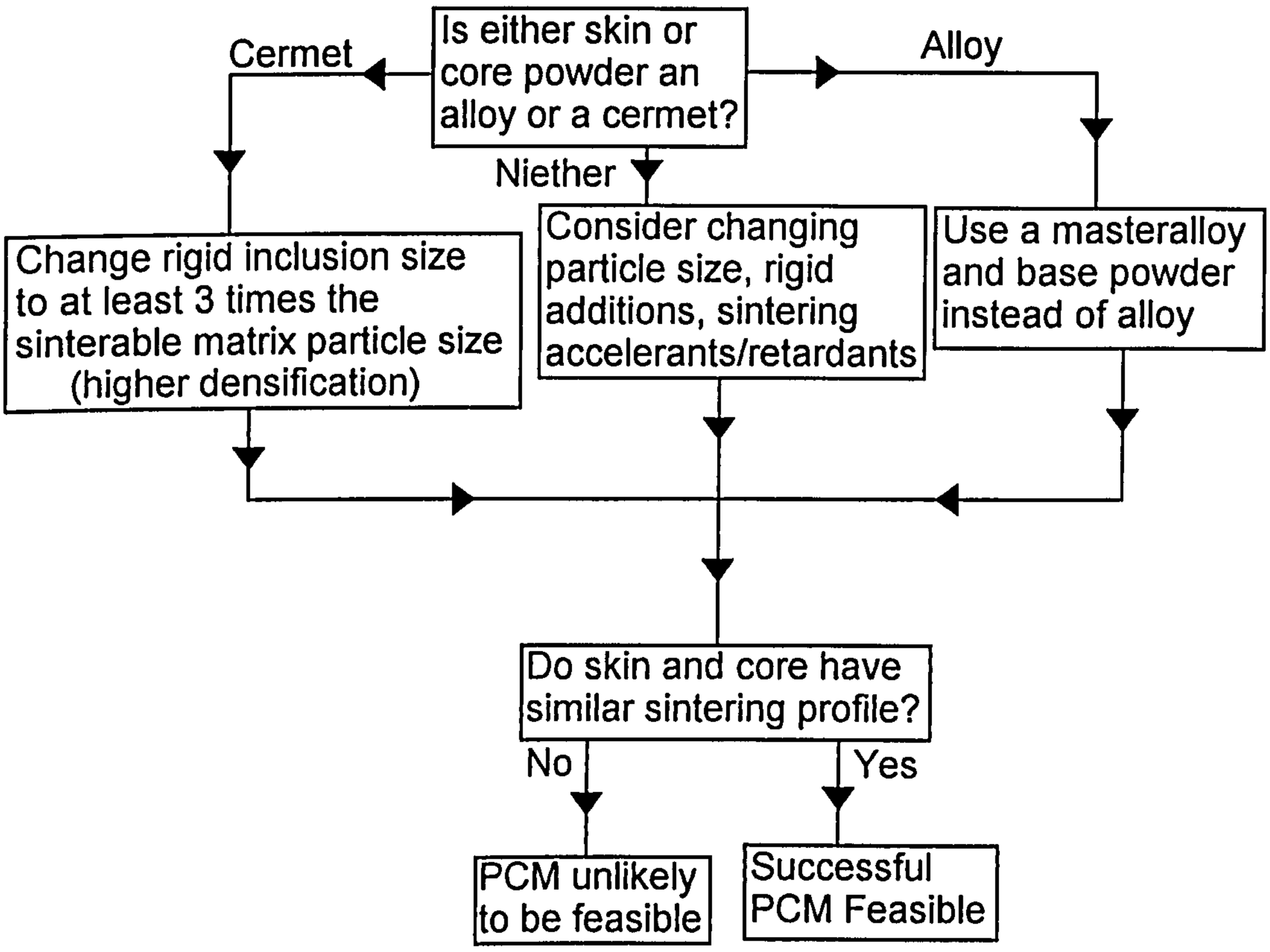

Figure 11.2 Flowchart for matching skin and core powder system sintering profiles

The flowchart in figure 11.3 deals with the necessary steps to achieve a desired skin profile, by the use of finite element analysis to determine the process conditions and the feedstock material properties. First pass models can then be used to obtain the required feedstock composition to achieve the required specific heat capacity, PVT and thermal conductivity. At the present time, no suitable first pass model for the rheology is available, so an iterative loop was inserted to check the rheology of the sample feedstock.

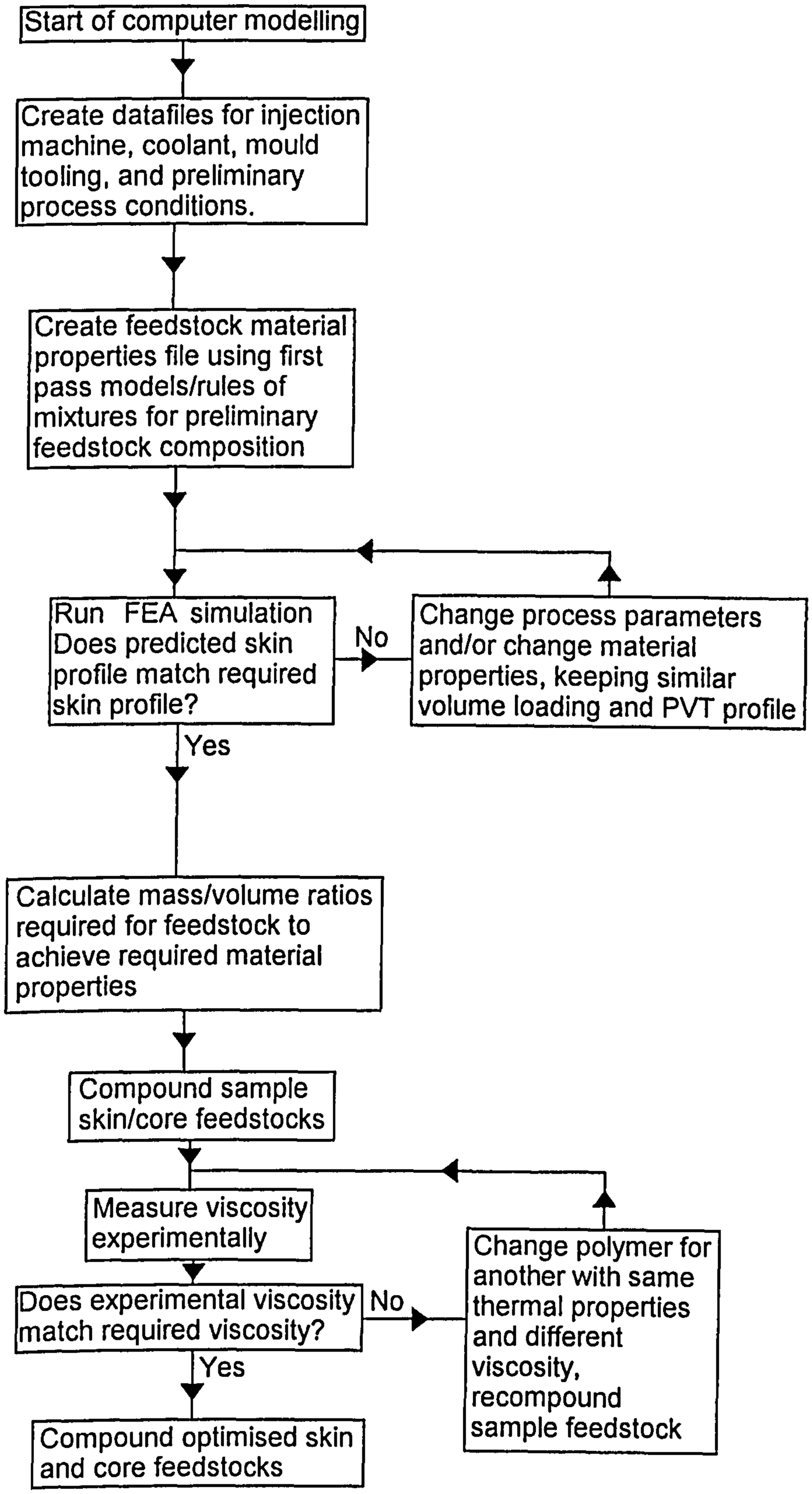

Figure 11.3 Computer modelling flowchart

11.2 Skin and core sintering compatibility

The most important factor which determines the feasibility of PCM is the sintering behaviour of the skin and core powders. Figure 11.4 shows some example sintering profiles for three different example powders. From figure 11.4, it is apparent that if powders A and B have different densification rates, then differential shrinkage will occur during sintering. German[63, pp 484-487] and Mutsuddy and Ford[12, pp321] state that differential shrinkage will lead to the formation of residual stresses in the mouldings.

If the residual stresses in the mouldings exceed the skin-core interfacial bond strength, then the interface will delaminate. This would be an unacceptable defect, leading to the rejection of the sintered PCM components. If the residual stresses do not exceed the interfacial bond strength between powder A and B, then the residual stresses will result in warpage or distortion of the powder co-injected mouldings. Warpage is the bending or twisting of the mouldings. An example of shape distortion is where the aspect ratio has altered during sintering. The acceptance or rejection of such shape distortion or warpage will be dependent on the final required dimensional and geometrical tolerances for the final application. This in turn, determines the level of acceptable residual stresses, which also determines the acceptable differential shrinkage tolerances.

If powders A and C have identical densification rates, but only powder A reaches full density, and powder C reaches an intermediate level of densification, then differential shrinkage has occurred, and remains after sintering has completed. There are many reasons for powder C's inability to attain full density. One example is excessive grain growth as reported by Baik and Bae[201]. Another example is constrained sintering, as reported by Rahaman[91].

If powder C is the core and powder A is the skin, then compressive stresses will occur as a result of the skin densifying more than the core. The end result will be that the skin will crack or the core will be under compressive forces. The compression of the core may cause it to sinter more densely, or lead to the residual stresses being frozen into the mouldings after sintering. If powder A is the core and powder C is the skin, the core will densify more than the skin. If the interface bonding strength is greater than the level of residual stresses, then the core will pull the skin material with it as it densifies, distorting and warping the skin. If the residual stresses are greater than the interface bonding strength, then the interface will delaminate. The acceptance or rejection of skin distortion will depend on the level of dimensional tolerances deemed acceptable. Delamination within a moulding is an unacceptable defect, leading to its rejection.

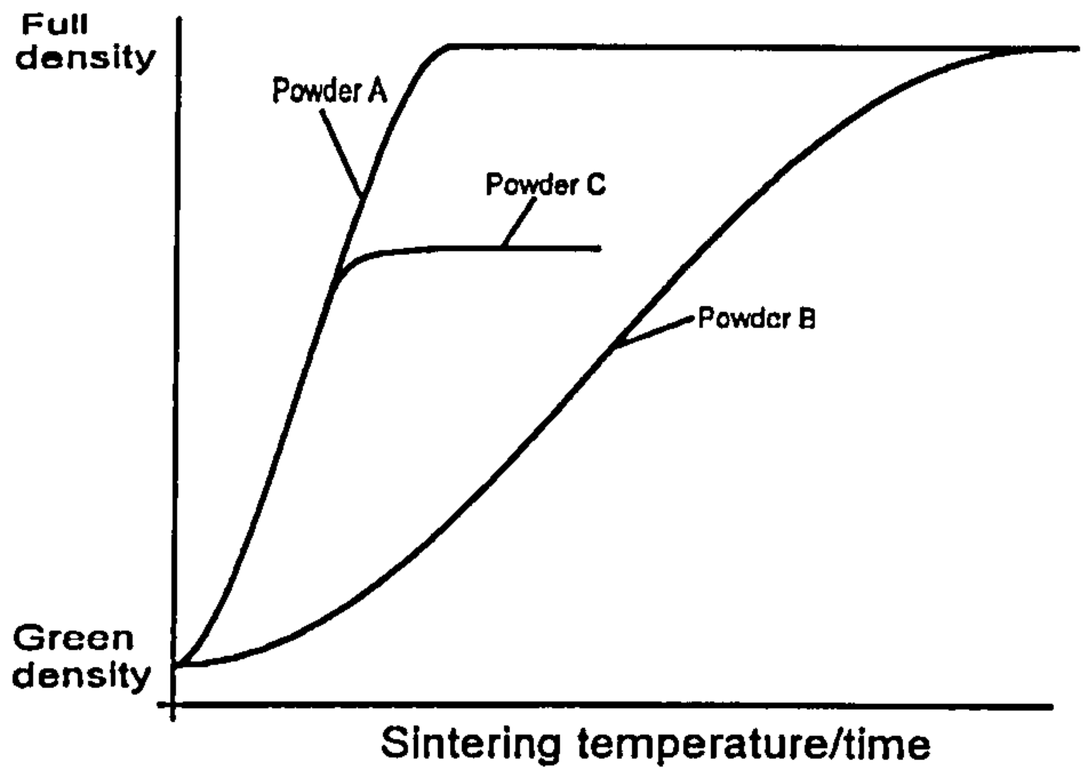

Figure 11.4 Sintering profiles of three distinct powders

To achieve successful PCM, it is vital that the skin and core powder systems are optimised, such that their sintering rates are nominally identical at all points of the sintering temperature/time profile and achieve full densification at the same point of temperature and time. If the initially selected skin powder and core powder do not have compatible sintering profiles, there are numerous methods available to match their sintering profiles. This is discussed further in sections 11.3 to 11.6 inclusive.

11.3 Effect of rigid inclusion size on the densification of cermets

It has been demonstrated during the experimental work on the die pressing of the alumina and iron cermet composites that the alumina particle diameter affected the densification of the cermets. Comparing the SEM images in figures 8.11, 8.12, 8.13, 8.14, 8.15 and 8.16 it was apparent that increasing the alumina particle inclusion diameter increased the densification of the iron matrix. This was further confirmed by density measurements, illustrated by figure 8.17. This is in general agreement with Weiser and De Jonghe[202], Kimura et al.[203], Lafer et al.[82], Besson and Evans[83], Taylor et al.[84], Thibault and Bouvard[85], Zavaliangos et al.[86], Lange et al.[87], Yamaguchi et al.[88], Fan and Rahaman[89] and Turner and Ashby[90] as they collectively conclude that the retarding effect on the sintering of the composite increases with decreasing particulate inclusion diameters at constant volume fractions.

An attempt was made to examine mathematically the effect of altering the particle inclusion diameter on the total number of inclusion particles for a constant volume fraction. This was done to offer a possible explanation for the results obtained in the die pressing of iron-alumina cermet pellets.

The volume of a sphere of radius r, is:

$$V_s = \frac{4\pi r^3}{3} \qquad \text{Eqn (11.1)}$$

Where V_s = Volume of a single sphere

r = Radius of a single sphere

If there are n spheres of similar radius, the total volume of the n spheres is:

$$V_t = \frac{n4\pi r^3}{3} \qquad \text{Egn (11.2)}$$

Where V_t = Total volume of all of the spheres
n = Total number of spheres

Thus for the rigid non sinterable alumina inclusions:

$$\frac{n_p 4\pi r_p^3}{3} = V_p \qquad \text{Eqn (11.3)}$$

and for the sinterable iron matrix particles:

$$\frac{n_m 4\pi r_m^3}{3} = V_m \qquad \text{Eqn (11.4)}$$

Where: r_m = Radius of the iron matrix particles
r_p = Radius of the rigid alumina inclusions
n_m = Number of iron matrix particles
n_p = Number of rigid alumina inclusions
V_m = Total volume of iron matrix particles
V_p = Total volume of rigid alumina inclusions

Since the volume fractions are known, the ratio of rigid alumina inclusions to the iron matrix particles can be calculated:

$$\frac{V_p}{V_m} = \frac{\frac{n_p 4\pi r_p^3}{3}}{\frac{n_m 4\pi r_m^3}{3}} \qquad \text{Eqn (11.5)}$$

Equation 11.5 simplifies to:

$$\frac{V_p}{V_m} = \frac{n_p}{n_m}\left(\frac{r_p}{r_m}\right)^3 \qquad \text{Eqn (11.6)}$$

and rearranging equation 11.6 yields:

$$\frac{n_m}{n_p} = \frac{V_m}{V_p}\left(\frac{r_p}{r_m}\right)^3 \qquad \text{Eqn (11.7)}$$

Equation 11.7 illustrates that if the volume ratio of matrix particles to rigid inclusions is kept constant, the number ratio of the matrix particles to the rigid inclusions is directly proportional to the cube of the radius ratio of the rigid inclusions and the matrix particles. Equation 11.7 was used to generate figures 11.5 and 11.6 to illustrate the effect of varying the diameter ratio of the alumina to the iron powders on the number ratio of alumina to iron particles. Figure 11.5 shows that as the ratio of inclusion and

matrix diameter decreases below 1, the number ratio of rigid inclusions to the matrix particles increases exponentially. When the ratio of the rigid inclusions to the matrix diameter is greater than 1, the number ratio of rigid inclusions to matrix particles is relatively low and within the same order of magnitude.

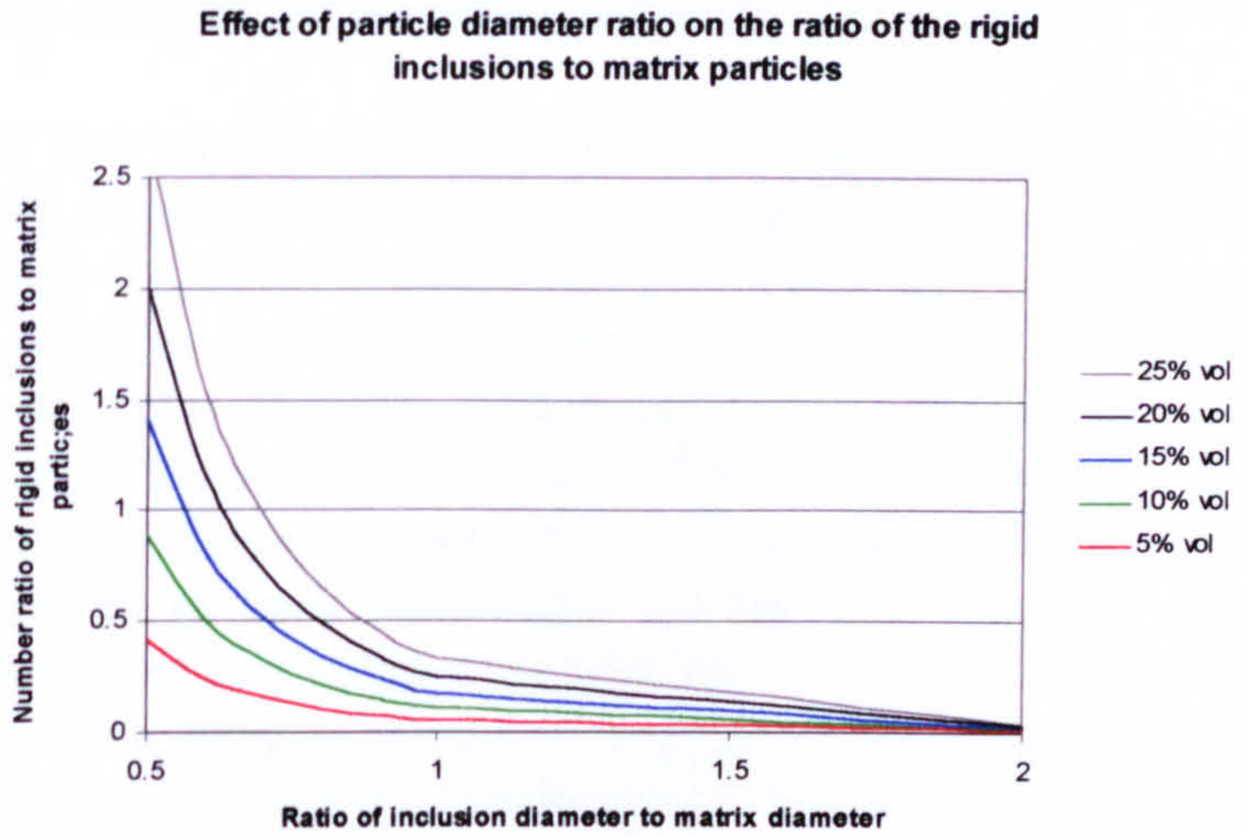

Figure 11.5 Effect of the radius ratio of the alumina inclusions to the iron matrix particles on the quantity ratio of rigid alumina particles to iron matrix particles. (the radius ratio range was selected to be from 0.5 to 2)

The effect of particle size ratio on the number ratio was re-plotted using logarithmic axes to cover a wider range of particle size ratios as illustrated by figure 11.6. This illustrates that for a rigid inclusion volume loading of 15% for a matrix particle diameter of 5.0μm, there are 176 0.5μm diameter rigid inclusions for every single matrix particle. There are nearly 3 matrix particles to every single 4.0μm diameter rigid particle and there is a single particle of 13.0μm diameter rigid inclusion for every 100 matrix particles.

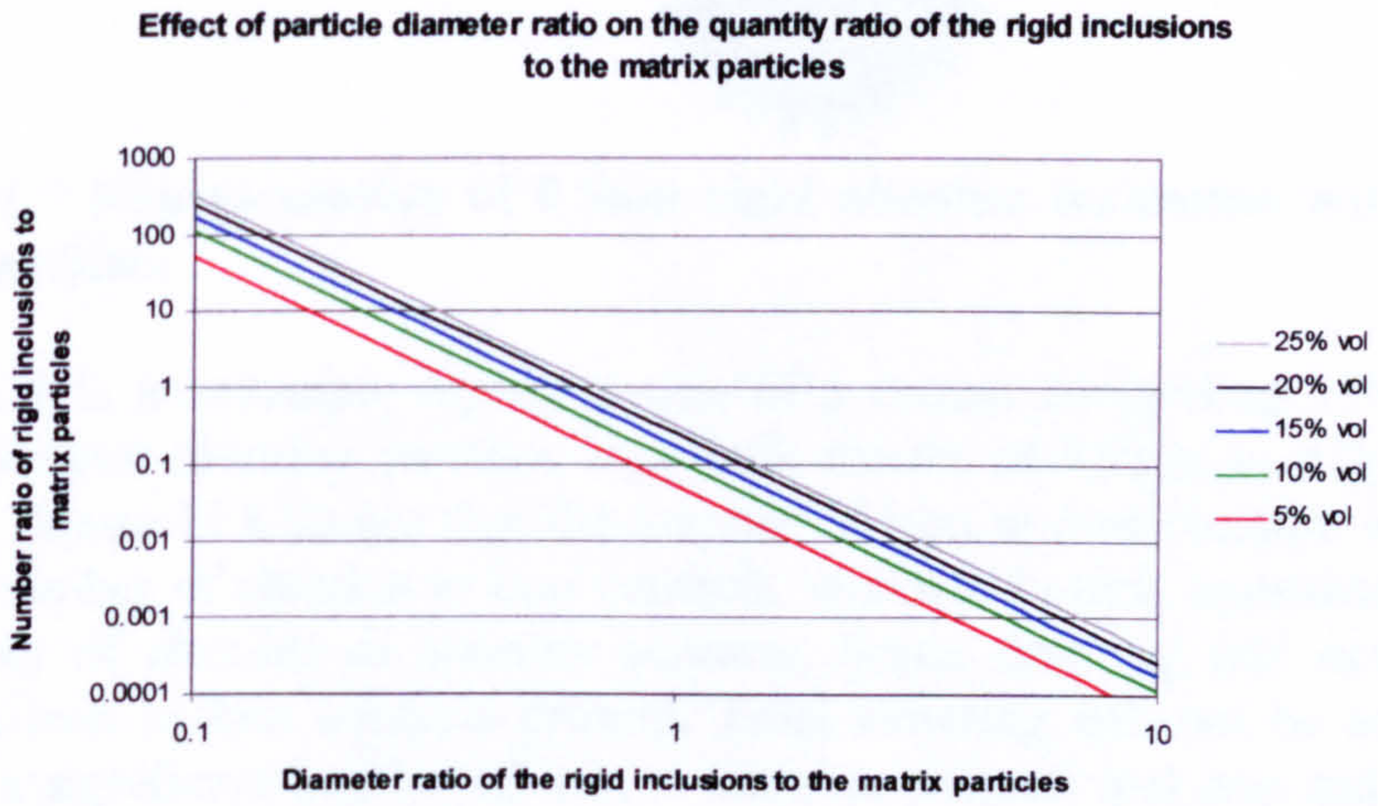

Figure 11.6 Effect of the radius ratio of the alumina inclusions to the iron matrix particles on the quantity ratio of rigid alumina particles to iron matrix particles. (The radius ratio range was selected to be from 0.1 to 10, which covers the experimental radius ratios encountered in the present work.)

The particle ratios refer to the volume, so to obtain the relative particle ratios in terms of area, the numbers were raised to the power of 2/3 for the purpose of figures 11.7, 11.8 and 11.9. The black circles represent iron matrix particles and the grey circles represent rigid inclusions of alumina. The diameters chosen for both powders were selected from the die pressing work for the purposes of figures 11.7 to 11.9.

Figure 11.7 is an example representation of a cermet comprising 15% by volume of 0.5μm diameter alumina particles in a bulk matrix of 4.0μm to 6.0μm diameter iron powder particles. Figure 11.7 illustrates that where the alumina particles are smaller than the iron particles, the number of iron to iron contacts is extremely low. There are high numbers of iron to alumina contacts and there is also a high quantity of alumina to alumina contacts. If there is a low number of iron to iron contacts, this implies that there is a low probability of possible potential neck formations. This implies that sintering is effectively retarded as neck formations are the first stage of sintering. The cermet sintering temperatures encountered are typically 1250°C and despite the high numbers of alumina to alumina particle contacts, negligible sintering will take place between alumina particles as the sintering temperature is too low. With decreasing diameters and increasing volume loading of the rigid inclusions, there is a higher probability of rigid inclusion agglomerates forming. The internal porosity of the inclusion agglomerates becomes increasingly inaccessible to the matrix material.

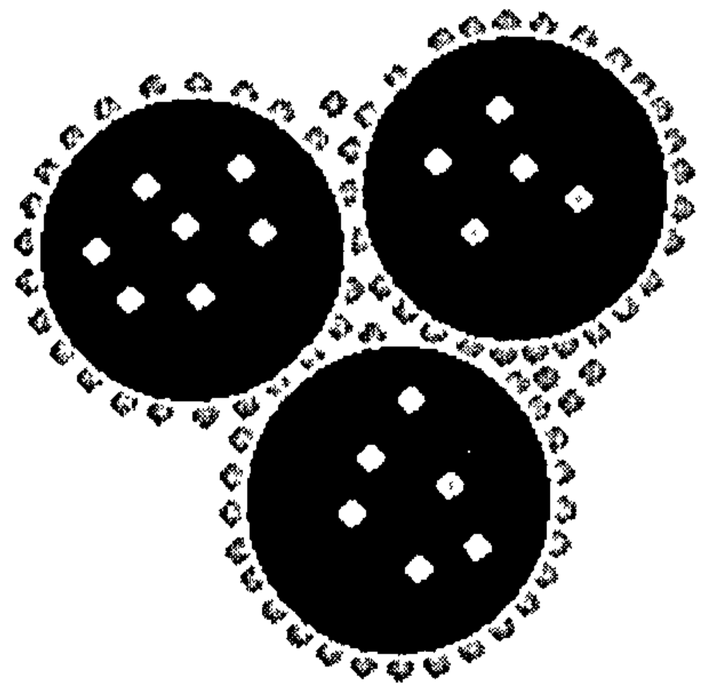

Figure 11.7 Representation of 0.5μm rigid alumina inclusions within 5.0μm iron matrix particles

Figure 11.8 is an example representation of a cermet comprising 15% by volume of 4.0μm diameter alumina particles in a bulk matrix of 4.0μm to 6.0μm iron powder particles. Figure 11.8 shows that the number of iron to iron contacts is slightly higher than the number of alumina to iron contacts, which is in turn, considerably higher than the number of alumina to alumina contacts. Some sintering will occur as there are numerous iron to iron contacts present. Total sintering will not be achieved because there are a significant number of iron to alumina contacts and iron and alumina do not sinter readily with each other. There is a possibility that as the cermet sinters, implying a reduction in volume, the rigid alumina inclusions could form a mechanically interlocking rigid network throughout the mouldings and thus limit the amount of sintering shrinkage taking place. The probability of a mechanically interlocking network of rigid alumina inclusions forming during sintering increases with increasing rigid alumina inclusion volume loading.

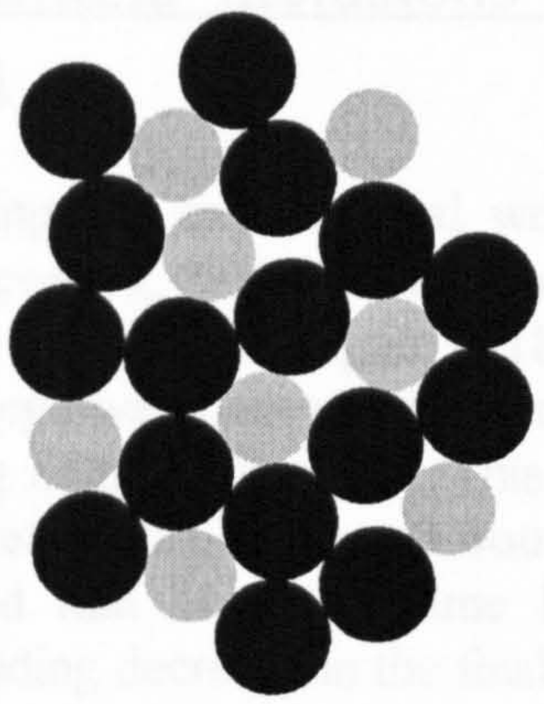

Figure 11.8 Representation of 4.0μm rigid alumina inclusions within 5.0μm iron matrix particles

Figure 11.9 is an example representation of a cermet comprising 15% by volume of 13.0μm alumina particles in a bulk matrix of 4.0μm to 6.0μm iron powder particles. Figure 11.9 shows that the number of iron to iron contacts is significantly higher than the number of alumina to iron contacts. The number of alumina to alumina contacts is extremely low. Substantial sintering will occur as there are numerous iron to iron contacts present, implying a high number of potential neck formations, which is the initial stage of sintering. With increasing rigid alumina inclusion size, implying a lower number of alumina particles, the greater the distance between adjacent alumina particles for the same volume loading. It is considered that the probability of a mechanically interlocking network of alumina particles during sintering is reduced, and sintering is then achievable. This permits higher volume loadings of alumina to be used before mechanical interlocking occurs during sintering. It is emphasised that the influence of rigid alumina inclusions on the sintering behaviour of the iron matrix powder is relative to the sintering behaviour of a pure 100% iron matrix powder, as other variables, for example, the iron matrix powder size influences sintering as well as the rigid inclusions to matrix powder particle diameter ratio.

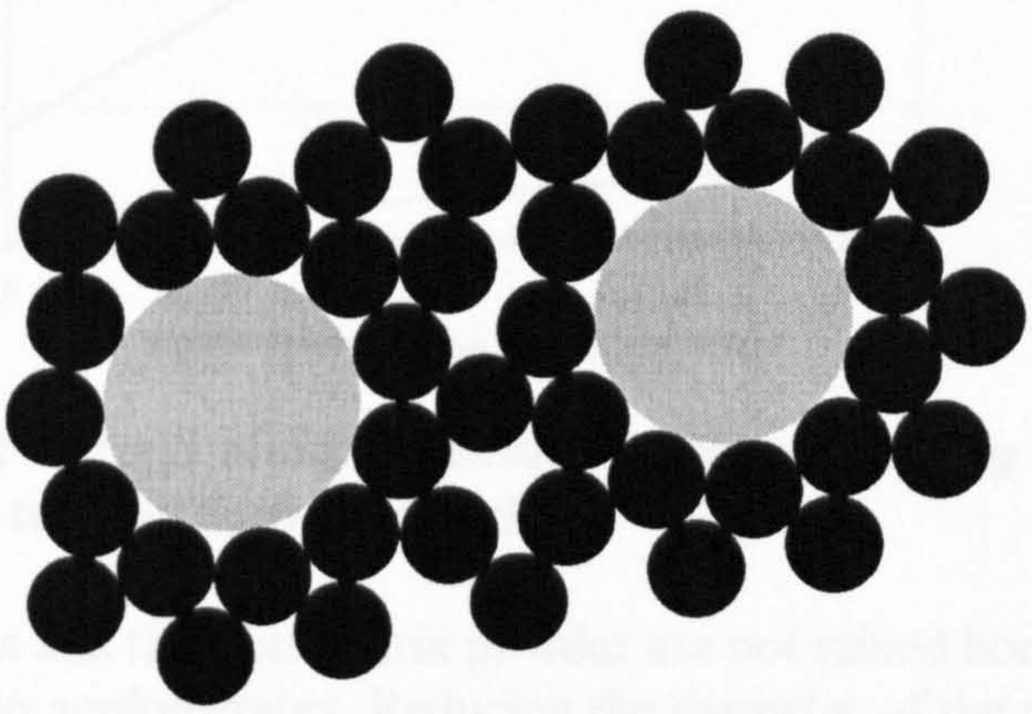

Figure 11.9 Representation of 13.0μm rigid alumina inclusions within 5.0μm iron matrix particles

11.4 Effect of rigid alumina inclusions volume loading on the densification of cermets

It has been demonstrated during the experimental work on the die pressing of the alumina and iron cermet composites, that the alumina volume loading affected the densification of the cermets as illustrated in figure 8.18. It was demonstrated that the alumina volume loading had a negative effect on the cermet densification, which became less pronounced with increasing alumina diameter. This agrees with the previous work carried out by Rahaman[91], Li et al.[78], Delie and Bouvard[92] and Kimura et al.[203] and they collectively concluded that as the volume loading of the rigid inclusions increased, there was a corresponding decrease in the final sintered density.

Equation 11.7 was used to generate figure 11.10. Figure 11.10 illustrates the effect of powder volume loading on the ratio of rigid alumina inclusions to iron matrix particles. If the volume loading of the rigid alumina inclusions were to be increased further, there would be an upper limit to the highest possible rigid alumina inclusion volume loading, because a rigid, interlocking network of rigid alumina inclusions would form, and this is discussed further by Li et al.[78]. This would limit the amount of shrinkage possible as the sintering temperatures encountered do not permit the sintering of alumina particles to other adjacent alumina particles, resulting in a porous cermet.

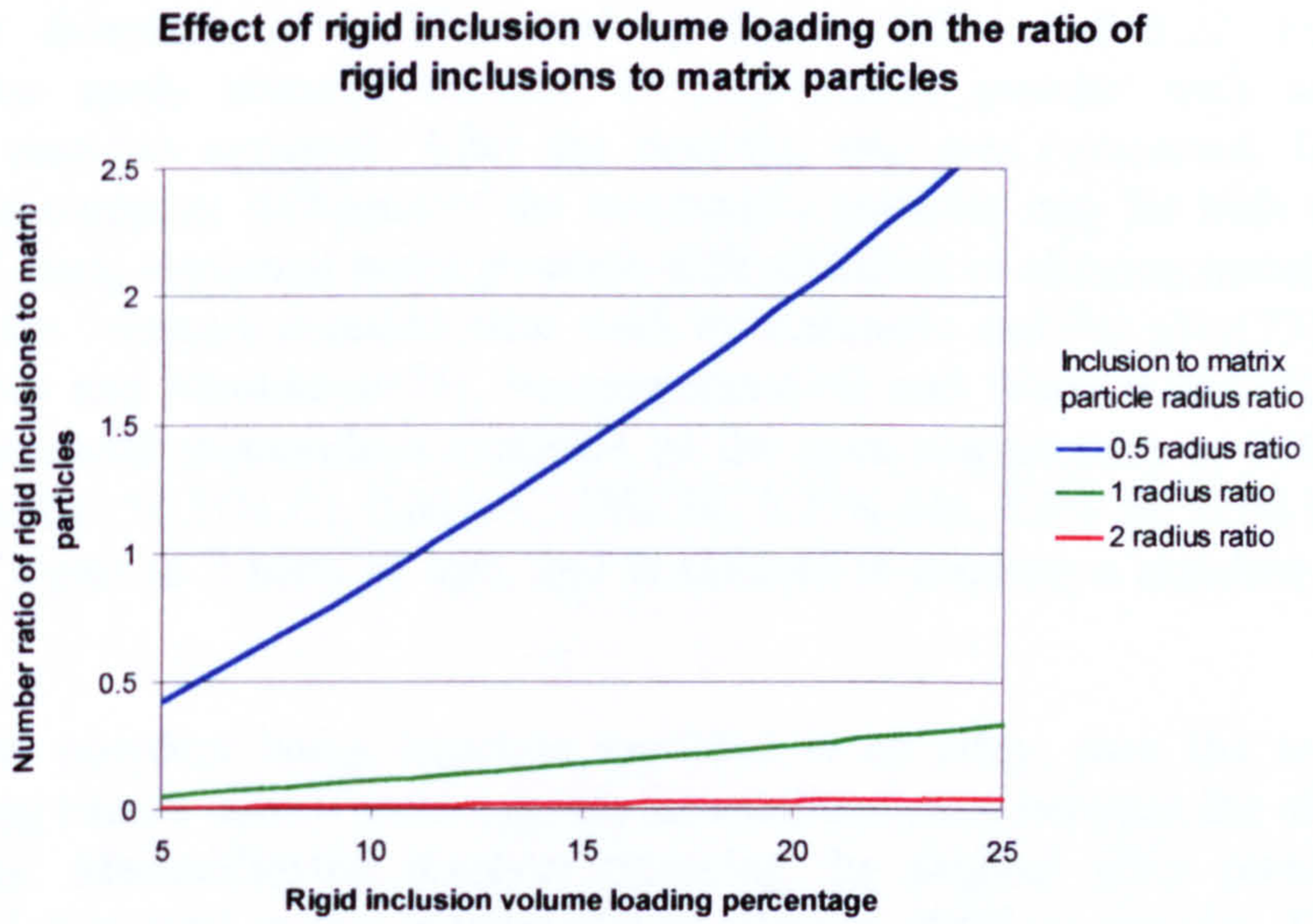

Figure 11.10 Effect of rigid alumina inclusion volume loading on the ratio of rigid alumina inclusions to iron matrix particles

If the rigid inclusions and the iron matrix powder are not mixed homogeneously, this will lead to rigid inclusion agglomerates. Reducing the diameter of the rigid inclusions means that the number ratio of rigid inclusions to the matrix particles is more influenced by rigid inclusion volume loading variations. Rigid inclusion agglomerates have higher levels of rigid inclusion volume loadings than for the rest of the bulk cermet. This would be a potential source of differential sintering throughout the mouldings and is another reason

would be a potential source of differential sintering throughout the mouldings and is another reason for choosing the rigid inclusion diameter to be at least 3 times the matrix powder diameters. If rigid inclusion agglomerates form during the compounding stage, then the effect of the powder system inhomogenieties on the sintering behaviour of the cermet will be affected by the particle size of the rigid inclusions.

It is concluded that for sintering compatibility to be achieved for a cermet-based feedstock, care must be exercised over the choice of volume loading and size of the rigid inclusions. It is suggested that mathematically-based sintering models in the open literature such as the master sintering curve could be adapted to predict the sintering of composites. This could incorporate the effect of the ratio of particle diameters and rigid inclusion volume loadings on the relative numbers of sinterable particle to sinterable particle contacts and the number of sinterable to rigid non-sinterable inclusions.

11.5 Sintering of alloy powders

During the experimental phase of the present work, it was demonstrated that a metal alloy powder could be substituted for an elemental metal matrix powder and additions of alloying metals. This was demonstrated experimentally in the model corrosion resistant system of an iron core and stainless steel skin, by using a 66% mass iron powder and 33% mass of alloying elements instead of 100% stainless steel alloy, with no apparent delamination as illustrated by figures 8.21a and 8.22. Figure 8.22a illustrates the partly sintered mixture of iron matrix powder with additions of masteralloy particles apparent. After the sintering step was completed, figure 8.22d illustrates the complete diffusion of the masteralloy particles into the bulk matrix. The technique of using elemental metal powders with additions of alloying metal powders is not new, as the literature revealed prior work by Antonova and Privalov[73], Chan and Lin[74], Garin and Mannheim[75], Naramsimhan[76] and Wada et al.[77]. There are various commercial masteralloys available on the open market such as 316L stainless steel masteralloy (54.21% Cr, 0.04% C, 38% Ni, 0.25% Mn, 0.5% Si, 7.0% Mo), which is mixed as 1 part to 2 parts of iron, and is claimed to produce a stainless steel 316L grade alloy.

If one of the powders being injection moulded is an alloy, then the technique of masteralloying can be used if sintering incompatibilities exist between the alloy and the other powder. Masteralloying involves replacing the original alloy powder with a mixture of an elemental matrix powder and an alloying additions powder. The alloying additions powder contains the required alloying elements, which diffuse into the elemental matrix powder during sintering, to create the desired alloy.

If the non-alloy powder is the same elemental powder used for the alloy powder system and the alloying addition particle size for powder is chosen to be at least 3 times greater than the matrix particle size, then both powder systems will have compatible sintering profiles. If the diffusion time of the masteralloy particles into the elemental metal matrix is longer than the chosen sintering dwell times, then the dwell times during sintering should be increased to permit complete diffusion of the masteralloying particles into the matrix.

This technique could potentially be used to produce a complex ceramic such as silicon aluminium oxy-nitride (Sialon), as outlined in the patents by Lumby et al.[204], Jack and Wilson[205] and Paris and Grollier-Baron[206]. This could be achieved by mixing two distinctly different ceramics such as alumina and silicon nitride or aluminium nitride and silica. Attempts were made at producing a ceramic co-injection moulding comprising a sialon skin and an alumina core, but efforts were hampered by the lack of sintering furnaces that operate in the order of 2000°C. It is considered that the fabrication of a model sialon skin on an alumina or silica core by powder co-injection moulding is feasible.

11.6 Other techniques for matching skin and core sintering profiles

There are three potential techniques for achieving sintering compatibility. Small additions of sintering aids such as silane to iron powder[64] or magnesia to alumina powders[207] are all examples of sintering aid additions. Sintering aids work by the mechanism of liquid phase sintering[5, pp247-282]. This technique provides one means of equalising the sintering profiles of the core and skin powders. If both powders A and B have the same sintering rate, but only one powder reaches full density, then a sintering aid could be added to the powder that does not achieve full density, to equalise the sintering profiles.

Small additions of sintering retardants to the powders to be sintered could also be used, as demonstrated in the experimental work on the die-pressing of alumina and iron cermets. However, it would mean that the sintering temperature/time profile would have to be extended, to permit the skin and core powders to attain full density, thus increasing the processing costs and time.

If both powders A and B have the same sintering rate, but only one powder reaches full density, then rigid non-sinterable inclusions could be added to the powder which attains full density. The rigid non-sinterable inclusion diameters should be selected such that they are 3 or more times greater than the sinterable powder diameter.

Sintering is dependent on the surface area of the sintering particles. Increasing the surface area implies higher surface energy and the sintering rate increases with increased surface energy. The particle surface area is dependent on diameter. Changing the particle size provides one means of equalising the sintering profiles of the skin and core powder. If none of the above described techniques succeed in equalising the sintering profiles, then it is considered that successful PCM would be highly unlikely.

11.7 Skin profile control

If skin profile control is required for PCM, an extra stage is necessary before formulating, compounding and co-injection moulding the feedstocks. For a desired skin profile, C-Mold can be used to run co-injection moulding simulations to determine the following:

(a) Optimum injection moulding process conditions and feedstock properties
The optimum process conditions and feedstock properties required to achieve the desired skin profile are determined from the use of C-Mold. The required process conditions can be programmed into the injection moulding machine. The required feedstock material property data can be used to design the feedstock composition to achieve the required material properties. This will be discussed further in this chapter.

(b) Optimum mould cavity geometry
The optimum mould cavity geometry that minimises the probability of weld lines, meld lines, sink marks, air traps and so on, can be determined from C-Mold simulations. The mould cavity geometry data can be passed to the mould tooling manufacturer for a suitable first time mould cavity geometry. This approach would eliminate the costly and time consuming trial and error approaches by removing the need to manufacture test feedstock batches, trialling injection moulding process conditions and testing different mould cavity geometries.

Before computer simulations can be carried out to determine the optimum feedstock material properties, mould geometry and process conditions required to achieve a given skin profile, it is necessary to create injection moulding machine, coolant, mould material and simulation files. The injection moulding machine file contains data such as the plasticating capacity, maximum shot weight, tie bar dimensions data and so on. The coolant file contains the thermal properties data of the coolant fluid that is used to cool the mould cavity. The mould material file contains the thermal property data of the mould cavity material. The simulation parameters file contains the simulation settings relating to the modelling convergence criteria and the level of tolerance/precision required. Examples of these data files can be found in appendix E.

11.8 Effect of feedstock composition on the feedstock material properties

It is necessary to create a preliminary feedstock material property file before modelling simulations can start. This can be generated by creating a test feedstock that is typical for the skin and core being injection moulded. The first pass models can be used to determine the test feedstock specific heat capacity, thermal conductivity and PVT from the mass fractions, volume fractions and the intrinsic properties of each feedstock component. (Examples can be found in appendix G). A mould geometry file would need to be created which describes the dimensions of the mould cavity, which is then meshed using C-Mold modeller.

At the present time, this is an iterative approach to determining the required feedstock properties, mould geometry and process conditions for a desired skin profile, but is considered to be more cost and time effective. Once the required feedstock material properties are determined to achieve the desired skin profile, the first pass models can be used to determine the optimum mass/volume ratios for the individual components of the optimised feedstock.

It has been identified that the powder system and binder system composition, powder system morphology and the powder volume fraction all interact to produce the final feedstock material properties. This section discusses the four main material properties in terms of feedstock design. A diagram is presented, illustrating the effects of feedstock composition has on the final feedstock material properties. Techniques are identified to alter the feedstock's material composition to achieve the desired properties.

11.8.1 Specific heat capacity

Figures 10.6 to 10.12 illustrate the good agreement between the experimental and calculated specific heat capacity vs temperature curves and appear to verify the suitability of the rule of mixtures method (equation 6.1). This is in agreement with the work by Ishida and Rimdusit[145] into calculating the feedstock specific heat capacity. Equation 6.1 indicated that the feedstock specific heat capacity was dependent on the algebraic sum of the individual component's heat capacities. (Heat capacity is defined as the product of specific heat capacity and mass) The specific heat capacity rule of mixtures has been shown to be scientifically valid as long as certain criteria are satisfied. The binder components and powder components must be totally inert and no new products are formed during compounding. The specific heat capacity vs temperature curve for the feedstock can be mathematically re-evaluated each time the composition is changed, provided that raw specific heat capacity data exist for the individual constituents.

The peaks observed during specific heat capacity determination of the binder system are due to transitions within the individual binder components. Changing the binder components will affect the temperature at which these transitions occur and the underlying specific heat capacity. Changing the binder component mass fractions will affect the magnitude of the transition peaks. It is considered that composition variations within the feedstocks account for the differences in magnitude of the peaks in the experimental and calculated specific heat capacity curves.

It was observed that the peaks due to the transitions within the waxes, for both the experimental and calculated curves were in alignment with respect to temperature. The melting peak due to the Exxon LMWPP in the granulated feedstocks was to the contrary. It was thought to be due to mechanical working and thermal history through the compounder. The specific heat capacity of the LMWPP component was carried out on a sample that had not been subjected to compounding. The specific heat capacity of the feedstocks was carried out on a sample that had been subjected to compounding.

Metal powders accounts for 84% to 96% of the total mass of typical metal feedstocks and ceramic powder accounts for 74% to 90% of the total mass of typical ceramic feedstocks. The major contribution to the feedstock's specific heat capacity comes from the powder system. Changing the powder system for another powder system with a different specific heat capacity will significantly affect the baseline specific heat capacity of the feedstock. Figures 10.13 and 10.14 show the effect of varying the powder volume and mass loadings respectively, on the feedstock specific heat capacity, which become more pronounced at increasing processing temperatures.

Polymers have only 1 distinct melting transition and for specific heat capacity determination purposes, it is sufficient to measure the polymer's specific heat capacity at a few selected temperature points over the expected processing temperature range, with most of the test temperatures concentrated around the melting temperature. Due to the multiple component nature of the binder system in PCM and PIM, which implies several melting points within the binder system, it is essential to characterise the specific heat capacity vs temperature curve. More temperature test points are therefore necessary during specific heat capacity determination and thus the required level of data quality for the feedstock specific heat capacity is much higher than for polymers for computer modelling purposes. From the feedstock composition design point of view, the ability to tailor the specific heat capacity vs temperature profile is very restricted because the feedstock specific heat capacity is dependent on the intrinsic specific heat capacity of the powder system. Variations in the volume loading of the powder system due to the pressures and temperatures encountered do not affect the mass ratios. Thus specific heat capacity is not dependent on pressure and temperature.

11.8.2 Thermal conductivity

Figures 10.38 to 10.44 demonstrate that the series model provided the best fit with the experimental thermal conductivity data. However, the series model tended to slightly overestimate the feedstock's thermal conductivity. This was because the geometrical arrangement of powder particles in the binder system was closer to a combined parallel and series arrangement, as illustrated in figure 11.11, which could be considered as a grid of squares. Some of the squares contain a particle and some binder and that square's thermal conductivity could be calculated using the SPBM model.

The thermal conductivity of the alternating horizontal layers that comprise a series of binder squares and SPBM squares, can be calculated using the parallel model. The series model could then be used to calculate the total thermal conductivity of all the horizontal layers of the feedstock. It is considered that this method would give a better calculation of the feedstock thermal conductivity.

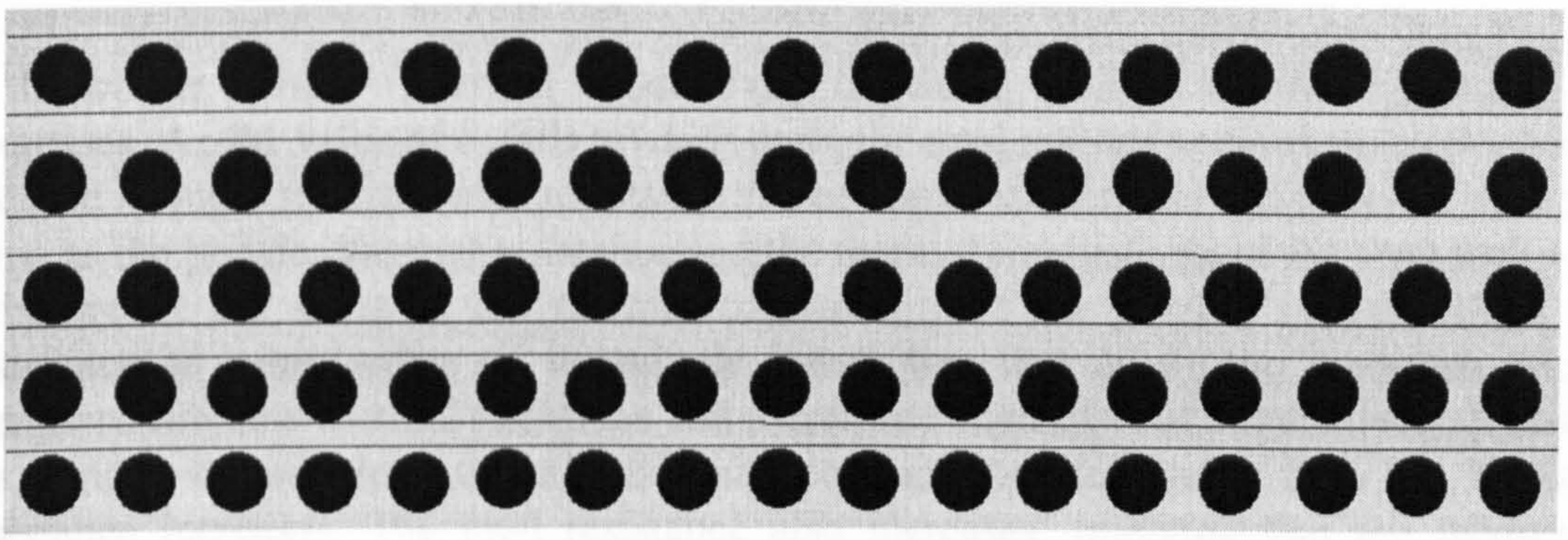

Figure 11.11 Representation of powder particles and binder matrix

All of the thermal conductivity models used in figure 10.46 are in general agreement that changing the binder systems' thermal conductivity has an effect on the feedstock thermal conductivity. Figure 10.47 indicated that changing the powder system to another with a different thermal conductivity had virtually no effect on the thermal conductivity of the feedstock. This was a common feature of all of the thermal conductivity models.

The effect of binder thermal conductivity and powder thermal conductivity on the feedstock thermal conductivity can be explained by making an analogy with resistor networks in electronics. The powder has a high thermal conductivity and therefore low thermal resistance, r and the binder components have relatively low thermal conductivity, and therefore high thermal resistance, R as illustrated by figure 11.12.

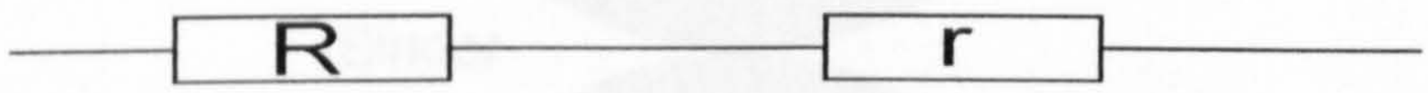

Figure 11.12 Schematic of two electrical resistors in series

The total resistance of the series resistance network is defined to be the algebraic sum of the individual resistances as equation 11.8 shows.

$$R_{total} = R + r \qquad \text{Eqn (11.8)}$$

If the powder system's thermal conductivity increases, then its thermal resistance, r decreases. As the value of r falls towards zero, the total resistor network will effectively become a single resistor with resistance R. The feedstock thermal resistance is now the same as the binder thermal resistance. The thermal conductivity of the feedstock will therefore be the same as the thermal conductivity of the binder system. Since resistor R's resistance is many orders of magnitude greater than that of r, the feedstock has a comparatively high thermal resistance and therefore a low thermal conductivity. This implies that powders with very high thermal conductivity such as silicon powder, with a quoted thermal conductivity value of $400 Wm^{-1}K^{-1}$ can be successfully injection moulded.

If the binder system's thermal conductivity increases, then its thermal resistance R, decreases. As the value of R falls towards zero, the total resistor network will effectively become a single resistor, with resistance r. The feedstock thermal resistance is now the same as the powder thermal resistance and the thermal conductivity of the feedstock will therefore be the same as the thermal conductivity of the powder system. Since r's resistance is many orders of magnitude lower than that of R, the feedstock has a comparatively low thermal resistance and therefore a high thermal conductivity. If either the binder or powder system's thermal conductivity decreases, then its thermal resistance increases. The total resistance also increases, implying that the feedstock thermal conductivity decreases accordingly.

The thermal conductivity models used in figure 10.45 all agree that increasing the powder volume loading increases the thermal conductivity of the feedstock, as expected. This effect is exponentially proportional to the volume loading. This is in agreement with the collective conclusions of Sharkawy et al.[151], Wong and Bollampally[152], Tavman[153][154], Maiti and Ghosh[155] and Agari and Uno[156]. It is explained by considering two powder particles and considering the effect of a separation distance d, between the surfaces of the two powder spheres, as illustrated by figure 11.13. The series heat flow model was used to plot figure 11.14.

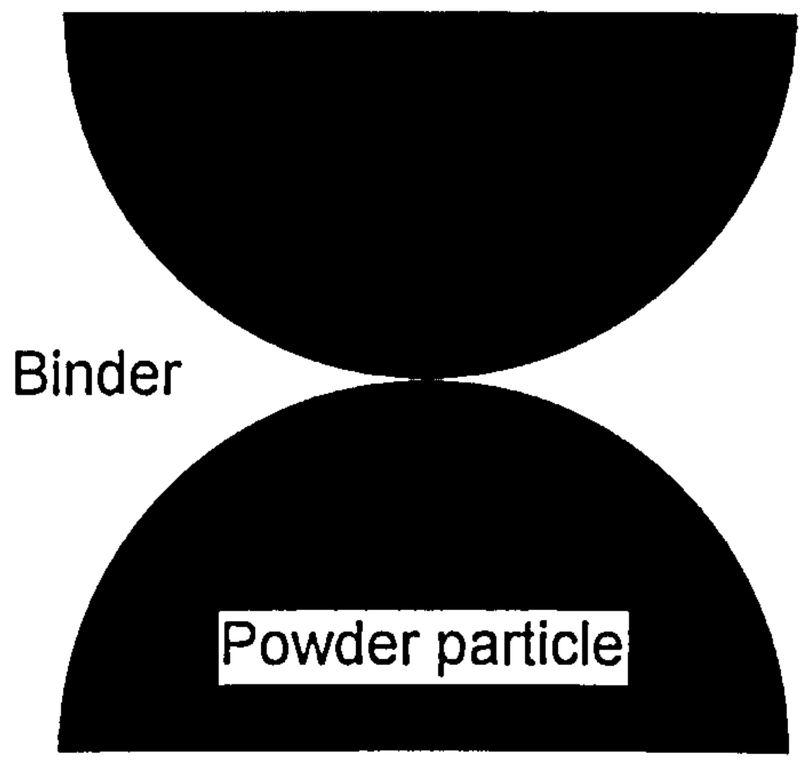

Figure 11.13 Two powder particles in a point contact arrangement

Figure 11.14 shows that the composite thermal conductivity only increases significantly when the separation distance is extremely small, or when the powder particles are in intimate contact with each other. The composite thermal conductivity is in the same order of magnitude as the binder thermal conductivity, when the separation distance is greater than about 0.1 of the radius.

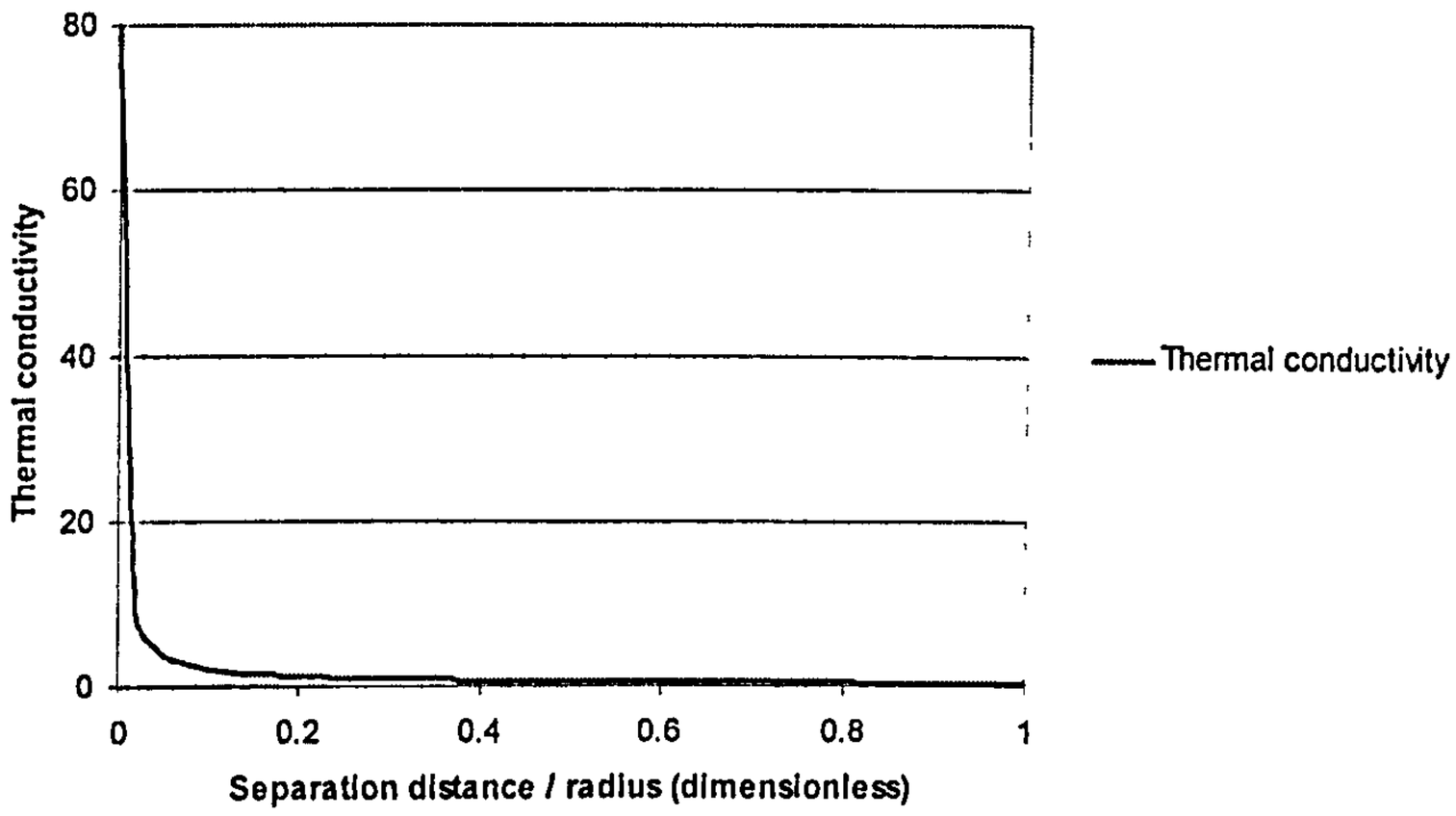

Figure 11.14 Effect of inter-particle separation distance on the total thermal conductivity (Powder thermal conductivity = 80 $Wm^{-1}K^{-1}$ and binder thermal conductivity = 0.2 $Wm^{-1}K^{-1}$)

As the powder volume loading increases, the average inter-particle separation distance decreases. There is little change in the feedstock thermal conductivity until the volume loading approaches a critical powder volume loading where the vast majority of powder particles are in intimate contact with each other or average inter-particle separation distance is less than 1/10th of the particle radius.

In practice, many of the feedstock's powder volume loadings are chosen to be below their critical powder volume loading as there would be significant mechanical inter-particle interlocking and high inter-particle friction, giving rise to injection moulding problems as the viscosity would be high. If there were a high number of particle to particle contacts within the feedstock, the series flow model could be used to calculate the thermal conductivity on a specific case of two particles in intimate contact with each other. If the particles are assumed to have a thermal conductivity of 80 $Wm^{-1}K^{-1}$ and the binder has a thermal conductivity of 0.2 $Wm^{-1}K^{-1}$, Figure 11.15 illustrates that the total thermal conductivity will still be relatively low. The total thermal conductivity of the composite is represented by the area under the graph.

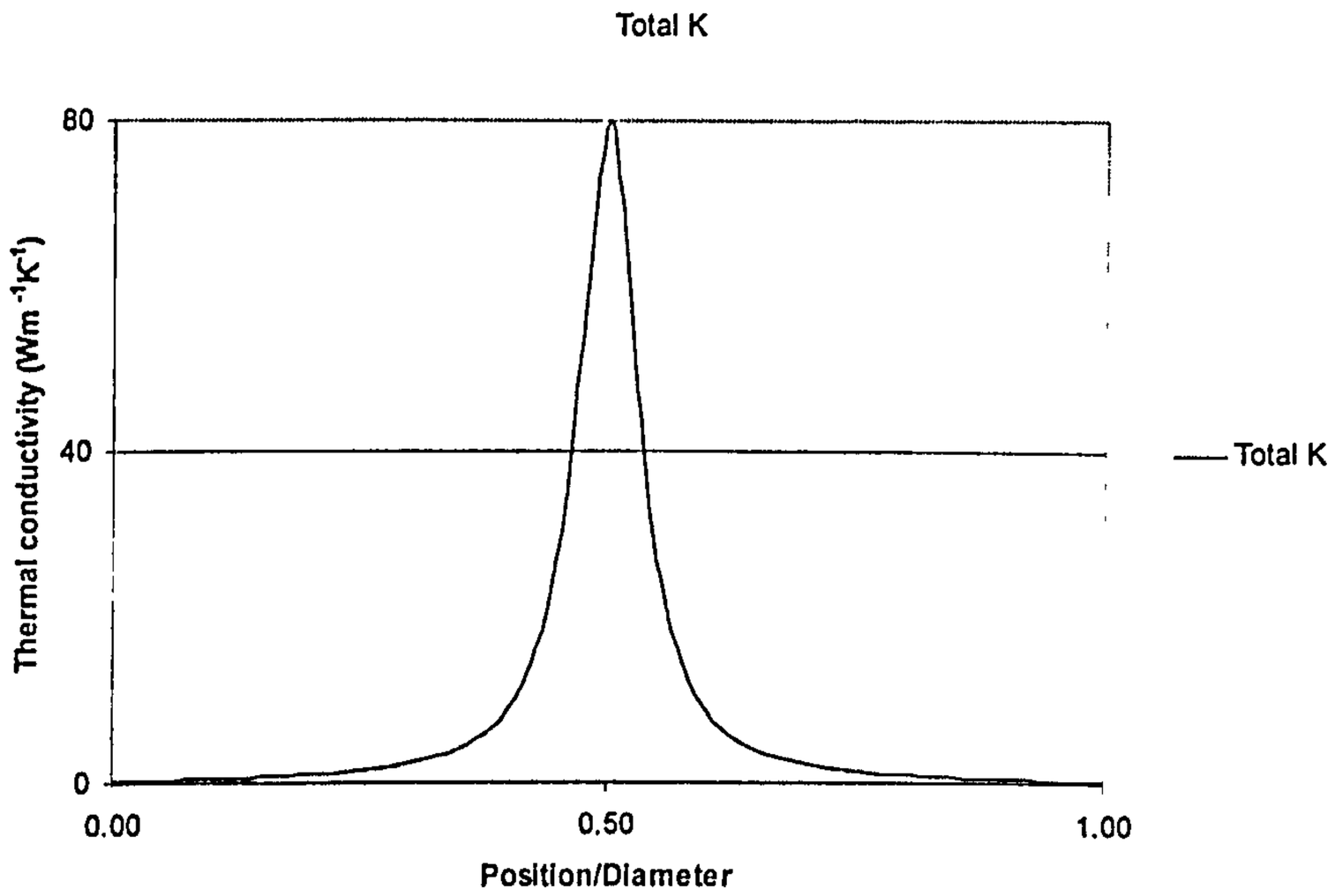

Figure 11.15 2-D graph of thermal conductivity vs diametric position

If the thermal conductivity were to be re-plotted as a 3 dimensional graph, the graph surface would be relatively flat, but with a singularity about the centre, further illustrating that the overall thermal conductivity of the composite is relatively low.

The binder's specific volume is influenced by temperature and pressure, implying that the powder volume loading is dependent on temperature and pressure. Figures 10.27 to 10.32 illustrate the effect of pressure and temperature on the powder volume fraction. The thermal conductivity is dependent on the volume ratios of the feedstock components and it is implied that the feedstock thermal conductivity is dependent on temperature and pressure. If thermal conductivity models are used, the effect of pressure and temperature may need to be taken into account.

Varying the powder volume loading to modify the feedstock thermal conductivity is not recommended as this will modify the PVT behaviour and rheology of the feedstock. From the PCM viewpoint, this will lead to differential sintering between the skin and core powders, unless the volume loading of the other feedstock is also changed as well. This means that its own thermal conductivity, rheology and PVT behaviour will also change.

Changing the waxes in the binder system offers the best method of modifying the feedstock thermal conductivity. This is because many polymers within the same generic class tend to have nominally similar thermal properties, but have a wide range of rheological behaviour. Changing the waxes will have minimal impact on other feedstock material properties, as generally, polymers are more compressible and have higher thermal expansivities than waxes. They have similar rheological characteristics, and vary in their thermal properties. One possible example would be to use napthalene, which has a thermal conductivity of 0.4 $Wm^{-1}K^{-1}$ instead of paraffin wax which has a thermal conductivity of 0.2 $Wm^{-1}K^{-1}$.

11.8.3 Specific volume

There have been no previous recorded attempts to use the modified 2 domain Tait equation to model the specific volume of the feedstocks as a function of pressure and temperature. Figures 10.21 to 10.26 illustrate that the 2d-modified Tait equation can be used to model the PVT behaviour of feedstocks. There was initial concern that the 2 domain Tait model would be inadequate due to the fundamental differences in the densities, thermal expansivities and compressibilities between the PIM/PCM feedstocks and polymers.

The additions of powders which have higher densities than typical polymers implies that the specific volume of the feedstocks is lower than for polymers. The volume loading and the powder density influences the specific volume of the feedstock. The powder thermal expansivities are considerably lower than those of typical polymers, implying that the thermal expansivity of the feedstock decreases with increasing powder volume loading and is influenced by the binder system's thermal expansivity. The powder compressibilities are considerably lower than those of typical polymers, the compressibility of the feedstock decreases with increasing powder volume loading and the binder system's compressibility accounts for all of the feedstock compressibility.

For the purpose of calculating the specific volume using a rule of mixtures approach, several assumptions were made. The polymer was more compressible than the waxes. If this assumption were wrong, the effect could be considered to be negligible because the rule of mixtures is based upon the mass ratios. The powder system accounts for 85% to 95% by mass of the feedstock, and the empirical model used in C-Mold is not sophisticated enough to deal with more than two distinct domains. The polypropylene transition was taken to be the major dominant transition as far as C-Mold was concerned because the LMWPP was the major component, accounting for 59.7% by mass of the binder system. If the binder system was changed such that the major constituent was a wax instead of a polymer, then the dominant transition would change accordingly and the PVT data by the rule of mixtures approach would need to be recalculated.

If both the skin and core feedstocks use exactly the same binder system composition and identical powder volume loadings, then the PVT behaviour of the skin and core feedstocks can be considered to be nominally identical. This is because the thermal expansivity of the powder system will be several orders of magnitude lower than the binder system, and the powder system is incompressible. Compatible PVT behaviour for both the skin and core is important for the feasibility of successful PCM, as this will minimise residual stress development. It is considered that as long as the skin and core feedstocks use exactly the same powder volume loading and similar binder compositions, there would be little practical need to modify the PVT behaviour of the feedstocks to achieve a given skin profile. This minimises the risk of differential shrinkage and delamination.

If for any reason, different binder systems must be used for the skin and core feedstocks, then PVT determination will be necessary to match the PVT profiles for both the skin

and core feedstock. The caveat of identical powder volume loadings remains to avoid differential shrinkage.

PVT data is used by C-Mold to predict cooling, shrinkage and warpage. The cooling of the feedstocks affects its skin profile, and will be discussed further. Computer modelling software is routinely used to model the shrinkage and warpage that polymer mouldings undergo during the injection cycle and final cooling to room temperature. Under certain circumstances, the shrinkage may lead to non-isotropic residual stressing of the mouldings, which usually manifests itself as warpage in polymers. In PIM/PCM, if the mouldings have frozen-in residual stresses, they do not manifest themselves until during debinding and sintering, which leads to rejection of the warped mouldings.

It is suggested that the application of C-Mold could be extended to predict warpage and shrinkage and hence predict frozen-in stresses, as this would provide a means of optimising the injection moulding conditions to minimise warpage and frozen-in stresses as well as achieving the desired skin profile, because this increases the efficiency of the PCM/PIM cycle.

11.8.4 Rheology

The rheology of the feedstocks and the Exxon LMWPP were characterised as illustrated by figures 10.48 to 10.55. Figures 10.48 to 10.51 indicate that the dominant flow regime was pseudoplasticity. Pseudoplasticity is also known as shear thinning and implies that the log of viscosity is inversely proportional to the log of shear rate. The addition of metal powders or waxes has little effect on the flow regime when compared to the rheology of the polypropylene. Figures 10.52 to 10.54 illustrate that the ceramic feedstock's rheology obeys an apparently linear relationship between log shear viscosity and log shear rate. This implies that the addition of ceramic powder influences the overall rheology at low shear rates. This is thought to be a consequence of the high interparticle friction and increased surface roughness, when compared to the metal powders. It was also observed during the rheology work, that monitoring the pressure at low shear rates with respect to time, produced a sawtooth profile, accompanied by an acoustic emission of hammering sounds. This implied that barrel wall friction and/or die wall friction were significant at low shear rates for the ceramic feedstocks.

Figures 10.48 to 10.55 also demonstrate that the Cross-WLF rheology model can be used to model the rheology of the feedstocks as a function of temperature. The effect of pressure on viscosity was not taken into account. D_3 is the pressure sensitivity parameter in the Cross-WLF equation. This explains why the values of D_3 are 0 Pa. The powder volume loading varies with temperature and pressure and the viscosity varies with powder volume fraction. It was thought that this would be a potential limitation of the Cross-WLF model for the feedstocks, but figures 10.48 to 10.54 indicate that this was not the case. There have been no previously recorded attempts to use the Cross-WLF equation to model the rheology of feedstocks, but the present work has demonstrated that the Cross-WLF equation can be used to model feedstock rheology.

Due to insufficient data and the difficulty in rheological determination of the paraffin wax, stearic acid, and carnauba waxes, it was not possible to calculate the feedstock viscosity as a function of the individual binder component's viscosities and the powder volume loading and powder particle size. Further work is needed to develop a better rheology prediction model that takes into account particle size, powder volume loading, the individual viscosities of the binder components, and also that the powder volume loading changes as a function of temperature and pressure, as previously determined in the PVT characterisation of the feedstocks.

Due to the present difficulty of determining the binder composition to achieve the required skin profile, it is necessary to test the optimised feedstock for its experimental rheology. If it does not agree with the required rheology determined by C-Mold simulations, then the most suitable way of changing the rheology profile, without changing the other material properties, is to change the polymer only. Although rheology is dependent on powder sizes, it is not recommended to change the particle size and powder volume loading, as this will affect the sintering profile. Generic classes of polymers have nominally identical specific heat capacity and thermal conductivity, but vary widely in their rheology. The new formulated feedstock must be tested to determine if its new rheology is similar to the rheology for the required skin profile.

11.8.5 Summary of the effects of feedstock composition on the feedstock material properties

This section discusses how the powder system composition, powder morphology, binder composition, polymer rheology and the powder volume loading affects the feedstock material properties. As discussed previously in section 11.8.1, the feedstock specific heat capacity is dominated by the powder system composition and the powder components specific heat capacities.

Increasing the powder particle size decreases the surface energy and hence reduces the driving forces for sintering. This implies that the particle size affects the sintering behaviour. At the same time, German[63, pp163-164] reports increasing the particle size leads to a decrease in the shear viscosity, hence altering the feedstock rheology. This is because increasing the particle size leads to a reduction in the surface area, and the number of particles per unit volume. This leads to fewer particle-particle interactions per unit volume of the feedstock, and hence lower overall inter-particle friction. This implies that changing the powder particle size will affect both the sintering behaviour and the feedstock rheology. Thus, another means of modifying the feedstock rheology without substantially changing the sintering behaviour is required. The feedstock rheology is influenced by two main factors as illustrated by the Metzner[121] model, equation 4.22, section 4.3.3. The Metzner equation implies that the binder system rheology and the powder volume loading both affect the feedstock rheology. Altering the powder volume loading is not recommended as this will affect the sintering behaviour, feedstock thermal conductivity and the PVT of the feedstock.

Decreasing the powder volume loading leads to a decrease in the densification achieved during sintering due to the lower green moulding density. Altering the powder volume

loading alters the feedstock thermal conductivity, and this has been discussed earlier in section 11.8.2. Changing the feedstock thermal conductivity influences the thermodynamics of mould filling and cooling. This may affect the skin profile. Equation 6.3 is a rule of mixtures for the PVT behaviour of the feedstock and is dependent on the mass fractions of the feedstock components. Varying the powder volume loading also alters the powder mass loading. The variation of powder mass loading leads to changes in the PVT behaviour of the feedstock.

The majority of waxes have similar rheological behaviour. In contrast, polymers vary widely in their rheology. Equation 4.20 is a rule of mixtures approach to calculating the binder rheology from the individual binder components and is dependent on the volume fractions within the binder system. This implies that there are two techniques for controlling the feedstock rheology. The first is to replace the polymer with another with different rheological characteristics. The second is to alter the wax to polymer volume ratio, provided that the thermal characteristics of the waxes and polymers are similar. Section 11.8.2 discusses the effect of the binder system thermal conductivity on the feedstock thermal conductivity. Changing one of the binder components with another of significantly different thermal conductivity will alter the thermal conductivity of the feedstock, and could alter the thermodynamics of injection moulding.

Figure 11.16 brings together the points made in this section and illustrates the dominant factors in feedstock design that influence the final feedstock properties. The C-Mold computer software could be used to determine the required feedstock material properties and the suitable injection moulding process conditions in order to achieve the required skin profile. Figure 11.16 can be used as a guide to designing a suitable feedstock composition to achieve the required feedstock material properties. This feedstock could then be compounded and used in PCM. Well matched skin and core feedstocks permit the subsequent co-injection moulding of the two distinct feedstocks and sintering.

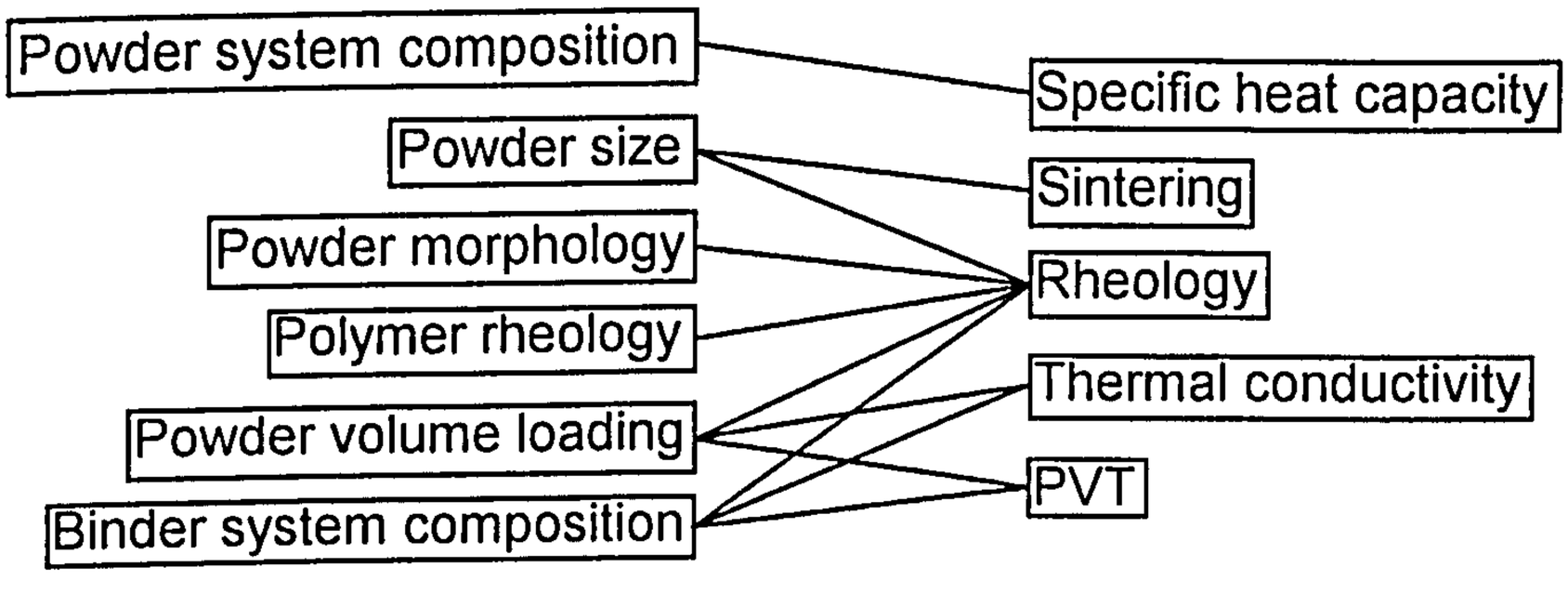

Figure 11.16 How feedstock design affects the final feedstock properties.

11.9 Effect of material properties on the skin profile

This section discusses the effects that the feedstock material properties have on the skin profile.

11.9.1 Effect of viscosity on the skin profile

It has been demonstrated that rheology has an effect on the polymer skin profile as illustrated by figures 9.14 to 9.19. This is explained by flow dynamics. The effect is due to the viscosity ratio between the skin and core feedstock[106, pp65-67] It is also pointed out that rheology is dependent on pressure, shear rate and temperature. The material thermal properties affect the viscosity, along with injection time and are discussed further on in this chapter.

If a low viscosity core polymer flows into a mould cavity that has been partly filled by a highly viscous skin polymer, the core will jet through the skin to fill the mould extremities with core polymer. This will result in thicker skin profiles on surfaces parallel to the flow direction, and thinner skins at the extremities that are perpendicular to the flow direction, as illustrated in part (a) of figure 11.17.

In an opposite example, if a high viscosity core polymer flows into a mould cavity that has been partly filled with a low viscosity skin polymer, the core will purge the skin to the extremities of the mould cavity, resulting in very thin skin layers on the surfaces parallel to the flow direction. The thin skin layers will have solidified in contact with the cold mould walls and cannot be purged by the molten highly viscous core. An accumulation of skin material will form at the extremities perpendicular to the flow direction, as illustrated in part (b) of figure 11.17.

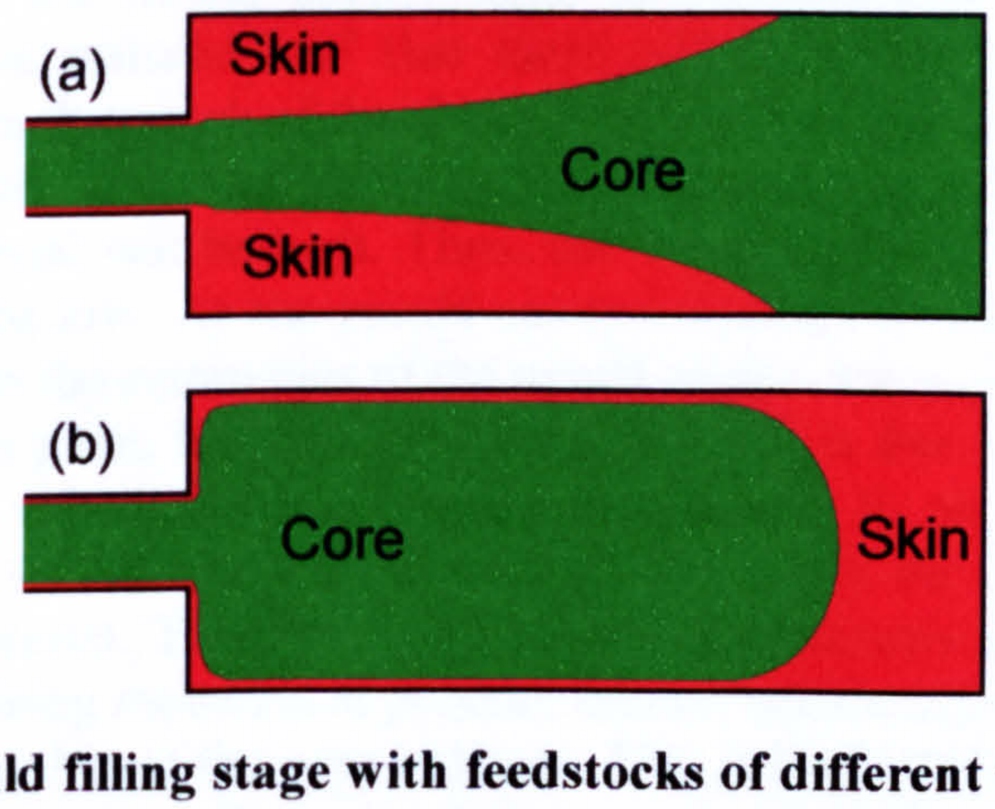

Figure 11.17 Mould filling stage with feedstocks of different viscosity. Part (a) has a viscous skin, and a fluid core, part (b) has a fluid skin, and a viscous core

The effect of viscosity on the skin profiles in powder co-injection moulding was not investigated, but it is expected that it would be broadly similar as in polymer co-injection moulding.

11.9.2 Effect of specific heat capacity, thermal conductivity and mould filling time on the skin profile

From the C-Mold modelling simulations, it has been demonstrated that the specific heat capacity of the skin and core polymers had a negligible effect on the skin profile as illustrated by figures 9.27 and 9.28. It was also demonstrated that the specific heat capacity of the skin and core feedstocks had a negligible effect on the skin profile, as illustrated by figures 10.56 and 10.57. It has also been demonstrated that the thermal conductivity of the skin and core polymers had a negligible effect on the skin profile, as illustrated by figures 9.29 and 9.30. It was also demonstrated that the thermal conductivity of the skin and core feedstocks had a negligible effect on the skin profile, as illustrated by figures 10.58 and 10.59. It is thought that further work is necessary in which the mesh element size could be decreased and the number of layers increased to give more detail on the skin profile as a function of thermal properties.

From the C-Mold simulations and polymer co-injection work, it has been demonstrated that the mould filling time affects the skin profile, as illustrated by figures 9.19 to 9.26. This is because for a longer mould filling time, the polymer is in contact with the mould walls for a longer time period while the mould cavity is being filled. As the contact time increases between the polymer and the mould walls, more thermal energy is transferred, and a greater proportion of the polymer volume will have decreased in temperature and solidified. Longer injection times lead to thicker solid polymer layers near the injection point. Figure 11.18 illustrates the effect of a low mould filling time versus a high mould filling time for two nominally identical polymers.

Figure 11.18(a) illustrates that if the mould filling time is high, the volume fraction of solidified material to molten material will be high. Since the frozen material occurs at regions adjacent to the mould cavity walls, this implies that most of the solidified material will be skin material, and that there will be a low volume of molten skin material. This implies that much of the skin material will solidify on the mould walls near the injection point and have thick profiles. The volume fraction of solidified skin material to molten skin material will be high. Thus, the volume ratio of molten skin to molten core materials will be low. As the mould cavity continues to fill, the core material will penetrate further into the extremities of the mould cavity. Since most of the core material is still molten at this point, the cross-sectional area that is free of solid material will be large and the core volume fraction remains unchanged. In cases of excessive mould filling times, one of two effects will occur. The first is that the core material will break through the skin material. This occurs where the vast majority of the skin material has solidified. The remaining molten skin polymer cooled sufficiently to increase its viscosity to much greater than that of the core polymer. This is illustrated in figure 11.19(a). The second is that a short shot will result, where at a certain point within the mould cavity, the cross-sectional area will have solidified completely before the mould has completely filled.

Figure 11.18b illustrates that if the mould filling time is low, the volume fraction of solidified material to molten material will be low. Since most of the solidified material occurs at regions adjacent to the mould cavity walls, the solidified material will be skin

material. The volume fraction of solidified skin to molten skin material will be low. Thus the volume fraction of molten skin to molten core will be high. As the mould cavity continues to fill, both the skin and core material continue to move into the mould cavity extremities. The cross-sectional area that is free of solidified material will be relatively high and thus a more uniform distribution of skin and core material will result. In the event of extremely short mould filling times, the core can purge the skin material to the extremities, as illustrated by figure 11.19(b).

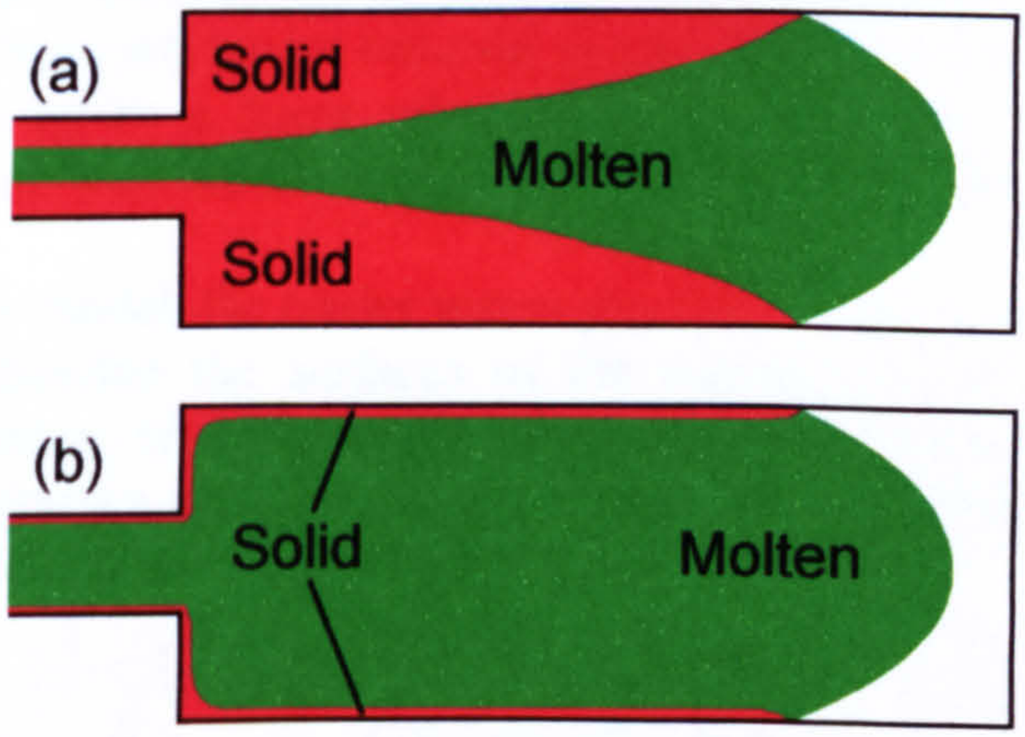

Figure 11.18 Effect of different mould filling times on the frozen layer profile. (a) has a high mould filling time. Part (b) has a low mould filling time (The skin and core material regions have been omitted for clarity) Red represents solid polymer and green represents molten polymer.

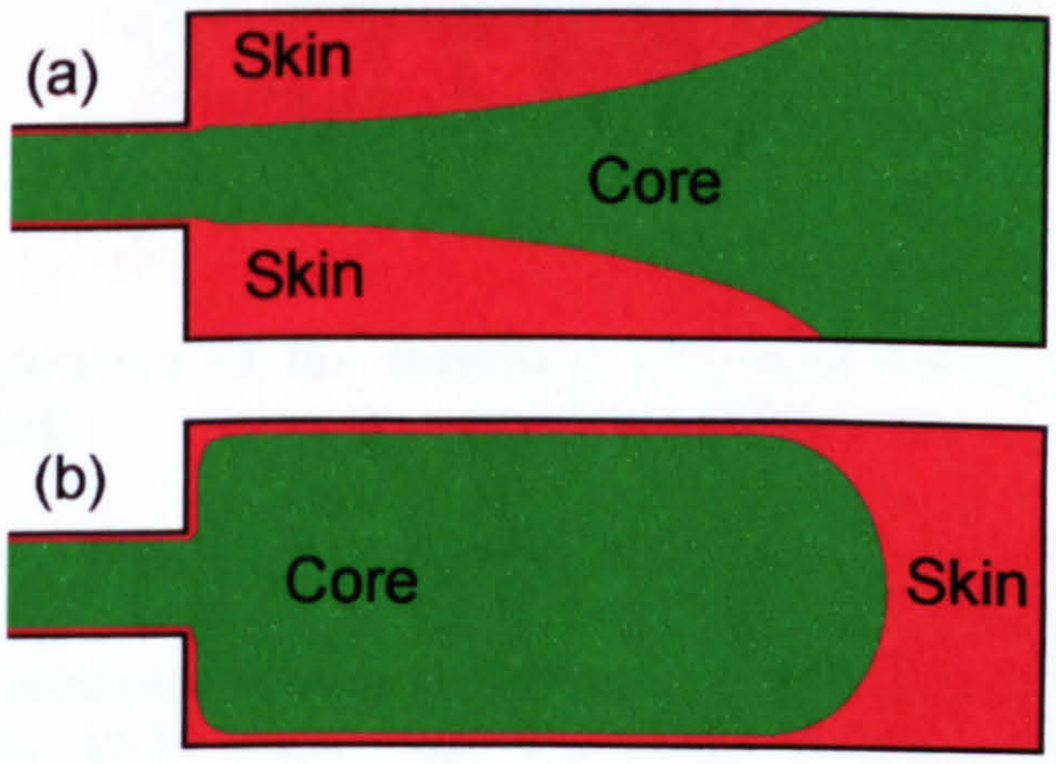

Figure 11.19. Effect of different mould filling times on the skin profile. (a) has a high mould filling time. Part (b) has a low mould filling time. (the frozen polymer regions have been omitted for clarity) Red represents the skin material and green represents the core material.

The effect of mould filling time was not investigated for the powder co-injection mouldings, but it is expected that it will be broadly similar to that for polymer co-injection moulding.

11.10 Solvent debinding

There are two possible mechanisms for the removal of the waxes during solvent debinding, the shrinking core model and gravity driven debinding.

In the gravity-driven debinding mechanism, the binder waxes melt under the action of the applied heat and migrate vertically downwards though the mouldings under the dominant effect of gravity. They then escape into the porous ceramic substrate. If gravity-driven debinding was the dominant binder removal mechanism, the binder removal rate vs time would be expected to be a linear relationship, as the binder region would descend uniformly across the horizontal cross-sectional area into the porous ceramic substrate.

In the shrinking core model, the binder waxes physically dissolve into the solvent and the solvent can only dissolve the surfaces of the remaining waxes. As the waxes are removed, the remaining binder's surface area decreases. Thus the rate of remaining binder removal decreases with decreasing surface area. Figure 11.20 illustrates the shrinking binder wax core model.

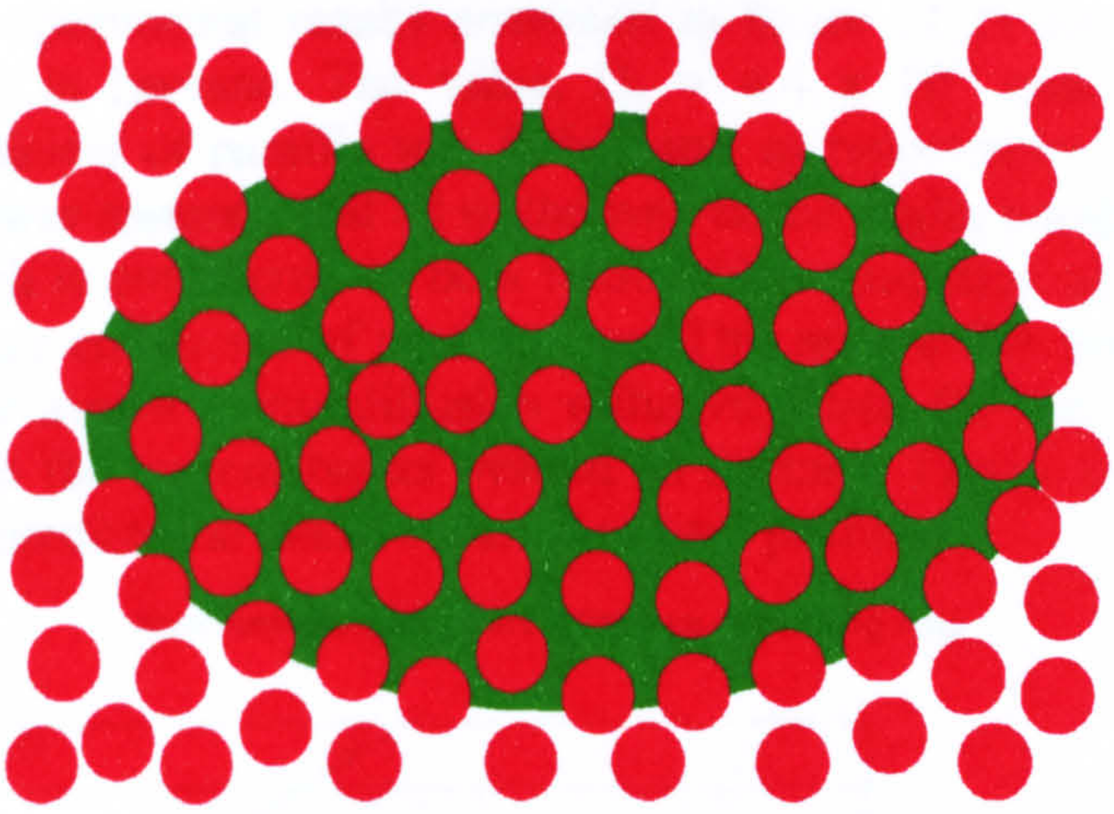

Figure 11.20 Illustration of the shrinking wax core model (Capillary pore size effects are neglected)

The author[21, pp58-59] carried out a study in 1995 to study solvent debinding over a period of time and figure 11.21 illustrates the binder removal percentage as a function of time. Figure 11.21 illustrates that the rate of wax removal decreases with increasing time parabolically. Figure 11.21 implies that the waxes were removed according to the shrinking core mechanism rather than the gravity driven mechanism. Increasing the debinding time to beyond the time required for 90% or more binder waxes removal would mean that the balance of economics would be affected in terms of the time and energy involved.

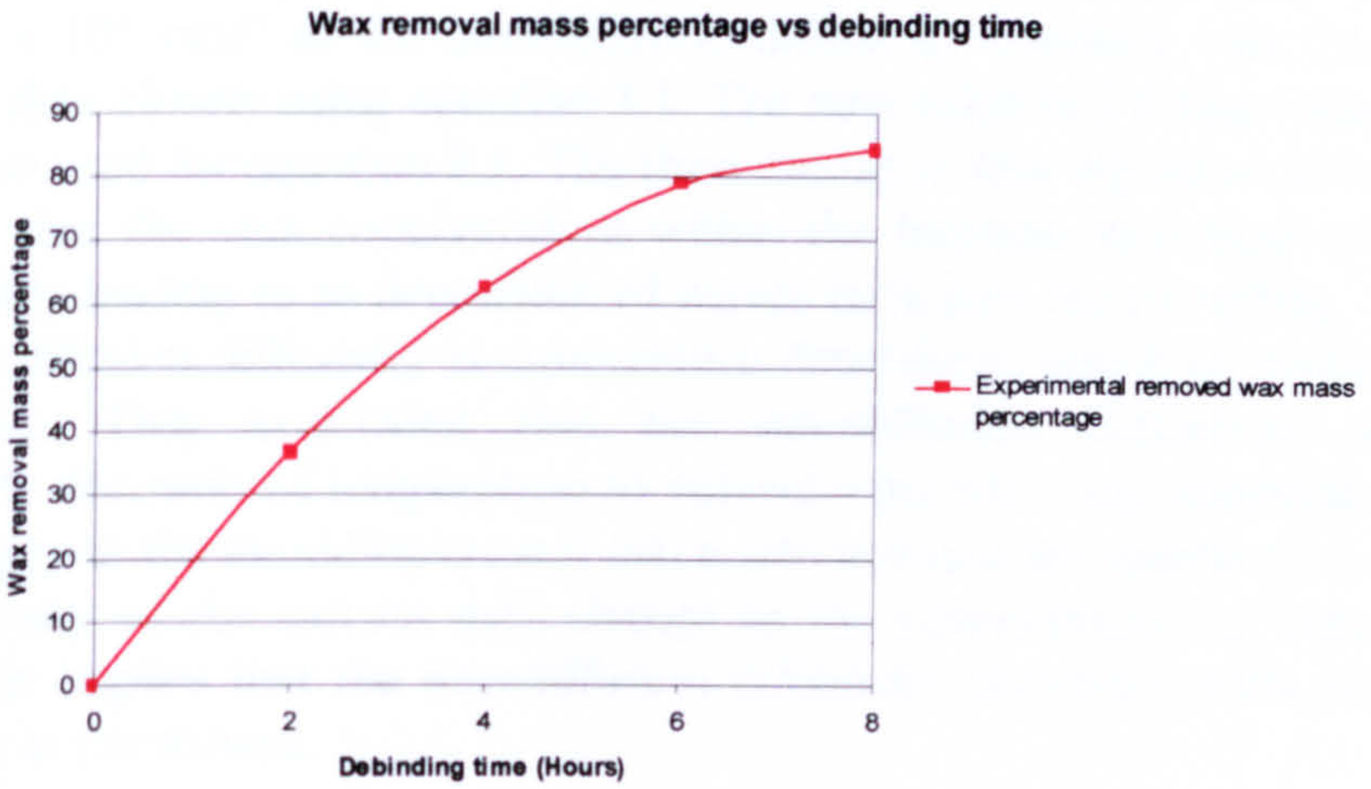

Figure 11.21 Wax removal percentage vs time.

Equation 3.1 was used to predict the binder removal as a function of time and directly compared to the experimental results presented in figure 11.21 for a 3mm thick PIM moulding debound in heptane. The value, $D_x = 4.4 \times 10^{-6}$ cms^{-1} was used as the interdiffusion coefficient of paraffin wax in heptane, as reported by Tsai and Chen[49]. In this example, it was assumed that all of the wax-based binder components were 100% paraffin wax, which is considered to be a reasonable assumption as 80% by mass and volume of the waxes comprised of paraffin wax. This assumption was made because of the lack of openly available interdiffusion diffusivity data for the carnauba wax and stearic acid used in the current binder system, in heptane. Figure 11.22 illustrates that equation 3.1 over-predicts the binder removal vs time profile.

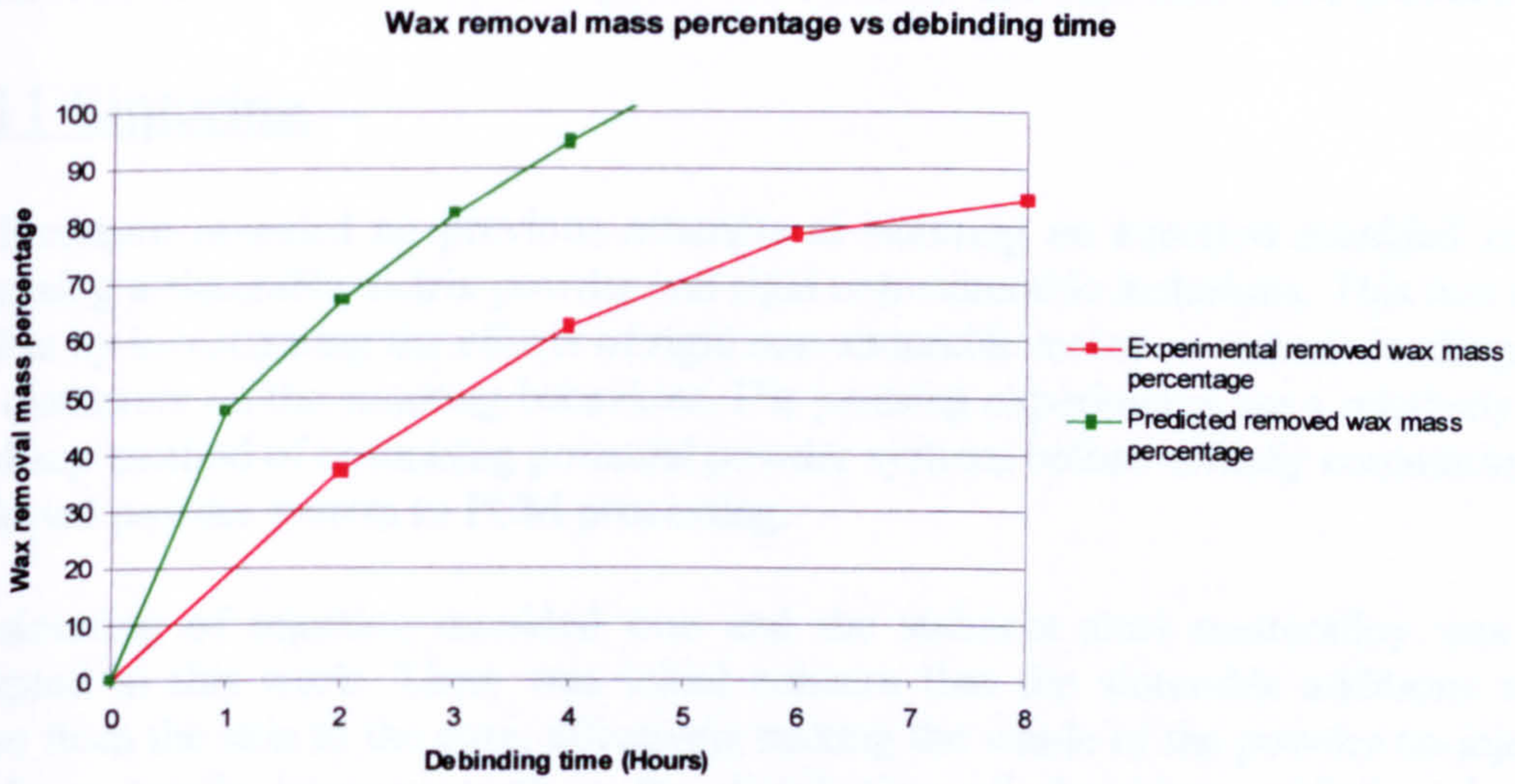

Figure 11.22 Comparison of experimental and predicted wax removal versus time

The over prediction is due to one or more reasons. The first is that the interdiffusion diffusivity of the carnauba wax and stearic acid could be lower than that of the paraffin wax, even though paraffin wax comprised 80% of the wax based components The second is that the interdiffusion diffusivity, D_x, of the paraffin wax may be too high. The

value of D_x was manually adjusted until the predicted curve fitted the actual data. A value of 1.8×10^{-6} cms^{-1} as the interdiffusion diffusivity constant was found to fit the experimental data closely using equation 3.1. The new value is 2.5 times smaller than the literature value used for equation 3.1. The third reason is that equation 3.1 does not take into account that the wax concentration within the heptane increased with debinding time, potentially leading to re-deposition of waxes back into the moulding. The fourth is that the interdiffusion diffusivity is temperature dependent, which is confirmed by Tsai and Chen[49]. They concluded that the interdiffusion diffusivity was roughly proportional to the ratio of temperature to solvent viscosity. Any temperature gradients present throughout the moulding are not taken into account by equation 3.1. The fifth is that the viscosity of the solvent may change as the concentration of dissolved waxes increases. This implies that the interdiffusion diffusivity decreases with increasing wax concentration in the solvent.

It is reported by Tsai and Chen[49] that using higher temperatures leads to swelling of the solvent, and can be a potential source of cracks in the mouldings during solvent debinding. However it is also stated that this may be counteracted by the swelling of the polymer within the binder system.

According to equation 3.1, the wax debinding time is inversely proportional to the half thickness, which indicated that the optimum debinding time for a 6mm thick PCM sample would be twice the debinding time required for a 3mm thick PIM sample. The experiments on the 3mm PIM disc indicated that 8 hours debinding time led to the removal of 85% of the waxes according to figure 11.21. Accordingly, the optimum debinding time for the 6 mm thick mouldings would be 16 hours, but a debinding time of 24 hours was used during the experimental stage of the project. This was deemed to be sufficient as there were no apparent gross defects in the final sintered PCM products.

11.11 Sintering

The literature revealed no previous attempts at sintering an injection moulded cermet comprising a sinterable matrix powder and rigid non-sinterable inclusions. This was made possible by investigating the effects of rigid non-sinterable inclusion volume loadings and their diameters on the sintering behaviour. Die pressing experiments are a relatively easy and cheap method of optimising potential powder systems before actually committing the developed powder system to PCM processing.

The sintering of injection moulded iron and the stainless steel masteralloy was also attempted in this work. There was initial concern that the sinterable additions might diffuse from the skin to the core, effectively making the whole of the powder co-injected mouldings totally homogeneous in the distribution of chromium, nickel and other alloying additions, typical in the manufacturing of stainless steels. This would detrimentally affect the corrosion resistance of the skin, and would negate the material cost savings inherent in using a cheap core material. Subsequent SEM analysis and chromium x-ray dot maps showed this to be unfounded.

It is thought that mechanisms of surface diffusion[63, pp 356-357]. and surface transport[12, pp248-250] are the dominant processes of the diffusion of the masteralloying additions into the iron matrix. The masteralloy particle volume appears to decreases during sintering, implying reducing surface area, and hence a reducing surface diffusion rate. Although the sintering profiles were essentially the same as for the sintering of iron based mouldings, there were no localised regions of high concentration chromium or nickel present after sintering. This was supported by x-ray chromium dot maps. This implies that no allowance needs to be made regarding the sintering dwell time to incorporate the diffusion time necessary for homogenisation of the skin material. Thus the technique of using masteralloying additions should not impact on the economics of PIM or PCM processing.

12 Conclusions

This section presents the conclusions of the present work and falls into three distinct groups.

12.1 Powder co-injection moulding

The principle of co-injection moulding has been demonstrated successfully in this research through the manufacture of:

(a) a cermet (alumina/iron) skin and iron core.
(b) a stainless steel skin (using a masteralloy and carbonyl iron) and iron core.
(c) a zirconia toughened alumina skin and alumina core.

Two conditions are critical to successful powder co-injection moulding. The first is that the two feedstocks must be well matched in their PVT behaviour to minimise the development of differential shrinkage or deformation in the co-injected green mouldings. The second is that the powders used in the feedstocks are compatible in their sintering behaviour and are at nominally identical powder volume loadings. This minimises the differential shrinkage and/or the occurrence of gross defects during subsequent sintering.

Cermet based feedstocks, stainless steel masteralloy-based feedstocks and zirconia-alumina feedstocks can be injection moulded. The mouldings produced in this study were free from gross defects as revealed by unaided visual inspection. This has not been reported previously in conventional PIM. This result has application to the PCM process, as demonstrated by the production of three model PCM systems.

In an ideal PCM system, minimal feedstock development time and costs can be achieved by ensuring that similar identical powder volume loadings and similar binder systems are used for both the skin and core feedstocks and that the skin powder and core powder have similar sintering profiles.

If the prototype core and skin feedstocks do not have similar sintering profiles, further work must be carried out. In order to modify the different sintering profiles until compatibility is achieved. This can be done by using different particle sizes or adding sintering aids. The technique of die pressing of sample pellets offers a relatively cheap means of optimising sintering behaviour before commissioning the new feedstock to the PCM process.

The die-pressing work indicated that when sintering cermets, as a "rule of thumb" the inclusion particle diameter should be at least three times that of the matrix powder particle diameter. The effect of having a non-uniform distribution of rigid inclusions in the sinterable matrix of a cermet can be minimised by increasing the rigid inclusion particle diameters.

12.2 Feedstock material properties

Feedstock characterisation is essential in order to optimise the PCM process and for productive modelling using software packages such as C-Mold. Of particular importance, is the availability of quantitative values for thermal properties such as specific heat capacity and thermal conductivity, together with reliable PVT and rheology data.

The current work has shown that a rule of mixtures can be used to give a good prediction of specific heat capacity as a function of temperature. With the exception of the iron-alumina cermet feedstock, the rule of mixtures was found to slightly over-predict the feedstock specific heat capacity. The specific heat capacity of the powder provides the major contribution to the feedstock specific heat capacity. Increasing the volume loading of the powder system leads to an increase in the feedstock specific heat capacities. The predicted values of specific heat capacities determined from the rule of mixtures model, were accurate enough to provide an excellent correlation with experimentally determined values.

It has been shown that the series thermal conductivity model gives a good prediction of the feedstock thermal conductivity, based on the thermal conductivities of individual feedstock components. The thermal conductivity of the feedstocks is exponentially proportional to the powder volume loading and directly proportional to the binder thermal conductivity. As the powder thermal conductivity increases, the feedstock thermal conductivity tends towards an asymptotic limit. The binder composition has a greater effect on the feedstock thermal conductivity than the powder system composition, and gives one means of controlling the feedstock thermal conductivity.

It has been demonstrated that the 2-domain Tait model, which is commonly used to model the PVT behaviour of polymers, can also be used to model the PVT behaviour of feedstocks. The compressibility of the feedstocks is dominated by the compressibility of the binder system. The powder volume loading during injection moulding is affected by both temperature and pressure. The initial volume loading of feedstocks decreases with increasing temperature. The volume loading of the feedstocks increases with increasing applied material pressures during injection moulding. This has possible implications where the feedstock viscosity is highly dependent on the powder volume loading.

It has been demonstrated that the Cross-WLF model, which is commonly used to model the rheological behaviour of polymers can also be used to model the rheological behaviour of feedstocks.

12.3 Computer modelling

It has been demonstrated that the C-Mold finite element modelling software can be used to predict the skin profile for the polymer co-injection moulding of a gear cog mould geometry with reasonable accuracy. However, the C-Mold software assumes that the core region is located symmetrically within the moulding and experimental

determination of the skin to core boundary locations for all of the polymer mouldings shows that this is not a valid assumption.

C-Mold predicts that the effect of varying the specific heat capacity and/or the thermal conductivity of the powder based feedstocks had a negligible effect on the skin profile. The thermal properties of the feedstock are influenced by the feedstock composition. This implies that the thermal properties can be controlled by altering the feedstock composition.

C-Mold predicts that the skin profile is not affected significantly by the polymer viscosity. Increasing the injection filling time leads to higher skin thickness fractions and further radial penetration of the core material.

Validation of the modelling approach using C-Mold has been demonstrated by successfully predicting the skin profile of both metal and ceramic co-injection moulded components. This work has demonstrated that the design of the feedstock composition and injection moulding process conditions can be optimised by the use of computer based injection moulding software in order to achieve the desired surface engineered skin profile.

The research has also demonstrated the complex interactions between feedstock properties, processing conditions and component characteristics. A simple methodology has been proposed which considers all of the stages necessary for successful powder co-injection moulding processes.

13 Recommendations for further work

This section presents recommendations for further work, which fall into three distinct groups.

13.1 Powder co-injection moulding

Develop a range of ferrous matrix alloys and other ceramic particulate additions such as silicon carbide, titanium nitride, titanium carbide, or tungsten carbide. The use of a non-ferrous alloy matrix would allow the introduction of diamond particulates as a potential wear resistant phase. This would have many applications such as grinding wheels. Chemical compatibility between the matrix material and the reinforcement must be ensured so that the interfacial properties are optimised, for example, strength and toughness. The relative particle size must also be considered to ensure the sintering profiles of the skin and core are compatible. Care must be taken to select rigid inclusions that are chemically and physically inert in the presence of the matrix material selected. An appropriate choice of rigid inclusion diameter in relation to the sinterable matrix particle diameters is also important.

Investigate the potential applications of using other commercially available masteralloy powders and use the same skin matrix powder for the core.

Investigate the potential applications of producing complex ceramic materials from simple ceramics. Lumby et al[204], Jack and Wilson[205] and Paris and Grollier-Baron[206] all outline in their United States patents techniques of forming Sialons from either alumina and silicon nitride, or from silica and aluminium nitride, or from various combinations of silica, alumina, silicon nitride and aluminium nitride, with small additions of sintering aids such as magnesia or yttria. This will permit further exploitation of PCM, and provide impetus for commercial powder companies to develop novel masteralloy powders to widen the range of masteralloy powders currently commercially available. It also offers a novel in-situ process of producing Sialon skins surrounding a silica or alumina core.

Investigations could be carried out to determine whether the solvent debinding mathematical models apply to solvent debinding of powder co-injected mouldings, once the pre-exponential frequency factors and activation energies are found or determined for the solvents and binder components used in PCM.

PCM presently uses a two-stage debinding process and there is a growing trend in the PIM industry moving away from the technique of solvent debinding to a single thermal debinding step. Work would need to be undertaken to determine whether it is feasible to use a single debinding step in debinding PCM components.
The current work on PCM has used organically based binder systems. There has been a growing trend for the use of water-based binder systems in PIM. If both the core and skin powders used in PCM are inert in the presence of water as a debinding solvent,

then work could be undertaken to examine the feasibility of using a water-based binder system in PCM.

13.2 Feedstock material properties

The series model that was used to model the thermal properties of the feedstocks was observed to slightly overestimate the true thermal conductivity. Work could be undertaken to develop a more suitable thermal conductivity model.

The feedstock thermal conductivity and specific heat capacity data were obtained under a heating regime. In the mould cavity, the material being injection moulded undergoes rapid cooling. This could potentially lead to errors in the C-Mold prediction. The determination of the feedstock thermal conductivity and specific heat capacity data should be repeated, but under a cooling profile. This would permit a more realistic modelling and prediction of the injection moulding process with the use of C-Mold. In addition, the use of high cooling rates in the determination of specific heat capacity will reveal any presence of supercooling, and the C-Mold simulations should be re-run to allow the study of the effects of supercooling on the predicted skin profile.

The feedstock PVT's were calculated by a rule of mixtures approach. This approach was not experimentally verified in the present work. Measuring the feedstock PVT experimentally would provide the opportunity to verify or disprove the rule of mixtures approach to calculating the PVT of feedstocks.

If further PVT experiments, using a confining fluid technique show that there are more than two distinct domains or that there are significant volume changes at changes of state for any of the binder system constituents, then this implies that the current 2-domain Tait model is inadequate. A multiple domain modified Tait equation could be developed and substituted for the 2-domain modified Tait equation. This would require rewriting or modifying the C-Mold modelling software.

The binder composition used in the research work has 4 melting transitions altogether, which would indicate that there are 5 distinct domains and 4 volume changes and a 5-domain modified Tait equation could be derived to achieve improved accuracy of the modelling of PVT curves.

It was not possible to determine the thermal expansion coefficients for either the solid or molten domains, and the determination of the compressibility of the solid domain. Assumptions were made regarding the thermal expansion and compressibility of the binder system. Experimental work would therefore be needed to clarify these assumptions.

Work have been undertaken by Chang et al.[208] to investigate whether the cooling rate had any effect on the specific volume of the material being injection moulded. They conclude that the melt to solid transition temperature and the specific volume increases with increasing cooling rate. A modified 2-domain Tait equation is presented to include the effect of cooling rate, introducing two new parameters in the process, a material

constant θ, and a variable, cooling rate, q. Chang et al. imply that that the final density of the ejected mouldings decreases with increasing cooling rate. The cooling rate is dependent upon the thermal conductivity, specific heat capacity and density of the feedstock being injection moulded. This could lead to effects in the solvent/thermal debinding and sintering stages due to variations in the powder to binder volume ratio. It is suggested that research work should be undertaken to determine if the typical cooling rates encountered in the injection moulding of ceramic/metal feedstock, influence significantly the specific volume, and to determine if the cooling rates should be incorporated into the 2-domain Tait equation used in the C-Mold software.

At the present time, there are no suitable rheology models that calculate the feedstock viscosity as a function of the powder volume loading and individual binder components viscosities. The iterative loop that checks the feedstock viscosity in the PCM methodology could be eliminated if a suitable rheology model could be determined.

13.3 Computer modelling

It was observed that C-Mold makes an assumption that the core region is located centrally within the mould cavity. This implies that the bottom skin layer thickness and the top layer skin thickness are equal. Travelling microscope studies of the sectioned polymer cogs revealed this to be an incorrect assumption. The asymmetry in the actual skin profiles may be down to the cross-sectional thickness being 6 mm in the gear cog, which is considered to be an unusually high cross-sectional thickness for polymer injection moulding as the cooling times are proportional to the square of half the cross-sectional thickness. Since no other mould geometry was studied, it was not possible to investigate if non-symmetrical skin profiles exist in mouldings injected into other mould geometries of a lower cross-sectional thickness. An investigation should therefore be carried out for mould geometries that have thinner cross-sectional thicknesses to see if this effect still occurs. C-Mold was used with a single simple mould geometry, the gear cog mould, and further work is required to determine if C-Mold predicts the skin profile with sufficient accuracy for complex mould geometries.

If residual stresses form during the injection moulding of PCM components, the stresses are frozen in during cooling. Evidence of frozen in stresses become evident during subsequent sintering by the PCM components warping. The C-Mold software suppliers have indicated that C-Mold can be used to predict warpage in injection moulded polymer components. It is suggested that work could be undertaken to determine if C-Mold could be used as a tool to predict warpage during sintering as a result of stresses created in the injection moulding stage.

The actual skin profiles were measured to a higher degree of accuracy than for the data of predicted skin profiles obtained from the results of the C-Mold simulations. This can be improved by using a smaller mesh element size and a higher number of layers. However, this would lead to a substantial increase in the computation time required to run an analysis. However, as computers become more powerful and cheaper, and with improvements in the quality of the written software, it would be worthwhile running the simulations again with a smaller mesh element size.

Further work needs to be carried out to determine the cause of the disagreement between the predicted and actual skin profile for the model ceramic co-injection system, and if it is confirmed to be the consequence of a flow instability, then finding a way of preventing or eliminating the flow instability would be worthwhile.

14 References

[1] Veltl, G., Harwig, T., Petzold, F. and Kunze, H. D. (1995). Investigations on metal injection moulding of 316L stainless steel. *Materials and manufacturing processes,* 10(3), 425 – 438.

[2] Hyatt, J. W. and I. S. (1872). *Improvement in process and apparatus for manufacturing pyroxyiline*. US patent 133,229.

[3] Schwartzwalder, K. (1949). Moulding of ceramic materials. *Injection Society bulletin*, 28, 459.

[4] Oxley, D. F. and Sandiford, D. J. H. (1971). Serving up a new plastic sandwich. Plastics and polymers, 27(9), 38 – 42.

[5] German, R. M. (1994). *Powder metallurgy science.* 2nd ed. Metal Powder Industry Metallurgy Institute, Princeton, NJ.

[6] Bose, A. (1995). The technology and commercial status of PIM. *Journal of the Minerals, Metals and Materials Society*, 47(8), 26 – 30.

[7] Anonymous (1996). Leading technology and ultrahard materials transformed into innovative watch design. *Powder metallurgy*, 39(3), 172 – 173.

[8] Deguchi, T., Ito, M., Obata, A., Koh, Y., Yamagishi, T. and Oshida, Y. (1996). Trial production of titanium orthodontic brackets fabricated by metal injection molding (MIM) with sintering. *Journal of dental research*, 75(7), 1491 – 1496.

[9] Martyn, M. T. and James, P. J. (1994). The processing of hard metal components by PIM. *International journal of refractory metals and hard materials,* 12(2), 61 – 69.

[10] Kuhn, H. A. and Dax, R. F. (1996). Powder metallurgy product and process development at Concurrent Technologies Corporation. *International journal of powder metallurgy*, 32(3), 229 – 236.

[11] Xie, Z., Huang, Y., Wu, J. and Zheng, L. (1995). Microwave debinding of a ceramic injection moulded body. *Journal of materials science letters*, 14(11), 794 – 795.

[12] Mutsuddy, B. B. and Ford, R. G. (1995). *Ceramic injection molding.* Chapman and Hall, London.

[13] Pease, L. F. (1990). Overview of MIM in North America; world market size and forecast. *Metal powder reports*, 45(5), 345 – 354.

[14] Alcock, J. R. and Stephenson, D. J. (1996). Powder injection moulding: some novel developments. *Materials world,* 4(11), 629 – 630.

[15] Duszczyk, J. (1995). The workshop on advanced sintering materials. *International journal of powder metallurgy*, 31(2), 177.

[16] Matthews, F. L. and Rawlings, R. D. (1994). *Composite materials: engineering and science.* Chapman and Hall, London, 287 – 320.

[17] McCrum, N. G., Buckley, C. P., and Bucknall, C. B. (1995). *Principles of polymer engineering.* Oxford University Press, Oxford. Chapter 6, 13 – 15.

[18] Meyer, W, (1989). Co-injection: versatility spurs automotive potential. *Plastics technology*, April 1989, 109 – 112.

[19] Mascia, F. (1992). The co-injection technology: a new way for producing parts in the automotive industry. In: *New alternative materials for the automotive industries.* Automotive Automation Ltd, Selsdon, Surrey, England.

[20] Betts, T. (1997). Co-injection moulding: old news or not? *Plastics world*, 55(3), 13 – 15.

[21] Alvain, O., Bravo, B., Hanson, S. and Knight, P. (1996). *Metal co-injection moulding.* MSc group project, Cranfield University, Chapter 3, 25 – 30.

[22] Alcock, J. R., Logan, P. M., Staphenson, D. J. (1996). Metal co-injection moulding. *Journal of materials science letters*, 15(23), 2033 – 2035.

[23] Mapleston, P. (1994). Versatile CAE software speeds part development. *Modern plastics*, 71(2), 44 – 47.

[24] Moulding simulation software available (1991). *Plastics news*, 2(46), 10.

[25] Alcock, J. R., Logan, P. M., and Stephenson, D. J. (1998). Surface engineering by co-injection moulding. *Surface and coatings technology*, 195(1-2), 65 – 71.

[26] Shimizu, T., Murakoshi, Y., Wechwitayakhlung, K., Sano, T. and Negishi, H. (1997). Characterisation of the moulding methods and the binder system in the MIM process. *Journal of materials processing techno*logy, 63(1-3), 753 – 758.

[27] Hsu, K. C., Lin, C. C. and Lo, G. M. (1994). Effect of wax composition on injection moulding of 304L stainless steel. *Powder metallurgy*, 37(4), 272 – 276.

[28] Amaya, H. E. (1990). Solvent dewaxing: principles and application. In: *Proceedings of the 1990 powder metallurgy conference and exhibition, part 3: Advances in power metallurgy processing.* Metal Powder Industries Federation, Princeton, NJ, 233 – 246.

[29] Stevens, R. (1986) *An introduction to Zirconia,* Magnesium Elektron Publication No 113, Magnesium Elektron Ltd, Manchester, England, 2nd Ed, 17 - 30.

[30] Pease, L. F., and Blomacher, M. (1990). Cost Reduced Feedstocks for Metal Injection Molding. In: *Advances in powder metallurgy*, Vol. 3, Pittsburgh, Pennsylvania, USA, 20-23 May 1990. Metal Powder Industries Federation, Princeton, New Jersey, 341-358.

[31] Wigotsky, V. (1994). Compounding: working simpler. *Plastics engineering*, 50(40), 22 – 26.

[32] Chung, J. T. (1983). Counter-rotating, partially intermeshing, conical twin screw extruder. *Plastics Compounding,* 6(4), 59 - 60, 62, 64, 67.

[33] Ebenhoch, J. S. and Krueger, D. C. (1997). Proceedings of the 1997 international conference on powder metallurgy and particulate materials. *Advances in powder metallurgy and particulate materials,* 3(3), 18-201 - 18-208.

[34] Hens, K. F. And Kupp, D. (1995). Advanced production methods for different PIM feedstocks, In: *Proceedings of the 1995 International Conference and Exhibition on Powder Metallurgy and Particulate Materials,* Metal Powder Industries Federation, Princeton, NJ, USA, 6/45 - 6/54.

[35] Edirisinghe, M. And Evans, J. R. G. (1986). Compounding ceramic powders prior to injection moulding. *British Ceramic Proceedings,* (38), 67 - 80.

[36] Hogan, T. A. and Bradley, N. L. (1997) Mixing and preparation of highly filled feedstocks for ceramic injection moulding. In: *Proceedings of the 1997 55th Annual Technical Conference,* Society of Plastics Engineers, Brookfield, CT, USA, 265 - 270.

[37] Ess, J. W. and Hornsby, P. R. (1987). Twin screw extrusion compounding of mineral filled thermoplastics: Dispersive mixing effects. *Plastics and Rubber Processing and Applications,* 8(3), 147 - 156.

[38] Hunt, K. N. and Evans, J. R. G. (1988). Influence of mixing route on the properties of ceramic injection moulding blends. *British Ceramic Transactions and Journal,* 87(1), 17 - 21.

[39] Buerkle, E. (1988). Quality improvement in injection moulding as function of the plasticising system, *Industrial and Production Engineering,* 12(3), 20, 22 - 25.

[40] Martin, C. (1993). Basic screw design geometries and system configurations to manufacture plastic compounds via twin screw extruders. In: *Proceedings of the 63rd Annual convention of the Wire Association International,* Wire Association International Inc, Guilford, CT, USA, 174 - 179.

[41] Rios, A. C., Gramann, P. J. and Osswald, T. A. (1998). Comparative study of mixing in co-rotating twin screw extruders using computer simulation. *Advances in Polymer Technology,* 17(2), 107 - 113.

[42] Appello, M. (2000). Characterisation of dispersion of carbon black in high density polyethylene using dielectric measurements. *Plastics, rubber and composites,* 29(5), 207-211.

[43] Kalyon, D.M., Lawal, A., Yazici, R., Yaras, P. and Ralikar, S. (1999). Mathematical modelling and experimental studies of twin screw extrusion of filled polymers. *Polymer engineering and science,* 39(6), 1139-1151.

[44] Shorr, N. (1995). Preheating turns on efficiency. *Modern plastics*, 72(6), 83.

[45] Spencer, R. S. and Gilmore, G. D. (1950). Role of pressure, temperature and time in the injection moulding process. *Modern plastics*, 27, 143.

[46] Angermann, H. H. and van der Biest, O. (1995). Binder removal in powder injection moulding. *Reviews in particulate materials*, 3, 35-69.

[47] Trunec, M. and Cihlar, J. (1997). Thermal debinding of injection moulded ceramics. *Journal of the European Ceramic Society*, 17(2 – 3), 203 – 209.

[48] Hammond, P. D. and Evans, J. R. G. (1995). The use of overpressure in thermolytic debinding of moulded ceramic bodies. *Journal of the European Ceramic Society*, 15(2), 117 – 125.

[49] Tsai, D-S. and Chen, W-W. (1995). Solvent debinding kinetics of alumina green bodies by powder injection moulding. *Ceramics international*, 21(4), 257 – 264.

[50] Cartier, T., Ferrato, M. and Baumard, J-F. (1995). Supercritical debinding of injection moulded ceramics. *Journal of the American Ceramics Society*, 78(4), 1787 – 1792.

[51] Cartier, T., Delhomme, E. and Baumard, J-F. (1997). Mechanisms of binder removal involved in supercritical debinding of injection moulded ceramics. *Journal de physique III*, 7(2), 291 – 302.

[52] Cartier, T., Ferrato, M. and Baumard, J-F. (1995). Influence of the debinding method on the mechanical properties of plastic formed ceramics. *Journal of the European Ceramics Society*, 15(9), 899 – 909.

[53] Finn, C. K. (1991). Vacuum binder removal and collection. *International journal of powder metallurgy*, 27(2), 127 – 132.

[54] Ebenhoch, P., Trubenbach, P. and Weinand, D. (1992). Process parameters for a fast catalytic debinding system. Powder injection moulding symposium, Metal Powder Industries Federation, Princeton, NJ., 385 – 392.

[55] Kim, S. W., Lee, H. W., Song, H. and Kim, B-H. (1996). Pore structure evolution during solvent extraction and wicking. *Ceramics international*, 22(1), 7 – 14.

[56] Vetter, R., van den Brand Horninge, W. R., Vervoort, P. J. and Majewska-Glabus, I. (1994). Square root wick debinding model for powder injection moulding. *Powder metallurgy*, 37(4), 265 – 271.

[57] Moore, J. A., Harding, B. P., Lograsso, B. K., and Anderson, L. E. (1995). Atmosphere control during debinding of PIM parts. *Journal of materials engineering and performance*, 4(3), 275 – 282.

[58] Shuquan, L., Baiyun, H. and Xuanhui, Q. (1996). Debinding mechanisms and kinetics for PW in PW – WC feedstocks under air atmosphere. *Transactions of the Non-ferrous Metals Society of China*, 6(2), 72 – 75.

[59] Angermann, H. H. and van der Biest, O. (1994). Removal of low molecular weight components in thermal debinding of MIM compacts. *International journal of powder metallurgy*, 30(4), 445 – 452.

[60] Angermann, H. H. and Van Der Biest, O. (1993). Progress in conventional thermal debinding of PIM parts with a novel thermoplastic based binder formulation. In: *Proceedings of the 3rd international conference on powder metallurgy in aerospace, defence and demanding applications.* Metal Powder Industries Federation, Princeton, NJ., 325 – 332.

[61] Arii, T., Terayama, K., and Fiji, N. (1996). Controlled rate thermal analysis: study of the process of superhard material debinding. *Journal of thermal analysis*, 47(6), 1649 – 1661.

[62] Duncavage, D. P. and Finn, C. W. P. (1993). Debinding and sintering of injection moulded 316L stainless steel. In*: Advances in powder metallurgy and particulate materials*, 5, Metal Powder Industry Metallurgy Institute, Princeton, NJ.

[63] German, R. M. (1990). *Powder injection moulding.* 1st ed. Metal Powder Industries Federation, Princeton, NJ.

[64] Takekawa, J. (1996). Enhancement of sintering of injection moulded ferrous mixed powder compacts by Silane treatment. *Materials transactions, JIM,* 37(2), 157 – 162.

[65] Skorokhod, V. V. (1995). Development of the ideas of YA. I. Frenkel in the contemporary rheological theory of sintering. *Powder metallurgy and metal ceramics, 34(9,10), 521 - 527.*

[66] Shinagawa, K. (1996). Finite element simulation of sintering process. *JSME International Journal, 39(4), 565 - 572.*

[67] Zhang, W. (1996). Calculations of internal stresses during sintering in two dimensions. *Journal of the American ceramic society*, 79(8), 2141 - 2144.

[68] Belen'kii, V. Z. (1993). Mathematical analysis of Ivensen's model for the shrinkage of pore volume during the sintering of a porous body. *Powder metallurgy and metal ceramics,* 32(8), 704 - 708.

[69] Liu, Y. and Patterson, B. R. (1994). Determination of pore mobility during sintering. *Metallurgical and materials transactions: A,* 25A(1), 81 - 87.

[70] Ashby, M. F. (1987). *A program for constructing maps for hot isostatic pressing.* Cambridge University Press, Cambridge, U.K.

[71] Shu, H. and Johnson, D. L. (1997). A practical approach to sintering. *American ceramic society bulletin*, 76(2), 72 – 76.

[72] Shu, H. and Johnson, D. L. (1996). Master sintering curve: a practical approach to sintering. *Journal of the American ceramic society*, 79(12), 3211 – 3217.

[73] Antonova, M. M. and Privalov, Y. G. (1986). Sintering behaviour of compacts from a mixture of titanium and iron powders in hydrogen. *Soviet Powder Metallurgy and Metal Ceramics,* 25(4), 291 - 296.

[74] Chan, T. Y. and Lin, S. T. (1997). Sintering of elemental carbonyl iron and carbonyl nickel powder mixtures. *Journal of Materials Science,* 32(8), 1963 - 1967.

[75] Garin, J. L. and Mannheim, R. L. (1998). Manufacturing of Mo-25 Re and Mo-50 Re alloys by means of powder sintering at medium temperatures. *Materials and Manufacturing Processes,* 13(5), 731 - 747.

[76] Narasimhan, K. S. (2001). Sintering of powder mixtures and the growth of ferrous powder metallurgy. *Materials Chemistry and Physics,* 67(1-3), 56 - 65.

[77] Wada, N., Kankawa, Y. and Kaneko, Y. (1997) Comparison between Cu-Ni alloy powder and Cu, Ni powder mixture by metal injection moulding. *Journal of the Japan Society of Powder and Powder Metallurgy,* 44(7). 596 - 603.

[78] Li, J., Kawasaki, A. and Watanabe, R. (1997). Effects of content and size of Al_2O_3 particle dispersion on the sintering densification rate of Y-PSZ/Al_2O_3 composites. *Journal of the Japan Society of Powder and Powder metallurgy,* 44(12), 1083 - 1088.

[79] Nakada, Y. and Kimura, T. (1997). Effects of shape and size of inclusions on the sintering of ZnO-ZrO_2 composites. *Journal of the American Ceramic Society,* 80(2), 401 - 406.

[80] Nakada, Y., Yamazaki, M. and Kimura, T. (1997). Effect of ZrO2 inclusions on the densification and microstructure development of Ag-matrix composites. *Journal of the Japan Society of Powder and Powder metallurgy,* 44(11), 1043 - 1048.

[81] Shinagawa, K. and Hirashima, Y. (1998). Constitutive model for sintering of mixed powder compacts, In: *Proceedings of the 1998 5th International Symposium on functionally graded materials, FGM 98,* Dresden, Germany. Trans Tech Publications, Uetikon-Zuerich, Switzerland, 1041 - 1046.

[82] Lafer, M., Bouvard, D. and Stutz, P. (1993). Influence of alumina Inclusions on the densification of superalloy powder. *Powder metallurgy international,* 25(1), 23.

[83] Besson, J. and Evans, A. G. (1992). The effect of reinforcements on the densification of a metal powder. *Acta metallurgica et materialia*, 40(9), 2247 – 2256.

[84] Taylor, D. C., Dunand, D. C. and Mortenson, A. (1993). Initial-stage hot-pressing of monosized Ti and 90-percent Ti-10 percent TiC powders. *Acta metallurgica et materialia*, 41(3), 955 – 965.

[85] Thibault, P., Bouvard, D., Stutz, P. and Baccino, R. (1994). *Hot isostatic pressing 93.* Elsevier Science, Amsterdam.

[86] Zavaliangos, A., Lam, A. and Wen, J. (1996*).* *Advances in powder metallurgy and particulate material,* 16. Metal Powder Industries Federation, Princeton, NJ.

[87] Lange, F. F., Atteraas, L. and Zok, F. (1991). Deformation consolidation of metal powders containing steel inclusions. *Acta metallurgica et materialia*, 39(2), 209.

[88] Yamaguchi, K., Takakura, N. and Imatani, S. (1997). Compaction and sintering characteristics of composite metal powders. *Journal of materials processing technology*, 63(1-3), 364 – 369.

[89] Fan, C-L. and Rahaman, M. (1992). Factors controlling the sintering of ceramic composites: Conventional processing. *Journal of the American Ceramic Society*, 75(8), 2056 - 2065.

[90] Turner, C. D. and Ashby, M. E. (1996). The cold isostatic pressing of composite powders --I. Experimental investigations using model powders. *Acta materialia*, 44(11), 4521 – 4530.

[91] Rahaman, M. N. (1995). *Ceramic processing and sintering.* 1st ed. Marcel Dekker, Inc. New York, 595-601.

[92] Delie, F. and Bouvard, D. (1998). Effect of inclusion morphology on the densification of powder composites, *Acta materialia,* 46(11), 3905 – 3913.

[93] Lord, H. A. and Williams, G. (1975). Mould filling studies for the injection moulding of thermoplastic materials. *Polymer engineering and science*, 15(8), 582 – 553.

[94] Wang, C. and McCabe, T. (1993). Computer model simulates powder injection moulding. *Advanced materials and processes*, 44(4), 27 - 29.

[95] Najmi, L. A. and Lee, D. (1991). Modelling of mould filling process of powder injection moulding. *Polymer engineering and science*, 31(15), 1137 – 1148.

[96] Najmi, L. A. and Lee, D. (1994). Application of mould filling software to powder injection moulding. *International journal of powder metallurgy*, 30(2), 231 – 240.

[97] Anonymous (1993). New mould analysis software for beginners and sophisticated users. *Plastics technology*, 39(9), 12, 17, 21.

[98] Anonymous (1989). Advanced CAE technology C-Mold. (*Plastics technology*, 35(4), 83.

[99] Aksit, M. F. and Lee, D. (1995). A lumped parameter analysis of powder injection moulding. *International journal of powder metallurgy*, 31(4). 351 – 363.

[100] Kwon, T. H. and Park, J. B. (1995). Finite element analysis modeling of powder injection molding filling process including yield stress and slip phenomena. *Polymer engineering and science*, 35(9), 741 – 753.

[101] Anonymous (1991). Mould analysis for gas and co-injection arrives. *Plastics technology*, 37(2), 14.

[102] Kirkland, C. (1990). Co-injection process simulation introduced. *Plastics world*, 48(13), 27.

[103] AC Technology web page on the suite of C-Mold software. http://catalyst.sun.com.cgi-bin/displayprod.pl/12969.

[104] Sherman, R. (1994). Making the most of CAE software. *Plastics design forum*, 19(10), 47 – 49.

[105] Trudesdell, C. (1968). *Essays in the history of mechanics.* Springer-Verlag, Berlin.

[106] Cogswell, F. N. (1981). *Polymer melt rheology: a guide for industrial practice.* E. Horwood, Chichester.

[107] Whorlow, R. W. (1980). *Rheological techniques.* E. Horwood, Chichester.

[108] Brydson, J. A. (1981). *Flow properties of polymer melts*, 2nd ed. Godwin in association with the Plastics and Rubber Institute, London.

[109] Rabinowitsch, B., cited in Brydson, J. A. (1981). *Flow properties of polymer melts*, 2nd ed. Godwin in association with the Plastics and Rubber Institute, London; sections 2.2.2 to 2.2.6.

[110] Bagley, E. B. (1957). Ends corrections in capillary flow of polyethylene. *Journal of applied physics*, 28(5), 624 – 627.

[111] Charley, R. V. (1961). Melt flow indexing of polypropylene. *British plastics*, 34, 476 – 481.

[112] Bartos, O. and Holomet, J. (1971). Unstable flow of amorphous polymer through capillaries. *Polymer engineering and science*, 11(4), 324 – 334.

[113] den Otter, J. L., Wales, J. L. S. and Schijf, J. (1967). The velocity profile of molten polymers during laminar flow. *Rheologica acta*, 6(3), 205 – 209.

[114] Chauffoureaux, J. C., Dehennan, C. and van Rijckevorsil, J. (1979). Flow and thermal stability of rigid PVC. *Transactions of the Society of Rheology*, 23(1), 1 – 24.

[115] Uhland, E. (1979). Das anomale Flussverhalten von Polyathylen hoher Dichte. *Rheologica acta,* 18(1), 1 – 24.

[116] Mooney, M. (1931). Explicit formulas for slip and fluidity. *Journal of rheology*, 2(2), 210 – 222.

[117] Kamal, M. R. and Nyun, H. (1980). Capillary viscometry: a complete analysis including pressure and viscous hating effects. *Polymer engineering and science*, 20(2), 109 – 119.

[118] Van Wazer, J. R. (1963). *Viscosity and flow measurement: a laboratory handbook of rheology.* Interscience, New York.

[119] Shah, J. and Nunn, R. E. (1987). Rheology of metal injection moulding feedstock. *Powder metallurgy international*, 19, 38 – 40.

[120] Kaanevskii, I. M., Aminov, A. N. and Vasil'eva, V. V. (1990). Dependence of the viscosity of mixtures of petroleum products on the composition. *Chemistry and technology of fuels and oils*, 26(7-8), 431 – 433.

[121] Metzner, A. B. (1985). Rheology of suspensions in polymeric liquids. *Journal of rheology*, 29(6), 739 – 775.

[122] Williams, M. L., Landel, R. F. and Ferry, J. D. (1955). The temperature dependence of relaxation mechanisms in amorphous polymers and other glass forming liquids. *Journal of the American chemical society*, 77, 3701 – 3707.

[123] Cross, M. M. (1965). Rheology of non-Newtonian fluids: a new flow equation for pseudoplastic systems *Journal of colloid science*, 20, 417 - 437.

[124] Zoller, P. (1982). A study of the pressure-volume-temperature relationships of four related amorphous polymers: polycarbonate, polyarylate, phenoxy and polysulfone. *Journal of polymer science*, polymer physics edition, 20(8), 1453 – 1464.

[125] Zoller, P. and Bolli, P. (1980). Pressure-volume-temperature relationships of solid and molten poly(ethylene-terphthalate). *Journal of macromolecular science-physics,* B18(3), 555 – 568.

[126] Walsh, D., Dee, G. and Ougizawa, T. (1990). Pressure-volume-temperature measurements of polymers and polymer mixtures. *Makromolecular chimie-makromolecular symposia*, 38, 255 – 266.

[127] Ougizawa, T., Dee, G. T. and Walsh, D. (1991). Pressure volume temperature properties and equations of state in polymer blends: characteristic parameters in polystyrene/poly(vinyl methyl ether) mixtures. *Macromolecules*, 24(13). 3834 – 3837.

[128] le Neindre, B. and Tufeu, R. (1981). Application of the Tait equation to the determination of thermophysical properties of fluids under pressure. In: *Proceedings of the international CODATA conference*, 1981, Kyoto, Japan, 411 - 414.

[129] Tait, P. G. (1888). Compressibility of water, glass, and mercury. *Physics and chemistry of the voyage of H. M. S. Challenger*. 2(4), 3 – 73, plus Appendix G.

[130] Dymond, J. H. and Malhotra, R. (1988). The Tait equation: 100 years on. *International journal of thermophysics*, 9(6), 941 - 951.

[131] Nanda, V. S. and Simha, R. J. (1964). Theoretical interpretation of Tait equation parameters. *Journal of chemical physics*, 41, 1884 - 1885, 3870.

[132] Simha, R., Wilson, P. S. and Olabisi, O. (1973). Pressure-volume-temperature properties of amorphous polymers: empirical and theoretical predictions. *Kolloid-Zeitschrift und Zeitschrift fur polymere*, 251(6), 402 - 408.

[133] Zoller, P. (1979). The pressure-volume-temperature properties of three well characterised low density polyethylenes. *Journal of applied polymer science,* 23(4), 1051-1056.

[134] Zoller, P. (1979). Pressure-volume-temperature relationships of solid and molten polypropylene and poly(butene-1). *Journal of applied polymer science,* 23(4), 1057 - 1061.

[135] Matveyev, Y.I and Askadskii, A.A. (1985). Effect of rate of temperature variation and of deformation rate on glass transition in polymers. *Polymer science USSR (English translation of Vysokomolekulyarnye soyedineniya series A),* 27(11), 2648 - 2654.

[136] Oehmke, F. and Wiegmann, T. (1994). Measuring PVT curves at high cooling rates. *Proceedings of the 52nd annual technical conference,* part 2 of 3, 2247 - 2248.

[137] Toratani, H. and Takamizawa, K. (1994). Effect of pressure on the relation between glass transition temperature and molecular weight for monodispersed polystyrenes. *Polymer journal*, 26(7), 797 - 803.

[138] Benediktov, M. V., Dushchenko, V. P., Kolupaev, B. S. and Tarasenko, Y. G. (1972). Thermal properties of filled plasticised PVC. Soviet Plastics, (5), 49 - 51.

[139] Zoller, P. and Hoehn, H. H. (1982). Pressure-volume-temperature properties of blends of poly (2,6-dimethyl-1, 4-phenylene ether) with polystyrene. *Journal of polymer science*, polymer physics edition, 20, 1385 – 1397.

[140] Jain, R. K., Simha, R. and Zoller, P. (1982). Theoretical equation of state of polymer blends: the poly (2,6-dimethyl-1, 4-phenylene ether)-polystyrene pair. *Journal of polymer science*, 20(9), 1399 – 1408.

[141] Rodgers, P. (1993). Pressure-volume-temperature relationships for polymeric liquids: a review of equations of state and their characteristic parameters for 56 polymers. *Journal of applied polymer science*, 48(6), 1061 – 1080.

[142] *C-Mold reference manual* (1996). AC Technology, New York.

[143] Zoller, P. and Fakhreddine, Y. (1994). Pressure-volume-temperature studies of semicrystalline polymers. *Thermochimica acta*, 238, 397 – 415.

[144] Chiu, C-P. and Liu, K-A. (1995). A method for measuring PVT relationships of thermoplastics using an injection moulding machine. *Polymer engineering and science*, 35(19), 1505 – 1510.

[145] Ishida, H and Rimdusit, S. (1999) Heat capacity measurement of boron nitride filled polybenzoxazine. *Journal of thermal analysis and calorimetry*, 58(3), 497 - 507.

[146] Krupa, I. and Chodak, I. (1998). Effect of matrix-filler interactions on the thermal capacity of LDPE/graphite composites. *Journal of macromolecular science*, A35(7-8), 1159 - 1164.

[147] TA Instruments (a subsidiary of Waters Corporation) (c1996). *Modulated DSC™ compendium: basic theory and experimental considerations*. TA Instruments, Leatherhead, UK.

[148] Reading, M., Luget, A. and Wilson, R. (1994). Modulated differential scanning calorimetry. *Thermochimica acta*, 238, 295 – 307.

[149] Wunderlich, B., Jin, Y. and Boller, A. (1994). Mathematical description of DSC based on periodic temperature modulation. *Thermochimica acta*, 238, 277 – 293.

[150] Boller, A., Jin, Y. and Wunderlich, B. (1994). Heat capacity measurement by modulated DSC at constant temperature. *Journal of thermal analysis*, 42, 307 – 330.

[151] El-Sharkawy, A. A., Halil, A. S., Abousehly, A. M., and El-Hakim, A. A. (1992). Thermophysical properties of polyvinyl chloride filled with calcium carbonate. *High Temperatures - High Pressures*, 24(3), 323 - 328.

[152] Wong, C. P. and Bollampally, R. S. (1999). Thermal conductivity, elastic modulus, and coefficient of thermal expansion of polymer composites filled with ceramic particles for electronic packaging. *Journal of applied polymer science,* 74(14), 3396 - 3403.

[153] Tavman, I. H. (1998). Effective thermal conductivity of isotropic polymer composites. *International communications in heat and mass transfer,* 25(5), 723 - 732.

[154] Tavman, I. H. (1996). Thermal and mechanical properties of aluminium powder filled high density polyethylene composites. *Journal of applied polymer science,* 62(12), 2161- 2167.

[155] Maiti, S. N. and Ghosh, K. (1994). Thermal characteristics of silver powder filled polypropylene composites. *Journal of applied polymer science,* 52 (8), 1091 - 1103.

[156] Agari, Y and Uno, T. (1985). Thermal conductivity of polymer filled with carbon materials: Effect of conductive particle chains on thermal conductivity. *Journal of applied polymer science,* 30(5), 2225 - 2235.

[157] Kowalski, L., Kuszczyk, J. and Katgerman, L. (1999). Thermal conductivity of metal powder-polymer feedstock for powder injection moulding. Jo*urnal of materials science*, 34(1), 1 – 5.

[158] Imura, S. and Takegoshi, E. (1974). Effect of gas pressure on the effective thermal conductivity of packed beds. *Heat transfer – Japanese research*, 3(4), 13 – 26.

[159] Kampf, H. and Karsten, G. (1970). Effects of different types of void volumes on the radial temperature distribution of fuel pins. *Nuclear applied technology*, 9, 288 – 300.

[160] Flinta, J. E. (1958). Thermal conductivity of uranium dioxide. In: *Fuel elements conference*, Paris, TID-7546, 516 – 525.

[161] Russell, H. W. (1935). Principles of heat flow in porous insulators. *Journal of the American Ceramics Society*, 18(1), 1 – 5.

[162] Eucken, A. (1932). The thermal conductivity of ceramic refractory materials. *VDI Forschung*, VDI Verlag, Berlin, 353, 1 - 16.

[163] Bruggeman, D. A. G. (1935). Berechnung vershiedene physikalischer konstanten von heterogenen substanzen. *Annals of physics*, 24(636), 6736 – 6764.

[164] Kanari, K. (1977). Thermal conductivity of composite materials, *Dai 14 kai Nippon Sinpojiumu Ronbunshu,* Kobunshi high polymers, Japan, 26, 557 - 561.

[165] Lichtenecker, K (1926). Development of a geometric mean model. *Physik Z,* 27, 115.

[166] Mitoff, S. P. (1960). Properties calculations for heterogeneous systems. *Advanced in materials research*, 3, 305 – 329.

[167] Maxwell, J. C. (1904). *A Treatise on electricity and magnetism.* Vol 1, 3rd ed, Oxford.

[168] Rayleigh, Lord. (1892). On the influence of obstacles arranged in rectangular order upon the properties of a medium. *Phil. Mag.* 34, 481 - 502.

[169] Runge, I. (1925). Zur elektrishen leitfahigkeit metallischer aggregate. *Zeitschr f. techn. physik.* 6(2), 61 - 79.

[170] De Vries, D. A. (1952). The thermal conductivity of soil. Mededelingen van de landbouwhogeschool te *Wageningen,* 52(1), 1 - 73.

[171] Deissler, R. G. and Eian, C. S (1952*). Investigation of effective thermal conductivities,* NACA RM E52 CO5.

[172] Deissler, R. G. and Eian, C. S (1953*). Effective thermal conductivities of MgO, stainless steel and uranium oxide powders in various gases,* NACA RM E53 GO3.

[173] Swift, D. L. (1966). Thermal conductivity of spherical metal powders including the effect of an oxide coating. *International journal of heat and mass transfer,* 9, 1061.

[174] Patterson, J. D. (1985) Error analysis and equations for the thermal conductivity of composites. *Thermal conductivity 18,* Plenum press, New York.

[175] Progelhof, R. C., Throne, J. L. and Ruetsch, R. R. (1976). Methods for predicting the thermal conductivity of composite systems. *Polymer engineering and science,* 16(9), 615 – 625.

[176] British Standards Institute. (1986*). Method for determining thermal insulating properties.* BS874.

[177] Marcus, S. M. and Blaine, R. L. (1994). Thermal conductivity of polymers, glasses and ceramics by modulated DSC. *Thermochimica acta*, 243(2), 231 – 239.

[178] de Groot, J. J., Kestin, J. and Sookiazian, H. (1974). Instrument to measure the thermal conductivity of gases. *Physica*, 75, 454 – 482.

[179] Healey, J. J., de Groot, J. J. and Kestin, J. (1976). The theory of the transient hot-wire method for measuring thermal conductivity. *Physica*, 82(C), 392 – 408.

[180] Kestin, J. and Wakeham, W. A. (1978). A contribution to the theory of the transient hot-wire technique for thermal conductivity measurements. *Physica*, 92(A), 102 – 116.

[181] Clifford, A. A., Kestin, J. and Wakeham, W. A. (1980). A further contribution to the theory of the transient hot-wire technique for thermal conductivity measurements. *Physica*, 100(A), 370 – 374.

[182] Drotnig, W. H. (1985). An automated thermal conductivity probe and applications to powders. In: *Thermal conductivity*, 18, Plenum Press, New York, 247 – 257.

[183] Haarman, J. W. (1973). Thermal conductivity measurements of He, Ne, Ar, Kr, N_2, and CO_2, with a transient hot wire method. *American institute of physics conference proceedings*, 11(193), 193 – 198.

[184] British Standards Institute. (1997). *Determination of thermal diffusivity by the laser flash (or heat pulse) method.* BS821, section 2.

[185] British Standards Institute. (1990). *Method for the determination of thermal diffusivity by the laser flash (or heat pulse) method.* BS7124, section 4.2.

[186] Taylor, R. E. and Clark, L. M. (1974). Finite pulse time effects in flash diffusivity method. *High Temperature High Pressures,* 6(1) 65 - 72.

[187] Kumada, T. and Kobayasi, K. (1976). Evaluation of error incurred in determining thermal properties by laser flash. *Journal of Nuclear Science Technology,* 13(6), 315 - 320.

[188] Gao, M. Williams, S. G. K. and Rowe, D. M. (1993). Laser flash method for measuring thermal conductivity of thermoelectric materials. *Hongwai Jishu/Infrared Technology,* 15(6) 9 - 14.

[189] Kestin, J. and Paul, R. (1980). Absolute determination of the thermal conductivity of the noble gases at room temperature up to 35MPa. *Physica* 100(A), 349 - 369.

[190] Assael, M. J., Dix, M., Lucas, A. and Wakeham, W. A. (1981). Absolute determination of the thermal conductivity of the noble gases and two of their binary mixtures as a function of density. *Journal of the Chemical Society Faraday transactions*, 1(77), 439 - 464.

[191] Clifford, A. A., Gray, P., Johns, A. I., Scott, A. C and Watson, J. T. R. (1981). Thermal conductivities of argon, nitrogen and hydrogen between 300 and 400K and up to 25 MPa. *Journal of the Chemical Society Faraday transactions*, 1(77), part 11, 2679 - 2691.

[192] Nieto de Castro C, A, and Roder, H. M. (1981). Thermal conductivity of argon at 300.65K. Evidence for a critical enhancement. In: *Proceedings of the 8th symposium of thermophysical properties,* Gaitherburg, MD, USA, ASME, New York, 241 - 246.

[193] Maitland, G. C., Rigby, M., Smith, E. B. and Wakeham, W. A. (1981). *Intermolecular forces*. Clarendon, Oxford, chapter 5.

[194] *C-Mold reference manual* (1996). AC Technology, New York.

[195] Ougizawa, T., Dee, G. T. and Walsh, D. J. (1989). PVT properties and equations of state for polystyrene molecular weight dependence of the characteristic parameters in equation-of-state theories. *Polymer*, 30(9), 1675.

[196] Ougizawa, T., Dee, G. T. and Walsh, D. J. (1992). The pressure volume temperature properties of polyethylene, poly(dimethyl siloxane), poly(ethylene glycol) and poly(propylene glycol) as a function of molecular weight. *Polymer*, 33(16), 3462 - 3469.

[197] *C-Mold User's guide: Filling and post filling* (1996). AC technology, New York. 27-3 to 27-6.

[198] Cubberly, W. H. Metals Handbook: Properties and selection: Non-ferrous alloys and pure metals, American society for metals, 9th Ed, 2, 743.

[199] Cubberly, W. H. Metals Handbook: Stainless steels, tool materials and special purpose metals, American society for metals, 9th Ed, 3, 33-35.

[200] Schneider, S. J. Engineered materials handbook: Ceramics and Glasses, The materials information society, ASM International, 4.

[201] Baik, S. and Bae, I-J. (1997) Abnormal grain growth of alumina. *Journal of the American ceramic society,* 80(5), 1149 - 1156.

[202] Wieser, M. W. and De Jonghe, L. C. (1988) Inclusion size and sintering of composite powders. *Journal of the American ceramic society,* 71(3), 125 - 127.

[203] Kimura, T., Kajiyama, H., Kim, J. and Yamaguchi, T. (1989) Effect of inclusion size on the densification of ZnO-$Zn_7Sb_2O_{12}$, *Journal of the American ceramic society,* 72(1), 140 - 141.

[204] Lumby, R. J., Wills, R. R. and Hosley, R. F. (1976). *Method of forming ceramic products.* US patent 3,991,148.

[205] Jack, K. H. and Wilson, W. I. (1982). *Ceramic materials.* US patent 3,991,166.

[206] Paris, R. A. and Grollier-Baron, T. (1982). *Method of producing sialon products.* US patent 4,360,506.

[207] Krueger, S. and Long, G. (1991). The effect of green density and the role of magnesium oxide additive on the densification of alumina measured by small angle neutron scattering. *Journal of the American ceramic society.* 74(7), 1578 - 1584.

[208] Chang, R. Y., Chen, C. H. and Su, K. S. (1996). Modifying the Tait equation with cooling rate effects to predict the pressure-volume-temperature behaviours of amorphous polymers: modelling and experiments. *Polymer engineering and science*, 36(13), 1789 - 1795.

Appendix A: Derivation of the series model and the parallel model

Derivation of mathematical equations for the thermal conductivity of mixtures for two simple geometries

The parallel and series heat energy flow formulae can be found in the following reference: Patterson, J. D. (1985) Error analysis and equations for the thermal conductivity of composites. *Thermal conductivity 18,* Plenum press, New York.

The derivation of the parallel and series heat flow models are presented here. These allow the calculation of the thermal conductivity of a mixture of any number of substances with known individual thermal conductivities and known volume ratios.

1. Parallel heat energy flow

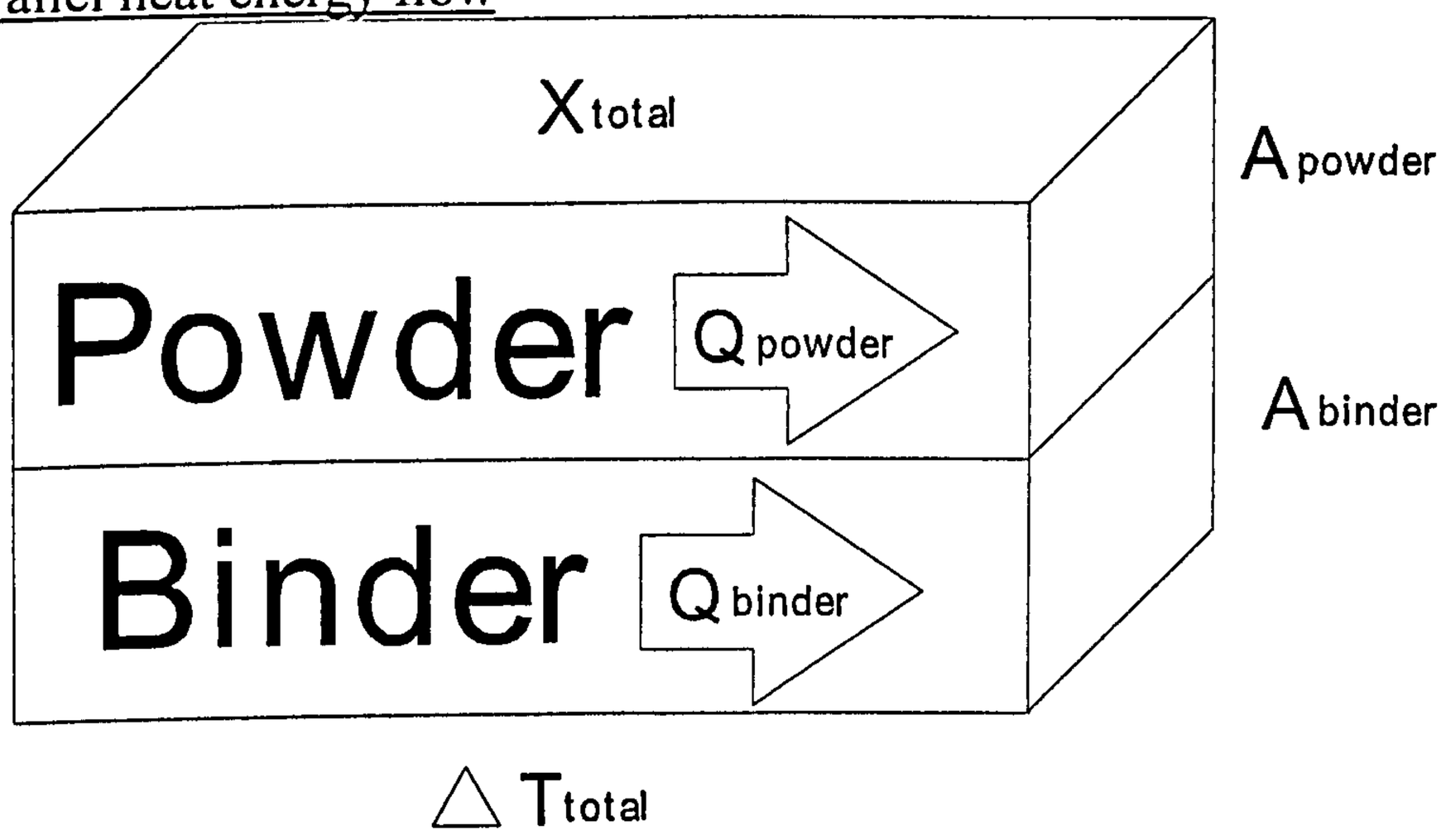

Figure A.1 Diagram of a material arrangement in parallel

The incoming heat, Q_{total} will split into two components, Q_{powder} and Q_{binder}, such that:

$$Q_{total} = Q_{powder} + Q_{binder} \qquad \text{Eqn (A.1)}$$

Considering the heat flow rates:

$$\frac{\partial Q_{total}}{\partial t} = \frac{\partial Q_{powder}}{\partial t} + \frac{\partial Q_{binder}}{\partial t} \qquad \text{Eqn (A.2)}$$

If the powder has a thermal conductivity k_{powder}, the binder has a thermal conductivity k_{binder}, and the composite has a thermal conductivity k_{total}, recall from the definition of thermal conductivity:

$$\frac{\partial Q_{powder}}{\partial t} = -A_{powder}.k_{powder}.\frac{\Delta T}{\Delta x}$$ Eqn (A.3)

$$\frac{\partial Q_{binder}}{\partial t} = -A_{binder}.k_{binder}.\frac{\Delta T}{\Delta x}$$ Eqn (A.4)

$$\frac{\partial Q_{total}}{\partial t} = -A_{total}.k_{total}.\frac{\Delta T}{\Delta x}$$ Eqn (A.5)

Substituting equations A.3, A.4 and A.5 into equation A.2 and rewriting yields:

$$k_{total}A_{total} = A_{binder}.k_{binder} + A_{powder}.k_{powder}$$ Eqn (A.6)

Extending the equation to the general solution for a composite comprising of n plates in parallel yields:

$$k_{total}A_{total} = \sum_{i=1}^{i=n} A_i k_i$$ Eqn (A.7)

Only the volume ratio of the binder to powder is known. The area ratios are constant for any change in x, hence volumetric ratios can be substituted yielding:

$$k_{total} = \frac{V_1k_1+V_2k_2+.....+V_{n-1}k_{n-1}+V_nk_n}{V_{total}}$$ Eqn (A.8)

Thus, for a composite with n parallel components with known volume ratios, the thermal conductivity of the feedstock can be calculated using equation A.8.

2. Series heat energy flow

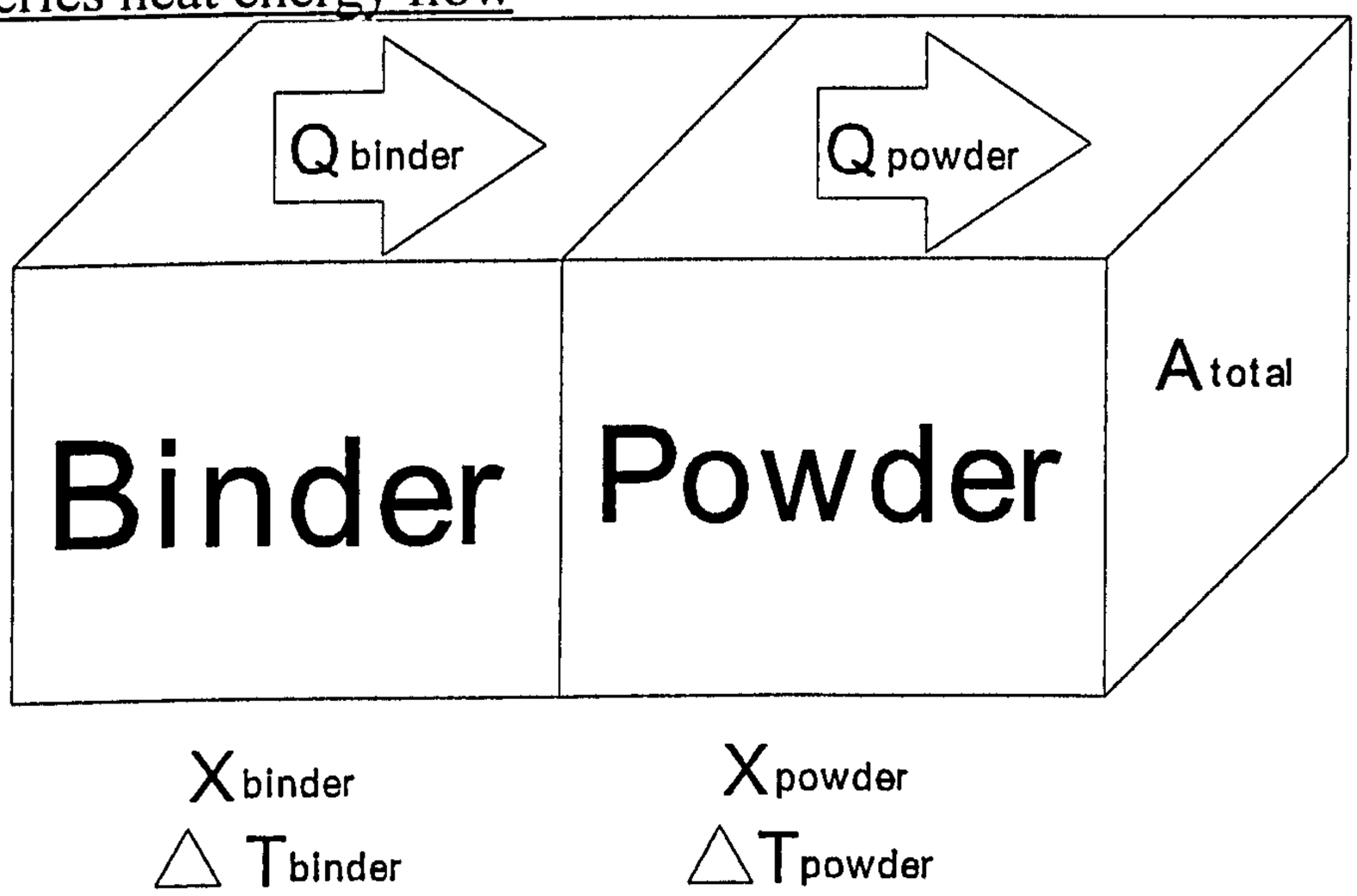

Figure A.2 Representation of materials arranged in series

Considering the heat flows:

$$\frac{\delta Q_{total}}{\delta t} = \frac{\partial Q_{powder}}{\partial t} = \frac{\partial Q_{binder}}{\partial t} \qquad \text{Eqn (A.9)}$$

Also, the total thickness is the sum of the individual thicknesses:

$$\Delta x_{total} = \Delta x_{powder} + \Delta x_{binder} \qquad \text{Eqn (A.10)}$$

Also, considering the temperature differences:

$$\Delta T_{total} = \Delta T_{powder} + \Delta T_{binder} \qquad \text{Eqn (A.11)}$$

rearranging equation A.11 yields:

$$\frac{\Delta T_{powder}}{\Delta T_{total}} + \frac{\Delta T_{binder}}{\Delta T_{total}} = 1 \qquad \text{Eqn (A.12)}$$

$$\frac{\partial Q_{powder}}{\partial t} = -A.k_{powder} \cdot \frac{\Delta T_{powder}}{\Delta x_{powder}} \qquad \text{Eqn (A.13)}$$

$$\frac{\partial Q_{binder}}{\partial t} = -A.k_{binder} \cdot \frac{\Delta T_{binder}}{\Delta x_{binder}} \qquad \text{Eqn (A.14)}$$

$$\frac{\partial Q_{total}}{\partial t} = -A.k_{total} \cdot \frac{\Delta T_{total}}{\Delta x_{total}} \qquad \text{Eqn (A.15)}$$

Hence substituting equations A.13, A.14 and A.15 into equation A.9 yields:

$$k_{total} \cdot \frac{\Delta T_{total}}{\Delta x_{total}} = k_{binder} \cdot \frac{\Delta T_{binder}}{\Delta x_{binder}} = k_{powder} \cdot \frac{\Delta T_{powder}}{\Delta x_{powder}} \qquad \text{Eqn (A.16)}$$

Splitting Equation A.16 into two equations yields:

$$k_{total} \cdot \frac{\Delta T_{total}}{\Delta x_{total}} = k_{binder} \cdot \frac{\Delta T_{binder}}{\Delta x_{binder}} \qquad \text{Eqn (A.17)}$$

$$k_{total} \cdot \frac{\Delta T_{total}}{\Delta x_{total}} = k_{powder} \cdot \frac{\Delta T_{powder}}{\Delta x_{powder}} \qquad \text{Eqn (A.18)}$$

Rearranging equation A.17 yields:

$$\frac{k_{total}}{k_{binder}} \cdot \frac{\Delta x_{binder}}{\Delta x_{total}} = \frac{\Delta T_{binder}}{\Delta T_{total}} \qquad \text{Eqn (A.19)}$$

Rearranging equation A.18 yields:

$$\frac{k_{total}}{k_{powder}} \cdot \frac{\Delta x_{powder}}{\Delta x_{total}} = \frac{\Delta T_{powder}}{\Delta T_{total}} \qquad \text{Eqn (A.20)}$$

Substituting equations A.19 and A.20 into equation A.12 and rearranging yields:

$$\frac{x_{powder}}{k_{powder}} + \frac{x_{binder}}{k_{binder}} = \frac{x_{total}}{k_{total}} \qquad \text{Eqn (A.21)}$$

Extending equation A.21 for the general case of a composite containing n plates in series is:

$$\frac{x_{total}}{k_{total}} = \sum_{i=1}^{i=n} \frac{x_i}{k_i} \qquad \text{Eqn (A.22)}$$

In the case of the powder filled feedstock, only the volume ratio of the binder to powder is known. The thickness ratios are constant for any change in the crossectional area, thus the thickness ratios can safely be substituted with volume ratios, yielding:

$$\frac{V_{powder}}{k_{powder}} + \frac{V_{binder}}{k_{binder}} = \frac{V_{total}}{k_{total}} \qquad \text{Eqn (A.23)}$$

Therefore for a composite with n components with known volume ratios, the general solution for the composite conductivity is:

$$k_{total} = \frac{V_{total}}{\frac{V_1}{k_1} + \frac{V_2}{k_2} + \ldots\ldots + \frac{V_{n-1}}{k_{n-1}} + \frac{V_n}{k_n}} \qquad \text{Eqn (A.24)}$$

Both the parallel and series case have been considered and the thermal conductivity of any composite material can be calculated from the volume fraction/ratios and thermal conductivities of all of the individual components of the composite. The series and parallel equations can be used to determine the lower and upper limits of the composite thermal conductivity.

Appendix B: derivation of the SPBM Model

Equations were derived from first principles to model the heat flow through a single spherical particle within a bulk matrix cube.

Spherical particulates within a bulk matrix model (SPBM Model)

Consider a single sphere with radius r within a regular cube of length 2r.

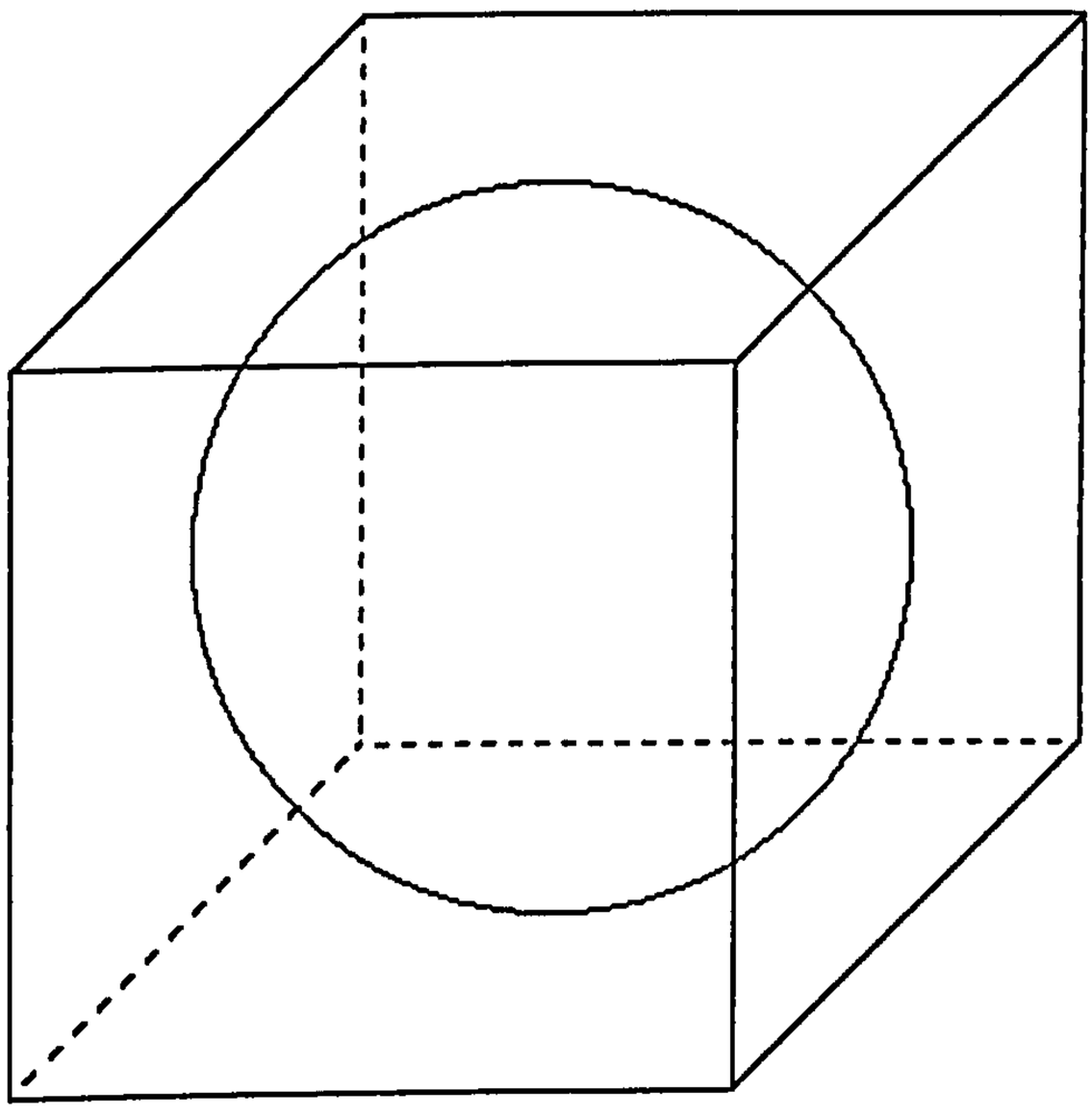

Figure B.1 Geometric representation of a sphere bounded by a cube

The volume of the cube will be $(2r)^3 = 8r^3$, and the volume of the sphere is $\frac{4}{3}\pi r^3$. This gives a volume fraction of :

$$\text{Volume fraction} = \frac{\frac{4}{3}\pi r^3}{8r^3} \qquad \text{Eqn (B.1)}$$

Cancelling r^3 and simplifying equation B1 yields:

$$\text{Volume fraction} = \frac{\pi}{6} = 0.5236 \qquad \text{Eqn (B.2)}$$

The volume fraction of 0.5236 is lower than the powder volume fractions encountered in PIM feedstocks, but it is useful as a first approximation.

Due to tri-axial symmetry, the cube can be divided into 8 identical cubes, where each cube has dimensions r, and a sector of a sphere with radius r, and subtended angles of 90° as in figure B.2.

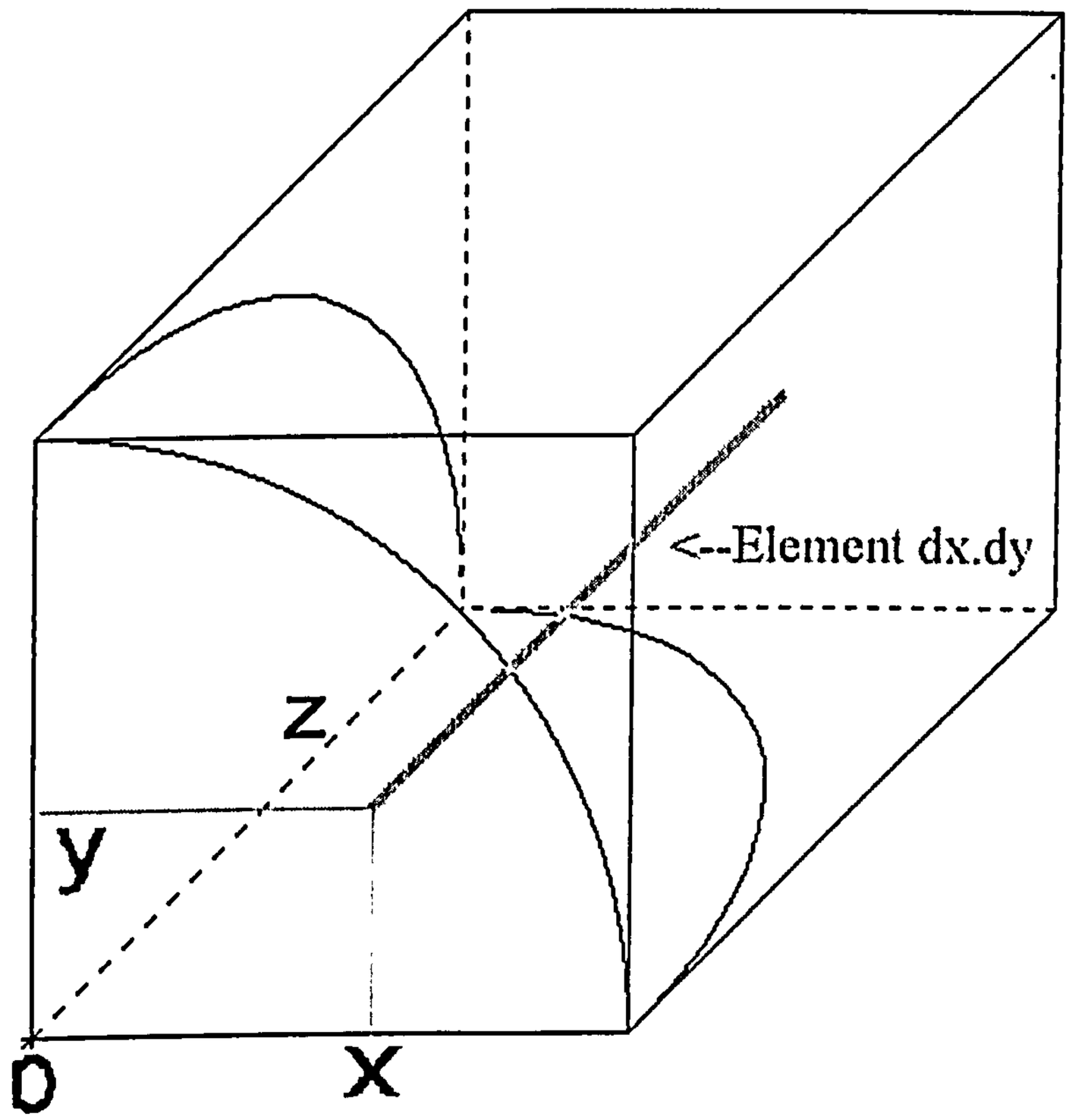

Figure B.2 Quadrant of figure B.3

Assuming that the heat flow direction is parallel to the z axis, the sphere has a thermal conductivity of k_p and that the thermal conductivity of the cube material is k_b. Consider a single regular rectangular element of dimensions r parallel to the z axis, and a cross-sectional area of dx.dy. This can be considered to be two materials in series for the purpose of calculating the thermal conductivity of the single element. Pythagoras's theorem gives the relationship between the cartesian co-ordinates of the point and the polar co-ordinate distance from the origin.

$$r^2 = x^2 + y^2 + z^2 \qquad \text{Eqn (B.3)}$$

Rearranging equation B.3 for z yields:

$$z = (r^2 - x^2 - y^2)^{\frac{1}{2}} \qquad \text{Eqn (B.4)}$$

This gives the z-axis distance from the x-y plane to the sphere's surface, and the distance from the sphere-matrix interface is (r-z). The series flow equation, equation A.24 can be used to calculate the thermal conductivity of the single element.

$$\frac{r}{ke} = \frac{r-(r^2-x^2-y^2)^{\frac{1}{2}}}{k_b} + \frac{(r^2-x^2-y^2)^{\frac{1}{2}}}{k_p} \qquad \text{Eqn (B.5)}$$

Where K_c = Thermal conductivity of the single element
K_b = Thermal conductivity of the binder
K_p = Thermal conductivity of the powder particulates

Simplifying equation B.5 yields:

$$\frac{r}{k_e} = \frac{k_p r - k_p(r^2-x^2-y^2)^{\frac{1}{2}} + k_b.(r^2-x^2-y^2)^{\frac{1}{2}}}{k_b.k_p} \qquad \text{Eqn (B.6)}$$

$$k_e = \frac{k_b.k_p.r}{k_p r - k_p(r^2-x^2-y^2)^{\frac{1}{2}} + k_b.(r^2-x^2-y^2)^{\frac{1}{2}}} \qquad \text{Eqn (B.7)}$$

To calculate the thermal conductivity of the whole composite, it is necessary to sum up all of the individual elements. Since they are arranged in parallel, the general form of equation A.6 can be used:

$$k_{total}A_{total} = \sum_{i=1}^{i=n} A_{e_i}k_{e_i} \qquad \text{Eqn (B.8)}$$

Where A_{e_i} = Cross-sectional area of the ith element (m^2)
k_{e_i} = Thermal conductivity of the ith element ($Wm^{-1}k^{-1}$)
A_{total} = Total cross-sectional area (m^2)
k_{total} = Total thermal conductivity ($Wm^{-1}k^{-1}$)
n = is the number of elements

However, total cross-sectional area $A_{total} = r^2$, and A_{e_i} is $x_i.y_j$, and equation B.8 becomes:

$$k_{total}.r^2 = \sum_{j=1}^{j=n}\sum_{i=1}^{i=n} x_i y_j k_{e_i} \qquad \text{Eqn (B.9)}$$

Substituting equation B.7 into equation B.9 gives the complete equation for the evaluation of the thermal conductivity of the composite for the sphere and an extra term is added in to account for the binder region outside the sphere.

$$k_{total}.r^2 = \left(\sum_{j=1}^{j=n}\sum_{i=1}^{i=n} x_i y_j \frac{k_b.k_p.r}{k_p r - k_p(r^2-x^2-y^2)^{\frac{1}{2}} + k_b.(r^2-x^2-y^2)^{\frac{1}{2}}}\right) + k_b\left(r^2 - \tfrac{1}{4}\pi r^2\right) \qquad \text{Eqn (B.10)}$$

Equation B.10 can be evaluated in a number of ways:

1. Double integration with respect to x and y

Converting equation B.10 to integral form yields:

$$k_{total} = \frac{1}{r^2}\left(\int_0^{r(r^2-y^2)^{\frac{1}{2}}}\int_0^{} \frac{k_b.k_p.r}{k_p r - k_p(r^2-x^2-y^2)^{\frac{1}{2}} + k_b.(r^2-x^2-y^2)^{\frac{1}{2}}}.dxdy\right) + k_b(1-\tfrac{1}{4}\pi) \quad \text{Eqn (B.11)}$$

Equation B.11 represents the full version of the SPBM model.

2. Numerical methods

Appendix C deals with the numerical method of evaluating equation B.10, and the method outlined in appendix C was used with equation B.10

Comparison of the SPBM model with Maxwell, Rayleigh, Runge and De Vries models

Section 4.6.2 introduced Maxwell's model, along with Rayleigh, Runge and De Vries models. All of these models are derived from Legendre functions and Laplace equations. In contrast, the SPBM model considers the heat flows through in terms of elements and summing up the elements in a series or parallel arrangement using either numerical approximation or double integration.

To aid direct comparison, graphs were plotted of these models for two scenarios. The first is the effect of varying the powder thermal conductivity on the feedstock thermal conductivity as illustrated by figure B.1. The second illustrates the effect of varying the binder thermal conductivity on the feedstock thermal conductivity. The powder volume fraction used for both scenarios was 0.5236.

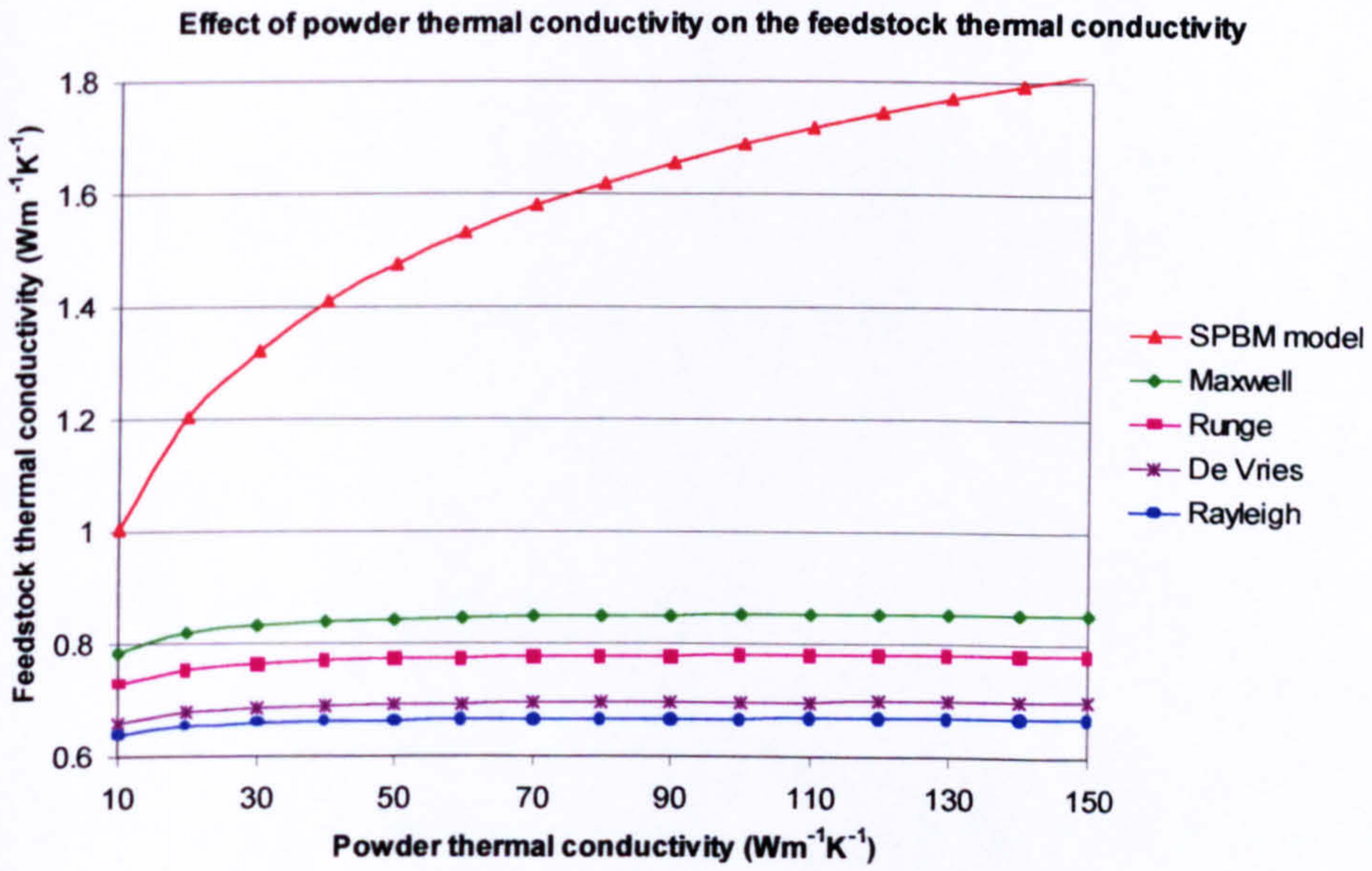

Figure B.3 Effect of varying the powder thermal conductivity on the feedstock thermal conductivity

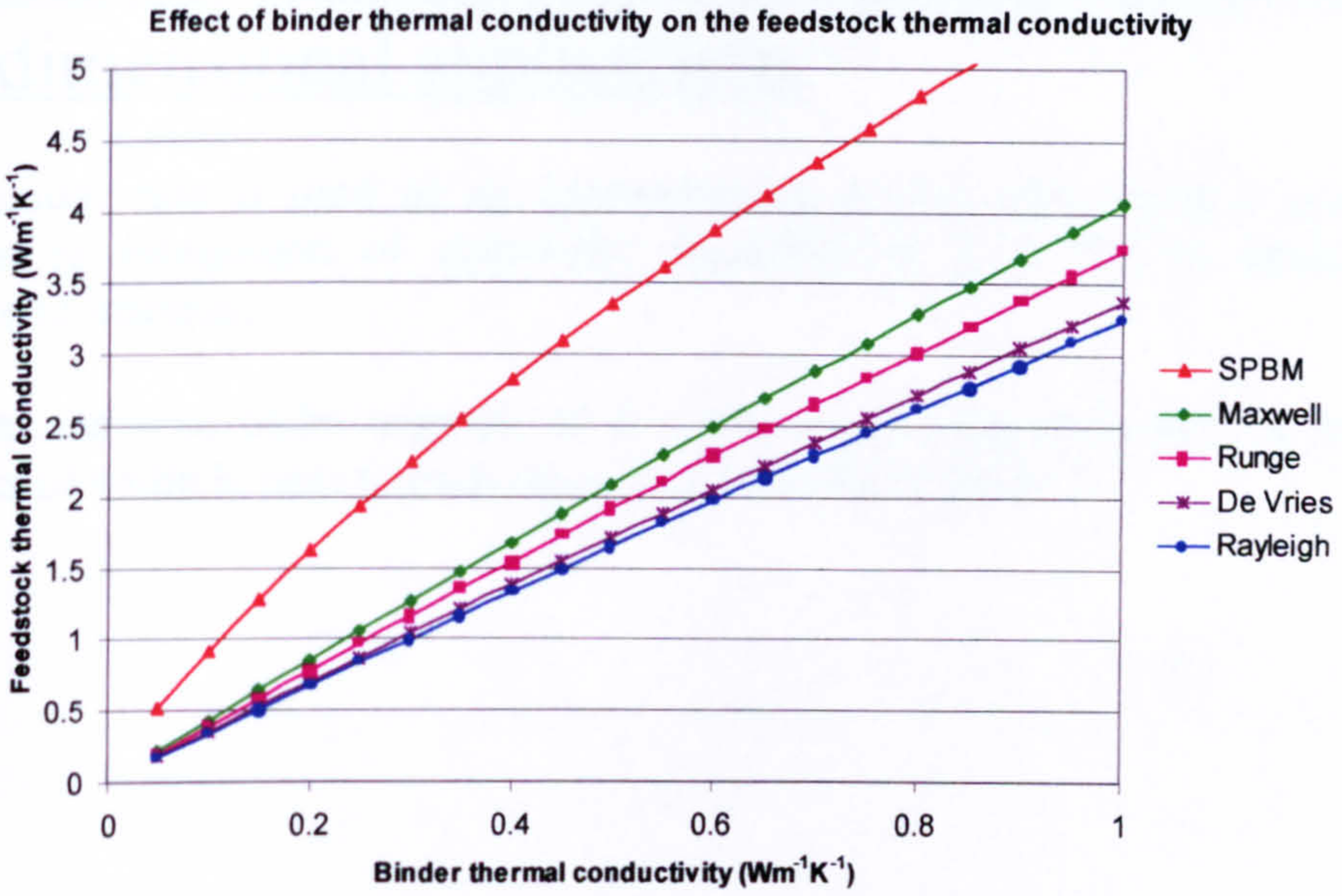

Figure B.4 Effect of varying the binder thermal conductivity on the feedstock thermal conductivity.

It is apparent that none of the models displayed figures B.3 and B.4 show any agreement even though the volume loading is fixed at 52.36% and that the spheres are arranged in a simple cubic lattice. The reasons for the disagreement between the models are thought to have its origins in the distinct ways that the models were derived from first principles.

Appendix C: Modification of the trapezium rule for three dimensional applications

The trapezium rule is used as an approximation of the area under a graph, as an alternative to integration of equations, especially if y = f(x) is mathematically impossible to integrate.

Recall that the area under a graph of y = f(x) can be approximated to be a set of trapeziums of width h, next to each other, as illustrated in figure 1.

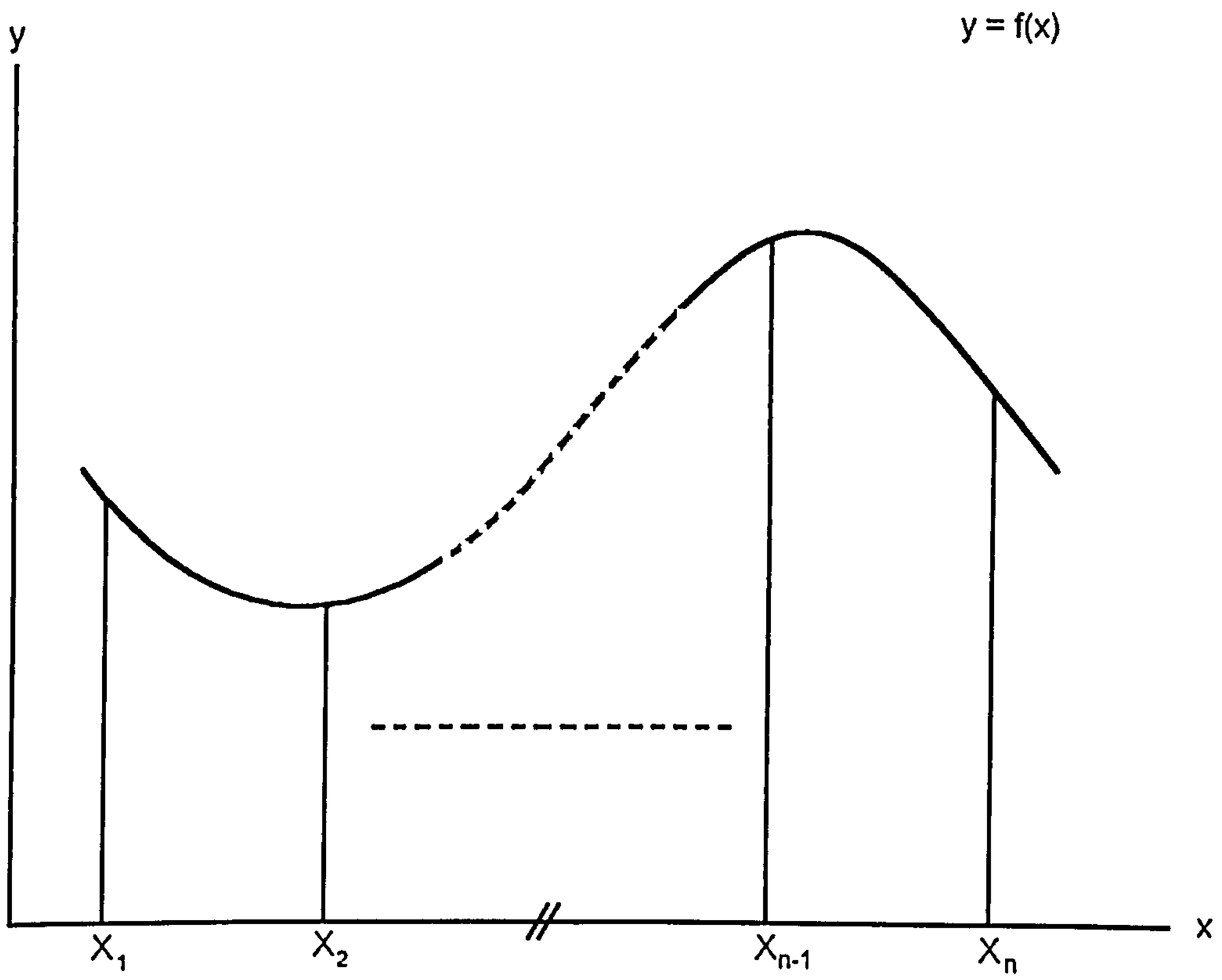

Figure C.1 Use of trapezium rule on a typical graph

$$\text{Area of a single trapezium} = \frac{h(a+b)}{2} \qquad \text{Eqn (C.1)}$$

Where h = width of trapezium
a = Length of left hand side
b = Length of right hand side

The area under the graph between $x = x_1$ to $x = x_n$ is the numerical sum of all the elemental trapezium areas inside the interval $x = x_1$ to $x = x_n$.

$$\int_{x=x_1}^{x=x_n} f(x).dx \approx \frac{h(y_1+y_2)}{2} + \frac{h(y_2+y_3)}{2} + \ldots\ldots + \frac{h(y_{n-2}+y_{n-1})}{2} + \frac{h(y_{n-1}+y_n)}{2} \qquad \text{Eqn (C.2)}$$

Simplifying equation C.2 yields:

$$\int_{x=x_1}^{x=x_n} f(x).dx \approx \frac{h}{2}(y_1 + y_2 + y_2 + y_3 + \ldots\ldots + y_{n-2} + y_{n-1} + y_{n-1} + y_n) \qquad \text{Eqn (C.3)}$$

Collecting up identical terms in equation C.3 yields:

$$\int_{x=x_1}^{x=x_n} f(x).dx \approx \frac{h}{2}(y_1 + 2(y_2 + y_3 + \ldots\ldots + y_{n-2} + y_{n-1}) + y_n) \qquad \text{Eqn (C.4)}$$

The accuracy of the numerical calculation improves with decreasing h, and the number of elements is equal to:

$$\text{Number of elements} = \frac{(x_n - x_1)}{h} \qquad \text{Eqn (C.5)}$$

<u>Modified 3 dimensional trapezium rule</u>

The trapezium rule can be extended for functions of the form z = f(x,y)

$$\text{Volume of a single 3 dimensional trapezium} = \frac{h^2(a+b+c+d)}{4} \qquad \text{Eqn (C.6)}$$

Where h^2 = cross-sectional area of the 3 dimensional trapezium
a,b,c,d = lengths of the four corners of the 3 dimensional trapezium

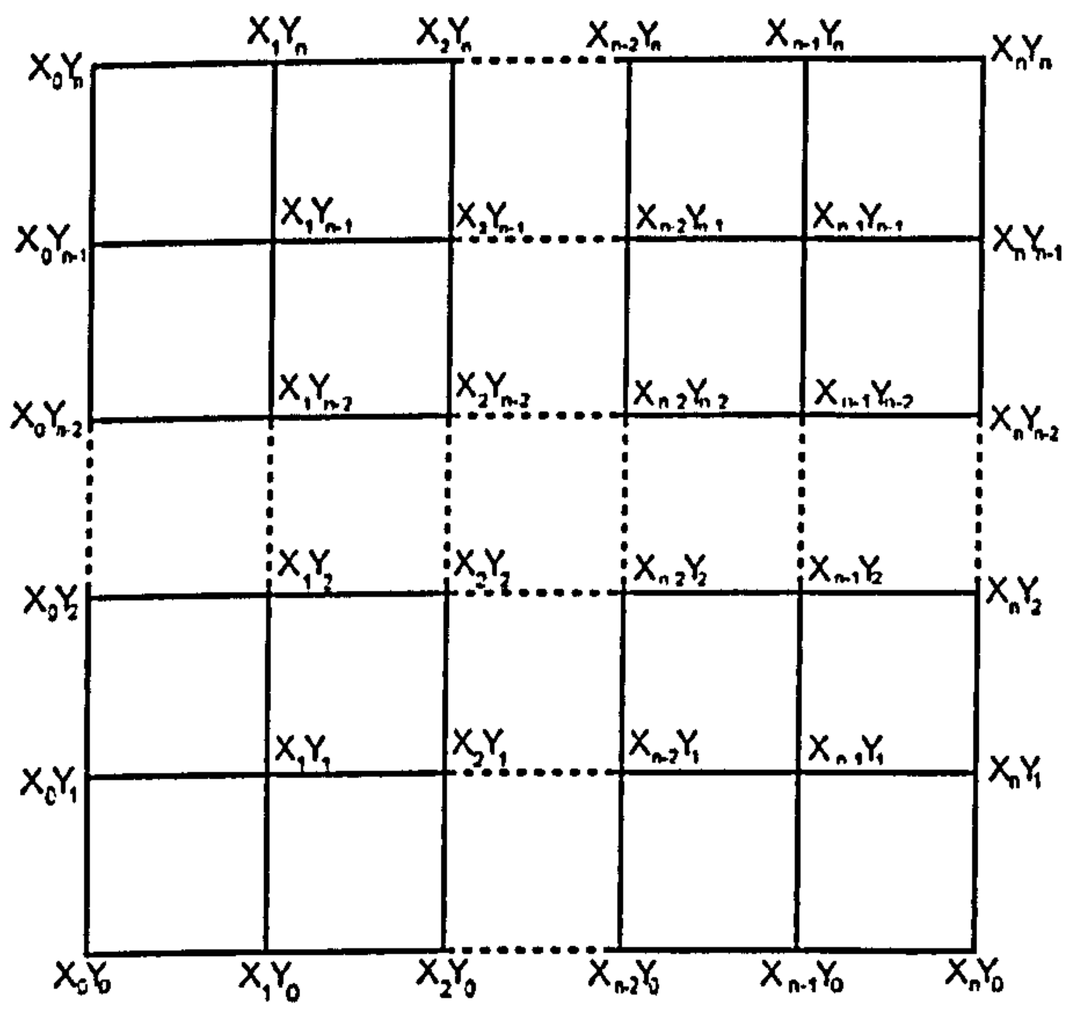

Figure C.2 Plan view of an arrangement of trapeziums for z = f(x,y)

The volume under the graph between $x = x_0$ to $x = x_n$ and $y = y_0$ to $y = y_n$ is the numerical sum of all the individual elemental trapezium volumes inside the interval.

$$\int_{y=y_0}^{y=y_n}\int_{x=x_0}^{x=x_n} f(x,y).dxdy \approx \frac{h^2(z_{00}+z_{10}+z_{01}+z_{11})}{4} +$$

$$\frac{h^2(z_{10}+z_{20}+z_{11}+z_{21})}{4} +$$

$$\frac{h^2(z_{01}+z_{02}+z_{11}+z_{12})}{4} +$$

$$\frac{h^2(z_{11}+z_{21}+z_{12}+z_{22})}{4} + \ldots\ldots\ldots$$

$$+\frac{h^2(z_{n-2,n-2}+z_{n-2,n-1}+z_{n-1,n-2}+z_{n-1,n-1})}{4}$$

$$+\frac{h^2(z_{n-1,n-2}+z_{n,n-2}+z_{n-1,n-1}+z_{n,n-1})}{4}$$

$$+\frac{h^2(z_{n-2,n-1}+z_{n-1,n-1}+z_{n-2,n}+z_{n-1,n})}{4}$$

$$+\frac{h^2(z_{n-1,n-1}+z_{n-1,n}+z_{n,n-1}+z_{n,n})}{4} \qquad \text{Eqn (C.7)}$$

Simplifying equation C.7 yields:

$$\int_{y=y_0}^{y=y_n}\int_{x=x_0}^{x=x_n} f(x,y).dxdy \approx \frac{h^2}{4}\left(\begin{array}{c}(z_{00}+z_{10}+z_{01}+z_{11})+\\(z_{10}+z_{20}+z_{11}+z_{21})+\\(z_{01}+z_{02}+z_{11}+z_{12})+\\(z_{11}+z_{21}+z_{12}+z_{22})+\ldots\ldots+\\(z_{n-2,n-2}+z_{n-2,n-1}+z_{n-1,n-2}+z_{n-1,n-1})\\+(z_{n-1,n-2}+z_{n,n-2}+z_{n-1,n-1}+z_{n,n-1})\\+(z_{n-2,n-1}+z_{n-1,n-1}+z_{n-2,n}+z_{n-1,n})\\+(z_{n-1,n-1}+z_{n-1,n}+z_{n,n-1}+z_{n,n})\end{array}\right) \qquad \text{Eqn (C.8)}$$

Collecting identical terms in equation C.8 yields:

$$\int_{y=y_0}^{y=y_n}\int_{x=x_0}^{x=x_n} f(x,y).dxdy \approx \frac{h^2}{4}\left(\begin{array}{c} (z_{0,0}+z_{n,0}+z_{0,n}+z_{n,n})+ \\ 2\left(\left(\sum_{i=1}^{i=n-1} z_{i0}\right)+\left(\sum_{j=1}^{j=n-1} z_{0j}\right)+\left(\sum_{i=1}^{i=n-1} z_{in}\right)+\left(\sum_{j=1}^{j=n-1} z_{nj}\right)\right) \\ 4\left(\sum_{j=1}^{j=n-1}\sum_{i=1}^{i=n-1} z_{ij}\right) \end{array} \right)$$

Eqn (C.9)

The accuracy of the numerical calculation improves with decreasing h, increasing the total number of elements.

$$\text{Number of elements} = \frac{(x_n-x_0)(y_n-y_0)}{h^2} \qquad \text{Eqn (C.10)}$$

Equation C.10 is the general solution of the modified 3 dimensional trapezium equation to calculate the volume under a graph of $z = f(x,y)$ for the boundaries of $x = x_0$ to $x = x_n$ and $y = y_0$ to $y = y_n$

Appendix D: SPBM model calculation computer program

```
/* This program calculates the composite thermal conductivity of a */
/* sphere inside a cube, and the sphere has a different thermal */
/* conductivity to the cube matrix */
#include <stdio.h>
#include <setjmp.h>
#include <math.h>
#include <ctype.h>

main()
{

/* kb is the binder thermal conductivity */
/* kp is the powder sphere thermal conductivity */
/* ke is the thermal conductivity of the ith element */
/* kt is the cumulative thermal conductivities of all the elements of the composite */
/* k is the thermal conductivity of the whole composite */
/* r is the radius of the sphere */
/* r2 is radius squared */
/* steps is the number of elements */
/* steps2 is the square of the steps */
/* h is the element thickness */
/* h2 is h squared, which gives the cross-sectional area of the element */

/* setting up the data types: */
double kb, kp, h, h2, kt, r, r2, kpr, numer;
long steps, i, j, steps2;
double k11, k12, k21, k22, ke, x1, x2, y1, y2;
double a11, a12, a21, a22, diff, k;


/* Start of Input parameters*/

kb = 0.200000000000;          /* binder thermal conductivity */
kp = 80.00000000000;          /* particle thermal conductivity */
r = 0.000001;                 /* radius of sphere */

/* End of input parameters */


kt=0.0;                       /* Reset kt to zero */
ke=0.0;                       /* reset ke to zero */
steps =1000;                  /* setting of the number of steps */
steps2 = steps*steps;         /* steps2 gives the total number of elements to evaluate */
```

```
h = r/(float)steps;        /* calculation of the element thickness */
h2=h*h;                    /* calculation of the element cross-sectional area */
numer = r*kp*kb;           /* Numerator equation */
kpr=kp*r;                  /* Product of powder thermal conductivity and radius */
diff=kb-kp;                /* Difference of powder thermal conductivity and binder thermal
conductivity */
r2=r*r;                    /* radius squared */

/* setting up two loops for working through each individual element */
 for (j=0;j<steps;j++)
 {
 for (i=0;i<steps;i++)
 {
 x1=h*(float)i;
 /* Calculating minimum x-axis position for the ith element */

 x2=h*(float)(i+1);
 /* Calculating maximum x-axis position for the ith element */

 y1=h*(float)j;
 /* Calculating minimum y-axis position for the ith element */

 y2=h*(float)(j+1);
 /* Calculating maximum y-axis position for the ith element */

 a11=x1*x1+y1*y1;
 /* Using pythagoras to calculate distance from the origin for the bottom left corner of
 element */

 a21=x2*x2+y1*y1;
 /* Using pythagoras to calculate distance from the origin for the bottom right corner of
 element */

 a12=x1*x1+y2*y2;
 /* Using pythagoras to calculate distance from the origin for the top left corner of
 element */

 a22=x2*x2+y2*y2;
 /* Using pythagoras to calculate distance from the origin for the top right corner of
 element */

 /* The four if-then loops test for whether any of the element corners is outside the
 sphere or not */
 /* if a corner of the element is outside the sphere then the thermal conductivity is set to
 kb */
```

```
/* k11, k12, k21 and k22 refer to the thermal conductivities of the element's four
corners. */

if(a11<=r2)
{
k11=numer/(diff*sqrt(r2-a11)+kpr);
}
else
{
k11=kb;
}

if(a21<=r2)
{
k21=numer/(diff*sqrt(r2-a21)+kpr);
}
else
{
k21=kb;
}

if(a12<=r2)
{
k12=numer/(diff*sqrt(r2-a12)+kpr);
}
else
{
k12=kb;
}

if(a22<=r2)
{
k22=numer/(diff*sqrt(r2-a22)+kpr);
}
else
{
k22=kb;
}

/* The average of the four thermal conductivity values for the element's corners are
averaged */
ke=(k11+k21+k12+k22)/(float)4;

/* The last calculated element's thermal conductivity is added to the cumulative total kt
*/
kt=kt+ke;
```

```
/* printf("i,j,ke,kt is %ld,%ld,%f,%f\n",i,j,ke,kt);          */
/* printf("k11,k21,k12,k22 is %f,%f,%f,%f\n",k11,k21,k12,k22);*/
}
}
/* The final cumulative kt total is divided by the sum of the element cross-sectional
areas */
/* to calculate the thermal conductivity of the whole composite */
k=kt/steps2;

/* Output to screen the numerical results */
printf("kb & kp are %f,%f\n",kb,kp);
printf("kt,k,steps are %f,%f,%ld",kt,k,steps2);
}
```

Appendix E: Machine, coolant, mould and parameters files

Machine parameter	Data value	Units
Machine manufacturer	Dassett	n/a
Model designation	DM30	n/a
Machine configuration	Horizontal	n/a
Machine type	Hydraulic	n/a
Clamp force	26.8	Tonne (metric)
Injection capacity (mass)	37	g
Injection capacity (volume)	40	cm^3
Maximum daylight	400	mm
Clamping stroke	220	mm
Horizontal tie rod clearance	254	mm
Vertical tie rod clearance	254	mm
Maximum clamping speed	12	cms^{-1}
Plasticating capacity	6	gs^{-1}
Maximum machine injection pressure	138	MPa
Injection rate	28	cm^3s^{-1}
Motor horse power	5.5	kW

Table E.1 Dassett DM30 injection moulding machine data used in C-Mold simulations

Parameter	Data	Units
Manufacturer	Castrol	n/a
Description	Oil	n/a
Density	0.836	gcm^{-3}
Specific heat capacity	2,250	$Jkg^{-1}K^{-1}$
Thermal conductivity	0.136	$Wm^{-1}K^{-1}$
Viscosity (C1)	6.476×10^{-5}	Pas
Viscosity (C2)	1,348	K
Viscosity (C3)	366.2	K

Table E.2 Coolant oil material properties data used in C-Mold simulations

Parameter	Data	Units
Manufacturer	Giffex	n/a
Mould material description	Tool steel P-20	n/a
Density	7.82	gcm^{-3}
Specific heat capacity	460	$Jkg^{-1}K^{-1}$
Thermal conductivity	36.5	$Wm^{-1}K^{-1}$
Linear thermal expansion coefficient	15×10^{-6}	K^{-1}

Table E.3 Gear cog mould tooling material data used in C-Mold simulations

Parameter	value	Units
Number of layers across full gap	12	n/a
Number of design outputs in filling	12	n/a
Number of detail outputs in filling	0	n/a
Pressure convergence criterion	0.5	%
Flow-rate convergence criterion	0.5	%
Melt-temperature convergence criterion	0.2	°C
Mould-melt heat transfer co-efficient	25,000	$Wm^{-2}K^{-1}$
Maximum number of pressure iterations	8	n/a
Maximum number of flow-rate iterations	125	n/a
Maximum number of melt-temperature iterations	100	n/a

Table E.4 Simulation parameter file used in C-Mold simulations

Appendix F: Polymer material properties data

ICI GXM43 polypropylene

Minimum processing temperature = 190°C
Maximum processing temperature = 288°C
Minimum mould temperature = 21°C
Maximum mould temperature = 60°C
Ejection temperature = 90°C
Constant polymer melt density = 0.77gcm^{-3}

Tait parameter	Data value	Units
B1s	1.10679 x 10^{-3}	m^3kg^{-1}
B2s	5.11 x 10^{-7}	$m^3kg^{-1}K^{-1}$
B3s	1.62932 x 10^{8}	Pa
B4s	4.74519 x 10^{-3}	K^{-1}
B1m	1.20226 x 10^{-3}	m^3kg^{-1}
B2m	9.13 x 10^{-7}	$m^3kg^{-1}K^{-1}$
B3m	8.79249 x 10^{7}	Pa
B4m	4.81736 x 10^{-3}	K^{-1}
B5	422.75	K
B6	1.18 x 10^{-7}	KPa^{-1}
B7	9.59 x 10^{-5}	m^3kg^{-1}
B8	0.15	K^{-1}
B9	2.06 x 10^{-8}	Pa^{-1}

Table F.1 2-domain modified Tait equation parameters

Temperature (°C)	Specific heat capacity ($Jkg^{-1}{}^{o}C^{-1}$)
254.5	2,000

Table F.2 Specific heat capacity vs temperature

Temperature (°C)	Thermal conductivity ($Wm^{-1}K^{-1}$)
215.5	0.15

Table F.3 Thermal conductivity vs temperature

Cross-WLF parameter	Data value	Units
n	0.24337	dimensionless
Tau*	23,304	Pa
D1	1.49 x 10^{11}	Pas
D2	263.15	K
D3	0	KPa^{-1}
A1	22.44	dimensionless
A2~	51.6	K
Transition temperature	135	°C

Table F.4 Cross WLF equation parameters

ICI GWM213 polypropylene

Minimum processing temperature = 190°C
Maximum processing temperature = 288°C
Minimum mould temperature =21°C
Maximum mould temperature = 60°C
Ejection temperature = 90°C
Constant polymer melt density = 0.77 gcm^{-3}

Tait parameter	Data value	Units
B1s	1.10679×10^{-3}	m^3kg^{-1}
B2s	5.11×10^{-7}	$m^3kg^{-1}K^{-1}$
B3s	1.62932×10^{8}	Pa
B4s	4.74519×10^{-3}	K^{-1}
B1m	1.20226×10^{-3}	m^3kg^{-1}
B2m	9.13×10^{-7}	$m^3kg^{-1}K^{-1}$
B3m	8.79249×10^{7}	Pa
B4m	4.01736×10^{-3}	K^{-1}
B5	422.75	K
B6	1.18×10^{-7}	KPa^{-1}
B7	9.59×10^{-5}	m^3kg^{-1}
B8	0.15	K^{-1}
B9	2.06×10^{-8}	Pa^{-1}

Table F.5 2-domain modified Tait equation parameters

Temperature (°C)	Specific heat capacity ($Jkg^{-1}°C^{-1}$)
254.5	3,100

Table F.6 Specific heat capacity vs temperature

Temperature (°C)	Thermal conductivity ($Wm^{-1}K^{-1}$)
215.5	0.15

Table F.7 Thermal conductivity vs temperature

Cross-WLF parameter	Data value	Units
n	0.35473	dimensionless
Tau*	16,000	Pa
D1	8.94×10^{6}	Pas
D2	263.15	K
D3	0	KPa^{-1}
A1	9.03	dimensionless
A2~	51.6	K
Transition temperature	135	°C

Table F.8 Cross WLF equation parameters

Solvay A3180 polyethylene

Minimum processing temperature = 177°C
Maximum processing temperature = 260°C
Minimum mould temperature = 32°C
Maximum mould temperature = 71°C
Ejection temperature = 90°C
Constant polymer melt density = 0.79 gcm^{-3}

Tait parameter	Data value	Units
B1s	1.10575×10^{-3}	m^3kg^{-1}
B2s	5.48×10^{-7}	$m^3kg^{-1}K^{-1}$
B3s	2.30357×10^{8}	Pa
B4s	4.05985×10^{-3}	K^{-1}
B1m	1.26054×10^{-3}	m^3kg^{-1}
B2m	9.69×10^{-7}	$m^3kg^{-1}K^{-1}$
B3m	1.00193×10^{8}	Pa
B4m	4.47097×10^{-3}	K^{-1}
B5	406.58	K
B6	1.54×10^{-7}	KPa^{-1}
B7	1.5481×10^{-4}	m^3kg^{-1}
B8	0.10275	K^{-1}
B9	3.38×10^{-8}	Pa^{-1}

Table F.9 2-domain modified Tait equation parameters

Temperature (°C)	Specific heat capacity ($Jkg^{-1}°C^{-1}$)
210	3,000

Table F.10 Specific heat capacity vs temperature

Temperature (°C)	Thermal conductivity ($Wm^{-1}K^{-1}$)
210	0.25

Table F.11 Thermal conductivity vs temperature

Cross-WLF parameter	Data value	Units
n	0.55675	dimensionless
Tau*	17,515	Pa
D1	4.87×10^{15}	Pas
D2	153.15	K
D3	0	KPa^{-1}
A1	34.47	dimensionless
A2~	51.6	K
Transition temperature	112	°C

Table F.12 Cross WLF equation parameters

Solvay TUB polyethylene

Minimum processing temperature = 190°C
Maximum processing temperature = 250°C
Minimum mould temperature = 32°C
Maximum mould temperature = 71°C
Ejection temperature = 90°C

Constant polymer melt density = 0.711gcm^{-3}

Tait parameter	Data value	Units
B1s	1.1068 x 10^{-3}	m^3kg^{-1}
B2s	6.82 x 10^{-7}	$m^3kg^{-1}K^{-1}$
B3s	1.7 x 10^{8}	Pa
B4s	5.0 x 10^{-3}	K^{-1}
B1m	1.243 x 10^{-3}	m^3kg^{-1}
B2m	9.6 x 10^{-7}	$m^3kg^{-1}K^{-1}$
B3m	9.51 x 10^{7}	Pa
B4m	4.2227 x 10^{-3}	K^{-1}
B5	389.15	K
B6	2.68 x 10^{-7}	KPa^{-1}
B7	1.36 x 10^{-4}	m^3kg^{-1}
B8	9.1722 x 10^{-2}	K^{-1}
B9	2.62 x 10^{-8}	Pa^{-1}

Table F.13 2-domain modified Tait equation parameters

Temperature (°C)	Specific heat capacity ($Jkg^{-1}°C^{-1}$)
150	2,600

Table F.14 Specific heat capacity vs temperature

Temperature (°C)	Thermal conductivity ($Wm^{-1}K^{-1}$)
210	0.27

Table F.15 Thermal conductivity vs temperature

Cross-WLF parameter	Data value	Units
n	0.22883	dimensionless
Tau*	28,555	Pa
D1	3.85 x 10^{20}	Pas
D2	153.15	K
D3	0	KPa^{-1}
A1	42.43	dimensionless
A2~	51.6	K
Transition temperature	112	°C

Table F.16 Cross WLF equation parameters

Exxon PP3536F1 low molecular weight polypropylene

Minimum processing temperature = 157°C
Maximum processing temperature = 180°C
Minimum mould temperature = 20°C
Maximum mould temperature = 40°C
Ejection temperature = 30°C
Constant polymer solid density = 0.905gcm^3

Tait parameter	Data value	Units
B1s	1.18×10^{-3}	m^3kg^{-1}
B2s	551.0×10^{-9}	$m^3kg^{-1}K^{-1}$
B3s	0.161×10^{9}	Pa
B4s	4.70×10^{-3}	K^{-1}
B1m	1.29×10^{-3}	m^3kg^{-1}
B2m	978.0×10^{-9}	$m^3kg^{-1}K^{-1}$
B3m	0.0866×10^{9}	Pa
B4m	4.82×10^{-3}	K^{-1}
B5	422.15	K
B6	118×10^{-9}	KPa^{-1}
B7	95.9×10^{-6}	m^3kg^{-1}
B8	0.15	K^{-1}
B9	19.8×10^{-9}	Pa^{-1}

Table F.17 2-domain modified Tait equation parameters

Temperature (°C)	SHC ($Jkg^{-1}{}^oC^{-1}$)	Temperature (°C)	SHC ($Jkg^{-1}{}^oC^{-1}$)
20	1,560	110	2,157
25	1,592	115	2,225
30	1,625	120	2,310
35	1,636	125	2,414
40	1,650	130	2,543
45	1,668	135	2,713
50	1,702	140	2,940
55	1,736	145	3,240
60	1,770	150	3,627
65	1,803	155	4,089
70	1,838	160	5,303
75	1,872	165	4,255
80	1,906	170	3,074
85	1,942	175	2,370
90	1,979	180	2,382
95	2,017	185	2,398
100	2,057	190	2,410
105	2,103	195	2,419

Table F.18 Specific heat capacity (SHC) vs temperature

Temperature (°C)	Thermal conductivity ($Wm^{-1}K^{-1}$)
20	0.198
40	0.205
60	0.207
80	0.204
100	0.215
120	0.216
140	0.225
160	0.313
180	0.190
200	0.200

Table F.19 Thermal conductivity vs temperature

Cross-WLF parameter	Data value	Units
n	0.23193	n/a
Tau*	55,075	Pa
D1	2.70×10^{11}	Pas
D2	263.15	K
D3	0	KPa^{-1}
A1	25.45	n/a
A2~	51.6	K
Transition temperature	142.8	°C

Table F.20 Cross WLF equation parameters

Appendix G: PCM Feedstock material properties

All of the PCM feedstocks have the same common processing properties:

Minimum processing temperature = 157°C
Maximum processing temperature = 180°C
Minimum mould temperature = 20°C
Maximum mould temperature = 40°C
Ejection temperature = 30°C

Iron 60% vol feedstock

Tait parameter	Data value	Units
B1s	0.202×10^{-3}	m^3kg^{-1}
B2s	38.0×10^{-9}	$m^3kg^{-1}K^{-1}$
B3s	0.763×10^{9}	Pa
B4s	4.57×10^{-3}	K^{-1}
B1m	0.206×10^{-3}	m^3kg^{-1}
B2m	57.2×10^{-9}	$m^3kg^{-1}K^{-1}$
B3m	0.411×10^{9}	Pa
B4m	3.56×10^{-3}	K^{-1}
B5	424.15	K
B6	110×10^{-9}	KPa^{-1}
B7	4.65×10^{-6}	m^3kg^{-1}
B8	0.13	K^{-1}
B9	17.0×10^{-9}	Pa^{-1}

Table G.1 2-domain modified Tait equation parameters

Temperature (°C)	SHC ($Jkg^{-1}°C^{-1}$)	Temperature (°C)	SHC ($Jkg^{-1}°C^{-1}$)
20	506	100	598
25	514.9	105	603.1
30	524.6	110	608.8
35	537.6	115	617.1
40	561.3	120	628.1
45	592.1	125	640.5
50	585.4	130	652.9
55	697.5	135	670.8
60	613.9	140	692.9
65	567.5	145	711.8
70	571	150	726.7
75	573.7	155	708.7
80	578.1	160	666.1
85	583.9	165	649.6
90	588.6	170	620.5
95	592.8		

Table G.2 Specific heat capacity vs temperature

Temperature (°C)	Thermal conductivity ($Wm^{-1}K^{-1}$)
20	0.498
40	0.562
60	0.464
80	0.437
100	0.442
120	0.443
140	0.418
160	0.386
180	0.367
200	0.377

Table G.3 Thermal conductivity vs temperature

Cross-WLF parameter	Data value	Units
n	0.26503	dimensionless
Tau*	53,578	Pa
D1	3.97×10^{18}	Pas
D2	263.15	K
D3	0	KPa^{-1}
A1	43.59	dimensionless
A2~	51.6	K
Transition temperature	142.3	°C

Table G.4 Cross WLF equation parameters

Constant polymer melt density = $4.780gcm^{-3}$

Stainless steel 60% vol feedstock

Constant polymer melt density = $4.883gcm^{3}$

Tait parameter	Data value	Units
B1s	0.198×10^{-3}	m^3kg^{-1}
B2s	38.2×10^{-9}	$m^3kg^{-1}K^{-1}$
B3s	0.763×10^{9}	Pa
B4s	4.58×10^{-3}	K^{-1}
B1m	0.202×10^{-3}	m^3kg^{-1}
B2m	55.3×10^{-9}	$m^3kg^{-1}K^{-1}$
B3m	0.424×10^{9}	Pa
B4m	3.24×10^{-3}	K^{-1}
B5	424.15	K
B6	110×10^{-9}	KPa^{-1}
B7	4.55×10^{-6}	m^3kg^{-1}
B8	0.13	K^{-1}
B9	17.0×10^{-9}	Pa^{-1}

Table G.5 2-domain modified Tait equation parameters

Temperature (°C)	SHC ($Jkg^{-1}°C^{-1}$)	Temperature (°C)	SHC ($Jkg^{-1}°C^{-1}$)
20	610.6	100	714.1
25	626.5	105	720.2
30	640.6	110	727.1
35	656.6	115	734.9
40	680.1	120	744.9
45	713	125	754.9
50	714.3	130	769.9
55	764.5	135	789.4
60	728.2	140	814.6
65	681.2	145	839.6
70	683.6	150	852.3
75	687.8	155	834.2
80	692.7	160	788.4
85	697.1	165	769.1
90	703.1	170	773.1
95	708.7	175	777.1

Table G.6 Specific heat capacity vs temperature

Temperature (°C)	Thermal conductivity ($Wm^{-1}K^{-1}$)
20	0.379
40	0.421
60	0.423
80	0.408
100	0.397
120	0.393
140	0.405
160	0.360
180	0.364
200	0.324

Table G.7 Thermal conductivity vs temperature

Cross-WLF parameter	Data value	Units
n	0.2664	n/a
Tau*	60,174	Pa
D1	3.58×10^{12}	Pas
D2	263.15	K
D3	0	KPa^{-1}
A1	29.31	n/a
A2~	51.6	K
Transition temperature	142.1	°C

Table G.8 Cross WLF equation parameters

Stainless steel masteralloy 60% vol feedstock

Constant polymer melt density = $4.883 gcm^3$

Tait parameter	Data value	Units
B1s	0.198×10^{-3}	m^3kg^{-1}
B2s	38.1×10^{-9}	$m^3kg^{-1}K^{-1}$
B3s	0.792×10^{9}	Pa
B4s	4.15×10^{-3}	K^{-1}
B1m	0.202×10^{-3}	m^3kg^{-1}
B2m	59.7×10^{-9}	$m^3kg^{-1}K^{-1}$
B3m	0.453×10^{9}	Pa
B4m	4.90×10^{-3}	K^{-1}
B5	423.15	K
B6	100×10^{-9}	KPa^{-1}
B7	4.79×10^{-6}	m^3kg^{-1}
B8	0.14	K^{-1}
B9	20.5×10^{-9}	Pa^{-1}

Table G.9 2-domain modified Tait equation parameters

Temperature (°C)	SHC ($Jkg^{-1}°C^{-1}$)	Temperature (°C)	SHC ($Jkg^{-1}°C^{-1}$)
20	534.2	100.0	591.2
25	544.3	105.0	595.3
30	554.1	110.0	600.0
35	568.6	115.0	607.6
40	588.7	120.0	617.0
45	615.5	125.0	627.5
50	627.9	130.0	640.3
55	647.8	135.0	658.8
60	670.6	140.0	685.0
65	573.3	145.0	708.0
70	575.1	150.0	710.6
75	579.8	155.0	683.7
80	581.2	160.0	645.8
85	581.6	165.0	628.7
90	585.2	170.0	632.3
95	588.5	175.0	635.4

Table G.10 Specific heat capacity vs temperature

Temperature (°C)	Thermal conductivity ($Wm^{-1}K^{-1}$)
20	0.373
40	0.429
60	0.489
80	0.469
100	0.448
120	0.433
140	0.449
160	0.391
180	0.375
200	0.375

Table G.11 Thermal conductivity vs temperature

Cross-WLF parameter	Data value	Units
n	0.38511	n/a
Tau*	25,759	Pa
D1	9.51×10^{13}	Pas
D2	263.15	K
D3	0	KPa^{-1}
A1	32.59	n/a
A2~	51.6	K
Transition temperature	142.3	°C

Table G.12 Cross WLF equation parameters

Iron-alumina cermet 60% vol feedstock

Constant polymer melt density = $4.4381 gcm^3$

Tait parameter	Data value	Units
B1s	0.217×10^{-3}	m^3kg^{-1}
B2s	40.6×10^{-9}	$m^3kg^{-1}K^{-1}$
B3s	0.761×10^{9}	Pa
B4s	4.57×10^{-3}	K^{-1}
B1m	0.222×10^{-3}	m^3kg^{-1}
B2m	60.6×10^{-9}	$m^3kg^{-1}K^{-1}$
B3m	0.407×10^{9}	Pa
B4m	3.32×10^{-3}	K^{-1}
B5	424.15	K
B6	92.5×10^{-9}	KPa^{-1}
B7	5.02×10^{-6}	m^3kg^{-1}
B8	0.13	K^{-1}
B9	17.0×10^{-9}	Pa^{-1}

Table G.13 2-domain modified Tait equation parameters

Temperature (°C)	SHC ($Jkg^{-1}°C^{-1}$)	Temperature (°C)	SHC ($Jkg^{-1}°C^{-1}$)
20	589.5	100	691.6
25	599.8	105	695.5
30	609.4	110	700.7
35	621.2	115	707.7
40	642.1	120	716.4
45	699.9	125	726.7
50	665.2	130	741.6
55	783.5	135	762.9
60	748.7	140	789.4
65	652.6	145	814.6
70	655.7	150	819.4
75	663.0	155.0	790.0
80	669.6	160	738.9
85	675.5	165	718.3
90	682.8	170	721.1
95	687.6		

Table G.14 Specific heat capacity vs temperature

Temperature (°C)	Thermal conductivity ($Wm^{-1}K^{-1}$)
20	0.441
40	0.456
60	0.422
80	0.385
100	0.386
120	0.388
140	0.399
160	0.366
180	0.358
200	0.337

Table G.15 Thermal conductivity vs temperature

Cross-WLF parameter	Data value	Units
n	0.22470	n/a
Tau*	68,813	Pa
D1	1.26×10^{13}	Pas
D2	263.15	K
D3	0	KPa^{-1}
A1	29.46	n/a
A2~	51.6	K
Transition temperature	142.2	°C

Table G.16 Cross WLF equation parameters

Alumina 50% vol feedstock

Constant polymer melt density = $2.1937 gcm^3$

Tait parameter	Data value	Units
B1s	0.437×10^{-3}	m^3kg^{-1}
B2s	94.8×10^{-9}	$m^3kg^{-1}K^{-1}$
B3s	0.606×10^{9}	Pa
B4s	4.61×10^{-3}	K^{-1}
B1m	0.449×10^{-3}	m^3kg^{-1}
B2m	142.0×10^{-9}	$m^3kg^{-1}K^{-1}$
B3m	0.334×10^{9}	Pa
B4m	3.37×10^{-3}	K^{-1}
B5	424.15	K
B6	110×10^{-9}	KPa^{-1}
B7	12.5×10^{-6}	m^3kg^{-1}
B8	0.13	K^{-1}
B9	17.0×10^{-9}	Pa^{-1}

Table G.17 2-domain modified Tait equation parameters

Temperature (°C)	SHC ($Jkg^{-1}°C^{-1}$)	Temperature (°C)	SHC ($Jkg^{-1}°C^{-1}$)
20	894.8	100	1,118
25	917.8	105	1,131
30	948.9	110	1,148
35	992.6	115	1,167
40	1,052	120	1,189
45	1,122	125	1,216
50	1,108	130	1,253
55	1,242	135	1,310
60	1,295	140	1,390
65	1,075	145	1,455
70	1,060	150	1,462
75	1,062	155	1,402
80	1,067	160	1,283
85	1,079	165	1,220
90	1,092	170	1,227
95	1,105	175	1,235

Table G.18 Specific heat capacity vs temperature

Temperature (°C)	Thermal conductivity ($Wm^{-1}K^{-1}$)
20	0.274
40	0.310
60	0.271
80	0.269
100	0.271
120	0.289
140	0.339
160	0.340
180	0.336
200	0.329

Table G.19 Thermal conductivity vs temperature

Cross-WLF parameter	Data Value	Units
n	0.41648	n/a
Tau*	3,824.5	Pa
D1	1.22×10^{15}	Pas
D2	263.15	K
D3	0	KPa^{-1}
A1	34.76	n/a
A2~	51.6	K
Transition temperature	142.3	°C

Table G.20 Cross WLF equation parameters

Alumina 55% vol feedstock

Constant polymer density = 2.3443gcm^3

Tait parameter	Data value	Units
B1s	0.410×10^{-3}	m^3kg^{-1}
B2s	81.2×10^{-9}	$m^3kg^{-1}K^{-1}$
B3s	0.674×10^{9}	Pa
B4s	4.60×10^{-3}	K^{-1}
B1m	0.420×10^{-3}	m^3kg^{-1}
B2m	121.0×10^{-9}	$m^3kg^{-1}K^{-1}$
B3m	0.374×10^{9}	Pa
B4m	3.35×10^{-3}	K^{-1}
B5	424.15	K
B6	110×10^{-9}	KPa^{-1}
B7	10.6×10^{-6}	m^3kg^{-1}
B8	0.13	K^{-1}
B9	17.0×10^{-9}	Pa^{-1}

Table G.21 2-domain modified Tait equation parameters

Temperature (°C)	SHC ($Jkg^{-1}°C^{-1}$)	Temperature (°C)	SHC ($Jkg^{-1}°C^{-1}$)
20	947.1	100	1,089
25	954.8	105	1,102
30	959.7	110	1,116
35	990.5	115	1,134
40	1,031	120	1,154
45	1,071	125	1,177
50	1,093	130	1,209
55	1,207	135	1,252
60	1,249	140	1,310
65	1,042	145	1,378
70	1,030	150	1,388
75	1,039	155	1,329
80	1,048	160	1,245
85	1,057	165	1,194
90	1,068	170	1,201
95	1,078	175	1,208

Table G.22 Specific heat capacity vs temperature

Temperature (°C)	Thermal conductivity ($Wm^{-1}K^{-1}$)
20	0.306
40	0.325
60	0.301
80	0.291
100	0.296
120	0.298
140	0.325
160	0.307
180	0.321
200	0.323

Table G.23 Thermal conductivity vs temperature

Cross-WLF parameter	Data value	Units
n	0.40849	n/a
Tau*	1,009.6	Pa
D1	1.92×10^{18}	Pas
D2	263.15	K
D3	0	KPa^{-1}
A1	40.39	n/a
A2~	51.6	K
Transition temperature	142.3	°C

Table G.24 Cross WLF equation parameters

Zirconia toughened alumina 55% feedstock

Constant polymer melt density = $2.5384 gcm^3$

Tait parameter	Data value	Units
B1s	0.379×10^{-3}	m^3kg^{-1}
B2s	73.7×10^{-9}	$m^3kg^{-1}K^{-1}$
B3s	0.687×10^{9}	Pa
B4s	4.59×10^{-3}	K^{-1}
B1m	0.388×10^{-3}	m^3kg^{-1}
B2m	110.0×10^{-9}	$m^3kg^{-1}K^{-1}$
B3m	0.382×10^{9}	Pa
B4m	3.32×10^{-3}	K^{-1}
B5	424.65	K
B6	105×10^{-9}	KPa^{-1}
B7	10.3×10^{-6}	m^3kg^{-1}
B8	0.13	K^{-1}
B9	17.0×10^{-9}	Pa^{-1}

Table G.25 2-domain modified Tait equation parameters

Temperature (°C)	SHC ($Jkg^{-1}°C^{-1}$)	Temperature (°C)	SHC ($Jkg^{-1}°C^{-1}$)
20	859.3	100	1,056
25	881.5	105	1,068
30	903.7	110	1,084
35	946.2	115	1,101
40	994.1	120	1,116
45	1,070	125	1,144
50	1,097	130	1,179
55	1,206	135	1,230
60	1,220	140	1,304
65	1,023	145	1,359
70	1,014	150	1,355
75	1,009	155	1,290
80	1,013	160	1,188
85	1,023	165	1,142
90	1,034	170	1,149
95	1,046	175	1,158

Table G.26 Specific heat capacity vs temperature

Temperature (°C)	Thermal conductivity ($Wm^{-1}K^{-1}$)
20	0.254
40	0.312
60	0.289
80	0.278
100	0.275
120	0.280
140	0.325
160	0.301
180	0.261
200	0.264

Table G.27 Thermal conductivity vs temperature

Cross-WLF parameter	Data value	Units
n	0.46529	n/a
Tau*	2,031.6	Pa
D1	2.67×10^{19}	Pas
D2	263.15	K
D3	0	KPa^{-1}
A1	47.01	n/a
A2~	51.6	K
Transition temperature	142.8	°C

Table G.28 Cross WLF equation parameters

Appendix H: Derivation of the specific heat capacity rule of mixtures

Equations were derived to allow the calculation of the specific heat capacity of a mixture of any number of substances with known individual specific heat capacities and known mass ratios.

Considering a multi-component system as a whole,

$$Q_{system} = m_{system} c_{system} (T_2 - T_1) \qquad \text{Eqn (H.1)}$$

Considering each nth component in the n component system,

$$Q_n = m_n c_n (T_2 - T_1) \qquad \text{Eqn (H.2)}$$

Considering the total energy to be the sum of the individual energies:

$$Q_{system} = Q_1 + Q_2 + ... + Q_{n-1} + Q_n \qquad \text{Eqn (H.3)}$$

The feedstock MDSC sample (nominally 10mg) was assumed to be a true representation of the bulk feedstock, and that each component was inert in the presence of the other components, and that the temperature variations throughout the feedstock could be considered to be negligible, thus substituting equations H.1 and H.2 into equation H.3 yields:

$$m_{system} c_{system} (T_2 - T_1) = (T_2 - T_1)(m_1 c_1 + m_2 c_2 + ... + ... + m_{n-1} c_{n-1} + m_n c_n) \qquad \text{Eqn (H.4)}$$

Equation H.4 simplifies to:

$$c_{system} = \frac{m_1 c_1 + m_2 c_2 + ... + m_{n-1} c_{n-1} + m_n c_n}{m_{system}} \qquad \text{Eqn (H.5)}$$

Where Q = energy (J)
c = specific heat capacity ($Jkg^{-1}{}^{o}C^{-1}$)
m = mass (kg)
(T_2-T_1) = temperature difference (°C)

Appendix I: Derivation of the specific volume rule of mixtures

Equations were derived to allow the calculation of the specific volume of a mixture of any number of substances with known specific volumes as a function of temperature and pressure and known mass or volume. Recall that specific volume is the reciprocal of density, which leads to equation I.1:

$$v = s_v m \qquad \text{Eqn (I.1)}$$

Where v = volume (m^3)
M = mass (kg)
S_v = specific volume (m^3kg^{-1})

Considering a multiple component system as a whole, the composite volume can be calculated from its composite mass and its composite specific volume, as shown:

$$v_{system} = m_{system} s_{v_{system}} \qquad \text{Eqn (I.2)}$$

Considering each nth component in the n component composite system, then the volume of the nth component is:

$$v_n = m_n s_{v_n} \qquad \text{Eqn (I.3)}$$

It follows that the total mass of the composite system is the sum of the masses of the individual components,

$$m_{system} = m_1 + m_2 + ... + m_{n-1} + m_n \qquad \text{Eqn (I.4)}$$

It also follows that the total volume of the composite system is the sum of the volumes of the individual components:

$$v_{system} = v_1 + v_2 + ... + v_{n-1} + v_n \qquad \text{Eqn (I.5)}$$

Where the masses are known for all of the components in the composite, substituting equations I.2 and I.3 into equation I.5 yields:

$$m_{system} s_{v_{system}} = m_1 s_{v_1} + m_2 s_{v_2} + ... + m_{n-1} s_{v_{n-1}} + m_n s_{v_n} \qquad \text{Eqn (I.6)}$$

Where the volumes are known for n components in a mixture, substituting equations I.2 and I.3 into equation I.4 yields:

$$\frac{v_{system}}{s_{v_{system}}} = \frac{v_1}{s_{v_1}} + \frac{v_2}{s_{v_2}} + ... + \frac{v_{n-1}}{s_{v_{n-1}}} + \frac{v_n}{s_{v_n}} \qquad \text{Eqn (I.7)}$$

It is more convenient to use equation I.6 for the calculation of the specific volume of a system, as the mass ratios of the components do not vary with temperature or pressure, unless degradation occurs.

If equation I.7 is used instead, corrections must be made for the different thermal expansivities and compressibilities of each component used, to allow for the variation of volumetric ratios of the components with temperature and pressure.

The specific volume of an injection mouldable material varies with both temperature and pressure. It is necessary to state that when using equation I.6 or I.7, the specific volumes of all of the components used must relate to the same temperature and pressure.

Equations I.6 or I.7 can be used to calculate the specific volume of the binder system as a function of the polymers and waxes. They can also be used in calculating the specific volume of the powder system as a function of two or more powders, such as the iron-alumina cermet powder system.

In the case of the powder system, zero compressibility may be safely assumed and the respective thermal expansivities may be used to calculate their specific volume as a function of temperature, because PVT data is not generally available for ceramics or metals, as it is for the vast majority of polymers.

Further manipulation of equations I.6 and I.7 leads to a useful relationship between the powder/binder volume fraction and the powder/binder mass fraction of a feedstock. This allows the calculation of the powder/binder volume fraction as a function of temperature and pressure as the specific volume changes as a function of temperature and pressure since the mass fraction remains constant. This allows the calculation of volume fraction as a function of temperature and pressure for use in other equations that are dependent on the volume fractions of the feedstock components.

$$\frac{1}{S_{vp}M_{pf}+S_{vb}M_{bf}} = \left(\frac{V_{pf}}{S_{vp}} + \frac{V_{bf}}{S_{vb}}\right) = \frac{1}{S_{v_{feedstock}}} \qquad \text{Eqn (I.8)}$$

Where
M_{pf} = mass fraction of the powder,
M_{bf} = mass fraction of the binder,
V_{pf} = volume fraction of the powder,
V_{bf} = volume fraction of the binder,
S_{v_p} = specific volume of the powder system,
S_{v_b} = specific volume of the binder system,
$S_{v_{system}}$ = specific volume of the system

The number of variables in the equation can be reduced from 6 to 4 by the appropriate substitution of the following relations:

$$M_{pf} + M_{bf} = 1 \qquad \text{Eqn (I.9)}$$

$$V_{pf} + V_{bf} = 1 \qquad \text{Eqn (I.10)}$$

Equations I.8, I.9 and I.10 are used in the chapter on thermal conductivity, to show the effect of temperature and pressure on the powder volume loading.

Appendix J: Calculation of the specific volume from the open literature density and expansivity data

Generally, materials expand with increasing temperature, leading to an increase in specific volume.

The amount of linear expansion is determined by the material's linear thermal expansion coefficient, a, ($^oC^{-1}$). The linear thermal expansion coefficient is defined as the increase per unit length per unit rise in temperature as shown by equation J.1

$$a = \frac{\Delta L}{L_0 . \Delta T} \qquad \text{Eqn (J.1)}$$

Where
ΔL = increase in length (m)
L_0 = original Length (m)
ΔT = change in temperature
a = linear thermal expansion coefficient

The amount of volumetric expansion is determined by the material's cubic thermal expansion coefficient, γ, ($^oC^{-1}$). The cubic thermal expansion coefficient is defined as the increase in volume per unit volume per unit rise in temperature, as shown by equation J.2.

$$\gamma = \frac{\Delta V}{V_0 . \Delta T} \qquad \text{Eqn (J.2)}$$

Where
ΔV = increase in volume (m^3)
V_0 = original Length (m)
ΔT = change in temperature
γ = cubic thermal expansion coefficient

And the relationship between linear and cubic thermal expansion coefficient is:

$$\gamma = 3a \qquad \text{(assuming isotropicity)} \qquad \text{Eqn (J.3)}$$

An equation was derived to allow the calculation of specific volume as a function of temperature and cubic thermal expansion coefficient.

Rearranging equation J.2 yields:

$$\Delta V = V_0 \gamma \Delta T \qquad \text{Eqn (J.4)}$$

Equation J4 gives the change in volume as a result of a temperature change, so the final volume will be the sum of the initial volume and the volume change, and hence the initial volume must be added to both sides of equation J.4.

$$V_0 + \Delta V = V_0 + V_0 \gamma \Delta T \qquad \text{Eqn (J.5)}$$

Simplifying equation J5 yields:

$$V_0 + \Delta V = V_0(1 + \gamma \Delta T) \qquad \text{Eqn (J.6)}$$

The volume terms can safely be substituted for specific volume terms and the final specific volume can be calculated from the initial specific volume, cubic thermal expansion coefficient and the temperature difference.

$$Sv_f = Sv_0(1 + \gamma \Delta T) \qquad \text{Eqn (J.7)}$$

Where Sv_f = final specific volume ($m^{-3}kg^{-1}$)
Sv_0 = original specific volume ($m^{-3}kg^{-1}$)
γ = cubic thermal expansion coefficient ($^0C^{-1}$)
ΔT = temperature difference (^0C)

Equation J.7 permits the determination of specific volume for a range of temperatures from the open literature density and expansivity data for any powder.

Appendix K: C-Mold modelling and injection moulding process parameters

Part A: Injection moulding process conditions

	Polymers	PCM	Units
Clamp force	300	300	kN
Clamp open stroke	130	120	mm
Start mould protect	54	70	mm
Mould protect pressure	1.0	3.0	MPa
Cooling time	15	10	s
Clamp open time	1.5	1.5	s
Clamp time limit	-	-	s

Table K.1 Dassett DM30 clamp settings

	Polymers	PCM	Units
Ejector forward time	2	2	s
Ejector forward speed	100	100	%
Ejector reverse speed	100	100	%
Ejector pressure	2.5	2.5	MPa
Ejector number of cycles	1	1	
Ejector dwell time	1	1	s
Ejector reverse time	1	1	s

Table K.2 Dassett DM30 ejector settings

	Polymers	PCM	Units
Shot size	20	20	mm
Injection high time	1	1	s
Injection high pressure	21.0	20.0	MPa
End 1st injection			mm
Transfer position	14	10	mm
Transfer pressure	20.0	15.0	MPa
Injection low time	15	55	s
Screw speed	200	220	rpm
Screw decompression	25	48	mm

Table K.3 Dassett DM30 injection barrel A (skin) settings

	Polymers	PCM	Units
Shot size	63	63	mm
Injection high time	5	10	s
Injection high pressure	15	20	MPa
Transfer position	4	10	mm
Transfer pressure	15	15	MPa
Injection low time	10	15	s
Screw speed	200	220	rpm
Screw decompression	28	48	mm

Table K.4 Dassett DM30 injection barrel B (core) settings.

The actual injection filling time is determined by the injection screw speed. Injection high time is a setting on the Dassett DM30 to sound an alarm if material injection does not start and complete within the injection high time setting.

	Polymers	PCM	Units
Front zone A (skin)	200	165	°C
Middle zone A (skin)	190	145	°C
Rear zone A (skin)	175	125	°C
Front zone B (core)	200	165	°C
Middle zone B (core)	190	145	°C
Rear zone B (core)	175	125	°C
Nozzle zone	200	165	°C

Table K.5 Dassett DM30 heating settings

	Polymers	PCM	Units
Injection low 1	1.0	2.0	MPa
Injection low 2	1.0	2.0	MPa
Injection low 3	1.0	2.0	MPa
Injection low 4	1.0	2.0	MPa
Injection low 5	1.0	2.0	MPa

Table K.6 Dassett DM30 injection pressure profile for barrel A (skin)

	Polymers	PCM	Units
Injection speed 1	40	65	%
Injection speed 2	40	65	%
Injection speed 3	40	65	%
Injection speed 4	40	65	%
Injection speed 5	40	65	%

Table K.7 Dassett DM30 injection speed profile for barrel A (skin)

	Polymers	PCM	Units
Injection low 1	1.0	2.0	MPa
Injection low 2	1.0	2.0	MPa
Injection low 3	1.0	2.0	MPa
Injection low 4	1.0	2.0	MPa
Injection low 5	1.0	2.0	MPa

Table K.8 Dassett DM30 injection pressure profile for barrel B (core)

	Polymers	PCM	Units
Injection speed 1	40	65	%
Injection speed 2	40	65	%
Injection speed 3	40	65	%
Injection speed 4	40	65	%
Injection speed 5	40	65	%

Table K.9 Dassett DM30 injection speed profile for barrel B (core)

	Polymers	PCM	Units
Injection unit speed	50	50	%
sprue break duration	1.5	1.5	s
sprue break delay	1.5	1.5	s

Table K.10 Dassett DM30 injection unit settings

Screw diameter = 25 mm Screw length - diameter = 20:1
Screw stroke = 83 mm Screw speed = 0-300 rpm
Maximum injection pressure = 21.0 MPa

Part B: C-Mold modelling process conditions

Maximum machine clamp force = 26.8 tonnes (metric)
Maximum machine injection volume = 40 cm^3
Maximum machine injection pressure = 138 MPa
Maximum machine injection rate = 28 cm^3s^{-1}

	Polymers	PCM	Units
Fill time	1	1	s
Timer for core injection	0.37	0.37	s
Fill - Pack switch over by volume	99	99	%

Table K.11 C-Mold mould cavity filling settings

	Polymer	PCM	Units
First inlet melt temperature (skin)	200	165	°C
Second inlet melt temperature (core)	200	165	°C

Table K.12 C-Mold inlet melt temperatures

	Polymers	PCM	Units
% stroke	0	0	%
% speed	40	65	%
% stroke	10	10	%
% speed	40	65	%
% stroke	20	20	%
% speed	40	65	%
% stroke	30	30	%
% speed	40	65	%
% stroke	40	40	%
% speed	40	65	%
% stroke	50	50	%
% speed	40	65	%
% stroke	60	60	%
% speed	40	65	%
% stroke	70	70	%
% speed	40	65	%
% stroke	80	80	%
% speed	40	65	%
% stroke	90	90	%
% speed	40	65	%
% stroke	100	100	%
% speed	40	65	%

Table K.13 C-Mold relative ram speed profile settings

	Polymer	PCM	Units
ID	1	1	
Temperature	20	20	°C
Total flow rate	10	10	litre min^{-1}
Total pressure drop	0	0	MPa
Coolant material	1	1	
ID	2	2	
Temperature	20	20	°C
Total flow rate	10	10	litre min^{-1}
Total pressure drop	0	0	MPa
Coolant material	1	1	

Table K.14 C-Mold coolant manifold control

	Polymer	PCM	Units
ID	1	1	
Temperature	n/a	n/a	°C
Insulation thickness	n/a	n/a	mm
ID	2	2	
Temperature	n/a	n/a	°C
Insulation thickness	n/a	n/a	mm

Table K.15 Hot runner manifold control (set to OFF as no hot runners were used)